LECTRON TRANSPORT IN FERROCENES LINKED BY MOLECULAR WIRES

A Thesis
Presented to
The Academic Faculty

by

Yu Li

In Partial Fulfillment
of the Requirements for the Degree
Doctor of Philosophy in the
School of Chemistry & Biochemistry

Georgia Institute of Technology
August 2007

ELECTRON TRANSPORT IN FERROCENES LINKED BY MOLECULAR WIRES

Approved by:

Dr. Laren M. Tolbert, Advisor
School of Chemistry & Biochemistry
Georgia Institute of Technology

Dr. Lawrence A. Bottomley
School of Chemistry & Biochemistry
Georgia Institute of Technology

Dr. Christoph J. Fahrni
School of Chemistry & Biochemistry
Georgia Institute of Technology

Dr. Mira Josowicz
School of Chemistry & Biochemistry
Georgia Institute of Technology

Dr. Mohan Srinivasarao
School of Polymer, Textile and Fiber Engineering
Georgia Institute of Technology

Date Approved: June 29, 2007

To My Parents and Dr. Laren M. Tolbert

ACKNOWLEDGEMENTS

There are many people to whom I am indebted for the completion of my study and this dissertation. First of all, I wish to express my deepest gratefulness to my research advisor, Dr. Laren M. Tolbert, for his support throughout my graduate career. Without him, I would never reach this point! Dr. Tolbert is also worth special thanks for providing a research environment which promotes independent thoughts and creativity.

A special thanks also goes out to Dr. Janusz Kowalik for his continuing encouragement and support during my graduate study. I really learned a lot from you in the numerous discussions about science and life.

I wish to thank Dr. Kenneth Hardcastle, Dr. Xikui Fang and Mr. Rui Cao at X-ray Crystallography Center of Emory University for performing the crystal structure analysis in this work.

I wish to thank my committee for taking time to review my work, to offer suggestions and to serve at my defense.

I wish to thank Dr. Mira Josowicz, Mr. Ryan Cantor and Dr. Hang Chen for helping me set up the electrochemical equipment. Dr. Mira Josowicz was always there whenever I need help and advice.

I wish to thank Dr. Veaceslav Coropceanu and Dr. Steve Barlow for their valuable inputs in understanding the mixed-valence compounds. Dr. Coropceanu has also conducted theoretical calculations for a number of model compounds in this work. Although these results are not included in this thesis due to the scope limitation, they will be covered elsewhere.

I wish to thank Dr. Jan Zukrowski at AGH University of Science and Technology (Krakow, Poland) for performing the Mossbauer experiments. His prompt response and sunshine emails made everything a joy.

I wish to thank my fellow lab mates past and present, Dr. Lorreta Crowe, Dr. Kyril Soltnsev, Jian Dong, Nguyen Vu, Dr. Jonas Jarvholm, Juan Vargas, Michael Salvitti , Christina Bauer, Robert Whetsell, and Dr. Luke Roberson for their help and friendship, which made the life in graduate school enjoyable.

Finally, I wish to thank my family. Their love is always endless and unconditional. They are in deep my heart no matter when and no matter where I am and they are. The same thanks also go out to my beloved friends. Yes, I know, you are looking at me!

TABLE OF CONTENTS

		Page
ACKNOWLEDGEMENTS		iv
LIST OF TABLES		viii
LIST OF FIGURES		ix
LIST OF SYMBOLS AND ABBREVIATIONS		xvii
SUMMARY		xix
CHAPTER		
1	Introduction	1
	Molecular Electronics and Wires	1
	Mixed-Valence Complexes and Electron Transfer Theory	5
	Solitonic Polymethine	11
	Experimental Approach and Objectives	13
	References	20
2	Electron Transport in Diferrocenyl Complexes Linked by –CH=CH-X-CH=CH- Spacers	23
	Introduction	23
	Experimental	26
	Results and Discussion	51
	Conclusion	114
	References	116
3	Greatly Enhanced Electronic Interaction in Diferrocenyl Complexes Linked by Pyrrole-Mediated Spacers: A Metal Ligand Redox-Matching Approach	120
	Introduction	120
	Experimental	123

Results and Discussion 132

Conclusion 176

References 178

4 Triferrocenes Bridged by Symmetric and Asymmetric Spacers: Synthesis, Structure, Electrochemistry and Mixed-Valence Studies 181

Introduction 181

Experimental 185

Results and Discussion 200

Conclusion 245

References 246

5 Doubly Bridged Binuclear Ferrocenophanes and Vinylene-Arylene-Vinylene Bridged Trinuclear Ferrocenophanes: Synthesis, Structure, Electrochemistry and Mixed-Valence Studies. 249

Introduction 249

Experimental 251

Results and Discussion 259

Conclusion 302

References 304

6 Bis(styrylpyrrole)s Linked by –CH=CH-X-CH=CH- Spacers: A Charge Mobility Study on Conjugated Organic Oligomers 306

Introduction 306

Experimental 309

Results and Discussion 319

Conclusion 351

References 353

APPENDIX: Additional Synthetic Procedures and Results 356

LIST OF TABLES

Page

Table 2.1: Selected steric parameters for bis(2-ferrocenylvinyl) compounds 65

Table 2.2: Electrochemical data (from Cyclic Voltammetry) for the compounds **FcCH=CHXCH=CHFc** 82

Table 2.3: LMCT band parameters, obtained from the spectral deconvolution of the mixed-valence species of Group A compounds 107

Table 2.4: IVCT and LMCT band parameters, obtained from the spectral deconvolution, and calculated Hush parameters for the mixed-valence species of Group B[a] compounds 112

Table 3.1: Electrochemical data (from Cyclic Voltammetry) for the compounds 149

Table 3.2: IVCT and LMCT band parameters, obtained from the spectral deconvolution, and calculated Hush parameters for the relevant radical cations 174

Table 4.1: Electrochemical data (from Cyclic Voltammetry) for the compounds 224

Table 4.2: IVCT and LMCT band parameters, obtained from the spectral deconvolution, and calculated Hush parameters for the relevant cationic species 237

Table 5.1: Electrochemical data (from Cyclic Voltammetry) for the compounds 282

Table 5.2: IVCT and LMCT band parameters, obtained from the spectral deconvolution, and calculated Hush parameters for the selected cationic species 297

Table 6.1: UV-Vis absorption and fluorescence parameters for the oligomers 327

Table 6.2: Electrochemical data (from Cyclic Voltammetry) for the oligomers 335

Table 6.3: Band shape data of the lowest energy band of the cationic species in CH_2Cl_2 344

Table 6.4: Optical transition energies of the oligomers 346

Table A.1: Electrochemical data (from Cyclic Voltammetry) for the compounds 365

LIST OF FIGURES

Page

Figure 1.1: Schematic representation of a molecular wire being addressed with an STM tips, reproduced from ref. 10 3

Figure 1.2: Schematic illustration of a molecular wire incorporated into a mixed valence systems 4

Figure 1.3: The Creutz-Taube ion 6

Figure 1.4: Optical and thermal ET processes in a symmetric mixed-valence complex 7

Figure 1.5: Potential energy surface for symmetrical mixed-valence complexes with negligible (A), weak (B) and strong (C) electronic coupling 8

Figure 1.6: Compounds used in previous studies 12

Figure 1.7: Schematic illustration of superexchange mechanism: electron-transfer type and hole-transfer type 14

Figure 1.8: Proposed model compounds in this work 17

Figure 2.1: Synthetic pathway of **FcCH=CHXCH=CHFc** compounds using conventional Wittig methodology 52

Figure 2.2: Synthetic pathway of **FcCH=CHXCH=CHFc** compounds through Horner-Wadsworth-Emmons reactions 53

Figure 2.3: Synthesis of **BFcVTh** and **BFcVEDOT** 55

Figure 2.4: Synthesis of **BFcVFu** and **BFcVPyr** 57

Figure 2.5: Synthesis of **BFcVPPh**, **BFcVP(S)Ph** and **BFcVP(O)Ph** 59

Figure 2.6: Synthesis of **BFcVC≡C**, **BFcVCH$^+$** and **BFcVC(O)** 61

Figure 2.8: ORTEP plot of **BFcVTh** 66

Figure 2.9: ORTEP plot of **BFcVFu**. 66

Figure 2.10: ORTEP plot (A) and packing form (B) of **BFcVPyr** 67

Figure 2.11: ORTEP plots of **(*Z*,*Z*)-BFcV*p*Ph** (A) and **(*E*,*E*)-BFcV*p*Ph** (B) 70

Figure 2.12: ORTEP plot (A) and unit cell packing form (B) of **BFcV*p*Ph(OC$_{12}$H$_{25}$)$_2$** 71

Figure 2.13: ORTEP plots of **(*E,E*)-BFcV*o*Ph** (A) and **(*E,Z*)-BFcV*o*Ph** (B) 73

Figure 2.14: ORTEP plot of **BFcVS** 74

Figure 2.15: ORTEP plot of **BFcVP(S)Ph** 74

Figure 2.16: Cyclic voltammograms of **BFcVS** in a CH_2Cl_2 solution with Bu_4NPF_6 (top, blue) and Bu_4NTFPB (bottom, green) as supporting electrolyte 77

Figure 2.17: Cyclic voltammograms of **BFcVPPh** in a CH_2Cl_2 solution with Bu_4NPF_6 (top, blue) and Bu_4NTFPB (bottom, green) as supporting electrolyte 77

Figure 2.18: Electrochemical isomerization of **BFcVS** 80

Figure 2.19: Cyclic voltammograms of **(*E,Z*)-BFcV*o*Ph** and **(*E,E*)-BFcV*o*Ph** in a CH_2Cl_2 solution containing 0.1 M Bu_4NTFPB 81

Figure 2.20: Schematic representation of the HOMO metal-d and ligand orbitals of ferrocene and energy perturbation from an electron-donating or withdrawing substituent 83

Figure 2.21: Cyclic voltammograms of **Fc(CH=CH)$_2$Fc**, **Fc(CH=CH)$_3$Fc** and **BFcVCH$^+$** in a CH_2Cl_2 solution containing 0.1 M Bu_4NTFPB 85

Figure 2.22: Cyclic voltammograms of **BFcVC≡C**, **BFcVC(O)** and **BFcVCH$_2$** in a CH_2Cl_2 solution containing 0.1 M Bu_4NTFPB 86

Figure 2.23: Cyclic voltammograms of **BFcVO**, **BFcVSe** and **BFcVCH=CHSCH=CH** in a CH_2Cl_2 solution containing 0.1 M Bu_4NTFPB 88

Figure 2.24A: Speculated electrochemical transformation of **BFcVPPh** to **BFcVP(O)Ph** 89

Figure 2.24B: Cyclic voltammograms of **BFcVP(S)Ph** and **BFcVP(O)Ph** in a CH_2Cl_2 solution containing 0.1 M Bu_4NTFPB 90

Figure 2.25A: Mechanism of charge injection and propagation in heteroatom centered bis(2-ferrocenylvinyl) complexes 91

Figure 2.25B: Proposed synthetic route for bis(2-ferrocenylvinyl)amine 92

Figure 2.26A: Cyclic and square wave voltammograms of **BFcV*p*Ph**, **BFcV*p*Ph(OR)$_2$** and **BFcV*m*Ph** in a CH_2Cl_2 solution containing 0.1 M Bu_4NTFPB 94

Figure 2.26B: Cyclic voltammograms of **BFcVFu**, **BFcVTh**, **BFcVEDOT** and **BFcVPyr** in a CH_2Cl_2 solution containing 0.1 M Bu_4NTFPB 95

Figure 2.27: Electrochemistry of aryl bridged biferrocenyl compounds 97

Figure 2.28: Mixed-valence spectra and spectral deconvolution of **BFcVEDOT** 100

Figure 2.29: Schematic illustration of the IVCT and IC transitions in a mixed-valence dinuclear complex, $[M^{II}M^{III}]$ 102

Figure 2.30: Spectrum evolution of mixed-valence species of **BFcVP(O)Ph** (A) and **BFcVP(S)Ph** (B) 104

Figure 2.31: Mixed-valence spectra of the monocationic species of **BFcVSe** (A), **BFcVCH=CHSCH=CH** (B), **BFcV*o*Ph** (C), **BFcV*m*Ph** (D) and **BFcVSC$_2$H$_4$** (E) 105

Figure 2.32: Mixed-valence spectra (A) and spectral deconvolution (B) of **BFcVS** 106

Figure 2.33: Spectra of mixed-valence species **Fc(CH=CH)$_2$Fc$^+$** (A & B) and **Fc(CH=CH)$_2$Fc$^+$** (C & D) with deconvoluted bands 109

Figure 2.34: A: Mixed-valence spectra of aryl bridged compounds: **BFcV*o*Ph** (black), **BFcV*m*Ph** (red), **BFcV*p*Ph** (purple), **BFcV*p*Ph(OR)$_2$** (blue), **BFcVTh** (green) and **BFcVFu** (orange). B: Deconvoluted spectrum of **BFcV*p*Ph** 110

Figure 2.35: Mixed-valence spectrum of **[BFcVPyr]$^+$** (A) and band deconvolution (B) in the NIR 111

Figure 3.1: Schematic representation of the hole transfer and electron transfer superexchange mechanisms 121

Figure 3.2: Synthetic route of diphosphonate **1** 132

Figure 3.3: Synthetic route of pyrrolealdehyde **4** 134

Figure 3.4: Synthetic route of butane-diketones **5** and **6** 135

Figure 3.5: Synthetic pathways for compounds **7**, **8**, **9c**, **10** starting from diphosphonate **1** 136

Figure 3.6: Synthetic pathway for compound **9a-b** starting from diketon **6** 137

Figure 3.7: Synthetic pathway of compounds **11a-b**, **12** starting from diketone **5** 138

Figure 3.8: Synthetic pathway for compounds **13**, **14** and **15** starting from **4** 139

Figure 3.9: ORTEP plot of compound **3** 141

Figure 3.10: ORTEP plot of compound **4** 142

Figure 3.11: ORTEP plots of compounds **9b** (A) and **9c** (B) 142

Figure 3.12: ORTEP plot of compound **10** 144

Figure 3.13: ORTEP plots of compounds **11a** (top) and **11b** (bottom) 145

Figure 3.14: Packing diagram of compound **11a**, viewed from slightly tilted z axis 146

Figure 3.15: ORTEP plot of compound **13** 147

Figure 3.16: Cyclic voltammograms of diferrocenyl compounds **11a**, **9b**, **9c** and **10** in CH_2Cl_2 containing 0.1 M Bu_4NTFPB 150

Figure 3.17: Cyclic voltammograms of compounds **11b**, **12** and **13** in CH_2Cl_2 containing 0.1 M Bu_4NTFPB 151

Figure 3.18: Cyclic voltammograms of diferrocenyl compounds **14** and **15** in CH_2Cl_2 containing 0.1 M Bu_4NTFPB 152

Figure 3.19: Plotted peak separation (ΔE_1s) comparisons of some key compounds using $Bu_4NPTFPB$ and Bu_4NPF_6 as the supporting electrolytes 157

Figure 3.20: Cyclic voltammograms of diferrocenyl compound **9c** in a CH_2Cl_2 solution containing 0.1 M Bu_4NPF_6 157

Figure 3.21: Evolution of the UV-Vis-NIR spectra of compounds **7** (A) and **9c** (B) in CH_2Cl_2 with progressive addition of trifluoroacetic acid (TFA) 159

Figure 3.22: Evolution of the UV-Vis spectra of compounds **11a** (A) and **14** (B) in CH_2Cl_2 with progressive addition of trifluoroacetic acid (TFA) 160

Figure 3.23: UV-Vis-NIR spectra of mixed-valence species $\mathbf{9c}^{+\bullet}$ in CH_2Cl_2 163

Figure 3.24: UV-Vis-NIR spectra of one-electron oxidized species of **13** in CH_2Cl_2 164

Figure 3.25: UV-Vis-NIR spectra of mixed-valence species of 2,5-diferrocenylpyrrole $\mathbf{11a}^{+\bullet}$ in CH_2Cl_2 165

Figure 3.26: Vis-NIR spectrum of mixed-valence species of 2,5-diferrocenylthiophene $\mathbf{12}^{+\bullet}$ in CH_2Cl_2 168

Figure 3.27: UV-Vis-NIR spectra of mixed-valence species $\mathbf{10}^{+\bullet}$ in CH_2Cl_2 169

Figure 3.28: UV-Vis-NIR spectra of one- and two-electron oxidized species of **14** in CH_2Cl_2 170

Figure 4.1: Chemical structure of a series of triferrocenes 183

Figure 4.2: Projected synthetic routes for **TFc4X**s (X = -, Th, and PyrNMe) 201

Figure 4.3: Synthesis of $FcCH_2P^+Ph_3I^-$, $[1,1'\text{-}Fc(CH_2P^+Ph_3)_2](I^-)_2$ and $1,1'\text{-}Fc[CH_2P(O)(OEt)_2]_2$ 202

Figure 4.4: Synthesis of **TFc4** and **TFc4PyrNMe** 205

Figure 4.5: Synthesis of **TFc4Th** 206

Figure 4.6: Synthesis of **TFc4S** 209

Figure 4.7: Synthesis of **TFc4CO**, **TFc2CO-A** and **TFc2CO-B** 210

Figure 4.8: Synthesis of **FcS-SFc**, **1,1'-Fc(SH)$_2$**, **FcCH=CHBr** and **1,1'-Fc(CH=CHBr)$_2$** 211

Figure 4.9: Synthesis of **BFc2S**, **TFc2S-A** and **TFc2S-B** 212

Figure 4.10: ORTEP diagram of **1,1'-Fc(CH=CHThCHO)$_2$** 215

Figure 4.11: ORTEP plot of **BFc2S** with 50% anisotropic displacement ellipsoids 216

Figure 4.12: ORTEP plot (A) and unit cell packing form (B) of **(*E,E*)-TFc2S** 217

Figure 4.13: ORTEP plot (A), topside view (B) and packing diagram (C) of **(*E,E*)-TFc2CO-A** 218

Figure 4.14: ORTEP plot (A), topside view (B) and packing diagram (C) of **(*E,E,E,E*)-TFc4Th** 219

Figure 4.15: ORTEP plot of **(*E,E,E,E*)-TFc4PyrNMe** 222

Figure 4.16: Cyclic voltammograms of FcCH=CHFc (**BFc2)** and **TFc2** in CH_2Cl_2/0.1 M Bu_4NTFPB 225

Figure 4.17: Cyclic voltammograms of **FcSSFc**, **BFc2S**, **TFc2S-A** and **TFc2S-B** in CH_2Cl_2/0.1 M Bu_4NTFPB 226

Figure 4.18: Cyclic voltammograms of **TFc2CO-A**, **TFc2CO-B** and **TFc4CO** in CH_2Cl_2/0.1 M Bu_4NTFPB 230

Figure 4.19: Cyclic voltammograms of cis/trans-**TFc4**, **(*E,E,E,E*)-TFc4**, **TFc4Th** and **TFc4PyrNMe** in CH_2Cl_2/0.1 M Bu_4NTFPB 232

Figure 4.20: Schematic representation of potential coordinate diagrams for photo-induced electron transfer in biferrocenium and triferrocenium ions with symmetrical bridging linker B 235

Figure 4.21: UV-Vis-NIR spectra of one-electron oxidized mixed-valence species. A: **TFc2$^+$** and **BFc2$^+$**; B: **TFc4$^+$** and **BFc4$^+$**; C: **TFc4Th$^+$** and **BFc4Th$^+$** 238

Figure 4.22: UV-Vis-NIR spectra of one-electron oxidized mixed-valence species, **TFc4PyrNMe$^+$** 240

Figure 4.23: UV-Vis-NIR spectra of one-electron oxidized mixed-valence species, **BFc2S**$^{+}$ and **TFc2S-A**$^{+}$ 243

Figure 5.1: Synthesis of compounds **1-4** using Witting methodology 260

Figure 5.2: Synthesis of compounds **5** and **6** 261

Figure 5.3: Synthesis of compounds **7-9** 265

Figure 5.4: Synthesis of compounds **10-15** 266

Figure 5.5: ^{1}H NMR spectra of the stacked *syn*-conformer (top) and non-stacked conformer (middle) of compound **7** and their singly-bridged analogue (bottom) in $CDCl_3$ 267

Figure 5.6: ^{1}H (top) and ^{13}C (bottom) NMR spectra of thiophenoferrocenophane **13** in $CDCl_3$ 271

Figure 5.7: Crystal structure of orthocycloferrocenophane **7** 274

Figure 5.8: Unit cell packing form of orthocycloferrocenophane **7** 275

Figure 5.9: Crystal structure of pyrroloferrocenophane **14** 277

Figure 5.10: ORTEP plot of compound **13** 279

Figure 5.11: Cyclic voltammograms of [4.4]ferrocenophane **1**, [5.5]ferrocenophane **2** and [6.6]ferrocenophane **3** in CH_2Cl_2/0.1 M Bu_4NTFPB 284

Figure 5.12: Cyclic voltammograms of dithia[5.5]ferrocenophane **4**, [5.5]ferrocenophane-dione **5** and [7.7]ferrocenophane-dione **6** in CH_2Cl_2/0.1 M Bu_4NTFPB 285

Figure 5.13: Cyclic voltammograms of orthocyclo-diferrocenophane **7** and furano-diferrocenophane **10** in CH_2Cl_2/0.1 M Bu_4NTFPB 286

Figure 5.14: Cyclic voltammograms of paracyclo-triferrocenophane **9**, furano-triferrocenophane **11**, thiopheno-triferrocenophane **13** and pyrrylo-triferrocenophane **15** in CH_2Cl_2/0.1 M Bu_4NTFPB 287

Figure 5.15: Schematic representation of potential coordinate and orbital configurational diagrams for photo-induced electron transfer in singly-bridged biferrocenium and doubly-bridged biferrocenium ions with symmetrical bridging linker B292

Figure 5.16: UV-Vis-NIR spectra of mixed-valence species **1**$^{+}$ and **2**$^{+}$ 293

Figure 5.17: UV-Vis-NIR spectra of mixed-valence species **4**$^{+}$ and **7**$^{+}$ 294

Figure 5.18: UV-Vis-NIR spectra of mixed-valence species **11**$^{+}$ and **13**$^{+}$ 295

Figure 5.19: UV-Vis-NIR spectra of mixed-valence species **15**$^{+}$ 296

Figure 6.1: Bis(styrylpyrrole) compounds 307

Figure 6.2: Chemical structures of a series of bis(styrylpyrrole)-based compounds 308

Figure 6.3: Synthetic route for the bis(styrylpyrrole)-based compounds 320

Figure 6.4: ^{1}H NMR spectrum of **3c** in $CDCl_3$ 323

Figure 6.5: ^{1}H NMR spectrum of **5a** in THF-d_8 324

Figure 6.6: ^{13}C NMR spectra of **3c** (top) and **5a** (bottom) in the aromatic and vinylic region 325

Figure 6.7: Normalized absorption (solid lines) and fluorescence (dashed lines) spectra of compounds **1a-c** (A) and **2a-c** (B) 328

Figure 6.8: Normalized absorption (solid lines) and fluorescence (dashed lines) spectra of compounds **3a-c** (A) and **4a-c** (B) 329

Figure 6.9: Normalized absorption (solid lines) and fluorescence (dashed lines) spectra of compounds **5a-c** (A) and **7a-c** (B) 330

Figure 6.10: Cyclic voltammograms of **3a**, **3b** and **3c** in a CH_2Cl_2 solution containing 0.1 M Bu_4NTFPB 336

Figure 6.11: Cyclic voltammograms of **5a**, **5b** and **5c** in a CH_2Cl_2 solution containing 0.1 M Bu_4NTFPB 337

Figure 6.12: Cyclic voltammograms of **1a**, **1b** and **1c** in a CH_2Cl_2 solution containing 0.1 M Bu_4NTFPB 338

Figure 6.13: Vis-NIR absorption spectra of the cationic species of **2a-c** (A) and **3a-c** (B) 342

Figure 6.14: Vis-NIR absorption spectra of the cationic species of **4a**, **4b** (A) and **5a-c** (B) 343

Figure 6.15: Molecular orbital diagram of the oligomers in neutral and cationic states 345

Figure 6.16: UV-Vis-NIR spectrum evolution of oligomer **3b** (A) and **6b** (B) upon progressive oxidation 349

Figure 6.17: Schematic energy diagram for radical cation **6b**$^{+}$ and the corresponding π-dimer **(6b)$_2$**$^{2+}$ 350

Figure A.1: Synthsis of compounds **4-8** 357

Figure A.2: Synthsis of compounds **9-13** 358

Figure A.3: ORTEP plot (A) and unit cell packing form (B) of compound **4** 364

Figure A.4: ORTEP plot of compound **7** 365

Figure A.5: Cyclic voltammograms of **4, 5** and **6** in a CH_2Cl_2 solution containing 0.1 M Bu_4NTFPB 366

Figure A.6: Cyclic voltammograms of **7** and **8** in a CH_2Cl_2 solution containing 0.1 M Bu_4NTFPB 367

Figure A.7: Cyclic voltammograms of **9, 10** and **11** in a CH_2Cl_2 solution containing 0.1 M Bu_4NTFPB 368

Figure A.8: Cyclic voltammograms of **12** and **13** in a CH_2Cl_2 solution containing 0.1 M Bu_4NTFPB 369

Figure A.9: UV-Vis-NIR spectra of the monocationic species $\mathbf{4}^+$, $\mathbf{5}^+$ and $\mathbf{6}^+$ 370

LIST OF SYMBOLS AND ABBREVIATIONS

IR	Infrared Spectroscopy
NMR	Nuclear Magnetic Resonance Spectroscopy
J	coupling constant
ppm	parts per million
δ	chemical shift (ppm)
Hz	Hertz
d	doublet
t	triplet
m	multiplet
UV-Vis	Ultra-Violet/Visible Spectroscopy
λ_{max}	wavelength maximum
ε_{max}	extinction coefficient maximum
CV	cyclic voltammetry
SWV	square wave voltammetry
E_{ox}	oxidation potential
E_{red}	reduction potential
ΔE	peak separation
TFPB	tetrakis(3,5-trifluoromethylphenyl)borate
E_g	bandgap energy
HOMO	highest occupied molecular orbital
LUMO	lowest unoccupied molecular orbital
ET	electron transfer
IVCT / IT	intervalence charge transfer

LMCT	ligand-to-metal charge transfer
MLCT	metal-to-ligand charge transfer
V_{ab} / H_{ab}	electronic coupling constant
α	delocalization parameter
bp	boiling point
mp	melting pointing
ORTEP	Oak Ridge Thermal Ellipsoid Plot
Å	angstrom
nm	nanometer
Ar	aromatic
Fc	ferrocene
AIBN	azobisisobutyronitrile
DMF	*N,N*-dimethylformamide
DMSO	dimethyl sulfoxide
MeOH	methanol
LDA	lithium diisopropylamine
THF	tetrahedrofuran
TMEDA	*N,N,N'N'*-tetramethylethylenediamine
TFA	trifluoroacetic acid

SUMMARY

Molecular wires and switches have been of great interest recently as the next generation of optoelectronic components. Long-range intramolecular electron/hole transfer is paramount in allowing a single molecule or group of molecules to conduct and process electrical signals. Particularly, mixed-valence compounds bearing different oxidation state as the termini have served as prototypical motifs for exploring the possibility of molecular wires and logic memory devices. As part of our efforts to understand the charge transport processes in transition metal complexes, we have synthesized a large variety of diferrocenyl compounds bridged by a "wire" fragment in the generic form "-CH=CH-X-CH=CH-", in which the X unit is a functional group/atom varying in the common range of linking group such as unsaturated double bond, triple bond, heteroatom, aromatic rings and heteroaromatic rings, etc. Systematic studies via structural, electrochemical, UV-Vis-NIR, Mossbauer and other spectroscopic techniques have provided us a great insight of the underlying mechanism of the electronic interaction between the redox-active sites. In this context, electron affinity of the bridging segment, structural configuration of the conjugation path and metal-ligand orbital mixing can all contribute to the effectiveness of certain wire in supporting electron transfer. By utilizing free coordinating electrolyte anions in electrochemistry, we have also found, in many cases, that the electronic communication in mixed-valence complexes is more subtle than originally expected.

Among the altering factors, redox-matching between the metal groups and the bridging organic fragment is most pivotal in determining the charge mobility of a mixed-valence system. This is presumably attributed to the narrow energy gap between the metal dpi orbital and the frontier HOMO of the organic component. The fact that 2,5-divinyl substituted pyrrole possess the same oxidation potential as ferrocene prompted us to develop a series of pyrrolene-spaced bisferrocenyl derivatives with various chain lengths, symmetry and electron density on the bridging component. All these compounds demonstrated greatly enhanced electronic coupling due to charge delocalization. In fact, the electronic communication between the metal centers is still significant at the iron-iron

distance of 17.5 Å. The pyrrolene moiety in the midway of the bridging unit, in essence, serves as an electronic relay in facilitating long-range electron transfer. This is particularly indicative in designing highly conductive polymers containing both metals and conjugated bridges.

A series of triferrocenes linked by symmetric and asymmetric wires have also been developed using appropriate synthetic approaches. For the symmetric triferrocenes, the redox processes are rather dynamic in the shortly-bridged and highly delocalized systems, for which charge relocalization is allowed during successive oxidations. The oxidation sequence of the redox-active sites is therefore governed by the Coulomb repulsion in the intermediate oxidation states. When the bridging conjugation path was lengthened and thus less effective, such charge relocalization was not observed. Instead, electronic interaction between the metal centers is believed to be mediated by charge draining effect. For triferrocenes linked by asymmetric components, the spacers not only act as an electron transfer path but also as a tuning element. Depending on the direction of the linking polar chain, the central ferrocene becomes a molecular switch, turning on or off the communication between the two end ferrocenes.

Since the long-range intramolecular coupling inevitably undergoes through a through-bond mechanism, we also developed a family of doubly bridged ferrocenes. The synthesis was achieved by double Wittig or HEW olefinations of the ferrocenedicarboxaldehydes with an appropriate bisylide. Although the yields were modest, we were able to obtain sufficient quantities for spectroscopic, electrochemical, and X-ray measurements. In all cases studied, the coupling was approximately double that for the equivalent singly-bridged analogues. Thus the use of parallel wires in such systems represents a facile approach to improve communication for molecular electronics. The synthetic methodology used for producing doubly-bridged ferrocenes necessarily allowed for statistical formation of cyclic compounds, including trimetallic, tetrametallic, and higher cycloferrocenophanes, especially when the linking groups were rigid aromatics. In fact, in some cases, only trimetallic cycles were obtained. The application for such cyclic systems is somewhat elusive at this point, however, their unique structural features have demonstrated great examples of structural self-assembly driven by steric strains and intramolecular π-π stacking.

Finally, to eliminate the metal ligand orbital mixing problem, we also bound the "wires" with two redox-active styrylpyrrole termini, for which the whole molecule was purely organic. It was found that when the π-conjugation was maintained, the oligomers were fully delocalized systems. The interpretation of the spectroscopic data of the cationic and dicationic species was thus conducted in the framework of polaron or molecular orbital theory. The band gap and formation of a radical cationic dimer of the singly oxidized species rely heavily on the charge distribution profile of the heterologue arylene oligomers. Their pronounced photophysical and photochemical properties imply the possible application as organic electronic and optical materials.

CHAPTER 1

INTRODUCTION

Molecular Electronics and Wires

In the past decades, the modern semiconductor industry has undergone revolutionary advances in increasing speed, decreasing size and reducing power consumption of electronic components. At present, this demand for more powerful computational devices is accomplished by the miniaturisation of existing silicon-based chips, the "top–down" approach, which is centered on the maturation of microlithography and related technology. It was predicted by Gordon Moore in 1968 that there would be a doubling of devices per chip every 18–24 months. This so-called "Moore's Law" has been enjoyed for almost 40 years. However, this approach will reach its physical limit in the next 5–10 years due to certain limiting factors. For example, when the oxide layers used in silicon chips reach a thickness of three atoms they become poorly insulating, resulting in charge leakage.[1] There are also financial implications such as the increasing costs for more complex production lines for the manufacture of ever-smaller devices on chips.

An alternative is the "bottom–up" approach, which begins at the molecular level with discrete molecules and is often adopted by chemists and materials scientists. Under this approach, molecules are designed and synthesized to possess some inherent electronic function, then studied with modern spectroscopic methods to further elucidate the structural requirement for the desired properties, and finally integrated into supermolecular architectures to build the electrical device. Such functionalized molecules were first hypothesized as the potential molecular electronics by Aviram and Ratner in 1974, who pointed out that discrete molecules could be used as alternatives to silicon chips.[2]

The subject of molecular electronics has been very controversial for many years and been viewed by critics as untentable speculation due to the fundamental limitations

associated with the difficulties of addressing a single molecule. Unfortunately, the direct measurement of the electronic characteristics of individual molecules awaited the development of methods for making molecular-scale electrical contacts. Thus, the first experiment measuring the conductance of a single molecule was only reported in 1997 by Mark Reed and co-workers.[3] Today, with the advent of advanced technologies such as the atomic force microscope (AFM) and the scanning tunneling microscope (STM), which finally enables one to image and address individual molecules, this branch of the field has progressed rapidly through the efforts of an interdisciplinary group of chemists, physicists and engineers. .

In the discipline of molecular electronics, there are many different electrical components[4] that need to be considered, for example switches, logic gates, diodes *etc*. and this area has attracted much interest in recent years with several reviews written on the topic.[5-9] Wires are the simplest of electrical devices, and as such are particularly suited to the development of some fundamental understanding and techniques required for the realization of molecule-scale electronics.

"Molecular wires" are generally defined as linear low-dimensional molecules possessing a pathway for transport of the electrons or holes from one reservoir to another through a defined distance gap. Structurally, such molecules inevitably contain a conjugated backbone. The electron or hole conduction occurs through their π-system, and this has been the basis of many such wires. Quantification of the conducting properties of a wire has been approached either directly or indirectly depending on the techniques used to analyze the wire properties. Whereas direct measurements often involve fabricating the molecules on some macroscopic system, a junction or surface--using techniques such as STM to obtain current–voltage characteristics to classify wires as metallic or semiconducting--indirect measurements have been carried out on the rate of electron transfer across the wire using spectroscopic techniques.

The direct measurement of the conductivity of a single molecular wire is exemplified by Tour's oligo(phenyleneethynylene) (OPE) molecules on a gold surface[10] as illustrated in Figure 1.1. To allow the "wire" to be attached on the metal surfaces, an attachment of "molecular alligator clips" is often required at the ends of the molecule. In the OPE wire, thioacetate was used as the preset attachment, which upon hydrolysis

formed a thiol. The thiol could then form gold-thiolates on exposure to gold surfaces. Molecular wires were inserted into an insulating layer of dodecanethiol molecules attached to a gold electrode. The conductivity of a molecular wire was measured using the STM probe tip, which was small enough and precisely controllable so that it could interact with individual molecules absorbed onto a metal. It was found that when the STM tip was maneuvered along the surface of the monolayer the current flowing was significantly greater when in contact with the wire than when the tip was placed over the insulating layer.

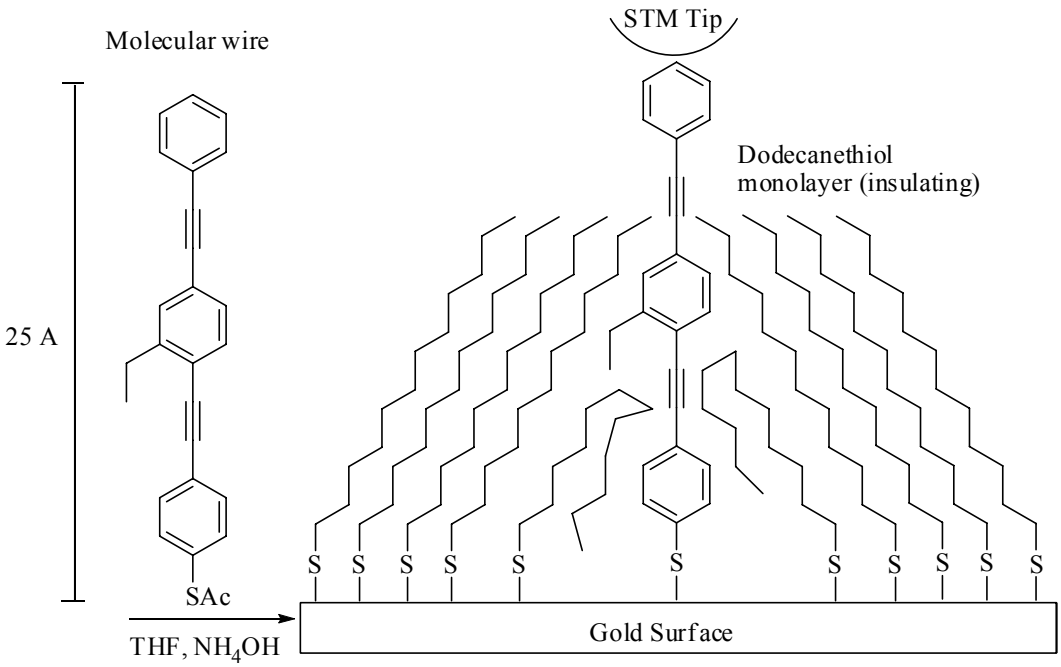

Figure 1.1 Schematic representation of a molecular wire being addressed with an STM tip, reproduced from ref. 10.

Despite the obvious advantage of such a straightforward measurement, the majority of the molecular wires intended for molecular electronics have never been tested in an actual circuit. One of the most important reasons is that there is not one generally accepted testbed that is readily acceptable to all investigators. Rather there are several

different testbeds in the literature,[3, 11-13] which have benn recently reviewed,[14] and the results from those molecular wires that have been tested are in many cases not comparable. These devices are difficult to make, yields are low, and obtaining reproducible results requires care and patience. Drawing conclusions about the activity of classes of compounds or building structure activity relationships among several classes using the data generated can be a difficult exercise.

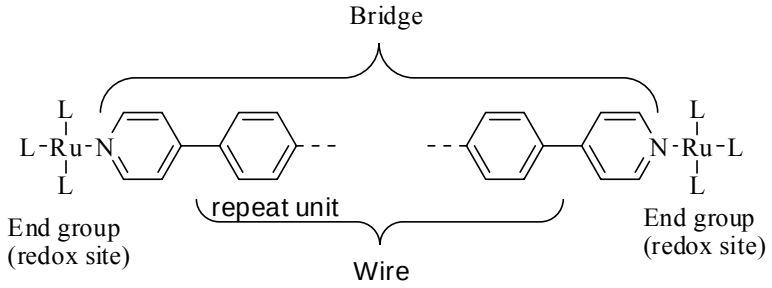

Figure 1.2 Schematic illustration of a molecular wire incorporated into a mixed valence systems. Reproduced from reference 15.

The indirect approach involves integration of the redox-active metal centers at either ends of the wire molecule (Figure 1.2). The metal centers act as donor and acceptor sites for the transfer of electrons across the bridge or wire. These donor–bridge–acceptor systems have the advantage of generating the electron *in-situ* so there is no need to connect the molecule to a macroscopic system. A key requirement is that there is good overlap between the d-orbitals of the metal and the p-orbitals of the bridging fragment, so that there is delocalization from one metal to the other, allowing the transfer of the electrons. The rate at which the electrons are transferred can be related to the properties of the wire (such as length, degree of conjugation *etc.*).[15]

A variation of this method is to use two isovalent metal centers. If one of the metals is then oxidized the complex can show an intervalence charge-transfer transition between the two end units. The timescale of the transition and intensity and shape of the absorption band provides quantitative information on the extent of coupling between the two metals, which can provide information related to the efficiency of the wire. To date,

this is the most often used and well-established approach due to its convenience for the fundamental study of the ubiquitous process of electron transfer.

Current research is focused on finding molecules that possess the exacting properties required to process information at the molecular scale. The research presented here in entirely devoted to study the intrinsic properties of molecules through modern computation, synthesis, physical organic chemistry, spectroscopy and modern computation. The task of devising such smart molecules must be left for later workers.

Mixed-Valence Complexes and Electron Transfer Theory

Mixed-valence compounds, in which an element exists, at least in a formal sense, in more than one oxidation state have attracted great research attention for decades due to the fact that they are ideal models for fundamental studies in electron transfer. In essence, data derived from the study of mixed-valence molecules made it possible to measure the rate constants and activation barrier for intramolecular electron-transfer. Much of the pioneering theoretical treatment was developed by Marcus and Hush, which is instrumental in advancing our understanding of electron-transfer theory.

Compounds containing multiple oxidation states are common species. The mixed-valence character of some minerals provides the basic for their color. Multiple-site metalloenzymes, which undergo multiple electron transfer, have mixed-valence forms. Prussian blue, which has a cyanide-bridged Fe(II)-Fe(III) structure, is generally considered as the first man-made mixed-valence compound. The intense colors exhibited by Prussian blue, and by mixed-valence compounds in general, are due to their unique electronic structure.[16, 17] In addition, the properties of mixed-valence compounds are rarely just the sum of the properties of the component parts taken separately. For example, the electrical conductivity of Fe_3O_4 ($FeO \bullet Fe_2O_3$), a mixed-valence Fe(II)Fe(III) oxide, is 10^6 times larger than the trivalent Fe_2O_3.

Among the commonly studied mixed-valence systems are the bridged bimetallic complexes.[18-21] Perhaps the most well known example of such a system is the Creutz-Taube ion. This complex consists of a pyrazine-bridged pentaammineruthenium mixed-valence dimer.[22, 23]

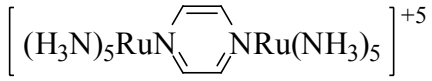

Figure 1.3 The Creutz-Taube ion.

The reason for interest in mixed-valence compounds like Creutz-Taube ion is that it provides the possibility of measuring the rate constants and activation barrier for intramolecular electron transfer,[22, 23] shown in eq. 1.1, in which we denote the mixed-valence complex in a generic form, M-B-M^+, where B is the bridging ligand, M and M^+ are the reduced and oxidized forms of the metal centers, respectively. The analogous, light-driven process, eq. 1.2, can often be observed as a broad, solvent-dependent absorption band. For symmetrical mixed-valence complexes, these bands typically appear in low-energy visible or near-infrared spectra. They are called intervalence transfer (IT), metal-metal charge transfer (MMCT), or intervalence charge transfer (IVCT) bands.[24-29] Hush has provided an analysis of IT band shapes based on parameters that also define the electron-transfer barrier.[24, 25] In the following discussion, we briefly provide an overview of the origins and significance of the IT bands described by the Marcus theory of out-sphere electron transfer (ET)[30-32] and by the Hush theory of mixed-valence complexes. Detailed accounts can be found elsewhere.[18, 24, 33]

$$M\text{-}B\text{-}M^+ \rightleftharpoons M^+\text{-}B\text{-}M \qquad \text{thermal process} \qquad (1.1)$$

$$M\text{-}B\text{-}M^+ \xrightarrow{h\upsilon} M^+\text{-}B\text{-}M \qquad \text{light-driven} \qquad (1.2)$$

The Franck-Condon principle implies that in the course of electron transfer, the positions of the atoms remain unchanged; the transfer of the electron can be regarded as quasi-instantaneous with respect to nuclear motion. In the special case of a symmetric mixed valence compound M-B-M^+, the inter-conversion of the two energetically degenerate forms depicted in Eq. 1.1 with no net free energy change is subject to a thermal activation barrier ΔG^*_{th}.

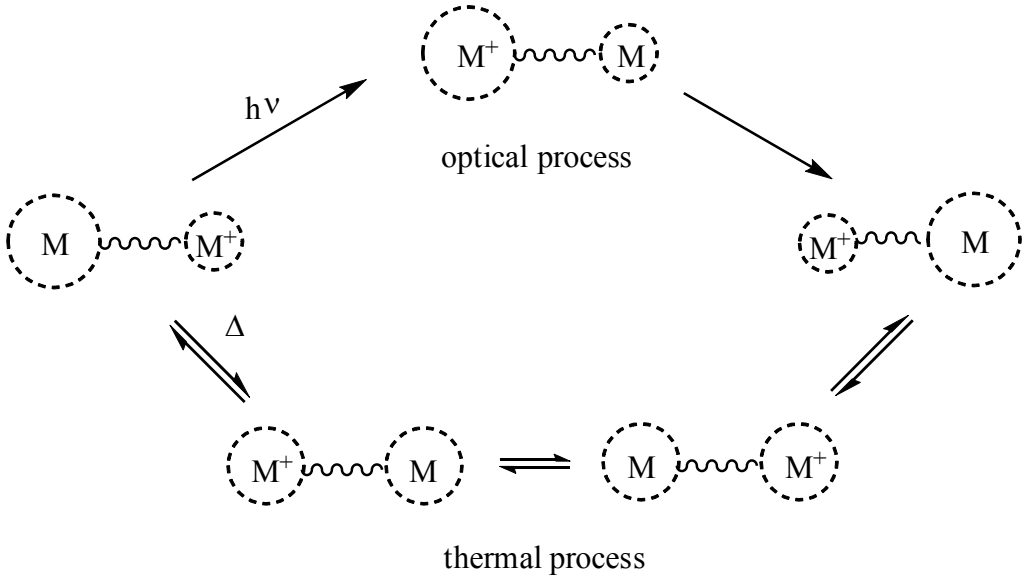

Figure 1.4 Optical and thermal ET processes in a symmetric mixed-valence complex.

In general, the metal-ligand bond lengths and force constants, and metal-solvent electrostatic interactions will be different around M and M^+. The interchange of charge therefore necessitates the reorganization of the inner-shell and outer-shell environments. The energy stemming from this reorganization is related to the ET activation barrier. This is the essence of the Marcus model. The consequences of the net nuclear rearrangement are depicted in Figure 1.4, where the dashed circles represent the corresponding geometry of the coordination sphere and solvation around the metal center. If spontaneous ET were to occur between M and M^+ in their equilibrium states, the product would be formed in a vibrationally excited state, with M having the M^+ configuration and vice-versa. This violates conservation of energy, and is depicted by the thermally forbidden upper reaction pathway in Figure 1.4. For ET to occur, the ligands and solvent must rearrange to a compatible configuration before the ET step. The formation of this activated complex in which ET takes place constitutes the thermal barrier, and is depicted by the lower pathway in Figure 1.4.

ET without prior rearrangement can be induced along the upper pathway by the absorption of light sufficiently energetic to form the excited state; it is this light absorption that gives rise to the intervalence transfer (IT) band. The energy relationships are demonstrated in Figure 1.5B as potential energy curves where one parabola describes

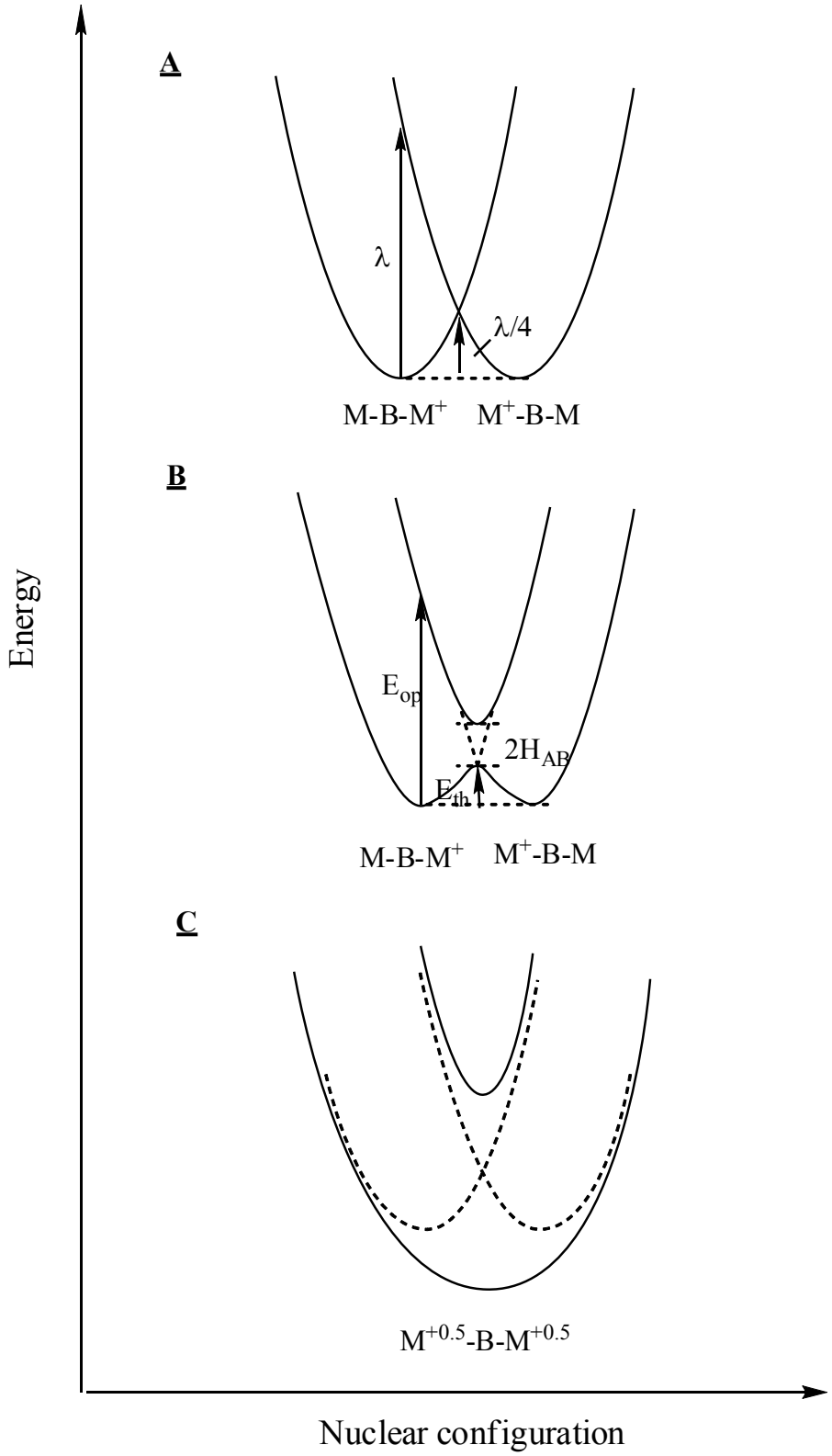

Figure 1.5 Potential energy surface for symmetrical mixed-valence complexes with negligible (A), weak (B) and strong (C) electronic coupling.

each of M-B-M^+ and M^+-B-M. The curves split at the intersection by $2H_{AB}$, where H_{AB} is a resonance energy between the states, *i.e.,* the electronic coupling between the two redox centers. In thermal ET, the system moves from left to right, passing over the barrier E_{th}. Optical ET occurs when sufficiently energetic light $h\nu = E_{op}$ is absorbed, effecting vertical passage from the lower to the upper curve. When H_{AB} is small and $E_{th} = \Delta G^*_{th}$, it turns out that optical and thermal ET are proportional:

$$E_{op} = h\nu = 4\ \Delta G^*_{th} \qquad (1.3)$$

The intervalence transfer, which corresponds to the vertical process in the energy diagram, usually appears in the visible and near-infrared regions of the absorption spectra in a symmetrical mixed-valence system. With the assumption of a dielectric continuum model,[16] the dependence of the absorption energy ν_{IT} of the intervalence transfer on solvent polarization is given by the following equation:

$$\nu_{IT} = \chi_i + e^2(1/2a_1 + 1/2a_2 - 1/d)(1/n^2 - 1/D) \qquad (1.4)$$

where χ_i is the contribution from inner sphere and other solvent-independent terms to the optical barrier of electron transfer, a_1 and a_2 are the radii of the donor and acceptor sites, respectively, d is the distance between the two sites, n is the solvent refractive indexes and D is the dielectric constant of the solvents. The relationship between the absorption energy, distance and solvent effects has been well established.[34]

Assuming a gaussian shape for the intervalence band and the weak electronic coupling as well as the perturbation approximation and the high temperature limit, it is possible to estimate the electronic coupling constant H_{AB} (often interchangeably termed V or V_{AB} in cm^{-1}) and the valence delocalization parameter (α) by using the integral intensity of the intervalence absorption band as follows:

$$H_{AB} = (2.05 \times 10^{-2})\ (\nu_{IT}.\varepsilon_{max}.\Delta\nu_{1/2})^{1/2}/r \qquad (1.5)$$

$$\alpha = H_{AB}/\nu_{IT} \qquad (1.6)$$

where v_{IT} (or v_{IVCT}) is the absorption maximum of the intervalence band, ε_{max} is the extinction coefficient, $\Delta v_{1/2}$ is the band half-width, and r is the metal-metal distance in Å . Both H_{AB} and α are in essence a measure of the extent of electronic delocalization between the metal centers and thus are used to describe the extent of electronic interaction in the ground state of the mixed-valence species. If the coupling between the metal centers is weak, the energy barrier for thermal electron transfer (E_{th}) is estimated as:[34]

$$E_{th} = (1/4)\, v_{IT} - H_{AB} + \alpha^2 v_{IT} \qquad (1.7)$$

A system of classifying mixed valence compounds on the basis of the interactions (H_{AB}) between the metal centers has been devised by Robin and Day.[35] In the Robin and Day classification, mixed-valence systems are characterized as Class I, II or III depending on the strength of the electronic interaction between the oxidized and reduced sites, ranging from essentially zero (Class I), to moderate (Class II), to very strong electronic coupling (Class III). The elucidation of the three categories can be readily appreciated from the potential energy curves shown in Figure 1.5, in which the generalized nuclear configuration term involves both inner and outer nuclear geometry; the parabolic potential curves depict the potential energy surface of the mixed-valence species.

In a class I mixed-valence system, the electronic interaction between the redox centers is negligible (for reasons such as large physical separation or very different environments) and only the properties of the discrete ions is observed. $H_{AB} = 0$ and the two potential energy profiles intersect (Figure 1.5A). The energy separation between the two states at equilibrium geometry is called the reorganization energy λ. The thermal energy barrier for electron transfer is one quarter of λ. In class III the extreme opposite is found, where the coupling is so strong that the characteristics of isolated M and M^+ are absent, replaced by the new properties of a completely delocalized $(M\text{-}B\text{-}M)^+$ unit . As shown in Figure 1.5C, when the electronic coupling is on the same order of the reorganization energy, two separate surface minima are no longer discernible and the energy surface features a single minimum at the intermediate geometry. For this class, Hush theory is not applicable.

Class II compounds exhibit characteristics of weak coupling ($0 < H_{AB} << \lambda$), with slightly perturbed M and M^+ character. The zero order potential energy curve is then no longer a valid model. It is for this class that the Hush model is useful. Increases in H_{AB} result in a lowering of E_{th} to the point where there is no thermal barrier and only one minimum exists: a class III compound. Borderline cases may be difficult to assign, although a number of criteria can be invoked to support an assignment. The Robin and Day classification has enjoyed considerable success and most of the redox systems studied to date are readily assigned to Class II.

Solitonic Polymethine

The theme for our previous research in low-dimensional materials has been the concept of "solitons in a box" (Figure 1.6).[36] These materials include one-dimensional ones such as polyacetylene, two-dimensional ones such as graphite, and intermediate dimensions such as the polyacenes. When end groups of varying electron accepting (redox potential) are separated by a polyene spacer, the effectiveness of the coupling ("wire" behavior) is a function of the nature of the spacer, whether it is (a) unsaturated and neutral, (b) charged, radical (polaronic) or (c) solitonic. In the case of solitonic systems, the end groups are separated by an odd-alternant hydrocarbon chain containing a non-bonding molecular orbital ("mid-gap wavefunction") such that charge injection can take place at relatively low potentials. Tolbert, Ogle and Zhao have discovered that the behavior of such systems is a function of the electron affinity of the end groups. In the case of phenyl end groups (**DPN**), the soliton is localized in the center of the chain. If the end group is strongly electron-attractive (e.g., pyridinium, **DPyN**), the soliton travels to one end of the chain, producing a symmetry collapse and the disruption of the formal resonance expected for such cyanine dyes. This is an example of a Peierls distortion in a single molecule. They were the first to demonstrate such symmetry collapse in such otherwise symmetrical systems,[36-39] and we believe such bistable systems may form the basis for a type of molecular switch which we propose below.

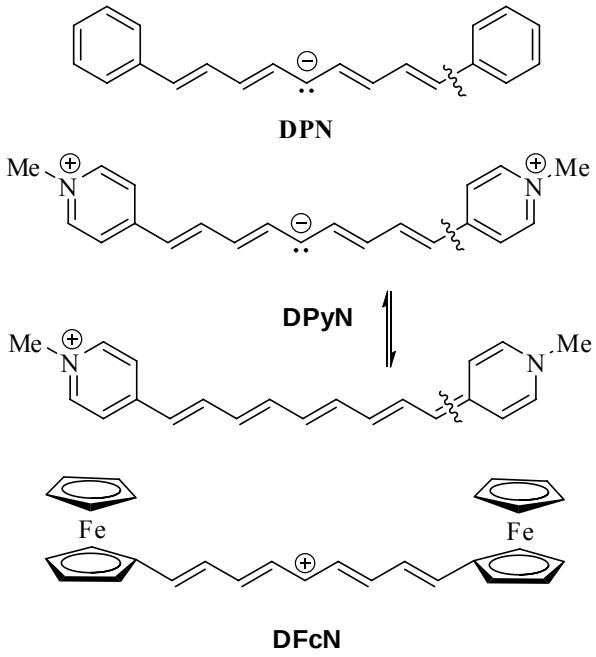

Figure 1.6 Compounds used in previous studies.

Chidsey and coworkers have demonstrated an approach to examining the function of molecular wires by attaching ferrocene to a surface through a conducting moiety.[40, 41] Our approach has been two redox end groups (e.g., ferrocene, **DFcN**, see Figure 1.6) to serve as a probe for communication of charged states. This also allows us to examine the optical absorption spectra of the intermediate species. In such cases, we have demonstrated that the chain is soliton-like when the two ferrocenes are at the same +2 oxidation state but undergoes symmetry collapse when one ferrocene is oxidized to ferrocenium.[42] For the cations **DFcN**, **N** = 1-13, the absorption maxima were characterized by much longer wavelengths than those of the analogous diphenylpolyenyl carbenium ions[43, 44] and carbanions of analogous length, indicating the presence of strong electronic coupling between the electropositive iron complex and the HOMO orbitals of the polyene chain.[45] In fact, such interaction are still at work when the metal centers is separated by a solitonic polymethine of thirteen carbons, while the undoped polyene is

ineffective in supporting electronic communication when the spacer is longer than six sp^2-carbons.[46]

Experimental Approach and Objectives

The current research was inspired by our previous success in achieving highly efficient molecular wires using solitionic moieties. However, "doping" (a misnomer) of organic systems requires addition of counterions, resulting in ionic systems for which solubility and processability become a problem. The work presented here was initially launched to address this issue by seeking a complementary neutral component and later extended drastically to a large volume of congruent reference molecules with the core focus on the essential factors defining the functioning molecular wires and switches. The methodology used in this research is still the indirect approach, adopting the prototype of mixed-valence compounds. It is devoted to contributing both to the mechanistic organic chemistry and to the related core processes in molecular electronics.

General Considerations

Due to the presence of several metal centers in different formal oxidation states, the mixed-valence compounds are built to provide for an intramolecular electron transfer. The dynamic aspect associated with this electron motion has been subject of much theoretical and experimental work. In particular, it has been shown that three electronic structures can occur[35]: (1) completely delocalized over the different sites (class III in Robin-Day's classification); (2) partially localized (class II); (3) fully localized (class I). The nature of the electronic structure and the rate for electron migration in such systems were shown to be directly linked to the nature and the length of the bridging groups. Polyenes, polyacetylenes and polyphenylene, in which the extended conjugation would facilitate such migration, were used as connectors in a number of mixed-valence complexes. Such mixed-valence compounds generally showed only limited electronic coupling between metal sites and most of them are borderline class I and class II compounds. In addition, it is generally accepted that the electronic coupling between the redox centers would exponentially decrease with the distance between them. In most of the bridged redox systems known today, such decrease proved to be too drastic for the

redox centers to maintain sufficient electronic communication when they are separated by more than 10-20 Å. To allow such systems processing information at molecular level, it is essential to develop highly coupling bridging group. This indeed raises two interleaved questions: (1) what are the underlying mechanisms in the mixed-valence systems with regard to electron transfer? and consequentially (2) what is the essence of designing a highly delocalized mixed-valence complex so that the charge mobility is maximized?

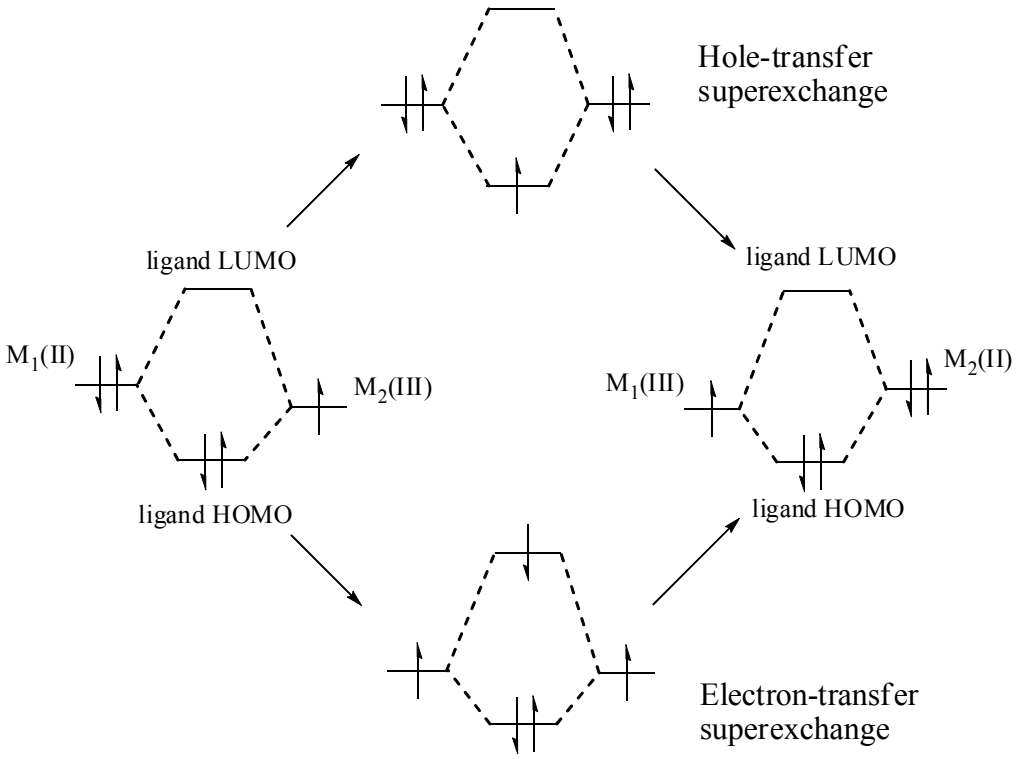

Figure 1.7 Schematic illustration of superexchange mechanism: electron-transfer type and hole-transfer type. The "ligand" denotes the bridging component between the metal centers.

Hoga and coworkers have performed systematic studies on a series of dinuclear Ru(II) complexes bridged with benzimidazole- and benzothiazole-based ligands[47-51], in which a superexchange mechanism is believed to be at play. As illustrated in Figure 1.7, two pathways are possible. In the hole-type superexchange pathway, an electron is promoted from the bridging ligand HOMO to the M(III) site, giving the symmetric

transition state with both metals in the reduced form. The missing electron from the bridging ligand HOMO is subsequently replaced by an electron from the other metal atom, resulting in a system where the valences have been swapped. Conversely, electron-type superexchange involves the transition of an electron from the M(II) state metal to the ligand LUMO, leaving a symmetric transition state with the metals in the oxidized form. Exchange is completed by the transfer of the electron to the opposing M(III) atom. The preferred pathway and the ease with which it is taken depend on the relative energies of the metal orbitals and the ligand HOMO or LUMO orbitals; metal-d and ligand HOMO orbital mixing leads to hole superexchange and metal-d and ligand LUMO orbital mixing leads to electron superexchange. Apparently, in either pathway, the effectiveness of orbital overlap between the organic component (i.e., the wire) and the metal centers is pivotal. In principle, the smaller the energy gap between the ligand frontier HOMO/LUMO and the metal-d orbital, the greater the efficiency of charge mobilization. Metal-metal distances should be less important when a high degree of electron delocalization is achieved, which consequentially utilizes long-range electron transfer.

Related to this, it is also crucial to realize that, in judging of the quality of certain conducting wires under mixed-valence circumstances, the end group effects must be taken into account. For instance, polyene bridged biferrocenium complex and binuclear Ru(II) mixed-valence compound, $[(NH_3)_5Ru\text{-}py\text{-}(CH{=}CH)_n\text{-}py\text{-}Ru(NH_3)_5]^{5+}$, demonstrated considerably different efficiency in supporting electron transfer as the latter compound exhibited unusual and quite remarkably slow attenuation of coupling with increasing distance.[52] The difference could be attributed to the different order of the orbital overlap between the metal and polyene-based ligand. This, in fact, reflects the gray field of the definition of where the wire actually begins in such systems. The "bridge" between the metal centers includes the primary coordination sphere of the metals whereas the "wire" (the polyene segment in the example above) does not (see Figure 1.2). Clearly such a definition is required for comparison between wires but must be regarded as an arbitrary choice. Nevertheless, assembly of a bridging unit with metal-incorporated moieties is not a simple sum up of related components. Rather they can substantially and mutually perturb the energy level of each other. Thus, given a certain bridging wire, good designs would be those with a suitable redox moiety, which will

result in greater orbital mixing after integrating them together and vice versa. Finally, the dependence of the metal and ligand components on environmental factors such as PH value, electric field, counterion, etc. is at the center of the art of composing switching elements.

Current Research Approach and Objectives

In the context stated above, this work is targeted to elucidate the fundamental issues for establishing efficient molecular wire systems in an integrated view. The model compounds developed in this study are illustrated in Figure 1.8.We still adopted ferrocene as the redox probe due to its functionalizable structure, its low oxidation potential, its stability in both neutral and charged form. The "wires" are in the generic form of "-CH=CH-X-CH=CH-", in which X is a functional group/atom varying diversely across the common linked groups such as unsaturated/saturated hydrocarbons, heteroatoms, aromatic rings and heteroaromatic rings. In a very broad view, wires of this type could be considered as a polyene derivatives, in which the length is relatively fixed to a certain extent to circumvent the through-space interaction between the metal centers; the inserted X group is essentially a variegate, which tunes the energy level of bridging ligand HOMO and the efficiency of orbital overlap between the metal and wire, giving rise to different degree of electronic coupling. The notion of this simple wire is that: if we consider "-CH=CH-CH^{+}-CH=CH-" solitonic due to the p-type doping on the polyene chain, the "-CH=CH-X-CH=CH-" wire containing an electron rich or deficient X group could be viewed as a n-type doped (X group is electron rich) or p-type doped (X group is electron deficient) neutral solitonic fragment, respectively. The effectiveness of such wire is surely determined by the nature of the central X group, both electronically and sterically. However, by using vinylene groups as the conductive spacers separating the functional groups X, we hope to minimize the steric effects and concentrate on the electronic effects.

Our approach is aiming at seeking the underlying mechanism in maximizing the electronic coupling in mixed-valence systems by systematic study of a broad variety of structurally similar bridging components. We expect the most efficient species would be those having lowest energy gap between the metal-d and frontier ligand orbitals (shown in Figure 1.7). In addition, the functional X group is intrinsically a potential switching

1. Singly-bridged biferrocenes

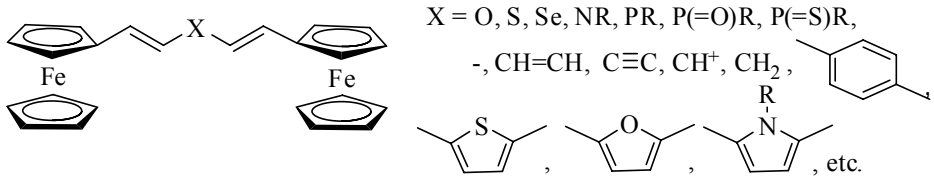

2. Doubly-bridged biferrocenes

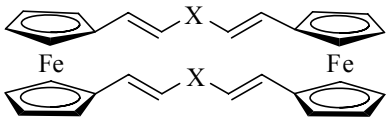

3a. Symmetrical triferrocenes

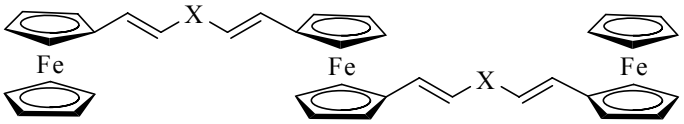

3b. Asymmetrical triferrocenes

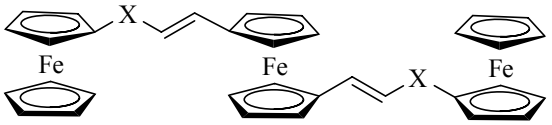

X = S, C(O)

4. Pyrrole-based organic wires

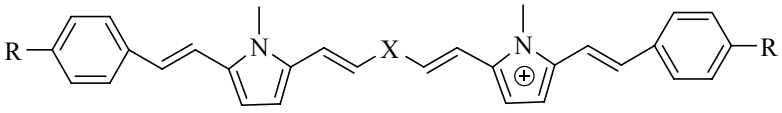

R = H, CN, OMe

X = S, -CH=CH-

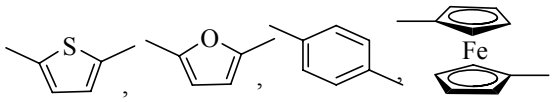

Figure 1.8 Proposed model compounds in this work.

element, which could be altered interiorly or exteriorly to adjust the communication between the metal centers.

Departing from the singly bridged systems, we deviate from our successful research on ferrocene-based complexes into two directions: doubly-bridged biferrocenes and spacer-linked triferrocenes (Figure 1.8). The former approach is based on the prerequisite that a through-bond interaction is at work. Apparently, as the metal centers are confined in a restricted framework and well separated, the merely possible communication between them in the mixed-valence state should be out of a through-bond process. The intuitive purpose of duel channels built in this architecture is aimed at enhancing such through-bond communications. For the latter triferrocenes, there are two types of model compounds: symmetrical and asymmetrical as shown in Figure 1.8. In either scenario, the chemical environments of the terminal ferrocenyl groups are identical and differ from that of the central ferrocene unit. The trinuclear systems are indeed a logic extension of the "closed-box" biferrocenyl systems. The additional metal moiety should perturb the electronic interacting patterns among the three redox-active sites as a function of the mediating X groups. It is especially intriguing when the X-centered spacer is redox-active by itself, which allows multiple charge transfers to occur by electron hopping along the metal and organic components. Revealing such underlying processes certainly has relevance for both mechanistic organic chemistry and polymeric materials. The asymmetrical triferrocenes are designed to have the central ferrocene unit as a switching element, turning on or off the communication between the two ferrocene ends, depending on the direction of the polar linking chain.

Finally, since the charge mobility in the metal harbored complexes relies largely on the effectiveness of orbital overlap between the metal and ligand components, we also develop a series of highly delocalized organic mixed-valence compounds,[53-57] for which the redox-active metal moieties are replaced by the low oxidation potential organic entities (Figure 1.8). By this means, the limitation caused by prototyping factors can be precluded so that the authentic potential of certain molecular wires in term of supporting electron transfer can be uncovered.

Obviously, this research is extensively synthesis-oriented. A large volume of compounds are designed and synthesized. The supporting methods include X-ray crystallography, electrochemistry, UV-Vis-NIR spectroscopy, ESR, Mössbauer and etc. X-ray structural analysis provides important steric information on the metal complexes in assisting our understanding of their physical and chemical properties. The coplanarity of the conjugation pathway along the bridging segment is very suggestive to the related electronic properties, although we recognize that the solid-state structure represents only one of many possible conformations in solution. Cyclic voltammetry further elucidates the properties of the mixed valence states, in which the communication between the redox sites is reflected by whether a peak separation exists and the magnitude of such a separation. The mixed-valence species can be reached by partial electrochemical or chemical oxidation. The intervalence transfer between the metal or redox centers derived from Vis-NIR spectra is extremely indicative to the degree of the electronic coupling and its fall off with distance and structural limitation.

References

1. Tour, J. M. *Acc. Chem. Res.* **2000,** 33, 791.
2. Aviram, A.; Ratner, M. A. *Chem. Phys. Lett.* **1974,** 29, 277.
3. Reed, M. A.; Zho, C.; Muller, C. J.; Burgin, T. P.; Tour, J. M. *Science* **1997,** 278, 252.
4. Ward, M. D. *J. Chem. Educ.* **2001,** 78, 321.
5. Tour, J. M.; Rawlett, A. M.; Kozaki, M.; Yao, Y.; Jagessar, R. C.; Dirk, S. M.; Price, D. W.; Reed, M. A.; Zhou, C.; Chen, J.; W. Wang, W.; Campbell, I. *Chem. Eur. J.* **2001,** 23, 5118.
6. Metzger, R. M. *Chem. Rev.* **2003,** 103, 3803-3834.
7. Carroll, R. L.; Gorman, C. B. *Angew. Chem., Int. Ed.* **2002,** 41, 4378-4400.
8. Mantooth, B. A.; Weiss, P. S. *Proc. IEEE* **2003,** 91, 1785-1802.
9. Salomen, A.; Cahen, D.; Lindsay, S.; Tomfohr, J.; Engelkes, V. B.; Frisbie, C. D. *Adv. Mater.* **2003,** 15, 1881-1890.
10. Chen, J.; Reed, M. A.; Asplund, C. L.; Cassell, A. M.; Myrick, M. L.; Rawlett, A. M.; Tour, J. M.; Van Patten, P. G.. *Appl. Phys. Lett.* **1999,** 75, 624-626.
11. Chen, J.; Reed, M. A.; Rawlett, A. M.; Tour, J. M. *Science* **1999,** 286, 1550.
12. Ranganathan, S.; Steidel, I.; Anariba, F.; McCreery, R. L. *Nano. Lett.* **2001,** 1, 491.
13. Fan, F.-R.; Yang, J.; Cai, L.; Price, D. W.; Dirk, S. M.; Kosynkin, D. V.; Yao, Y.; Rawlett, A. M.; Tour, J. M.; Bard, A. J. *J. Am. Chem. Soc.* **2002,** 1224, 5550.
14. James, D. K.; Tour, J. M. *Chem. Mater.* **2004,** 16, 4423.
15. Launay, J. *Chem. Soc. Rev.* **2001,** 30, 386.
16. Robin, M. B.; Day, P. *Adv. Inorg. Chem.* **1983,** 10, 247.
17. Allen, G.; Hush, N. S. *Prog. Inorg. Chem.* **1967,** 8, 357.
18. Creutz, C. *Prog. Inorg. Chem.* **1983,** 30, 1.
19. Haim, A. *Prog. Inorg. Chem.* **1983,** 30, 273.
20. Meyer, T. J. *Prog. Inorg. Chem.* **1983,** 30, 389.
21. Endicott, J. F.; Kumar, K.; Ramasami, T.; Rotzinger, F. P. *Prog. Inorg. Chem.* **1983,** 30, 141.

22. Creutz, C. T., H. *J. Am. Chem. Soc.* **1969,** 91, 3988.

23. Creutz, C.; Taube, H. *J. Am. Chem. Soc.* **1973,** 95, 1086.

24. Hush, N. S., *Prog. Inorg. Chem.* **1967,** 8, 391.

25. Hush, N. S. *Electrochim. Acta* **1968,** 13, 1005.

26. Crutchley, R. J. *Adv. Inorg. Chem.* **1994,** 41, 273.

27. Ward, M. D. *Chem. Soc. Rev.* **1995**, 187.

28. Kaim, W.; Bruns, W.; Poppe, J.; Kasack, V. J. *Mol. Struct.* **1993,** 292, 221.

29. Richardson, D. E.; Taube, H. *Coord. Chem. Rev.* **1984,** 60, 107.

30. Marcus, R. A., *J. Chem. Phys.* **1956,** 24, 966.

31. Marcus, R. A., *J. Chem. Phys.* **1965,** 43, 679.

32. Marcus, R. A.; Sutin, L., *Inorg. Chem.* **1975,** 14, 213.

33. Astruc, D., *Electron Transfer and Radical Processes in Transition-Metal Chemistry; VCH: New York* **1995**.

34. Power, M. J.; salmon, D. J.; Callahan, R. W.; Meyer, T. J. *J. Am. Chem. Soc.* **1976,** 98, 6731.

35. Robin, M. B.; Day, P., *Adv. Inorg. Chem. Radiochem.* **1967,** 10, 247.

36. Tolbert, L. M., *Acc. Chem. Res.* **1992,** 25, 561.

37. Tolbert, L. M.; Ogle, M. E., *J. Am. Chem. Soc.* **1989,** 111, 5958.

38. Tolbert, L. M.; Ogle, M. E., *Mol. Cryst. Liq. Cryst.* **1990,** 189, 279.

39. Tolbert, L. M.; Ogle, M. E., *J. Am. Chem. Soc.* **1990,** 112, 9519.

40. Devaraj, N. K.; Decreau, R. A.; Ebina, W.; Collman, J. P.; Chidsey, C. E. D., *J. Phys. Chem. B* **2006,** 110, 15955-15962. .

41. Sikes, H. D.; Smalley, J. F.; Dudek, S. P.; Cook, A. R.; Newton, M. D.; Chidsey, C. E. D.; Feldberg, S. W., *Science* **2001,** 291, 1519-1523.

42. Tolbert, L. M.; Zhao, X., *J. Am. Chem. Soc.* **1997,** 119, 2291.

43. Dähne, S.; u. Radeglia, R., *Tetrahedron* **1971,** 27, 3673.

44. Fabian, J.; Zahradnik, R.; Wiss, Z., *Tech. Univ., Dresden* **1977,** 26, 315.

45. Spotts, J. M.; Marder, S. R., *Adv. Mater.* **1992,** 4, 100.

46. Ribou, A.-C.; Launay, J.-P. ; Sachtleben, M. L.; Li, H.; Spangler, C. W., *Inorg. Chem.* **1996,** 35, 3735-3740.

47. Haga, M.-A.; Ali, M. M.; Koeski, S.; Fujimoto, K.; Yoshimura, A.; Nozaki, K.; Ohno, T.; Nakajima, K.; Stufkens, D., *J. Inorg. Chem.* **1996,** 35, 3335.

48. Haga, M.-A.; Ali, M. M.; Koseki, S.; Yoshimura, A.; Nozaki, K.; Ohno, T., *Inorg. Chim. Acta* **1994,** 226, 17.

49. Haga, M.-A.; Ano, T.-A.; Kano, K.; Yamabe, S., *Inorg. Chem.* **1991,** 30, 3843.

50. Ohno, T.; Nozaki, K.; Haga, M.-A., *Inorg. Chem.* **1992,** 31, 4256.

51. Haga, M.-A.; Matsumura-Inoue, T.; Yamabe, S., *Inorg. Chem.* **1987,** 26, 4148.

52. Joachim, C.; Launay, J. P., *J. Mol. Electronics* **1990,** 6, 37.

53. Barlow, S.; Risko, C.; Chung, S.-J.; Tucker, N. M.; Coropceanu, V.; Jones, S. C.; Levi, Z.; Bredas, J.-L.; Marder, S. R., *J. Am. Chem. Soc.* **2005,** 127, 16900-16911.

54. Bailey, S. E.; Zink, J. I.; Nelsen, S. F., *J. Am. Chem. Soc.* **2003,** 125, 5939-5947.

55. Coropceanu, V.; Malagoli, M.; Andre, J. M.; Bredas, J. L., *J. Am. Chem. Soc.* **2002,** 124, 10519-10530.

56. Lindeman, S. V.; Rosokha, S. V.; Sun, D.; Kochi, J. K., *J. Am. Chem. Soc.* **2002,** 124, 843-855.

57. Stephen, F.; Nelsen, S. F.; Konradsson, A. E.; Weaver, M. N.; Telo, J. P., *J. Am. Chem. Soc.* **2003,** 125, 12493-12501.

CHAPTER 2

ELECTRON TRANSPORT IN DIFERROCENYL COMPLEXES LINKED BY –CH=CH-X-CH=CH- SPACERS

Introduction

The notion of molecular "wires" has captured the imagination of chemists and physicists in semiconductor nanotechnology. Missing are clear concepts of what this term means and how it relates to structure and function. Although such wires are often portrayed as single conductive paths, and the measurement of single molecule conductance has emerged as a rich and provocative research area, most often such wires are used in ensembles connecting metallic surfaces.[1-3] Moreover, such wires often possesses a low dimensional long π-conjugation backbone that can carry electron in a molecular circuit through a distance of several nanometers.[4] However, directly addressing the conductivity of a distinct molecule, for instance, by assembling an electronic junction connected by the molecular wire, is still inconvenient for preliminary and fundamental studies, and interpretation of results is problematic. Therefore, an indirect approach using a donor-bridge-acceptor motif is still the most useful prototype for examination of the capability of a single molecule in supporting electron transfer. Molecules of this kind must not only satisfy the dimensional requirement, but also have the correct physical properties.

Electron transport across molecules is generally divided into two alternative types: *superexchange and hopping*. In the superexchange mechanism,[5, 6] the donor and acceptor orbitals are assumed to overlap with the highest occupied molecular orbital (HOMO) and lowest unoccupied molecular orbital (LUMO) of the bridging group, while the direct orbital overlaps between the donor and acceptor are negligible. Thus, the coupling between the donor and acceptor is furnished by indirect mixing of the donor and acceptor wave functions through the mediation of the bridging component. The efficiency

of such a mechanism is determined by the effective overlap between donor and acceptor. In the hopping mechanism, the electron (or hole) transiently resides on the midway bridging group so that a chemical intermediate is generated. Early works commonly treated them separately, but recent reports have also shown that both mechanisms can function at work simultaneously.[7-9]

Ferrocenes are ideal donor moieties, since, unlike conventional aromatics, the HOMO is localized not in the π-system, but in a non-bonding metal-centered d-orbital. Aside from that, the ease of the organic functionalization, the chemical stability of the neutral and charged species, the low oxidation potential to allow effective coupling with organic component, and the diamagnetism of the neutral state (thus enabling NMR characterization) have made ferrocenes one of the most employed candidates for implementing the wire-bridged complex. The mixed valence (MV) state of biferrocenyl complex is of most interest since the charge mobility in this system can be directly characterized by electrochemistry, X-ray structural analysis, electronic spectroscopy, ESR, Mossbauer spectroscopy, and other photophysical techniques.

Previously Tolbert and Zhao had shown that a solitonic-bridge, i.e., a polyenyl cation or anion, maintains electrical communication up to 13 carbon atoms.[10] However, the use of such bridges is complicated by the ionic nature of the substrates. In contrast, it has been very common to use a number of heteroatoms (silicon, phosphorus, or sulfur) to bind redox active molecules to surfaces. In this case, the pair of electrons on the heteroatom serves to substitute for the more mobile electron pair (or hole) within a soliton. Little discussion, however, has taken place over the nature of the conduction path. How well do such linking groups facilitate or block electronic communication? One of the most important targets of this study seeks to determine this effect.

Indeed, if we compare a diferrocenyl "soliton" molecule $(Fc(CH)_5Fc)^-$ with the isoelectronic molecule containing a heteroatom (**FcCH=CHXCH=CHFc**) instead, we see that the HOMO has a striking similarity to that for the solitonic molecule. However, the redox potential of the replacement group would be expected to have profound effects, as would the polarizability of the substituted group. We were concerned that the rather naïve views of resonance extant in the community lead to the assumption that resonance is equally effective whether through a double bond, a triple bond, heteroatom, an

aromatic ring, or a heteroaromatic ring. Since the range of molecules studied by various methods does not allow ready comparison, we determined to compare a range of molecular of type **FcCH=CHXCH=CHFc** in which a group X was varied across the common range of linking groups studied but for which the vinylene groups CH=CH served to minimize the steric effects which would otherwise intervene. According to the symmetrical structure, we gave this series of **FcCH=CHXCH=CHFc** compounds a generic applation in the form of **BFcVX**, where **BFcV** denotes the bis(2-ferrocenylvinyl) fragment and **X** stands for the central X functional atom/group.

In examining the capability of the bridging wire, -CH=CHXCH=CH-, in supporting intramolecular electronic interaction, our methods involve electrochemistry and near infrared (NIR) absorption spectroscopy of the mixed-valence species. If we considered a bis-ferrocenyl molecule for which the connecting bridge is insulating, then the half-wave potential of each ferrocene is identical and we observe a two-electron wave. Conversely, an effective bridge would alter the second half-wave potential, and the difference between the two potentials is an indication of the effectiveness of the wire. In addition, intervalence electron transfer can be detected and quantitatively studied from the characteristics of the intervalence band of mixed valence complexes. Basically, the intervalence transition is considered as a special case of charge transfer transition, the reduced site (Red) being the donor group, while the oxidized site (Ox) is the acceptor group. The mixing of the two electronic states Red-Ox and Ox-Red is due to an electronic coupling term V_{ab} which is also responsible of the intensity of the intervalence transition. Thus, V_{ab} and the derived delocalization parameter α can be determined by the following formulas[11, 12] according to Hush's theoretical treatment

$$V_{ab} = (2.05 \times 10^{-2}) (\nu_{max}.\varepsilon_{max}.\Delta\nu_{1/2})^{1/2}/R_{MM} \qquad (2.1)$$

$$\alpha = V_{ab}/\nu_{max} \qquad (2.2)$$

where V_{ab} is the coupling (cm^{-1}), ε_{max} is the maximum extinction coefficient, ν_{max} is the band position (cm^{-1}), $\Delta\nu_{1/2}$ is the full width at half-maximum (cm^{-1}), and R_{MM} is the metal-metal distance (Å).

As stated earlier, the effectiveness of certain organic wires using the prototype of binuclear complexes largely relies on the effective overlap between the d-orbital of the metal and the frontier p-orbital of the bridging fragment. We expect that electron transfer

from one metal to another to be more efficient when the energy gap between the metal orbital and organic fragment is narrowed, allowing enhanced charge delocalization. In the present series, the X group, in one sense, serves as an active gate for tuning the relevant energy levels. The consequential perturbation on the electronic properties could be revealed through current systematic studies.

Experimental

General Procedures

Purification of the different substrates was achieved by the following methods. Thin layer chromatography (TLC), which was used to monitor the progress of the reactions, was performed with Anatech precoated silica gel (SiO_2) GF plates with the R_f values obtained by the ratio of spot location to solvent front distance. Detection was accomplished by shortwave violet (UV) or iodine vapor. Column chromatography was carried out with use of silica gel (Scientific Absorbents, 20-50 μm), or alumina (Fisher, certified, 80-200 mesh) with neutral activity I which had been allowed to dry at 135 ^{o}C for at least 24 h immediately prior to use. A rotary evaporator was used to remove solvents *in vacuo* at reduced pressure achieved by Welch vacuum pump. Liquid were fractionally distilled under reduced pressure and were generally stored in a freezer at -30 ^{o}C. Solids were purified by either chromatography or recrystallization and dried at ca.1 torr pressure for at least 3 h. Melting points were determined on an Electrothermal capillary melting point apparatus and are reported uncorrected. Elemental analyses (EA) of new compounds were performed by Atlantic Microlab, Inc. (Norcross, Georgia). Molecular sieves (3Å and 4Å) used for adsorption of moisture in reagent storage and reactions were dried for at least two weeks at 135 ^{o}C.

All glassware including cannulas and syringes, were dried at 135 ^{o}C for at least 24 h prior to use. Anhydrous reaction conditions were established by allowing the glassware to cool under a gentle flow of argon, or in the case of syringes and cannulas, by allowing each to be flushed with argon immediately before sample introduction. In case of anaerobic reaction conditions, transfer of samples was generally conducted via stainless

steel cannulas or Hamilton gas-tight syringes. Inert conditions were maintained by an atmosphere of argon.

During the preparation of highly sensitive compounds, a number of operations were conducted in a vacuum atmosphere glove box, containing an atmosphere of argon. The atmosphere inside the glove box is constantly deoxygenated with a dry train contaning a BASF catalyst (R-311). The dry train was maintained by routine regeneration every two months. The glove box was flushed with argon (10-12 times of the volume of the dry box) prior to use if it has not been used for a long period of time or large quantity of solvent were used. Purified compounds were always stored under argon atmosphere in acid neutralized glassware and generally were kept in containers which allowed evacuation followed by argon purge. All samples were found to be reasonably stable when protected from light, air, and moisture.

Instrumentation

Infrared Spectroscopy:

Infrared, IR, spectra in the region of 2.5-25 μ (4,000 to 400 wave numbers, cm^{-1}) were recorded on a Nicolet 520 FTIR equipped with a Globar source and triglycine sulfate (TGS) detector. Liquids were run as a neat solution and solids as a potassion bromide (KBr) pellet.

Nuclear Magnetic Resonance Spectroscopy.

Nuclear magnetic resonance, NMR, spectra were recorded at ambient temperature in $CDCl_3$ (^1H 7.24 ppm), d_3-acetonitril (^1H 2. ppm), d_6-acetone (^1H 2.04 ppm) or Me_2SO-d_6 (^1H 2.49 ppm, ^{13}C 395. ppm) and chemical shifts were reported in ppm with the solvent peak as reference. The NMR spectra were recorded on a Varian Gemini 300 (^1H 300 MHz, ^{13}C 75.5 MHz) spectrometer furnished with a 5 mm probe or a Varian XL-400 (^1H 400 MHz, ^{13}C 100 MHz) spectrometer equipped with either a 5 mm or 10 mm probe. All ^{13}C were ^1H decoupled using WALTZ 16. Unless otherwise noted, all NMR spectra were recorded at ambient temperature. Variable temperature NMR experiments were conducted in a temperature range from -190 ^oC to +90 ^oC. When the temperature was changed, samples were allowed to equilibrate at that temperature for at least 15 min prior to spectral acquisition.

UV-Vis-NIR Spectroscopy

UV-Vis-NIR spectra were recorded on a Varian Cary 5E spectrophotometer, which has a scan range of 190 nm to 3000 nm. Spectra of the air stable compounds were conducted using a 1,000 $\pm$ 0.001 centimeter precision manufactured quartz cell and spectra for air sensitive compounds were recorded with a specially constructed, calibrated spectrophotometric cell. The cell walls were always gently wiped with laboratory tissue before spectral record. In all cases the spectra were recorded at 0.5 nm resolution with a scan increment of 0.5 or 1.0 nm and in the case of cations adjusted to correct for baseline.

For the intervalence absorption studies, a neutral substrate CH_2Cl_2 solution in a concentration ranging from 1 x 10^{-4} M to 4 x 10^{-4} M was made. To this solution, an oxidant (e.g. $FcPF_6$) in the solvent was added in 0.2-2.0 equivalents, the resulting solution was quickly mixed and immediately subjected to UV-Vis-NIR measurement under an argon protection. Generally, for each compound, a series of 5-10 progressive oxidation spectra were taken in order to determine the underlying mechanisms and the extinction coefficient.

Mass Spectrometry

Mass spectra, MS, were recorded using a VG analytical 70-SE spectrometer and are reported from electron ionization with the mass-to-charge ratio and the intensity indicated. High resolution mass spectra were used to determine the identity of the measured compounds. In some cases for the pure materials, both electron impact and chemical ionization methods were used in order to determine if the fragments and ratios obtained corresponded to only one particular compound with the same molecular weight.

Cyclic Voltammetry and Square Wave Voltammetry

Cyclic Voltammety (CV) and square wave voltammetry (SWV) were conducted with the standard three-electrode system, using a CHI 660 computer-controlled Electrochemical Workstation of CH Instruments, Inc. The three-electrode system consisted of a platinum button, with a size of 2 mm^2, as disk working electrode, a AgI/Ag reference electrode and a platinum wire as counter electrode. The potential scale was calibrated vs. the ferrocium/ferrocene couple. Freshly distilled methylene chloride was used as solvent. Supporting electrolytes included conventional tetrabutylammonium tetrafluoroborate (Bu_4NBF_4), tetrabutylammonium hexafluorophosphate (Bu_4NPF_6) and

self-synthesized tetrabutylammonium tetrakis(3,5-bis(trifluoromethyl)pheny1)borate (Bu_4NTFPB). Both Bu_4NBF_4 and Bu_4NPF_6 were purchased from Fluka as electrochemical grade reagent and used without further purification, however, highly purified Bu_4NTFPB was generally passed through an alumina column using anhydrous methylene chloride as eluent immediately before being applied to electrochemical studies.

All the experiments were carried out under an inert atmosphere. The solution systems in the electrochemical cell were bubbled with argon for at least 5 minutes before any measurement was taken. The scan rate of cyclic voltammetry ranged from 50 to 1000 mv/s to reveal the different reaction mechanisms. The sensitivity of square wave voltammetry was carefully tuned by changing the pulse width, i.e. frequency (e.g. 5 Hz), and pulse period. In most of the cases, the measurements were conducted at room temperature unless indicated otherwise.

Crystal Structure Analysis

A suitable crystal was coated with Paratone N oil, suspended in a small fiber loop and placed in a cooled nitrogen gas stream at 173 K on a Bruker D8 SMART APEX CCD sealed tube diffractometer with graphite monochromated MoK_α (0.71073Å) radiation. Data were measured using a series of combinations of phi and omega scans with 10 s frame exposures and 0.3^o frame widths.Data collection, indexing and initial cell refinements were all carried out using SMART[13] software. Frame integration and final cell refinements were done using SAINT[14] software. The final cell parameters were determined from least-squares refinement on F^2 reflections. The SADABS[15] program was used to carry out absorption corrections.

The structure was solved using Direct methods and difference Fourier techniques (SHELXTL, V6.12).[16] Hydrogen atoms were placed their expected chemical positions using the HFIX command and were included in the final cycles of least squares with isotropic U_{ij} 's related to the atom's ridden upon. The C-H distances were fixed at 0.93 Å(aromatic and amide), 0.98 Å (methine), 0.97 Å (methylene), or 0.96 Å (methyl). All non-hydrogen atoms were refined anisotropically. Scattering factors and anomalous dispersion corrections are taken from the *International Tables for X-ray*

Crystallography.[17] Structure solution, refinement, graphics and generation of publication materials were performed by using SHELXTL, V6.12 software.

All the crystal structure analyses were performed at X-ray Crystallography Center of Emory University, supervised by Dr. Kenneth Hardcastle.

Chemical Materials

All chemical materials were purchased from Aldrich and Acros if not otherwise stated. (Ferrocenylmethyl)triphenylphosphonium iodide ($FcCH_2PPh_3I$),[18] 1-ferrocenyl-2-bromoethene,[19] bis(diethylphosphinylmethyl)sulfide,[20] tetraethyl 1,4-xylylenediphosphonate,[21] tetraethyl 1,2-xylylenediphosphonate,[22] tetraethyl 1,3-xylylenediphosphonate,[23] tetraethyl 2,5-dimethoxy-1,4-xylylenediphosphonate,[24] tetraethyl 2,5-didodecyloxy-1,4-xylylenediphosphonate,[25] sodium tetrakis(3,5-bis(trifluoromethyl)phenyl)borate (NaTFPB),[26, 27] triphenylmethylium tetrakis(3,5-bis(trifluoromethyl)pheny1)borate (Trityl TFPB)[26] and ferrocenylvinylthiophene-2-yl-carbaldehyde[28] were synthesized according to the literature procedures.1,5-Diferrocenylpentadiene (**$BFcVCH_2$**) and 1,5-diferrocenylpentadienylium tetrafluoroborate (**$BFcVCH_2^+$**) were prepared following the synthetic procedures described in Dr. Xiaodong Zhao's Ph.D. thesis.[29]

Synthesis

1,4-Diferrocenylbuta-1,3-diene [$Fc(CH=CH)_2Fc$].

1,3-Dioxan-2-yl methyltributylphosphonium bromide.[30] A mixture of 2-bromomethyl-1,3-dioxolane (8.04 g, 46.2 mmol) and tri-*n*-butylphosphine (9.83 g, 46.2 mmol) was heated with an oil bath for 4 days at 90 ^oC. After cooling, an essentially quantitative yield of the desired phosphonium bromide was obtained as a colorless glass. No further purification is necessary, the reagent is used as a standard solution in anhydrous DMF for further reactions. ^1H NMR ($CDCl_3$): δ 5.25 (1H, t, J = 4.2 Hz), 3.9, 4.05 (4H, d), 3.08, 3.04 (2H, dd, J_{PCH} = 13.2 Hz, J = 4.2 Hz), 2.47 (6H, m), 1.48 (12H, m), 0.95 (9H, t, J = 6.9 Hz).

3-Ferrocenyl-2-propenal. Ferrocenecarboxaldehyde (2.14 g, 10 mmol) and 1,3-dioxan-2-yl methyltributylphosphonium bromide (11 mL of a 1.0 M solution in DMF, 11

mmol) were dissolved in dry DMF (100 mL) and heated with stirring to 80-90 °C. A solution of sodium ethoxide (12 mL of a 1.0 M solution in EtOH, 12 mmol) was then added dropwise over a period of 15 min, after which the reaction was heated at 90 °C for 48 h. The resulting mixture was poured into H_2O (ca. 200 mL) and then extracted with ethyl ether (4 x 150 mL) and the combined extract dried over $MgSO_4$. After filtration, the ether was removed under vacuum. The crude acetal was obtained as a dark red oil and was not purified further. It was dissolved in tetrahydrofuran (THF) (50 mL) to which a 5% aqueous solution of H_2SO_4 was then added (25 mL). After being stirred at 25 °C for 2 h, the mixture was poured into H_2O (*ca*. 200 mL), extracted with ethyl ether (3 x 150 mL), and then washed with brine (2 x 100 mL) and dried over $MgSO_4$. After filtration and removal of the ether, dark crude product was obtained, which was purified by chromatography over silica gel, eluting with 3% EtOAc in hexane. The product was obtained as dark red crystals (1.5 g, 63%); m.p. 92-94 °C. ^{1}H NMR ($CDCl_3$): δ 9.54 (1H, d, J = 7.7 Hz), 7.39-7.45 (1H, d, J = 15.6 Hz), 6.3-6.38 (1H, dd, J = 15.6, J = 7.7 Hz), 4.51 (4H, m), 4.17 (5H, s). ^{13}C NMR ($CDCl_3$): δ 193.47, 155.41, 126.56, 78.04, 72.23, 70.27, 69.51.

1,4-Diferrocenylbuta-1,3-diene [**Fc(CH=CH)$_2$Fc**]. To a suspension of ferrocenylmethyltriphenylphosphonium iodide (590 mg, 1 mmol) in dry THF (25 mL) at 0 °C under argon, was added potassium *tert*-butoxide (134 mg, 1.2 mmol, 20% excess) in one portion. The solution was stirred for 30 min, whereupon it turned rapidly from yellow to wine red, at this point, 3-ferrocenyl-2-propenal (240 mg, 1 mmol) was added as a solution in anhydrous THF (10 mL) via a cannula. The resultant mixture was slowly warmed to room temperature and stirred for ca. 3 h before 10 mL of water was introduced to quench the reaction. After being extracted with diethyl ether (3 x 25 mL), the organic extract was washed with saturated aqueous NaCl, dried over Na_2SO_4, and evaporated. The orange-red residue was purified by flash column chromatography on silica gel (CH_2Cl_2/hexane (1:3)) to yield a red solid (239 mg, 52%). The compound is stable in solid, however, more air sensitive in solutions. Obtained sample is a mixture of trans/cis isomers. ^{1}H NMR ($CDCl_3$): δ 6.09-6.02 (2H, m), 5.79, 5.74 (0.7H, two triplets, J = 6.9 Hz), 5.45, 5.41 (1.3H, two triplets, J = 6. 9 Hz), 4.30, 4.27 (4H, two triplets, J =1.8 Hz), 4.17, 4.14 (4H, two triplets, J = 1.8 Hz), 4.09, 4.08 (10H, two singlets). IR (KBr

pellet, cm^{-1}): 3078.3, 3025.1, 1610.9 (br), 1406.1(alkene C-H in-plane), 1102.5, 1042.8, 983.8, 836.6 (alkene C-H out-of-plane bend). MS m/e (intensity): 422 (100, M^+), 354 (10), 300 (11), 236 (10), 211 (16), 186 (12), 121 (14), 44(4).

1,6-Diferrocenylhexa-1,3,5-triene [Fc(CH=CH)$_3$Fc].

(*E*)-But-2-ene-1,4-diylbis(tributylphosphonium) dichloride. A mixture of tri-n-butylphosphine (7.1 mL, 28 mmol) and cis-1,4-dichloro-2-butene (1.5 mL, Acros) in dry xylene (30 mL) was stirred at room temperature under argon for 14 h. The resultant slurry was then heated under reflux for 4 h. After cooling, the mixture was allowed to settle into two layers. The top xylene layer was decanted, the heavy product layer was washed twice with comparable amount of hexane and evaporated to dryness, which afforded a colorless glass-like liquid (7.5 g, 100%). This phosphonium dichloride was dissolved into anhydrous methanol (20 mL) before being used for next reactions. ^{1}H NMR ($CDCl_3$): δ 6.50 (2H, br), 3.57 (4H, br), 2.39 (12H, m), 1.53 (24H, m), 0.97 (18H, t, J = 4.2 Hz).

1,6-Diferrocenylhexa-1,3,5-triene [**Fc(CH=CH)$_3$Fc**]**.** Ferrocenecarboxaldehyde (2.14 g, 10 mmol) and (*E*)-but-2-ene-1,4-diylbis(tributylphosphonium) dichloride (10 mL of a 0.5 M MeOH solution, 5 mmol) were placed in a 250 mL round bottom flask and dissolved in DMF (70 mL). A solution of sodium methoxide (11 mL of a 1.0 M solution in methanol, 11 mmol) was added dropwise with stirring, and the resulting mixture, stirred at 25 °C for 48 h and then at 90 °C for 2 h. After cooling to room temperature, the mixture was cooled at 0 °C in refrigerator for 1 day and filtered, yielding a red product which was purified by solvent extraction with EtOH for several hours followed by vacuum drying. Pure title compound was of metallic copper color (1.69 g, 75%), m.p. 190 °C. ^{1}H NMR ($CDCl_3$): δ 6.26 (2H, br), 6.11 (4H, br), 4.48 (4H, m), 4.36 (4H, m), 4.16 (10H, s). IR (KBr pellet, cm^{-1}): 3078.2, 2931, 1652.6, 1615.4(br), 1408.4, 1385.7, 1103.1, 998.4, 825.3, 477.2. MS m/e (intensity): 448.2 (100, M^+), 378 (8), 259.1 (48), 219 (27), 176.7 (70), 115.8 (22), 38.1 (14).

1,6-Diferrocenylhexa-3-yn-1,5-diene (BFcVC≡C). Cuprous iodide (7.6 mg, 0.04 mmol) was added to a mixture of bis(triphenylphosphine)palladium dichloride (56 mg, 0.08 mmol) and diethylamine (30 mL) solution of 1-ferrocenyl-2-bromoethene (1.16 g, 4 mmol) under an argon atmosphere in a flask equipped with a gas inlet needle and a magnetic stirrer. A slow current of acetylene was passed through the reaction mixture for

8 h at room temperature, the reaction completion was monitored by TLC. After removal of diethylamine under reduced pressure, water (30 mL) was added to the residue. The mixture was extracted with methylene chloride (3 x 30 mL), dried over $MgSO_4$ and evaporated. The residue was purified by column chromatography on silica gel using hexane to elute the remained ferrocenyl bromoethene, hexane/CH_2Cl_2 to elute the desired compound as a deep red solid (0.76 g, 85%). The NMR indicated a mixture of cis/trans isomers. ^{1}H NMR ($CDCl_3$): 7.0-6.45 (2H, m) [6.87 (d, J = 15.6 Hz), 6.70 (d, J = 15.3 Hz), 6.56 (d, J = 11.7 Hz), 6.41 (d, J = 11.7 Hz)], 6.0-5.5 (2H, m) [5.89 (d, J = 15.3 Hz), 6.87 (d, J = 15.6 Hz), 5.60 (d, J = 11.7 Hz), 5.53 (d, J = 11.7 Hz)], 4.8 (1.5H, t, J = 1.8 Hz), 4.42-4.29 (6.5H, m), 4.19, 4.17, 4.16 (10H, 3 singlets). ^{13}C NMR ($CDCl_3$): δ 144.2, 139.9, 137.8, 105.5, 104.7, 103.7, 90.7, 82.6, 82.3, 81.3, 75.3, 70.3, 69.9, 69.7, 67.3, 67.0. IR (KBr pellet, cm^{-1}): 3088.7w, 3024.0w, 2173.5w, 2119.5m, 1716.9 (br), 1599.9m, 1408.8w, 1285.9m, 1245.6m, 1102.9m, 1027.4m, 998.8m, 945.7m, 814.2s, 503.0s. MS m/e (intensity): 446.1 (100, M^+), 379 (5), 324 (8), 260.1 (7), 223.1 (21), 186 (7), 121 (7), 57.1 (46), 43(6). Exact mass for $C_{26}H_{22}Fe_2$: 446.04203 observed: 446.04107.

Sonogashira, K.; Tohda, Y.; and Hagihara N.; Tetrahedron Letters, 1975, 4467-4470.
Stephans, R. D.; Castro, C. E., J. Org. Chem. (28), 1963, 3313.

1,6-Diferrocenylhexa-1,5-diene ($BFcVC_2H_4$).

Tetramethylene bis(triphenylphosphonium) bromide. A solution of 1,4-dibromobutane (4.3 g, 20 mmol) and triphenylphosphine (13.62 g, 52 mmol, 30% excess) in dimethyl formamide (DMF) (150 mL) was heated under reflux for 12 h. After a while, white crystals began to separate from the solution. The precipitate was collected, washed with petroleum ether. The solid was then dissolved in hot methylene chloride and crystallized by slow addition of hexane. The final product was obtained as white crystals (11.7 g, 79%). The compound was dried under vacuum at 110 ^{o}C for 24 h. before being used, m.p. 287-289 ^{o}C. ^{1}H NMR ($CDCl_3$): δ 7.94-7.86 (12H, m), 7.75-7.63 (18H, m), 4.05 (4H, br), 2.44 (4H, br).

1,6-Diferrocenylhexa-1,5-diene (**$BFcVC_2H_4$**). To a suspension of tetramethylene bis(triphenylphosphonium) bromide (0.74 g, 1 mmol) in dry THF (30 mL) maintained at –78 ^{o}C was added n-buthyllithium (1.5 mL of a 1.6 M solution in hexane, 2.4 mmol). The resulting yellow colored solution was stirred for 30 min at –78 ^{o}C, and at room

temperature for 2 h. The orange suspension was added to a solution of ferrocenecarboxaldehyde (0.43 g, 2 mmol) in THF (10 mL) at – 78 ^{o}C. The red mixture was stirred at –78 ^{o}C for 2 h, gradually warmed to room temperature and stirred for another two hours before being quenched by the addition of water (10 mL). The volatile solvent was evaporated under reduced pressure. The resulting aqueous solution was diluted with 30 mL of water and extracted with chloroform (3 x 30 mL). The organic layers were combined, dried over $MgSO_4$, and evaporated. Purification was achieved by chromatography of the crude material on silica gel using chloroform as the eluent. The first band was collected and concentrated to afford an orange-red solid (0.38 g, 85%). m.p. 77-78 ^{o}C. ^{1}H NMR ($CDCl_3$): 6.11 (2H, d, J = 11.1 Hz), 5.84 (0.5H, m), 5.51 (1.5H, m), 4.34 (3H, t, J = 1.8 Hz), 4.30 (1H, t, J = 1.8 Hz), 4.20 (3H, t, J = 1.8 Hz), 4.16 (1H, t, J = 1.8 Hz), 2.40 (3H, td, major), 2.22 (1H, m, minor). IR (KBr pellet, cm^{-1}): 3092.7w, 2921.9w, 1718.4w(br), 1645.7w, 1466w, 1409w, 1197.5w, 1104.1m, 1045m, 999.8m, 807.5s(br), 769.4s, 472.5s. MS m/e (intensity): 450.2 (100, M^+), 448.2 (14.5), 220 (100), 152.6 (16), 115.8 (32), 58 (3.5). Exact mass for $C_{26}H_{26}Fe_2$: 450.07333; observed: 450.07163.

The NMR indicated a mixture of cis/trans isomers, with cis configuration as a major component.

Bis(2-ferrocenylvinyl)sulfide (BFcVS).

Method A: Conventional Wittig reaction procedures.

Dimethylthioether-a,a'-bis(triphenylphosphonium) bromide. This phosphonium salt was prepared by modifying the literature procedure.[31] Triphenylphosphine (10.5 g, 40 mmol) and bis(chloromethyl)sulfide (TCI, 97%) (2.62 g, 20 mmol) were mixed into a 100 mL flask and heated slowly to 150 ^{o}C in a silicone oil bath with stirring by a glass rod. The reaction was remained at this temperature for 45 min. The resultant light-brown solid was then heated at reflux three times with 30 mL 5% aqueous HCl, during which the triphenylphosphine remained undissolved. The filtered solution was stirred with active charcol, filtered, and then treated with saturated solution of KBr, which caused immediate precipitation in large amount. The solid was filtered and crystallized from H_2O to afford a colorless crystalline solid (4.3 g, 30%). The compound was dried under vacuum at 110 ^{o}C for at least two days before being used; m.p. 302-304 ^{o}C, lit. [31] 302-

304 °C. ^{1}H NMR ($CDCl_3$): δ 7.66-7.75 (18H, m), 7.77-7.97 (12H, m), 5.64 (4H, d, J = 9.3 Hz).

Bis(2-ferrocenylvinyl)sulfide (**BFcVS).** To a suspension of dimethylthioether-a,a'-bis(triphenylphosphonium) bromide (1.86 g, 2.5 mmol) and ferrocencarboxaldehyde (1.07 g, 5 mmol) in anhydrous MeOH (20 mL) at 0°C, was added sodium methoxide (11mL of a 0.5M solution in MeOH, 5.5 mmol) under argon with stirring. The mixture was brought to room temperature, red solid started to separate from the solution upon 2 h stirring. After stirred for 4 more hours, the solution was concentrated to about 10 mL, cooled at 0°C, and filtered to result in an orange powder which was washed twice with 5 mL petroleum ether. Further purification was achieved by recrystallization the crude product from MeOH to yield the title compound as a red crystalline solid (0.93 g, 81%). It is a cis/trans mixuture. m.p. 135-142 °C. ^{1}H NMR ($CDCl_3$): δ 6.389 (ca. 1.2H, d, J_{trans} = 15 Hz), 6.381 (0.4H, d, J = 5.2 Hz), 6.27 (1.2 H, d, J_{trans} = 15 Hz), 6.24 (0.6H, d, J_{cis} = 10.5 Hz), 6.12 (0.6H, d, J_{cis} = 10.5 Hz), 4.54 (1.2H, t, small), 4.36-4.32, 4.26-4.23 (6.8H, m), 4.15, 4.14 (10H, 2 singlets). ^{13}C NMR ($CDCl_3$): δ 129.8, 128.3, 125.6, 120.8, 119.5, 117.9, 83.1, 81.2, 69.5, 69.2, 69.0, 66.7, 66.5. IR (KBr pellet, cm^{-1}): 3085.2, 3018.5, 1635.3 (br), 1594, 1408.8, 1246.6, 1103, 1043.1, 930.2, 808.6, 722.9, 484.4. MS m/e (intensity): 454 (100, M^+), 301.1 (59), 274 (7), 227 (16), 186 (28), 121 (16), 56 (3.5). Exact mass for $C_{24}H_{22}Fe_2S$: 454.01410; observed: 454.00929. Anal. Calcd for $C_{24}H_{22}Fe_2S$: C, 63.49; H, 4.88; S, 7.06. Found: C, 63.24; H, 4.99; S, 7.01.

Method B: Horner-Wadsworth-Emmons (HWE) reaction procedures affording exclusive (*E,E*)-product.

Bis(diethylphosphinylmethyl)sulfide. A mixture of bis(chloromethyl)sulfide (5.24 g, 40 mmol) and an excess of triethylphosphite (19.9 g, 120 mmol) was heated slowly to 170 °C under an air-condenser whose effluent led to an ice-cooled dewar condenser, and the evolving ethyl chloride was distilled off simultaneously. After heating at the same temperature overnight, vacuum was applied at 180 °C to distill off the excess of triethylphosphite. The resulting oil was purified by distillation to afford a colorless oil (10 g, 75%), lit.[20] b.p. 172-176 °C/0.2 torr.

(*E,E*)-Bis(2-ferrocenylvinyl)sulfide [**(*E,E*)-BFcVS**]**.** To a suspension of NaH (0.2 g, 4.8 mmol of a 60% suspension in oil, washed with hexane) in dry THF (20 mL) was

added bis(diethylphosphinylmethyl)sulfide (735 mg, 2 mmol) in THF (20 mL), and after 10 min. a solution of ferrocenecarboxaldehyde (856 mg, 4 mmol) in THF (15 mL). The reaction mixture was heated at reflux under vigorous stirring for 8 h, cooled to room temperature, water (30 mL) was added to quench the reaction. After the volatile solvent was removed under vacuum, the aqueous solution was extracted with chloroform (3 x 30 mL). The organic layer was dried over $MgSO_4$, and evaporated under reduced pressure. The residue was purified by silica gel column chromatography, eluting with CH_2Cl_2/hexane (1:1). The first red band was collected and concentrated to afford a orange red crystalline solid (581 mg, 64%). The trace amount of non-(*E,E*) isomers (ca. 2-5%) could be easily separated by recrystallizing the mixture from acetone, which was isolated from the solution first. (*E,E*)-isomer: ^{1}H NMR (CD_3CN): δ 6.47 (4H, s), 4.43 (4H, t, J = 1.8 Hz), 4.27 (4H, t, J = 1.8 Hz), 4.17 (10H, s). ^{1}H NMR (Acetone-d_6): δ 6.57 (4H, s), 4.53 (4H, t, J = 1.8 Hz), 4.37 (4H, t, J = 1.8 Hz), 4.28 (10H, s). ^{13}C NMR (CD_2Cl_2): E/E isomer: δ 128.80, 117.12, 82.27, 68.67, 68.31, 65.84. IR (neat, cm^{-1}): 3084.9m, 3018.1m, 2920.6w, 1718.4m (br), 1591.3m, 1406.7m, 1372.2m, 1241.9m, 1101.1s, 996.0m, 926.8s, 803.8s, 497.1s.

Bis(4-ferrocenylbutadienyl)sulfide (BFcVCH=CHSCH=CH). To a suspension of dimethylthioether-a,a'-bis(triphenylphosphonium) bromide (0.74 g, 1 mmol) and 3-ferrocenylpropenal (0.48 g, 2 mmol) in anhydrous MeOH (10 mL) at 0 ^{o}C, was added sodium methoxide (4.6 mL of a 0.5 M solution in MeOH, 2.3 mmol) under argon with stirring. The mixture was brought to room temperature, red solid started to separate from the solution upon 2 h stirring. After stirred for 6 more hours, the solution was concentrated to about 5 mL, cooled at 0 ^{o}C. The precipitate was filtered, washed with water (10 mL), cold methanol (5 mL) and petroleum ether. The red residue was purified by silica gel flash column chromatography, eluting with CH_2Cl_2. The first red band was collected and concentrated to afford a deep red solid (0.36 g, 71%); m.p. 152-154 ^{o}C. ^{1}H NMR ($CDCl_3$): δ 6.0-6.6 (8H, m), 4.37-4.43, 4.35, 4.27 (8H, m), 4.18 (10H, m). ^{13}C NMR ($CDCl_3$): δ 133.2, 132.1, 130.3, 129.7, 128.7, 125.6, 123.3, 122.1, 120.3, 83.3, 82.9, 69.5, 69.3, 68.5, 67.2, 67.1, 66.9. IR (KBr pellet, cm^{-1}): 3088.7, 3018.3, 2360.8, 1616.5, 1569.7, 1409.2, 1242.8, 1104.1, 1000.1, 930.4, 809.5, 766.1, 729.5. MS m/e

(intensity): 506.1 (100, M^+), 422.1(21), 286.6 (22), 250.4 (18), 176.7 (23), 115.8 (19), 58.9 (5). Exact mass for $C_{28}H_{26}Fe_2S$: 506.04540, observed: 506.04692.

Bis(2-ferrocenylvinyl) ether (BFcVO).

Bis(bromomethyl)ether. The compound was prepared by modifying the literature procedure.[32] To a 250 mL three neck round-bottom flask, equipped with an addition funnel, charged with water (3 mL), bromine (~50 g, 0.31 mol) was slowly added during 30 min with mild stirring at 0 ^oC. A mixture of paraformaldehyde (10 g, 0.33 mol) and red phosphorus (2.4 g, 0.077 mol) was then added spatula by spatula (very exothermic! frequently caused flame and smoke during the addition.) until no obvious reaction was observed. The two-layer product was closed and set aside for 1 day. The heavy crude ether layer was then separated, washed with water and saturated aqueous $Na_2S_2O_4$ solution several times to remove the unreacted bromine. After final extraction with ethyl ether, the organic layer was dried over Na_2SO_4 and evaporated under vacuum to give a pale yellow liquid product (16.5 g), which was dried by P_2O_5 for 1 day. The liquid turned to be spectroscopically pure (by NMR) and was used without further purification. b.p. 146-159 ^oC. ^1H NMR ($CDCl_3$): δ 5.68 (4H, s).

Dimethylether-a,a'-bis(triphenylphosphonium) bromide. The compound was synthesized by modifying literature procedure.[31] Triphenylphosphine (17.1 g, 65 mmol) were combined with bis(bromomethyl) ether (6.12g, 30 mmol) in a wide-necked flask and heated in an oil bath with stirring by a glass rod. At 100 ^oC, the mixture started to solidify and after 30 min at 180 ^oC, the formation of the salt was completed. The brown salt was heated at reflux with anhydrous benzene for 2 h, and filtered after cooling. The resulting powder was dissolved in $CHCl_3$, boiled 1 h with active charcoal, concentrated to minimum volume and allowed to crystallize in refrigerator overnight to yield a pale yellow crystal (18.6 g, 85%). The compound was vacuum-dried at 110 ^oC for one day before being used; m.p. 285-290 ^oC, lit.[31] 290-294 ^oC. ^1H NMR ($CDCl_3$): δ 7.74-7.85 (18H, m), 7.53-7.60 (12H, m), 6.81 (4H, d, J = 6 Hz).

Bis(2-ferrocenylvinyl)ether (**BFcVO**). In a round-bottom flask equipped with a reflux condenser, thoroughly dried ether bisphosphonium bromide above (0.72 g, 1 mmol) were dissolved in 15 mL absolute MeOH under argon. Sodium methoxide (4.6 mL of a 0.5 M solution in MeOH) was added dropwise to the stirred solution, followed

by addition of ferrocenecarboxaldehyde (428 mg, 2 mmol) in THF (5mL). The reaction mixture was then heated at reflux for 16 h and monitored by TLC for the completion. After cooling and evaporation of the solvent, the residue was dissolved in ethyl ether, washed in turn with water and brine, dried over Na_2SO_4 and concentrated under reduced pressure. The targeted compound was obtained by silica gel column chromatography with CH_2Cl_2/hexane (1:1) or ethyl acetate/hexane (2:8) as eluent, which is a brown solid (yield 52%) and identified as a *cis/trans* isomeric mixture by NMR. MS m/e (intensity): 438.1 (100, M^+), 342 (11), 212.1 (21), 176.6 (15), 115.8 (24), 58 (5). Exact mass for $C_{24}H_{22}OFe_2$: 438.03694; observed: 438.03724.

Bis(2-ferrocenylvinyl)selenide (BFcVSe).

Bis(diethylphosphomethyl)selenide.[33, 34] Diethyl iodomethylphosphonate (Acros) (4.9 g, 17.6 mmol) in 15 mL of dry THF was added to a suspension of Na_2Se (Alfa Aesar, 99.8%) (1.3 g, 10.4 mmol) in THF (10 mL) under argon. The resulting solution was stirred at room temperature for 2 h, then treated with 30 mL of water. After filtration (to remove the red selenium by-product), the filtrate was extracted with diethyl ether (3 x 30 mL). The combined organics were washed with brine, dried over $MgSO_4$ and evaporated under vacuum. The residue was purified by silica gel column chromatography, eluting with hexane/ethyl acetate (7:3) to afford a colorless oil (2.96 g, 88.6%). ^{1}H NMR ($CDCl_3$): δ 4.10 (8H, dq, $J_{P,H}$ = 8 Hz，$J_{H,H}$ = 7 Hz), 2.92 (4H, d, $J_{P,H}$ = 11 Hz), 1.33 (12H, t, J = 7 Hz).

(*E,E*)-Bis(2-ferrocenylvinyl)selenide (**BFcVSe**). To a suspension of NaH (0.2 g, 4.8 mmol of a 60% suspension in oil, washed with hexane) in dry THF (20 mL) was added bis(diethylphosphomethyl)selenide (0.77 g, 2 mmol) in THF (20 mL), hydrogen evolution was immediately observed upon the addition. After 10 min, ferrocenecarboxaldehyde (0.86 g, 4 mmol) in THF/HMPA (10mL/2mL) was added. The reaction mixture was heated at reflux for 2 h, cooled to room temperature, diluted with ether 40 mL ether, washed with saturated aqueous NH_4Cl, dried over Na_2SO_4 and evaporated. The dark residue was purified by silica gel column chromatography, eluting with CH_2Cl_2. The first yellow band was collected, concentrated to yield an orange-red solid (0.67 g, 67%); m.p. 110-112 ^{o}C. ^{1}H NMR ($CDCl_3$): δ 6.65 (d, minor), 6.61 (4H, d, J =2 Hz), 4.36 (4H, t, J = 1.8 Hz), 4.24 (4H, t, J = 1.8 Hz), 4.15 (5H, s). ^{13}C NMR ($CDCl_3$):

δ 134.0, 113.1, 83.5, 69.5, 69.1, 66.7. IR (KBr pellet, cm^{-1}): 3088.8, 3018.9, 1639.2, 1596.2, 1409.1, 1219.9, 1104, 1041.3, 945.3, 809.3, 481.1. MS m/e (intensity): 502 (40, M^+), 422 (15), 301.1 (100), 212 (19), 186 (28), 121 (19), 44.9 (8). Exact mass for $C_{24}H_{22}Fe_2Se$: 501.95855, observed: 501.95885. Anal. Calcd for $C_{24}H_{22}Fe_2Se$: C, 57.42; H, 4.42. Found: C, 57.04; H, 4.45.

Bis(2-ferrocenylvinyl)phenylphosphine (BFcVPPh).

1,1-Dichloro-2-ferrocenylethene.[35] To a solution of ferrocenecarboxaldehyde (4.28 g, 20 mmol) and triphenylphosphine (20.96 g, 80 mmol) in anhydrous acetonitrile (60 mL) at 0 ^oC under argon atmosphere, CCl_4 (6.15 g, 40 mmol) was added in one portion. The mixture was allowed to reach room temperature and stirred for one hour. Then the dark solution was poured into 200 mL water and extracted with ether (3 x 100 mL). The organic layer was washed with brine, dried over Na_2SO_4 and evaporated under vacuum. The residue was flash-chromatographed on a silica gel column with CH_2Cl_2/hexane (1:1) as eluent, which afforded a light brown crystalline solid (3.85g, 69%). The reaction was ran for several times, but never reached the literature yield (85%). ^1H NMR ($CDCl_3$): δ 6.52 (1H, s), 4.57 (2H, t), 4.28 (2H, t), 4.17 (5H, s).

Ethynylferrocene.[35] To a solution of 1,1-dichloro-2-ferrocenylethene (2.52 g, 9 mmol) in dry THF (15 mL) at 0 ^oC, *n*-BuLi (12.4 mL of a 1.6 M solution in hexane, 19.8 mmol) was slowly added under stirring. The reaction mixture was brought to room temperature and stirred for 15 minutes until the reaction was complete (monitored by TLC), then 20 mL of water was added into it. The resultant solution was extracted with diethyl ether and dried over Na_2SO_4. After column chromatography on silica gel ($CHCl_3$), 1.55 g red crystalline solid was obtained with 82% yield. ^1H NMR ($CDCl_3$): δ 4.46 (2H, t, J = 1.8 Hz), 4.22 (5H, s), 4.19 (2H, t, J = 1.8 Hz), 2.72 (1H, s).

Bis(2-ferrocenylvinyl)phenylphosphine (**BFcVPPh**). To a solution of ethynylferrocene (1.05 g, 5 mmol) and AIBN (32.8 mg, 0.2 mmol) in anhydrous toluene in a pyrex vial, phenylphosphine (Strem Chemicals, 99%) (0.275 mL, 2.5 mmol, with extremely unpleasant smell) was quickly added under argon. The system was sealed and heated with oil bath at 60 ^oC for 48 h. After removal of the solvent, the residue was purified by chromatography on silica gel using $CHCl_3$/hexane (1:2) as eluent. The first band was collected and evaporated under reduced pressure to give a bright red crystalline

solid product (0.98 g, 74%). The NMR and TLC both indicated a mixture of trans/trans, cis/trans and cis/cis isomers. Unfortunately they are very difficult to be separated. (E,E)-isomer: ^{1}H NMR($CDCl_3$): δ 7.56-7.51 (2H, m), 7.37-7.29 (3H, m), 7.02-6.9 (2H, dd, *J* = 12.6, 26.4$_{(HP)}$ Hz, vinyl), 6.06-6.01 (2H, dd, *J* = 12.6, 3.0$_{(HP)}$ Hz, vinyl), 4.69 (4H, t, *J* =1.8 Hz), 4.27 (4H, t, *J* = 1.8 Hz), 4.12 (10H, s). ^{13}C NMR (75 MHz, $CDCl_3$): δ 141.69 (d, *Jcp* = 20.5 Hz) , 131.63 (d, *Jcp* = 17.1 Hz), 131.21 (d, *Jcp* = 16.5 Hz), 128.62 (d, *Jcp* = 5.1 Hz), 127.89, 126.28 (d, *Jcp* = 13.1 Hz), 81.81 (d, *Jcp* = 3.4 Hz), 70.81 (d, *Jcp* = 10.3 Hz) , 70.4(d, *Jcp* = 11.4 Hz), 69.51. IR (KBr pellet, cm^{-1}): 3087.9, 2986.4, 2923.6, 1700.14, 1592.1(br), 1452.8, 1255.4, 1103, 998.6, 816.1, 744.2, 480.7. MS m/e (intensity): 530.1 (100, M^+), 465.1 (12.5), 422 (33), 265 (9.4), 211.1 (17), 121 (8), 57.1 (4), 43 (3). Exact mass for $C_{30}H_{27}Fe_2P$: 530.05492, observed: 530.05627. Anal. Calcd for $C_{30}H_{27}Fe_2P$: C, 67.98; H, 5.13. Found: C, 67.72; H, 5.18.

Bis(2-ferrocenylvinyl)phenylphosphine Sulfide [BFcVP(S)Ph]. To a solution of bis(2-ferrocenylvinyl)phenylphosphine (**BFcVPPh**) (133 mg, 0.25 mmol) in anhydrous THF (10 mL) was added elemental sulfur (32 mg, 1 mmol). The reaction mixture was stirred overnight under argon and filtered. After removing the volatile solvent of the filtrate under reduced pressure, the residue was subjected to column chromatography on silica gel using CH_2Cl_2/hexane (1:1) as eluent. The title compound was obtained as a red crystalline solid (134 mg, 95%). (Z,Z)-isomer: ^{1}H NMR ($CDCl_3$): δ 8.03-7.96 (2H, m), 7.52-7.48 (3H, m), 7.0-6.8 (2H, dd, J = 13.5, 43.8$_{(HP)}$ Hz, vinyl), 6.0-5.89 (2H, dd, *J* = 13.5, 19.8$_{(HP)}$ Hz, vinyl), 4.89 (2H, m), 4.58 (2H, m), 4.28 (2H, m), 4.23 (2H, m), 4.08 (10H, s). ^{13}C NMR (75 MHz, $CDCl_3$) δ 144.64, 134.21 (d, *Jcp* = 85.6 Hz), 131.55 (d, *Jcp* = 10.8 Hz), 130.84 (d, *Jcp* = 10.3 Hz), 128.38 (d, *Jcp* = 12.6 Hz), 118.87 (d, *Jcp* = 83.8 Hz), 78.72 (d, *Jcp* = 8.0 Hz), 72.30 (d, *Jcp* = 23.4 Hz), 70.53(d, *Jcp* = 26.8 Hz), 69.71. IR (neat, cm^{-1}): 3082.9m, 2923.4w, 1584.4s, 1434.8m, 1264.5m, 1103.7s, 1041.6m, 998.9s, 815.3s, 735.8s, 691.4s, 669.4s. MS m/e (intensity): 562 (100, M^+), 497 (85), 432 (12), 319.1 (17), 299 (15), 121 (8), 57.3 (36), 43.8 (18). Exact mass for $C_{30}H_{27}SFe_2P$: 562.02652, observed: 562.02699.

Bis(2-ferrocenylvinyl)phenylphosphine Oxide [BFcVP(O)Ph]. To a solution of bis(2-ferrocenylvinyl)phenylphosphine (**BFcVPPh**) (133 mg, 0.25 mmol) in anhydrous THF (10 mL) was added iodine (63 mg, 0.25 mmol) in one portion and three drops of

water. The reaction mixture was stirred overnight, the completion of the reaction was monitored by TLC. After filtration and removing the volatile solvent of the filtrate under reduced pressure, the residue was subjected to column chromatography on silica gel using CH_2Cl_2 and CH_2Cl_2/ether (9:1) as eluent. The title compound was obtained as an orange red solid (100 mg, 73%) and identified as exclusive (*E,E*)-isomer by NMR. ^{1}H NMR($CDCl_3$): δ 7.82-7.75 (2H, ddd, J = 9.0 $_{(HP)}$, 4.2, 1.8 Hz), 7.52-7.48 (3H, m), 7.35 (2H, dd, J = 17.1, 19.5$_{(HP)}$ Hz, vinyl), 6.21 (2H, dd, *J* = 17.1, 22.2$_{(HP)}$ Hz, vinyl), 4.49 (4H, t, J =1.8 Hz), 4.37 (4H, t, J = 1.8 Hz), 4.15 (10H, s). ^{13}C NMR (75 MHz, $CDCl_3$) δ 147.28 (d, *Jcp* = 4.5 Hz), 133.39 (d, *Jcp* = 106 Hz), 131.77 (d, *Jcp* = 2.3 Hz), 130.90 (d, *Jcp* = 9.6 Hz), 128.78 (d, *Jcp* = 11.9 Hz), 115.21 (d, *Jcp* = 107.8 Hz), 80.26 (d, *Jcp* = 20.5 Hz), 70.76, 69.81, 69.36 (d, *Jcp* = 6.3 Hz). IR (neat, cm^{-1}): 3076.6w, 2947.2w, 1769.4m, 1715.0m, 1602.3s, 1434.9m, 1236.9m, 1171.1s, 1104.9s, 1064.7m, 997.3m, 974.9m, 854.2s, 743.4s, 722.1s, 693.2s. MS m/e (intensity): 546 (93, M^+), 481 (100), 389 (18), 273 (13), 208 (22), 121 (8). Exact mass for $C_{30}H_{27}OFe_2P$: 546.04902, observed: 546.04983.

1,5-Diferrocenylpenta-1,4-diene-3-one [BFcVC(O)].

2-Acetylvinylferrocene [FcCH=CHC(O)Me]. An aqueous solution of KOH (20 mL of a 2 M solution) was added at 0 ^{o}C to a solution of ferrocenecarboxaldehyde (1.98 g, 9.25 mmol) in acetone (40 mL). The reaction mixture was stirred for 2 h at 0 ^{o}C and poured into cold water. The precipitate was filtered off and dried in air. The crude product was passed through a short silica gel column (1:1 hexane/CH_2Cl_2) to afford a red crystalline solid (2.05g, 88%); m.p. 78-80 ^{o}C. ^{1}H NMR ($CDCl_3$): δ 7.4 (1H, d, J = 16 Hz), 6.31 (1H, d, J = 16 Hz), 4.51 (2H, t, J = 2 Hz), 4.49 (2H, t, J = 2 Hz), 4.16 (5H, s), 2.29 (3H, s)..

1,5-Diferrocenylpenta-1,4-diene-3-one [**BFcVC(O)**]. Method A: A solution of ferrocenecarboxaldehyde (0.86 g, 4 mmol), 2-acetylvinylferrocene (1.02 g, 4 mmol), and potassium hydroxide (1.5 g) in ethanol was heated at 60 ^{o}C for 8 h under an argon atmosphere. The completion of the reaction was monitored by TLC. After the crude product was filtered off, washed with water, ethanol, and ether, and then dried, the title compound was obtained as a purple red solid (1.45 g, 80%). Silica gel column with $CHCl_3$ may be necessary to achieve the analytically pure sample; m.p. 169-171 ^{o}C. ^{1}H

NMR ($CDCl_3$): δ 7.6 (2H, d, J = 15.9 Hz), 6.58 (2H, d, J = 15.9 Hz), 4.56 (4H, t, J = 1.8 Hz), 4.45 (4H, d, J = 1.8 Hz), 4.18 (10H, s). ^{13}C NMR ($CDCl_3$): δ 187.6, 144.4, 123.5, 79.6, 71.5, 70.0, 69.1. IR (KBr pellet, cm^{-1}): 3095.2w, 1661.6m, 1638.6s, 1611.8s, 1573.6s, 1395.8m, 1276.9m, 1206.7m, 1166.4m, 1104.5m, 999.5m, 981.7m, 817.5s, 477.2s. MS m/e (intensity): 450.1 (100, M^+), 385 (48), 290.9 (6.5), 220 (12), 176.7 (8), 115.8 (17), 38.1 (7).

Method B:[36] A solution of ferrocenecarboxaldehyde (0.86 g, 4 mmol), acetone (0.116 g, 2 mmol), and potassium hydroxide (1.5 g) in ethanol was heated at 60 ^oC for 8 h under an argon atmosphere. The completion of the reaction was monitored by TLC. After the crude product was filtered off, washed with water, ethanol, and ether, and then dried, the title compound was obtained as a purple red solid (1.14 g, 62%).

1,4-Bis(2-ferrocenylvinyl)benzene (BFcV*p*Ph).

Method A: Conventional Wittig reaction approach.

p-Xylylene-bis(triphenylphosphonium bromide).[37] A solution of α,α'-dibromo-*p*-xylene (5.28 g, 20 mmol) and triphenylphosphine (13.62 g, 52 mmol, 30% excess) in dry xylene (150 mL) was heated under reflux for 12 h. After a while, white crystals began to separate from the solution. The precipitate was collected, washed with dry xylene and petroleum ether. The solid was then dissolved in hot chloroform and crystallized by slow addition of hexane. The final product was obtained as white crystals (13.1 g, 83%). The compound was dried under vacuum at 110 ^oC for 24 h. before being used, m.p. 275-278 ^oC. ^1H NMR ($CDCl_3$): δ 7.77-7.71 (12H, m), 7.68-7.64 (18H, m), 6.91 (4H, s), 5.38 (4H, d, J = 13.5 Hz).

1,4-Bis(2-ferrocenylvinyl)benzene **(BFcV*p*Ph).** To a suspension of *p*-xylylene-bis(triphenylphosphonium bromide) (1.58 g, 2 mmol) and ferrocencarboxaldehyde (0.94 g, 4.4 mmol) in anhydrous MeOH (20 mL) at 0 ^oC, was added sodium methoxide (9.6 mL of a 0.5M solution in MeOH, 4.8 mmol) under argon with stirring. The mixture was brought to room temperature and stirred for 10 hours before it was concentrated to about 10 mL and cooled at 0 ^oC. The resultant red solid was filtered and washed with 10 mL petroleum ether. Recrystallization of the crude product from benzene yielded a red crystalline solid (0.72 g, 72%). This turned to be a mixture of three cis/trans isomers (by TLC), which could be separated by column chromatography on silica gel, eluting with

$CHCl_3$/hexane (1:5). The first band was collected as the pure trans/trans isomer. m.p. > 180 °C, decomposed. ^{1}H NMR ($CDCl_3$): (*E,E*)-isomer δ 7.40 (4H, s), 6.91-6.86 (2H, d, J = 15.9 Hz), 6.72-6.66 (2H, d, J = 15.9 Hz), 4.48 (4H, t, J = 1.8 Hz), 4.29 (4H, t, J = 1.8 Hz), 4.15 (10H, s); cis-cis isomer δ 7.329 (4H, s), 6.42-6.38 (2H, d, J = 11.7 Hz), 6.32-6.29 (2H, d, J = 11.7 Hz), 4.20 (4H, t, J = 1.8 Hz), 4.16 (4H, t, J = 1.8 Hz), 4.11 (10H, s); (*E,Z*)-isomer δ 7.34 (4H, s), 6.90-6.85 (1H, d, J = 15.9 Hz), 6.70-6.65 (1H, d, J = 15.9 Hz), 6.43-6.39 (1H, d, J = 11.7 Hz), 6.32-6.29 (1H, d, J = 11.7 Hz), 4.24 (4H, t, J = 1.8 Hz), 4.18 (4H, t, J = 1.8 Hz), 4.11 (10H, s).

Method B: HWE reaction for exclusive (*E,E*)-product.

(*E,E*)-1,4-Bis(2-ferrocenylvinyl)benzene [**(*E,E*)-BFcV*p*Ph**]**.** To a 100 mL round-bottom flask, under argon and equipped with a reflux condenser, was added THF (20 mL), NaH (116 mg, 4.8 mmol), a solution of tetraethyl 1,4-xylylenediphosphonate[21] (756 mg, 2 mmol) in THF (10 mL) and after 10 min, a solution of ferrocenecarboxaldehyde (856 mg, 4 mmol) in THF (15 mL). The reaction mixture was heated at reflux under vigorous stirring for 4 h, cooled to room temperature, water (15 mL) was added to quench the reaction. After the volatile solvent was removed under vacuum, MeOH (15 mL) was added and filtered. The residue was then washed twice with 10 mL of MeOH to afford the semi-pure product which was recrystallized from CH_2Cl_2 to yield a red powder (740 mg, 74%). Pure compound showed very low solubility in common organic solvents such as $CHCl_3$ and ether, moderate in THF. ^{1}H NMR ($CDCl_3$): δ 7.37 (4H, s), 6.87-6.82 (2H, d, J = 15.9 Hz), 6.66-6.61 (2H, d, J = 15.9 Hz), 4.53 (4H, t, J = 1.8 Hz), 4.34 (4H, t, J = 1.8 Hz), 4.18 (10H, s). ^{13}C NMR ($CDCl_3$): δ 126.71, 126.30, 126.06, 83.74, 69.31, 68.14, 67.08. IR (neat, cm^{-1}): 3094.4w, 2920.5w, 1625.4m(br), 1511.4m, 1413.7m, 1276.1m, 1102.8m, 1043.7m, 1028.7m, 1003.4m, 955.8s, 931.2m, 820.8s, 709.4m (br), 478.2s.

1,2-Bis(2-ferrocenylvinyl)benzene (BFcV*o*Ph).

Method A: Conventional Wittig reaction approach.

o-Xylylene-bis(triphenylphosphonium bromide). A solution of α,α'-dibromo-*o*-xylene (5.28 g, 20 mmol) and triphenylphosphine (13.62 g, 52 mmol, 30% excess) in dry xylene (150 mL) was heated under reflux for 12 h. After a while, white crystals began to separate from the solution. The precipitate was collected, washed with dry xylene and

petroleum ether. The solid was then dissolved in hot chloroform and crystallized by slow addition of hexane. The final product was obtained as white crystals (12.6 g, 80%). The compound was dried under vacuum at 110 ^{o}C for 24 h. before being used; m.p. 295-296 ^{o}C. ^{1}H NMR ($CDCl_3$): δ 7.75-7.85 (18H, m), 7.64-7.70 (12H, m), 7.0 (2H, m), 6.9 (2H, m), 5.28 (4H, d, J = 15 Hz).

1,2-Bis(2-ferrocenylvinyl)benzene **(BFcV*o*Ph).** General Wittig reaction procedure as for **BFcV*p*Ph** was followed. *o*-Xylylene-bis(triphenylphosphonium bromide) (1.58 g, 2 mmol) and ferrocencarboxaldehyde (0.94 g, 4.4 mmol) was allowed to react for 10 h in presence of sodium methoxide (9.6 mL of a 0.5 M solution in MeOH, 4.8 mmol). The red solid product (0.65 g, 65%) is a mixture of two cis/trans isomers, small amount of which was separated by column chromatography on silica gel or preparative TLC chromatography, eluting with $CHCl_3$/hexane (1:3). ^{1}H NMR ($CDCl_3$): (*E,Z*)-isomer δ 7.65-7.62 (1H, d, J = 7.8 Hz), 7.28-7.24 (1H, m), 7.23-7.18 (2H, t, J = 7.8 Hz), 6.95 (1H, d, J = 16.2 Hz), 6.82 (1H, d, J = 16.2 Hz), 6.48 (1H, d, J = 11.4 Hz), 6.39 (1H, d, J = 11.4 Hz), 4.44 (2H, t, J = 1.8 Hz), 4.25 (2H, t, J = 1.8 Hz), 4.10 (10H, s), 4.08 (2H, t, J = 1.8 Hz), 4.00 (2H, t, J = 1.8 Hz). (*E,E*)-isomer: ^{1}H NMR ($CDCl_3$): δ 7.53 (2H, dd, J = 5.7 Hz, J = 3.3 Hz), 7.28 (2H, dd, J = 5.7 Hz, J = 3.3 Hz), 7.05 (2H, d, J = 15.9 Hz), 6.78 (2H, d, J = 15.9 Hz), 4.53 (4H, t, J = 1.8 Hz), 4.33 (4H, t, J = 1.8 Hz), 4.20 (10H, s). ^{13}C NMR ($CDCl_3$): δ 136.02, 129.48, 127.32, 126.64, 124.48, 83.92, 69.60, 69.42, 67.27. IR (neat, cm^{-1}): 3076.7w, 2914w, 1685.2w(br), 1624.2m, 1590.7w, 1407.5m, 1243.9m, 1102.8s, 1040m, 1024.1m, 998.8s, 957.5s, 804.5m, 758.9s, 485.7s. MS m/e (intensity): 498.1 (100, M^{+}), 433 (8.0), 311.1 (7.5), 245.5 (17), 179.9 (3), 115.8 (4.0).

Method B: HWE reaction leading to exclusive (*E,E*)-product.

(*E,E*)-1,2-Bis(2-ferrocenylvinyl)benzene. General HWE reaction procedure as for **(*E,E*)-BFcV*p*Ph** was followed. Tetraethyl 1,2-xylylenediphosphonate[22] (756 mg, 2 mmol) and ferrocencarboxaldehyde (856 mg, 4 mmol) was heated at reflux in THF for 4 h in presence of NaH (116 mg, 4.8 mmol). The reaction mixture was quenched with water and extracted with diethyl ether. Purification was achieved by column chromatography on silica gel (1:1 CH_2Cl_2/hexane) to yield the pure compound as a red crystalline solid (617 mg, 62%). ^{1}H NMR ($CDCl_3$): δ 7.53 (2H, dd, J = 5.7 Hz, J = 3.3

Hz), 7.28 (2H, dd, J = 5.7 Hz, J = 3.3 Hz), 7.05 (2H, d, J = 15.9 Hz), 6.78 (2H, d, J = 15.9 Hz), 4.53 (4H, t, J = 1.8 Hz), 4.33 (4H, t, J = 1.8 Hz), 4.20 (10H, s). ^{13}C NMR ($CDCl_3$): δ 136.02, 129.48, 127.32, 126.64, 124.48, 83.92, 69.60, 69.42, 67.27. IR (neat, cm^{-1}): 3076.7w, 2914w, 1685.2w(br), 1624.2m, 1590.7w, 1407.5m, 1243.9m, 1102.8s, 1040m, 1024.1m, 998.8s, 957.5s, 804.5m, 758.9s, 485.7s.

(*E, E*)-1,3-Bis(2-ferrocenylvinyl)benzene (BFcV*m*Ph). General HWE reaction procedure as for **(*E,E*)-BFcV*p*Ph** was followed. Tetraethyl 1,3-xylylenediphosphonate[23] (756 mg, 2 mmol) and ferrocencarboxaldehyde (856 mg, 4 mmol) was heated at reflux in THF for 4 h in presence of NaH (116 mg, 4.8 mmol). The crude material was washed twice with MeOH and recrystallized from CH_2Cl_2/hexane to afford an orange red powder (0.8 g, 80%). ^{1}H NMR ($CDCl_3$): δ 7.47 (1H, s), 7.31 (3H, m), 6.89 (2H, d, J = 16.2 Hz), 6.70 (2H, d, J = 16.2 Hz), 4.49 (4H, t, J =1.8 Hz), 4.30 (4H, t, J =1.8 Hz), 4.15 (10H, s). ^{13}C NMR ($CDCl_3$): δ 138.45, 129.18(v), 127.31, 126.20, 124.43, 123.57(v), 83.54, 69.47, 69.29, 67.12. IR (neat, cm^{-1}): 3089w, 3038w, 1718w, 1634m, 1592m, 1569w, 1407m, 1103m, 1041m, 957m, 929m, 826m, 805s, 779s, 693m, 484s. Anal. Calcd for $C_{30}H_{26}Fe_2$: C, 72.32; H, 5.26. Found: C, 72.39; H, 5.31.

2,5-Bis(2-ferrocenylvinyl)-1,4-dimethoxybenzene [BFcV*p*Ph(OMe)$_2$].

Method A: Conventional Wittig reaction approach.

1,4-Dichloromethyl-2,5-dimethoxybenzene. 1,4-dimethoxybenzene (4.6 g, 0.033 mol) and paraformaldehyde (6 g, 0.2 mol) was added into a solution of conc. HCl (30 mL) and glacial acetic acid (50 mL), the mixture was sonicated in a water bath for 2 h. The resultant white emulsion was filtered and washed with water (50 mL). The collected solid was recrystallized from acetone to give a white crystalline solid material (4.3 g, 55%). ^{1}H NMR ($CDCl_3$): δ 6.93 (2H, s, benzene), 4.65 (4H, s, CH_2Cl), 3.87 (6H, s). ^{13}C NMR ($CDCl_3$): δ 151.3, 127.1, 113.7, 56.4, 41.5.

2,5-Dimethoxy-*p*-xylylene-bis(triphenylphosphonium chloride). A solution of 1,4-dichloromethyl-2,5-dimethoxybenzene (4.7 g, 20 mmol) and triphenylphosphine (13.62 g, 52 mmol, 30% excess) in dry xylene (150 mL) was heated under reflux while being stirred for 12 h. After a while, a crystalline solid began to separate from the solution. The precipitate was collected, washed with dry xylene and petroleum ether. The solid was then dissolved in hot chloroform and crystallized by slow addition of hexane.

The final product was obtained as pale yellow crystalline solid (12.3 g, 81%). The compound was dried under vacuum at 110 ^{o}C for 24 h. before being used; m.p. 271-275 ^{o}C. ^{1}H NMR ($CDCl_3$): δ 7.73-7.62 (30H, m), 6.95 (2H, s), 5.26-5.31 (4H, d, J = 13.2 Hz), 3.66 (6H, s).

2,5-Bis(2-ferrocenylvinyl)-1,4-dimethoxybenzene [**BFcV*p*Ph(OMe)$_2$**]. General Wittig reaction procedure as for **BFcV*p*Ph** was followed. 2,5-dimethoxy-*p*-xylylene-bis(triphenylphosphonium chloride) (1.58 g, 2 mmol) and ferrocencarboxaldehyde (0.94 g, 4.4 mmol) was allowed to react for 10 h in the presence of sodium methoxide (9.6 mL of a 0.5 M solution in MeOH, 4.8 mmol). The orange red solid product (0.7 g, 70%) consists of two cis/trans isomers, small amount of which was separated by column chromatography on silica gel or preparative TLC chromatography, eluting with $CHCl_3$/hexane (1:3). m.p. 130 ^{o}C. ^{1}H NMR ($CDCl_3$): (*E,E*)-isomer: δ 7.04 (2H, s), 6.93 (2H, d, J = 15.9 Hz), 6.84 (2H, d, J = 15.9 Hz), 4.49 (4H, t, J = 1.8 Hz), 4.28 (4H, t, J = 1.8 Hz), 4.15 (10H, s), 3.90 (6H, s). (*Z,Z*)-isomer: δ 7.01 (2H, s), 6.48 (2H, d, J = 11.4 Hz), 6.35 (2H, d, J = 11.4 Hz), 4.24 (4H, t, J = 1.8 Hz), 4.13 (4H, t, J = 1.8 Hz), 4.11 (10H, s), 3.62 (2H, s). IR (KBr pellet, cm^{-1}): 2931.2w, 2828.2w, 1627.4(br), 1502.2m, 1461.7m, 1409.2m, 1209.4s, 1105.1m, 1043.1s, 963.7m, 819.1m, 480.1m. MS m/e (intensity): 558.2 (100, M^+), 413 (5), 357.1 (8.5), 277.6 (10), 234.3 (4), 69.1 (8.0), 38.1 (38.1). Exact mass for $C_{32}H_{30}Fe_2O_2$: 558.09446, observed: 558.09496.

Method B: HWE reaction leading to exclusive (*E,E*)-product.

(*E,E*)-2,5-Bis(2-ferrocenylvinyl)-1,4-dimethoxybenzene. General HWE reaction procedure as for **(*E,E*)- BFcV*p*Ph** was followed. Tetraethyl 2,5-dimethoxy-1,4-xylylenediphosphonate[24] (876 mg, 2 mmol) and ferrocencarboxaldehyde (856 mg, 4 mmol) was heated at reflux in THF for 4 h in presence of NaH (116 mg, 4.8 mmol). The crude product was washed twice with MeOH (10 mL) and recrystallized from CH_2Cl_2/hexane to afford an orange red powder (840 mg, 75%). The pure compound demonstrated low solubility resembling **(*E,E*)-**DFc4-*p*-Ph. ^{1}H NMR spectrum is identical to the data described above. Good ^{13}C NMR data was not obtained due to poor solubility. IR (neat, cm^{-1}): 3080w, 2927.3w, 2821w, 1678.6w, 1627.8m, 1502.7m, 1458.1m, 1406.2m, 1266m, 1207.2s, 1133.4 (br), 1104.3m, 1037.6s, 965.2m, 809.9m.

(*E,E*)-2,5-Bis(2-ferrocenylvinyl)-1,4-didodecyloxybenzene (BFcV*p*Ph($OC_{12}H_{25}$)$_2$). General HWE reaction procedure as for **(*E,E*)-BFcV*p*Ph** was followed. Tetraethyl 2,5-didodecyloxy-1,4-xylylenediphosphonate[25] (1.5 g, 2 mmol) and ferrocencarboxaldehyde (856 mg, 4 mmol) was heated at reflux in THF for 4 h in presence of NaH (116 mg, 4.8 mmol). The crude material was washed with MeOH and passed through a short column on silica gel ($CHCl_3$) to yield a red crystalline solid (1.42 g, 82%). ^{1}H NMR (CD_2Cl_2): δ 7.0 (2H, d, J = 16.2 Hz), 7.04 (2H, s, aryl), 6.89 (2H, d, J = 16.2 Hz), 4.49 (4H, t, J = 1.8 Hz), 4.30 (4H, t, J = 1.8 Hz), 4.14 (10H, s), 4.05 (4H, t, J = 6.6 Hz, CH2O-dodecyl), 1.89-1.29 (40H, m), 0.89 (6H, t, J = 6.9 Hz). ^{13}C NMR (CD_2Cl_2): δ 152.70, 129.04, 128.64, 123.08, 112.47, 86.37, 71.71, 71.35, 71.12, 68.93, 34.09, 31.86, 31.55, 28.52, 24.87, 16.07. IR (neat, cm^{-1}): 3109.9w, 3043.5w, 2916s, 2848.4s, 1629m, 1501m, 1454.7m, 1420m, 1391m, 1263m, 1201.0s, 1106.3m, 1038.9m, 966.6s, 805.5s.

2,5-Bis(2-ferrocenylvinyl)thiophene (BFcVTh).

Thiophene-2,5-dicarboxaldehyde. To a solution of 2,5-dibromothiophene (2.9 g, 12 mmol) in dry ether (150 mL) was added dropwise n-butyllithium (35 mL of a 2.5 M solution in hexane, 87.5 mmol, 3.5 equiv.) at –78 ^{o}C. The mixture was stirred for 15 min. and then 9 mL of N,N-dimethylformamide was added. After stirring for 1 h, the reaction mixture was allowed to warm gradually to room temperature and water (100 mL) was added to quench the reaction. The aqueous solution was separated and extracted with ether (2 x 100 mL). The combined ether extracts were washed with brine (2 x 100 mL), dried over Na_2SO_4 and evaporated to give a yellow oil. Chromatographic purification was achieved on silica gel (hexane/CH_2Cl_2 = 5:1) to afford a white solid (0.97 g, 58%), m.p. 79-80 ^{o}C. Small amount of mono-formylthiophene was also obtained as byproduct. ^{1}H NMR ($CDCl_3$): δ 10.03 (2H, s), 7.83 (2H, s). ^{13}C NMR ($CDCl_3$): δ 183.9, 149.3, 135.7.

2,5-Bis(2-ferrocenylvinyl)thiophene (**BFcVTh**).

Method A: To a suspension of ferrocenylmethyltriphenylphosphonium iodide (1.18 g, 2 mmol) in dry THF (50 mL) at 0 °C under argon, was added potassium *tert*-butoxide (0.246 g, 2.2 mmol, 10% excess). The solution was stirred for 30 min, whereupon it turned rapidly from yellow to wine red, at which point, 5-(*E*)-ferrocenylvinylthiophene-2-yl-carbaldehyde[28] (0.64 g, 2 mmol) was added as a solution

in anhydrous THF (20 mL). The resultant mixture was slowly warmed to room temperature and subsequently heated at reflux for ca. 8 h. It was then cooled, poured into ice water, and extracted with diethyl ether (3 x 25 mL). The organic extract was washed with brine, dried over Na_2SO_4, and evaporated to dryness to yield a brown solid. This was purified by column chromatography on silica gel (CH_2Cl_2/hexane (1:1)) to yield 0.82 g (82%) of red crystalline solid. (*E,E*)-isomer: ^{1}H NMR ($CDCl_3$): δ 6.79 (2H, s, thiophene), 6.74 (2H, d, J = 15.6 Hz, vinyl), 6.62 (2H, d, J = 15.9 Hz, vinyl), 4.42 (4H, t, J = 1.7 Hz), 4.28 (4H, t, J = 1.7 Hz), 4.14 (10H, s). ^{13}C NMR ($CDCl_3$): δ 141.61, 126.97, 125.54, 119.80, 83.27, 69.50, 69.40, 66.96. IR (KBr pellet, cm^{-1}): 3084.9, 3010.4, 2927.8, 1772, 1652.7 (br), 1622.4, 1475.9, 1435.3, 1230 (br), 1104.4, 1027.93, 943.9, 818.1, 763.9, 571.6. MS m/e (intensity): 504.2 (100, M^+), 439 (5.0), 370 (7.5), 249.1 (29), 176.7 (4), 115.8 (7.0).

Method B: The compound was also synthesized analogously to the above procedure from ferrocenylmethyltriphenylphosphonium iodide (3.54 g, 6 mmol, 3 equiv.), potassium *tert*-butoxide (0.74 g, 6.6 mmol) and thiophene-2,5-dicarboxaldehyde (140 mg, 1 mmol). The reaction mixture was stirred 18 h at room temperature before being quenched by water. Pure sample (0.75 g, 75%) was obtained by column chromatography in the same manner as above. However, this method affords a mixture of cis,trans, trans,trans, and cis,cis isomers.

2,5-Bis(2-ferrocenylvinyl)-3,4-ethylenedioxythiophene (BFcVEDOT).

3,4-Ethylenedioxythiphene-2,5-dicarboxaldehyde. The dialdehyde was prepared according to literature procedure.[38] ^{1}H NMR ($CDCl_3$): δ 10.04 (2H, s), 4.45 (4H, s). ^{13}C NMR ($CDCl_3$): δ 181.22, 147.45, 124.32, 65.38.

2,5-Bis(2-ferrocenylvinyl)-3,4-ethylenedioxythiophene (**BFcVEDOT**)**.** To a stirred suspension of $FcCH_2PPh_3I$ (2.58 g, 4.4 mmol) in THF (60 mL) maintained at 0 ^oC was added potassium *tert*-butoxide (0.5 g, 4.4 mmol) in one portion. The resulting red solution was stirred for 30 min at r.t. before being treated with 3,4-ethylenedioxythiphene-2,5-dicarboxaldehyde (0.4 g, 2 mmol) in THF (15 mL) through cannulation. The reaction mixture was heated to reflux for 3 h, cooled, quenched by water (40 mL), extracted by diethyl ether (3 x 60 mL). The organic extracts was washed with brine, dried over Na_2SO_4 and evaporated under reduced pressure. The residue was

then stirred in MeOH (20 mL), filtered before subject to column chromatography on silica gel ($CHCl_3$) to give a deep red crystalline solid (0.8 g, 71%). NMR spectrum indicated this product is a configuration mixture consisting of approx. 85% (*E, E*)-isomer, which was isolated by recrystallization from CH_2Cl_2/hexane (1:2). (*E, E*)-isomer: ^{1}H NMR ($CDCl_3$): δ 6.72 (2H, d, J = 15.9 Hz), 6.55 (2H, d, J = 15.9 Hz), 4.42 (4H, t, J =1.8 Hz), 4.29 (4H, s), 4.26 (4H, t, J = 1.8 Hz), 4.14 (10H, s). ^{13}C NMR ($CDCl_3$): δ 138.38, 124.67, 115.63, 115.04, 83.89, 69.51, 69.23, 66.80, 65.12. IR (neat, cm^{-1}): 3093.3w, 2940.5w, 1774.9w, 1622.1w(br), 1507.6m, 1458.9m, 1434.5s, 1361.8s, 1274.8m, 1080.3s, 939.4s, 816.8m, 483.3s. MS m/e (intensity): 562 (100, M^+), 281 (16), 186 (5), 121 (4). Exact mass for $C_{30}H_{26}O_2SFe_2$: 562.03168, observed: 562.03523.

2,5-Bis(2-ferrocenylvinyl)-N-dodecylpyrrole (BFcVPyr).

Preparation of 1,8-diferrocenyl-octa-1,7-diene-3,6-dione.[39] Commercial LDA (5 mL of a 2 M solution in THF/n-heptane, 10 mmol) was first added to precharged THF (15 mL) in a 100 mL round-bottle flask at –78 ^{o}C under argon. To this stirred solution, 4-ferrocenyl-but-3-enone (2.28 g, 9 mmol) in THF (15 mL) was added slowly. After 45 min, anhydrous $CuCl_2$ (1.35 g, 10 mmol) dissolved in 15 mL DMF was added at once at the same temperature. The reaction mixture was stirred for an additional 1 h and then allowed to reach room temperature and stirred for further 1 h. The reaction mixture was treated with 3% aqueous HCl and extracted with chloroform. The organic extract was washed with 3% aqueous HCl and with water and dried over $MgSO_4$. After removal of the solvent, the residue was pre-purified by flash chromatography on silica gel using chloroform/ether (95:5) as eluent to afford the crude product. This was dissolved in a minimum amount of CH_2Cl_2 (ca. 5 mL) and treated with hexane (60 mL) to cause precipitate. Upon filtration, the product was obtained in the form of brown needles (1.75 g, 77%); m.p. > 130 ^{o}C, decomposed. ^{1}H NMR ($CDCl_3$): δ 7.53 (2H, d, J = 16.2 Hz), 6.38 (2H, d, J = 16.2 Hz), 4.52 (4H, t, J = 2 Hz), 4.44 (4H, t, J = 2 Hz), 4.17 (10H, s), 2.99 (4H, s). ^{13}C NMR ($CDCl_3$): δ 198.63, 144.83, 123.94, 78.88, 71.45, 69.99, 69.06, 34.22. IR (KBr pellet, cm^{-1}): 3095, 2922.4, 1677.3, 1647.1, 1618.8, 1599.4, 1358.3, 1145.7, 1042.6, 972.8, 817.3, 490.5. MS m/e (intensity): 506 (100, M^+), 488 (12.5), 441 (20), 252 (13), 239 (17), 201 (15), 121 (15), 55.9 (4). Exact mass for $C_{28}H_{26}Fe_2O_2$: 506.06316, observed: 506.05918.

2,5-Bis(2-ferrocenylvinyl)-*N*-dodecylpyrrole **(BFcVPyr).**

A mixture of 1,8-diferrocenyl-octa-1,7-diene-3,6-dione (506 mg, 1 mmol), dodecylamine (741 mg, 4 mmol) and *p*-toluenesulfonic acid (*p*-TSA) monohydrate (10 mg) was dissolved in 20 mL xylene. The reaction mixture was stirred and heated at reflux for 12 h. After cooling, 30 mL saturated aqueous $NaHCO_3$ was added and the organic layer was extracted twice with 20 mL CH_2Cl_2. The combined organic extracts were dried over $MgSO_4$, and concentrated under reduced pressure. The residue was passed through a silica gel column using CH_2Cl_2/Hexane (1:2) as eluent. The first band was collected and concentrated to yield the title compound as a yellow solid (365 mg, 55.7%), m.p. 106-107 ^oC. ^1H NMR ($CDCl_3$): δ 6.61 (2H, d, J = 15.9 Hz), 6.51 (2H, d, J = 15.9 Hz), 6.43 (2H, s), 4.41 (4H, t, J = 1.8 Hz), 4.25 (4H, t, J = 1.8 Hz), 4.13(10H, s), 3.92 (2H, t, J = 5.1 Hz), 1.9-1.25 (20H, m), 0.87 (3H, t, J = 6 Hz). ^{13}C NMR ($CDCl_3$): δ 132.9, 124.4, 115.0, 106.4, 84.6, 69.4, 69.0, 66.6, 43.5, 32.1, 31.6, 29.9, 29.6, 27.1, 22.9, 14.3. IR (KBr pellet, cm^{-1}): 3093.2, 2954.7, 2918.6, 2849, 1652.7, 1467.8, 1411.3, 1105.2, 1025.2, 999.8, 817, 766.4, 485.3. MS m/e (intensity): 655 (100, M^+), 458 (2.0), 356 (2.5), 327.6 (33), 121 (3.0). Exact mass for $C_{40}H_{49}Fe_2N$: 655.25638, observed: 655.25624.

2,5-Bis(2-ferrocenylvinyl)furan (BFcVFu). A mixture of 1,8-diferrocenyl-octa-1,7-diene-3,6-dione (253 mg, 0.5 mmol) and *p*-toluenesulfonic acid (*p*-TSA) monohydrate (5 mg) was dissolved in 20 mL xylene. The reaction mixture was stirred and heated at reflux for 16 h. After cooling to r.t., 30 mL saturated aqueous $NaHCO_3$ was added and the organic layer was extracted twice with 20 mL CH_2Cl_2. The combined organic extracts were dried over $MgSO_4$, and concentrated under reduced pressure. Purification was achieved by column chromatography on silica gel using CH_2Cl_2/hexane (1:1) as eluent. The first band was collected and concentrated to afford a red crystalline solid (125 mg, 51%); m.p. > 180 ^oC, decomposed. ^1H NMR ($CDCl_3$): δ 6.82 (2H, d, J = 15.9 Hz), 6.45 (2H, d, J = 15.9 Hz), 6.22 (2H, s), 4.45 (4H, t, J = 1.8 Hz), 4.29 (4H, t, J = 1.8 Hz), 4.17 (10H, s). ^{13}C NMR ($CDCl_3$): δ 153.0, 125.7, 114.5, 109.3, 83.5 69.5, 67.0, 66.8. IR (KBr pellet, cm^{-1}): 3090.2, 2917.6, 2850.3, 1652.7, 1635.3 (br), 1436.2 (br), 1104.4, 1026.7, 953.2, 813.1, 780.3, 485. MS m/e (intensity): 488 (100, M^+), 329 (3.0), 302 (5.5), 244 (23), 186 (4.4), 121 (7.0), 55.9 (2.3). Exact mass for $C_{28}H_{24}Fe_2O$: 488.05259, observed: 488.04988.

Tetrabutylammonium tetrakis(3,5-bis(trifluoromethyl)pheny1)borate ($Bu_4N^+TFPB^-$). This compound was prepared as a supporting electrolyte in the electrochemical studies. Tetrabutylammonium bromide (2.6 g, 7 mmol) and sodium tetrakis(3,5-bis(trifluoromethyl)phenyl) borate (6.2 g, 7 mmol) were dissolved in methanol (20 mL) and stirred for 15 minutes at room temperature. Distilled water (40 mL) was then added into the clear solution at a comparable rate to cause a white precipitate isolate from the solution immediately. The solid was filtered off, dried overnight under vacuum at 60^{o}C, and passed through a neutral alumina column using CH_2Cl_2 as eluent to afford a white crystalline solid after solvent evaporation (7.2 g, 93%). For electrochemical purpose, the salt needs to pass through a neutral alumina column again using dry CH_2Cl_2 as eluent prior to use. ^{1}H NMR ($CDCl_3$): δ 7.68 (8H, d, J = 2.1 Hz) 7.53 (4H, s), 2.95 (8H, t, J = 8.4 Hz), 1.52 (8H, m), 1.30 (8H, tt, J = 7.5 Hz), 0.90 (12H, t, J = 7.5 Hz).

Results and Discussion

Synthetic Procedures

In this study, more than twenty bis(ferrocenylvinyl) derivatives (**BFcVX**) were synthesized. Bearing in mind the fact that this family of compounds shares a similar symmetrical skeleton, we tried to seek a general synthetic pathway to prepare this series of molecules with minimal synthetic complexities. According to the structural characteristics of the compounds this kind, the conventional Wittig reaction intuitively emerged as the most convenient approach for fulfill the synthetic mission. By addition of two equivalents of ferrocenecarboxyaldehye (FcCHO) to the bis(ylide) of the appropriate bis(triphenylphosphine) bromide/chloride (i.e. $(BrPh_3PCH_2)_2$-X), we could easily prepare a number of the desired compounds with acceptable yields. **BFcVCH_2**, **BFcV$(CH_2)_2$**, **BFcVCH=CH** (or **Fc$(CH=CH)_3$Fc**), **BFcVS**, **BFcVO**, **BFcV*p*-C_6H_4**, **BFcV*o*-C_6H_4**, **BFcV*p*-$C_6H_2(OMe)_2$** and **BFcVCH=CHSCH=CH** were synthesized through this approach. The synthetic route was shown in Figure 2.1. In the latter case, instead of ferrocenecarboxyaldehye, ferrocenylpropenal was used as the coupling aldehye. In each case, a mixture of *cis* (*Z*) and *trans* (*E*) isomers was obtained, as evidenced by NMR

spectroscopy, due to the non-stereoselectivity of the conventional Wittig reaction. Separation of the isomers by column chromatography or recrystallization proved to be very difficult and only partially feasible for some of the compounds.

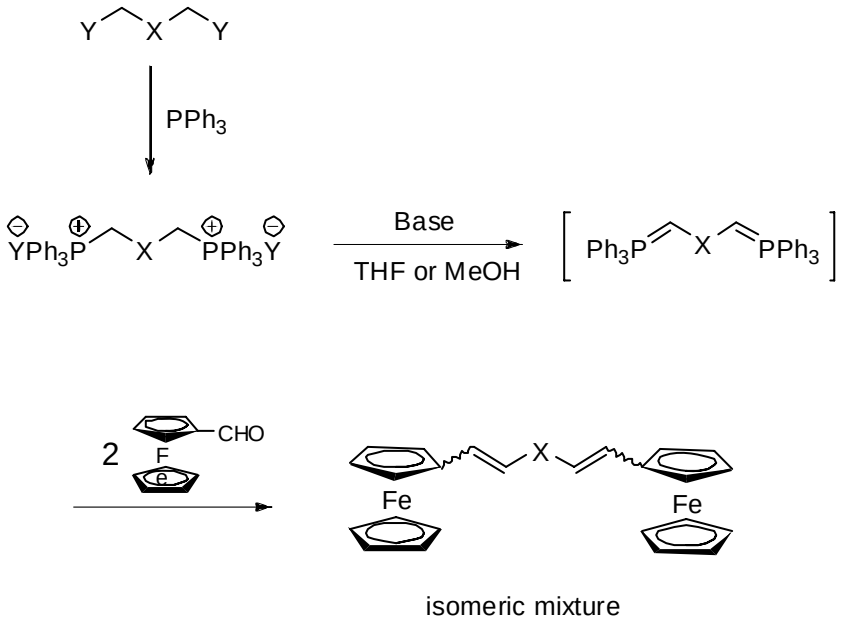

Figure 2.1 Synthetic pathway of **FcCH=CHXCH=CHFc** compounds using conventional Wittig methodology.

In contrast, the Horner-Wadsworth-Emmons (HWE) reaction[40, 41] was known to produce *E*-alkenes stereospecifically. We also utilized such an approach in preparing the (*E,E*)-bis(2-ferrocenylvinyl) compounds by olefination reactions between two equivalents of FcCHO and an appropriate diphosphonate in the presence of NaH. The synthetic route and compounds applicable to this approach are shown in Figure 2.2. In general, the synthetic precursors, bis(diethylphosphinylmethylene) derivatives ($[(EtO)_2P(O)CH_2]_2X$), were prepared through Arbuzov reaction[42] by refluxing a bishalide with triethylphophite.

In the HWE olefination step, heating is essential to allow the reaction to proceed and to promote the generation of double bonds in *E*-form. When the X group was a phenylene moiety, the product was obtained as exclusive *trans,trans*-isomer in high yield in all cases. It was also found that the coupling reaction would not take place without heating,

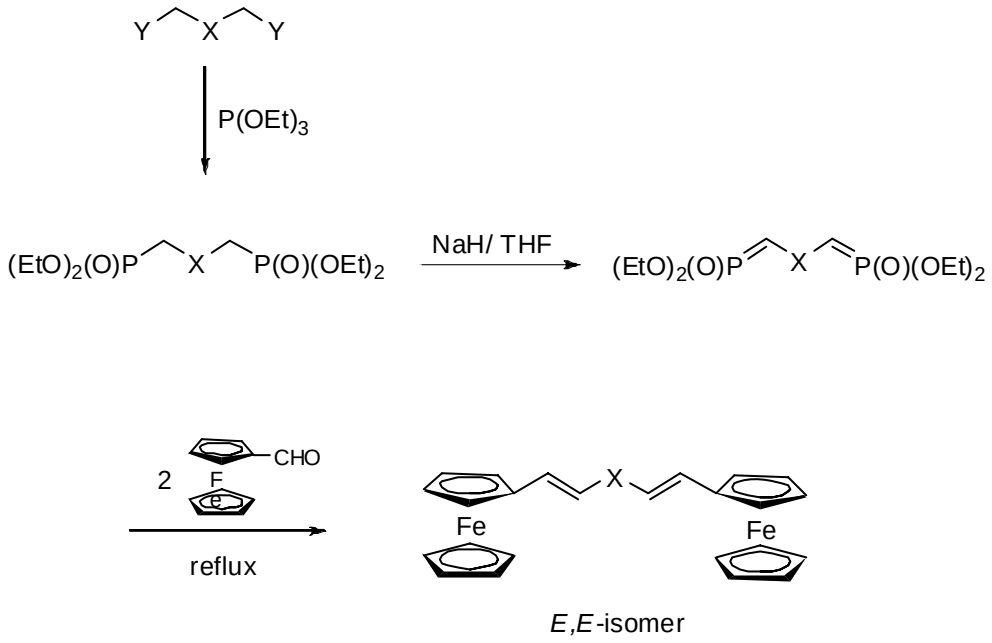

Y = Br or Cl

X = S, Se, *p*-C_6H_4, *o*-C_6H_4, *m*-C_6H_4,
2,5-$(OR)_2$-*p*-C_6H_2 (R = CH_3 and $C_{12}H_{25}$)

Figure 2.2 Synthetic pathway of **FcCH=CHXCH=CHFc** compounds through Horner-Wadsworth-Emmons reactions.

which is presumably due to the decreased nucleophilicity of the intermediate carbanion attributable to the stabilization of the neighboring aromatic ring. However, the bulkiness of the aromatic ring favors the formation of the intermediate oxaphosphatane with a steric arrangement that the ferrocene unit is *anti* to the aromatic moiety, which eventually led to the *trans* vinyl bond upon elimination of the diethyl phosphate. When the X group was a heteroatom such as S and Se, the HWE reaction proceeded smoothly at room temperature but only afforded a *cis/trans* isomeric mixture with improved *E,E*-stereochemistry (approx. 70%) in comparison with the outcome of the corresponding Wittig reaction. When the same reactions were conducted under reflux, however, nearly 95% *E,E*-adduct was observed as evidenced by ^{1}H NMR spectroscopy. The pure *trans,trans*-isomer could be conveniently isolated by recrystallization from CH_2Cl_2/hexane (1:1). The enhanced stereoselectivity with higher temperature is ascribed to the interconversion among the oxaphosphetane intermediates to the thermodynamically more stable arrangement leading to the *E*-alkene.[43] Our efforts to transform Wittig to HWE reaction for other compounds to achieve exclusive *E,E*-product were unsuccessful due to either the instability of the intermediate carbanion (e.g. X = O) or the lack of stablizing effect favorable to the *E* final product (e.g. X = CH_2). Finally, under the HWE methodology, although it is predictable that heteroarylene-centered diphosphonate should give rise to exclusive (*E,E*)-2,5-bis(2-ferrocenylvinyl)heteroaryl products as had been observed for the phenylene series, the synthetic precursors, i.e. the 2,5-bis(halomethyl)heteroarylene derivatives, were extremely unstable and subjected to extensive decomposition upon being exposed to air. For this reason, we resorted to other synthetic methods to prepare these compounds.

As shown in Figure 2.3, 2,5-bis(2-ferrocenylvinyl)thiophene (**BFcVTh**) and 3,4-ethylenedioxy-2,5- bis(2-ferrocenylvinyl)thiophene (**BFcVEDOT**) were synthesized via the Wittig reaction of two equivalents of ferrocenylmethyltriphenylphosphonium iodide ($FcCH_2P^+Ph_3I^-$) with thiophene-2,5-dicarboxaldehyde and 3,4-ethylenedioxythiophene-2,5-dicarboxaldehyde, respectively. This synthetic route is in an inverse manner in comparison with the Wittig procedures for other compounds depicted in Figure 2.1. The 2,5-thiophenedialdehydes were readily prepared from thiophene and 3,4-ethylenedioxythiophene (EDOT) through the conventional dilithiation and consequential formylation procedures[38] (Figure 2.3). Whereas both the bis(2-ferrocenylvinyl)

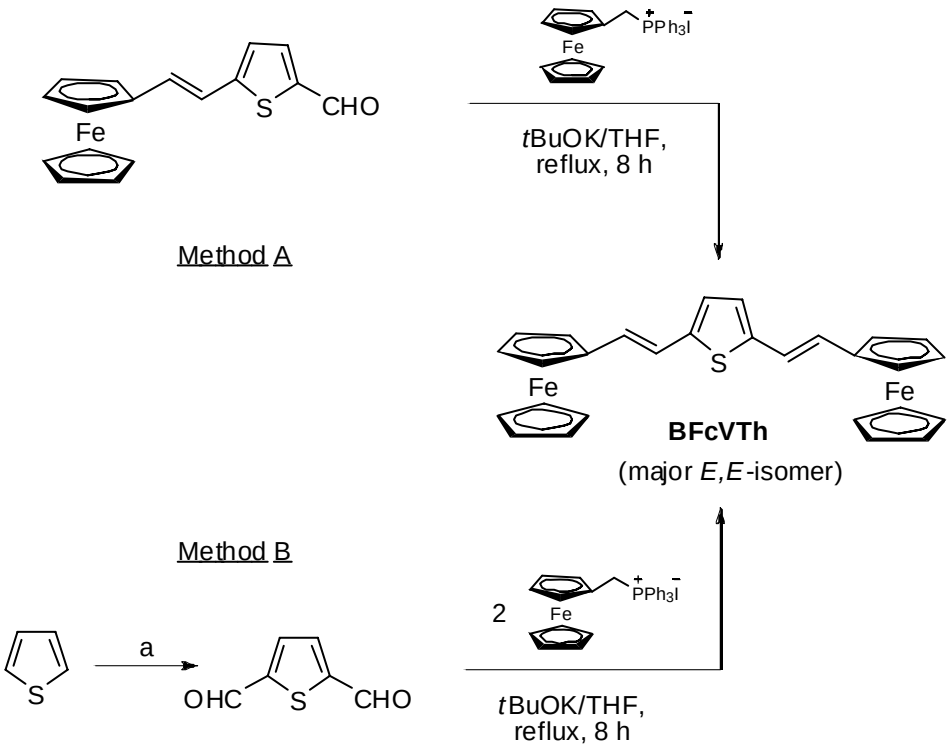

a. 1) BuLi/THF, -78 ^{o}C, 2) DMF, aq. HCl

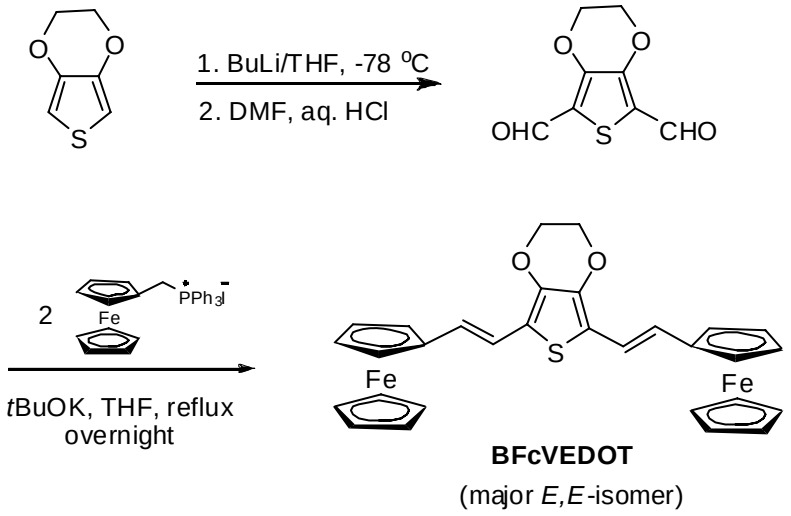

Figure 2.3 Synthesis of **BFcVTh** and **BFcVEDOT**.

compounds were achieved in high yield as an E/Z isomeric mixture at room temperature, comparison studies showed that reflux is an important promoting factor for (*E,E*)-product (roughly 85%), which could be isolated as a pure species upon recrystallization from CH_2Cl_2/hexane (1;1). The literature synthetic procedure for **BFcVTh**[28] (method A in Figure 2.3) apparently required a few more steps in preparing the synthetic precursor, 2-(2-ferrocenylvinyl)-5-formylthiophene. It is also notable that $FcCH_2P^+Ph_3I^-$ is a very handy ferrocenylvinyl synthon as extensively used in our later work.

However, our efforts to synthesize 2,5-bis(2-ferrocenylvinyl)pyrrole using the same method adapted for the thiophene derivatives were unsuccessful. Although pyrrole-2,5-dicarboxyaldehyde was smoothly prepared according to the literature procedures,[44] the Wittig reaction between the dialdehyde and two equivalents of $FcCH_2P^+Ph_3I^-$ only afforded a mono-coupled compound due to the deactivation of the second formyl group on the pyrrole ring. Further olefination of the isolated 2-(2-ferrocenylvinyl)-5-formyl-pyrrole resembling method A for **BFcVTh** (Figure 2.3) was proved to be fruitless.

We then switched to a different approach to develop an N-substituted pyrrolene derivative which served the same purpose for our current study. A literature survey indicated that the well-known Paal-Knorr ring closure reaction was an efficient method leading to formation of pyrrole nucleus as presented in Figure 2.4. Under this approach, 1,4-bis(2-ferrocenylvinyl)butanedione was first prepared, by modifying the literature procedure,[39] through a metal (e.g, silver or copper) promoted oxidative coupling mechanism. The dimerization of carbanions was performed by treating ketone enolate $\mathbf{1}^-$, which was prepared from 2-ferrocenylvinylketone and lithium diisopropylamide in THF at -78 ^oC, with $CuCl_2$ in DMF. The use of DMF as co-solvent was very crucial in the copper promoted oxidative coupling of lithium enolates. 2-Ferrocenylvinylketone was oxidatively dimerized to bis(2-ferrocenylvinyl)-1,4-diketone **2** in good yield (70%). In principle, this 1,4-diketone could alternatively be prepared by a Mannich reaction of 2-ferrocenylvinylketone, formaldehyde and dimethylamine hydrochloride, affording an emamine[45], followed by a cyanide-catalyzed Micheal-type condensation, Stetter reaction,[46] with ferrocenepropenal (FcCH=CHCHO). The synthetic procedure we used took the advantage of fewer preparation steps and avoidance of using synthetically more expensive FcCH=CHCHO. The 1,4-diketone **2** was an excellent starting material

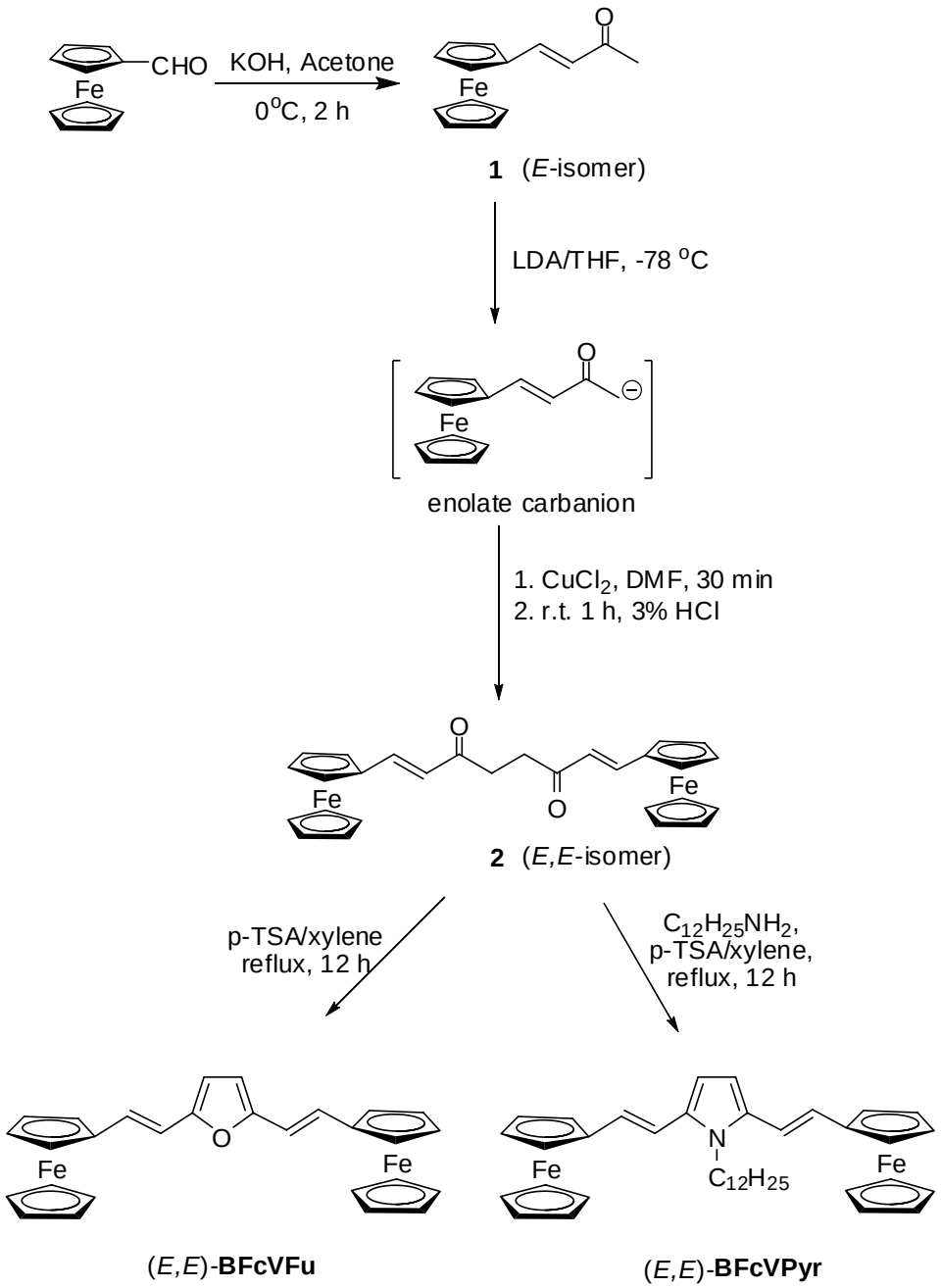

Figure 2.4 Synthesis of **BFcVFu** and **BFcVPyr**.

for synthesis of bis(2-ferrocenylvinyl)pyrroles modified at nitrogen with different functional groups as shown in the later chapters.

The 1,4-diketone **2** was then allowed to react with dodecylamine in xylenes with catalytic amount of *para*-toluenesulfonic acid (*p*-TSA) in presence to form N-dodecyl-2,5-bis(2-ferrocenylvinyl)pyrrole (**BFcVPyr**). The reaction presumably proceeded via initial formation of an imine, followed by a nucleophilic attack of the imine nitrogen on the second carbonyl carbon atom, resulting in a ring formation. Elimination of water aromatized the ring and completed the pyrrole formation. A few points should be stressed on this Paal-Knorr reaction. First, xylenes were carefully chosen as the reaction medium due to a high boiling point and low solvent polarity. Although acidic solvents such as acetic acid were commonly used in this kind of preparation due to the acid-catalyzed nature of this reaction, unfortunately, this pyrrolene-bridged biferrocene was very unstable in strong acidic environment. Second, multi-fold amounts of primary amine were used as a promoting factor for high yields. Third, low molecular weight amines such as *n*-butylamine were also applied to this pyrrole formation reaction, however, their volatility under high temperatures, which was a requirement for this type of reaction under current procedures, precluded their use.

As an extension of the ring closure reaction, we also successfully synthesized 2,5-bis(2-ferrocenylvinyl)furan (**BFcVFu**) from **2** (Figure 2.4) by reflux of the diketone in xylenes with catalytic amounts of *p*-TSA, which yielded the desired product in moderate yield (51%). Compared to the literature procedure,[28] the current preparation was certainly simpler and more convenient. For further ring closure reactions, 1,4-diketone **2** was also expected to be an effective synthon in forming the thiophene derivative, i.e. **BFcVTh**, with the assistance of the Lawesson's reagent[47] as we shall see in the similar preparation in Chapter 3. Owing to the limitation of the extent of current research, this will be left for future works. Finally, for both pyrrole and furan derivatives described above, only the (*E,E*)-products were obtained due to the predefined *trans* configuration of the double bonds in 1,4-diketone **2**.

Bis(2-ferrocenylvinyl)phenylphosphine, **BFcVPPh**, was synthesized by radical addition of phenylphosphine to ethynylferrocene in the presence of the radical initiator azobis(isobutyrofuran) (AIBN) (Figure 2.5). This preparation was modified from

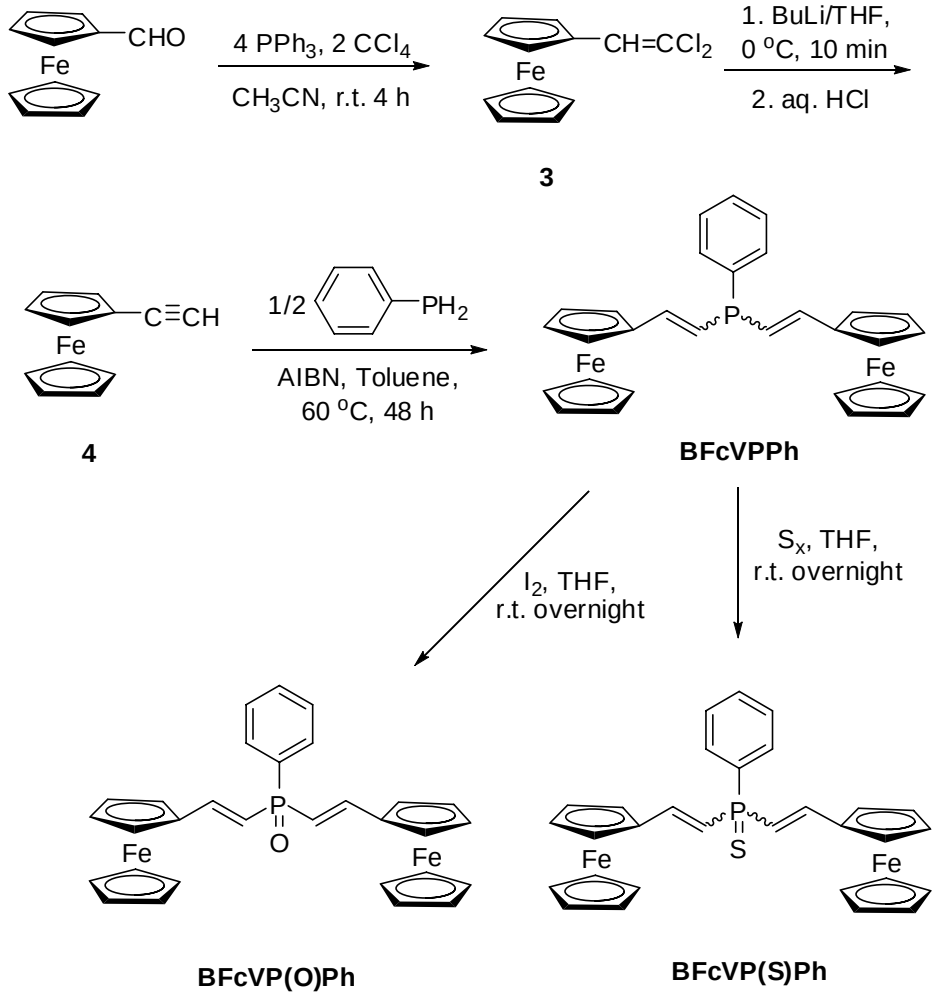

Figure 2.5 Synthesis of **BFcVPPh**, **BFcVP(S)Ph** and **BFcVP(O)Ph**.

Kobayashi's synthetic procedures.[48] Phenylphosphine, having two reactive hydrogens, was added to two ethynylferrocenes, which was prepared via two steps from ferrocenecarboxaldehyde,[49] by the *anti*-Markownikoff's rule to give the 1:2 adduct in high yield. ^{1}H NMR spectrum of the isolated product showed predominant *trans* vinylene protons with minor *cis* vinylene protons present. Stirring this phenylphosphine derivative with excessive elemental sulfur in THF under argon furnished the sulfurized compound, bis(2-ferrocenylvinyl)-phenylphosphine sulfide (**BFcVP(S)Ph**), in high yield (Figure 2.5). The corresponding bis(2-ferrocenylvinyl)phenylphosphine oxide, **BFcVP(O)Ph**, was conveniently obtained by the treatment of **BFcVPPh** with one equivalent of iodine, a weak oxidant, and a small amount of water in THF overnight (Figure 2.5). These two transformations could be easily observed by ^{1}H NMR spectroscopy, in which the *para*-phenyl proton was noticeably shifted to low field upon oxidation or thiolation. Interestingly, whereas the stereochemistry of **BFcVP(S)Ph** was basically inherited from the precedent compound **BFcVPPh**, the final **BFcVP(O)Ph** only exhibited exclusive (*E,E*)-adduct, which implied that isomerization of *cis* vinyl bonds to the *trans* moiety underwent during the oxidation process with the assistance of iodine.

Bis(2-ferrocenylvinyl)-1,2-acetylene, **BFcVC≡C**, was prepared through a modified Stephans-Castro reaction[50, 51] (Figure 2.6), which was commonly used to synthesize acetylenes by coupling of copper(I) arylacetylene with halogenoalkenes or halogenoarenes. For **BFcVC≡C,** a synthetic precursor, 1-bromo-2-ferrocenylethene (FcCH=CHBr), was first prepared via Wittig coupling of bromomethyltriphenyl-phosphonium bromide[52] with ferrocenecarboxaldehyde.[19] Cuprous iodide was added to a mixture of bis(triphenylphosphine)palladium dichloride and diethylamine solution of FcCH=CHBr under an inert atmosphere. A slow current of acetylene gas was then passed through the reaction mixture for 8 hours at room temperature. After usual workup and column chromatography, the symmetrical disubstituted acetylene, **BFcVC≡C**, was achieved as a bright red solid in very good yield (85%). The final product was characterized as an inseparable E/Z isomeric mixture by ^{1}H NMR spectroscopy. This presumably arose from the non-stereo-specified starting material FcCH=CHBr.

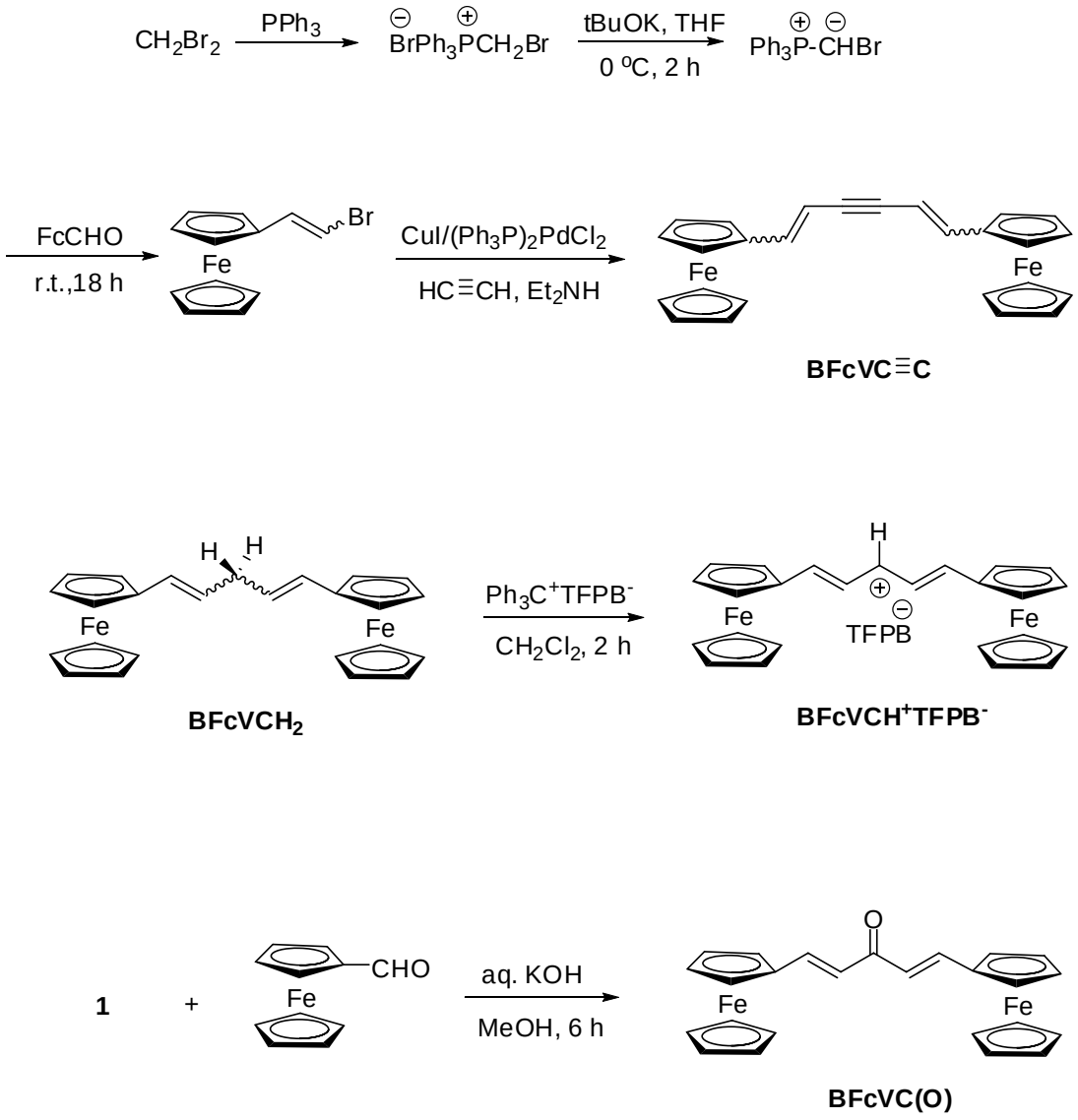

Figure 2.6 Synthesis of **BFcVC≡C**, **BFcVCH**$^+$ and **BFcVC(O)**.

BFcVCH$^+$ was prepared according to Dr. Xiaodong Zhao's thesis,[29] where the α,ω-diferrocenyl polymethine cation was paired with tetrafluoroborate anion. In our study, we also synthesized the same cationic species with tetrakis(3,5-bis(trifluoromethyl)phenyl)borate (TFPB) as the counterion (Figure 2.6). The solubility of the new polymethine salt, **BFcVCH**$^+$**TFPB**$^-$, in organic solvent was therefore highly increased so that in the recrystallization step only hexane precipitated the product from its

methylene chloride solution. **BFcVCH$^+$TFPB$^-$** had the same green color as **BFcVCH$^+$BF$_4^-$** does and lasted for months in a desiccators.

Whereas most of the bis(2-ferrocenylvinyl) compounds prepared here were fairly stable both in solid/liquid state and in solutions, there were a few exceptions. **Fc(CH=CH)$_2$Fc** and **Fc(CH=CH)$_3$Fc** were observed to have low stabilities in solutions. An unknown brick red solid was observed to precipitate from solution over time, which was believed due to decomposition or polymerization as previously suggested by Spangler.[53] Thus, during the purification procedures, fast recrystallization or flash chromatography was always performed to avoid this pitfall. **BFcVPPh** should also be kept out of solution for long periods of time due to the possible oxidation to the corresponding phenylphophine oxide. Last, **BFcVPyr** is acid-sensitive, purification through column chromatography was thus conducted in a flash manner with basic alumina as adsorbant.

Cis/trans Isomers and Their Influence on Physical and Chemical Properties

It is noteworthy that in this series of **FcCH=CHXCH=CHFc** compounds, not all of them had well-defined geometry around the double bonds. Some of the compounds were inevitably obtained as a *cis/trans* isomeric mixture due to the limitation of the currently available synthetic methods for a specific structure. For instance, **BFcVC≡C**, **BFcVPPh** and **Fc(CH=CH)$_2$Fc** contained all the three configurational isomers as evidenced by NMR spectroscopy. The initial Wittig approach almost always afforded *cis/trans* isomeric mixtures with *trans,trans* isomer as the major component. Efforts to separate the isomers by slow chromatography or recrystallization turned out to be either extremely tedious or fruitless since those isomers showed very little difference in these purification techniques. Isomerization to the thermodynamically more stable product using conventional methods was also futile. We attempted to convert the *cis,trans* and *cis,cis* isomers into the *trans,trans* isomer with catalytic amount of I_2 or p-TSA under heat for several compounds, but none of them produced satisfactory transformations. Instead, I_2 or acid often led to partial oxidation or decomposition of the bisferrocenylvinyl compounds. Therefore, we later applied the Horner-Emmons-

Wordwoth reaction in order to prepare the configurationally pure trans-trans products as we have discussed in the earlier section.

However, it is our intention to address the isomeric mixture issue properly before further discussion. In general, the melting points of the *trans,trans* isomers are usually higher and shaper than the isomeric mixture and the *trans,cis*, *cis,cis* counterparts due to the better packing forms in solid. The regio-regularity and planar conjugation facilitate the possible intermolecular interactions such as π-π stacking between the neighboring molecules. For the same reason, the solubility of *trans,trans* isomer is commonly lower than that of the other isomers and isomeric mixtures. It is especially the case when the X group is an aromatic ring. While the products obtained from Wittig reaction are well soluble in CH_2Cl_2, the exclusive *trans,trans* compounds prepared from HWE reaction dissolve in the same solvent to a limited extent. The extreme examples are *p*-phenylene derivatives **BFcV*p*Ph** and **BFcV*p*Ph(OMe)$_2$**, which are very poorly soluble in CH_2Cl_2, acetone and CH_3CN.

Despite the obvious discrepancy in physical properties, a series of comparison studies of several compounds did not show any significant differences between their isomers in electrochemistry and mixed-valence absorptions, which are the major concerns of this study. Taking **BFcVS** for instance, the cyclic voltammograms of a various ratios of isomeric mixtures showed identical two well-shaped one-electron oxidation waves with peak positions and peak-separation same as that obtained from the pure **(*E,E*)-BFcVS**. The UV-Vis and mixed-valence absorptions of these samples are virtually identical as well. Although the detailed discussion shall be given in later sections, it is necessary to point out at this point that the experimental 'no difference' properties could be the consequences of two general reasons: first, the standard techniques involved here for these properties are not sensitive enough to probe the differences under the conditions of measurements; second, the E/Z configurational differences of this particular series of compounds are not significant to influence the physical or chemical properties investigated in the current work. Based on these facts, it is reasonable to compare the same property among different compounds under the same experimental conditions although the stereochemical issues could not be fully resolved via synthetic or advanced purifying manner for all of the compounds.

X-ray Crystal Structures

Single crystals were grown either by slow solvent evaporation of the corresponding CH_2Cl_2 solutions or by layered diffusion of hexane into the concentrated CH_2Cl_2 solutions of the substrates. Nearly all of the arylene-centered derivatives afforded good crystals for X-ray studies, which should depend on the packing effects originated from the aromatic moieties in the conjugation fragment. In contrast, single crystals of the linear hydrocarbon and heteroatom incorporated analogues turned out to be very difficult to achieve owing to the absence of such packing effects. Aside from that, relatively low solubility (e.g. **Fc(CH=CH)$_2$Fc** and **Fc(CH=CH)$_3$Fc**), poor solid morphology due to steric mixture (e.g. **BFcVPPh**) and flexible backbones could also account for the poorly organized features for compounds this kind. Due to these reasons, **BFcVS** and **(*Z,Z*)-BFcVP(S)Ph** became the only linearly bridged compounds which eventually offered good crystals for X-ray crystallographic analysis.

The identities of **BFcVTh** (ORTEP plot in Figure 2.8), **BFcVFu** (Figure 2.9), **BFcVPyr** (Figure 2.10), **(*Z,Z*)-BFcV*p*Ph** (Figure 2.11), **BFcV*p*Ph(OC$_{12}$H$_{25}$)$_2$** (Figure 2.12), **(*E,E*)-BFcV*o*Ph** (Figure 2.13A), **(*Z,E*)-BFcV*o*Ph** (Figure 2.13B)**, BFcVS** (Figure 2.14) and **BFcVP(S)Ph** (Figure 2.15) were confirmed by the single-crystal X-ray analysis. The selected steric parameters for these compounds are collected in Table 2.1. For all compounds, the ferrocenyl moieties have adopted normal eclipsed conformations for the cyclopentadienyl (Cp) rings. Systematic structural studies revealed a number of interesting features, which provided the opportunity to assess the impact of the π-system chain lengthening, stereochemistry, and substituent modification on metrical parameters and crystal packing preference. Owing to the large volume of structural information derived from the crystallographic data for this group of compounds, in the following discussions, we will only focus on the main structural features and interpret the most important aspects that might have potential correlation between stereochemistry and the relevant physical and chemical properties.

The crystal structures of compounds **(*E,E*)-BFcVTh** and **(*E,E*)-BFcVFu** (Figure 2.8 and 2.9) are very similar. They both adopt a *syn* conformation with respect of the two ferrocenyl units and crystallize in a *pseudo*-plane-symmetric form with the mirror plane

Table 2.1 Selected steric parameters for bis(2-ferrocenylvinyl) compounds.

	BFcVTh	**BFcVFu**	**BFcVPyr**	**BFcV*p*Ph**	**BFcV*p*Ph**
vinyl,vinyl	*E,E*	*E,E*	*E,E*	*Z,Z*	*E,E*
Fc to Fc	*syn*	*syn*	*syn*	*anti*	*Anti*
Fe-Fe (space), Å	10.85	10.37	12.84	11.97	13.49
Fe-Fe (bond), Å	16.72	16.56	16.69	16.84	17.86
Planes					
Cp1(subs)-Cp2(subs)	15.34	1.81	26.68	0	0
Cp1(subs)-Ar	8.41	1.49	12.94	58.34	1.98
Cp2(subs)-Ar	8.41	2.74	22.79	58.34	1.98

	BFcV*p*Ph'[a]	**BFcV*o*Ph**	**BFcV*o*Ph**	**BFcVS**	**BFcVP(S)Ph**
vinyl,vinyl	*E,E*	*E,E*	*E,Z*	*E,E*	*Z,Z*
Fc to Fc	*anti*	*syn*	*syn*	*anti*	*Anti*
Fe-Fe (space), Å	13.53	10.138	7.74	9.77	9.43
Fe-Fe (bond), Å	16.77	14.02	14.08	13.14	13.32
Planes					
Cp1(subs)-Cp2(subs)	0	65.72	86.63	52.74	3.16
Cp1(subs)-Ar	21.41	17.7	61.55	N/A	N/A
Cp2(subs)-Ar	21.41	59.92	76.77	N/A	N/A

[a] 2,5-didodecyl substituted *para*-phenylene derivative **BFcV*p*Ph(OC$_{12}$H$_{25}$)$_2$**.

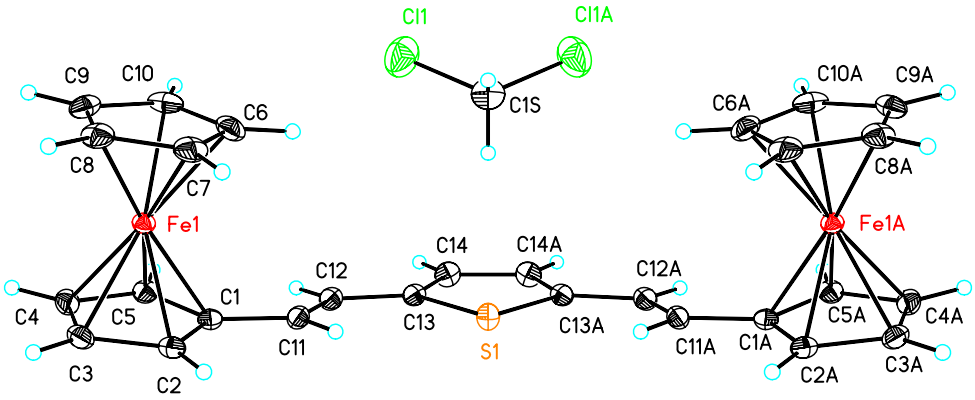

Figure 2.8 ORTEP plot of **BFcVTh**.

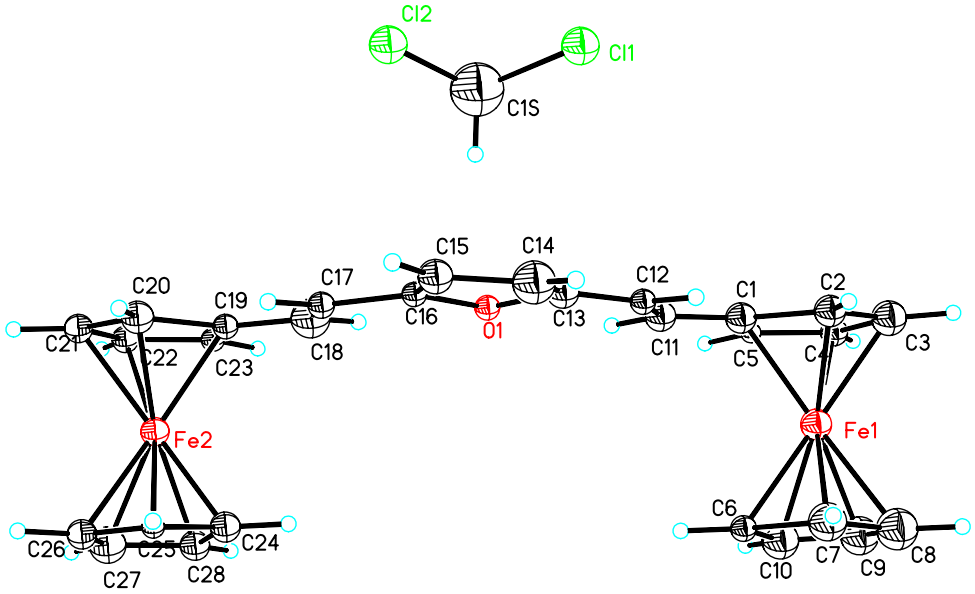

Figure 2.9 ORTEP plot of **BFcVFu**.

A

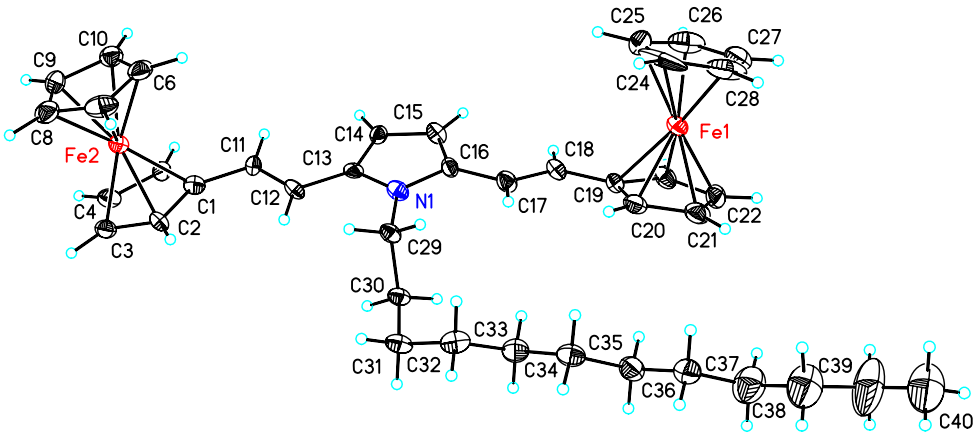

B

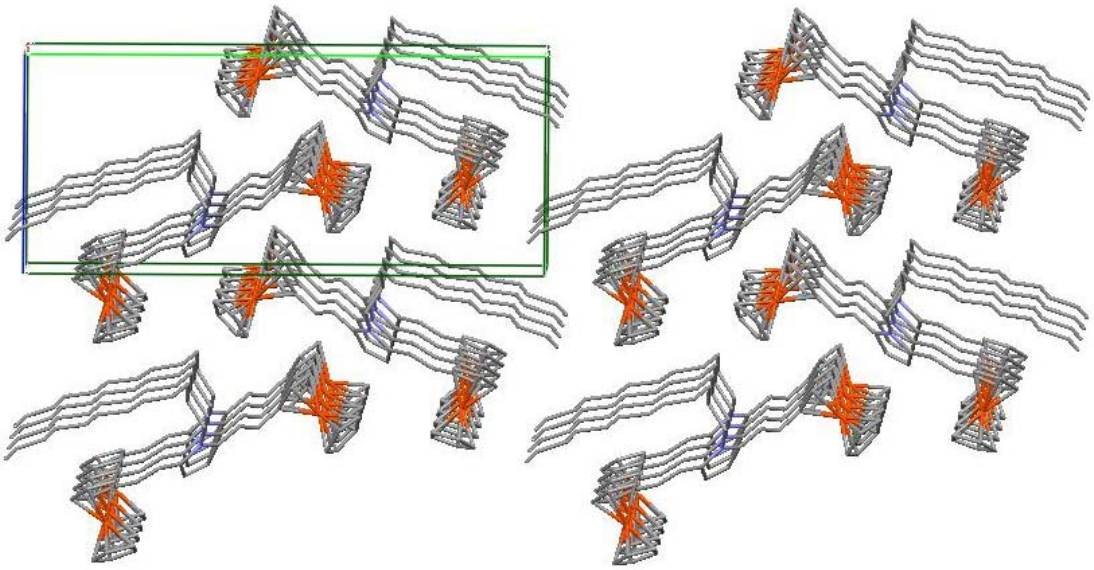

Figure 2.10 ORTEP plot (A) and packing form (B) of **BFcVPyr**.

passing through the heteroatom (S or O) and perpendicular to the aromatic ring. The substituted Cp rings are essentially coplanar with the 2,5-substituted heteroaromatic ring. This is clearly evident from the dihedral angles between the central furan ring, taking **BFcVFu** for instance, and the ending substituted Cp rings (2.74^{o}, max), and the dihedral angle between the two substituted Cp rings (1.81^{o}, virtually perfectly parallel), which secure a high degree of conjugation. The iron-iron through-space distances for **BFcVTh** and **BFcVFu** are 10.85 Å and 10.37 Å, respectively, while the corresponding sums of the intervening bonds in the conjugation path are longer, 16.72 Å and 16.56 Å. These close structural similarities between **BFcVTh** and **BFcVFu** set the foundation that their electronic differences should stem from the electron distribution along the conjugation chain, which is in turn governed by the heteroatom inside the aromatic nucleus. Their shorter through-space iron-iron distances, when compared with that of 1,4-bis(2-ferrocenylvinyl)benzene (13.49 Å), should also contribute the stronger metal-metal intramolecular interaction manifested by electrochemistry.

Compared to the nearly parallel arrangement of the two ferrocenyl moieties in **BFcVTh** and **BFcVFu**, the two ferrocenyl groups in **BFcVPyr** (Figure 2.10) tilt 26.68^{o} with respect to each other, which is ascribed to the steric effects arising from the long-chain alkyl fragment attached to the central pyrrolene ring, leading to a longer metal-metal distance (through-space). Owing to the same reason, the pyrrolene ring is no longer coplanar with the substituted Cp rings, giving rise to a maximum 22.79^{o} dihedral angle between the pyrrolene and substituted Cp rings. Interestingly, in spite of the noticeable steric hindrance, the two ferrocenyl units do not embrace an *anti* conformation to minimize the steric congestion, but appear as *syn*. Aside from that, the dodecyl hydrocarbon chain attached on the nitrogen of the pyrrole nucleus does not linearly zig-zag to one direction as most often observed in other structures incorporating the same alkyl chain. It bends roughly 90 degree at the forth carbon from the nitrogen atom so that the entire chain shapes as an ‘L’. Both of the structural arrangements above could be better understood when the packing factors are taken into account, as shown in Figure 2.10B (viewed from slightly tilted a axis). The crystal packing form of **BFcVPyr** suggests the ferrocenyl *syn* conformation and L-shaped alkyl orientation allow the more efficient and tighter packing along the molecular layers. With these arrangements, the

layered (along b axis) ferrocenyl moieties engage in the classic offset edge-to-edge (OEE) intermolecular motif and the bending alkyl chains align parallelly to each other along the layer propagation.

The single crystal structure of **(*Z*,*Z*)-BFcV*p*Ph** (Figure 2.11) was obtained from the corresponding Wittig product. The X-ray analysis of its geometric isomer, (***E*,*E*)-BFcV*p*Ph**, was previously reported on several occasions.[54] Both of them have *anti* conformation with respect to the ferrocenyl units. For both steric isomers, the dihedral angle of the two substituted Cp rings is 0^{o}, namely the two ferrocenyl moieties are perfectly parallel to each other. However, while the *p*-phenylene ring in ***(E,E)*-BFcV*p*Ph** is virtually coplanar with the substituted Cp rings, dihedral angle of 1.98^{o}, the *p*-phenylene group in **(*Z*,*Z*)-BFcV*p*Ph** is severely distorted away (58.34^{o}) from the ferrocenyl alignment plane as shown in Figure 2.11A. The iron-iron through-space (11.97 Å) and through-bond distances (16.84 Å) of **(*Z*,*Z*)-BFcV*p*Ph** are shorter than those (13.49 Å and 17.86 Å, respectively) of **(*E*,*E*)-BFcV*p*Ph** due to the steric differences.

The stereochemistry of didodecyloxy substituted (2,5 on the *p*-phenylene ring) compound, **BFcV*p*Ph($OC_{12}H_{25}$)$_2$** (Figure 2.12), resembles that of **(*E*,*E*)-BFcV*p*Ph** in terms of conformation, structural symmetry and bond distance as indicated in Table 2.1. However, the structural modification on the central phenylene moiety apparently twists the phenylene ring out of the conjugation plane between the two substituted Cp rings by a dihedral angle of 21.41^{o}. This could be attributed to the steric effects similar to what was observed in compound **BFcVPyr**. Different from that of **BFcVPyr**, where the dodecyl backbone bends approximately 90^{o} on the one-third way of propagation, the same long alkyl chain in **BFcV *p*Ph($OC_{12}H_{25}$)$_2$** adopts a normal linear orientation from the beginning to the end along the hydrocarbon skeleton. In addition, the two side chains attached on the 2,5-position of *p*-phenylene group align on the same plane but extend to the opposite direction. The unit cell packing diagram of **BFcV *p*Ph($OC_{12}H_{25}$)$_2$** (Figure 2.12B) presented two types of molecule orientations between the adjacent layers. With respect to the ferrocenyl moieties, the layered ferrocenyl units adopt a face-to-edge motif; from the viewpoint of the long alkyl chains, the long chains from adjacent layers forming a crossing 'X' shape with respect to each other. Apparently, this packing form is governed by the long hydrocarbon-chains.

A

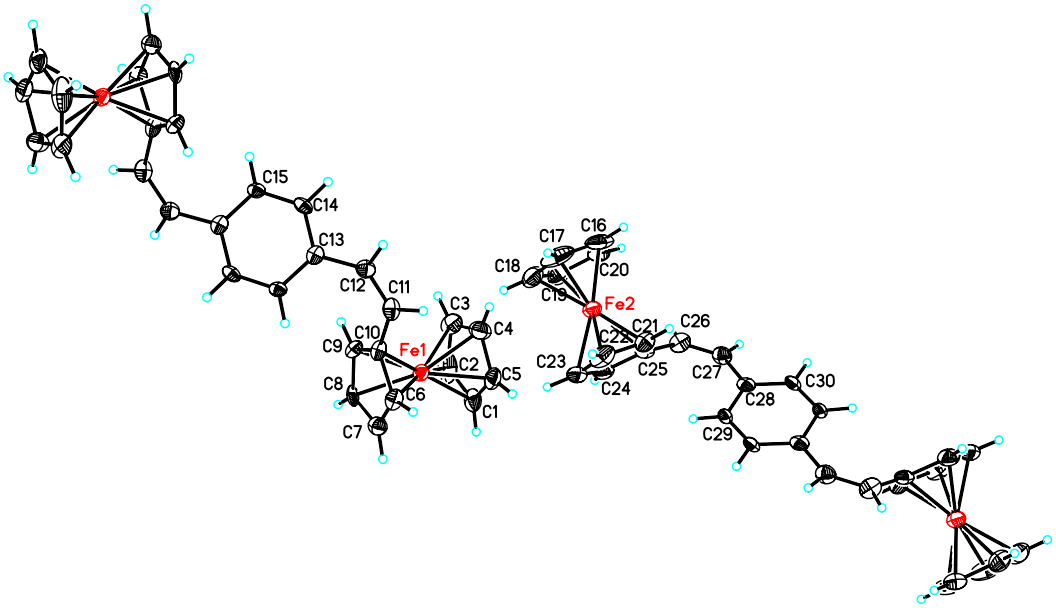

B

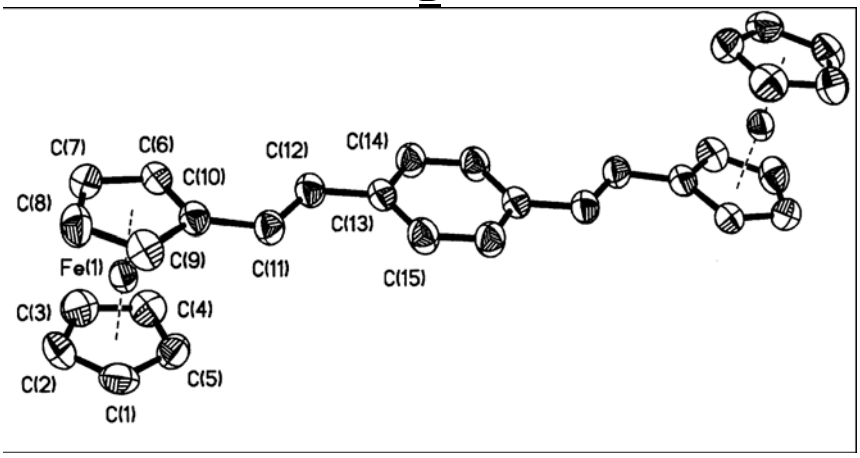

Figure 2.11 ORTEP plots of **(*Z*,*Z*)-BFcV*p*Ph** (A) and **(*E*,*E*)-BFcV*p*Ph**[54] (B).

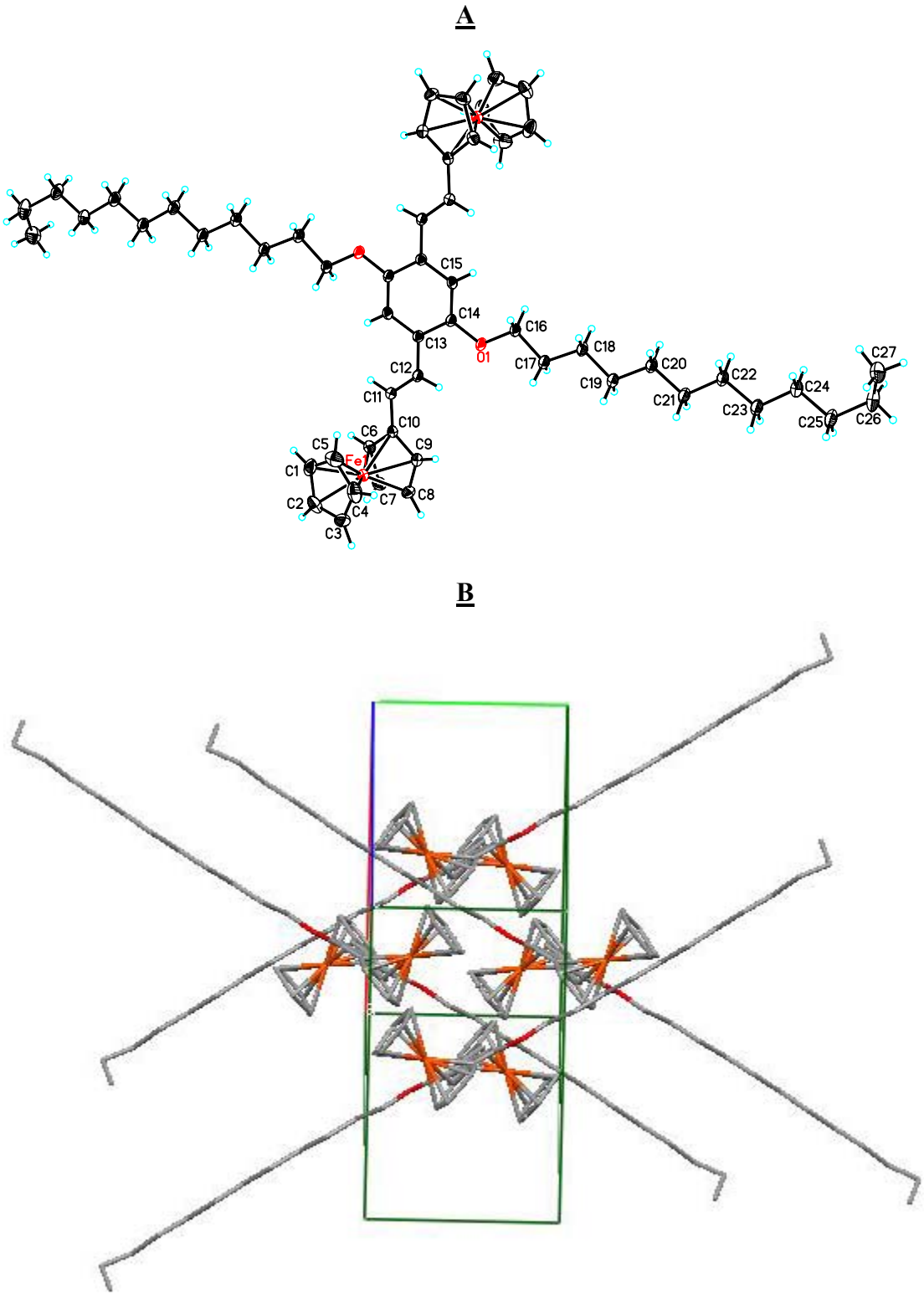

Figure 2.12 ORTEP plot (A) and unit cell packing form (B) of **BFcV*p*Ph(OC$_{12}$H$_{25}$)$_2$**.

For compound **BFcV*o*Ph**, two geometric isomers, (*E,E*)- and (*E,Z*)-forms, were isolated and crystallized from the corresponding HWE and Wittig products. Compared to their *para*-analogues, the *ortho*-substituted bis(2-ferrocenylvinyl)benzenes contain significant steric congestions due to the close proximity of the two bulky ferrocenylvinyl fragments attached on the 1- and 2- positions of the central phenylene ring. This is clearly reflected in their crystal structures as shown in Figure 2.13. Both the (*E,E*)- and (*E,Z*)-forms demonstrate serious distortion, in the view of the steric arrangement of the *o*-phenylene and two substituted Cp rings, along the conjugation pathway. The extreme case occurrs in the (*E,Z*)-form. Due to its overall unfavorable *cis,trans* configurations of the vinyl bonds, one of the ferrocenyl groups, i.e. the Fe(1)-incorporating ferrocene, adopts an orientation virtually perpendicular to both the *o*-phenylene ring and the other ferrocenyl unit to release the strain. Apart from that, the Cp ring of the second ferrocenyl group still distorts 61.55^{o} from the phenylene plane. The progressive conjugation is obviously afflicted due to these distortions. For the same reason, however, the iron-iron through-space distance of the (*E,Z*)-isomer is substantially shortened to 7.74 Å in contrast to that of the (*E,E*)-isomer (10.07 Å), while the through-bond distances of the (*E,Z*) and (*E,E*) forms are essentially the same (approximately 14 Å). In theory, these significant structural differences should be reflected in their electronic and redox behaviors.

Upon replacing the rigid aromatic unit with a heteroatom, S, the linking fragment in **BFcVS** is rather flexible as shown in Figure 2.14. The two ferrocenyl units adopt an *anti* conformation and a 42.84^{o} torsion angle between the two substituted Cp rings. Since the vinyl groups are virtually coplanar to the attached Cp rings, the relative spatial arrangement of the two ferrocenyl units is essentially an outcome of the displacement of the central C(12)-S and S-C(13) bonds. The C(12)-S bond length (1.74 Å) and C(12)-S-C(13) angle (105.4^{o}) are in the expected range. The metal-metal through-space and through-bond distances are very close to those of **(*E,E*)-BFcV*o*Ph**.

Although **BFcVP(S)Ph** was synthetically obtained as an isomeric mixture, the single crystal isolated from the substrate solution was identified as the (*Z,Z)*-isomer

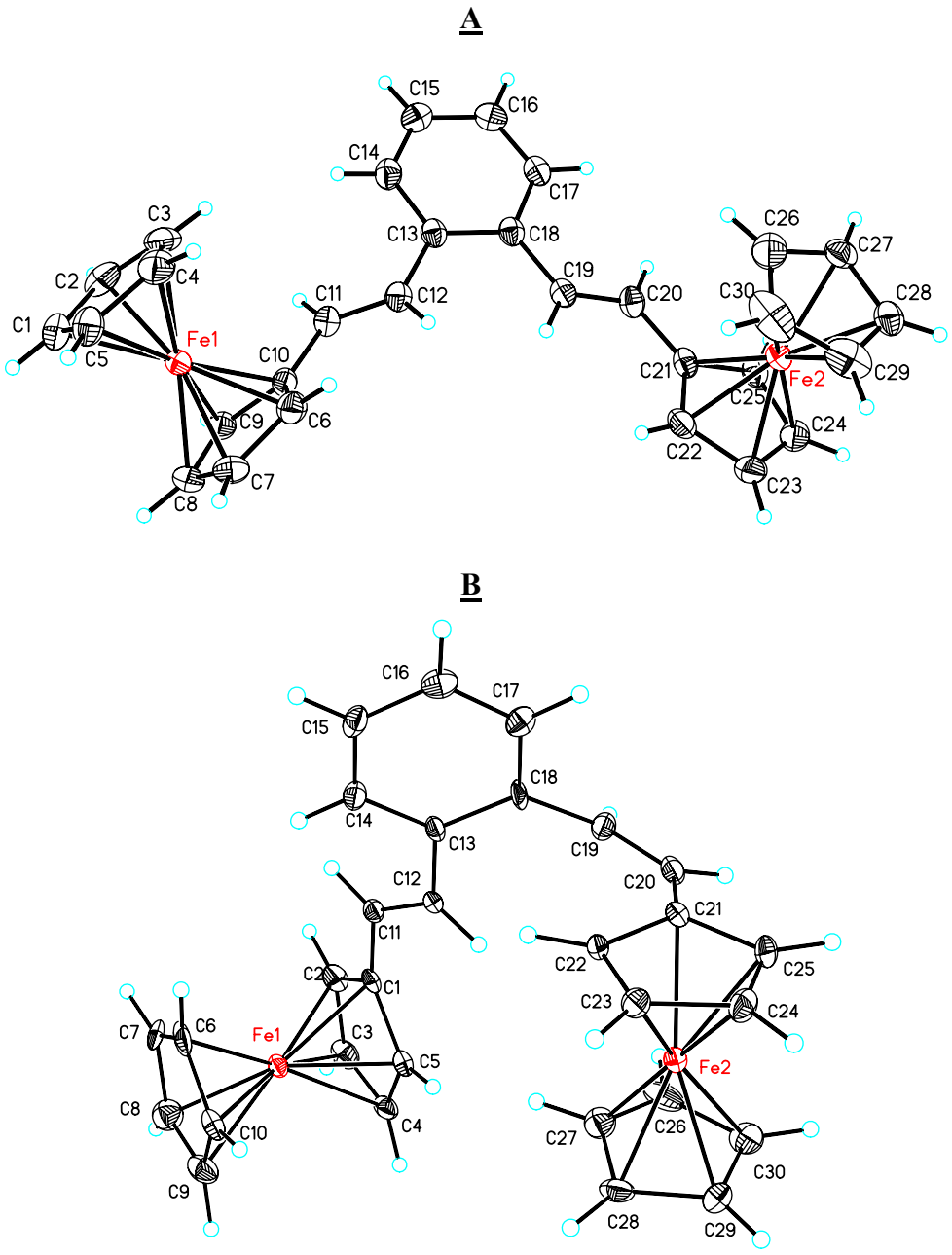

Figure 2.13 ORTEP plots of **(*E,E*)-BFcV*o*Ph** (A) and **(*E,Z*)-BFcV*o*Ph** (B).

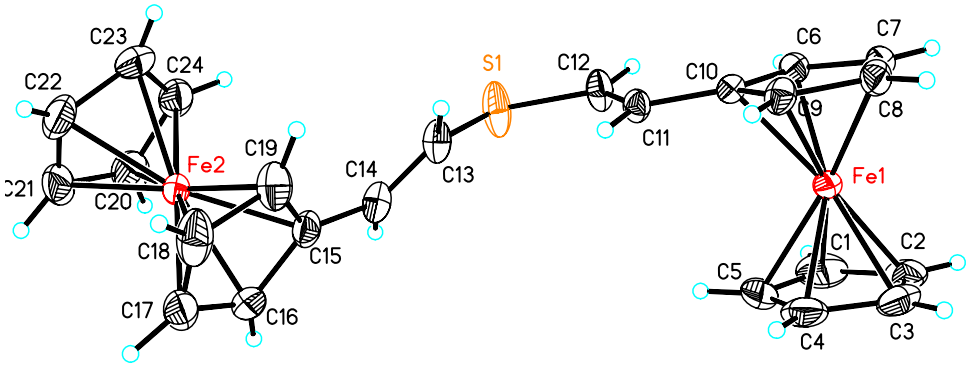

Figure 2.14 ORTEP plot of **BFcVS**.

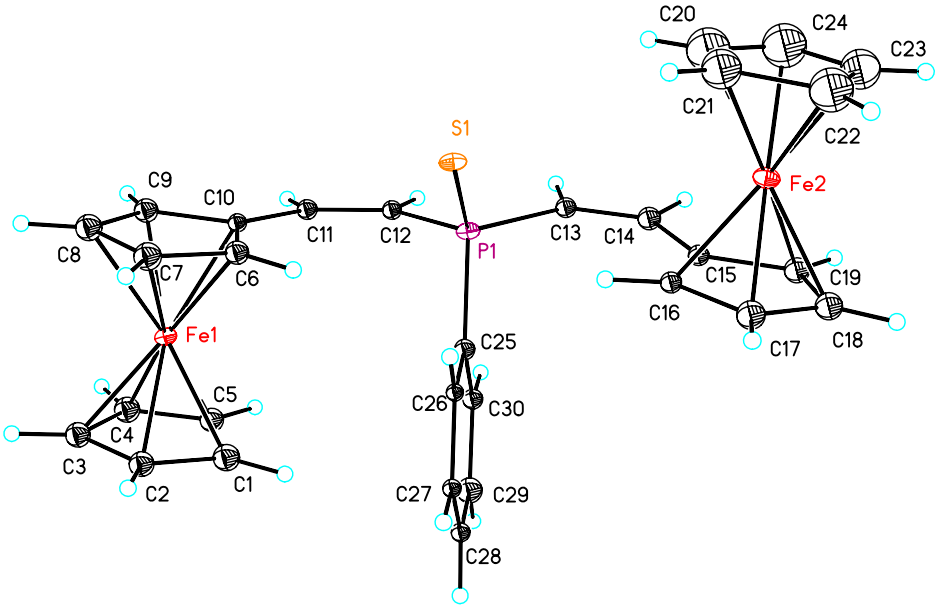

Figure 2.15 ORTEP plot of **BFcVP(S)Ph**.

(Figure 2.15). The most remarkable structural feature of the (*Z,Z*)-isomer is its *pseudo*-coplanarity along the conjugation path. The disposition of the two ferrocenes is *anti*. The phenylene ring attached on the phosphorus atom displaces nearly perpendicular to the bridging plane and takes a face-to-edge orientation to the co-sided ferrocenyl group. This steric arrangement certainly has important consequences in minimizing the steric conflict between the aryl and metallocenyl groups, and contributes to the non-distorted

conjugation pathway. While most of the bond lengths and angles lie in the normal range, the C(10)-C(11)-C(12) and C(13)-C(14)-C(15) angles are 133.82° and 132.96°, respectively, which are notably greater than the common sp^2 bond angles. In contrast, the C(12)-P(1)-C(13) angle (100.47°) is smaller than expected, resulting a shorter C(12)-C(13) through-space distance (2.77 Å) similar to that of **BFcVS**.

Electrochemistry

General considerations

Previous polarographic studies in our laboratory have used conventional $Bu_4N^+PF_6^-$, BF_4^- or ClO_4^- as the supporting electrolyte. However, not until recent years, has the use of the more nucleophobic counterions, $B(C_6F_5)_4^-$ ($THPB^-$) and $B[3,5\text{-}C_6H_3(CF_3)_2]_4^-$ ($TFPB^-$) been found to give wider peak separations than the conventional anions.[55, 56] The improved electrochemistry arises from the weakly coordinating nature of the bulky anions.[57] Geiger and co-workers have performed extensive studies on the fluoroarylborate anions, the reported larger peak separation was ascribed to the low ion-pairing effect.[55, 58, 59]

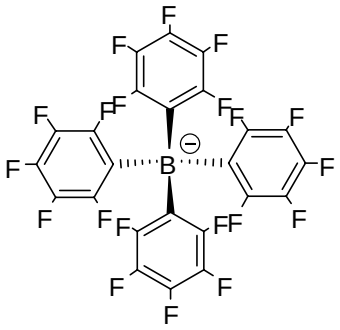

tetrakis(pentafluorophenyl) borate (**PFPB**)

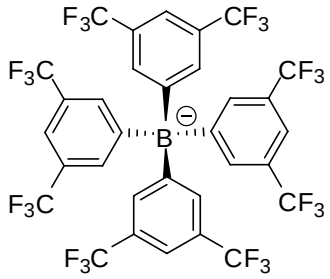

tetrakis(3,5-bis(trifluoromethyl) phenyl)borate (**TFPB**)

Our first handle on one of the fluoroarylborate anions, $TFPB^-$, dates back to our earlier search for solubility-promoting couter-anion for multiply-charged oligoferrocenyl complexes. Later applications of this bulky species as supporting electrolyte anion in electrochemistry show two remarkable advantages as follows:

1) It significantly enlarges the peak separations (ΔE) between the successive redox processes. This is particularly valuable for weakly-interacting systems, which are more sensitive to ion-pairing effect. Although the conventional supporting electrolyte anions, PF_6^-, BF_4^-, and ClO_4^-, are generally considered as low ion-pairing counterions comparing to halide, their nucleophilic effects are more important than previously estimated.[57] For partially oxidized compounds, the ideal experimental condition is the one having minimized peripheral effects that could affect the intrinsic electronic interaction in the mixed valent system. Taking **BFcVS** for instance, this biferrocenyl compound showed a single two-electron oxidation process (-50 mV vs. Fc/Fc^+) in the solution of $Bu_4N^+PF_6^-$ in CH_2Cl_2, but two well separated one-electron waves (ΔE = 180 mV) when the supporting electrolyte was changed to $Bu_4N^+TFPB^-$ (see Figure 2.16). Utilizing the 'free'-coordinating $TFPB^-$ basically allows the first positive charge generated on one of the ferrocenes to be more delocalized along the bridging fragment to effectively perturb the second oxidation process otherwise won't take place. By enlarging ΔE, the comproportionation constant (Eq. 2.5) will be exponentially increased to favor the monocationic form as shown below,

$$\text{Fc-B-Fc} + [\text{Fc-B-Fc}]^{2+} \rightarrow 2\,[\text{Fc-B-Fc}]^{+} \qquad (2.3)$$

$$K_c = [[\text{Fc-B-Fc}]^{+}]^2 / \text{Fc-B-Fc} \times [\text{Fc-B-Fc}]^{2+} \qquad (2.4)$$

$$\Delta E = (RT/F)\ln K_c \qquad (2.5)$$

where -B- denotes the bridging fragment between the ferrocenyl groups and K_c is the conproportionation constant.

2) The bulky anions stabilize multiply-charged cations in the most often used electrochemical solvents such as CH_2Cl_2 and CH_3CN. Multiply-oxidized cations commonly encounter solubility problems in low-polarity CH_2Cl_2 and even in CH_3CN.[60, 61] This problem consequentially causes electrode passivation and gives rise to stripping-type CV waves[62, 63] which obscure the thermodynamic and mechanistic information ideally available in voltammetric experiments. The emergence of the large weakly-coordinating anions, has tremendously ameliorated the solvent-based effects[64] and promoted better resolved electrochemical behavior. In our laboratory, numerous multiply-oxidized compounds have shown greatly improved results when $Bu_4N^+TFPB^-$ is

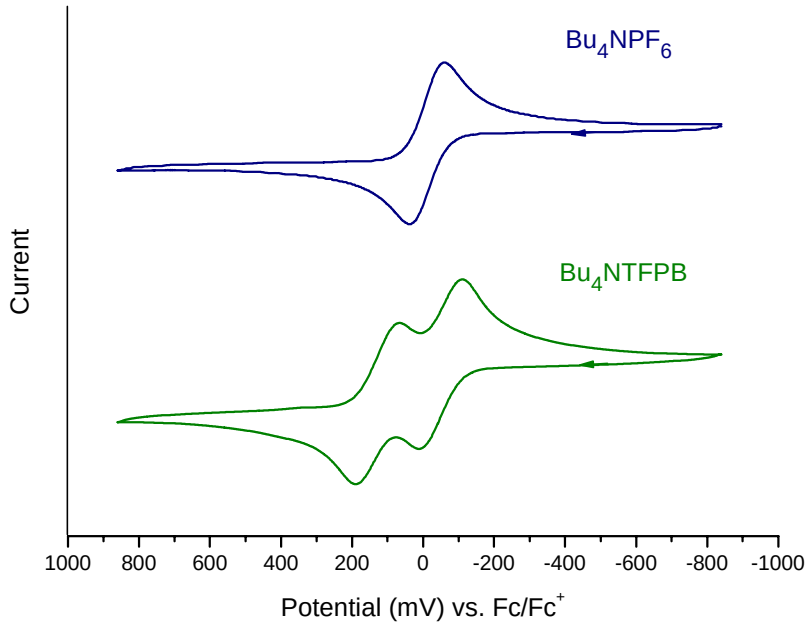

Figure 2.16 Cyclic voltammograms of **BFcVS** in a CH_2Cl_2 solution with Bu_4NPF_6 (top, blue) and Bu_4NTFPB (bottom, green) as supporting electrolyte. Scan rate: 50 mV/s.

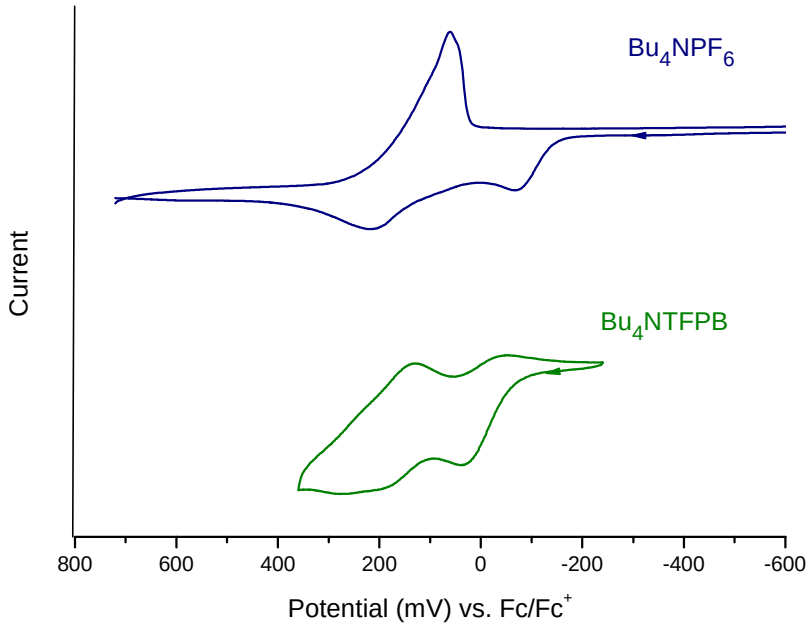

Figure 2.17 Cyclic voltammograms of **BFcVPPh** in a CH_2Cl_2 solution with Bu_4NPF_6 (top, blue) or Bu_4NTFPB (bottom, green) as the supporting electrolyte. Scan rate: 50 mV/s.

used as the supporting electrolyte. Taking **BFcVPPh** for instance (Figure 2.17), the cyclic voltammogram of this compound indicates the electrochemistry is fully irreversible after the anodic reactions in CH_2Cl_2 with PF_6^- as the counterion. However, two semi-reversible waves are observed upon changing the supporting electrolyte to $Bu_4N^+TFPB^-$ in the same solvent. Whereas this is rather a comprehensive set of parameters leading to such improvement than simply attributed to the low ion-pairing and increased solubility, the stabilization effects derived from employing fluoroarylborate in electrochemistry are very notable and deserve more fundamental studies in future work.

For these reasons, we selected $Bu_4N^+TFPB^-$ and the oxidatively more reliable solvent, CH_2Cl_2, as the electrochemical medium throughout the current work. According to the literature, although there is no apparent difference between $PFPB^-$ and $TFPB^-$ as supporting electrolyte anions,[55, 58] we focused on $TFPB^-$ simply because it is synthetically more economic. The synthetic precursor, Na^+TFPB^-, could be easily prepared from commercially available 3,5-bis(trifluoromethyl)bromobenzene via a multiple-step one-pot reaction in excellent yield (90%).[26, 27] Methathesis ion exchange of Na^+TFPB^- with $Bu_4N^+Br^-$ readily afforded the electrolyte, $Bu_4N^+TFPB^-$. This ammonium salt was recrystallized several times from CH_2Cl_2/Et_2O and always freshly passed through alumina chromatographic column (CH_2Cl_2) just before use.

E/Z Configuration and its Impact on Electrochemistry

As we have discussed in previous sections, isomeric mixtures are an inevitable issue for some of the compounds in this series of biferrocenyl compounds. Whether or not the stereochemistry will affect the electrochemical behavior is essential to be addressed properly.

It was our plan to go through both Wittig and HWE methodologies to obtain more than five bisferrocenylvinyl compounds comprising both the isomeric mixture and (*E,E*)-pure product. Diligent separation of the isomeric mixture through very slow column chromatography also provided us with very small amount of pure (*E,Z*)-isomer such as **(*E,Z*)-BFcV*p*Ph** and **(*E,Z*)-BFcVTh**. Furthermore, synthetically we also made two geometric isomers of **Fc(CH=CH)$_3$Fc** with the central vinyl bond predefined as *cis* and *trans* from the starting material. With this sample library at hand, we were able to

conduct comparative studies of the impact of stereochemistry on its corresponding electrochemical behaviors. It was found that most of the compounds exhibited no electrochemical variations with the steric arrangement of the double bonds.

Apart from the two general reasons pointed out earlier, the observed electrochemical consistency among the steric isomers could also be explained by the mechanism of electronic interaction. The iron-iron distance in this series of compounds ranges roughly from 8 Å to 14 Å, which is long enough to exclude the through-space interaction since it has been well established that the direct metal-metal orbital-overlapping interaction only affects within very close proximity (roughly 3-4 Å) and drops exponentially with lengthening distance. Thus, the peak separation (ΔE), which is routinely used to address the degree of electronic coupling between the metal centers, must be a result of through-bond effect. When no obvious distortion presents in the bridging fragment, the *cis*-*trans* configurational difference could play very little role under such through-bond mechanism.

Additionally, our earlier study[10] on diferrocenyl complex bridged by polymethine cation has revealed that the synthetic precursor **BFcVCH$_2$**, a geometric mixture, was all converted to the thermodynamically favorable (*E,E*)-cationic form upon hydride extraction as shown below.

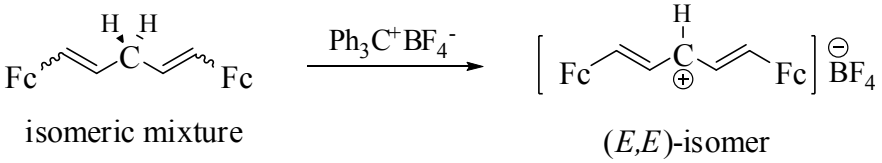

isomeric mixture (*E,E*)-isomer

Enlightened by this fact, we postulated that the *Z*-vinyl bonds could also be isomerized to the *E* form during the anodic oxidation reaction. This hypothesis was later circumstantially substantiated by a simple experiment illustrated in Figure 2.18. A small amount of the isomeric mixture of **BFcVS** was first electrochemically oxidized to the dicationic species upon being exposed to a constant potential 200 mV positive than the second oxidation wave of **BFcVS**. After the transformation was completed, the brown colored dicationic solution was immediately reduced back to the original neutral compound by exposure to a constant potential 400 mV negative than the first oxidation of

BFcVS. The two reversed redox processes were strictly protected by an inert argon atmosphere. After column chromatographic purification, almost 90% of the **BFcVS** was recovered. The NMR result manifested that all the isomers have been converted to the (*E,E*)-form. Therefore, it is very likely that isomerization during the redox processes accounts for the electrochemical uniformity among the geometric isomers, which is especially the case when the thermal barrier for such isomerization is low (e.g., for the linear biferrocenes).

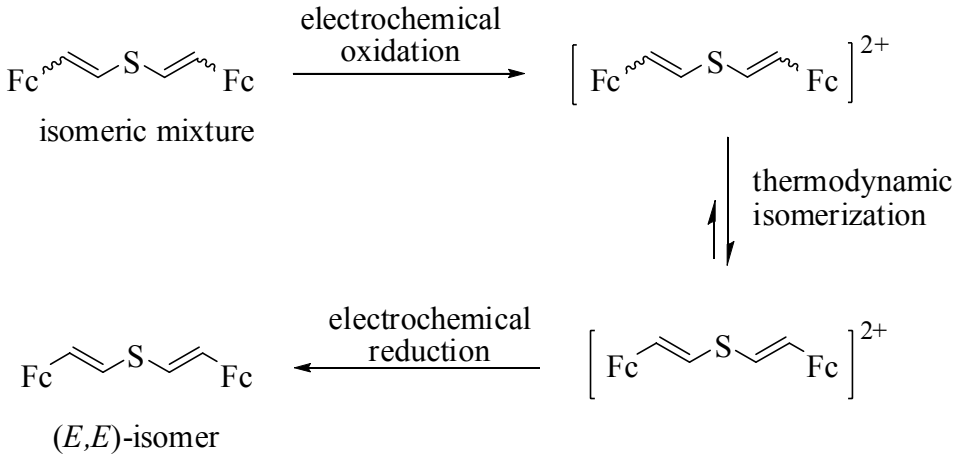

Figure 2.18 Electrochemical isomerization of **BFcVS**.

The *ortho*-phenylene derivatives, however, show different couplings as a function of stereochemistry. The (*E,E*)-isomer shows a 110 mV coupling, while the (*E,Z*)-isomer shows zero coupling (see Figure 2.19). The crystal structures of both isomers (*vide supra)* illustrate why and also provide an answer to the continuing question: what is the role of through-space interaction. The structure of the (*E,Z*)-isomer indicates that, while the center-to-center distance between iron nuclei is close, the π system is so distorted from planarity as to preclude resonance coupling. Despite the closer iron-iron distance in the (*E,Z*)-isomer, the lack of such coupling indicates that through-space communication is insignificant in these systems. Moreover, due to the rigidity of the central aromatic ring,

the *cis*-to-*trans* isomerization is not plausible because of the high thermal barrier required for such process to occur.

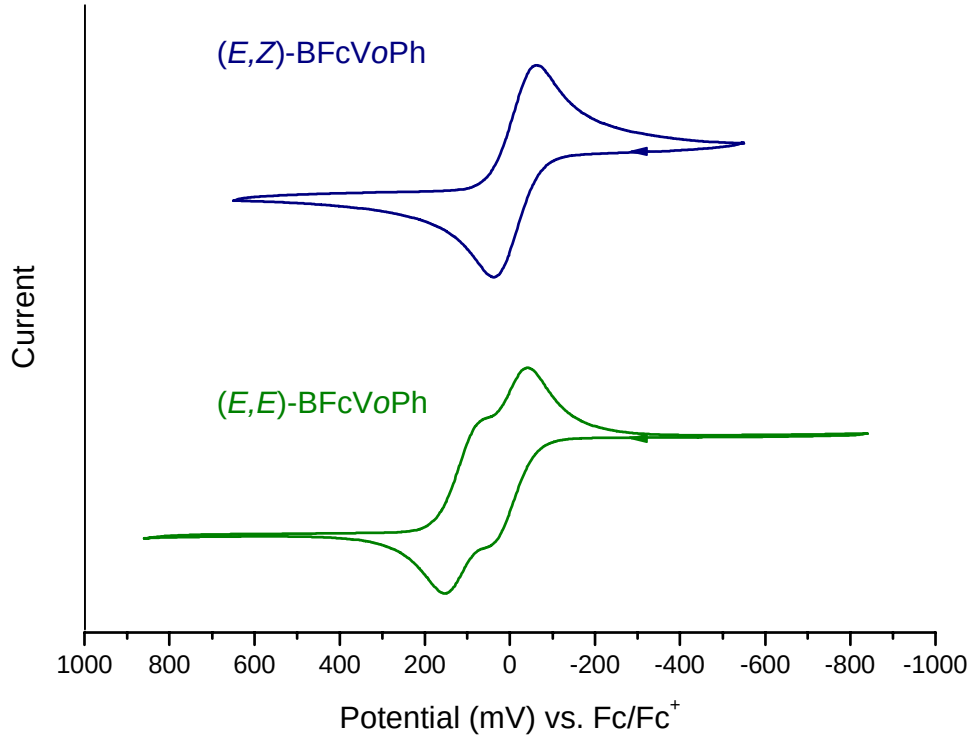

Figure 2.19 Cyclic voltammograms of **(*E,Z*)-BFcV*o*Ph** and **(*E,E*)-BFcV*o*Ph** in a CH_2Cl_2 solution containing 0.1 M Bu_4NTFPB. Scan rate: 50 mV/s.

Electrochemistry Results and Discussions

The cyclic voltammetry (CV) results of the biferrocenyl compounds are summarized in Table 2.2. The half wave potentials were reported versus Fc/Fc^+ redox couple. For compounds having peak separation less than 100 mV, square wave voltammetry (SWV) was applied to resolve the wave overlaps.

For biferrocenyl compounds herein, the first oxidation potential (E_1) and peak separation (ΔE) are very important parameters in revealing how the bridging linkage alters the electronic property of the metal complexes. The former directly associates with the electron sufficiency or deficiency of the linking ligand, which is substantially tuned

Table 2.2 Electrochemical data[a] (from Cyclic Voltammetry) for the compounds **FcCH=CHXCH=CHFc**.

No.	X	E_1 (mV)	E_2 (mV)	E_3 (mV)	ΔE [b] (mV)	K_c [c]
1	**-**	-35	190		225	6300
2	**C=C**	-80	100		180	1100
3	**CH^+**	-75	210		285	6.5×10^4
4	**C≡C**	50	175		125	130
5	**CH_2**	-25	90		115	≈ 88
6	**CH_2 -CH_2**	0 [d]	-		0	--
7	**C(O)**	+110	235		125	130
8	**O**	-90	110		200	2400
9	**S**	-50	130		180	1100
10	**CH=CHSCH=CH**	-30	45		75	≈ 19
11	**Se**	+50	125		75	≈ 19
12	**PPh**	-20	160		180	1100
13	**P(S)Ph**	+60	210		150	340
14	**P(O)Ph**	+140	240		100	≈ 50
15	***p*-C_6H_4**	-30	60		90	≈ 33
16	***o*-C_6H_4**	0	110		110	≈ 72
17	***m*-C_6H_4**	0 [d]	-		0	-
18	***p*-$C_6H_2(OR)_2$**	-50	55		105	≈ 60
19	**C_4H_2O**	-80	80		160	500
20	**C_4H_2S**	-60	80		140	230
21	**EDOT[e]**	-138	70	1040	208	3200
22	**C_4H_2NR**	-262	93	793	355	10^6

[a] Obtained in CH_2Cl_2 containing 0.1 M Bu_4NTFPB (0.1M). E (mV versus Fc/Fc^+) are the arithmetic average of anodic and cathodic peak potentials. Scan rate: 50 mv/s. [b] $\Delta E = E_2 - E_1$. [c] $\Delta E = (RF/T)\ln K_c$. [d] Two-electron redox process. [e] 3,4-ethylenedioxythiophene.

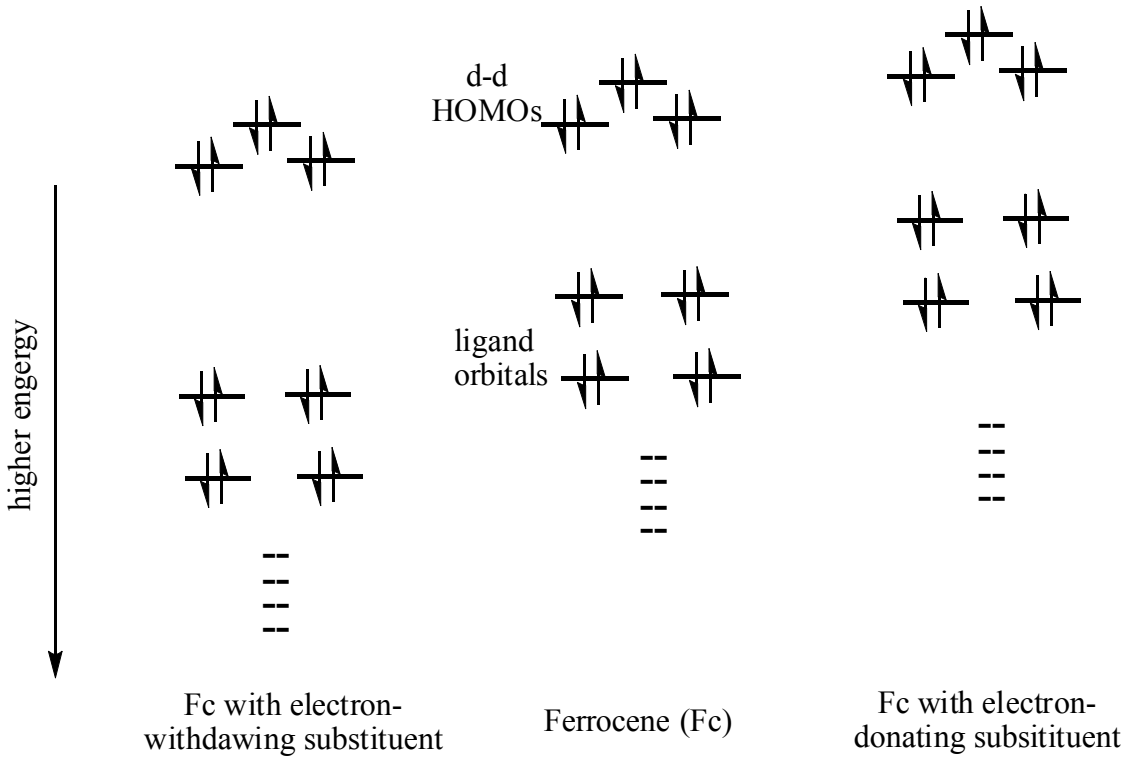

Figure 2.20 Schematic representation of the HOMO metal-d and ligand orbitals of ferrocene and energy perturbation from an electron-donating or withdrawing substituent.

by the X functional group in this series of bisferrocenylvinyl compounds. An electron-rich group lowers E_1, causing a negative shift in comparison to the oxidation potential of the unsubstituted ferrocene; an electron-poor unit increases E_1, giving rise to a positive shift. The degree of such shifting reflects the electron donating or withdrawing capability of the linking unit. This phenomenon can be illustrated in molecular orbital view as shown in Figure 2.20, where the energy level of the metal-based[65] HOMO is varied by the perturbation from the substituents on the Cp ring.

ΔE, which results from stepwise oxidations, is widely considered as one of the most convenient probes for estimating the strength of intramolecular interaction in multiple redox-center containing compounds. While the highly delocalized bimetallic compounds commonly demonstrate large ΔE, the weakly coupled systems show a small or negligible peak separation. It is crucial to realize, however, that charge mobilization is

not the only cause for wave splitting in electrochemistry, other factors such as through-space electrostatic effect, through-bond inductive effect, etc. could also lead to discrete oxidations. Thus, it is important to interpret the electrochemical data carefully and use multiple techniques to disclose the intrinsic natures whenever a controversy arises.

As shown in Table 2.2, in this series of bis(2-ferrocenylvinyl) compounds, nearly all of them except **BFcV*m*Ph** and **BFcVC$_2$H$_4$** demonstrated two metal-based oxidation waves with peak separation ranging from 75 to 350 mV. In order to examine the detailed electrochemical behaviors, in the following discussion, we will divide the compounds into three subgroups according to the functionality of the central X unit and summarize them at the end.

1. X = hydrocarbons. The cyclic voltammograms are shown in Figure 2.21-22. In this group of linearly linked biferrocenyl compounds, **BFcVCH$^+$** showed the largest ΔE, 285 mV, 65 mV higher than the length more favored **Fc(CH=CH)$_2$Fc**. The stronger electronic coupling arises from the solitonic nature of the polymethine cationic chain, which has previously been reported by Tolbert and Zhao.[10] The cyclic voltammogram of **BFcVCH$^+$**, shown in Figure 2.21, however, did not display two well shaped oxidation waves, which was also observed in previous study.[29] Alternating the counterion of **BFcVCH$^+$** from BF_4^- to $TFPB^-$ did not offer any better resolution. The discernible fact is the ionic **BFcVCH$^+$** species was often seen to stick on the surface of the working electrode, which could account for the abnormal electrochemical behaviors. The semi-reversible reduction wave at ca. -600 mV is attributed to the bridging ligand based redox process.

The CV of **Fc(CH=CH)$_2$Fc** and **Fc(CH=CH)$_3$Fc** showed wave separations of 220 mV and 180 mV, respectively. Compared to the smaller (150 mV and 115 mV, respectively) records reported by Spangler,[53] the enlarged ΔEs essentially arose from the better electrolyte anion used in our case. These two literature known compounds were included in this study mainly for the purpose of comparison. **Fc(CH=CH)$_3$Fc** is especially a good referential compound for other bis(2-ferrocenylvinyl) derivatives which could be treated as a variation of **Fc(CH=CH)$_3$Fc** where the central vinylene group is altered by a specific X linking unit. Replacing the central double bond of **Fc(CH=CH)$_3$Fc** with a triple bond gives **BFcVC≡C**, resulting in the first oxidation

shifted to positive (50 mV vs. Fc/Fc^+) and the peak separation decreased to 125 mV (Figure 2.22). The positive shift of the first oxidation originated from the electron deficiency of the ethynyl bond and the decreased peak separation is ascribed to the greater bond alternation along the conjugation backbone. When X becomes carbonyl group (**BFcVC(O)**), the first oxidation wave was even more positively shifted, 125 mV vs Fc/Fc^+, which is attributed to the electron-withdrawing nature of the -C(O)- group. **BFcVC(O)** also demonstrated a ΔE of 125 mV, which suggested the highly polarized carbon atom of the carbonyl group still facilitated an electronic interaction along the conjugation path. However, such interaction is rather derived from accumulated inductive effect than charge mobilization.

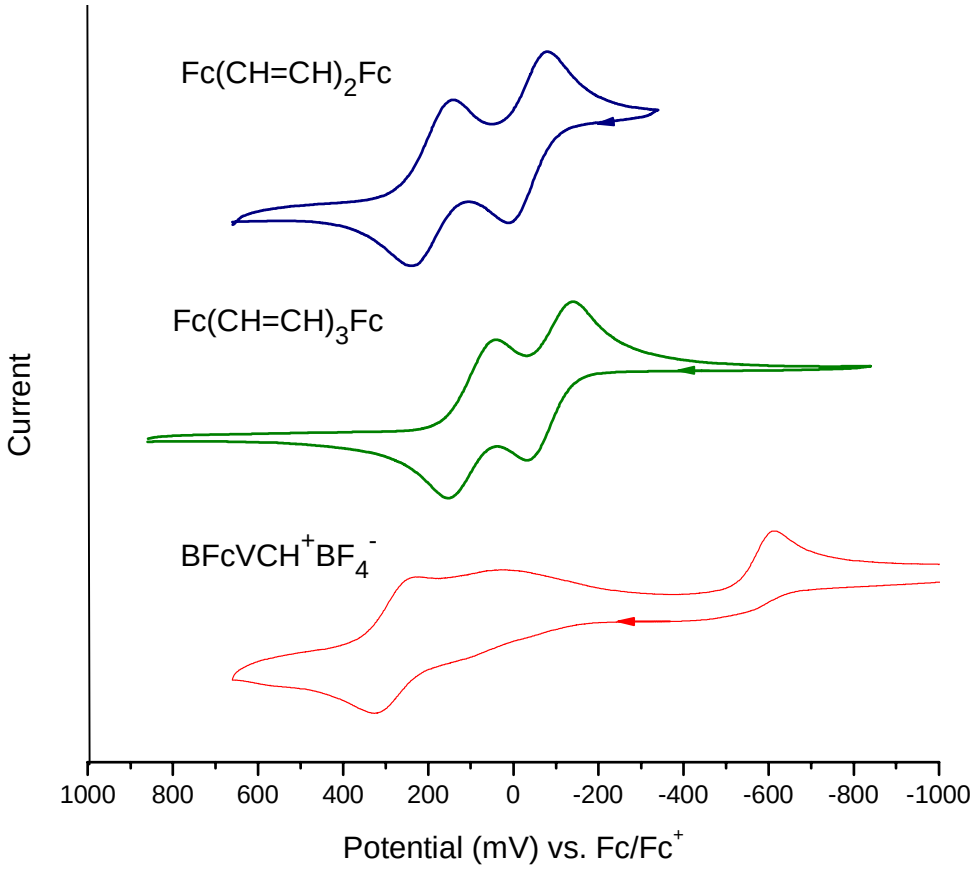

Figure 2.21 Cyclic voltammograms of **$Fc(CH=CH)_2Fc$**, **$Fc(CH=CH)_3Fc$** and **$BFcVCH^+$** in a CH_2Cl_2 solution containing 0.1 M Bu_4NTFPB. Scan rate: 50 mV/s.

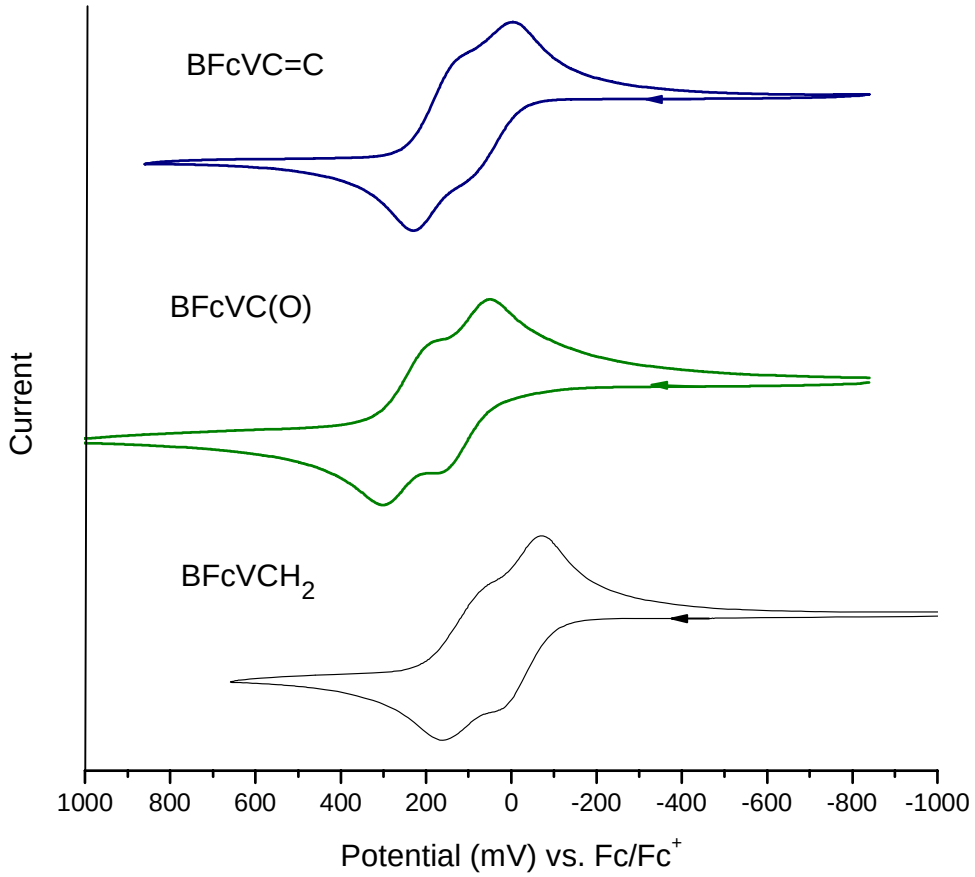

Figure 2.22 Cyclic voltammograms of **BFcVC≡C**, **BFcVC(O)** and **$BFcVCH_2$** in a CH_2Cl_2 solution containing 0.1 M Bu_4NTFPB. Scan rate: 50 mV/s.

To our surprise, the -CH_2- centered **$BFcVCH_2$**, the synthetic precursor of **$BFcVCH^+$**, amazingly revealed two distinguishable oxidation waves in well resolved 1:1 ratio (Figure 2.22). The ΔE is rather small, 105 mV, but clearly reproducible. This observation is quite against to the intuition since the conjugation is considered broken with -CH_2- inserted between two vinylene groups. To further affirm the unexpected result, we deliberately prepared the -CH_2CH_2- centered analogue **$BFcVC_2H_4$** which only demonstrated a single two-electron oxidation process. Thus, the electronic communication between the two ferrocene ends did vanish when the conjugation path is further corrupted.

Although the reason for the observed weak coupling in **$BFcVCH_2$** can not be clearly disclosed yet, there are two possibilities could account for the cause. The first

possibility, which is more likely, is that the peak separation might simply arise from the through-bond inductive effect under current electrochemical conditions. The greatly improved electrochemistry by using the virtually non-coordinating electrolyte anion could allow such subtle effect still being effective through a reasonably 'short' distance. The second possibility, which is a rather challenging one, is that a homo-conjugation[66-68] (shown below) in the intermediate state furnished the electron transport since the calculated distance between the two vinyl carbons connected by the $-CH_2-$ group is 2.53 Å, within the possibility to allow such cross-conjugation to occur.

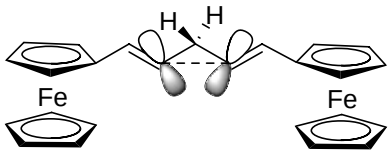

Postulated cross-conjugation in **BFcVCH$_2$**.

2. X= heteroatom. One of the most important contributions of this study is to investigate whether a heteroatom, such as S, O, N, P, etc., can effectively mediate the charge transfer process along a π-conjugation. Different from the shortly bridged diferrocenyl complexes such as **Fc-S-Fc**,[69] **Fc-Se-Fc**,[70] and **Fc-PPh-Fc**,[71] the notion for compounds of **FcCH=CHXCH=CHFc** is that the lone-pair of the heteroatoms, especially those with high polarizability (e.g. N and S), might provide a mechanism for electron transfer by overlapping with the adjacent C-sp^2 orbitals.

Indeed, all heteroatom-centered bis(2-ferrocenylvinyl) derivatives revealed two one-electron oxidations with peak separations ranging from 75 mV to 200 mV (Figure 2.16-17, 2.23-24 and Table 2.2). In the chalcogenide series (X = O, S and Se), **BFcVO** (Figure 2.23) was the most effective (ΔE = 200 mV). This might be attributed to the small size of oxygen and the shortest through-space carbon-carbon distance in the central =CH-X-CH= fragment. The third oxidation wave appeared in the CV of **BFcVO** is tentatively assigned to the bridging ligand based redox process. In contrast, **BFcVSe** (Figure 2.23) exhibited the smallest wave separation, 75 mV, presumably arising from the hardness of the lone-pair electrons in selenium and the unfavorable bond length.

Interestingly, the electrochemical behavior of **BFcVS** (Figure 2.16) is very close to that of **Fc(CH=CH)$_3$Fc**. Both compounds demonstrated a ΔE of 180 mV, suggesting S atom is an electrochemical equivalence of -C=C- bond in terms of supporting electronic interaction. Such equivalency was also observed in other S containing systems in our later studies (see Chapter 4). Insertion of one more vinyl bond at each side of S atom of **BFcVS** gives **BFcVCH=CHSCH=CH** (Figure 2.23) and resulted in a shrunk ΔE (75 mV) because of the decayed coupling between the redox centers with the lengthening distance.[10, 53]

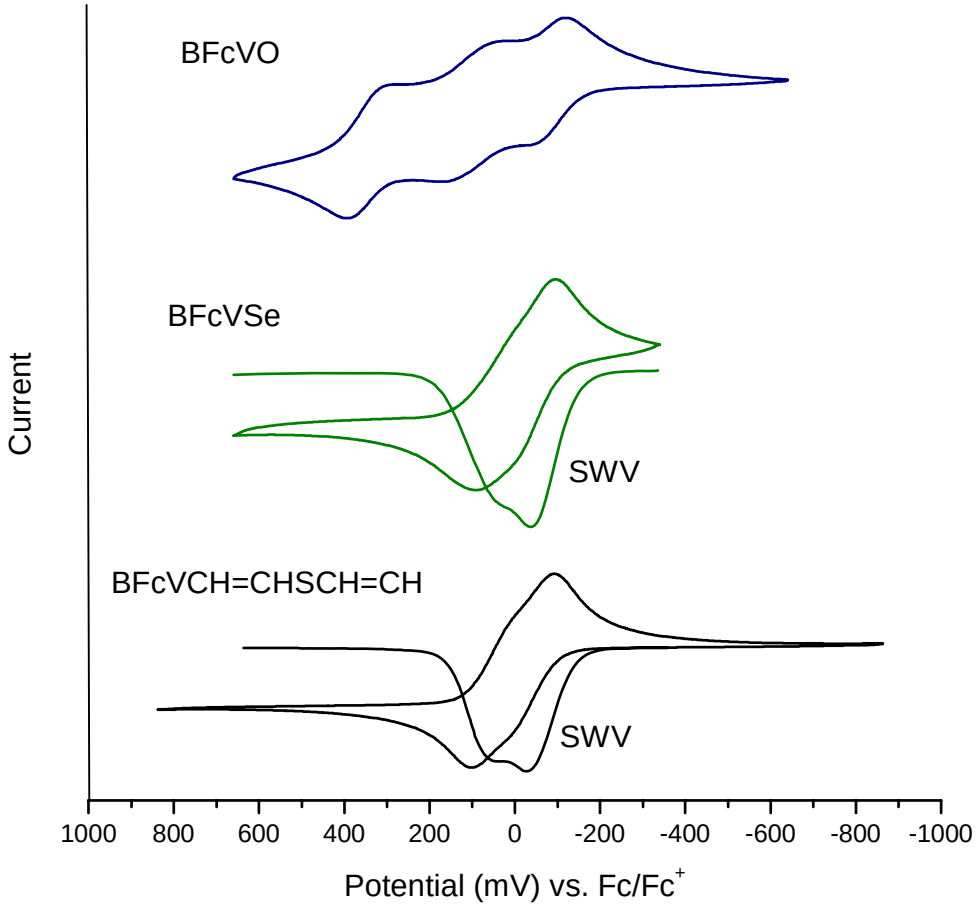

Figure 2.23 Cyclic voltammograms of **BFcVO**, **BFcVSe** and **BFcVCH=CHSCH=CH** in a CH_2Cl_2 solution containing 0.1 M Bu_4NTFPB. Scan rate: 50 mV/s.

As mentioned earlier, the cyclic voltammogram of **BFcVPPh** did not present two well-shaped reversible oxidation waves. This situation was especially worsened when PF_6^- was used as the electrolyte anion, whereby the returning reduction sweep only offered a stripping wave indicating the compound was possibly decomposed during the anodic reactions. Replacing PF_6^- with $TFPB^-$ moderated the wave stripping problem by increasing the solubility of the cationic and dicationic species of **BFcVPPh**, resulting in two semi-reversible waves with a peak separation of 170 mV. Initially we proposed that the irreversibility could arise from a possible chemical oxidation process during the anodic sweeping. For instance, the trace amount of oxygen presented in the reaction media could transform the phenylphosphine compound into the corresponding phenylphosphine oxide during the electrochemical process.

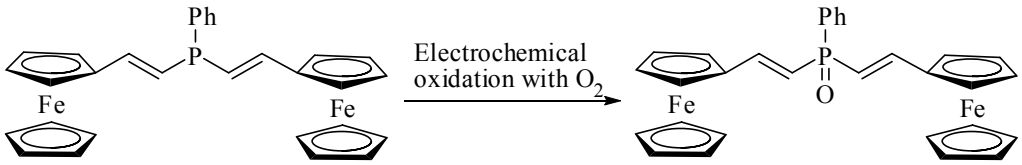

Figure 2.24A Speculated electrochemical transformation of **BFcVPPh** to **BFcVP(O)Ph**.

To justify this hypothesis, we later synthetically prepared two **BFcVPPh** derivatives, **BFcVP(O)Ph** and **BFcVP(S)Ph**. Both of them were, however, electrochemically stable and showed two reversible waves with ΔE of 100 mV and 150 mV (Figure 2.24B), respectively. -P(O)- and -P(S)- behave very similarly as a carbonyl group (*vide supra*), moving the first oxidation wave to positive and decreasing the through-bond coupling due to their electron-withdrawing nature. Logically, such effects were more significant for -P(O)- than -P(S)-. Based on these facts, we can conclude that the abnormal electrochemical behavior of **BFcVPPh** should mainly derive from the decomposition of the bridging ligand upon oxidation.

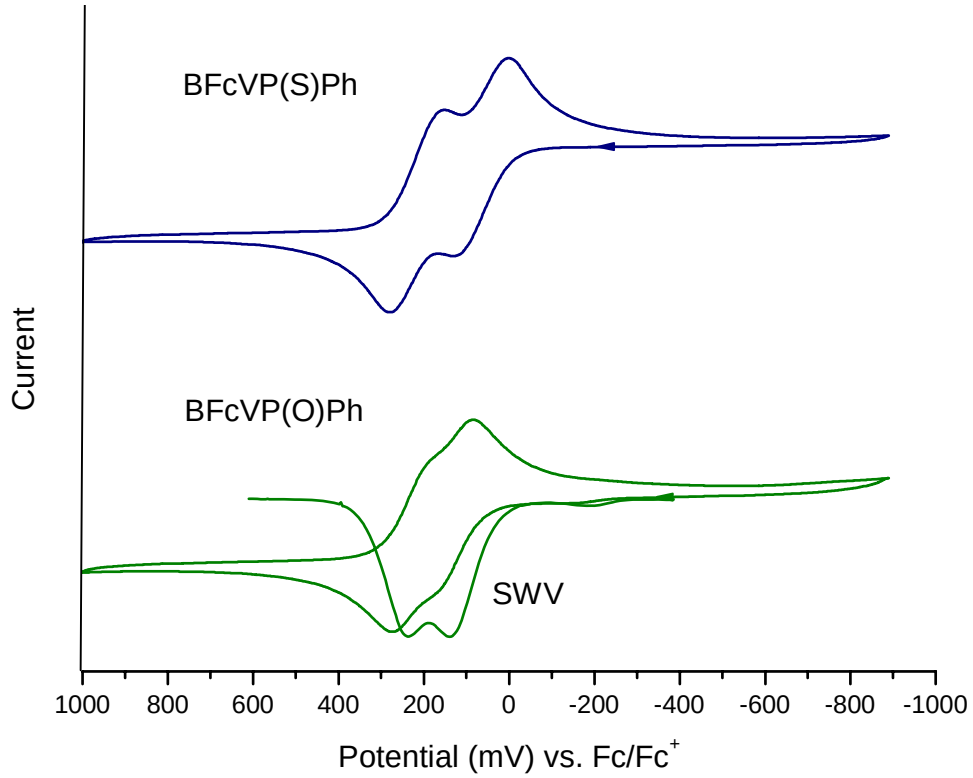

Figure 2.24B Cyclic voltammograms of **BFcVP(S)Ph** and **BFcVP(O)Ph** in a CH_2Cl_2 solution containing 0.1 M Bu_4NTFPB. Scan rate: 50 mV/s.

To make a short summary, the heteroatom centered bis(2-ferrocenylvinyl) derivatives exhibit electronic coupling in the order of O > S, PPh > P(S)Ph > P(O)Ph > Se. This coupling sequence is a comprehensive variant of atom size, bond length, polarizability of the lone-pair and electron density on the heteroatom. For this series, resonance apparently trumps electron affinity. That is, in order for efficient communication, valence bond structures involving formal double bonds with the heteroatom are involved, and overlap is more efficient with Row II elements as illustrated in Figure 2.25A.

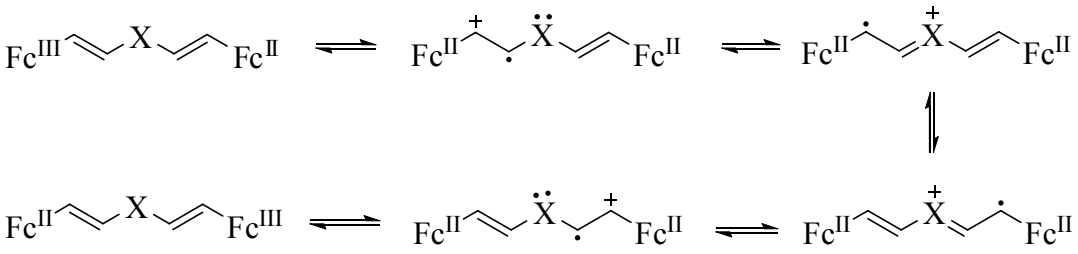

Figure 2.25A. Mechanism of charge injection and propagation in heteroatom centered bis(2-ferrocenylvinyl) compounds.

In this context, we can predict that the size more advantageous and lone-pair more polarizable nitrogen would be a more efficient heteroatom in supporting charge transport. However, linear divinyl amines are extremely difficult to synthesize owing to the fact that the intermediate vinylamine would rather transform to the thermodynamically more stable imine form, which consequently inhibits further addition reaction (Figure 2.25B). Thus, synthesis of linear divinyl amine is barely known without extra stabilizing factors. Nevertheless, we were able to prepare a biphenyl end-capped analogue **A** (Figure 2.25B) via a $TiCl_4$ involved reductive coupling of aniline with Ph_2CHCHO.

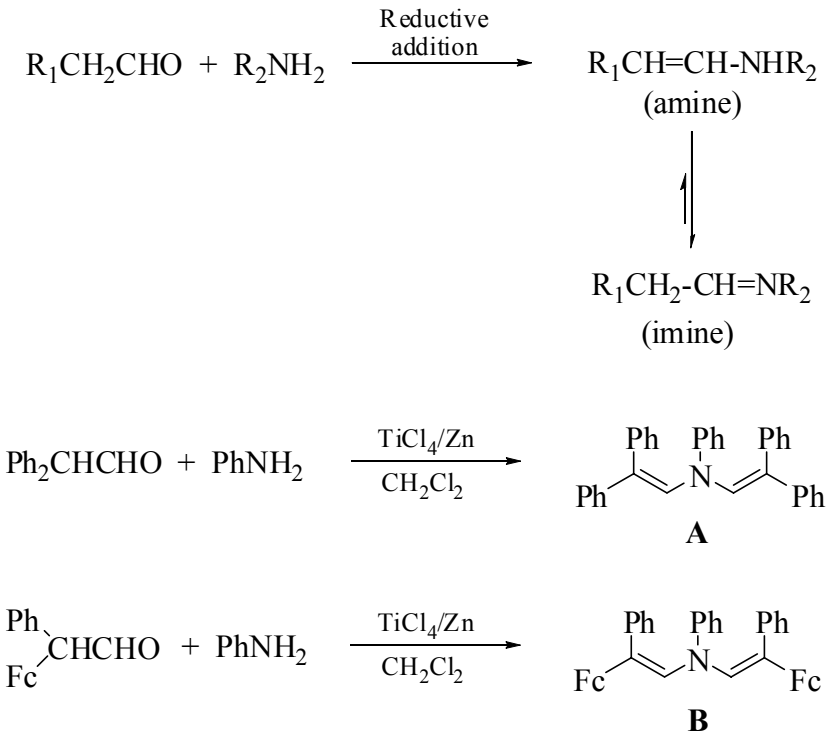

Figure 2.25B. Proposed synthetic route for bis(2-ferrocenylvinyl)amine.

The divinylamine-based formal potential of **A** was collected as 0.3 V vs. Fc/Fc^+ couple. This rather low oxidation potential indicates that divinylamine could be a very good candidate as the charge transfer mediator since the intermediate resonance forms shown in Figure 2.25 would be therefore reinforced as the charge traverses across the conducting path with the high electron affinity of nitrogen atom. Moreover, in the view of superexchange charge transfer, the energy level of the ligand orbital in this system is more compatible to that of the ferrocene d-orbital, which will lead to greaterorbital overlap between the bridging ligand and metal centers. Currently, the synthesis of structurally similar diferrocenyl compound **B** (Figure 2.26) is undergoing in our laboratory.

3. X = aromatic rings. Previously reported biferrocences linked by vinylene-arylene-vinylene spacers[28] (e.g. **BFcV*p*Ph** and **BFcVTh**) did not show any wave separation in electrochemistry with the conventional electrolyte anion such as PF_6^- in present. For this reason, the authors often concluded that vinylene-arylene-vinylene is an ineffective 'molecular wire'. Consequentially, no further investigation such as

intervalence absorption on the mixed-valence state of these compounds was performed. In fact, such conclusion might be imprudent in considering that substantial electronic interactions may still occur even in the absence of any observable peak separation. Pickup's ruthenium complexes[72, 73] and Swager's transition-metal containing conjugated polymers[74, 75] have demonstrated such examples in several occasions. With the assistance of improved electrolyte, we believed the overlooked electronic coupling should emerge to surface. Therefore, in this work, we also examined a number of bis(2-ferrocenylvinyl) compounds with the most commonly used arylenes and heteroarylenes as the central mediator, i.e. the X group. As shown in Table 2.2, a lowered first oxidation (vs. Fc/Fc^{+}) was observed in all cases of this series of arylene-mediated compounds due to the extended conjugation and the electron-donating effect from the bridging ligand. With free-coordinating supporting electrolyte anion, $TFPB^{-}$, all compounds except the *meta*-phenylene derivative presented ferrocene-based peak separations ranging from 90 mV to 355 mV. To circumvent the complexity caused by the variation of stereochemistry, the following discussions are all associated with the corresponding (*E,E*)-isomers. The unique dependence of electrochemistry on stereochemistry demonstrated by the *ortho*-phenylene derivatives has been discussed in previous section.

The *para*-phenylene group is one of the most popular linkers in conducting polymers such as polyphenylenevinylene (PPV) and polyphenyleneethynylene (PPE). For steric reasons, there has been comparatively little work done on the corresponding *ortho* species, while the *meta* derivatives are expected to have inefficient charge propagation through a *meta*-phenylene. Indeed, *para*-phenylene showed a coupling of 90 mV, while the *meta* isomer showed a zero coupling (Figure 2.26A), in keeping with the meta-para dichotomy for transmission effects. The (*E,E*)-*ortho*-phenylene compound exhibited a 20 mV larger peak separation than its *para* analogue. The enhanced coupling is ascribed to the shorter conjugation pathway and the shorter iron-iron distance. Essentially, the metal-metal separation for the *para*-phenylene derivative could be considered as four conjugated double bonds apart, but three double bonds for the *ortho*-phenylene analogue. In this sense, compared to the coupling strength of **Fc(CH=CH)$_3$Fc** (ΔE = 180 mV), the weakened coupling in **BFcV*o*Ph** (110 mV) stems from the relative electron-deficiency of the phenylene ring due to the aromaticity. Finally, introduction of

two electron-donating alkoxy groups on the 2,5 positions of the *p*-phenylene ring slightly enlarged the peak separation as shown for compound **BFcV*p*Ph(OR)$_2$** (Figure 2.26A).

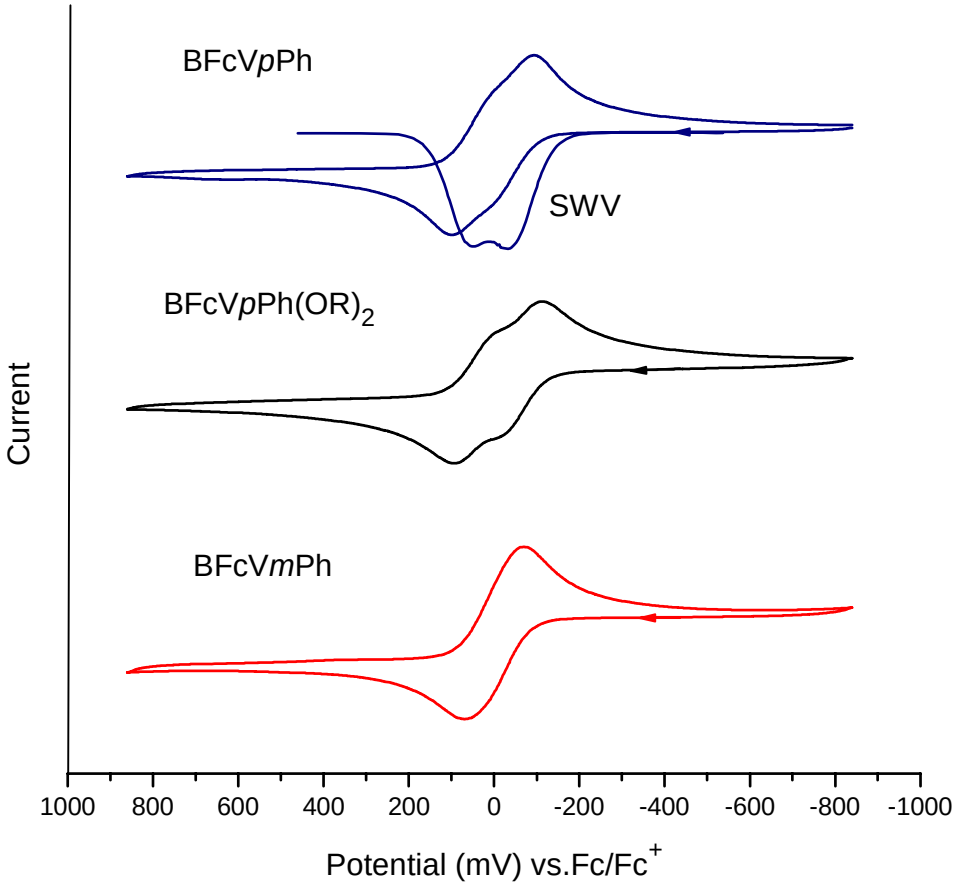

Figure 2.26A Cyclic and square wave voltammograms of **BFcV*p*Ph**, **BFcV*p*Ph(OR)$_2$** and **BFcV*m*Ph** in a CH_2Cl_2 solution containing 0.1 M Bu_4NTFPB. Scan rate: 50 mV/s.

The *sine qua non* of linking groups are the heteroaromatic rings represented by furan, thiophene and pyrrole (see Figure 2.26B). The coupling strength increases with the increased electron-density and decreased aromaticity of the heteroaromatic rings. In the case of thiophene, we also examined 3,4-ethylenedioxythiophene (EDOT), which exhibited nearly 50% enhanced coupling in comparison to the unsubstituted thiophene due to the electron-donating effect from the peripheral substituents. The third oxidation

wave of the EDOT derivative is assigned to the oxidation of the bridging ligand, which is presumably EDOT-based.

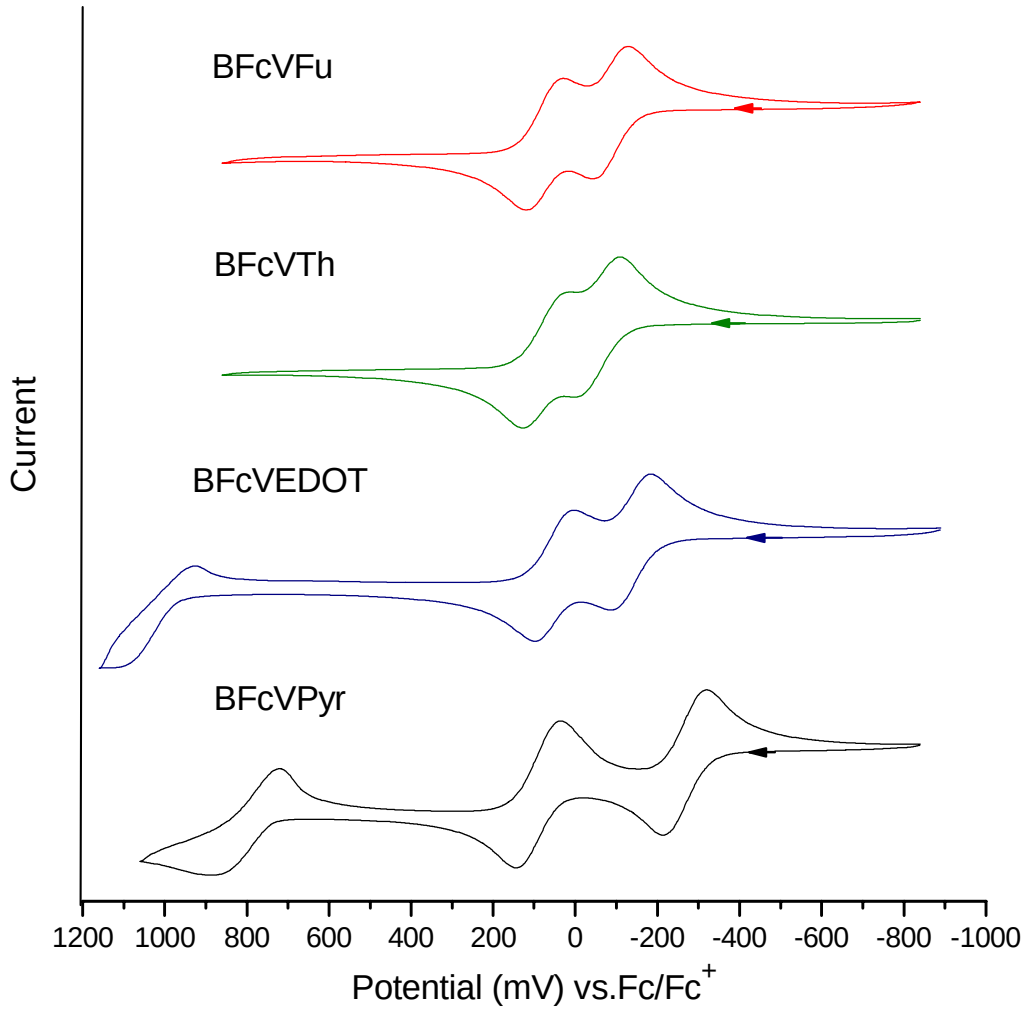

Figure 2.26B Cyclic voltammograms of **BFcVFu**, **BFcVTh**, **BFcVEDOT** and **BFcVPyr** in a CH_2Cl_2 solution containing 0.1 M Bu_4NTFPB. Scan rate: 50 mV/s.

In the aromatic series, probably the most exciting discovery is the N-alkyl-2,5-pyrrolene mediated compound **BFcVPyr**, which showed remarkably enlarged electronic coupling compared to any other compound. This compound also displayed three instead of two widely separated oxidation waves, with ΔE_1 (E_2-E_1) and ΔE_2 (E_3-E_2) of 350 mV and 650 mV, respectively, indicating that the N-alkyl-2,5-divinylpyrrolene moiety was also involved in the redox process within the sweeping extent, which corresponds to the

third oxidation process. The first oxidation was significantly shifted to negative, -265 mV vs. Fc/Fc^{+}, manifesting the strong electron-donating effect from the pyrrolene moiety. In spite of the obvious advantages, a recent literature survey did not show any report on pyrrolene spaced biferrocenyl compound. We later conducted systematic studies on a series of pyrrolene-bridged systems and concluded that the unusual strong communication between the linked redox centers is originated from the high degree of charge delocalization in the mixed-valence state. The full discussion will be given in Chapter 3.

Finally, for aryl bridged biferrocenyl complexes, there is a well-obeyed correlation between the first oxidation and electronic coupling strength (ΔE) as plotted in Figure 2.27, that is, the coupling strength increases as the first oxidation potential decreases. Given the fact that metal-metal distances for this series of compounds fall in a comparable range, under superexchange mechanism, the through-bond electronic communication is presumably governed by the effectiveness of orbital mixing between the bridging ligand and metal centers. An electron-rich bridging linker not only causes an elevated energy level of the metal orbitals, resulting in relaxed first oxidation, but also gives rise to a narrowed band gap between the bridging ligand HOMO and metal $d\pi$ orbitals (Figure 2.20), leading to more efficient conducting path as the electron or charge traverses across the conjugated backbone. The only exception for such correlation is the *ortho*-phenylene derivative (the last entry in Figure 2.27), in which the enlarged coupling mainly arose from the shorter metal-metal distance.

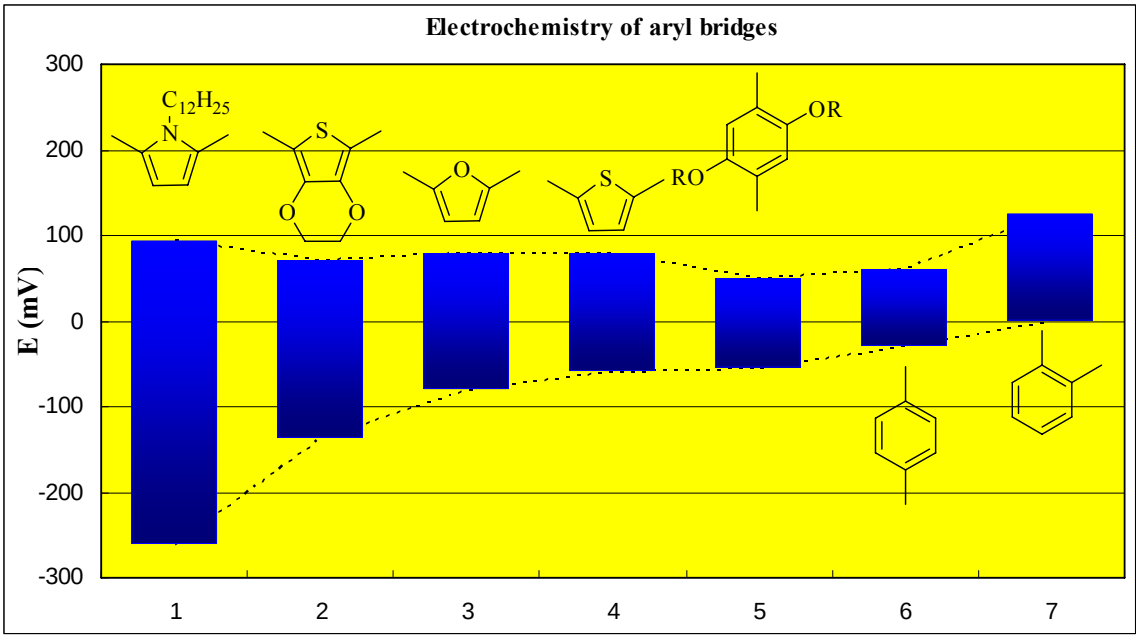

Figure 2.27 Electrochemistry of aryl bridged biferrocenyl compounds.

Mixed-Valence Electronic Absorptions

Methodology

In general, the mixed-valence state of a multinuclear compound could be achieved either electrochemically or chemically for intervalence electron transfer studies. We will briefly discuss the *cons* and *pros* of these two most commonly used methods.

The apparent advantage of electrochemical oxidation method is that it offers a better control of generating the mixed-valent state. The common practice is to set the anodic poterntial at the middle position between two successive waves so that only the former oxidation state is achieved. This method is especially effective when the oxidation waves are well separated. However, it could encounter serious problems when a weakly coupling system is involved. The working electrode used in this kind of procedure is usually a surface-enlarged electrode, e.g. Au or Pt mesh, which is served to alleviate the solution mixing problems controlled by substrate diffusions. Unfortunately, this kind of electrode generally broadens the oxidation waves due to the big anodic surface. When the neighboring peaks are closlye-spaced, differentiation between them becomes difficult or impossible under experimental conditions. In addition to that, another intrinsic drawback

of the electrochemical approach, which has been widely recognized, is that it can only provide underestimated value when the molar extinction coefficient is concerned since the coulomb loss owing to the circuit resistance is congenitally inevitable. Other disadvantages of this method include complicated apparatus setup, difficulty to achieve the homogeneous solution, etc.

In contrast, chemical oxidation method uses carefully selected oxidizing agent as the means to achieve the mixed-valence species. The experimental setup is virtually the same as the regular apparatus used for absorption spectroscopy. The desired mixed-valence state could be either achieved beforehand (i.e. synthetically isolated substance) or generated *in situ* by adding certain amount of oxidant into the solution of the starting material. Homogeneous solution can be conveniently obtained by usual mixing manner. The only problem, which is the major drawback, of chemical oxidation method is that it does not have a good control on the oxidation states. Undesired higher oxidation state could also be formed if the oxidant is not fully compatible with the substrate (ideally, the oxidation strength of oxidizing agent should only afford the monocation not the dication in our case). The commonly used compromise to alleviate this problem is to use 0.1-0.5 equivalent oxidant in the oxidation procedure to drive the disproportionation equilibrium in favor to the monocationic side.

$$2\ [\text{Fc-B-Fc}]^{+} \rightarrow [\text{Fc-B-Fc}] + [\text{Fc-B-Fc}]^{2+} \quad \text{disproportionation process} \quad (2.6)$$

From our experimental experience, we found chemical oxidation is more convenient, easier to manipulate and offers more accurate results. Thus, we adapted this method for all the mix-valence absorption studies. Connelly and Geiger have reviewed the chemical redox agents for organometallic chemistry.[76] After a series of comparisons, we found that $Fc^{+}PF_6^{-}$ and $Ar'_3N^{+\bullet}SbCl_6^{-}$ (TBA or magic blue, Ar' = *p*-BrC_6H_4) are very good oxidation reagents for the diferrocenyl compounds, especially $Fc^{+}PF_6^{-}$. The mild oxidation strength of $Fc^{+}PF_6^{-}$ (0.0V vs Fc/Fc^{+}) can just oxidize the first ferrocene moiety but not the second one, provided that most of the compounds in this work have a negatively shifted first oxidation and their second oxidation potential is generally higher than the Fc/Fc^{+} couple. When a stronger oxidant is required, magic blue was used (0.76 V vs Fc/Fc^{+}). It is noteworthy that both the oxidants and their reduced forms do not have

any absorption in the low energy region to interfere the mixed-valence spectrum. The general procedure has been described earlier in the experimental section. For weak coupling compounds, 0.1-1.0 equivalent of oxidant was used to minimize the possible disproportionation. $Fc^+PF_6^-$ absorbs around 622 nm with an extinction coefficient of 374 ,[65] which is essentially negligible compared to the absorption of the ferrocenium moiety of the mixed-valence species herein. In addition, low energy especially the near-IR absorption is the area we are mostly interested in.

Corrected Mixed-Valence Spectra and General Concerns

The mixed-valence spectra of biferrocene compounds are often complicated by the overlapping of the coexisting absorptions arising from different types of electronic transitions in the low energy area. This is especially the case for the current mixed-valence species herein due to the large variety of the bridging ligands "-CH=CH-X-CH=CH-" employed. Therefore, spectral deconvolution is generally required to revolve the discrete bands into gaussian components. Hereby, gaussian means that $\varepsilon/\nu = f(\nu)$ is the gaussian function, not $\varepsilon = f(\lambda)$. In other words, gaussian fitting should be performed versus energy unit, wave numbers, instead of wavelength. Such curve fittings were conveniently fulfilled with the Origin Peak Fitting Module (PFM).[77]

For the mixed-valence species of bis(2-ferrocenylvinyl) derivatives, several absorption bands could exhibit in the visible and NIR region, including Cp-to-Fe^{III} charge transfer, bridging ligand π-π* transition, bridging ligand to metal charge transfer (LMCT), intervalence charge transfer (IVCT) and Fe^{III} interconfigurational transition (IC). To gain basic understanding of these bands and the deconvolution process, the mixed-valence spectra of **BFcVEDOT** showing scanning range up to 3000 nm are exemplified in Figure 2.28. Figure 2.28A shows the spectrum evolution of **BFcVEDOT** upon being oxidized by increasing amount of oxidant. The first intense band appears around 600 nm is a typical Cp-to-Fe^{III} charge transfer band[65, 78] belonging to the ferrocenium moiety. The second intense band located ca. 800 nm corresponds to the bridging ligand π-π* transition originated from the ferrocenyl chromophore. This band *only* appears in the extensively conjugated systems, especially those with electron-rich linking component, with λ_{max} and ε_{max} highly dependent on the extent of conjugation.

A

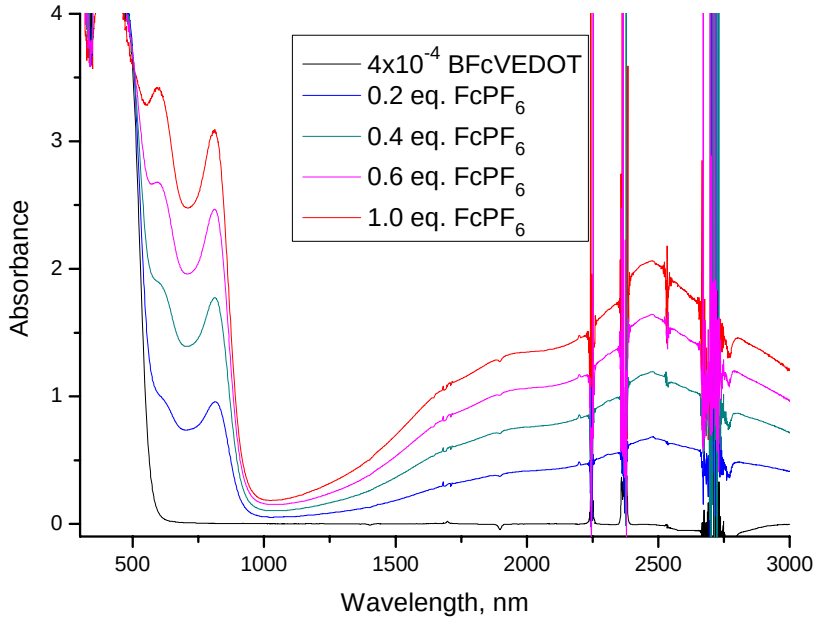

B

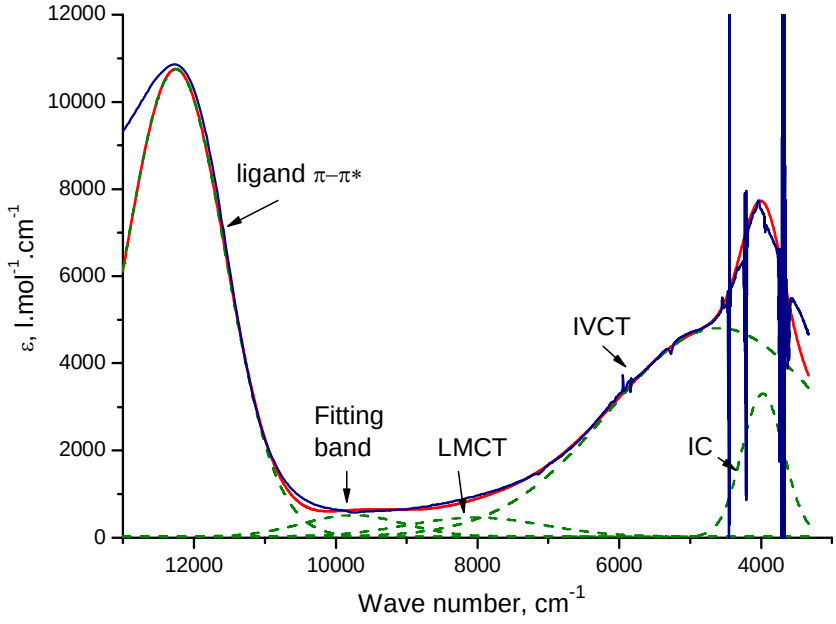

Figure 2.28 Mixed-valence spectra and spectral deconvolution of **BFcVEDOT**.

Therefore, heteroatom or saturated carbon centered derivatives clearly did not show such band due to the broken conjugation along the bridging fragment.

In contrast to the simplicity of the visible bands, the absorptions in the NIR are not straightforward. The vertical lines appearing beyond 2200 nm are the artifacts coming from solvent absorption exceeding the compensation capacity of the double beam spectrophotometer. Upon deconvolution of the broad envelope in the NIR, four gaussains were revealed as shown in Figure 2.28B, resulting in the fitting curve (red line) matching very well to the original spectrum (blue line). The major broad gaussian component is apparently ascribed to the IVCT transition between the metal centers; the adjacent weak band centered at ca. 8000 nm (1250 nm) is assigned to the LMCT derived from the electron transition from the bridging ligand to the Fe^{III} d-orbital; another weak band appearing at higher energy around 10000 cm^{-1} (1000 nm) was proved to be necessary for good spectral fits and has been noticed in other diferrocenyl systems.[53] Finally, there is a sharp band, which overlaps with the tailing section of the IVCT band, at the border between the NIR and IR. It has been noticed that this mysterious band unquestionably belongs to the diferrocenyl system as evidenced by its continuous increase of intensity upon progressive oxidation (Figure 2.28A). Later, we also found that this narrow band (half bandwidth around 800 cm^{-1}) does not necessarily associate with a mixed-valence diferrocenyl system, instead, it always appears with any ferrocenium ion substituted with a strong electron-donating ancillary. Unfortunately, an extensive literature survey could not reveal any record on such band owing to the fact that nearly all the relevant reports associated with ferrocenium complexes cut the low energy absorption spectrum at 2200 nm, presumably to avoid showing the strong solvent noises depicted above. However, it has been well established that the Ru^{III} and Os^{III} complexes often demonstrate interconfigurational (IC) transition bands derived from the $d\pi \rightarrow d\pi$ transitions between the Kramer's doublets[79, 80] as illustrated in Figure 2.29. The IC bands are nominally parity or LaPorte forbidden but gain intensity through spin-orbit coupling and metal ligand mixing. They appear in the near-IR (between 4000 to 6000 cm^{-1}) as narrow ($\Delta\varepsilon_{1/2}$ < 1000 cm^{-1}), relatively weak bands,[81, 82] which are almost the same characteristics as the band we observed in the ferrocenium complexes. Therefore, we tentatively assigned this band, centered around 2400 nm, to an IC transition.

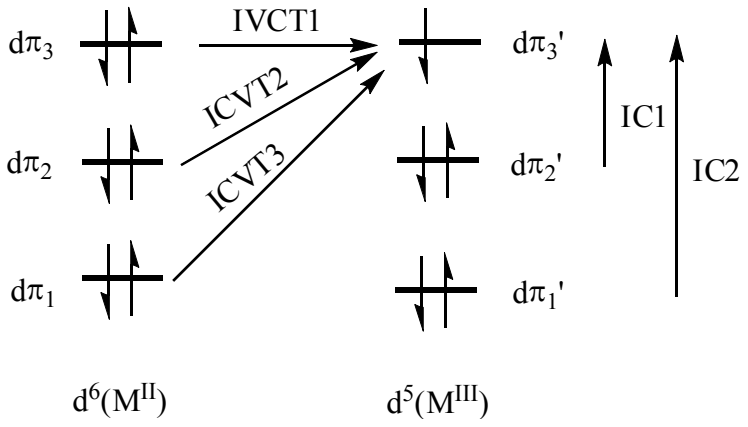

Figure 2.29 Schematic illustration of the IVCT and IC transitions in a mixed-valence dinuclear complex, $[M^{II}M^{III}]$.

Finally, it is worth mentioning that the appearance, band-shape, absorption maximum and intensity of all the bands discussed above are very case-dependent for the series of mixed-valence species herein. The IVCT transition is of the most interest since it provides the spectral information associated with the strength of the electronic interaction.

Results and Discussion

According to the characteristics of their mixed-valence absorption, the **FcCH=CH-X-CH=CHFc** compounds could be divided into two groups: A and B. While group A includes compounds not showing the IVCT band in the mixed-valence state, group B contains those exhibiting an IVCT transition. The former compounds clearly belong to class I under Robin-Day's classification,[83] which are insulating systems. For group B compounds, the strengths of electronic coupling could be analyzed from their spectral parameters by the Hush formula[12] (Eq. 2.1 and 2.2).

Group A include compounds in which X = Se, P(O)Ph, P(S)Ph, CH=CHSCH=CH, CH_2, CH_2CH_2, C(O), *m*Ph and *o*Ph. It basically contains nearly all of the conjugation-broken compounds and two phenylene derivatives, **BFcV*m*Ph** and **BFcV*o*Ph**, which do not have a favorable resonance form in supporting electron transfer.

The sample spectra are shown in Figure 2.30-31, where Figure 2.30 demonstrates the spectrum evolution of **BFcVP(O)Ph** and **BFcVP(S)Ph** upon progressive oxidation with 0.2-2.0 equivalents of oxidant in present. As can be seen, for each mixed-valence species, only a weak low-energy band with λ_{max} falling in the range of ca. 770-1280 nm was revealed, which is assigned to the bridging ligand to Fe^{III} LMCT transition. The spectral data are collected in Table 2.3. Obviously, the absorption maxima and intensities of the LMCT bands are both associated with the extent of conjugation and electron density on the bridging ligand. Therefore, the LMCT band of **[BFcVCH=CHSCH=CH]**$^+$ (Figure 2.31B) appears at the longest wavelength (λ_{max} = 1275 nm) with the greatest intensity (ε_{max} = 1750 L•M^{-1}•cm^{-1}) due to the longest conjugation in this series. In contrast, the corresponding ε_{max} of **[BFcVP(O)Ph]**$^+$ is very low (300 L•M^{-1}•cm^{-1}) due to the low electron density on the bridging ligand caused by the electron-withdrawing –P(=O)- group (Table 2.3). For each case of the group A compounds, except the LMCT band, no additional absorption, i.e. an IVCT band, was observed in the NIR, which implied that this group of compounds are rather insulating. This conclusion seems inconsistent with the electrochemical results, where most of the compounds demonstrated a peak separation, implying the existing of electronic coupling. However, it is important to realize that interpretation of ΔE data is less straightforward than that of IVCT data because the former depends on stabilizing factors in the Fe^{II}/Fe^{II}, Fe^{II}/Fe^{III} and Fe^{III}/Fe^{III} species, and on through-space electrostatic and through-bond inductive effects. The lack of IVCT band in the mixed-valence species above suggested that there is no intrinsic correlation between ΔE value and intervalence transition.

Interestingly, the mixed-valence absorption of **[BFcVS]**$^+$ in the NIR (Figure 2.32) is much broader than a normal LMCT band. Whereas the predominant absorption centered at ca. 1090 nm is clearly ascribed to a LMCT transition (Figure 2.32A), there is a noticeable band buried by the tailing segment of the LMCT band, which indeed possesses the IVCT feature upon spectral deconvolution (Figure 2.32B). Although this IVCT band is very weak in terms of both intensity (ε_{max} = 440 l.M^{-1}.cm^{-1}) and calculated electronic coupling constant (V_{ab} = 202 cm^{-1}), it is the first example demonstrating that

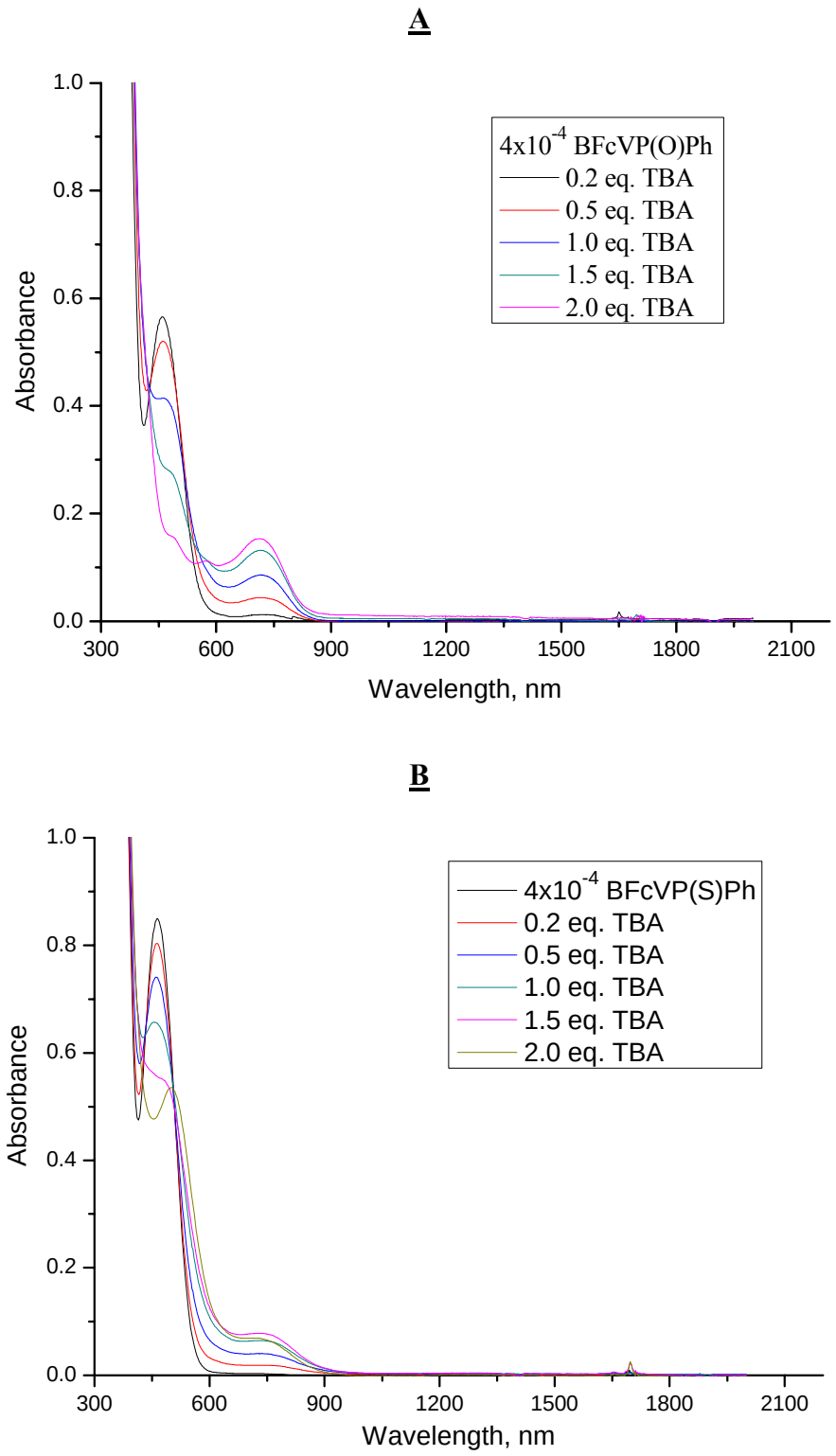

Figure 2.30 Spectrum evolution of mixed-valence species of **BFcVP(O)Ph** (A) and **BFcVP(S)Ph** (B). TBA = magic blue.

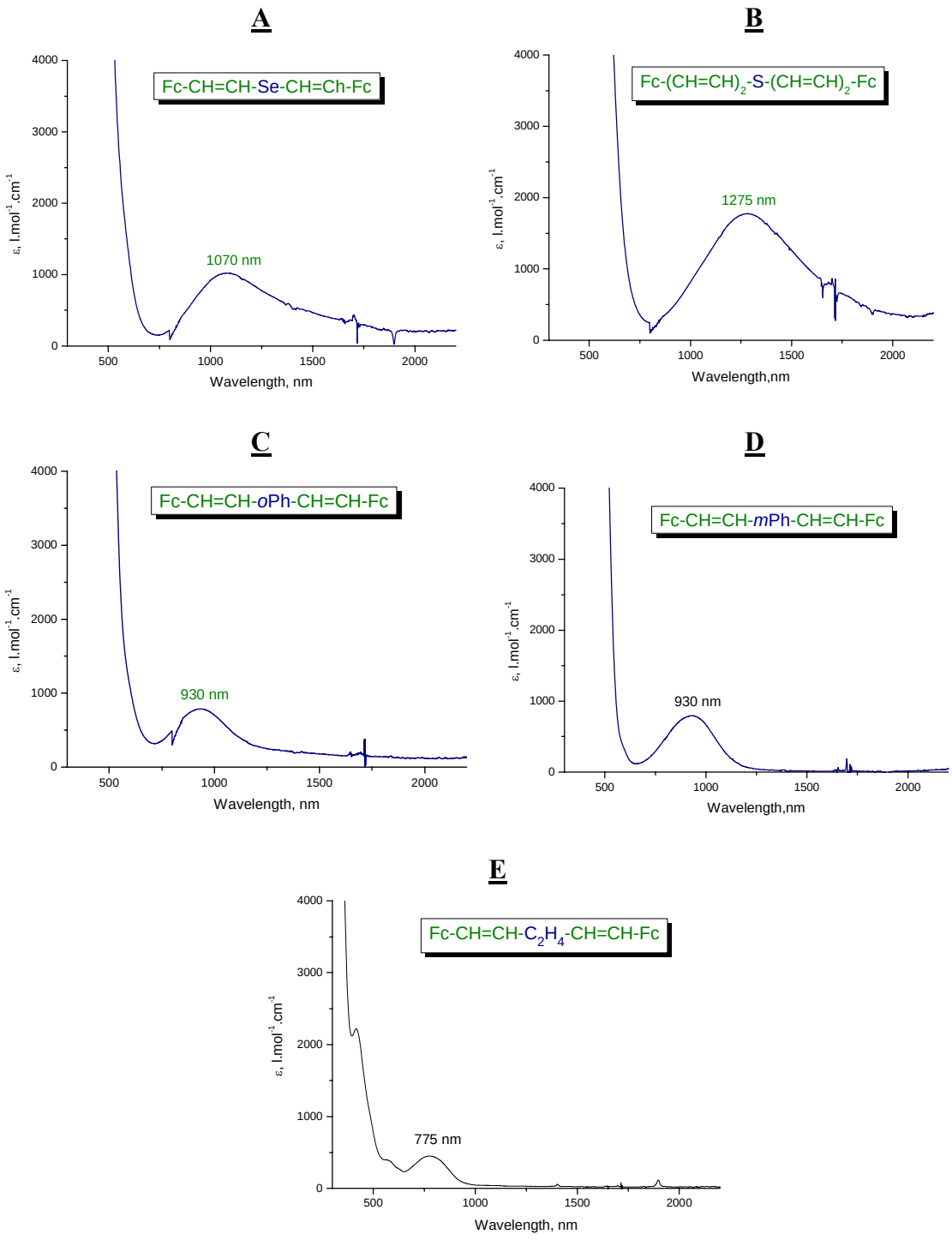

Figure 2.31 Mixed-valence spectra of the monocationic species of **BFcVSe** (A), **BFcVCH=CHSCH=CH** (B), **BFcV*o*Ph** (C), **BFcV*m*Ph** (D) and **BFcVSC$_2$H$_4$** (E).

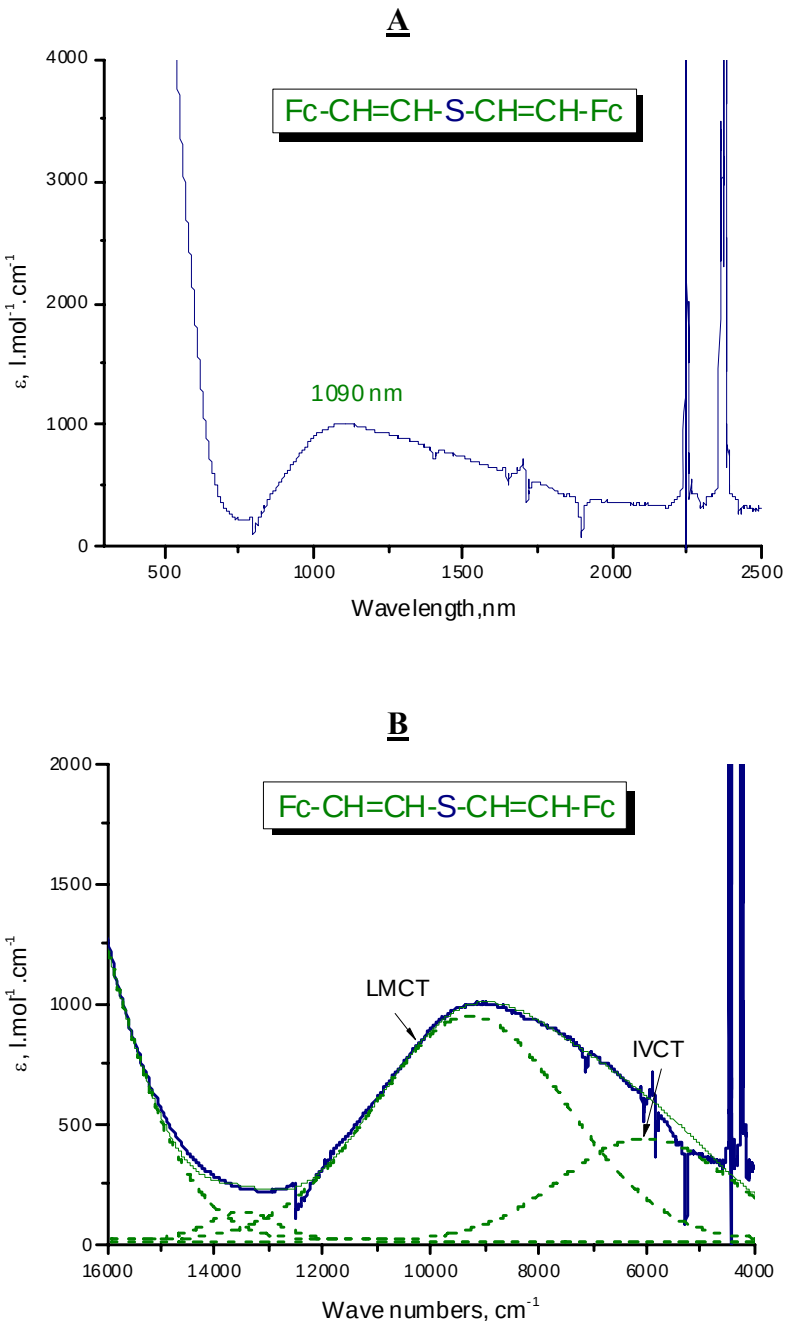

Figure 2.32 Mixed-valence spectra (A) and spectral deconvolution (B) of **BFcVS**.

Table 2.3 LMCT band parameters, obtained from the spectral deconvolution of the mixed-valence species of Group A[a] compounds.

Compounds	ν_{max} [cm^{-1}]	ε_{max} [$M^{-1}cm^{-1}$]	$\Delta\nu$ [cm^{-1}]
$[BFcVCH_2]^+$	12850	420	3020
$[BFcVC_2H_4]^+$	12850	420	3020
$[BFcVP(O)]^+$	13980	300	2630
$[BFcVP(S)]^+$	13430	230	2670
$[BFcVSe]^+$	9265	990	4330
	5270[b]	160	4200
$[BFcVCH=CHSCH=CH]^+$	7860	1750	3370
$[BFcV\textit{m}Ph]^+$	10700	780	2700
$[BFcV\textit{o}Ph]^+$	10770	780	3600
	6060[b]	162	4486

[a] See text; [b] suspected IVCT band upon spectral deconvolution.

heteroatom can also serve as the supporting element for electron transfer in the context of photo-driven process. Thus, **BFcVS** belongs to group B. Based on this, we also expected that **$[BFcVPPh]^+$** and **$[BFcVO]^+$** should also present IVCT bands similar to that of **$[BFcVS]^+$** since both compounds showed even greater ΔE in electrochemistry. Unfortunately, these two mixed-valence species are chemically unstable so that no absorptions could be observed in the low-energy area.

Besides **BFcVS**, group B also includes compounds in which X = -, CH=CH, *p*-Ph, *p*-$Ph(OR)_2$, Th, Fu, EDOT and Pyr. Apparently all of them comprise a persistent π-conjugation. The mixed-valence spectra are shown in Figure 2.33-35, and the spectroscopic data obtained after spectral deconvolution are gathered in Table 2.4. **$Fc(CH=CH)_2Fc$** and **$Fc(CH=CH)_3Fc$** have been previously studied by Spangler and coworkers.[53] The reported results are also included in Table 2.4. In comparison to the

literature records, our current data presented two major differences which both associate with the different experimental conditions used in developing and measuring the mixed-valence species, i.e. electrochemical (Spangler) and chemical (this work) oxidation. First, the IVCT ν_{max} (or λ_{max}) of current results are shifted (ca. 300 cm^{-1}) to lower energy. It is well known that the IVCT band can be altered significantly by external factors such as solvent, ion-pairing, concentration of counterion, temperature, etc. according to Marcus theory out-sphere electron transfer[12, 84]: $\lambda_{IVCT} = \lambda_{in} + \lambda_{out}$., where the λ_{in} and λ_{out} are the interior and out-sphere reorganization energy in the light-induced electron transfer process, respectively. Most likely, the red-shift of the current IVCT bands came from the low concentration of PF_6^- (ca. 1-3 x 10^{-4} M, essentially the same as that of the mixed-valence species) present, in comparison to the high concentration of counterion (0.1 M $Bu_4N^+PF_6^-$) used in electrospectroscopic measurement. Second, the calculated ε_{max} of IVCT is at least 25% greater than the literature result due to the advantages of chemical oxidation over electrochemical oxidation in moderating the underestimation of ε_{max} as discussed earlier. This in turn contributed to the higher V_{ab} and α values.

The spectra of a series of aryl bridged mixed-valence species are shown in Figure 2.34A. In order to illustrate the electronic transition trend, the corresponding spectra of **[BFcV*m*Ph]**$^+$ and **[BFcV*o*Ph]**$^+$ are also included. Whereas **[BFcV*m*Ph]**$^+$ and **[BFcV*o*Ph]**$^+$ only showed a narrow weak band in the high energy NIR ascribed to the LMCT, the rest of the aryl bridged mixed-valence species all presented a dominating broad band in the low energy NIR clearly derived from IVCT transition between the two metal sites. However, it is reasonable to question the nature of the low energy band demonstrated by **[BFcV*p*Ph]**$^+$ since this band appears in the crossing area between the LMCT and IVCT transitions. The spectral deconvolution (Figure 2.34B) gave two underlying gaussians. While the intense gaussian centered at 7850 cm^{-1} is obviously assigned to the IVCT transition according to the band position and half bandwidth (4400 cm^{-1}), the weak band centered at ca. 11010 cm^{-1} and buried by the IVCT leading segment is assigned to the bridging ligand to metal charge transfer similar to that of **[BFcV*m*Ph]**$^+$ and **[BFcV*o*Ph]**$^+$. Apparently, the significance of such LMCT transition is greatly depressed due to the competing IVCT transition as manifested by its low intensity (ε_{max} = 310 $L \bullet M^{-1} \bullet cm^{-1}$) comparing with other phenylene analogues (ε_{max} = 780 $L \bullet M^{-1} \bullet cm^{-1}$).

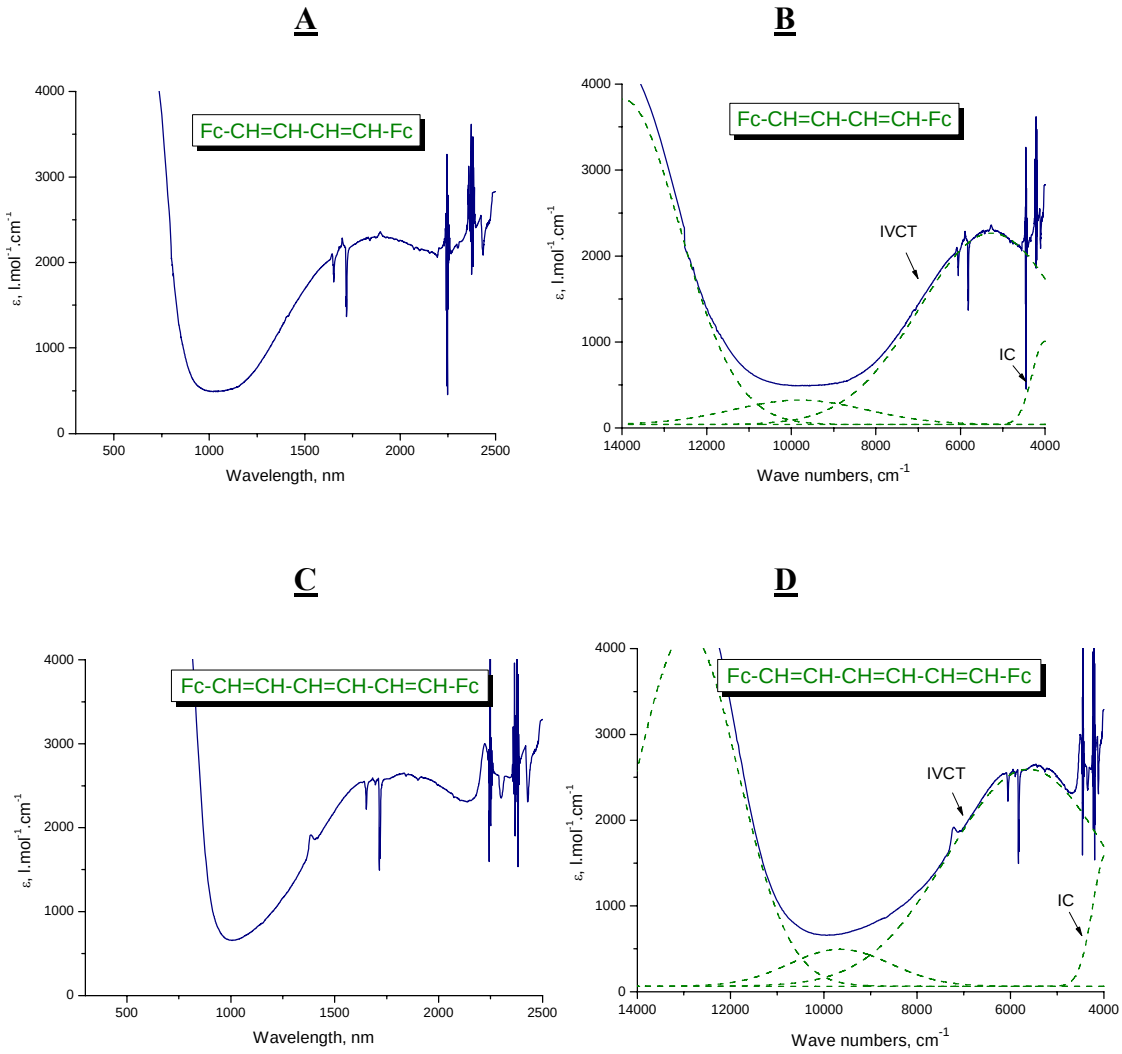

Figure 2.33 Spectra of mixed-valence species **$Fc(CH=CH)_2Fc^+$** (A & B) and **$Fc(CH=CH)_2Fc^+$** (C & D) with deconvoluted bands

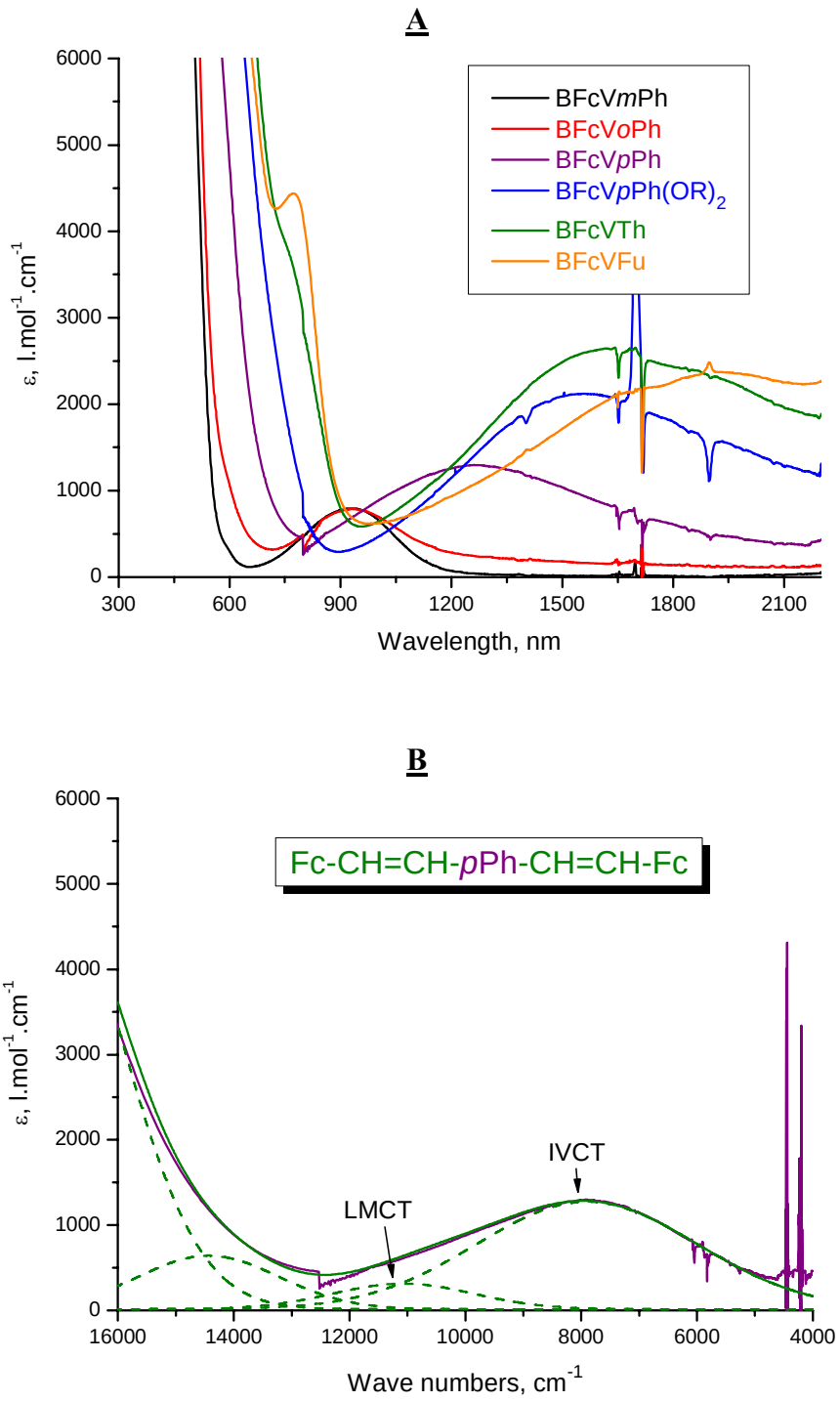

Figure 2.34 A: Mixed-valence spectra of aryl bridged compounds: **BFcV*o*Ph** (black), **BFcV*m*Ph** (red), **BFcV*p*Ph** (purple), **BFcV*p*Ph(OR)$_2$** (blue), **BFcVTh** (green) and **BFcVFu** (orange). B: Deconvoluted spectra of **BFcV*p*Ph**.

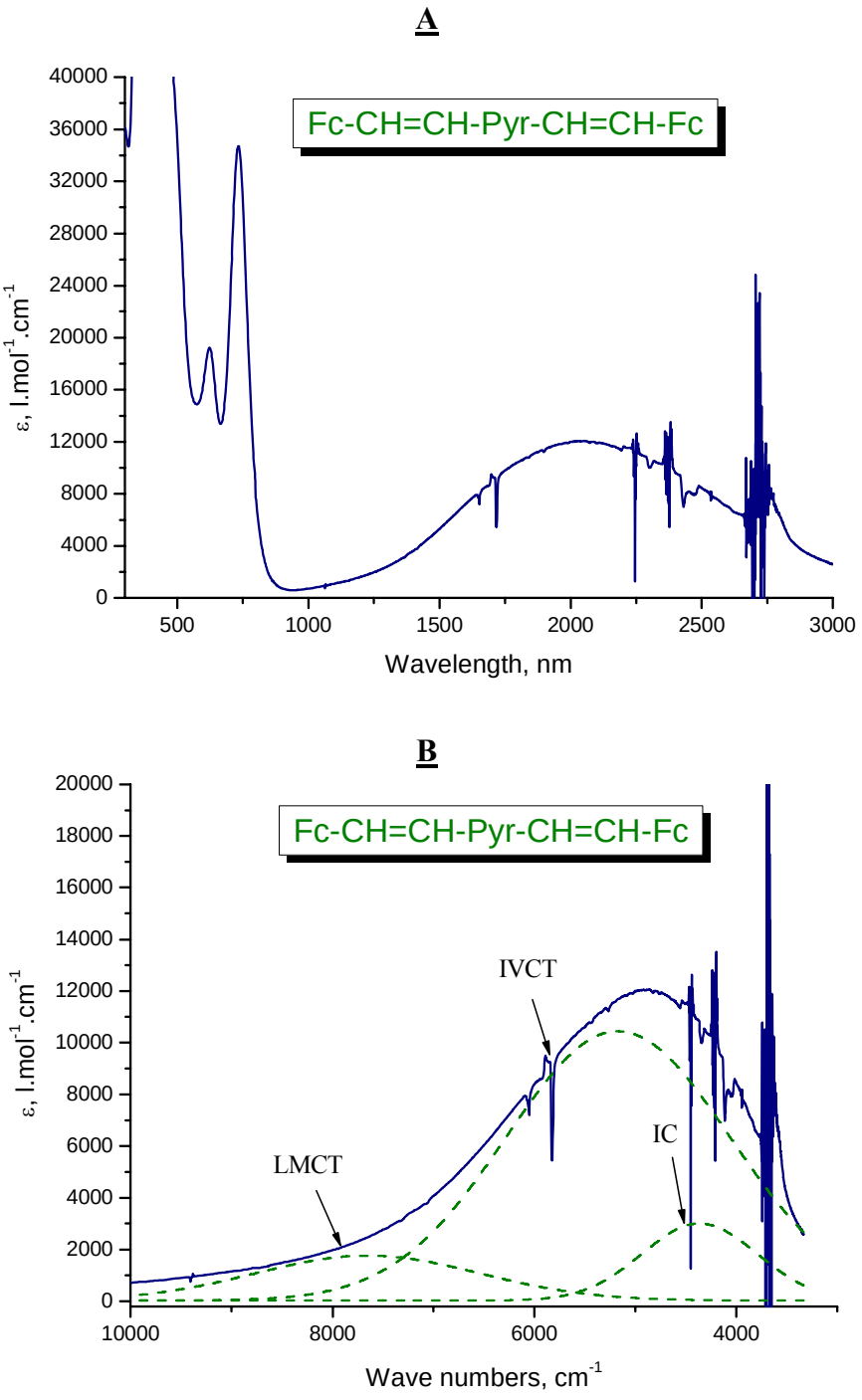

Figure 2.35 Mixed-valence spectrum of **[BFcVPyr]**$^{+}$ (A) and band deconvolution (B) in the NIR.

Table 2.4 IVCT and LMCT band parameters, obtained from the spectral deconvolution, and calculated Hush parameters for the mixed-valence species of Group B[a] compounds.

	ν_{max} [cm^{-1}]	ε_{max} [$M^{-1}cm^{-1}$]	$\Delta\nu$ [cm^{-1}]	R_{mm} [b] [Å]	V_{ab} [c] [cm^{-1}]	α [d]
$Fc(CH=CH)_2Fc^+$	5290	2280	3900	9.21 [f]	483	0.091
$Fc(CH=CH)_2Fc^+$ [e]	5500	1570	4340	9.21 [f]	430	0.078
$Fc(CH=CH)_3Fc^+$	5660	2590	4100	11.54 [f]	436	0.077
$Fc(CH=CH)_3Fc^+$ [e]	6010	2100	3800	11.54 [f]	390	0.065
$[BFcVS]^+$	9257 [g]	965	4176			
	6020	440	3640	9.78	206	0.034
$[BFcV\textit{p}Ph]^+$	11040 [g]	310	2930			
	7850	1300	4400	13.49	322	0.041
$[BFcV\textit{p}Ph(OR)_2]^+$	6430	2095	3780	13.53	342	0.053
$[BFcVFu]^+$	5250	2520	4600	10.37	488	0.093
$[BFc4Th]^+$	6130	2770	4000	10.85	492	0.08
$[BFcVEDOT]^+$	4700	5100	3720	10.85 [f]	564	0.12
$[BFcVPyr]^+$	5153	10100	2730	12.64	611	0.119

[a] See text. [b] spatial iron-iron distance obtained from crystal structure if not otherwise stated. [c] Hush coupling constant $V = 2.06 \times 10^{-2}(\varepsilon_{max} \cdot \Delta\nu_{1/2} \cdot \nu_{max})^{1/2}/R_{mm}$. [d] delocalization efficient $\alpha = V_{ab}/\nu_{max}$. [e] obtained from ref. 53. [f] obtained from theoretical calculation. [g] LMCT transition as described in text.

It is noteworthy that the IVCT absorption maxima (λ_{IVCT}) of the aryl series are continuously shifted to longer wavelength (Figure 2.34A) with the increasing electron-density on the bridging ligand, which is in turn determined by the aryl group. This suggested that the electron-density on the bridging ligand has substantial meaning in perturbing the effective overlap between the diabatic orbitals as described by Hush intervalence charge transfer theory[12] (Chapter 1). Accompanied with that, the corresponding IVCT extinction coefficients (ε_{IVCT}) are consequentially promoted as the λ_{IVCT} moves to lower energy. The extreme case comes when the X group is a pyrrolene nucleus (Figure 2.35). **[BFcVPyr]**$^+$ demonstrated a very pronounced IVCT band with absorption intensity approximately 4-5 times greater than that of the phenylene derivatives. As a consequence, the V_{ab} and α values (Table 2.4) increase as the electron density of the aryl group becomes richer, which is in good agreement with the increasing order of ΔE values obtained from electrochemistry

Finally, it is interesting to compare the V_{ab} values of the polyene-bridged compounds, **Fc(CH=CH)$_2$Fc** and **Fc(CH=CH)$_3$Fc**, with those of the aryl linked **FcCH=CHXCH=CHFc** derivatives. Despite the fact that most of the arylene mediated compounds showed noticeably smaller ΔE in electrochemistry, their V_{ab} values are even superior to the polyene bridged analogues as evidenced by **BFcVFu** and **BFcVTh** vs. **Fc(CH=CH)$_3$Fc** and **BFcVEDOT** vs. **Fc(CH=CH)$_2$Fc**. Furthermore, the small V_{ab} values for the *para*-phenylene derivatives are presumably derived from the larger metal-metal distance. If we preclude this distance factor, the resulting electron coupling constant would be in the same magnitude as that of **Fc(CH=CH)$_2$Fc** or **Fc(CH=CH)$_3$Fc**. This again suggested that the metal-ligand orbital mixing is at pivot under superexchange mechanism.

Conclusions

More than twenty binuclear ferrocene complexes in the form of **FcCH=CHXCH=CHFc** have been successfully synthesized, most of which are novel compounds or compounds prepared in improved chemistry and greater yield. Our approach is to place the redox mediator X between two ferrocenylvinyl groups such that the steric effects are comparable in all cases. The nature of the linking bridge is greatly altered by the central X group, its capability in facilitating electronic communication was found not a straightforward function of the oxidation potential of the bridge, but rather exhibits a more complex dependence on distance, oxidation potential, stereochemistry, and orbital overlap. Through current systematic studies, we have uncovered some surprisingly effective linkers (e.g. X = CH^+, EDOT, Pyr), as well as others (e.g. X = C≡C) which suppress communication in a counterintuitive fashion. In the process of electrochemical investigations, we also discovered a profound counterion effect on the oxidation potentials. It was thus necessary, in every case, to use a very hydrophobic counterion, i.e. $[(CF_3)_2C_6H_3]_4B^-$, to avoid ion pairing, which would have skewed the results.

In particular, for this series of diferrocenyl compounds, the stereochemistry, namely the *cis-trans* configuration of the vinyl bonds, was found to be a relatively insensitive factor in influencing intramolecular electronic coupling, presumably due to the through-bond interaction mechanism and bond isomerization during the redox processes. The only exception is (*E,Z*)-1,2-bis(2-ferrocenylvinyl)benzene (X = *ortho*-phenylene), in which the steric strain is obviously severe so as to fully distort the planarity of the conjugation path and the bond isomerization is hindered due to the rigidity of the aromatic rings which result in higher thermal barrier for such process to take place. For the heteroatom mediated systems, all compounds showed a peak separation in electrochemistry. This was not only surprising since such connector between a π-conjugation often considered as a sink, but also inspiring because it is a common practice in material science and surface chemistry to intimately connect a number of chalcogens, nitrogen, silicon and other moieties to nanostructured materials electronically, understanding of the nature of such communication is thus essential.

Indeed, we found that the effectiveness of a heteroatom as an electron transfer linker relies mostly on the atom size and the polarizability of the lone-pair electrons. In many cases, such as X = **O**, **S** and **PPh**, the coupling strength, judged by ΔE, is at the same magnitude as that of double bond, i.e. **Fc(CH=CH)$_3$Fc**. Intervalence absorption studies (V_{ab} and α values, derived from intervalence charge transfer band) have pointed out, however, that electronic communications in heteroatom centered systems are much weaker than π-conjugated systems (e.g. **BFcVS** << **Fc(CH=CH)$_3$Fc**), or even totally vanishing (X = **Se** and **CH=CHSCH=CH**) despite the presence of a peak separation. The disparity between electrochemical and spectroscopic results is mainly because ΔE value could arise from multiple causes such as electrostatic effect, inductive effect, charge delocalization, etc. and therefore can only be treated as a rough indication of electronic coupling. Thus, for binuclear complexes in which the bridging component does not have a throughout conjugation, they all demonstrated characteristics of Robin-Day's class I or borderline features of class I-II.

In contrast, all π-conjugation linked diferrocenyl compounds presented considerable V_{ab} and α values in spite of their smaller ΔEs and disadvantageous metal-metal distance. The aryl and heteroaryl bridged series are especially indicative since both electrochemical and intervalence NIR spectroscopic results have conceded that electronic communication between the bridged redox sites is presumably governed by the energy level of the bridging unit. As the electron density on the bridging ligand increases (e.g. X = **EDOT** or **Pyr**), the energy level of the bridging component is more approaching to that of the metal d-orbitals, which will result in greater metal ligand orbital mixing and consequential stronger metal-metal communication. Although all of such aryl bridged complexes still belong to class II, judged from their a values, the trend is very implicative as it pointed out that redox-match between the metal and linking organic components is essential in leading to a highly charge-delocalized and conductive system.

References

1. Chen, J.; Reed, M. A.; Asplund, C. L.; Cassell, A. M.; Myrick, M. L.; Rawlett, A. M.; Tour, J. M.; Van Patten, P. G., *Appl. Phys. Lett.* **1999,** 75, 624-626.

2. Carroll, R. L.; Gorman, C. B., *Angew. Chem., Int. Ed.* **2002,** 41, 4378-4400.

3. Metzger, R. M., *Chem. Rev.* **2003,** 103, 3803-3834.

4. Sikes, H. D.; Smalley, J. F.; Dudek, S. P.; Cook, A. R.; Newton, M. D.; Chidsey, C. E. D.; Feldberg, S. W., *Science* **2001,** 291, 1519-1523.

5. Anderson, P. W., *Phys. Rev.* **1959,** 115, 2.

6. Marcus, R. A., *J. Chem. Phys.* **1965,** 43, 679-701.

7. Petrov, E. G. M., V., *J. Phys. Chem. A* **2001,** 105, 10176.

8. Sim, E., *J. Phys. Chem. B* **2004,** 108, 19093.

9. Weiss, E. A.; Ahrens, M. J.; Sinks, L. E.; Gusev, A. V.; Ratner, M. A.; Wasielewski, M. R., *J. Am. Chem. Soc. 2004, 126, 5577.* **2004,** 126, 5577.

10. Tolbert, L. M.; Zhao, X., *J. Am. Chem. Soc.* **1997,** 119, 2291.

11. Hush, N. S., *Coord. Chem. ReV.* **1985,** 64, 135.

12. Hush, N. S., *Prog. Inorg. Chem.* **1967,** 8, 391.

13. SMART Version 5.628, **2003**, Bruker AXS, Inc., Analytical X-ray Systems, 5465 East Cheryl Parkway, Madison WI 53711-5373.

14. SAINT Version 6.36A, **2002**, Bruker AXS, Inc., Analytical X-ray Systems, 5465 East Cheryl Parkway, Madison WI 53711-5373.

15. SADABS Version 2.10, **2003**, George Sheldrick, University of Göttingen.

16. SHELXTL V6.12, **2002**, Bruker AXS, Inc., Analytical X-ray Systems, 5465 East Cheryl Parkway, Madison WI 53711-5373.

17. A. J. C. Wilson (ed), International Tables for X-ray Crystallography, Volume C. Kynoch, Academic Publishers, Dordrecht, **1992**, Tables 6.1.1.4 (pp. 500-502) and 4.2.6.8 (pp. 219-222).

18. Pauson, P. L.; Watts, W. E., *J. Chem. Soc.* **1963**, 2990-2996.

19. Barlow, S.; Henling, L. M.; Day, M. W.; Schaefer, W. P.; Green, J. C.; Hascall, T.; Marder, S. R., *J. Am. Chem. Soc.* **2002,** 124, 6285-6296.

20. Mikolajczyk, M.; Popielarczyk, M.; Grzejszczak, S., *Phosphorus and Sulfur and the Related Elements* **1981,** 10, 369-373.

21. Kauffman, J. M.; Moyna, G., *J. Org. Chem.* **2003,** 68, 839-853.

22. Xu, B.; Zhang, J.; Pan, Y.; Peng, Z., *Synth. Met.* **1999,** 107, 47-51.

23. Plater, M. J.; Jackson, T., *Tetrahedron* **2003,** 59, 4673-4658.

24. Iwase, Y.; Kamada, K.; Ohtab, K.; Kondo, K., *J. Mater. Chem., 2003, 13,* **2003,** 13, 1575-1581.

25. Mbiegbei, D. A.; Roll, C. P.; Klemmi, E., *Designed Monomers and Polymers* **2002,** 5, 245-275.

26. Bahr, S. R.; Boudjouk, P., *J. Org. Chem.* **1992,** 57, 5545-5547.

27. Reger, D. L.; Wright, T. D.; Little, C. A.; Lamba, J. J. S.; Smith, M. D., *Inorg. Chem.* **2001,** 40, 3810-3814.

28. Justin Thomas, K. R.; Lin, J. T.; Wen, Y. S., *Organometallics* **2000,** 19, 1008-1012.

29. Zhao, X., *Ph.D. Thesis, Georgia Institute of Technology.* **1996**.

30. Spangler, C. W.; McCoy, R. K., *Synth. Commun.* **1988,** 18, 51-59.

31. Dimroth, K.; Follmann, H.; Pohl, G., *Chem. Ber.* **1965,** 95, 642.

32. Beeby, M. H.; Mann, F. G., *J. Chem. Soc.* **1949**, 1799-1803.

33. Silveira, C. C.; Santos, P. C. S.; Braga, A. L., *Tetrahedron Let.* **2002,** 43, 7517-7520.

34. Comasseto, J. V.; Petragnani, N., *J. Organomet. Chem.* **1978,** 152, 295-304.

35. Luo, S. J.; Liu, Y. H.; Liu, C. M.; Liang, Y. M.; Ma, Y. X., *Synth. Commun.* **2000,** 30, 1569-1571.

36. Kamiyama, S.; Kasahara, A.; Izumi, T.; Shimizu, I.; Watabe, H., *Bull. Chem. Soc. Jpn.* **1981,** 54, 2079-2082.

37. Nakaya, T.; Imoto, M., *Bull. Chem. Soc. Jp.* **1966,** 39, 1547-1551.

38. Mohanakrishnan, A. K.; Hucke, A.; Lyon, M. A.; Lakshmikantham, M. V.; Cava, M. P., *Tetrahedron* **1999,** 55, 11745-11754.

39. Ito, Y.; Konoike, T.; Harada, T.; Saegusa, T., *J. Am. Chem. Soc.* **1977,** 99, 1487-1493.

40. Horner, L.; Hoffmann, H. M. R.; Wippel, H. G., *Ber.* **1958,** 91, 61-3.

41. Wadsworth, W. S., Jr.; Emmons, W. D., *J. Am. Chem. Soc.* **1961,** 83, 1733.

42. Arbuzov, A. E., *J. Russ. Phys. Chem. Soc.* **1906,** 38, 687.

43. Thompson, S. K.; Heathcock, C. H., *J. Org. Chem.* **1990,** 55, 3386-3388.

44. Muchowski, J. M.; Hess, P., *Tetrahedron Let.* **1988,** 29, 777-780.

45. Hauser, C. R.; Pruett, R. L.; Mashburn, J. T. A., *Inorg. Chem.* **1961,** 26, 1800-1801.

46. Stetter, H., *Angew. Chem. Int. Ed.* **2003,** 15, 639-647.

47. Lecher, H. Z.; Greenwood, R. A.; Whitehouse, K. C.; Chao, T. H., *J. Am. Chem. Soc.* **1956,** 78, 5018-5022.

48. Kobayashi, E.; Obata, T.; Asohima, S.; Furukawa, J., *Polymer J.* **1993,** 25, 1049.

49. Luo, S. J.; Liu, Y. H.; Liu, C. M.; Liang, Y. M.; Ma, Y. X., *Synth. Commu.* **2000,** 30, 1569.

50. Sonogashira, K.; Tohda, Y.; N., H., *Tetrahedron Let.* **1975**, 4467-4470.

51. Stephans, R. D.; Castro, C. E., *J. Org. Chem.* **1963,** 28, 3313.

52. Driscoll, J. S. G. J., D. W.; Pustinger, J. V.; Harris, J. E.; Matthews, C. N., *J. Org. Chem.* **1964,** 29, 2427-2431.

53. Ribou, A.-C.; Launay, J.-P. ; Sachtleben, M. L.; Li, H.; Spangler, C. W., *Inorg. Chem.* **1996,** 35, 3735-3740.

54. Mata, J. A.; Peris, E.; Llusar, R.; Uriel, S.; Cifuentes, M. P.; Humphrey, M. G.; Samoc, M.; Luther-Davies, B., *Eur. J. Inorg. Chem.* **2001**, 2113-2122.

55. Barrière, F.; Camire, N.; Geiger, W. E.; Mueller-Westerhoff, U. T.; Sanders, R., *J. Am. Chem. Soc.* **2002,** 124, 7262-7263.

56. LeSuer, R. J.; Geiger, W. E., *Angew. Chem. Int. Ed.* **2000,** 112, 254-256.

57. Strauss, S. H., *Chem. Rev.* **1993**, 927-942.

58. Camire, N.; Mueller-Westerhoff, U. T.; Geiger, W. E., *J. Organomet. Chem.* **2001,** 637-639 823-826.

59. Barriere, F.; Geiger, W. E., *J. Am. Chem. Soc.* **2006,** 128, (12), 3980-3989.

60. Brown, G. M.; Meyer, T. J.; Cowan, D. O.; LeVanda, C.; Kaufman, F.; Roling, P. V.; Rausch, M. D., *Inorg. Chem.* **1975,** 14, 506.

61. Rulkens, R.; Lough, A. J.; Manners, I.; Lovelace, S. R.; Grant, C.; Geiger, W. E., *J. Am. Chem. Soc.* **1996,** 118, 12683.

62. Garcia, B.; Casado, C. M.; Cuadrado, I.; Alonso, B.; Moran, M.; Losada, J., *Organometallics* **1999,** 18, 2349-2356.

63. Ganter, C.; Kaulen, C.; Englert, U., *Organometallics* **1999,** 18, 5444-5446.

64. Reed, C. A., *Acc. Chem. Res.* **1998,** 31, 133-139.

65. Sohn, Y. S.; Hendrickson, D. N.; Gray, H. B., *J. Am. Chem. Soc.* **1971,** 93, 3603-3612.

66. Gleiter, R.; Merger, R.; Imgartinger, H., *J. Am. Chem. Soc.* **1992,** 114, 8927-8932.

67. Winstein, S., *J. Am. Chem. Soc.* **1959,** 81, 6524.

68. Paquette, L. A., *Angew. Chem., Int. Ed. Engl.* **1978,** 17, 106-117.

69. Connor Salazar, D. C.; Cowan, D. O., *J. Organomet. Chem.* **1991,** 408 227-231.

70. Shu, P.; Bechgaard, K.; Cowan, D. O., *J. Org. Chem.* **1976,** 41, 1849-1852.

71. Delgado-Pena, F.; Talham, D. R.; Cowan, D. O., *J. Organomet. Chem.* **1983,** 253 C43-C46.

72. Cameron, C. G.; Pickup, P. G., *Chem. Commun.* **1997**, 303-304.

73. Cameron, C. G.; Pickup, P. G., *J. Am. Chem. Soc.* **1999,** 121, 11773-11779.

74. Kingsborough, R. P.; Swager, T. M., *Adv. Mater.* **1998,** 10, 1100-1104.

75. Zhu, S. S.; Swager, T. M., *J. Am. Chem. Soc.* **1997,** 119, 12568-12577.

76. Connelly, N. G.; Geiger, W. E., *Chem. Rev.* **1996,** 96, 877-910.

77. *http://www.mpassociates.gr/software/distrib/science/microcal/pfm.html*.

78. Geoffroy, G. L.; Wrighton, M. S., *Organometallic Photochemistry, Academic Press, New York,* **1979**.

79. Sen, J.; Taube, H., *Acta Chem. Scand. Ser. A* **1979,** 33, 125-135.

80. Hill, N. J., *J. Chem. Soc., Faraday Trans. 2* **1972,** 68, 427.

81. Demadis, K. D.; El-Samanody, E.-S.; Coia, G. M.; Meyer, T. J., *J. Am. Chem. Soc.* **1999,** 121, 535-544.

82. Kober, E. M.; Goldsby, K. A.; Narayana, D. N. S.; Meyer, T. J., *J. Am. Chem. Soc.* **1983,** 105, 4303-4309.

83. Robin, M. B.; Day, P., *Adv. Inorg. Chem. Radiochem.* **1967,** 10, 247.

84. Marcus, R. A., *J. Chem. Phys.* **1965,** 43, 679.

CHAPTER 3

GREATLY ENHANCED ELECTRONIC INTERACTION IN DIFERROCENYL COMPLEXES LINKED BY PYRROLE-MEDIATED SPACERS: A METAL LIGAND REDOX-MATCHING APPROACH

Introduction

Mixed-valence metallic complexes linked by a conjugated organic component are the most widely used prototype in the study of intramolecular electron transfer in molecular level.[1-4] In the past, we have studied a large variety of diferrocenyl compounds bridged by a conjugated spacer, -CH=CH-X-CH=CH-, for which X represents a functional group with different level of electron-donating ability. Systematic analysis of these compounds via electrochemical and spectroscopic techniques revealed that electron transfer in the mixed-valence species relies largely on the energy level of the bridging unit. Effective electronic coupling in long distance only takes place when the redox potential of the bridging unit is high enough to match that of the redox-active metal centers. This is ascribed to the underlying superexchange hole-charge transfer mechanism.[5, 6]

As illustrated in Figure 3.1, the superexchange hole-transfer process in a mixed valence complex involves two sequential electron-transfer events occurring first between the π-HOMO of the bridging ligand (donor) and the Fe^{III} (acceptor) dπ-orbital and, second, between the π-HOMO of the bridging ligand (acceptor) and the Fe^{II} (donor) dπ-orbital. This mechanism is called 'hole transfer' is due to the electron hole migrates from the right to the left cross the complex via the mediation of the HOMO orbital of the bridging ligand. This term is opposite to 'electron transfer' mechanism, in which the electron hops from the Fe^{II} donor dπ-orbital to the ligand LUMO π-orbital and sequentially moves to the Fe^{III} acceptor site. Such process is apparently unfavorable or forbidden due to the high energy required to initiate the electron movement from Fe^{II}

electron donor to the empty π-orbital of the bridging ligand. However, people often use 'electron transfer' to refer to the metal-metal charge transfer (MMCT) process, without worrying that the actual undergoing mechanism, the 'hole transfer', described above. In this work, we will follow this convention, mutually exchange the two terms to refer to the MMCT or IVCT process.

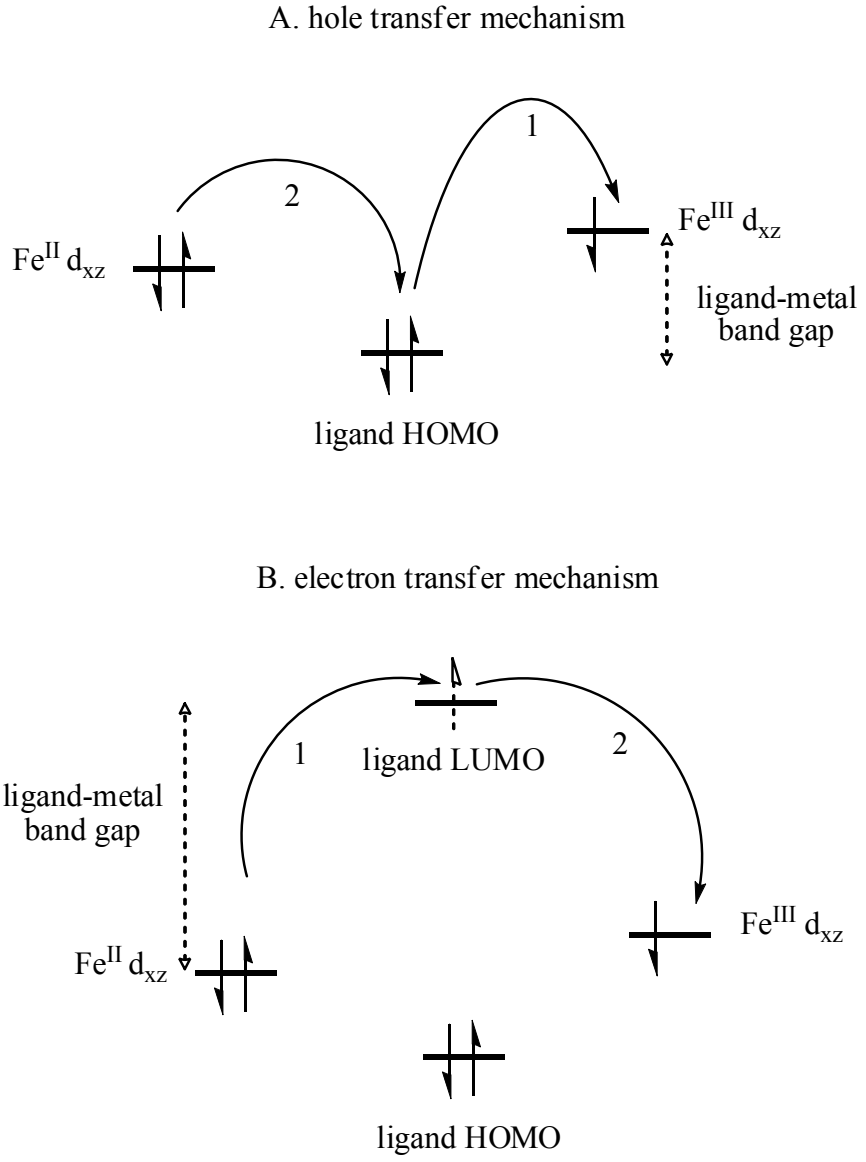

Figure 3.1 Schematic representation of the hole transfer and electron transfer superexchange mechanisms.

Based on the superexchange hole transfer mechanism, the smaller the energy gap between the HOMO of the bridging ligand and ferrocenium/ferrocene *d*π-orbitals, the greater the degree of the metal-metal intervalence charge transfer will occur. In principle, the intuitive approaches to narrow such energy band-gaps are either to lower the energy level of the metal *d*π-orbitals or to raise the HOMO orbitals of the bridging organic component, or, to merge these two processes into one. In other words, given a specific di-homometallic species (e.g. metallocenes or metallic complexes) separated by certain distance, modification of the metal complex ligand (e.g. octamethylferrocene) or introducing substituents on the bridging ligand can each perturb the energies of the interested orbitals. Careful selection of bridging ligand with compatible HOMO energy level close to that of the metallic species is always imperative in common practice. Having said that, however, extending conjugation of the bridging ligand to promote ligand HOMO energy level should be considered with caution, since the metal-metal electronic coupling weakens quickly as the metal-metal separation grows, as regulated by the Hush's rule (see equation 3.1).[7] Conceptually, longer conjugated bridging ligands require multiple electron hopping in order to traverse the gap between the metal centers, which will inevitably cause more energy loss and lead to less effective electronic communication.

$$H_{ab} = 2.06 \times 10^{-2}(\varepsilon_{max} \cdot \Delta v \cdot E_{IT})^{1/2}/r \qquad [3.1]$$

Electrochemistry provides convenient way to gather information on the energy levels of the metal complex and its bridging ligand as the oxidation potential values of these species are important indicators of the energy required to remove the electron from the corresponding redox-active centers. Essentially, the metal-metal through-ligand charge transfer (or hole transfer) could be considered as sequential redox processes among the metal centers and the bridging ligand unit. Thus, metal-ligand redox matching is crucial to minimize the metal-ligand energy gap to reach the optimized state for hole transfer.[8, 9]

Previous diferrocenyl compounds linked by polyene,[10] polymethine,[11] cumulene,[12] vinylene-arylene-vinylene[13] (Ar = *p*-phenylene, 2,5-thiophene, 2,5-furanylene) showed limited ability to facilitate the intervalence charge transfer process owing to the redox-mismatching between the redox-active metal center and bridging spacer, which accounts

for larger metal-ligand band gap. Curiously, pyrrolene-mediated differocenyl complex which offers considerable electron-donating advantage has not yet been reported.

In this study, we first examine the electrochemistry of two non-metal contained model compounds, diphenyl end-capped *N*-methyl-2,5-bis(arylvinyl)pyrrole **7** and **8**, to simulate the chemical environments of the 2,5-divinyl substituted pyrrole ligand similar to that of diferrocenyl terminated analogue **9c**. As the oxidation potentials of the pyrrole moiety in **7** and **8** closely resemble that of unsubstituted ferrocene, such metal-ligand redox-matching sets a solid foundation for the charge transfer studies in pyrrolene-based diferrocenyl systems. Based on this, we then investigate a series of pyrrolene-mediated diferrocenyl compounds, **9a-c**, **10** and **11a-b**, with different conjugation lengths and tuning substituents on the N atom of the pyrrolene nucleus. These compounds not only demonstrate significantly enhanced electronic interaction in both electrochemical and mixed-valence spectroscopic examinations, but also manifest electron hopping along the conjugated backbone is of importance when the energy level of the ligand HOMO orbital approaches to that of metal dπ orbitals. This provides us great insight in designing electronic devices such as molecular wires and molecular relays.

In order to enhance our understanding of the underlying electron transfer mechanism in the compounds stated above, two relevant referencel compounds **12** and **13** are also prepared and studied. As a logic extension, α,ω-diferrocenyl complexes bridged by pyrrolenevinylene oligomeric units, **14** and **15**, are also studied. As we shall see, both electrochemical and spectroscopic behaviors of these oligomers depend heavily on the energy level of the organic component and the metal-metal distance, which fundamentally changed the redox sequences and corresponding mechanisms.

Experimental

General Methods

All chemicals were purchased from Aldrich or Acros and used without further purification unless specified otherwise. All ^{1}H NMR spectra were acquired with a Varian Mercury 300 MHz instrument using $CDCl_3$ as the solvent unless otherwise specified. Chemical shifts are reported relative to tetramethylsilane. ^{13}C NMR spectra were

obtained at 75.5 MHz. IR analysis was performed on a Nicolet 520 FTIR spectrometer. UV-Vis-NIR analysis was recorded on a Varian Cary 5E UV-Vis-NIR spectrometer. X-ray structural analysis was conducted by the X-ray crystallography center of Emory University (Atlanta, GA). Elemental analysis was performed by Atlantic Microlab Inc. (Norcross, GA).

Electrochemical experiments were performed under argon on dry dichloromethane solutions ~10^{-4} M in sample and 0.1 M in $[^nBu_4N]^+[TFPB]^-$ (and $[^nBu_4N]^+[PF_6]^-$) using a BAS 100B analyzer in a three-electrode cell equipped with a 2.0 mm^2 platinum disk working electrode, a platinum wire counter electrode, and a AgI/Ag *pseudo* reference electrode (Chapter 2). Potentials were referenced by the addition of freshly sublimated ferrocene to the cell and are quoted relative to the nearest 5 mV relative to the ferrocene/ferrocenium (Fc/Fc^+) couple.

Standard procedures were employed in drying solvents. Thus, methylene chloride was distilled from sodium, hexane from calcium hydride, and THF from sodium benzophenone ketyl.

Column chromatography was performed on silica gel (40 mesh, 60Å, Fisher) or basic alumina. Deactivated silica gel chromatography was achieved by washing the packed column with corresponding eluent containing 3% of triethylamine and then with pure eluent to remove the triethylamine.

Synthesis

Tetraethyl *N*-Methylpyrrole-2,5-diylbismethylphosphonate (1). The title compound was prepared according to literature procedure[16] with slight modification. A solution of diethyl phosphite (11.52 g, 83.4 mmol) in DMF (20 mL) was slowly added to a suspension of NaH (2 g, 83.4 mmol) in DMF (80 mL) under nitrogen at -15 ^oC. When hydrogen evolution had ceased, the *N*-methyl-2,5-bis[(trimethylamino) methyl]pyrrole diiodide[14] (9 g, 18.8 mmol) was added at room temperature and the mixture was heated at 80°C for 8 h. After cooling, the mixture was poured onto ice and extracted with $CHCl_3$ (150 mL); the organic layer was dried and evaporated under reduced pressure. The residue was purified by flash column chromatography on silica gel using EtOAc-> EtOAc/MeOH (95:5) as eluent. Final product (yield 65%) was obtained as pale yellow oil

(Lit b.p.160 ^{o}C/0.1 mmHg).[16] ^{1}H NMR ($CDCl_3$): δ 6.0 (2H, m, pyr), 4.05 (8H, m, OCH_2), 3.60 (3H, s, NMe), 3.20 (4H, d, $J_{(CH-P)}$ = 18 Hz, CH_2P), 1.25 (12H, m, Me).

Diethyl N-methylpyrrol-2-ylmethylphosphonate (2). The title compound was prepared according to literature procedure.[16] A suspension of sodium hydride in oil (55% by weight; 1.67 g, corresponding to 0.92 g, 38 mmol) was thoroughly washed with THF and suspended in THF (50 mL). To this suspension maintained under nitrogen, cooled to - 15--20 "C, and magnetically stirred, a solution of diethyl phosphite (5.32 g, 38.5 mmol) was slowly added: once the evolution of hydrogen had ceased, the temperature was raised to room temperature, and the *N*-methylpyrrol-2-ylmethyl- trimethylammonium iodide[15] (in Figure 3.3) (3.27 g, 11.7 mmol) was added; the mixture was then heated at reflux for 15 h, cooled, and poured onto water. The mixture was extracted with diethyl ether (3 x 30 mL), and the organic phase washed with water, dried, and evaporated at reduced pressure to leave an oily residue which was distilled to give the compound **2** (1.2 g, 44%), b.p. 130 ^{o}C at 1 mmHg. ^{1}H NMR ($CDCl_3$): δ 6.55 (1H, m), 6.05 (2H, s), 4.05 (4H, m), 3.8 (3H, s), 1.35 (6H, t, J = 1.8 Hz).

(*E*)-*N*-methyl-2-(2-ferrocenyl)vinylpyrrole (3). To a stirred suspension of NaH (0.48 g of a 60% suspension in oil, 12 mmol, washed with dry hexane) in dry THF (40 mL) was added a solution of diethyl *N*-methylpyrrol-2-ylmethylphosphonate **2** (2.54g, 11 mmol) in THF (20 mL) dropwise under argon at r.t. The resulting suspension was stirred for 20 minutes before the ferrocenecarboxaldehyde (2.14 g, 10 mmol) in THF (30 mL) was added slowly and the reaction mixture was heated to reflux for 4 h. After cooling the colored mixture was quenched with water (5 mL). Volatile solvent was then removed under reduced pressure, the residues dissolved in CH_2Cl_2 (60 mL), washed with H_2O (3 x 40 mL), dried over $MgSO_4$ and evaporated to afford the crude product. Purification was achieved through flash column chromatography on silica gel using CH_2Cl_2/hexane (1:1) as eluent affording a red crystalline solid (2.76 g, 95%); m.p. 88-89 ^{o}C. ^{1}H NMR ($CDCl_3$): δ 6.63 (1H, d, J = 15.9 Hz), 6.62 (1H, m), 6.54 (1H, d, J = 15.9 Hz), 6.42 (1H, dd, J = 3.6, 1.8 Hz), 6.16 (1H, dd, J = 3.6, 2.7 Hz), 4.44 (2H, t, J =1.8 Hz), 4.28 (2H, t, J =1.8 Hz), 4.16 (5H, s), 3.66 (3H, s).). ^{13}C NMR ($CDCl_3$): δ 132.83, 124.59, 122.92, 114.98, 108.29, 105.67, 84.46, 69.43, 69.01, 66.61, 29.99. MS m/e (intensity): 291 (100, M^{+}), 226 (38), 211 (8), 169 (12), 121 (5), 56 (4).

(*E*)-*N*-methyl-5-(2-ferrocenylvinyl)-pyrrole-2-carboxaldehyde (4). Formylation of the 2-substituted-*N*-methylpyrrole derivative **3** was achieved by Vilsmeier reaction.[17, 18] The Vilsmeier reagent was prepared by mixing dimethyl formamide (DMF) (5 mL) with phosphorus oxychloride (1.61 g, 10.5 mmol) at 0 ^{o}C under Argon. This was transferred via cannula to an ice-cooled solution of *N*-methylpyrrole **3** (2.91 g, 10 mmol) in DMF (50 mL). After the addition, the reaction mixture was allowed to warm to r.t. and stirred for 6 h. The resulting deep red solution was quenched with water and subsequently treated with excess of 10% aqueous NaOH solution. The red suspension was extracted with CH_2Cl_2, and washed with more diluted NaOH, water and brine solution sequentially. The combined organic extracts were dried over $MgSO_4$ and evaporated to dryness to afford the crude product, which was purified by column chromatography on silica gel using CH_2Cl_2/hexane (1:1) as eluent. The tiitle compound was obtained as a red crystalline solid (1.78 g, 56%); m.p.116 ^{o}C. ^{1}H NMR ($CDCl_3$): δ 9.46 (1H, s), 6.89 (1H, d, J = 15.9 Hz), 6.88 (1H, d, J = 4.2 Hz), 6.53 (1H, d, J = 15.9 Hz), 6.47 (1H, d, J = 15.9 Hz), 4.47 (2H, t, J =1.8 Hz), 4.35 (2H, t, J =1.8 Hz), 4.15 (5H, s), 3.99 (3H, s). ^{13}C NMR ($CDCl_3$): δ 178.90, 142.67, 132.87, 125.45, 112.43, 107.33, 82.63, 70.09, 69.71, 67.36, 32.63. Anal. Calcd for $C_{18}H_{17}NOFe$: C, 67.73; H, 5.37. Found: C, 67.44; H, 5.36.

1,4-Diferrocenyl-butane-1,4-dione (5). Commercial LDA (5 mL of a 2M solution in THF/n-heptane, 10 mmol) was first added to precharged THF (5 mL) in a 100 mL round-bottle flask at –78 ^{o}C under argon. To this stirred solution, acetylferrocene (2.05 g, 9 mmol) in THF (10 mL) was added slowly. After 30 min, anhydrous $CuCl_2$ (1.35 g, 10 mmol) dissolved in 10 mL DMF was added at once at the same temperature. The reaction mixture was stirred for an additional 30 min and allowed to reach room temperature and stirred for further 1 h. The reaction mixture was treated with 3% aqueous HCl and extracted with chloroform. The organic extract was washed with 3% aqueous HCl and with water and dried over $MgSO_4$. After removal of the solvent, the residue was purified by chromatography on silica gel using chloroform as eluent to afford 1.48 g (72%) in the form of brown needles. ^{1}H NMR ($CDCl_3$): δ 4.89 (4H, t, J = 1.8 Hz), 4.54 (4H, t, J = 1.8 Hz), 4.31 (10H, s), 3.12 (4H, s). ^{13}C NMR ($CDCl_3$): δ 203.05, 72.22, 70.63, 69.97, 69.36, 33.2.

1,8-Diferrocenyl-octa-1,7-diene-3,6-dione (6). Refer to Chapter 2.

(*E,E*)-N-methyl-2,5-distyrylpyrrole (7). To a stirred solution of diphosphonate **1** (0.38 g, 1 mmol) in THF (30 mL) was added sodium bis(trimethylsilyl)amide (2.2 mL of a 1.0 M solution in THF, 2.2 mmol) dropwise at r.t. under argon. The resulting deep red solution was stirred for 15 minutes before benzaldehyde (0.212 g, 2 mmol) in THF (15 mL) was introduced slowly. The reaction mixture was heated to reflux for 4 h, cooled and quenched with water (5 mL). The volatile solvent was then removed under reduced pressure, and the residue was dissolved in CH_2Cl_2 (30 mL), washed with H_2O (3 x 30 mL), dried over $MgSO_4$ and evaporated to afford the crude product. Purification was achieved through flash column chromatography on silica gel using CH_2Cl_2 as eluent to give an orange solid (0.26 g, 91%); m.p. 189-190 ^oC. (lit.[19] 190-191 ^oC).^1H NMR ($CDCl_3$): δ 7.47 (4H, d, J = 7.2 Hz), 7.35 (4H, t, J = 7.5 Hz), 7.23 (2H, t, J = 7.5 Hz), 7.0 (2H, d, J = 15.9 Hz), 6.89 (2H, d, J = 15.9 Hz), 6.57 (2H, s), 3.72 (3H, s). ^{13}C NMR ($CDCl_3$): δ 138.04, 133.97, 128.98, 127.28, 126.76, 126.21, 117.13, 107.90, 30.90. IR (neat, cm^{-1}): 3019w, 1733w, 1699w, 1615m, 1590m, 1491m, 1473m, 1407m, 1386m, 1266m, 1072m, 1043m, 947s, 742s, 685s, 530s. MS m/e (intensity): 285.1 (100, M^+), 194.1 (7), 181.1 (7), 165.1 (5), 115.1 (8), 77 (7), 63 (3).

(*E,E*)-N-methyl-2,5-bis(4-methoxystyryl)pyrrole (8). Synthetic procedures described for compound **7** were used to prepare the title compound from *p*-methoxybenzaldehyde (0.272 g, 2 mmol) and diphosphonate **1** (0.38 g, 1 mmol). The reaction mixture was heated at reflux for 6 h; the crude product was recrystallized from CH_2Cl_2/hexane to yield an orange solid (0.26 g, 75%); m.p. 219-220 ^oC. ^1H NMR ($CDCl_3$): δ 7.38 (4H, d, J = 8.7 Hz, Ar), 6.87 (4H, d, J = 8.7 Hz, Ar), 6.85(4H, s, vinyl), 6.50 (2H, s, Pyr), 3.82 (6H, s, -OMe), 3.68 (3H, s, -NMe). ^{13}C NMR ($CDCl_3$): δ 159.09, 133.91, 130.95, 127.35, 126.23, 115.32, 114.38, 107.15, 55.58, 30.86. IR (neat, cm^{-1}): 2938w, 2835w, 1764w, 1662w, 1621m, 1598m, 1571m, 1505s, 1442m, 1301m, 1247s, 1104s, 1020s, 946s, 810m, 756m. MS m/e (intensity): 345.2 (100, M^+), 172.6 (13), 121 (8), 42.9 (8).

(*E,E*)-*N*-dodecyl-2,5-Bis(2-ferrocenylvinyl)-pyrrole (9a). Refer to Chapter 2.

(*E,E*)-*N*-phenyl-2,5-Bis(2-ferrocenylvinyl)-pyrrole (9b). A mixture of 1,8-diferrocenyl-octa-1,7-diene-3,6-dione (253 mg, 0.5 mmol), aniline (415 mg, 5 mmol) and *p*-toluenesulfonic acid (*p*-TSA) monohydrate (5 mg) was dissolved in xylene (20 mL).

The reaction mixture was stirred and heated at reflux for 12 h. After cooling, 30 mL saturated aqueous $NaHCO_3$ was added and the organic layer was extracted twice with 20 mL CH_2Cl_2. The combined organic extracts were dried over $MgSO_4$, and concentrated under reduced pressure. The residue was purified by flash column chromatography on silica gel using CH_2Cl_2/hexane (1:2) as eluent. The first band was collected and concentrated to give a red solid product (166 mg, 61%); m.p. 152-154 ^oC. ^1H NMR ($CDCl_3$): δ 7.52 (2H, d, J = 7.8 Hz), 7.48 (1H, d, J = 2 Hz), 7.30 (2H, dd, J = 7.8 Hz, J = 2 Hz), 6.55 (2H, s), 6.48 (2H, d, J = 15.9 Hz), 6.14 (2H, d, J = 15.9 Hz), 4.23 (4H, t, J = 1.8 Hz), 4.16 (4H, t, J = 1.8 Hz), 4.07 (10H, s). ^{13}C NMR ($CDCl_3$): δ 138.0, 134.4, 129.3, 128.4, 124.2, 116.0, 106.8, 84.4, 69.3, 68.9, 66.6. IR (KBr pellet, cm^{-1}): 3088.5, 3028.7, 1626.6, 1595.6, 1496.7, 1412.1, 1103.7, 1025.58, 943.7, 819, 771.9, 694.1, 485.8. MS m/e (intensity): 563 (100, M^+), 488 (9.0), 432 (3.5), 376 (7.8), 281.6 (27.4), 242 (2.3), 121 (4). Exact mass for $C_{34}H_{29}Fe_2N$: calcd: 563.09988, observed: 563.10218.

***(E,E)-N*-methyl-2,5-bis(2-ferrocenylvinyl))-pyrrole (9c).** Synthetic procedures described for compound **7** were followed to prepare the title compound from ferrocenecarboxaldehyde (1.28 g, 6 mmol) and diphosphonate **1** (1.14 g, 3 mmol). The reaction mixture was heated at reflux for 6 h and the crude product was purified either by flash column chromatography on silica gel (CH_2Cl_2) or by recrystallization twice from MeOH to offer an orange red crystalline solid (1.11 g, 74%); decomposed > 200 ^oC. ^1H NMR ($CDCl_3$): δ 6.61 (2H, d, J = 15.9 Hz), 6.54 (2H, d, J = 15.9 Hz), 6.44 (2H, s), 4.42 (4H, t, J =1.8 Hz), 4.26 (4H, t, J =1.8 Hz), 4.14 (10H, s), 3.61 (3H, s). ^{13}C NMR ($CDCl_3$): δ 133.72, 124.70, 114.94, 106.44, 84.52, 69.42, 69.05, 66.55, 30.88. IR (neat, cm^{-1}): 3096w, 1771w, 1716w, 1683m, 1652m, 1558m, 1409m, 1300m, 1231m, 1102m, 1027m, 947m, 815m, 754s, 483s. FABMS: *m/z* 501 [M^+]. Anal. Calcd for $C_{29}H_{27}NFe_2$: C, 69.49; H, 5.43. Found: C, 69.44; H, 5.40.

***N*-methyl-2,5-bis((1E,3E)-4-ferrocenylbuta-1,3-dienyl)pyrrole (10).** Synthetic procedures described for compound **7** were followed to prepare the title compound from ferrocenepropenal (0.48 g, 2 mmol) and diphosphonate **1** (0.42 g, 1.1 mmol). The reaction mixture was heated at reflux overnight; the crude product was washed with 10 mL MeOH before being passed through a short basic alumina column (CH_2Cl_2) to achieve a purple red crystalline solid (0.33 g, 60%); decomposed > 210 ^oC. ^1H NMR

(CD_2Cl_2): δ 6.66 (2H, dd, J = 15 Hz, J = 10.8 Hz), 6.56 (2H, dd, J = 14.7 Hz, J = 10.8 Hz), 6.46 (2H, s, pyr), 6.45 (2H, d, J = 15 Hz), 6.35 (2H, d, J = 14.7 Hz), 4.41 (4H, t, J =1.8 Hz), 4.27 (4H, t, J =1.8 Hz), 4.13 (10H, s), 3.58 (3H, s). ^{13}C NMR (CD_2Cl_2): δ 134.03, 129.70, 127.69, 127.40, 118.25, 107.47, 83.92, 69.46, 69.23, 66.83, 29.91. IR (neat, cm^{-1}): 3096w, 2919m, 2850m, 1721w, 1602m, 1522w, 1440m, 1370m, 1234m, 1103m, 1025m, 975s, 808m, 730m, 485s. MS m/e (intensity): 553 (64, M^+), 366 (8), 276 (5), 186 (78), 121 (100), 55.9 (12).

***N*-Dodecyl-2,5-diferrocenylpyrrole (11a)**. A mixture of 1,4-diferrocenyl-tetrane-1,4-dione **5** (227 mg, 0.5 mmol), dodecylamine (741 mg, 4 mmol) and p-toluenesulfonic acid (p-TSA) monohydrate (10 mg) was dissolved in 20 mL xylene. The reaction mixture was stirred and heated at reflux for 12 h. After cooling, 30 mL saturated aqueous $NaHCO_3$ was added and the organic layer was extracted twice with 20 mL CH_2Cl_2. The combined organic extracts were dried over $MgSO_4$, and concentrated under reduced pressure. The residue was purified by flash column chromatography on silica gel using CH_2Cl_2/hexane (1:2) as eluent. The first band was collected and concentrated to give a yellow crystalline solid (242 mg, 80%); m.p. 108 ^oC. ^{1}H NMR ($CDCl_3$): δ 6.28 (2H, s), 4.35 (4H, t, J = 1.8 Hz), 4.23 (4H, t, J = 1.8 Hz), 4.18 (10H, s), 3.90 (2H, t, J = 5.1 Hz), 1.25 (20H, br), 0.88 (3H, t, J = 6.3 Hz). ^{13}C NMR ($CDCl_3$): δ 130.5, 108.8, 80.4, 69.6, 69.1, 68.0, 43.6, 32.1, 31.5, 29.9, 29.7, 29.6, 29.3, 26.8, 22.9, 14.4. MS m/e (intensity): 603.2 (100, M^+), 434 (5.0), 367.9 (4), 301.6 (13), 248 (3), 120.9 (3.4), 57.1 (3), 44 (3.5). Exact mass for $C_{36}H_{45}Fe_2N$: calcd: 603.22508, observed: 603.22542.

***N*-Phenyl-2,5-diferrocenylpyrrole (11b).** The tiitle compound was prepared in the same manner as that for compound **11a**. 1,4-Diketone **5** (227 mg, 0.5 mmol), aniline (415 mg, 5 mmol) and *p*-toluenesulfonic acid (*p*-TSA) monohydrate (5 mg) was dissolved in xylene (20 mL) and heated at reflux for 12 h. The crude product was purified by flash column chromatography on silica gel using CH_2Cl_2/Hexane (1:2) as eluent. A yellow crystalline solid resulted (242 mg, 80 %); m.p. > 195 ^oC, decomposed. ^{1}H NMR(CD_2Cl_2): δ 7.54 (2H, d, J = 7.2 Hz), 7.52 (1H, d, J = 1.5 Hz), 7.33 (2H, dd, J = 7.2 Hz, J = 1.5 Hz), 6.17 (2H, s), 4.06 (4H, t, J = 1.8 Hz), 4.02 (10H, s), 3.89 (4H, t, J = 1.8 Hz). ^{13}C NMR (CD_2Cl_2): δ 140.45, 129.97, 128.97, 79.32, 69.67, 67.98, 66.53. ^{13}C NMR ($CDCl_3$): δ 140.26, 132.39, 130.15, 128.97, 128.88, 108.20, 79.31, 69.63, 67.66, 66.87.

IR (neat, cm^{-1}): 3078.6w, 1597.3m, 1496.3m, 1418.6m, 1326.9m, 1103.7m, 1000.1m, 854.3m, 757.8s, 683s. MS m/e (intensity): 603.2 (100, M^+), 434 (5.0), 367.9 (4), 301.6 (13), 248 (3). Exact mass for $C_{30}H_{25}Fe_2N$: calcd: 511.06858, observed: 511.06731.

2,5-Diferrocenylthiophene (12). A mixture of $FcCOCH_2CH_2COFc$ **5** (227 mg, 0.5 mmol) and Lawesson's reagent (242 mg, 0.6 mmol) in dry toluene (10 mL) was heated at reflux under argon for 4 hours. The reaction mixture was concentrated and subjected to flash column chromatography on silica gel using CH_2Cl_2/Hexane (1:2) as eluent to furnish a red crystalline solid (191 mg, 84.5%); m.p. 196-198 ^oC. ^1H NMR ($CDCl_3$): δ 6.82 (2H, s), 4.58 (4H, t, J = 1.8 Hz), 4.29 (4H, t, J = 1.8 Hz), 4.13 (10H, s). ^{13}C NMR ($CDCl_3$): δ 140.9, 122.6, 80.74, 70.22, 68.84, 66.91. MS m/e (intensity): 452 (100, M^+), 410.1 (8), 331 (28), 226 (54), 186 (10), 121 (21), 55.9 (5). Exact mass for $C_{24}H_{20}Fe_2S$: 451.99845, observed: 451.99586.

(*E*,*E*)-*N*-methyl-2-(2-ferrocenyl)vinyl-5-styrylpyrrole (13). To a stirred suspension of NaH (80 mg, a 60% suspension in oil, 2 mmol, washed with dry hexane) in dry THF (20 mL) was added a solution of diethyl benzylphosphonate (Aldrich) (0.274 g, 1.2 mmol) in THF (10 mL) dropwise under argon at r.t. The resulting suspension was stirred for 20 minutes before the (*E*)-1-methyl-5-(2-ferrocenylvinyl)-pyrrole-2-carboxaldehyde **4** (0.29 g, 1 mmol) in THF (15 mL) was added slowly and the reaction mixture was heated to reflux for 6 h. After cooling the colored mixture was quenched with water (5 mL). Volatile solvent was then removed under reduced pressure, the residues dissolved in CH_2Cl_2 (40 mL), washed with H_2O (3 x 30 mL), dried over $MgSO_4$ and evaporated to afford the crude product. Purification was achieved through flash column chromatography on silica gel using CH_2Cl_2/hexane as eluent to afford a red crystalline solid (0.34 g, 87%); m.p. 148 ^oC. ^1H NMR ($CDCl_3$): δ 7.44 (2H, d, J = 8.7 Hz), 7.33 (2H, t, J = 8.4 Hz), 7.21 (1H, t, J = 8.4 Hz), 6.97 (1H, d, J = 15.9 Hz), 6.86 (1H, d, J = 15.9 Hz), 6.63 (1H, d, J = 15.9 Hz), 6.56 (1H, d, J = 15.9 Hz), 6.53 (1H, d, J = 3.9 Hz), 6.45 (1H, d, J = 3.9 Hz), 4.43 (2H, t, J =1.8 Hz), 4.27 (2H, t, J =1.8 Hz), 4.14 (5H, s), 3.67 (3H, s). ^{13}C NMR ($CDCl_3$): δ 138.19, 134.60, 133.09, 128.90(Ar), 127.11, 126.11 (Ar), 125.43, 117.31, 114.75, 107.73, 106.66, 84.32, 69.42, 69.12, 66.63, 30.88. IR (neat, cm^{-1}): 3093w, 2919m, 2844m, 1616m, 1589m, 1565w, 1441m, 1297m, 1233m,

1102m, 1035m, 946s, 810m, 758s, 692s, 486s. FABMS: *m/z* 393 [M^+]. Anal. Calcd for $C_{25}H_{23}NFe$: C, 76.34; H, 5.89. Found: C, 76.66; H, 6.1.

(*E,E,E,E*)-2,5-Bis[2-[5-(2-ferrocenylvinyl)-*N*-methylpyrrol-2-yl]vinyl]-*N*-methylpyrrole (14). Synthetic procedures described for compound **7** were followed to prepare the title compound from (*E*)-1-methyl-5-(2-ferrocenylvinyl)-pyrrole-2-carboxaldehyde **4** (0.29 g, 1 mmol) and diphosphonate **1** (0.21 g, 0.55 mmol). The reaction mixture was heated at reflux for 6 h, the crude product was washed with ca. 10 mL MeOH, then passed through a short basic alumina column (CH_2Cl_2) to gain a purple red crystalline (0.18 g, 51%); decomposed > 210 ^oC. ^1H NMR (CD_2Cl_2): δ 6.79 (4H, d, J = 15.2 Hz), 6.63-6.44 (6H, m), 4.44 (4H, t, J = 1.8 Hz), 4.28 (2H, t, J = 1.8 Hz), 4.15 (10H, s), 3.63 (9H, s, NMe). ^{13}C NMR (THF-d_8): δ 133.88, 125.13, 123.59, 122.53, 115.29, 114.01, 106.50(s), 84.99, 69.01, 68.53, 29.95, 29.64. IR (neat, cm^{-1}): 3090w, 2950w, 1741w, 1646m, 1618m, 1538m, 1442m, 1386m, 1269m, 1103m, 1040m, 940s, 814m, 752s, 480s. FABMS: *m/z* 711 [M^+].

(*E,E,E,E*)-1,4-Bis[2-[5-(2-ferrocenylvinyl)-*N*-methylpyrrol-2-yl]vinyl]-2,5-dodecyloxybenzene (15). To a stirred suspension of NaH (60 mg, a 60% suspension in oil, 1.5 mmol, washed with dry hexane) in dry THF (10 mL) was added a solution of tetraethyl (2,5-bis(dodecyloxy)-1,4-phenylene)bis(methylene)diphosphonate[20] (0.373 g, 0.5 mmol) in THF (15 mL) dropwise under argon at r.t. The resulting solution was stirred for 20 minutes before the (*E*)-1-methyl-5-(2-ferrocenylvinyl)-pyrrole-2-carboxaldehyde **4** (0.29 g, 1 mmol) in THF (15 mL) was added slowly and the reaction mixture was heated to reflux for 2 h. After cooling, the colored mixture was quenched with water (5 mL). The volatile solvent was then removed under reduced pressure, the residues dissolved in CH_2Cl_2 (60 mL), washed with H_2O (3 x 30 mL), dried over $MgSO_4$ and evaporated. The crude product was then stirred in MeOH (15 mL) for 10 min. and filtered. After repeating the washing and filtration processes one more time, the final product was obtained as an orange red solid (516 mg, 96%). Analytical sample was achieved by passing through a short silica gel column using CH_2Cl_2 as eluent, m.p. 160 ^oC. ^1H NMR ($CDCl_3$): δ 7.13 (2H, d, J = 15.9 Hz, vinyl), 7.07 (2H, d, J = 15.9 Hz, vinyl), 6.99 (2H, s, Ar-center), 6.62 (2H, d, J = 15.9 Hz, vinyl), 6.56 (2H, d, J = 15.9 Hz, vinyl), 6.55 (2H, d, J = 3.9 Hz, Pyr), 6.48 (2H, d, J = 3.9 Hz, Pyr), 4.43 (4H, t, J = 1.8 Hz), 4.27 (2H, t, J = 1.8 Hz), 4.15 (10H,

s), 4.04 (4H, t, J = 6.3 Hz, CH_2O-dodecyl), 3.67 (6H, s, NCH_3), 1.87-1.28 (40H, m), 0.89 (6H, t, J = 6.9 Hz). ^{13}C NMR ($CDCl_3$): δ 151.21, 134.49, 134.14, 126.81, 125.10, 121.57, 117.65, 114.83, 111.0, 107.71, 106.79, 84.46, 69.76, 69.42, 69.1, 66.64, 32.18, 30.89, 29.90, 29.76, 29.62, 26.57, 22.95, 14.38. IR (neat, cm^{-1}): 3093w, 3033w, 2916s, 2848s, 1761w, 1611m, 1504m, 1443m, 1388m, 1337m, 1229m, 1197m, 1024m, 940s, 813m, 743m, 481s. FABMS: *m/z* 1076 [M^+].

Results & Discussion

Synthesis

Preparation of Synthons

Starting from commercially available *N*-methylpyrrole, tetraethyl *N*-methylpyrrole-2,5-diylbismethylphosphonate, **1**, was prepared through multiple step reactions following literature procedures[16] as shown in Figure 3.2. This is a very useful precursor for assembling the 2,5-divinylpyrrolene fragment through conventional Horner-Wadsworth-Emmons (HWE) condensation with the corresponding aldehydes. The alternative strategy to build such fragments is to inversely couple the 2,5-formylpyrrole

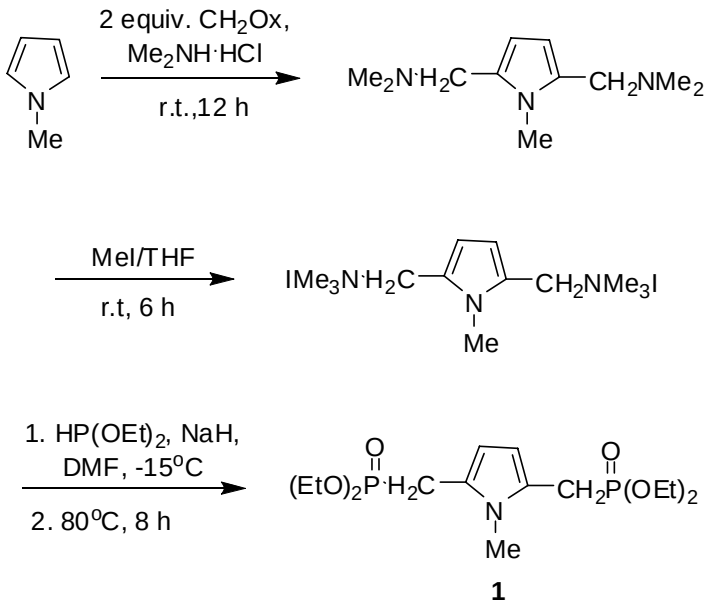

1

Figure 3.2. Synthetic route of diphosphonate **1**.

derivatives with the mono-phosphonate via the same HWE methodology. However, our previous attempts to bring about reaction turned out to be unsuccessful, presumably due to the depreciated reactivity of the second aldehyde upon the first olefinic coupling. Only mono-condensed product was recovered (see Chapter 2). The employment of bisphosphonate **1** in HWE reactions eliminated such problem. The methyl group was selected as the side substituent on the pyrrole nucleus for several considerations. First, the starting material, *N*-methylpyrrole was commercially available. Second, *N*-aliphalic substituted pyrrole derivatives are generally more synthetically stable than their pyrrole analogues, which are more sensitive to acid triggered oxidative processes. Whereas the steric hindrance derived from the *N*-substituent is one of the major concerns for polypyrroles, it is not severe for oligo- or poly(pyrrolenevinylene) systems, since the aromatics are held well apart by the vinyl linkers. Third, the oxidation potential of *N*-alkyl substituted pyrrole is lower than that of other pyrrole derivatives due to the electron-donating ability from the alkyl group. Finally, when higher solubility (e.g. pyrrolene oligomers and polymers) is required, the methyl group can be easily modified to other long alkyl chains with the same synthetic approach used here. The current investigation serves as an easy test case to understand the fundamentals of this system.

Diethyl *N*-methylpyrrol-2-ylmethylphosphonate **2** was also prepared according to literature procedures[16]. The synthetic pathway was very similar to that of bisphosphonate **1**. As shown in Figure 3.3, in the first step of the synthetic route, the Mannich reaction, only one equivalent of aqueous formaldehyde and dimethylaminehydrochloride was utilized so that the mono-Mannich base was formed. The predefined open side at the a-position of the pyrrole unit was very essential since the active α-H allowed subsquent introduction of functional groups for various purposes. The HWE reaction between phosphonate **2** and ferrocenecarboxaldehyde readily afforded (*E*)-2-ferrocenylvinyl-*N*-methylpyrrole **3** in high yield (87%). The vinyl linker between the ferrocenyl and pyrrolyl units was *trans* configured as most often seen in the HWE reactions, which was affirmed both by the coupling constant (15.9 Hz) of the two olefinic protons and by the strong IR band at ca. 950 cm^{-1} attributable to the out-of-plane C-H stretching mode from an (*E*)-disubstituted ethylene. Formylation of **3** at the 5-position of the pyrrolene ring was effected by conventional Vilsmeier reaction[17, 18] affording the corresponding aldehyde **4**.

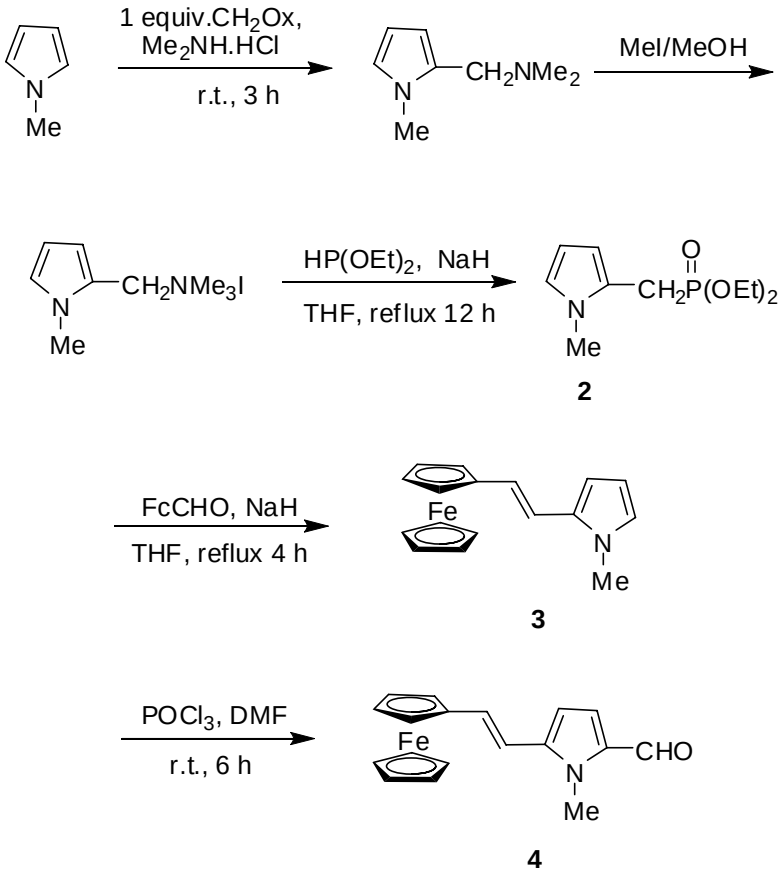

Figure 3.3. Synthetic route of pyrrolealdehyde **4**.

Unlike similar procedures on furan and thiophene analogues,[21, 22] formylation on the pyrrole ring only offered moderate yield (55%), which was attributed to the sensitivity of pyrrole unit to the acidic condition and the relative high reactivity of the protons on the 3- and 4-positions. Indeed, 4-formyl aldehyde and diformyl 4,5-dialdehyde were also isolated and characterized as major side products. Thus, the general practice to alleviate this problem was to employ shorter reaction time without heating.

1,4-Butanediones **5** and **6** (in Figure 3.4) were prepared by $CuCl_2$ promoted oxidative coupling[23] of the lithium anions generated by the lithination of the corresponding ferrocenylketones via lithium diisopropylamide (LDA), as we have discussed in chapter 2. The geometries of vinyl groups in **6** were synthetically predefined

in *E* forms. These two synthetic precursors were to be utilized in the ring closure reactions.

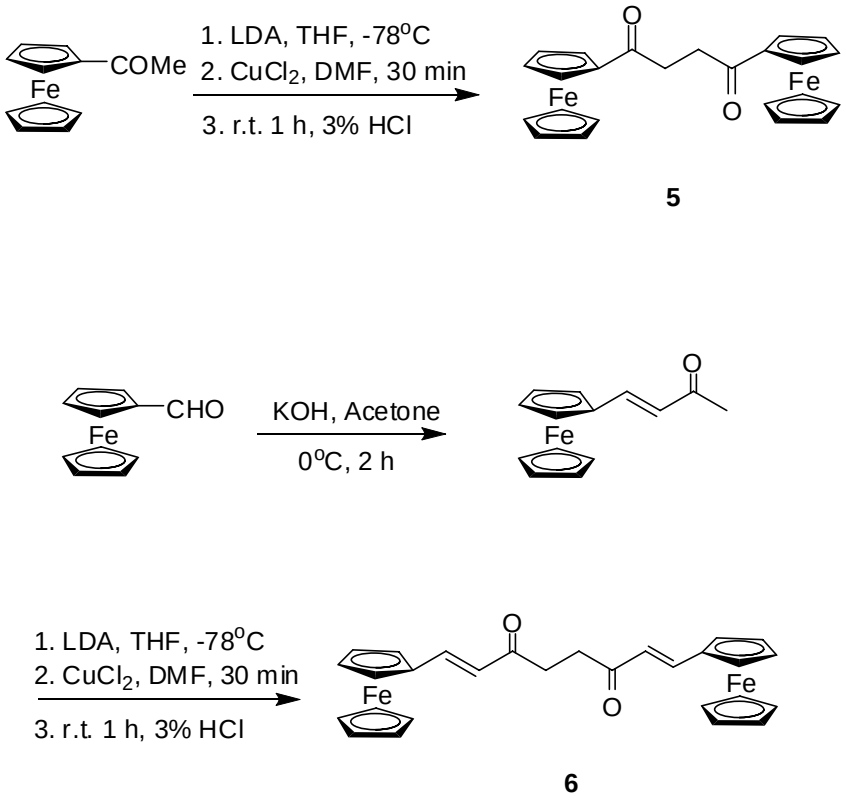

Figure 3.4. Synthetic route of butane-diketones **5** and **6**.

Preparation of Targeted Compounds

Bis(2-arylvinyl) (**7** and **8**), bis(2-ferrocenylvinyl) (**9c**) and bis(2-ferrocenylbutadienyl) (**10**) *N*-methylpyrroles were readily achieved through the HWE olefinations between the bisphosphonate **1** and the appropriate aldehydes (Figure 3.5) to give yields ranging from 45% to 85%. In each case, the newly formed olefinic protons were characterized by *E* stereochemistry. The HWE condensation fashion effectively avoided the possible geometrically unselective adducts prepared via the Wittig approach as previously observed (e.g. compound **7**).[24] Purifications were performed carefully through flash column chromatography on deactivated silica gel or basic alumina to minimize product loss due to their acid sensitivity. Even with this precaution, the

butadienyl bridged compound **10** was still obtained in a relatively low yield (45%) due to such column chromatography loss. The increased degree of conjugation in **10** must have accounted for the consequently enhanced sensitivities, which caused more decomposition during the purification process. Therefore, alternative purification procedures such as recrystallizing **10** from polar solvent (e.g. MeOH) are recommended to improve the outcome in the future, since high levels of olefinic conjugation lead to lower solubility in polar solvent as we indeed observed for compound **10**. Finally, both phenyl-capped compounds **7** and **8** are shiny and highly fluorescent materials in solutions. Their photochemical and photo-illuminating properties are not in this scope of study and will be discussed elsewhere (chapter 6).

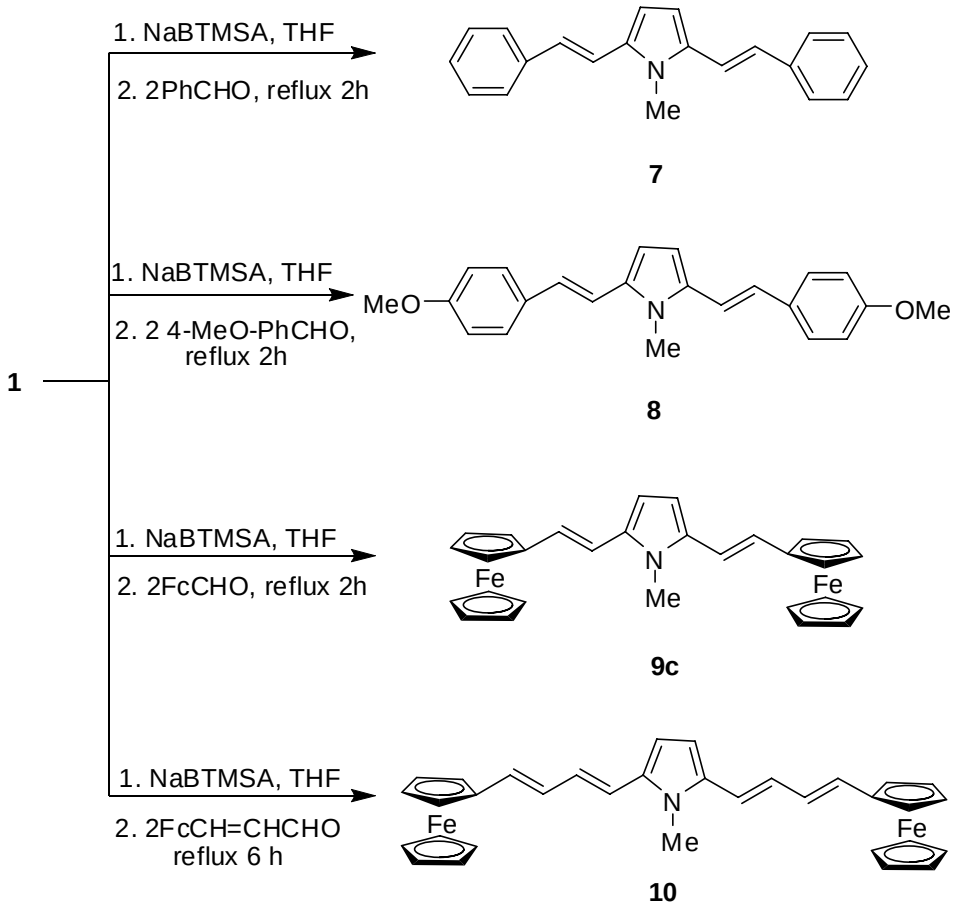

Figure 3.5. Synthetic pathway for compounds **7**, **8**, **9c**, **10** starting from diphosphonate **1**.

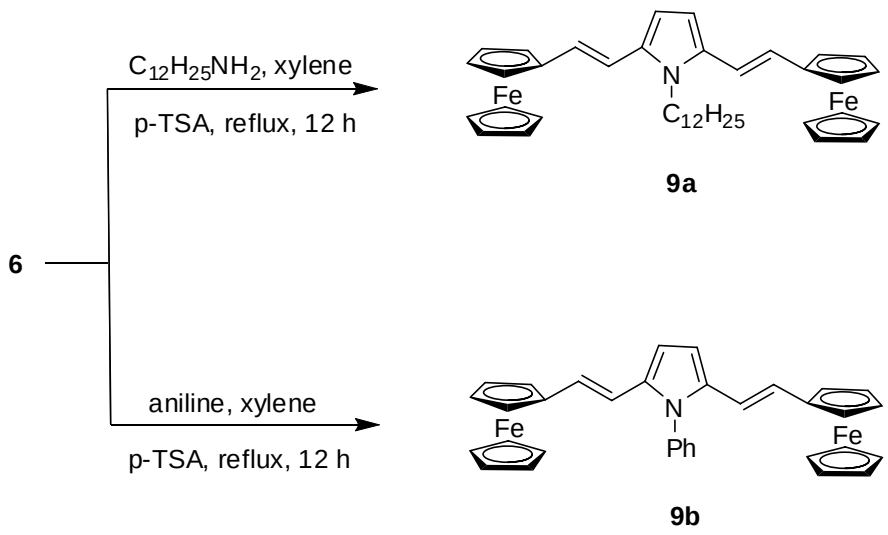

Figure 3.6. Synthetic pathway for compound **9a-b** starting from diketon **6.**

N-dodecyl and *N*-phenyl substituted 2,5-bisferrocenylvinylpyrroles, **9a** and **9b,** were prepared from (1E, 7E)-1,8-diferrocenylocta-1,7-diene-3,6-dione **6** via Paal-Knorr intramolecular ring closure condensations[25, 26] as shown in Figure 3.6, while *N*-dodecyl and *N*-phenyl substituted 2,5-diferrocenylpyrroles, **11a** and **11b**, were achieved from 1,4-diferrocenylbutane-2,3-dione **5** in the same synthetic manner (Figure 3.7). In general, excess amounts of primary amines were used in the presence of catalytical amount of p-toluenesulfonic acid (p-TSA) to promote higher yield in high-boiling xylene. In any event, decent yields were obtained. As the relevant mechanisms were previously discussed in Chapter 2, Paal-Knorr methodology was very essential for 2,5-substituted pyrroles such as **11a** and **11b** since compounds of this kind were fairly difficult to achieve otherwise. Although vinyl spaced 2,5-pyrroles **9a** and **9b** could alternatively be prepared via a similar synthetic pathway as that for *N*-methyl substituted compound **9c**, apparently several more intermediates and steps are required for such a synthesis to occur. The current approach obviously provided the most efficient preparations. On the other hand, *N*-methyl pyrrole derivative **9a** could not be obtained using Paal-Knorr reaction since the condensation reaction required high temperature (refluxing in xylene), for which volatile primary amines such as methylamine or butylamine were not suitable.

Therefore, both HWE and Paal-Knorr methodologies were employed for the most efficient and specific purposes. Again, acidic contacts were always minimized to eliminate the possible product loss during the purification procedures.

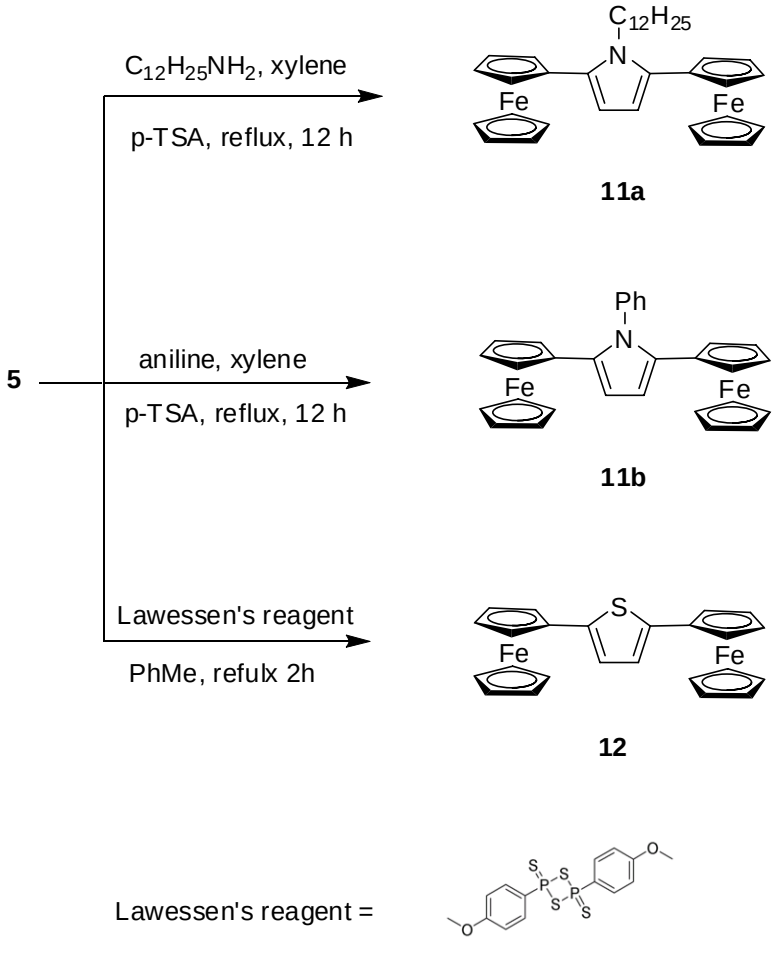

Figure 3.7. Synthetic pathway of compounds **11a-b**, **12** starting from diketone **5**.

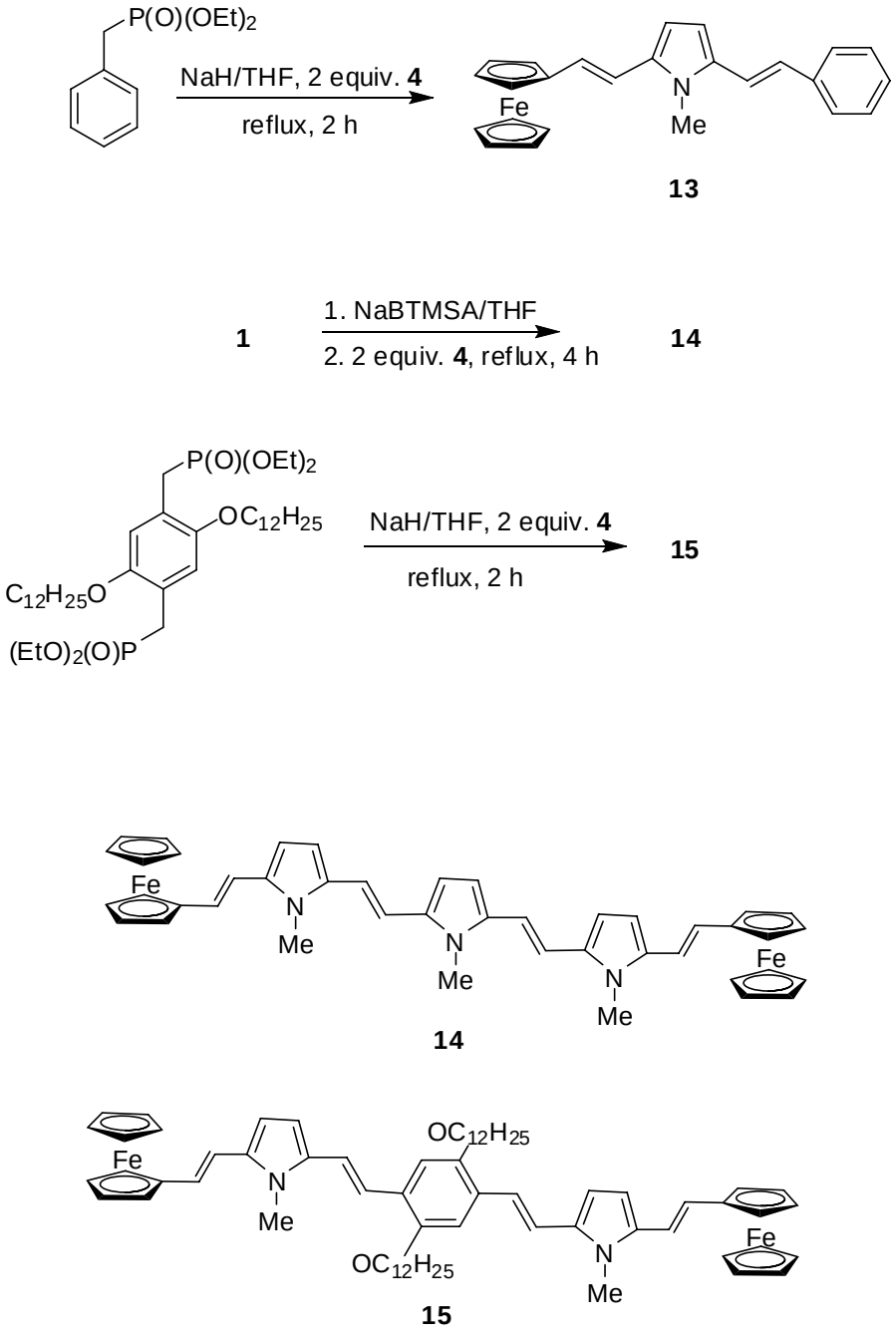

Figure 3.8. Synthetic pathway for compounds **13**, **14** and **15** starting from **4**.

For the sake of comparison, diferrocenylthiophene **12** was also synthesized from diketone **5** with Lawesson's reagent (LR)[27, 28] as the thionating and ring closing medium. The reaction was readily effected in refluxing toluene, affording a high yield of 84.5%. The related mechanism and applications of LR have recently been reviewed on several occasions.[29, 30] Generally, it is believed the central phosphorus/sulfur four membered ring in LR (in Figure 3.7) opens to form two reactive dithiophosphine ylides ($R\text{-}PS_2$) upon heating. These ylides were very effective species to convert a carbonyl into the corresponding carbothionyl group. Two successive such sulfurations on diketons **5**, followed by water elimination completed the heterocyclic formation. Compared to the literature procedures used in preparing of diferrocenylthiophene **12** (reference), the LR reaction we adopted herein required fewer steps and resulted in higher yield.

As illustrated in Figure 3.8, structurally asymmetric compound **13** and diferrocenyl end-capped aromatic oligomers **14** and **15** were prepared, again, through HWE olefination between pyrrolealdehyde **5** and diethylphenylmethylphosphonate (Aldrich), bisphosphonate **1**, and diethyl 2,5-didodecyloxyphenylmethylphosphonate,[20] respectively. The three compounds were all successfully achieved in moderate or high yields with all newly formed olefinic bonds (*E*)-configured, which were evidenced by NMR and IR spectroscopies. Compounds **13** and **14** were purified by flash column chromatography in the same manner as that for compound **9c.** Due to the highly conjugated and electron enriched backbone of **14**, it became more acid-sensitive. Therefore, it is always recommended either using basic alumina as the column absorbant or adopting other purification techniques as we mentioned earlier was employed. Owing to its long side hydrocarbon chains on the central phenylene group, highly-yielded compound **15** were conveniently purified by washing several times with small amount of MeOH.

X-ray Crystal Structure

Single crystals of **3, 4, 9b-c, 10, 11a-b,** and **13** were obtained by slow solvent evaporation of the concentrated substrate solution. The X-ray crystal analysis of **9a** has been described in Chapter 2. The ORTEP plots are shown in Figure 3.9-3.15. The ferrocenyl units in all compounds present normal eclipsed conformations unless otherwise stated. Most of the bond lengths and angles lie in the expected region.

As shown in Figure 3.9, the coplanarity of the substituted Cp ligand in **3** is fairly sustained with a methyl group attached on the pyrrolene nitrogen atom. The maximum torsion angle between the pyrrolene and the substituted Cp rings is 6.98^{o}, which is substantially smaller than the analogous value (34.90^{o}) in **4** (Figure 3.10). Apparently, the enlarged twist in **4** arises from the insertion of a formyl substituent at the 5-position of the pyrrolene nucleus, which causes the whole heteroaromatic unit to become more bulky so that more distortion is introduced to alleviate the steric crowdedness.

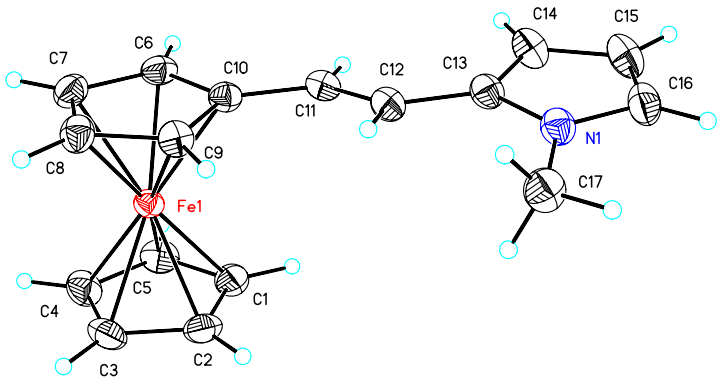

Figure 3.9. ORTEP plot of compound **3** with 50% anisotropic displacement ellipsoids.

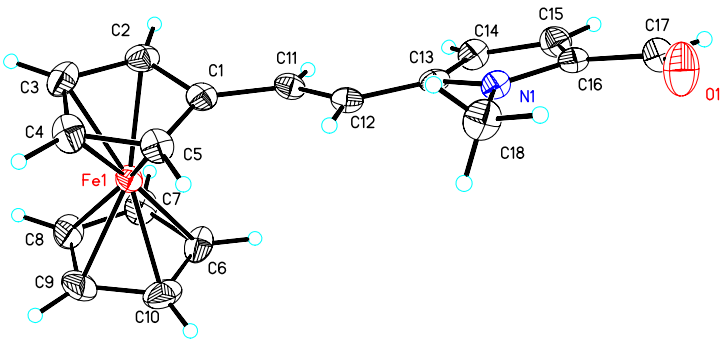

Figure 3.9. ORTEP plot of compound **4** with 50% anisotropic displacement ellipsoids.

A

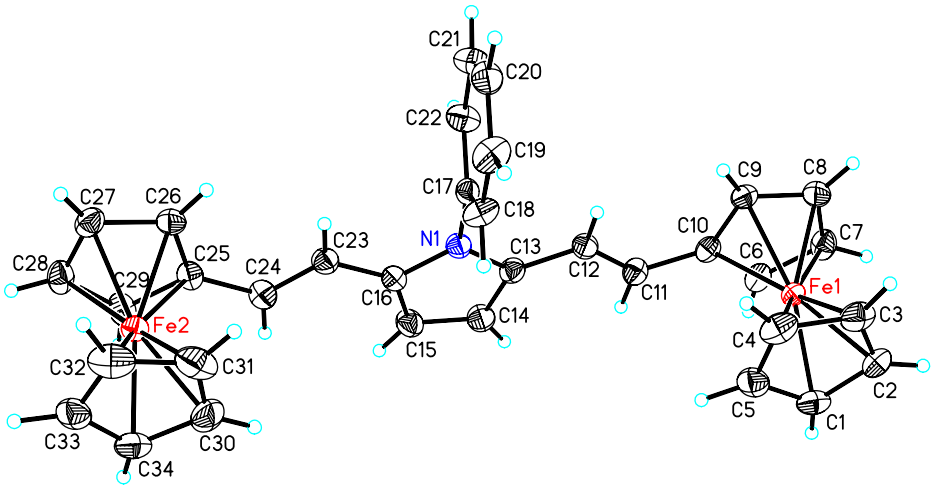

B

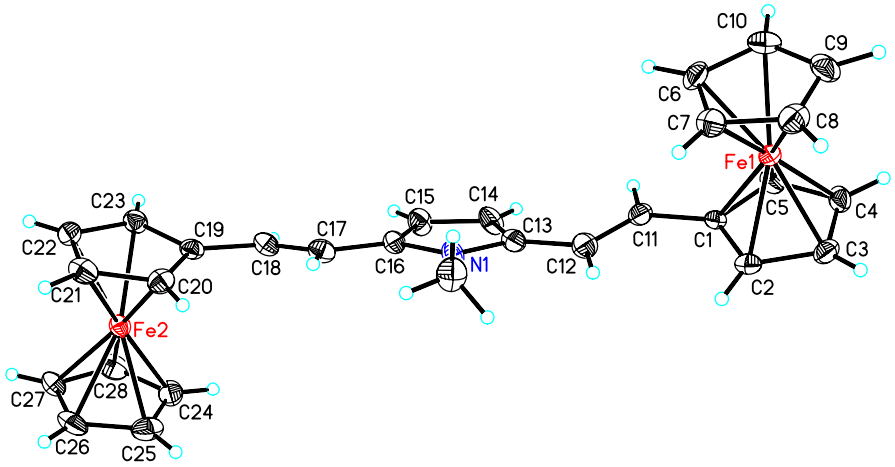

Figure 3.11. ORTEP plots of compounds **9b** (A) and **9c** (B) with 50% anisotropic displacement ellipsoids.

Different from that of *N*-dodecyl substituted **9a** (as described in Chapter 2), the two ferrocenyl units of *N*-methyl substituted analogue **9c** adopt an *anti* conformation with respect to each other (Figure 3.11B). The co-planarity along the conjugation pathway is moderately sacrificed to accommodate the steric hindrance arising from the methyl group, represented by a maximum dihedral angle between the pyrrolene unit and substituted Cp ring of 20.07^{o}. The iron-iron through-space and through-bond distances are measured as 12.64 and 16.73 Å, respectively. Despite its *anti* ferrocenyl arrangement, which generally means a longer metal-metal special separation, the iron-iron through-space distance of **9c** is even slightly shorter than that of *syn*-**9a** (12.83 Å).

Amazingly, the *N*-phenyl substituted compound **9b**, demonstrates very organized crystallographic features (Figure 3.11A) significantly different from its *N*-alkyl substituted analogues. The Cp(subs)-Pyr-Cp(subs) conjugation backbone is essentially coplanar, in close resemblance to that of the furanyl and thiophenyl centered bisferrocenylvinyl derivatives (Chapter 2). This is ascribed to the straightly perpendicular disposition between the central pyrrolene ring and its 'bulkier' but planar phenyl attachment on the nitrogen atom. Obviously this steric arrangement provides the minimum steric strain within the otherwise congested system. Due to the vertical alignment between the pyrrolene group and its phenylene attachment, there is no extra p-orbital over-lapping contributed from the aromatic phenylene group to the primary conjugation pathway, which could potentially result in more electron delocalization during the charge transfer process. Instead, the electron-deficient phenyl ring in this case functions merely as an electron-withdrawing group subject to the main conjugation backbone, which will logically lead to a less efficient electron-tunneling path between the two redox centers and is manifested in the electrochemistry (*vide infra*). Along with the *syn* (Fc-Fc) conformation, the iron-iron through-space distance turns out to be the shortest (12.12 Å) in comparison to the corresponding distances of **9a** and **9c**.

The availability of the crystal structure of the polyene linked compound **10** (Figure 3.12), in great sense, is attributed to the rigid pyrrolene ring incorporated in the midway of the conjugation pathway, since single crystal of polyene bridged species is fairly difficult to achieve due to the flexibility of the linear unstaturated chains. In fact, the two side butadienyl chains on the central pyrrole nucleus naturally bend along the conjugation

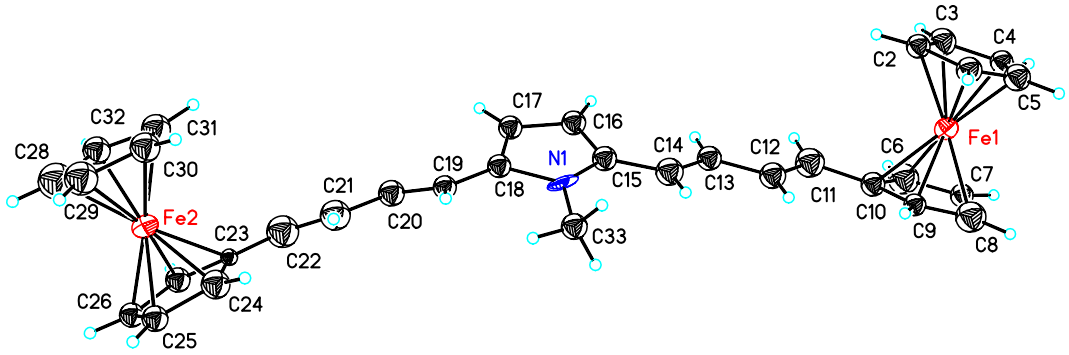

Figure 3.12. ORTEP plot of compound **10** with 50% anisotropic displacement ellipsoids.

path, with the terminal ferrocene units taking an *anti* displacement to each other. The central pyrrolene ring distorts 22.93° and 40.86° away from the Cp(sub, Fe1) and Cp(sub, Fe2) rings, respectively, while the distortion angle between the two Cp(sub) rings is 39.64°. The Fe1-N, N-Fe2 and Fe1-Fe2 through-space distances are measured as 8.90, 8.86 and 17.75 Å, respectively.

The spatial traffic of *N*-methyl-2,5-bisferrocenylpyrrole **11b** is rather busy as shown in Figure 3.13A. After several compromises, the pivot pyrrole linker and its phenyl substituent adopt a semi-orthogonal disposition with respect to each other, giving a dihedral angle of 75.2° between them. Both ferroenyl moieties are tilted (33.33° and 39.43°) with respect to the central pyrrolene ring, and display a semi-*anti* conformation in reference to the pyrrolene unit. The iron-iron through-space and through-bond distances are 8.54 Å and 11.21 Å, respectively. The stereochemistry of **11a** (Figure 3.13B) resembles that of **11b** due to the similar steric congestion. The dihedral angles between the pyrrolene ring and the two substituted Cp rings are 34.63° and 49.61°, respectively. The metal-metal through-space separation is 8.46 Å while the through-bond distance is virtually the same as that of **11b**. The long alkyl chain attached on the pyrrolene nucleus extends linearly along the carbon backbone without obvious bending. In fact, crystals of **11a** grow into a needle shape in various solvents, indicating that the crystal formation is

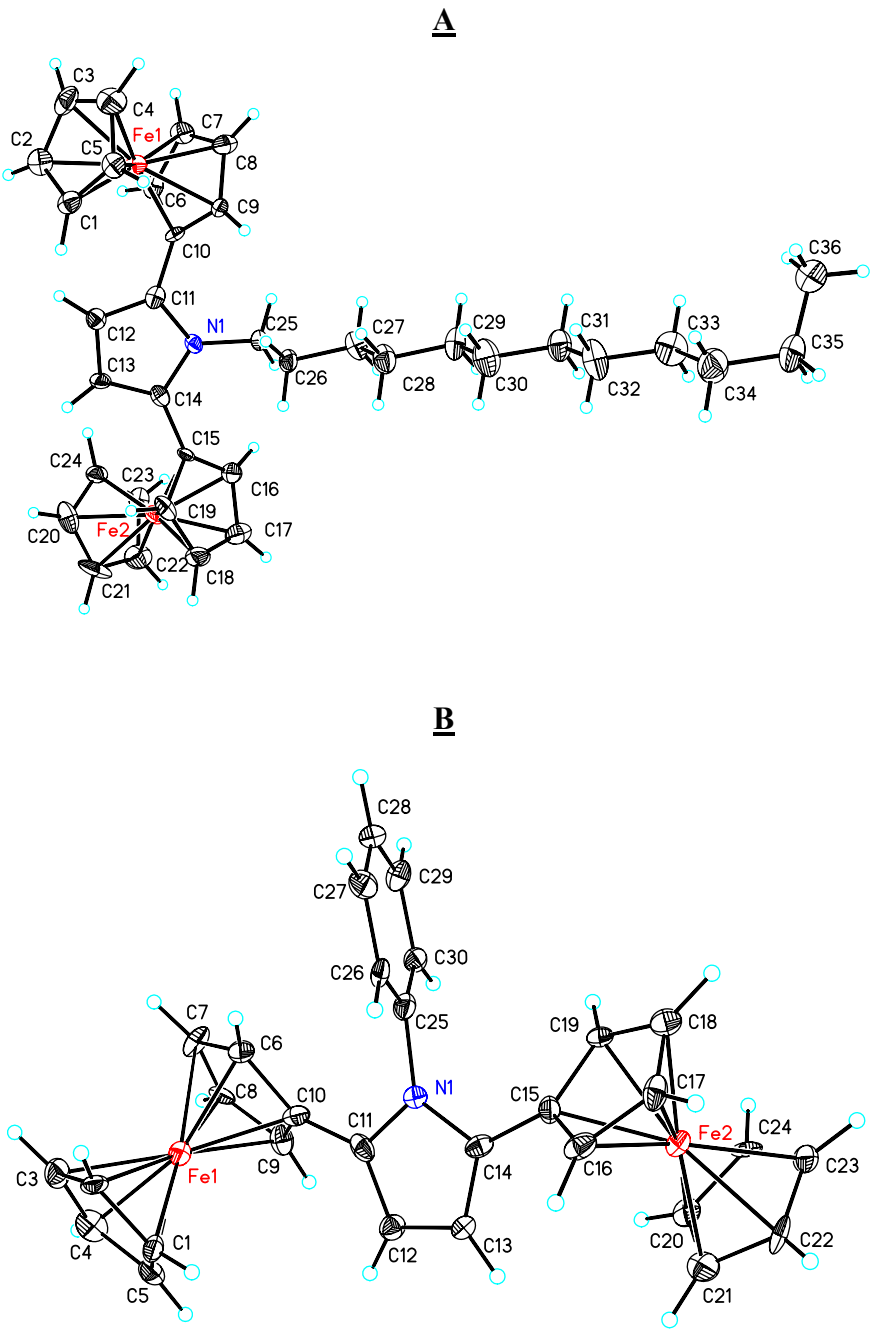

Figure 3.13. ORTEP plots of compounds **11a** (top) and **11b** (bottom) with 50% anisotropic displacement ellipsoids.

essentially governed by the alignment of the extended hydrocarbon subunits among the adjacent molecules. This can be clearly seen in the packing diagram of **11a** shown in Figure 3.14. Finally, it is noteworthy to mention that the ferrocene moieties in both **11a** and **11b** all demonstrate some degree of staggered feature, with staggering angles varying from 4^{o} to 14^{o}, which is believed to relieve the otherwise substantial steric hindrances.

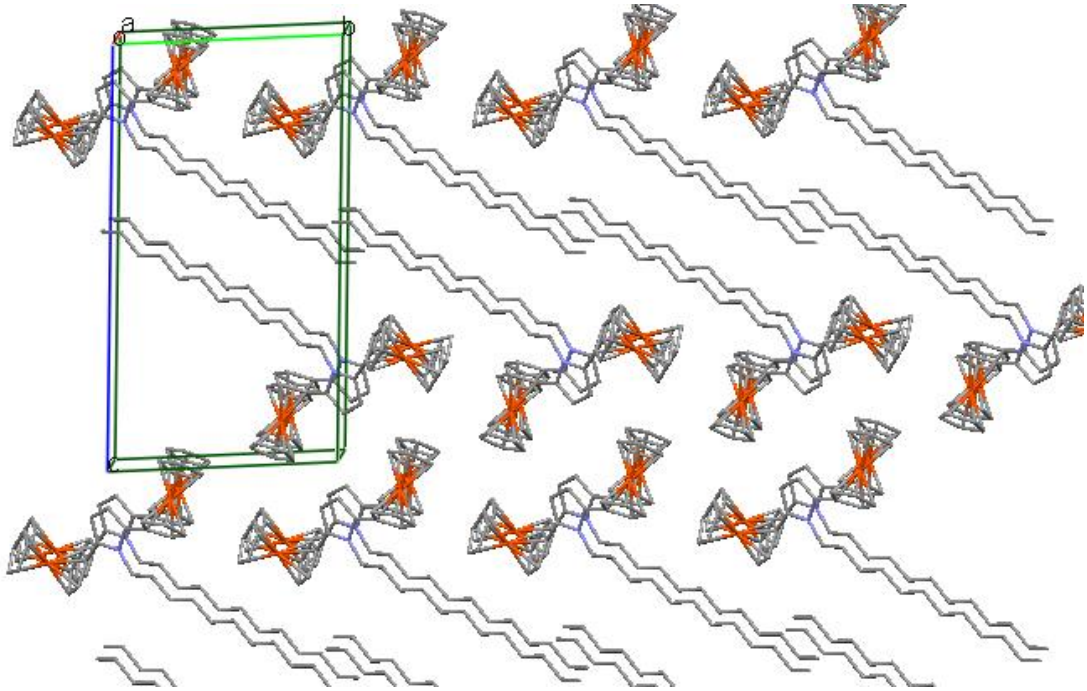

Figure 3.14. Packing diagram of compound **11a**, viewed from slightly tilted z axis.

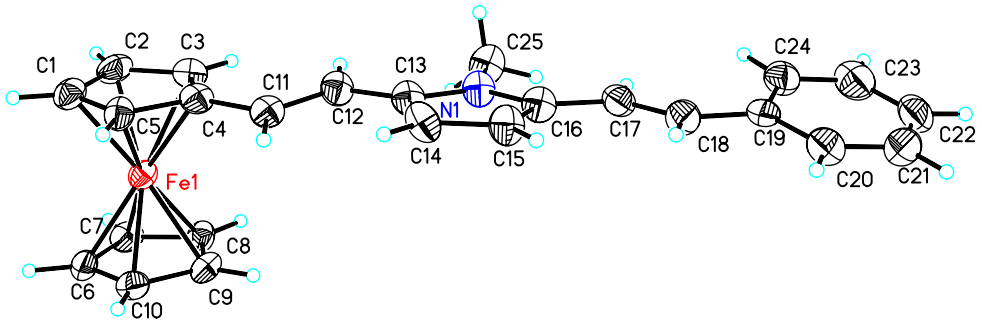

Figure 3.15. ORTEP plot of compound **13** with 50% anisotropic displacement ellipsoids.

Finally, the monoferrocenyl complex **13** exhibits a fairly coplanar conjugation pathway of its ancillary ligand, as shown in Figure 3.15. The torsion angle between the substituted Cp ring and the central pyrrolene ring is approx. 5.03°, the same value between the pyrrolene and phenyl rings, however, is much larger, 13.10°, presumably due to the titling of the terminal phenyl group from the rest of the conjugated fragment. Accordingly, the nitrogen to iron through-space distance is measured as 6.31 Å.

Electrochemistry

The cyclic voltammetric results are summarized in Table 3.1. All electrochemical data are reported versus the Fc/Fc^+ couple with Bu_4NTFPB and Bu_4NPF_6 as the supporting electrolytes in CH_2Cl_2. The following discussion is based on the data obtained from our conventional supporting electrolyte Bu_4NTFPB. However, comparison will also be made at the end of this section when alternative counterion PF_6^- is used.

The unique bis(2-ferrocenylvinyl)pyrrole compound **9a** we studied previously reveals three largely-separated oxidation waves, presumably arising from the two ferrocenyl groups and central pyrrole moiety. However, the interpretation of the electrochemical data is quite problematic. First, what is the cause of the first oxidation? Is it ferrocene based or pyrrole based? Second, what is the charge configuration of the intermediate dicationic species? In other words, if the first oxidation is a pyrrole based process, where do the two positive charges reside in the immediate following oxidation state (dication)? The charges could be Fc/pyrrole based, Fc^+--Pyr^+--Fc, or Fc/Fc based, Fc^+--Pyr--Fc^+, or

in a evenly distributed scenario, $[Fc—Pyr—Fc]^{2+}$. Finally, the large peak-separation generally implies efficient electronic communication and some degree of charge delocalization. The significantly enhanced electrochemistry of **9a** ($\Delta E_1 = E_2 - E_1 = 375$ mV and $\Delta E_2 = E_3 - E_2 = 500$ mV) suggests a high possibility of charge mobility. To what extent, is it delocalized?

The main reason we included two non-metal contained compounds **7** and **8**, in this study is to mimic the chemical environment of the *N*-alkyl-2,5-divinylpyrrolene moiety resembling that of **9c** derivatives. While the oxidation potentials of pyrrole and *N*-alkyl-pyrrole are reported in the literature as approximately 0.9 V and 0.7 V vs. Fc^+/Fc couple, respectively, the electrochemical information of *N*-alkyl-2,5-divinyl substituted pyrroles is barely known. As shown in Table 3.1, the phenyl end-capped 2,5-divinyl substituted pyrrole **7** reveals a single one-electron oxidation wave at 0.08 V (vs. Fc^+/Fc), which is significantly negative to the unsubstituted pyrrole derivatives due to its extended conjugation on the redox-active heteroaromatic ring. The *p*-methoxyphenyl end-capped pyrrole analogue **8,** however, displays two reversible one-electron peaks at -0.07 V and 0.43 V, which are assigned to the oxidations of the pyrrole moiety and the *p*-methoxyphenyl group, respectively. Clearly, the lowered pyrrole-based oxidation potential of **8**, compared to that of **7**, derives from the electron-donating effects from the *p*-methoxy substituents on the terminal phenyl groups.

It has been well recognized that the electron-richness of the ferrocenyl substitutent resembles that of *p*-methoxy phenyl group. Thus, if the first oxidation of **9c** happens at the 2,5-divinylpyrrolene moiety, the oxidation wave should appear around -80 mV, similar to that of **8**. Instead, E_1 of **9c** is considerably negative (-263 mV), which implies the redox process is rather ferrocene based than pyrrole based. The much lowered oxidation potential of the ferrocene unit is ascribed to the high electron-donating contribution from the pyrrolene moiety to its conjugated ancillary. Logically, the second oxidation should originate from the second ferrocenyl group since the electrochemical environment of the pyrrole unit is not favorable to conduct such process with a close proximity to the charged moiety ($-Fc^+$). In other words, the two positive charges in the dicationic species would rather be distant from each other to achieve an electrostatically

Table 3.1. Electrochemical data[a] (from Cyclic Voltammetry) for the compounds.

Compounds	E^o_1 (mV)	E^o_2 (mV)	E^o_3 (mV)	E^o_4 (mV)	ΔE_1 [d] (mV)
3	-70	730			800
7	80				-
8	-70	430			500
9a	-263	93	793		356
9b	-240	75	860		315
9c	-263	93	793		356
10	-240	0	408		240
11a	-200	280			480
11b	-240	245			485
12	-60	240			300
13	-140	410			550
14	-467	-304	155	540	163
15	-230	294	572		524
9c[b]	-210	0	304[c]		210
10[b]	-197	-84	140[c]		113
11a[b]	-140	104			244
12[b]	-24	130			154
13[b]	-117	192			309

[a] Obtained in CH_2Cl_2 solution containing 0.1 M Bu_4NTFPB (unless otherwise stated). Scan rate 50 mV/s. [b] supporting electrolyte switched to Bu_4NPF_6 with other conditions unchanged. [c] irreversible oxidation process. [d] $\Delta E_1 = E^o_2 - E^o_1$.

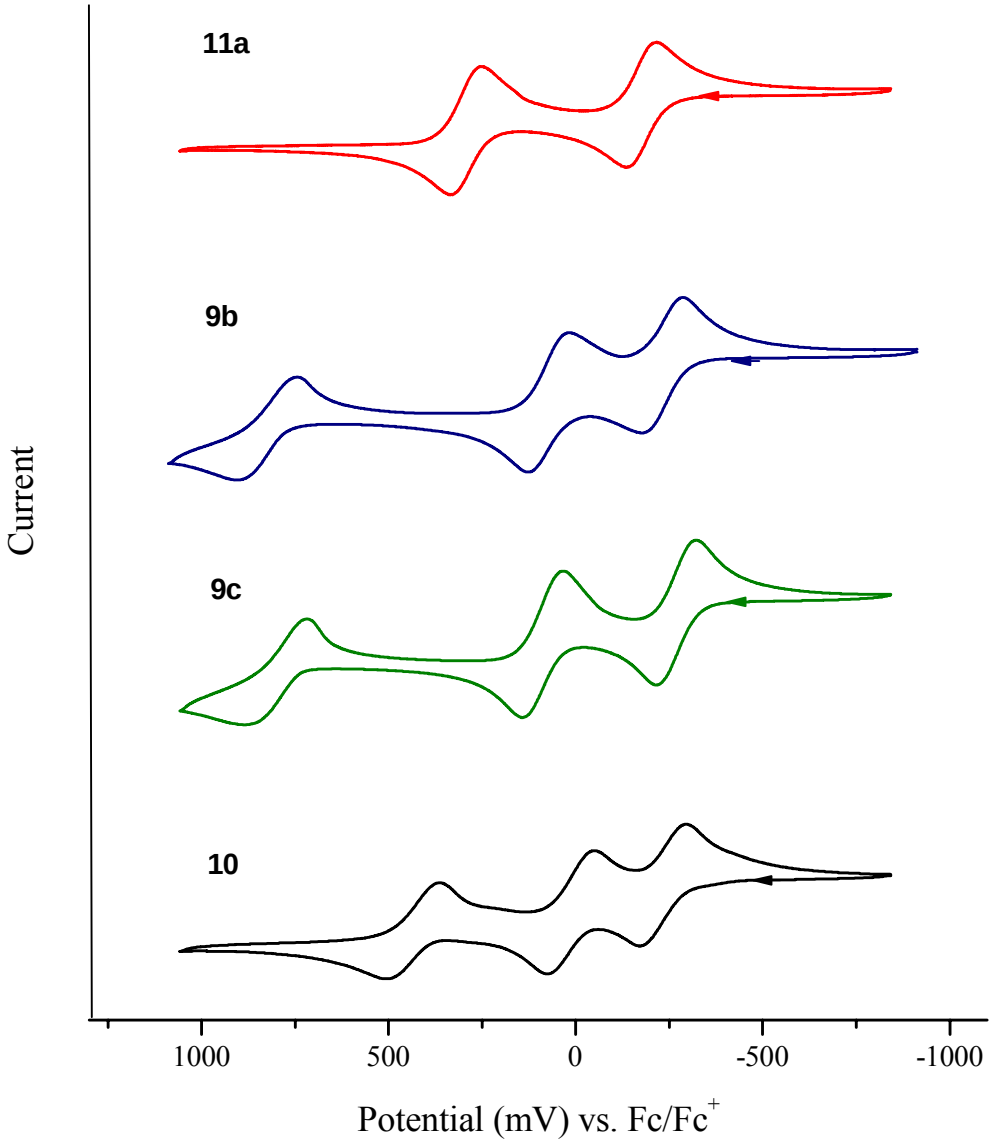

Figure 3.16. Cyclic voltammograms of diferrocenyl compounds **11a**, **9b**, **9c** and **10** in CH_2Cl_2 containing 0.1 M Bu_4NTFPB. Scan rate 50 mV/s. The oxidation potentials are reported versus the Fc/Fc^+ couple as the internal reference. The spectra above are diagramed in an increasing order of distances between the redox centers, for which the peak separation (ΔE_1) decreases as the steric separation between the metal centers is enlarged.

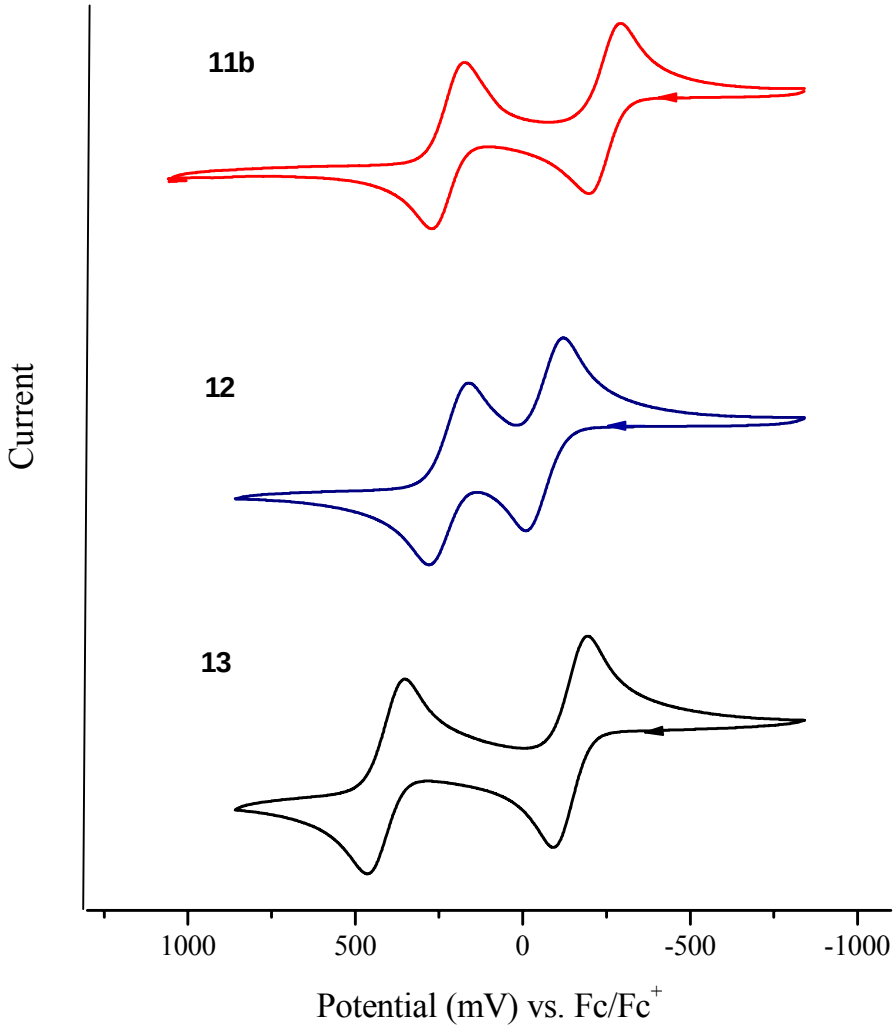

Figure 3.17. Cyclic voltammograms of compounds **11b**, **12** and **13** in CH_2Cl_2 containing 0.1 M Bu_4NTFPB. Scan rate 50 mV/s. The oxidation potentials are reported versus the Fc/Fc^+ couple as the internal reference.

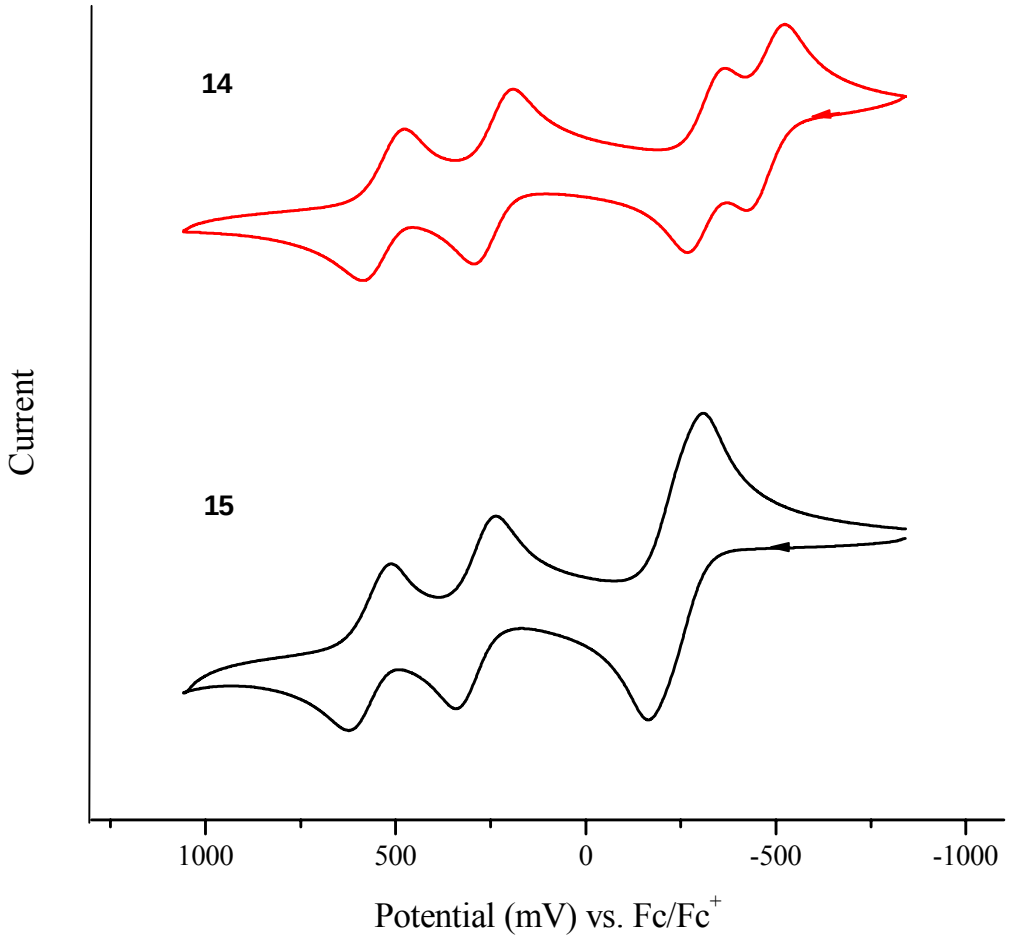

Figure 3.18. Cyclic voltammograms of diferrocenyl compounds **14** and **15** in CH_2Cl_2 containing 0.1 M Bu_4NTFPB. Scan rate 50 mV/s. The oxidation potentials are reported versus the Fc/Fc^+ couple as the internal reference.

more stable state. Consequentially, the last oxidation wave, E_3, must result from the pyrrolene moiety.

Whereas the CV of **9a** and **9c** are identical, the electrochemistry of **9b** exhibits three oxidation waves but slightly higher E_1 (-240 mV vs. Fc/Fc^+) and smaller ΔE_1 (315 mV) (Figure 3.16). This could be ascribed to the electron-withdrawing nature of the phenyl group attached on the pyrrolene N atom, since the phenyl ring functions as a pure electron accepting factor with a perpendicular orientation to its anchor, the pyrrole ring. The decreased electron density along the conjugation backbone increases the first oxidation potential and decreases the level of the intramolecular electron coupling.

Replacing vinyl with butadienyl groups as the two linking units between the ferrocenyl terminals and the central *N*-methyl-2,5-pyrrolene moiety basically elongates the distances between the redox centers. As a consequence, both ΔE_1 (240 mV) and ΔE_2 (408 mV) of **10** shrink to smaller values compared to those of **9c**, with E_1 (-250 mV) roughly unchanged (Figure 3.16).

Conversely, removing the vinyl linkers in **9a** and **9b** gives rise to shortly bridged compounds **11a** (Figure 3.16)and **11b** (Figure 3.17), for which the two ferrocenyl groups are attached at the 2- and 5- positions of the pyrrolene rings. The decreased metal-metal distances account for a greater electronic interaction as evidenced by the increased ΔEs, 480 mV and 485 mV for **11a** and **11b**, respectively. The first oxidations of both compounds appear in the similar region as that of **9c** (Table 3.1) and the variations must be a result of a comprehensive combination of the steric and substituent effects. Both compounds do not show the third peak within the media allowable measurement window, which is assumably pyrrole based.

For the sake of comparison, we also prepared and studied another analogous compound, 2,5-diferrocenylthiophene **12** (Figure 3.17). As indicated in Table 3.1, **12** shows much higher E_1 (-60 mV vs Fc/Fc^+) and smaller ΔE (300 mV) than its pyrrolene spaced analogs. Provided that the stereochemistry of **12** is substantially more favorable than that of the *N*-substituted pyrrole derivatives (**11a-b**) (*vide supra*) since the Cp-Th-Cp framework in **12** is virtually coplanar,[31, 32] current comparison examination exemplifies how an electron-richer aromatic ring (pyrrole) can facilitate the redox process (E_1), and most importantly, enhance the electron communications.

Up to this point, we have investigated a series of pyrrole-mediated diferrocenyl compounds, **11a-b**, **9a-c**, and **10**, with an increasing number of unsaturated sp^2-carbon spacers linking the two ferrocenyl termini to the central pyrrolene nucleus. The electronic coupling strength between the terminal metal centers drops with the increasing separation, which is consistent with the well-established theory.[10] To gain further insight, we also used conventional n-Bu_4NPF_6 as the supporting electrolyte in studying the electrochemical behaviors of **11a**, **9c** and **10**. The obtained CV data are also included in Table 3.1, which allows us to compare with similar systems recorded in the same measurement conditions.

Spangler et. al. have reported diferrocenylpolyenes Fc-n-Fc[10] (where n denotes the number of the bridging unstaturated carbons), whereupon peak separation was not observed when the metal-metal distance is beyond 11 Å (n > 6). Another relevant neutral a,w-diferrocenyl cumulene system reported by Skibar et. al.[12] did not demonstrate notable electronic communication between the electroactive ferrocenes when the cumulenic [*sp*-C]$_n$ linker is longer than six carbons (metal-metal distance of 6.5 Å). In our case, nevertheless, the ΔE_1 of **10** is still of significance (113 mV with PF_6^-) with virtually 12 sp^2-carbons as linking spacer and iron-iron through-space separation of 17.75 Å (*vide supra*). It is quite persuasive that the pyrrole moiety centered in the electron tunneling channel serves as an 'amplifier' in supporting the charge transfer process.

As another modification of **9c**, the monoferrocenyl complex **13** (Figure 3.17) demonstrates two reversible oxidation waves at -140 mV and 410 mV (vs. Fc^+/Fc) corresponding to a ferrocene- and a pyrrole-centered oxidation processes, respectively. Obviously the moderately negatively shifted E_1 is due to the replacement of one of the ferrocenyl groups in **9c** with a phenyl group, which lowers the electron-density of the ancillary ligand and causes the oxidation of the ferrocene unit to shift to higher potential. The rather large ΔE (E_2-E_1) (550 mV) indicates that the ferrocenyl and pyrrolenyl groups have a high degree of interaction with a very close proximity, one double bond away to each other. However, it is precautious to point out that this large peak separation may also be due to the chemical and environmental difference between the two redox-centers, even this difference is conceptually small.

Tri(pyrrolenevinyl) bridged diferrocenyl compound **14** exhibits four oxidation waves with very intriguing redox processes as shown in Figure 3.18. To understand the four processes requires considerations on the possible dynamics. The further negatively shifted first oxidation potential (-467 mV vs. Fc^+/Fc) suggests that this process involves the central pyrrole, since the central pyrrolene unit is the electron richest moiety by connecting with two pyrrolene group at each side. This speculation was later confirmed by the non-ferrocenyl but phenyl end-capped analog, Ph-Pyr3-Ph (see Chapter 6), for which the first oxidation of this compound appears at roughly the same position in **14**. However, the peak separation between the first and second oxidation waves (ΔE_1) is rather small (143 mV). Taking the chemical and electrostatic environment into account, the second oxidation is presumably ferrocene-based. The unexpected small ΔE_1 indicates that the location of the second oxidation is rather further to the first positive charge. The only possible explanation to this observation is the first charge on the central pyrrolene unit move to the further end during the second oxidation process so that the resulting dicationic charges are well separated to reach the most stable electronic state. Therefore, the oligo-pyrrolenevinylene incorporated system processes high charge mobility in the organic fragment. Based on this knowledge, the third and forth oxidation states can be inductively understood in the following equations,

Fc-V-Pyr-V-Pyr-V-Pyr-V-Fc → Fc-V-Pyr-V-Pyr^+-V-Pyr-V-Fc → **[** Fc-V-Pyr^+-V-Pyr-V-Pyr-V-Fc^+ ←→ Fc^+-V-Pyr-V-Pyr-V-Pyr-V-Fc^+ ←→….**]** → Fc^+-V-Pyr-V-Pyr^+-V-Pyr-V-Fc^+ → **[** Fc^+-V-Pyr^+-V-Pyr-V-Pyr^+-V-Fc^+ ←→ Fc^+-V-Pyr^+-V-Pyr^+-V-Pyr-V-Fc^+ ←→ Fc^+-V-Pyr-V-Pyr^+-V-Pyr^+-V-Fc^+ ←→…..**]**

where V and Pyr denote the vinylene and N-methylpyrrolene groups, respectively, for sake of simplicity. Apparently, for such a highly delocalized system, the exact charge locations are very difficult to be specified, especially for the dicationic and tetracationic species, in which multiple electronic configurational forms may exist to stabilize the whole system.

Replacing the central pyrrolene unit of **14** with 2,5-dialkoxy substituted para-phenylene, however, dramatically changes the electrochemical behavior as represented

by compound **15** (Figure 3.18). Compound **15** demonstrates three oxidation waves with a ratio of 2:1:1. The first oxidation appears at -230 mV (vs. Fc/Fc^+), roughly the position as that of **9c**, which presumably arises from the two ferrocenyl terminals. The co-oxidized feature implies that the two metal centers do not have any communication between each other due to the lengthened conjugation spacers. The second and third oxidations apparently rise from the two pyrrolene units sequentially.

As mentioned earlier, to understand the counterion effect, we have also examined electrochemistry of some key compounds using conventional Bu_4NPF_6 as the supporting electrolyte. The obtained data were also summarized in Table 3.1. In contrast to the data obtained with $TFPB^-$ as the couterion, the most striking difference in using PF_6^- as counter anion was that the peak separations dropped tremendously due to stronger ion-pairing effect in $[Fc\text{-}B\text{-}Fc]^+PF_6^-$ as we discussed in the earlier chapter. More interestingly, systematic comparisons suggested an emipirical rule that $\Delta E_{PF6-} \approx 0.5\ \Delta E_{TFPB-}$. In fact, this half-$\Delta E$ rule fell in a very narrow variation of 0.5-0.55, which can be easily seen in the plotted diagram shown in Figure 3.19. Aside from that, when Bu_4NPF_6 was applied as the supporting electrolyte, in many cases especially when a third oxidation was involved, the last oxidation wave (presumably pyrrole-based) was not longer reversible as exemplified in Figure 3.20. This has been observed commonly both in the literature[33, 34] and in our laboratory and has been discussed in Chapter 2.

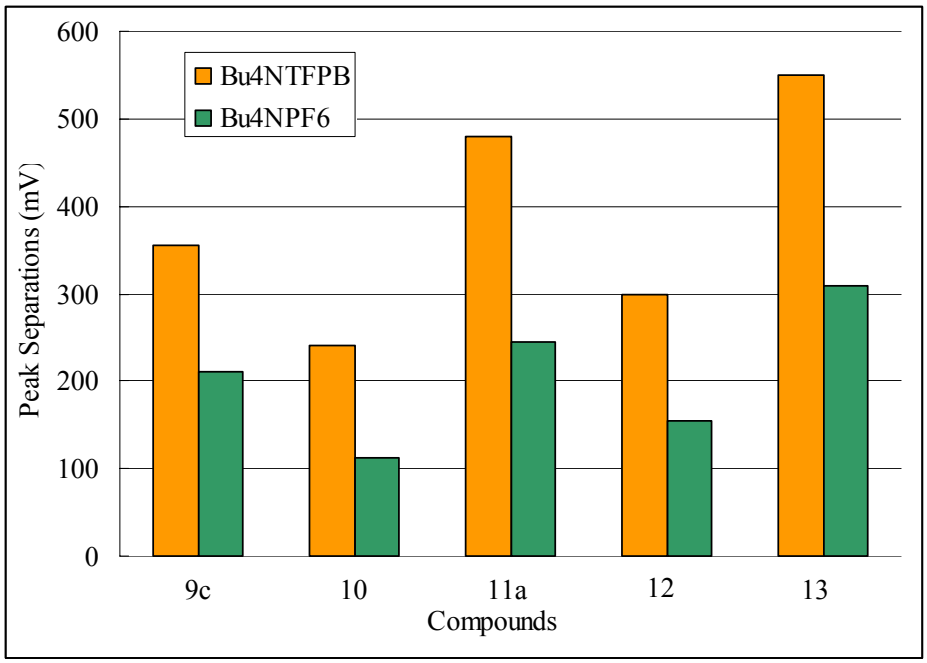

Figure 3.19. Plotted peak separation (ΔE_1s) comparisons of some key compounds using $Bu_4NPTFPB$ (orange bars) and Bu_4NPF_6 (green bars) as the supporting electrolytes.

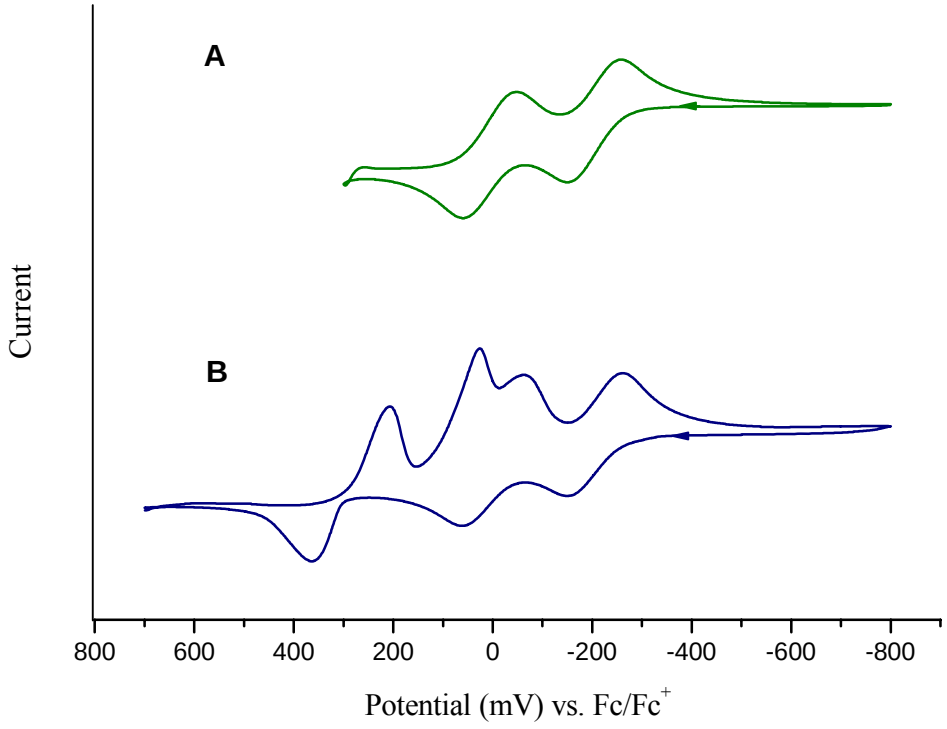

Figure 3.20. Cyclic voltammograms of diferrocenyl compound **9c** in CH_2Cl_2 containing 0.1 M Bu_4NPF_6. Scan rate 50 mV/s. The difference between A and B is the scan range.

Electronic Absorption of Pyrrole-Based Radical Cation in TFA

It has been well established that 2,5-substituted pyrrolyl derivatives are subjected to radical oxidation processes upon exposure to an acidic environment. It is crucial to have a basic understanding of the electronic absorption features of such pyrrole centered radical cationic species, especially for the systems we studying here, where both pyrrolyl and ferrocenyl redox-active moieties are integrated in a single molecule. Differentiating the electronic absorptions of the different redox-center based radical cations ($Fc^{\cdot+}$ or $Pyr^{\cdot+}$) is indispensable when the mixed valence species are concerned.

Five representative compounds were selected for the spectroscopic studies of their pyrrole-based radical cations. The radical cations were generated by progressive addition of dilute TFA (in CH_2Cl_2) into the substrate solution in the same solvent. The evolutions of the spectra of these compounds are shown in Figure 3.21-3.22. In general, upon successive oxidation by TFA, one or multiple low energy absorptions appeared and increased at the expense of the high energy π-π^* transition of the neutral compound. Detailed comparisons suggested that the positions and strength of these pyrrole-based radical cationic low energy absorptions (500-825 nm) were highly dependent on the degree of conjugation and the chemical environment.

For model compound **9c**, the corresponding radical cation exhibits three strong signature absorption maxima at 742 nm, 622 nm and 434 nm. The isosbestic point (λ_{max} = 409 nm) represents the interconversion of only two species, **9c**-**9c**$^{+\bullet}$. The radical cation of the diphenyl end-capped compound **7**, however, only showed very weak absorptions in the low energy area (667 nm, 612 nm and 529 nm as illustrated in the inset of Figure 3.21A), which suggested that the ferrocenyl substituent in **9c** could enhance the oscillator strength of the electronic transition for pyrrole-based radical cations. The bathochromic shift from the short wavelength absorption (519 nm) of **11a**$^{+\bullet}$ to the long wavelength absorption (823 nm) of **9c**$^{+\bullet}$, along with the absorption peaks of **9c**$^{+\bullet}$ manifests that higher degree of conjugation accounts for the significant red shift in the low energy absorptions (mostly in the visible region) of the pyrrole-based radical cations.

With no supporting theoretical calculations on hand at this moment, we can not offer sophisticated assignments for each absorption in these compounds. Conceptually, nevertheless, these low energy absorptions arise from the electronic transition from high

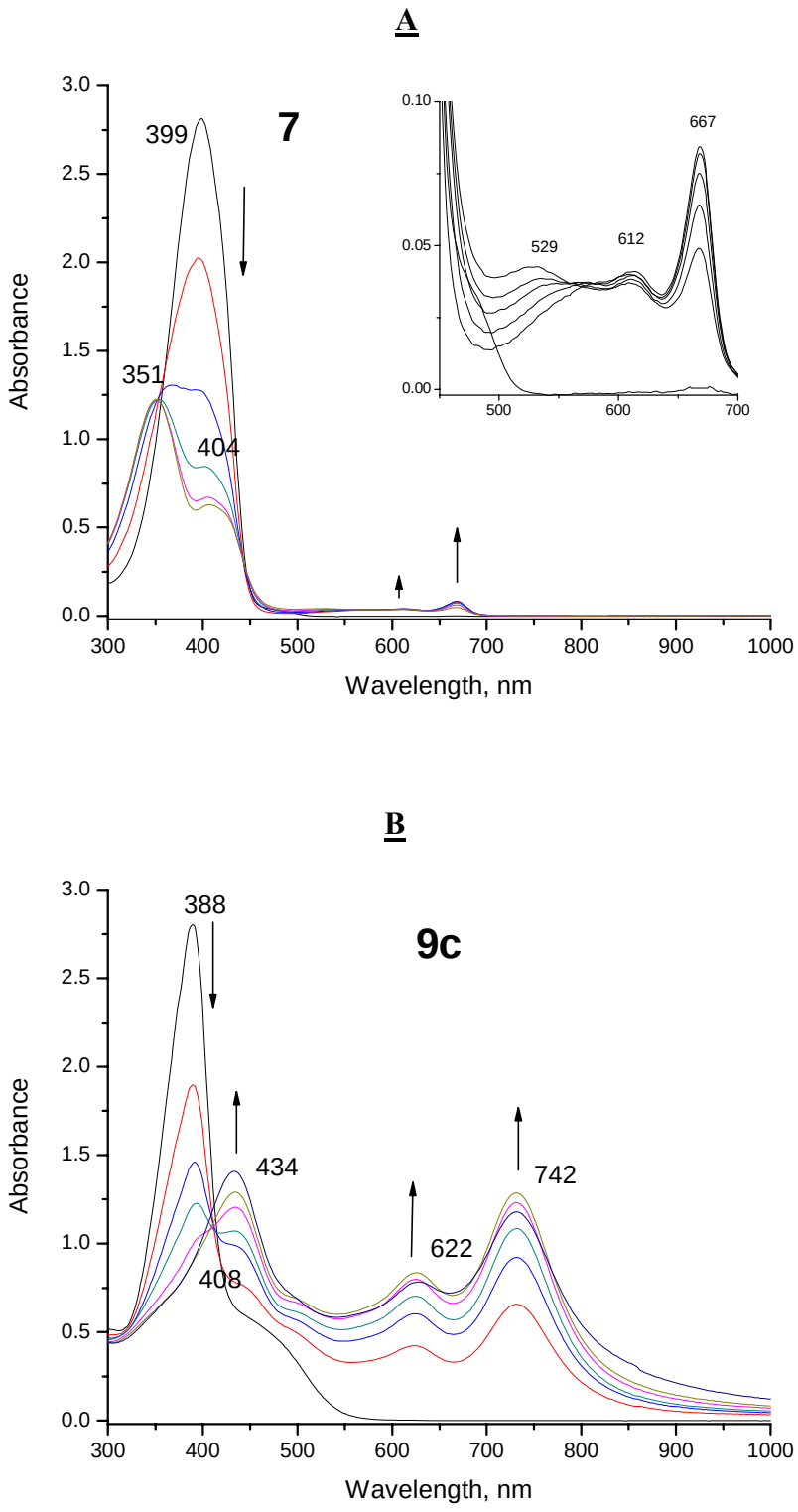

Figure 3.21. Evolution of the UV-Vis-NIR spectra of compounds **7** (A) and **9c** (B) in CH_2Cl_2 with progressive addition of trifluoroacetic acid (TFA). The amplified spectra of $\mathbf{7}^{+\bullet}$ in the region of 450-700 nm is shown in the inset diagram.

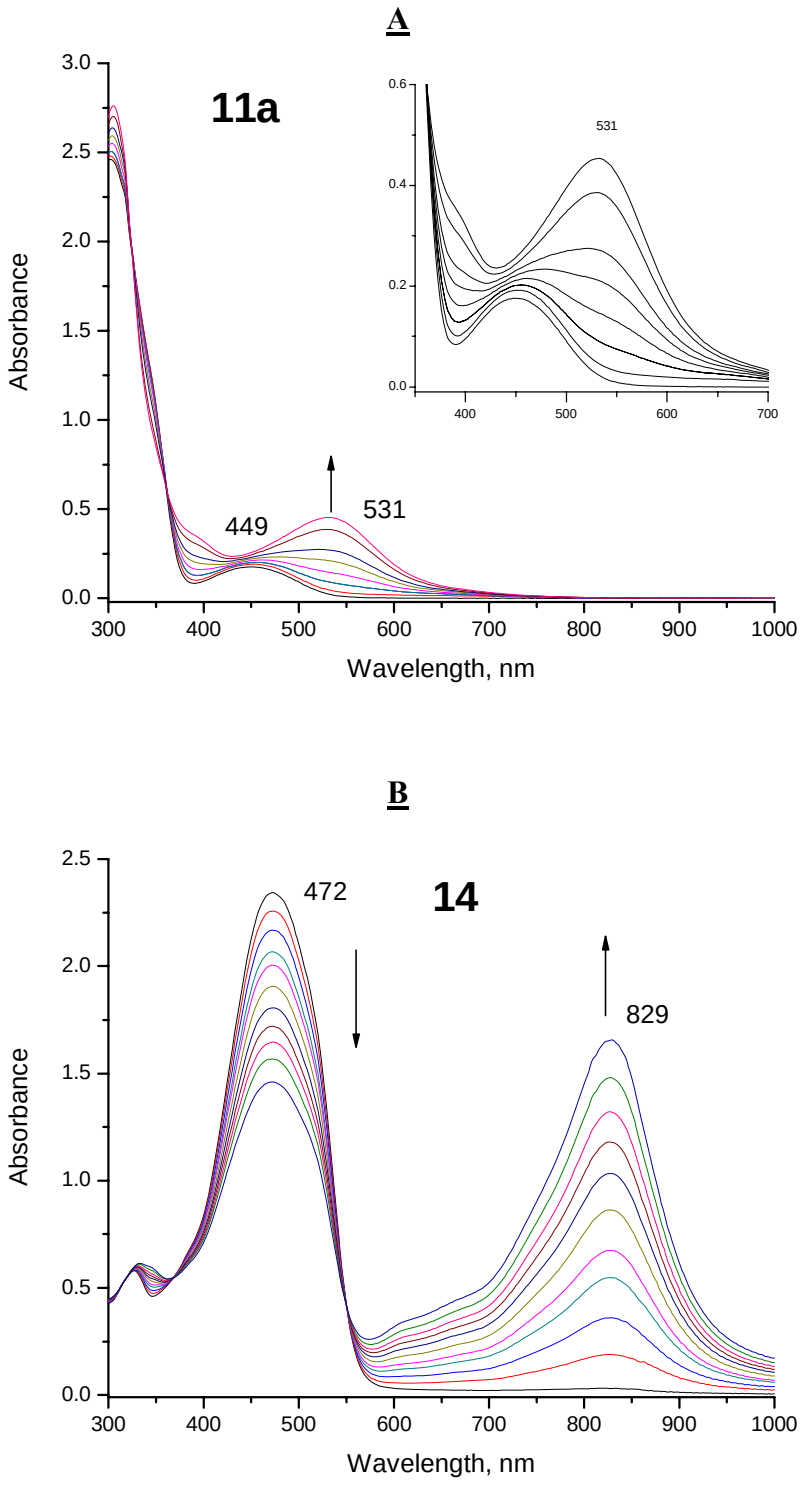

Figure 3.22. Evolution of the UV-Vis spectra of compounds **11a** (A) and **14** (B) in CH_2Cl_2 with progressive addition of trifluoroacetic acid (TFA). The amplified spectra of $\mathbf{11a}^{+\bullet}$ in the region of 450-700 nm is shown in the inset diagram.

energy orbitals to the pyrrole-based SOMOs.[35] In addition, in no case the signature absorption (ca. 620 nm) of the cationic ferrocenium species[36] observed. In other words, the radical cation initiated at the pyrrolyl moiety does not relocalize to the ferrocenyl unit in the acidic solution. Furthermore, for all compounds studied above, no further low energy bands are observed in the near-IR region beyond 1000 nm.

Mixed-Valence Absorption

General Considerations and Spectral Analysis

The neutral compounds were prepared as a 1-4 x 10^{-4} M solution in CH_2Cl_2 and oxidized with concentrated $Fc^+PF_6^-$ in the same solvent. The generated mixed-valence (MV) species were immediately subjected to UV-Vis-NIR spectroscopic measurements in an argon-protected cuvette. Generally, a series of such spectra were taken with oxidant varying from 0.2 to 1.0 equivalent to reveal the detailed oxidation process for each compound. That $Fc^+PF_6^-$ was selected as the oxidant was mainly due to its easy availability and moderate oxidizing strength, which avoided over-oxidizing the substrates with small ΔE into dicationic species. Moreover, the side-product, ferrocene, did not interfere the spectral region of interest. However, it would be more advantageous if the counterion of the ferrocenium were converted to $[BAr'_4]^-$ (Ar' = 3,5-$(CF_3)_2C_6H_3$). In this manner, the oxidation processes would exactly correlate with the electrochemical potentials and provide more favorable K_c (larger ΔE). For quantitative analysis, the concentration of oxidant was used as the concentration of the MV species for compounds with $\Delta E > 200$ mV (most of cases in this study) since the comproportionation constant ($K_c > 2400$) was of great significance in the equilibrium given in Equation 3.2.

$$[\text{neutral}] + [\text{dication}]^{2+} = 2[\text{monocation}]^{+} \qquad [3.2]$$

When the ΔE was small (e.g. for compound **10** ΔE = 113 mV with PF_6^- as counterion), disproportionation reaction must be taken into account. The common practice to ameliorate this problem is to use the data obtained from ~0.2 equivalent of oxidant applied, where the comproportionation equilibrium (Eq. 3.2) is favorable to the right, i.e. to the monocationic species. The concentration of the monocationic species at

equilibrium is determinded from the physically reasonable solution to the quadratic equation (Eq. 3.3), in which $[M^+]$ is the concentration of monocation at equilibrium, C_M is the concentration of M in reaction mixture (i.e. neutral, monocation and dication), C_{OX} is the concentration of $Fc^+PF_6^-$ in reaction mixture and K_c is the comproportionation constant.

$$(0.25 - (1/K_c))[M^+]^2 - (0.5C_M)[M^+] + (0.25C_{OX})(2C_M - C_{OX}) = 0 \qquad [3.3]$$

In general, the one-electron oxidized species in this study all demonstrated bands in visible region including a signature band around 620 nm assigned to the unsubstituted Cp-to-Fe^{III} transition and a ligand-based π-π^* band in the region of 500-850 nm depending on the degree of conjugation. At the meantime, a low energy band in the NIR area was also revealed for each monocationic species, however, the nature of this absorption is quite case-dependent and must be considered individually.

For vinylene-pyrrolene-vinylene bridged mono-radical cation $\mathbf{9c}^{+\bullet}$, the electronic absorptions including both high energy visible bands and NIR low energy band increased nearly linearly with continuous oxidative treatment before one equivalent of $Fc^+PF_6^-$ was reached (Figure 3. 23A). This indicates that this [Fc-B-Fc^+] MV species is quite stable and the high comproportionation constant derived from large peak separation is favorable to the monocationic state. Such proportional evolution is not observed in its thiophene- and furan-mediated analogues due to their weak electronic coupling and promoted disproportionation reaction (reversed Equation 3.2) leading to the dicationic [Fc^+-B-Fc^+] and neutral [Fc-B-Fc] species.

In Figure 3.23A, the absorption maxima at 622 nm and 726 nm are assigned to the LMCT transition from unsubstituted Cp ring to the Fe^{III} *dπ*-orbital and the bridging ligand based *π*-*π** transition, respectively. The broad and symmetrical band in the NIR region, centered at ca. 2060 nm, is initially attributed to the intervalence charge transfer between the metal d-d orbitals. Qualitatively, the highly increased intensity of this band, which is at least three times stronger than the similar diferrocenyl family compounds (Chaper 2), and the red-shifted absorption maxima imply that $\mathbf{9c}^{+\bullet}$ possesses more charge delocalized feature in the excited state. The high population of charge transfer is

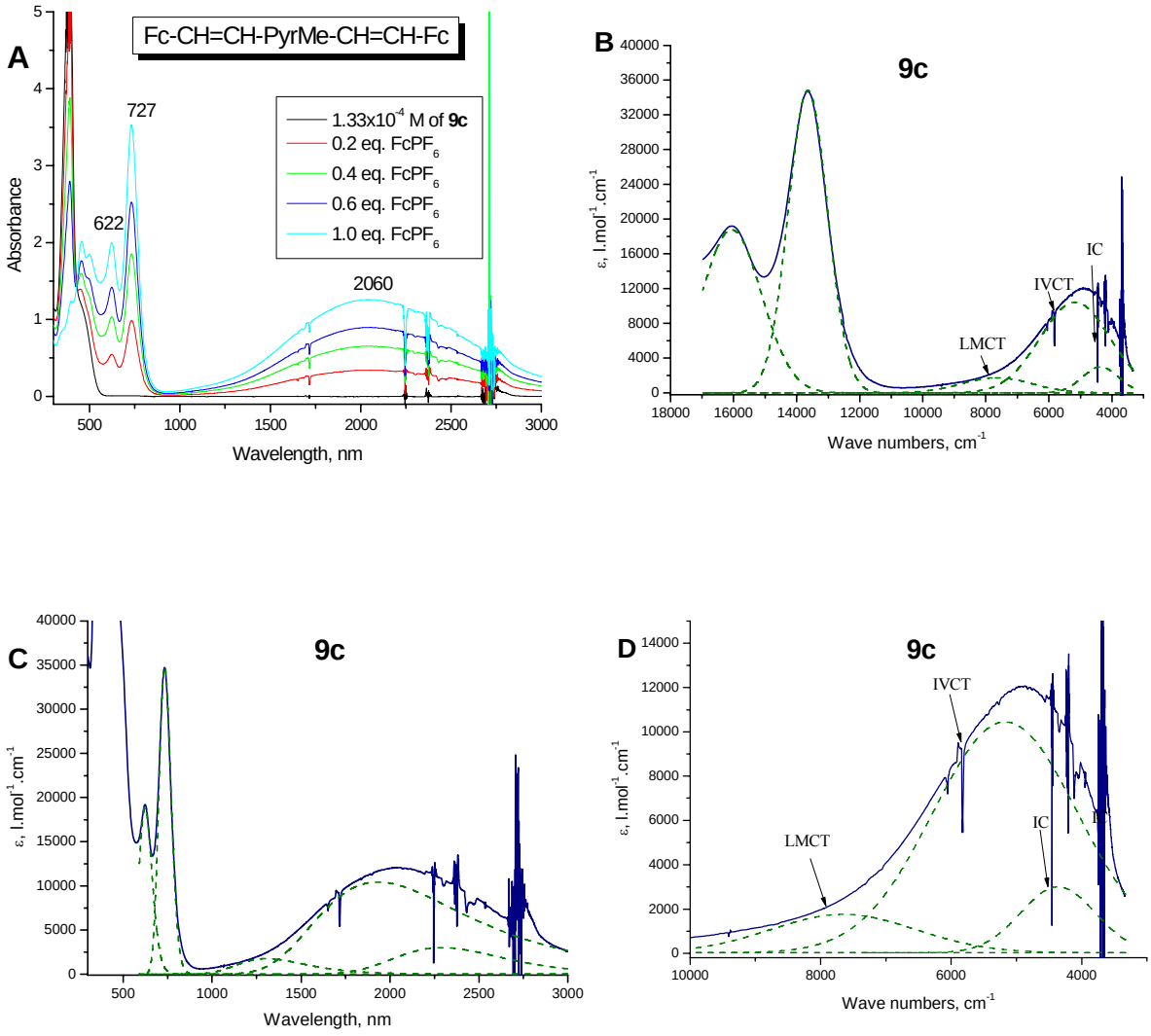

Figure 3.23. UV-Vis-NIR spectra of mixed-valence species $\mathbf{9c}^{+\bullet}$ in CH_2Cl_2: *A*: evolution spectra of **9c** obtained upon progressive oxidation with 0.2 to1.0 equivalent of oxidant. *B*: deconvoluted spectrum (X-axis in energy unit, cm^{-1}) assuming Gaussian-shaped bands. The dashed lines are the deconvoluted bands. *C*: spectrum with X-axis in wavelength unit after deconvolution. *D*: highlighted spectrum in the NIR and into IR region. .

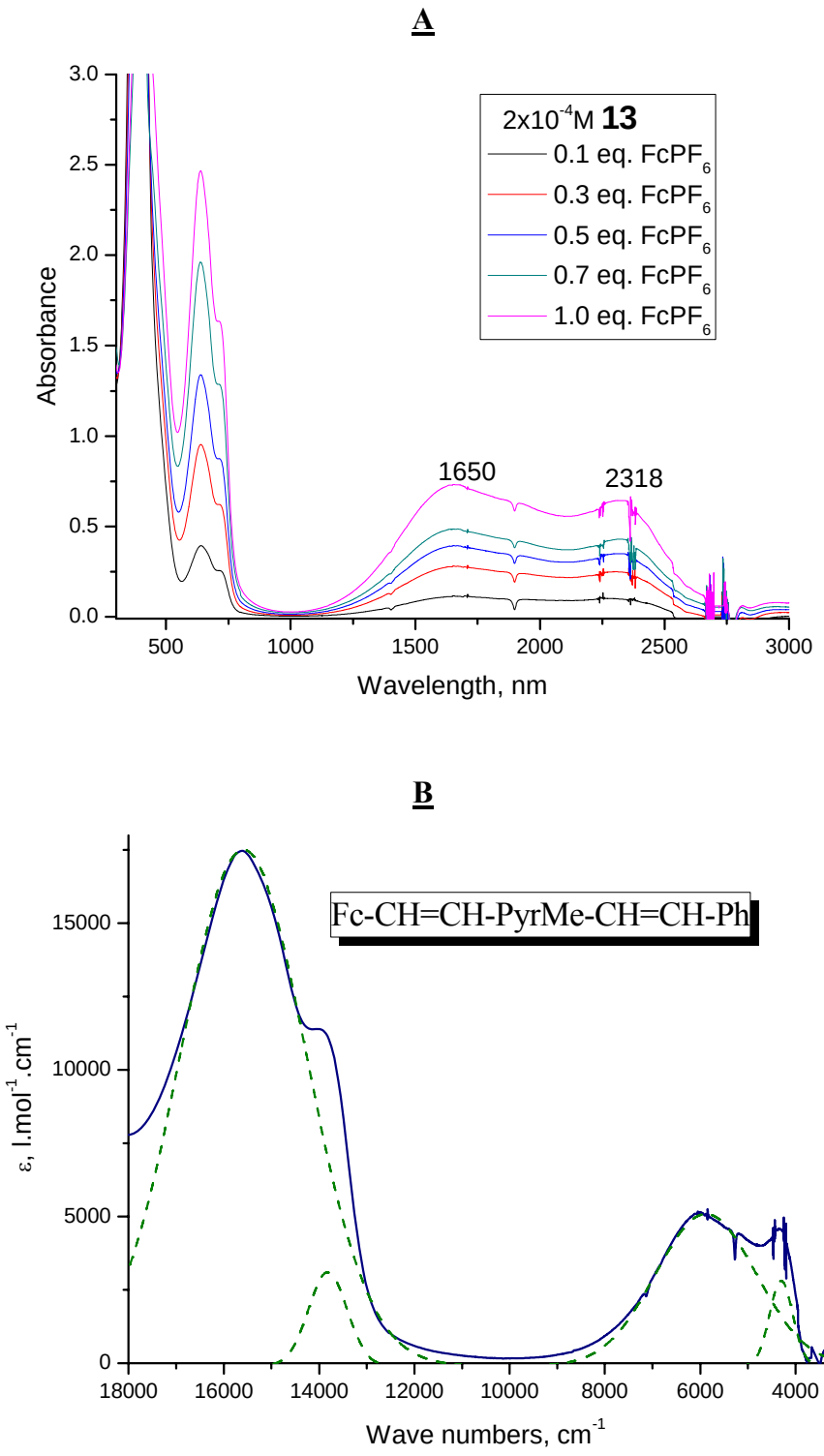

Figure 3.24. UV-Vis-NIR spectra of one-electron oxidized species of **13** in CH_2Cl_2. Top: evolution spectra of **13** with progressive addition of oxidant in 0.2-1.0 equivalent. Bottom: deconvoluted spectra (X-axis in energy unit, cm^{-1}) of $\mathbf{13}^{+\bullet}$ assuming Gaussian-shaped bands. Fitting bands presented in dashed lines.

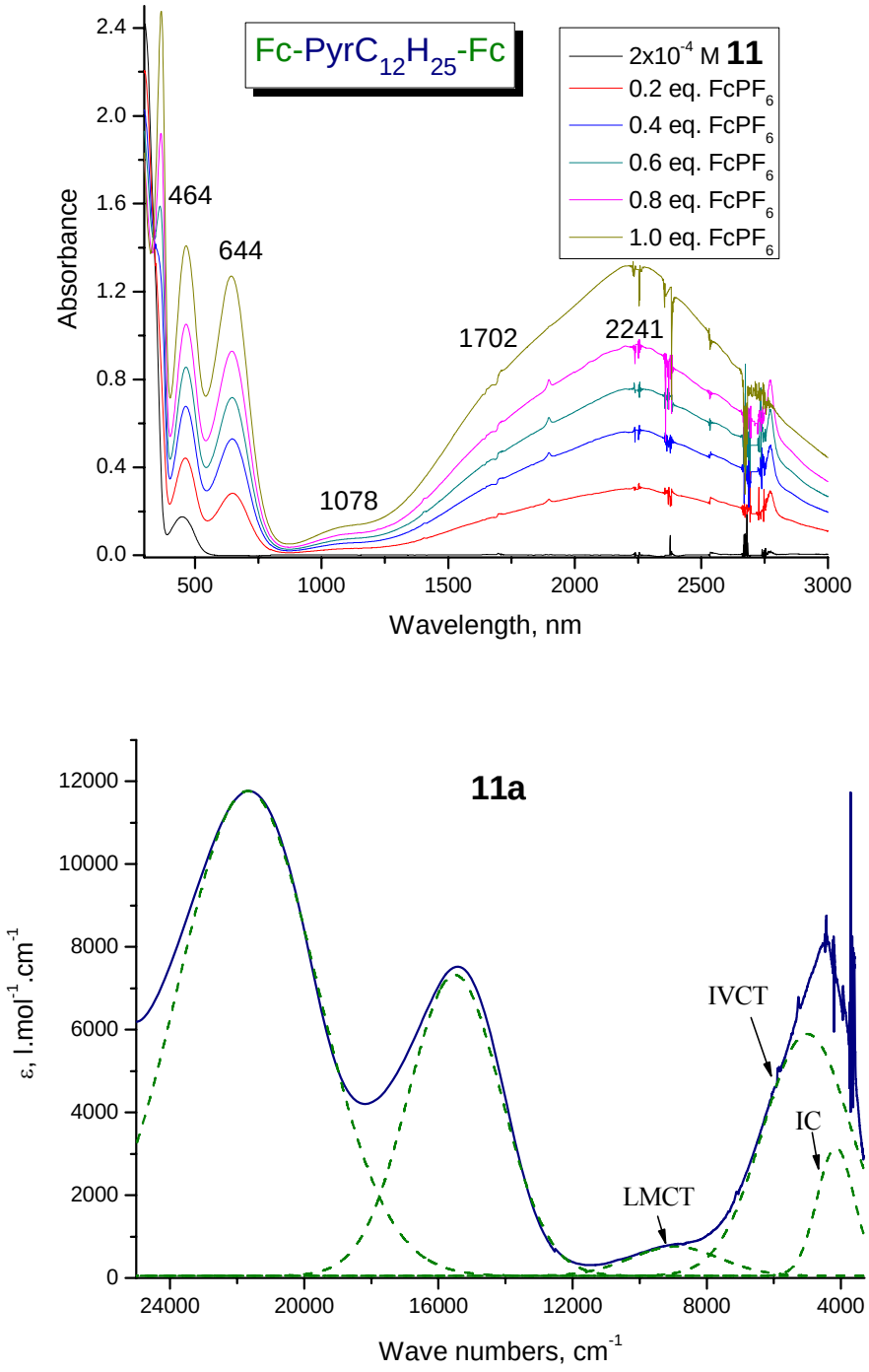

Figure 3.25. UV-Vis-NIR spectra of mixed-valence species of 2,5-diferrocenylpyrrole **11a** $^{+\bullet}$ in CH_2Cl_2. Top: evolution spectra of **11a** with progressive addition of oxidant in 0.2-1.0 equivalent. Bottom: deconvoluted spectra (X-axis in energy unit, cm^{-1}) assuming Gaussian-shaped bands. Deconvoluted bands are presented in dashed lines.

ameliorated with low energy barrier required for such transitions to occur. However, it is also noteworthy that this broad envelope indeed consists of multiple absorptions after deconvolution in energy unit (wave numbers), giving rise to three distinct Gaussian bands with absorption maxima at 7450 cm^{-1}, 5153 cm^{-1} and 4332 cm^{-1}, respectively (Figure 3.23B to D).

The presence of several near-IR bands in the spectrum of a mixed-valence complex is not uncommon, and their occurrence is generally explained by one of the four different possible causes. One can be the presence of a strong spin-orbit coupling effect, which becomes important only for complexes containing third-row transition metals.[37-39] A second source can be the presence of a double-exchange mechanism[40, 41] which becomes more probable as the bridge length and the energy level of the π-orbitals increase. The third source is associated with a possible low-lying excited state in some ferrocenium complexes, a $^2A_{1g}$ ferrocenium 'hole' state where the 'hole' resides in the a_{1g} orbital. The existence of such low-lying state is believed to be accountable for a secondary IVCT band observed by Hendrickson and coworkers in the biferricenium and biferricenylium cations.[42, 43] Finally, such multiple near-IR bands may be caused by the presence of a bridge with accessible redox sate levels, as has been recently proposed to explain the rich absorption spectrum of certain mixed-valence compounds with redox-active bridges.[44] Therefore, band assignment could be fairly difficult when multiple factors and mechanisms co-exist for species like $\mathbf{9c}^{+\bullet}$, for which the band gap between the metal center and redox-active bridging ligand is quite low, as has been demonstrated in the electrochemistry.

Based on our previous knowledge (Chapter 2), the far-end into-IR band of $\mathbf{9c}^{+\bullet}$ centered at 4332 cm^{-1} (2308 nm) is a typical interconfigurational (IC) transition band derived from the $d\pi \rightarrow d\pi$ transitions between the Kramer's doublets of Fe^{III}. This band is commonly observed as a narrow and low intensity band appearing around the border between NIR and IR region. The higher energy band centered at 7450 cm^{-1} (1342 nm) is assigned to a pyrrolene to Fe^{III} LMCT transition. This band is blue shifted and diminished in intensity (ε_{max} = 1715) compared to that of the reference species $\mathbf{13}^{+\bullet}$ (*vide infra*), presumably because of the modified chemical environment and the competing intervalence charge transfer process. Finally, the major and most intense band with λ_{max} at

5153 cm^{-1} (ε_{max} = 10100) is presumably ascribed to the bridge-mediated superexchange intervalence charge transfer (IVCT) between the two iron sites. The high intensity and low energy of this band are superior to any structural analogues, suggesting the great extent of delocalization and low energy barrier between the partial occupied and full-filled dπ orbitals. However, a partial contribution from LMCT transition to this broad band can not be fully ruled out due to the possible overlapping between the LMCT and IVCT bands. In fact, the structurally mimicking mono-ferrocenyl species $\mathbf{13}^{+\bullet}$ does show a strong low-energy ligand-to-metal charge transfer band at 6020 cm^{-1} (ε_{max} = 5020) as shown in Figure 3.24. As can be seen, the absorption spectrum of $\mathbf{13}^{+\bullet}$ bears in close resemblance to that of $\mathbf{9c}^{+\bullet}$ in terms of Cp-to-Fe^{III}, ligand-based π-π^* transition and IC bands. Although the terminal phenyl group in $\mathbf{13}^{+\bullet}$ is not as ideal as a 4-methoxyphenyl group in its electron-donating capability relative to replace a ferrocenyl group, the LMCT band of $\mathbf{13}^{+\bullet}$ provides very useful insight of the energy gap between the pyrrolene-based ligand orbital and Fe^{III} dπ orbital. Therefore, it is likely both LMCT and IVCT transitions coexist in the highly intense low-energy band of $\mathbf{9c}^{+\bullet}$, whereas they are mathematically not distinguishable due to close spacing.

Compared to the profound spectra of $\mathbf{9c}^{+\bullet}$, the absorption spectrum of the oxidized species derived from **11a** (Figure 3.25) is more straightforward with an absence of the possible overlap between the LMCT and IVCT bands. Apart from the obvious structural difference between **9c** and **11a**, the removal of the vinyl bonds between the pyrrolene and ferrocene moiety has some important consequences for 2,5-bis(ferrocenyl)pyrrole **11a**. The less extended and less coplanar conjugation along the bridging fragment considerably lowers the energy of the bridging unit, which accounts for the hypochromic shift of the ligand-based π-π* transition and the absence of the third oxidation wave in electrochemistry which is assumably pyrrole-based. In other words, the redox-match between the central pyrrole unit and its ferrocene groups is diminished due to the enlarged energy difference between them. The enhanced ΔE_1 is more a consequence of shorter metal-metal distance than effective charge delocalization in comparison with that of **9c**. Thus, the LMCT band in $\mathbf{11a}^{+\bullet}$ should be shifted out of the IVCT absorption region to a higher energy area so that overlapping between the two bands is not possible.

As shown in Figure 3.25, the mixed-valence spectra of **11a**$^{+\bullet}$ is very similar to that of **9c**$^{+\bullet}$. The spectra evolved in strictly linear fashion during the stepwise introduction of oxidant into the solution of neutral **11a**, which is ascribed to the high conproportionation constant derived from the large ΔE value (*vide supra*). Whereas the Cp-to-Fe^{III} transition band appears at the expected position (644 nm), the nearby ligand-based π-π* transition band resembling to that of **9c**$^{+\bullet}$ (λ_{max} = 726 nm) is not observed in the visible region, which confirmed our previous prediction that the pyrrole-based ligand orbital in **11a** and **11a**$^{+\bullet}$ is at a rather low-energy level. The spectrum of **11a**$^{+\bullet}$ also shows a very broad and intense band in the low energy region. Deconvolution of this band resulted in three gaussians (Figure 3.25B). The weak band centered at 9260 cm^{-1} (1079 nm) is clearly derived from the bridging-ligand-to-Fe^{III} LMCT transition, which is blue-shifted as expected; the most intense band centered at 5110 cm^{-1} (1956 nm) is assigned to the metal-metal IVCT transition; and the last into-IR band is still due to the IC transition within the Fe^{III} dπ orbitals. These assignments are quite clear which in turn gives us insight of the band analysis of **9c**$^{+\bullet}$. Again, the intensity of the IVCT band of **11a**$^{+\bullet}$ is substantially

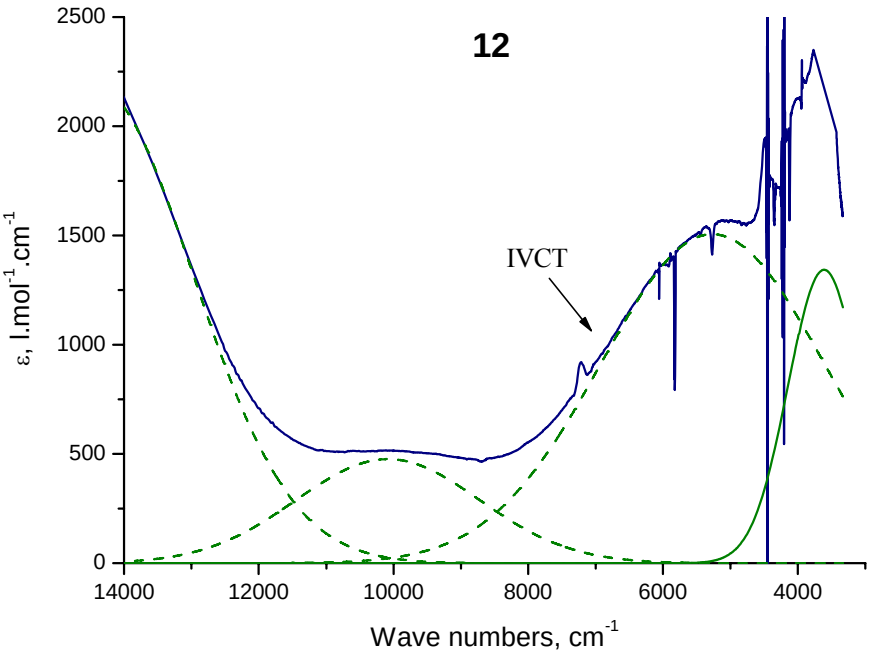

Figure 3.26 Vis-NIR spectrum of mixed-valence species of 2,5-diferrocenylthiophene **12**$^{+\bullet}$ in CH_2Cl_2. The dashed lines are deconvoluted bands.

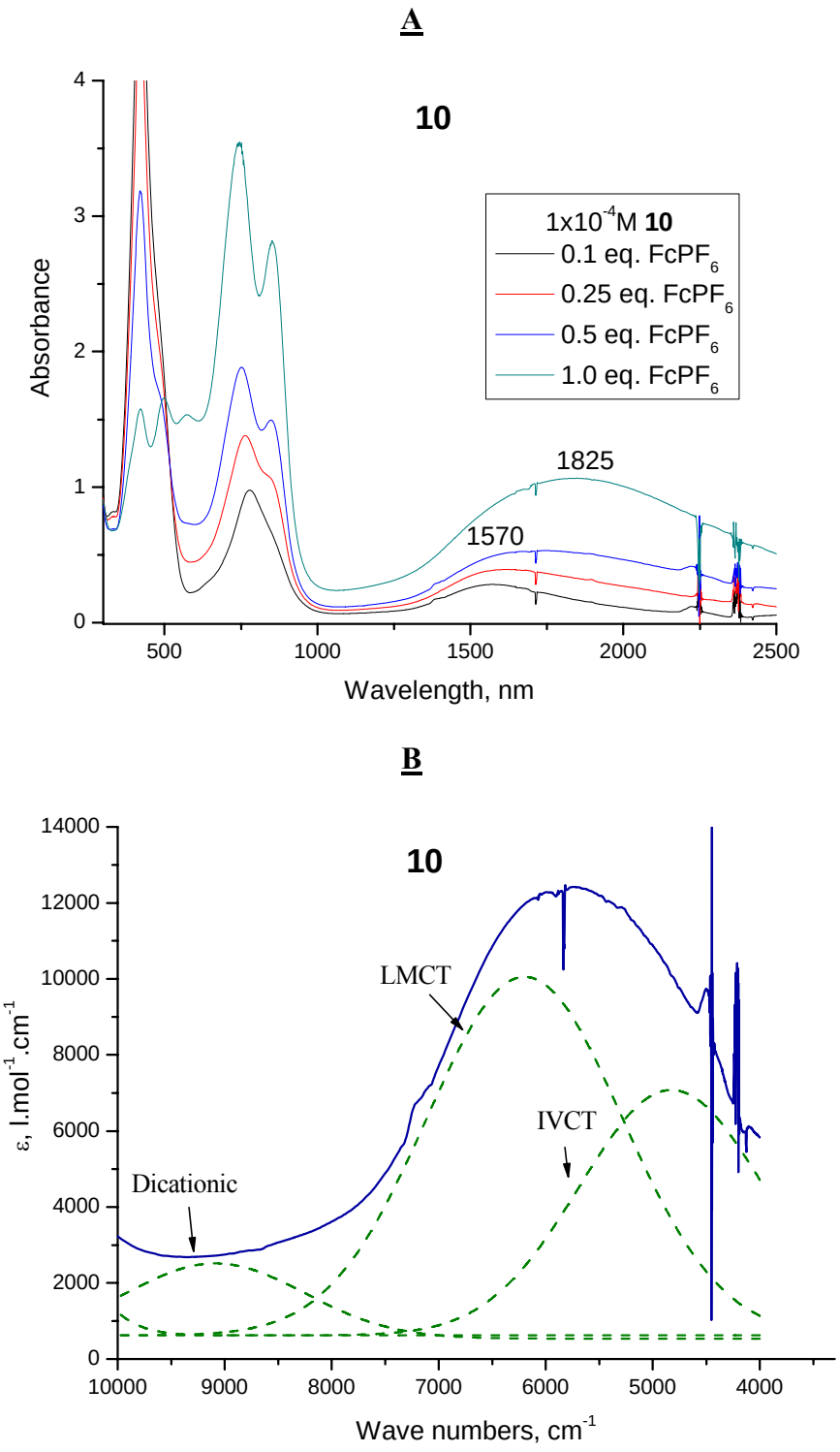

Figure 3.27. UV-Vis-NIR spectra of mixed-valence species $\mathbf{10}^{+\bullet}$ in CH_2Cl_2: *Top*: evolution spectra of **10** obtained upon progressive oxidation with 0.1 to1.0 equivalent of oxidant in. *Bottom*: deconvoluted spectrum of $\mathbf{10}^{+\bullet}$ in the NIR region (X-axis in energy unit, cm^{-1}), derived from spectrum obtained with 0.5 equivalent of oxidant. The low energy envelope contained both LMCT and ICVT bands (dashed lines).

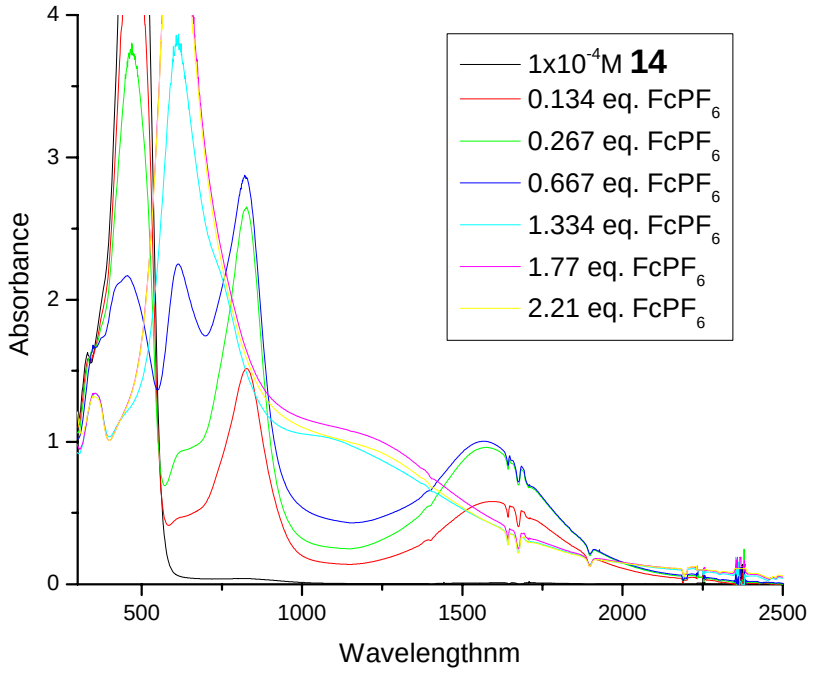

Figure 3.28. UV-Vis-NIR spectra of one- and two-electron oxidized species of **14** in CH_2Cl_2.

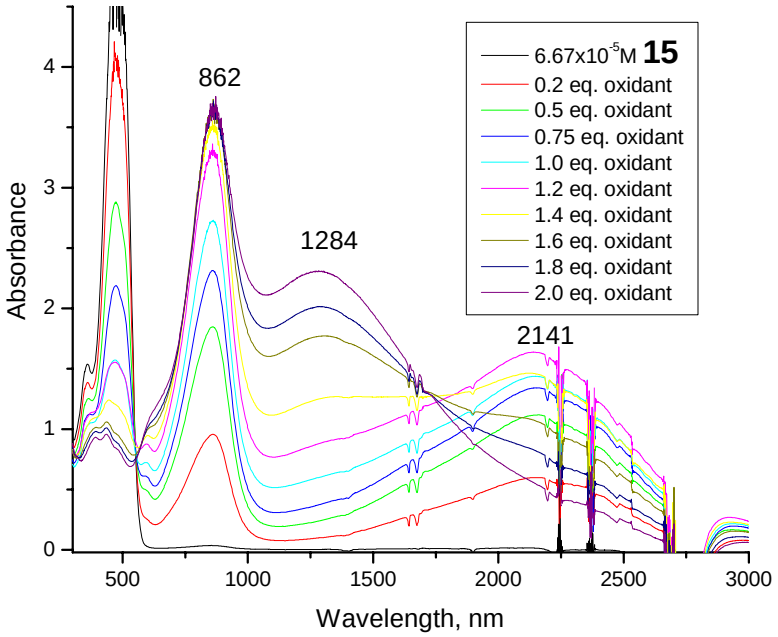

Figure 3.29. UV-Vis-NIR spectra of one- and two-electron oxidized species of **15** in CH_2Cl_2.

higher than that of 2,5-diferrocenylthiophene $\mathbf{12}^{+\bullet}$ (Figure 3.26), which manifests more effective electronic coupling between the two iron sites facilitated by the electron richer pyrrolene linker. Interestingly, the IC band of is also slightly stronger and broader than that of other compounds. The same feature was also observed in *N*-phenyl substituted analogue $\mathbf{11b}^{+\bullet}$. Although we could not provide a profound explanation at this moment, conceptually, however, it must relate to the perturbation of the pyrrole-centered ligand to the Fe^{III} dπ Kramer's doublets so that such transition is promoted.

The spectrum of monocationic $\mathbf{10}^{+\bullet}$ is markedly different and complicated as shown in Figure 3.27. Unlike its shorter-bridged analogue discussed above, in which the shape and position of low energy bands persisted with progressive treatment of oxidant before one equivalent of oxidant was introduced, the one-electron oxidized $\mathbf{10}^{+\bullet}$ demonstrated significant band-shape change and λ_{max} shifting upon stepwise oxidation. This observation could be attributed to the extended conjugation of the bridging ligand. The spectra of $\mathbf{10}^{+\bullet}$ demonstrated two bathochromically shifted bands (755 and 850 nm) in the ending visible region, which arose from HOMO-to-LUMO and SOMO-to-LUMO transitions due to the elongated conjugation. This implied the energy level of the bridging ligand was further elevated. On the other hand, the low-energy band appeared at λ_{max} = ca.1600 nm in the initial oxidation (0.1 equivalent of oxidant) of neutral compound **10** and was quite MLCT-featured, taking both the absorption energy and intensity into account. The sequential addition of oxidant caused the overall band-shape change (broader) and bathochromic shift in λ_{max} which was clearly due to the rising-up of a newly formed secondary band in lower energy. As one equivalent of oxidant was reach, the band-shape change and shift reached its maximum. Meanwhile, at this point, the obvious growth of one underlying band around 1150 nm indicated the appearance of corresponding dicationic species due to the small ΔE_1 of **10**, which made the interpretation of the spectra more complicated. Deconvolution of the spectrum obtained from 0.5 equivalent of oxidant present revealed two major NIR bands with λ_{max} at 6200 and 4830 cm^{-1}, respectively (Figure 3. 27B). Whereas the former higher energy band was assigned to the initially appearing LMCT transition, the latter was very likely an IVCT band. An accurate explanation to this band-shape transformation with different amount of oxidant present is difficult. However, it is likely that the LMCT and IVCT transitions are

competing processes and they have different level of dependence on the concentration of the counterion, which could essentially perturb their absorption strengths.

As we discussed in electrochemical section, the first oxidation of **14** was based on the central pyrrole moiety. Apart from that, the second oxidation wave is in close position to the first one and the dicationic species demonstrated a highly charge-delocalized feature. For these reasons, the electronic absorption of initially oxidized **14** gave rise to ligand-based SOMO-to-LUMO and HOMO-to-SOMO bands at 825 nm and 1563 nm, respectively (Figure 3.28). Both bands increased and saturated till half an equivalent of oxidant was added. Upon further addition, the disproportionation prevailed during the consequential oxidation treatment. Upon addition to two equivalents of oxidant, the two bands disappeared, while a new band around 1200 nm appeared. This new band was assigned to the HOMO-to-LUMO transition in the dicationic species.

In contrast to that of $\mathbf{14}^{+\bullet}$, the low energy band (maxima at 2153 nm) in $\mathbf{15}^{+\bullet}$ spectra (Figure 3.29) was highly skewed and red-shifted. As the initial oxidation of **15** was mainly ferrocene-based (*vide supra*), this low energy band was presumably derived from LMCT transitions. However, in many occasions, it has been reported that in a highly conjugated electron-rich α,ω-diferrocenyl system,[45, 46] it is very likely the positive charge could seep into the bridging segment upon initial oxidation. The broad and skewed NIR band of $\mathbf{15}^{+\bullet}$ certainly contained multiple transitions including LMCT, ligand-based π-π^* and IC bands.

Hush Formalism

The spectroscopic results are interpreted with the classical electron-transfer model of Marcus-Hush[7, 47] using equations shown below, where V is the electronic coupling parameter, α is the delocalization efficient and $\Delta\nu_{1/2}$ is the calculated half-band width derived from Hush's relationships. The experimental and calculated results of relevant compounds are summarized in Table 3.2. The electronic absorption data of $\mathbf{9a}^{+\bullet}$ is essentially identical to $\mathbf{9c}^{+\bullet}$. $\mathbf{14}^{+\bullet}$ and $\mathbf{15}^{+\bullet}$ are not included because the nature of the electronic absorption has been more associated with ligand-based transition instead of IVCT superexchange. The metal-to-metal adiabatic distances are adopted from single crystal structures.

$$V = 2.06 \times 10^{-2}(\varepsilon_{max} \cdot \Delta\nu_{1/2} \cdot \nu_{max})^{1/2}/r \quad [3.1]$$

$$\alpha = V/\nu_{max} \quad [3.4]$$

$$\Delta\nu_{1/2}\,[\text{Hush}] = (2310\nu_{max})^{1/2} \quad [3.5]$$

It is worth mentioning that we can apply the Hush formalism to the ligand-to-metal charge transfer in mono-ferrocenyl species $\mathbf{13}^{+\bullet}$ and in extensively conjugated diferrocenyl $\mathbf{10}^{+\bullet}$. Originally developed for the interpretation of intervalence charge transfer (IVCT) bands in extended solids, the Marcus-Hush model has been extended and applied to IVCT in mixed-valence organometallics[48, 49] and organic compounds,[50, 51] as well as to LMCT and metal-to-ligand charge transfer (MLCT) processes in charge-delocalized asymmetric complexes.[52-54] Ligand-to-metal charge transfer such as that in $Fc^{+}CH{=}CHPyrCH{=}CHPh$ can be viewed as a special case of "intervalence" electronic coupling, whereupon the radical cationic species possesses an asymmetrical structure. Accordingly, the March-Hush energy double wells no longer reside on the same isoenergetic level (see Chapter 1). Instead, the ligand well is elevated by a relative free enthalpy ΔG^{o} which can be estimated from the difference of electrochemical potentials (ΔE^{o}) between the pyrrolene and ferrocene moiety of a neutral complexes. In other words, the energy for such LMCT transition (E_{op}) will equal the sum of the Frank-Condon energy (E_{FC}) and the difference in energy (ΔE^{o}) between the equilibrium vibrational states of Fc^{+}-Pyr-Ph and Fc-Pyr^{+}-Ph, $E_{op} = E_{FC} + \Delta E^{o}$. In these cases, the donor and acceptor distance is determined from the crystal structure assuming the effective electron-transfer distance is the distance between the Fe and N atoms.

As shown in Table 3.2, all pyrrolene-mediated diferrocenyl radical cation systems feature absorption with relatively low IVCT energy ($\nu_{1/2}$) and greatly enhanced intensity (ε_{max}), which indicates the energy gap between the electron transfer Fe^{II} and Fe^{III} sites are decreased with perturbation of the pyrrolene bridging ligand on the relevant metal dπ orbitals. As a consequence, a high population of IVCT transition occurs and contributes largely to the resulting V and α parameters. Conversely, the experimental $\Delta\nu_{1/2}$ in these systems is narrower than the calculated Hush limit ($\Delta\nu_{1/2}$ [Hush]) for Robin-Day[55] Class II species, which generally implies a more delocalized feature. In contrast to all of

Table 3.2. IVCT and LMCT band parameters, obtained from the spectral deconvolution, and calculated Hush parameters for the relevant radical cations.

	ν_{max} [cm^{-1}]	ε_{max} [$M^{-1}cm^{-1}$]	$\Delta\nu$ (obs) [cm^{-1}]	$\Delta\nu$ (Hush) [cm^{-1}]	d_{mm} [Å]	V [cm^{-1}]	α
11a $^{+\bullet}$	5070	5910	3200	3422	8.54	743	0.146
11b $^{+\bullet}$	4700	5160	3040	3294	8.46	658	0.139
9a,c $^{+\bullet}$	5153	10100	2730	3450	12.64	611	0.118
9b $^{+\bullet}$	5160	10000	2800	3452	12.12	643	0.124
10 $^{+\bullet}$ (IVCT)	4830	7014	2200	3340	17.75	315	0.065
10 $^{+\bullet}$ [a] (LMCT)	6200	10140	2170	3784	8.86[a]	855	0.137
12 $^{+\bullet}$	5310	1500	4150	3502	7.14	522	0.098
13 $^{+\bullet}$ [a] (LMCT)	6020	5050	2450	3729	6.32[a]	885	0.147

[a]LMCT band corresponding to an electron transfer between pyrrole-based ligand to metal center. The electron transfer distance assumes from N to Fe atoms.

these, the corresponding values of thiophene bridged species, **12** $^{+\bullet}$, set very sharp comparison to the pyrrolene-bridged families. The ε_{max}, V and α parameters of **12** $^{+\bullet}$ are noticeably smaller than those of **11a**$^{+\bullet}$, whereas its half-wave width, $\Delta\nu_{1/2}$, is much broader, showing a more localized and typical Class II characteristics.

It is clear that the strength of electronic coupling decreases as the bridging fragment elongated which is evidenced by the variation of V values in a decreasing order of **11a**$^{+\bullet}$ > **9c**$^{+\bullet}$ > **10**$^{+\bullet}$ and **11b**$^{+\bullet}$ > **9b**$^{+\bullet}$. Meanwhile, it is interesting to notice that whereas the V value of *N*-phenyl substituted **11b**$^{+\bullet}$ is 86 cm^{-1} smaller than that of *N*-alkyl substituted **11a**$^{+\bullet}$ due to the electron-draining effect caused by the phenyl group on the bridging pyrrolene nucleus, such depressed electronic coupling does not happen on **9b**$^{+\bullet}$, instead, the V value of **9b**$^{+\bullet}$ is even slightly greater than **9c**$^{+\bullet}$ (and **9a**$^{+\bullet}$). The possible explanation for this disparity can be attributed to the steric difference presented in **11a-b** and **9b-c** (*vide supra*). The steric interference in the former complexes (**11a-b)** causes

serious distortion along the Cp-Pyr-Cp conjugation. Therefore, the electron withdrawing or donating ability of the *N*-substituent plays a more noticeable role in determining the electronic coupling between the metal centers, which leads to greater *V* value in **11a**$^{+\bullet}$ than in **11b**$^{+\bullet}$. In contrast, the difference in *V* values between **9b**$^{+\bullet}$ and **9c**$^{+\bullet}$ mainly arises from the shorter metal-metal distance of the former species as all the other Hush's parameters for both radical cations are essentially the same. This in turn is attributed to the greater coplanarity of the bridging ligand in **9b** as we have discussed in an earlier section.

Investigation of the ligand-to-metal charge transfer (LMCT) process in this series of compounds also gives rise to some important points. First, the reference mono-ferrocenyl species **13**$^{+\bullet}$ reveals very strong LMCT transition comparing to the thiophene ancillary analogues[56] in term of ε_{max} and parameter *V*. The transition takes place at rather a low energy (6020 cm^{-1}) implying the low band gap between the donor (pyrrolene-centered) and acceptor (ferrocenyl Fe^{III}) sites. The short donor-to-acceptor distance accounts for the large *V* value of **13**$^{+\bullet}$. Secondly, the degree and strength of LMCT transition in diferrocenyl complexes vary significantly with the magnitude of conjugation extension of the linking pyrrolene ligand. Whereas the LMCT transition in **11a**$^{+\bullet}$ is weak (ε_{max} = 806) with high energy requirement (ν_{max} = ca. 9000 cm^{-1}), the corresponding transition in highly conjugated **12**$^{+\bullet}$ is considerably stronger (ε_{max} = 10140 cm^{-1}, ν_{max} = 6200 cm^{-1}). In fact, as the former cationic species mainly demonstrates the IVCT band in the excited state, the latter shows a dominating LMCT transition accompanied with a weak IVCT transition. The vinylene-pyrrole-vinylene linked mixed-valence species **9c**$^{+\bullet}$, however, falls just in the middle of the two extremes, showing approximately equal amounts of LMCT and IVCT transitions, which makes interpretation ofthe differentiation between them extremely difficult. This obvious transformation in photo-induced electronic transition is ascribed both to the narrowed band-gap between the metal center and organic component as the conjugation of the bridging unit extended and to the shorter ligand-to-metal distance, assumingly from N to Fe atoms. In this sense, the central pyrrolene moiety acts essentially as an electron-hopping intermediate site in supporting the electron transfer process in large distance.

Finally, it is noteworthy to underline that, whereas Hush model is a very useful methodology in quantitatively analyzing the electronic coupling in Class II systems, it encounters well-recognized problems when applied to strongly coupled or highly delocalized systems were applied.[57-59] For the pyrrolene-mediated mixed-valence complexes herein, caution should be taken in fitting the experimental data into Hush model due to the obviously delocalized feature and complicated electronic transitions in some of the compounds.

Conclusion and Perspectives

We have prepared a series of pyrrolene-mediated diferrocenyl compounds with different lengths, and extended them to oligomers. Both electrochemistry and mixed-valence absorption studies reveal highly delocalized systems. This is presumably due to the redox-match and low energy band gap between the metal and linking organic orbitals. With the pyrrolene moiety as the mediator in the conjugated linking framework, the electronic interaction between the two ending metal centers is still of significance with metal-metal distance of 17.75 Å, whereas such electronic coupling could not be observed in any other similar system to date. In this context, the electron-rich pyrrolene unit essentially functions as an amplifier or promoter in supporting charge transfer process over large distances, which explicitly directs to potential applications in designing molecular devices such as electronic relays.

In contrast, electronic conductivity in conjugated organic polymers such as PPV, PVPV, polythiophene and polypyrrole depends on delocalization of charge along the polymer backbone. In polymers containing both metal centers and conjugated bridges, delocalization along the backbone is expected to enhance conductivities and charge mobilities relative to analogous polymers in which charge is localized. In such materials, the extent of charge delocalization will depend on the magnitude of the energy barriers to charge transfer along the backbone. The result achieved in current research provides important implications for extension to oligomers and polymers. We are now in the progress of preparing the vinylene-pyrrolene-vinylene bridged ferrrocenyl polymer shown below,

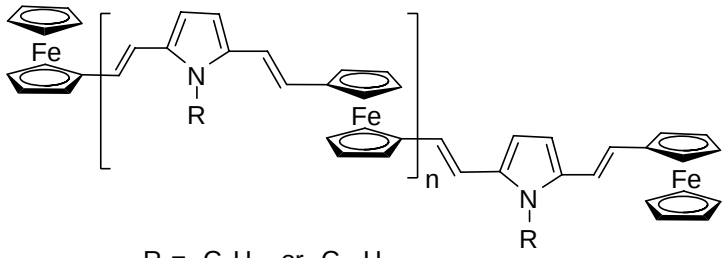

R = -C_6H_{13} or -$C_{12}H_{25}$

in which the long alkyl-chain substituent attached on the pyrrolene nucleus is anchored to increase the solubility. This polymer could be conveniently achieved by utilizing the HWE condensation reaction between 1,1'-$Fc(CHO)_2$ and appropriate pyrrolyl-diphosphonate. We believe this novel metal-contained polymer will demonstrate highly enhanced conductivity due to very low band gap and great charge delocalization.

References

1. Brunschwig, B. S.; Creutz, C.; Sutin, N., *Chem. Soc. Rev.* **2002,** 31, 168-184.

2. Weiss, D. S.; Cowdery, J. R.; Young, R. H., *Electron Transfer in Chemistry (Ed.: V. Balzani), Wiley-VCH, Weinheim* **2001**, 379–471.

3. Segal, D.; Nitzan, A.; Davis, W. B.; Wasielewski, M. R.; Ratner, M. A., *J. Phys. Chem. B.* **2000,** 104, 3817–3829.

4. Barlow, S.; O'Hare, D., *Chem. Rev.* **1997,** 97, 637 -669.

5. Low, P. J.; Paterson, M. A. J.; Puchmann, H.; Goeta, A. E.; Howard, J. A. K.; Lambert, C.; Cherryman, J. C.; Tackley, D. R.; Leeming, S.; Brown, B., *Chem. Eur. J.* **2004,** 10, 83–91.

6. Lambert, C.; Nöll, G.; Schelter, J., *Nat. Mater.* **2002,** 1, 69-73.

7. Hush, N. S., *Prog. Inorg. Chem.* **1967,** 8, 391.

8. Kingsborough, R. P.; Swager, T. M., *Adv. Mater.* **1998,** 10, 1100-1104.

9. Zhu, S. S.; Carroll, P. J.; Swager, T. M., *J. Am. Chem. Soc.* **1996,** 118, 8713-8714.

10. Ribou, A.-C.; Launay, J.-P. ; Sachtleben, M. L.; Li, H.; Spangler, C. W., *Inorg. Chem.* **1996,** 35, 3735-3740.

11. Tolbert, L. M.; Zhao, X., *J. Am. Chem. Soc.* **1997,** 119, 2291.

12. Skibar, W.; Kopacka, H.; Wurst, K.; Salzmann, C.; Ongania, K. H.; Fabrizi de Biani, F.; Zanello, P.; Bildstein, B., *Organometallics* **2004,** 23, 1024-1041.

13. Thomas, J. K. R.; Lin, J. T.; Wen, Y. S., *Organometallics* **2000,** 19, 1008-1012.

14. Kim, I. T.; Elsenbaumer, R. L., *Tetrahedron Let.* **1988,** 39, 1087-1090.

15. Carson, J. R.; Hortenstine, J. T.; Maryanoff, B. E.; Molinari, A. J., *J. Org. Chem.* **1977,** 42, 1096.

16. Berlin, A.; Bradamante, S.; Ferraccioli, R.; Pagani, G. A.; Sannicolo, F., *J. Chem. Soc. Perkin Trans. I* **1987**, 2631-2635.

17. de Meheas, M., *Bull. SOC. Chim. Fr.* **1962**, 1989.

18. Minkin, V. L. D., G. N., *Russ. Chem. Rev.* **1960,** 29, 599.

19. Van Der Looy, J. F. A.; Thys, G. J. H.; Dieltiens, P. E. M.; Schrijver, D. D.; Van Alsenoy, C.; Geise, H. J., *Tetrahedron* **1997,** 53, 15069-15084.

20. Egbe, D. A. M.; Tillmann, H.; Birckner, E.; Klemm, E., *Macromolecular Chemistry and Physics* **2001,** 202, (13), 2712-2726.

21. Justin Thomas, K. R.; Lin, J. T.; Wen, Y.-S., *J. Organomet. Chem.* **1999,** 575, 301-309.

22. Justin Thomas, K. R.; Lin, J. T.; Lin, K. J., *Organometallics* **1999,** 18, 5285-5291.

23. Ito, Y.; Konoike, T.; Harada, T.; Saegusa, T., *J. Amer. Chem. Soc.* **1977,** 99, 1487-1493.

24. Van Der Looy, J. F. A.; Thys, G. J. H.; Dieltiens, P. E. M.; Schrijver, D.; Van Alsenoy, C.; Geise, H. J., *Tetrahedron* **1997,** 53, 15069-15084.

25. Zakrzewski, J., *J. Organomet. Chem.* **1987,** 333, (1), 71-6.

26. Clerici, F. G., Maria Luisa; Trimarco, Pasqualina., *Tetrahedron* **1998,** 54, (21), 5763-5774.

27. Kiryanov, A. A.; Sampson, P.; Seed, A. J., *J. Org. Chem.* **2001** 66, 7925-7929.

28. Lecher, H. Z.; Greenwood, R. A.; Whitehouse, K. C.; Chao, T. H., *J. Am. Chem. Soc.* **1956,** 78, 5018-5022.

29. Jesberger, M.; Davis, T. P.; Barne, L., *Synthesis* **2003,** 13, 1929-1958.

30. Cava, M. P.; Levinson, M. I., *Tetrahedron* **1985,** 41, 5061-5087.

31. Mathur, P.; Singh, A. K.; Singh, V. K.; Singh, P.; Rahul, R.; Mobin, S. M.; Thoene, C., *Organometallics* **2005** 24, 4793-4798.

32. Yoda, M.; Kondo, T.; Okabe, T.; Matsuyama, H.; Sasaki, S.; Kuwatani, Y., *Chemistry Letters* **1997**, 35-36.

33. LeSuer, R. J.; Geiger, W. E., *Angew. Chem. Int. Ed.* **2000,** 112, 254-256.

34. Camire, N.; Mueller-Westerhoff, U. T.; Geiger, W. E., *J. Organomet. Chem.* **2001,** 637-639 823-826.

35. Nakazaki, J.; Chung, I.; Matsushita, M.; Sugawara, T.; Watanabe, R.; Izuoka, A.; Kawada, Y., *J. Mat. Chem.* **2003,** 13, 1011-1022.

36. Sohn, Y. S.; Hendrickson, D. N.; Gray, H. B., *J. Am. Chem. Soc.* **1971,** 93, 3603-3612.

37. Lay, P. A.; Magnuson, R. H.; Taube, H., *Inorg. Chem.* **1988,** 27, 2364–2371.

38. Kober, E. M.; Goldsby, K. A.; Narayane, D. N. S.; Meyer, T. J., *J. Am. Chem. Soc.* **1983,** 105, 4303–4309.

39. Laidlaw, W. M.; Denning, R. G., *J. Chem. Soc., Dalton Trans.* **1994**, 1987–1994.

40. Richardson, D. E.; Taube, H., *J. Am. Chem. Soc.* **1983,** 105, 40 - 51.

41. Halpern, J.; Orgel, L. E., *Discuss. Faraday Soc.* **1960,** 29, 32 - 41.

42. Morrison, W. H., Jr. ; Hendrickson, D. N., *J. Chem. Phys.* **1973,** 59, 380-385.

43. Sinha, U.; Lowery, M. D.; Hammack, W. S.; Hendrickson, D. N.; Drickamer, H. G., *J. Am. Chem. Soc.* **1987,** 109, 7340-7345.

44. Nelsen, S. F.; Ismagilov, R. F.; Powell, D. F., *J. Am. Chem. Soc.* **1998,** 120, 1924–1925.

45. Sato, M.; Kashiwagi, S.; Taniguchi, H.; Hiroi, M., *Jpn. J. Appl. Phys.* **1999,** 38, L1073-L1075.

46. Sato, M.; Fukui, K.; Sakamoto, M.; Kashiwagi, S.; Hiroi, M., *Thin Solid Films* **2001,** 393, 210-216.

47. Marcus, R. A.; Sutin, L., *Inorg. Chem.* **1975,** 14, 213.

48. Colbert, M. C. B.; Lewis, J. L., N. J. ; Raithby, P. R.; Younus, M.; White, A. J. P.; Williams, D. J.; Payne, N. N.; Yellowlees, L.; Beljonne, D.; Chawdhury, N.; Friend, R. H., *Organometallics* **1998,** 17, 3034-3043.

49. Zhu, Y.; Clot, O.; Wolf, M. O.; Yap, G. P. A., *J. Am. Chem. Soc.* **1998,** 120, 1812-1821.

50. Nelsen, S. F.; Tran, H. Q.; Nagy, M. A., *J. Am. Chem. Soc.* **1998,** 120, 298-304.

51. Lambert, C.; Noll, G., *J. Am. Chem. Soc.* **1999,** 121, 8434-8442.

52. Desjardins, P.; Yap, G. P. A.; Crutchley, R., *J. Inorg. Chem.* **1999,** 38, 5901-5905.

53. Evans, C. E. B.; Ducharme, D.; Naklicki, M. L.; Crutchley, R., *J. Inorg. Chem.* **1995,** 34, 1350-1354.

54. Evans, C. E. B.; Naklicki, M. L.; Rezvani, A. R.; White, C. A.; Kondratiev, V. V.; Crutchley, R. J., *J. Am. Chem. Soc.* **1998,** 120, 13096-13103.

55. Robin, M. B.; Day, P., *Adv. Inorg. Chem. Radiochem.* **1967,** 10, 247.

56. Zhu, Y.; Wolf, M. O., *J. Am. Chem. Soc.* **2000,** 122, 10121-10125.

57. Salaymeh, F.; Berhane, S.; Yusof, R.; De la Rosa, R.; Fung, E. Y.; Matamoros, R.; Lau, K. W.; Zheng, Q.; Kober, E. M.; Curtis, J. C., *Inorg. Chem.* **1993,** 32, 3895.

58. Westmoreland, T. D.; Wilcox, D. E.; Baldwin, M. J.; Mims, W. B.; Solomon, E. I., *J. Am. Chem. Soc.* **1989,** 111, 6106.

59. Dong, Y.; Hupp, J. T., *Inorg. Chem.* **1992,** 31, 3170.

CHAPTER 4

TRIFERROCENES BRIDGED BY SYMMETRIC AND ASYMMETRIC SPACERS: SYNTHESIS, STRUCTURE, ELECTROCHEMISTRY AND MIXED-VALENCE STUDIES

Introduction

The mixed-valence states of conjugated ferrocene dimers have attracted considerable attention for decades because they are valuable examples affording intrinsic information regarding intramolecular electron-exchange reactions.[1-5] It has been shown that the chemical structure of the conjugated spacer group and its length dramatically affect the electronic interaction between the ferrocene units. At the same time, polymeric and oligomeric ferrocene-based materials have also attracted great attention with respect to their electrochemical, electronic, and magnetic properties.[6, 7] A recent literature survey indicated, however, reports on trinuclear or tetranuclear ferrocene derivatives are considerably less frequent.[8-12] Aside from that, most of the known triferrocenes contain short and symmetrical bridges such as S, $Si(Me)_2$, and Se as shown below. The synthetic methods are often associated with radical anion or ring-opening polymerization. Thus, the distinct oligomeric materials such as triferrocenes or tetraferrocenes are only isolated as statistical products with yield in milligram quantity. Moreover, despite the fast development of synthetic chemistry, triferrocenes bridged by an extended conjugation backbone have not been recorded until recently.[13]

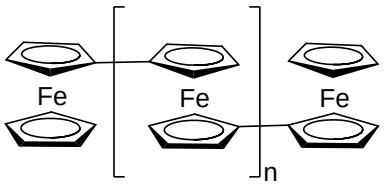

n = 1,2,3..

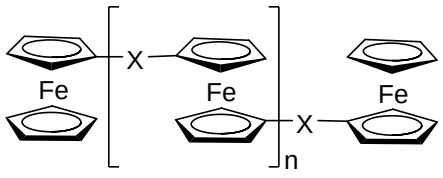

n = 1-6 x = S, Se, $Si(Me)_2$

The importance of studying trinuclear metallic systems is obvious. First, it extends our understanding of the long-range electron transfer processes through multiple redox-active sites. In biferrocenyl systems, charge transfer is restricted in a closed 'box', i.e. between the limits confined by the two redox-acive terminii. When an additional metal center is introduced, the limit is extended and the interactions among the three redox centers are expected to be more profound and dynamic, especially when the electronic couplings are strong. Apart from that, it has been well established that both superexchange[14, 15] and hopping mechanism[16, 17] can contribute to electron or hole transfer from a donor to an acceptor with the assistance of an intermediate pathway. In the superexchange mechanism, direct electron transfer between the distanced electron donor and acceptor is accomplished by indirect mixing of their wave functions, while in the electron/hole hopping process the charge is temporarily localized on the midway group and a chemical intermediate species is generated. Triferrocenes provide an excellent model in examining these mechanisms since the central ferrocene unit can be essentially viewed as a midway redox-active group in supporting the electron traverse between the terminal ferrocenes.

Second, triferrocenes possess apparent synthetic advantages with respect to structural design. Whereas in preparing oligo- and polyferrocenes little control can be made to vary the chemical environment of each ferrocenyl group, subtle structural design in triferrocene systems is plausible with the assistance of modern metallocene chemistry. In this context, the chemical environment of distinct ferrocene moiety could be intentionally defined through the spacers and substituents so that the redox sequence of the three ferrocenes can be actively controlled. By this means, the bridging ligand act not only as an electron conductor but also as a switching element, turning on or off the communication between the redox-active sites, which, in essence, is a prototype of electronic switches.

Finally, multimetallic complex linked by extensively conjugated spacers often encounters serious solubility problem without introducing a solubility promoting element, which sometimes is synthetically tedious. For triferrocenes or tetraferrocenes, however, such problem can be moderated by carefully design the conjugated linkers as we shall see later.

The studies herein mainly focused on a series of novel triferrocenes linked by conjugated spacers varying both in length and in symmetry. The structures of the triferrocenyl compounds are summarized in Figure 4.1.

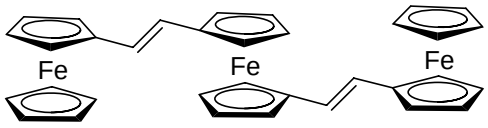

TFc2

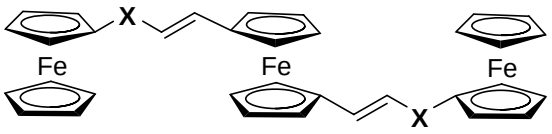

TFc2X-A (X = S, CO)

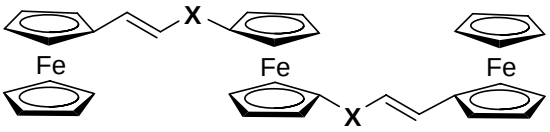

TFc2X-B (X = S, CO)

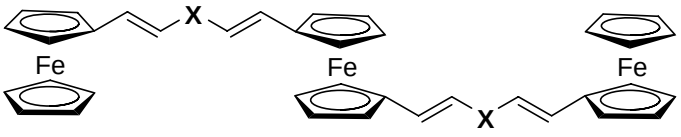

TFc4X (X = S, CO, CH=CH, 2,5-Th, 2,5-PyrNMe)

Figure 4.1 Chemical structure of a series of triferrocenes.

As can be seen, the linkers in the triferrocenyl complexes all consist of vinylene bonds and an X functional group/atom. We give each of the compounds a short name in a **TFcNX** fashion, in which TFc stands for the three ferrocenes, N and X denote the number of unsaturated sp^2 carbons and the functional group/atom of the conjugated spacer connecting the two adjacent ferrocenyl groups, respectively. In order to gain more insight of the relevant properties of the triferrocenes, we also included the corresponding biferrocenyl analogue to each of the triferrocenes for comparisons. These biferrocenes, which have been reported previously (Chapter 2 & 3), are abbreviated in the similar fashion as **BFcNX**.

Multifold objectives were implemented in the course of current work, which determined our selection of model compounds. In studying charge mobility, we started with a simple triferrocenyl compound, **TFc2**, in which the ferrocenes are spaced by a single vinyl bond. From there, the conjugation of the bridging components is lengthened by insertion of vinyl bond and X functional groups, giving rise to compounds as **TFc4X**, in which the central ferroecene is connected to the terminal ferrocenyl groups by a symmetrical spacer, –CH=CH-X-CH=CH- (Figure 4.1). In seeking the possibility to utilize the linking spacer as a redox switching element, four **TFc2X** compounds were prepared. Depending on the orientation of the polar linking chain, **TFc2X**s are divided into two subgroups **A** and **B** as shown in Figure 4.1. By this means, the electron-densities of the individual ferrocenyl groups in **TFc2X**s are varied by the asymmetric linkers. Lastly, it is noteworthy that pyrrolene bridged compound **TFc4PyrNMe** was deliberately included in this study with important perspective. Whereas the bridging units in the rest of the triferrocenes merely function as electron conductors or redox-tuners, none of them will explicitly participate in the redox processes. The vinylene-pyrrolene-vinylene fragment in **TFc4PyrNMe**, however, has a redox potential resembling that of unsubstituted ferrocene. Our previous research revealed that the charge delocalization and ligand redox activity in pyrrolene-mediated diferreocenyl systems are fairly high due to low band gap between the frontier HOMO ligand orbital and the iron dπ orbitals. Therefore, it is speculated that **TFc4PyrNMe** will exhibit more dynamic redox behaviors due to the possible involvement of the redox-active bridging ligand , which can essentially change the fundamental mechanism.

Experimental

General Methods

General methods described in Chapter 2 were followed. All chemicals were purchased from Aldrich or Acros and used without further purifications if not otherwise specified. 1,1'-Bis(N,N'-dimethylaminomethyl)ferrocene,[18] ferrocene-1,1'-diylbis(methyltrimethylammonium iodide),[18] 1,1'-ferrocenedialdehyde [$Fc(CHO)_2$][19] and 1,1'-ferrocenyl-bis(diethylmethylphosphonate)[20] were prepared according to the literature procedures. The syntheses of dimethylthioether-a,a'- bis(triphenylphosphonium) bromide (Chapter 2), (*E*)-(2-formylvinyl)ferrocene (Chapter2), (*E*)-1-methyl-5-(2-ferrocenylvinyl)-pyrrole-2-carboxaldehyde (Chapter 3) and 2-acetylvinylferrocene (Chapter 2) have been depicted in previous chapters.

Synthesis

Ferrocene-1,1'-diylbis(methyltriphenylphosphonium iodide) [$Fc(CH_2PPh_3I)_2$].[21] Ferrocene-1,1'-diylbis(methyltrimethylammonium iodide)[18] (7 g, 12 mmol) and triphenylphosphine (7.89 g, 30 mmol) were dissolved in absolute ethanol (1 L), and the solution was heated under reflux for 3 weeks (yellow precipitate started isolating from the reaction solution after stirring for 3 days), then concentrated to approximately 300 mL. After cooling, dry ethyl ether (300 mL) was poured into the reaction mixture under vigorous stirring. The yellow precipitate was filtered off, washed with ether, and dried to yield the title compound as a yellow powder (8.5 g, 71.5%). The salt was dried under vacuum at 120 ^oC for 2 days before being used; m.p. 217-219 ^oC, lit.[21] 220 ^oC. ^1H NMR ($CDCl_3$): δ 7.93-7.85 (12H, m), 7.7-7.68 (6H, m), 7.62-7.56 (12H, m), 5.52 (4H, d, $^2J_{HCP}$ = 13.2 Hz, CH_2), 4.44 (4H, m, Cp), 3.95 (4H, m, Cp).

1,1'-Bis(2-ferrocenylvinyl)ferrocne (TFc2).

Method A (Wittig reaction): To a suspension of ferrocenylmethyltriphenylphosphonium iodide (Chapter 2) (708 mg, 1.2 mmol) in dry THF (25 mL) at 0 C under argon, was added potassium *tert*-butoxide (134 mg, 1.2 mmol, 20% excess) in one portion. The solution was stirred for 30 min, whereupon it turned rapidly from yellow to wine red, at this point, 1,1'-ferrocenedialdehyde (121 mg, 0.5 mmol) was added as a solution in anhydrous THF (10 mL) via a cannula. The resultant mixture was slowly warmed to room temperature and stirred for ca. 3 h before

10 mL of water was introduced to quench the reaction. After being extracted with diethyl ether (3 x 25 mL), the organic extract was washed with saturated aqueous NaCl, dried over Na_2SO_4, and evaporated. The orange-red residue was purified by flash column chromatography on silica gel using CH_2Cl_2/hexane (1:3) as the eluent. The first band was collected and concentrated to provide the product as a red solid (236 mg, 78%). ^{13}C NMR ($CDCl_3$): δ 128.8, 125.4, 124.9, 83.2, 82.8, 70.6, 69.6, 69.3, 68.8, 68.3. IR (KBr pellet, cm^{-1}): 3081.6, 3002.6, 2928.3, 1771.4, 1700.5, 1635, 1434.7, 1238.1, 1104, 1040.9, 999.5, 819.5, 755.6, 697.3. MS m/e (intensity): 606 (100, M^+), 396 (6), 303.1 (17), 210 (9), 153.1 (7), 35.7 (3). Exact mass for $C_{34}H_{30}Fe_3$: 606.03957, observed: 606.03976 .

Method B(Wittig reaction): The title compound (322 mg, 53%) was also prepared from ferrocene-1,1'-diylbis(methyltriphenylphosphonium iodide) [$Fc(CH_2PPh_3I)_2$] (990 mg, 1 mmol), potassium *tert*-butoxide (268 mg, 2.4 mmol, 20% excess), and ferrocenecarboxaldehyde (513 mg, 2.4 mmol) in the same manner as above.

Method C (HWE reaction): To a stirred suspension of NaH (104 mg, a 60% suspension in oil, 2.6 mmol, washed with dry hexane) in dry THF (15 mL) was added a solution of 1,1'-ferrocenyl-bis(diethylmethylphosphonate)[20] (535 mg, 1.1 mmol) and 4 drops of 15-crown-5 in THF (20 mL) dropwise under argon at r.t. The resulting suspension was stirred for 10 minutes before ferrocenecarboxaldehyde (428 mg, 2 mmol) in THF (20 mL) was added slowly and the reaction mixture was heated at reflux for 12 h. After cooling the colored mixture was quenched with water (5 mL). The volatile solvent was then removed under reduced pressure, the residues sequentially washed with H_2O (3 x 20 mL) and MeOH (2 x 10 mL) with the assistance of sonication. After filtration, the crude product was further purified by recrystallization from CH_2Cl_2 to afford an orange red solid (0.48 g, 80%). The all-*E* compound is poorly soluble. ^1H NMR ($CDCl_3$): δ 6.40 (4H, s), 4.37 (4H, t, J = 1.8 Hz), 4.28 (4H, t, J = 1.8 Hz), 4.23 (4H, t, J = 1.8 Hz), 4.19 (4H, t, J = 1.8 Hz), 4.12 (10H, s). ^{13}C NMR ($CDCl_3$): δ 124.18, 110.44, 84.63, 70.20, 69.42, 68.82, 67.76, 66.55. MS m/e (intensity): 606 (100, M^+), 396 (9), 328.9 (19), 303 (17), 210 (18), 152.7 (11). 44 (4).

1,1'-Bis(4-ferrocenylbutadienyl)ferrocene (TFc4).

Ferrocene-1,1'-bis(2-formylvinyl) [**Fc(CH=CHCHO)$_2$**]. 1,1'-Ferrocenedialdehyde[19] (2.42 g, 10 mmol) and 1,3-dioxan-2-yl

methyltributylphosphonium bromide (Chapter 2) (24 mL of a 1.0 M solution in dimethylformamide (DMF), 24 mmol) were dissolved in dry DMF (100 mL) and heated with stirring to 80-90 °C. A solution of sodium ethoxide (26 mL of a 1.0 M solution in EtOH, 26 mmol) was then added dropwise over a period of 20 min, after which the reaction was heated at 90 °C for 48-72 h until $Fc(CHO)_2$ was fully consumed (monitored by TLC). The resulting mixture was poured into H_2O (ca. 200 mL) and then extracted with ethyl ether (4 x 150 mL) and the combined extracts dried over $MgSO_4$. After filtration the ether was removed under vacuum. The crude diacetal was obtained as a dark red oil and was not purified further. It was dissolved in tetrahydrofuran (THF) (50 mL) to which a 5% aqueous solution of H_2SO_4 was then added (25 mL). After being stirred at r.t. for 2 h, the mixture was poured into H_2O (*ca*. 200 mL), extracted with ethyl ether (3 x 150 mL), and then washed with brine (2 x 100 mL) and dried over Na_2SO_4. After filtration and removal of the ether, dark crude product was obtained. The crude product was subject to chromatography over silica gel, eluting with CH_2Cl_2/THF (5%), to give the semi-pure dark solid product, which was recrystallized with CH_2Cl_2/hexane. The final product was obtained as purple red crystals (1.76 g, 60%); m.p. 90-92 ^oC. ^1H NMR: δ 9.52 (2H, d, J = 7.7 Hz), 7.17 (2H, d, J = 15.6 Hz), 6.25-6.33 (2H, dd, J = 15.6 Hz, J = 7.7 Hz), 4.53 (4H, t, J = 1.8 Hz), 4.49 (4H, t, J = 1.8 Hz). ^{13}C NMR ($CDCl_3$): δ 193.0, 152.9, 127.8, 79.5, 73.7, 70.8. MS m/e (intensity): 294.1 (100, M^+), 238 (12), 175 (88), 147 (11), 121 (38), 91.1 (9), 55.9 (9), 39 (2).

1,1'-Bis(4-ferrocenylbutadienyl)ferrocene (**TFc4**).

Method A (Wittig reaction): To a suspension of ferrocenylmethyltriphenylphosphonium iodide (1.18 g, 2.2 mmol) in dry THF (35 mL) at 0 C under argon, was added potassium *tert*-butoxide (268 mg, 2.4 mmol, 20% excess) in one portion. The solution was stirred for 30 min, whereupon it turned rapidly from yellow to wine red, at this point, 1,1'-bis(2-formylvinyl)ferrocene (294 mg, 1 mmol) was added as a solution in anhydrous THF (10 mL) via a cannula. The resultant mixture was slowly warmed to room temperature and stirred for ca. 6 h before 10 mL of water was introduced to quench the reaction. After being extracted with diethyl ether (3 x 30 mL), the organic extract was washed with brine, dried over Na_2SO_4, and evaporated. The orange-red residue was purified by flash column chromatography on silica gel

(CH_2Cl_2/hexane (1:2)) to yield an orange red solid (69%, 21%). The compound is stable in solid, however, more air sensitive in solutions. ^{1}H NMR ($CDCl_3$): δ 6.06-6.44 (8H, m), 4.35-4.42 (4H, m, Cp-end), 4.21-4.32 (12H, m), 4.15 (5H, s), 4.12 (5H, s). MS m/e (intensity): 658 (100, M^+), 422 (5), 329 (22), 236 (16), 121 (11), 55.1 (8), 44 (13). Exact mass for $C_{38}H_{34}Fe_3$: 658.07087, observed: 658.06525.

Method B for (*E,E,E,E*)-product (HWE reaction): To a stirred suspension of NaH (104 mg, a 60% suspension in oil, 2.6 mmol, washed with dry hexane) in dry THF (15 mL) was added a solution of 1,1'-ferrocenyl-bis(diethylmethylphosphonate) (535 mg, 1.1 mmol) and 4 drops of 15-crown-5 in THF (20 mL) dropwise under argon at r.t. The resulting suspension was stirred for 10 minutes before (*E*)-(2-formylvinyl)ferrocene (480 mg, 2 mmol) in THF (20 mL) was added slowly and the reaction mixture was heated at reflux for 12 h. After cooling the colored mixture was quenched with water (5 mL). The volatile solvent was then removed under reduced pressure, the residues sequentially washed with H_2O (3 x 20 mL) and MeOH (2 x 10 mL) with the assistance of sonication. After filtration, the crude product was further purified by recrystallization from CH_2Cl_2 to afford an orange red solid (0.48 g, 73%). ^{1}H NMR($CDCl_3$): δ 6.43 (2H, dd, J = 15 Hz, J = 10.2 Hz), 6.38 (2H, dd, J = 14.7 Hz, J = 10.2 Hz), 6.27 (2H, d, J = 15 Hz), 6.21 (2H, d, J = 14.7 Hz), 4.37 (4H, t, J =1.8 Hz), 4.29 (4H, t, J =1.8 Hz), 4.25 (4H, t, J =1.8 Hz), 4.21 (4H, t, J =1.8 Hz), 4.12 (10H, s). ^{13}C NMR spectrum was not obtained due to the low solubility of the title compound. IR (neat, cm^{-1}): 3090w, 2920m, 1743m, 1612m, 1406m, 1258m, 1101m, 1022m, 999m, 981s, 921m, 801s(br), 725m, 528m, 482m. MS m/e (intensity): 658.1 (93, M^+), 472.1 (8), 355.1 (10), 329 (33), 291 (14), 236 (31), 186 (10), 121 (13).

(*E,E,E,E*)-1,1'-Bis[2-[5-(2-ferrocenylvinyl)-N-methylpyrrol-2-yl]vinyl]ferrocene (TFc4PyrMe). To a stirred suspension of NaH (104 mg, a 60% suspension in oil, 2.6 mmol, washed with dry hexane) in dry THF (15 mL) was added a solution of 1,1'-ferrocenyl-bis(diethylmethylphosphonate) (535 mg, 1.1 mmol) and 4 drops of 15-crown-5 in THF (20 mL) dropwise under argon at r.t. The resulting suspension was stirred for 10 minutes before (*E*)-1-methyl-5-(2-ferrocenylvinyl)-pyrrole-2- carboxaldehyde (Chapter 3) (638 mg, 2 mmol) in THF (20 mL) was added slowly and the reaction mixture was heated to reflux for 12 h. After cooling the colored mixture was

quenched with water (5 mL). The volatile solvent was then removed under reduced pressure, the residues dissolved in CH_2Cl_2 (60 mL), washed with H_2O (3 x 30 mL), dried over $MgSO_4$ and evaporated to afford the crude product. Purification was achieved through flash column chromatography on silica gel using CH_2Cl_2 as eluent to afford a red crystalline (0.47 g, 57.5%). ^{1}H NMR($CDCl_3$): δ 6.59 (2H, d, J = 15.9 Hz), 6.55 (2H, d, J = 15.9 Hz), 6.50 (2H, d, J = 15.9 Hz), 6.43 (2H, d, J = 15.9 Hz), 6.39 (2H, d, J = 3.9 Hz), 6.34 (2H, d, J = 3.9 Hz), 4.39 (4H, t, J =1.8 Hz), 4.36 (4H, t, J = 1.8 Hz), 4.24 (8H, s), 4.13 (8H, s), 3.38 (6H, s). ^{13}C NMR ($CDCl_3$): δ 133.58, 124.70, 123.40, 115.37, 114.93, 106.47, 85.47, 84.51, 69.97, 69.40, 69.06, 67.75, 66.63, 30.38. IR (neat, cm^{-1}): 3086w, 2920w, 2847w, 1773w, 1658m, 1620br, 1534m, 1443m, 1406m, 1272m, 1103m, 1041m, 1025m, 937s, 806s, 750m, 484s. FABMS: *m/z* 816 [M^+]. Anal. Calcd for $C_{48}H_{44}N_2Fe_3$: C, 70.62; H, 5.43. Found: C, 70.76; H, 5.55.

(*E,E,E,E*)-1,1'-Bis[2-[5-(2-ferrocenylvinyl)thiophen-2-yl]vinyl]ferrocene (TFc4Th).

Diethyl (5-bromothiophen-2-yl)methylphosphonate.[22] A 250 mL flask fitted with a reflux condenser was charged with 2-bromothiophene (9.7 mL, 100 mmol), paraformaldehyde (3.3 g, 110 mmol) and acetic acid (50 mL), hydrobromic acid in acetic acid (25 mL, 33%) was added and the solution was heated in a well ventilated fume cupboard at 50 ^{o}C for 3 h. After cooling the solution, the reaction mixture was extracted with CH_2Cl_2 (200 mL) and washed with cold water (2 x 50 mL). The organic layer was dried over $MgSO_4$, evaporated giving 24 g of a brown oil, which was mixed with triethylphosphite (16 mL). The viscous solution was stirred at 150 ^{o}C overnight. Evaporation of the excess of the triethylphosphite under reduced pressure yielded 30 g of a dark oil. Chromatographic separation on silica gel was achieved using ether to ether/methanol (99:1) to isolate a red oil (18 g, 57.6%). ^{1}H NMR ($CDCl_3$): δ 6.88 (1H, d, J = 3.9 Hz), 6.72 (1H, d, J = 3.9 Hz), 4.03 (4H, dq, J = 7.1, 7.4 Hz), 3.17 (2H, d, J_{HP} = 20.7 Hz), 1.27 (6H, t, J = 7.1 Hz).

(*E,E*)-1,1'-Bis[2-(5-bromothiophen-2-yl)vinyl]ferrocene [**Fc(CH=CHThBr)$_2$**]. To NaH (960 mg, a 60% suspension in oil, 24 mmol) washed twice with dry hexane was added (20 mL) and 15-crown-5 (132 mg, 0.6 mmol, 10%). A mixture of 1,1'-ferrocenedialdehyde (0.73 g, 3 mmol) and diethyl (5-bromothiophen-2-

yl)methylphosphonate (2.1 g, 6.6 mmol) in THF (25 mL) was added slowly and the suspension was stirred at r. t. overnight. The reaction mixture was quenched by adding water (20 mL) at 0 ^{o}C, and extracted with ether (80 mL). The organic phase was dried over Na_2SO_4, the solvent evaporated, and the residue was purified by column chromatography on silica gel (CH_2Cl_2). The product was isolated as a red powder (1.61 g, 96%). ^{1}H NMR ($CDCl_3$): δ 6.82 (2H, d, J = 3.6 Hz), 6.53 (2H, d, J = 15.9 Hz), 6.50 (2H, d, J = 3.6 Hz), 6.30 (2H, d, J = 15.9 Hz), 4.36 (4H, t, J = 1.8 Hz), 4.25 (4H, t, J = 1.8 Hz). ^{13}C NMR ($CDCl_3$): δ 145.21, 130.40, 125.95, 125.01, 120.24, 110.24, 84.96, 70.56, 68.09. IR (KBr pellet, cm^{-1}): 3086.8, 1766.6, 1622.6, 1466.8, 1428.1, 1222.4, 1041.8, 938.6, 788.6, 478.5. MS m/e (intensity): 559.8 (100, M^+), 557.8 (50), 227 (5), 171 (78), 139 (23), 89.1 (3), 56 (3).

(*E,E*)-1,1'-Bis[2-(5-formylthiophen-2-yl)vinyl]ferrocene [**Fc(CH=CHThCHO)$_2$**]. To a solution of (*E,E*)-1,1'-bis[2-(5-bromothiophen-2-yl)vinyl]ferrocene (1.12 g, 2 mmol) in THF (30 mL) at –78 ^{o}C was added slowly butyllithium (3.0 mL of a 1.6 M solution in hexane, 4.8 mmol, 20% excess) and the dark red mixture was stirred at –78 ^{o}C for 45 min. DMF (1.5 mL, 4.8 mmol) was added at –78 ^{o}C and the reaction was warmed to room temperature and stirred for 1.5 h. After hydrolysis with diluted HCl, the mixture was extracted with CH_2Cl_2 (2 x 30 mL), dried over $MgSO_4$ and concentrated. The residue was purified by flash chromatography on silica gel, eluting with CH_2Cl_2 to give the dialdehyde as a dark red crystalline solid (0.67 g, 73%). ^{1}H NMR ($CDCl_3$): δ 9.76 (2H, s), 7.48 (2H, d, J = 3.6 Hz), 6.82 (2H, d, J = 3.6 Hz), 6.63 (4H, s), 4.48 (4H, t, J = 1.8 Hz), 4.36 (4H, t, J = 1.8Hz). ^{13}C NMR ($CDCl_3$): δ 182.67, 153.52, 140.60, 137.76, 131.03, 125.38, 119.37, 83.0, 71.20, 68.73. IR (KBr pellet, cm^{-1}): 3075.9, 2788.4, 1890, 1654.3, 1613.6, 1472.4, 1436.3, 1379.6, 1236.1, 1044.4, 937.6, 795.9, 485. MS m/e (intensity): 458 (100, M^+), 257 (23), 229 (4), 195 (8), 139 (10), 115 (5). Anal. Calcd for $C_{24}H_{18}FeO_2S_2$: C, 62.89; H, 3.96. Found: C, 62.67; H, 4.08.

(*E,E,E,E*)-1,1'-Bis[2-[5-(2-ferrocenylvinyl)thiophen-2-yl]vinyl]ferrocene (**TFc4Th**). To a suspension of ferrocenylmethyltriphenylphosphonium iodide (704 mg, 1.2 mmol) in dry THF (25 mL) at 0 ^{o}C under argon, was added potassium *tert*-butoxide (134 mg, 1.2 mmol, 20% excess) in one portion. The solution was stirred for 30 min,

whereupon it turned rapidly from yellow to wine red, at this point, 1,1'-bis[2-(5-formylthiophenyl)vinyl]ferrocene (229 mg, 0.5 mmol) was added as a solution in anhydrous THF (10 mL) via a cannula. The resultant mixture was slowly warmed to room temperature, refluxed for 6 h and cooled to room temperature before 10 mL of water was introduced to quench the reaction. After the volatile solvent was evaporated, the aqueous phase was extracted with CH_2Cl_2 (3 x 30 mL), dried over Na_2SO_4, and evaporated. The orange-red residue was purified by flash column chromatography on silica gel using CH_2Cl_2/hexane (1:1) as eluent, the first band was collected and evaporated to yield the desired compound as a brown red solid (260 mg, 63%), m.p. >210 ^oC, decomposed; the second band was also recovered as the mono-condensed byproduct, a dark red solid (35 mg , 11%). Title compound: ^1H NMR($CDCl_3$): δ 6.74 (2H, d, J = 3.9 Hz), 6.71 (2H, d, J = 15.9 Hz), 6.69 (2H, d, J = 3.9 Hz), 6.68 (2H, d, J = 15.9 Hz), 6.58 (2H, d, J = 15.9 Hz), 6.52 (2H, d, J = 15.9 Hz), 4.42 (4H, t, J =1.7 Hz), 4.39 (4H, t, J =1.7 Hz), 4.29 (4H, t, J =1.7 Hz), 4.27 (4H, t, J =1.8 Hz), 4.16 (10H, s). ^{13}C NMR ($CDCl_3$): δ 141.64, 126.86, 125.91, 125.75, 125.53, 120.50, 119.91, 84.32, 83.35, 70.44, 69.52, 69.38, 68.25, 66.99. IR (KBr pellet, cm^{-1}): 3081.4, 3022.9, 1733.5, 1652.7, 1635.1, 1616.6, 1456.7, 1105.1, 1042.6, 939, 818.2, 463.6. MS m/e (intensity): 822.1 (100, M^+), 612.1 (16), 504 (5), 439.1 (9), 411.1 (16), 227.1 (18), 121 (8), 43.9 (11). Exact mass for $C_{46}H_{38}Fe_3S_2$: 822.04631, observed: 822.04434.

(*E,E,E*)-1-[2-[5-(2-ferrocenylvinyl)thiophen-2-yl]vinyl]-1'-[2-(5-formylthiophen-2-yl)vinyl]ferrocene. Mono-aldehyde byproduct from above: ^1H NMR($CDCl_3$): δ 9.74 (1H, s), 7.48 (1H, d, J = 3.9 Hz), 6.84 (1H, d, J = 3.9 Hz), 6.76 (1H, d, J = 16.2 Hz), 6.69 (2H, s, thiophene), 6.65 (1H, d, J = 15.9 Hz), 6.63 (1H, d, J = 16.2 Hz), 6.61 (1H, d, J = 15.6 Hz), 6.55 (1H, d, J = 15.9 Hz), 6.38 (1H, d, J = 15.6 Hz), 4.46 (2H, t, J =1.8 Hz), 4.44 (2H, t, J =1.8 Hz), 4.42 (2H, t, J =1.8 Hz), 4.35 (2H, t, J =1.8 Hz), 4.30 (2H, t, J =1.8 Hz), 4.28 (2H, t, J =1.8 Hz), 4.16 (5H, s). ^{13}C NMR ($CDCl_3$): δ 182.67, 153.68, 141.76, 141.56, 140.66, 137.62, 131.70, 127.05, 125.95, 125.53, 125.16, 125.04, 120.93, 119.80, 119.08, 84.87, 83.26, 82.77, 71.11, 70.41, 69.53, 69.47, 68.80, 68.15, 66.99.

1,1'-Bis[2-[2-ferrocenylvinyl]thiovinyl]ferrocene (TFc4S).

To a suspension of dimethylthioether-a,a'-bis(triphenylphosphonium) bromide (1.5 g, 2 mmol), ferrocencarboxaldehyde (0.43 g, 2 mmol) and 1,1'-ferrocenedialdehyde

(0.24 g, 1 mmol) in anhydrous MeOH (20 mL) at 0°C, was added sodium methoxide (9.2 mL of a 0.5M solution in MeOH, 4.6 mmol) under argon with stirring. The mixture was brought to room temperature and stirred overnight, whereupon red precipitate started to isolate from the solution after 2 h stirring. The solution was then concentrated to dryness, extracted with $CHCl_3$ (40 mL), which was washed with H_2O (30 mL), dried over MgSO4 and evaporated. The dark residue was purified by column chromatography on silica gel, eluting with CH_2Cl_2/hexane (1:1). The first two bands afforded BFc4S and the mono-coupled byproduct, followed by the desired compound in the third band. After solvent evaporation, the final product was obtained as an orange powder (170 mg, 23%). ^{1}H NMR ($CDCl_3$): δ 6.15-6.39 (ca. 8H, m), 5.9-6.0 (m, minor), 4.55 (ca. 4H, m) 4.23-4.35 (ca. 12H, m), 4.13-4.15 (8H, m). FABMS: 722.1 (100, M^+),

1,1'-Bis(5-ferrocenylpenta-3-one-1,4-dienyl)ferrocene (TFc4CO).

A solution of 1,1'-ferrocenedialdehyde (0.24 g, 1 mmol), 2-acetylvinylferrocene (see Chapter 2) (0.56 g, 2.2 mmol), and potassium hydroxide (1.0 g) in ethanol was heated at 60 °C for ca. 6 h under an argon atmosphere. After 2 h stirring, precipitate started separating from the reaction solution, the completion of the reaction was then monitored by TLC. The crude product was filtered off, washed with water, ethanol, and then dried. Further purification was achieved by flash column chromatography of the crude product on silica gel, eluting with CH_2Cl_2/THF (95:5). The final product was obtained as a purple solid (0.51 g, 71.5%). This compound is air sensitive, need to be handled carefully. ^{1}H NMR ($CDCl_3$): δ 7.55 (2H, d, J = 15.6 Hz), 7.47 (2H, d, J = 15.6 Hz), 6.53 (2H, d, J = 15.6 Hz), 6.51 (2H, d, J = 15.6 Hz), 4.53 (8H, t), 4.42 (8H, m, mid-Cp), 4.16 (10H, s). ^{13}C NMR ($CDCl_3$): δ 187.53, 144.91, 142.38, 124.56, 123.51, 80.98, 79.50, 73.0, 71.53, 70.55, 70.03, 69.28. MS m/e (intensity): 714.1(48, M^+), 434 (5.0), 367.9 (4), 301.6 (13), 248 (3), Exact mass for $C_{40}H_{34}O_2Fe_3$: 714.06070, observed: 714.05929.

(*E,E*)-1,1'-Bis[2-(ferrocenylcarbonyl)vinyl]ferrocene (TFc2CO-A). Sodium hydroxide (10 mL of 20% aqueous solution) was added into a stirred solution of 1,1'-ferrocenedialdehyde (1.21 g, 5 mmol) and acetylferrocene (2.74 g, 12 mmol) in methanol/THF (2:1) (30 mL). The reaction mixture was stirred at room temperature for ca. 48 h, whereupon the completion was monitored by TLC. The volatile solvent was

then evaporated and the aqueous phase was extracted with $CHCl_3$ (2 x 30mL). The organic extracts were dried over $MgSO_4$, concentrated under reduced pressure. Purification was achieved by column chromatography on silica gel, eluting with CH_2Cl_2/THF (98:2). Small amount of unreacted acetylferrocene, dialdehyde and mono-condensed byproduct were sequentially eluted, followed by the desired compound. Upon concentration, the final product was obtained as a deep red crystalline solid (2.38 g, 72%). ^{1}H NMR ($CDCl_3$): δ 7.61 (2H, d, J = 15.6 Hz), 6.67 (2H, d, J = 15.6 Hz), 4.83 (4H, t, J = 1.8 Hz), 4.55 (4H, t, J = 1.8 Hz), 4.52 (4H, t, J = 1.8 Hz), 4.47 (4H, t, J = 1.8 Hz), 4.18 (10H, s). ^{13}C NMR ($CDCl_3$): δ 192.51, 140.77, 121.5, 121.3, 80.9, 80.7, 73.0, 72.9, 72.7, 70.5, 70.3, 70.0, 69.8. IR (KBr pellet, cm^{-1}): 3093.1, 1649.4, 1587.7, 1449.9, 1378.5, 1247.2, 1082.8, 979.2, 821.7, 485.4. MS m/e (intensity): 662.1 (100, M^+), 597 (42), 359 (33), 331 (17), 238 (8), 121 (13), 55.9 (3). Exact mass for $C_{36}H_{30}O_2Fe_3$: 662.02940, observed: 662.03711. Anal. Calcd for $C_{36}H_{30}Fe_3O_2$: C, 65.31; H, 4.57. Found: C, 65.73; H, 4.49.

Note: using THF as co-solvent is crucial which avoided the intermediate mono-condensation aldehyde isolating from the reaction mixture. The reaction time can be shortened by heating under reflux.

(*E,E*)-1,1'-Bis[(2-ferrocenylvinyl)carbonyl]ferrocene (TFc2CO-B). A solution of 1,1'-diacetylferrocene (0.54 g, 2 mmol), ferrocenecarboxaldehyde (0.95 g, 4.4 mmol), and potassium hydroxide (1.5 g) in ethanol (50 mL) was heated at 60 ^{o}C for ca. 6 h under an argon atmosphere. After 2 h stirring, a brick-red precipitate started separating from the reaction solution, the completion of the reaction was then monitored by TLC. The crude product was filtered off, washed with water, ethanol, and then dried. Further purification was achieved by flash column chromatography of the crude product on silica gel, eluting with CH_2Cl_2/THF (95:5). The final product was obtained as a pink red solid (0.63 g, 48%). ^{1}H NMR ($CDCl_3$): δ 7.7 (2H, d, J = 15.6 Hz), 6.67 (2H, d, J = 15.6 Hz), 4.85 (4H, t, J = 2.0 Hz), 4.62 (4H, t, J = 1.8 Hz), 4.53 (4H, t, J = 2.0 Hz), 4.47 (4H, t, J = 1.8 Hz), 4.17 (10H, s). ^{13}C NMR ($CDCl_3$): δ 191.71, 143.67, 119.97, 82.35, 79.47, 74.53, 71.58, 70.1, 69.34, 69.1. MS m/e (intensity): 662.1 (100, M^+), 597 (42), 359 (33), 331 (17), 238 (8), 121 (13), 55.9 (3). Exact mass for $C_{36}H_{30}O_2Fe_3$: 662.02940, observed: 662.02646.

Ferrocenyl(2-ferrocenylvinyl) Sulfide (BFc2S).

Ammonium ferrocenesulfonate monohydrate (**$FcSO_3NH_4 \cdot H_2O$**).[23] To a stirred solution of ferrocene (20 g, 107.5 mmol) in acetic anhydride (350 mL), was slowly added chlorosulfonic acid (7.25 mL, 109 mmol) at room temperature. The reaction mixture was stirred overnight and cooled with ice/water. 600 mL of ice/water was carefully added to the mixture. The unreacted ferrocene precipitated and was removed by filtration. The solution was evaporated to dryness under vacuum and the residue was extracted with methanol in a Soxhlet apparatus. The methanol solution was concentrated and conc. $NH_3 \cdot H_2O$ was added to adjust pH to 10. The precipitated solid was collected by filtration to give **$FcSO_3NH_4 \cdot H_2O$** (17.5 g, 54%) as a monohydrate in form of brown yellow plates. ^{1}H NMR (DMSO-d_3): δ 7.09 (4H, br), 4.29 (2H, t), 4.17 (5H, s), 4.05 (2H, t).

Ferrocenylsulphonyl chloride (**$FcSO_2Cl$**).[23] Ammonium ferrocenesulfonate monohydrate (6 g, 20 mmol) was added in portion to phosphorus trichloride (60 mL), preheated to 50 ^{o}C, at such a rate as to maintain gentle refluxing. The mixture was then heated in an oil bath for 4 h at 70 ^{o}C, diluted with boiling ligroin (30 mL), and filtered. The orange filtrate was evaporated under reduced pressure and the residual solid crystallized from ligroin, giving $FcSO_2Cl$ (4.08 g, 72%) as crimson needles, m. p. 100 ^{o}C, which rapidly darkened in moisture air. ^{1}H NMR ($CDCl_3$): δ 4.84 (2H, t), 4.58 (2H, t), 4.43 (5H, s).

Ferrocenethiol (**FcSH**) and Diferrocenyl Disulfide (**FcS-SFc**). To a stirred solution of lithium aluminum hydride (1.9 g, 50 mmol) in THF (50 mL) under argon, ferrocenesulphonyl chloride (4.08 g, 14.3 mmol) in the same solvent (50 mL) was added during 20 min. After refluxing for 2 h, a mixture of concentrated HCl and distilled water (1:5) purged with argon was added dropwise and extracted with ether. The organic layer was washed with brine, dried over Na_2SO_4 and evaporated, yielding ferrocenethiol as a pale brown foul-smelling oil (2.03 g, 65%). ^{1}H NMR ($CDCl_3$): δ 4.31 (2H, t), 4.17 (5H, s), 4.14 (2H, t), 2.57 (1H, s).

Ferrocenethiol is very unstable and spontaneously dimerizes within two days in a closed flask. Diferrocenyl Disulfide was thereby obtained as a yellow plate, m.p. 190 ^{o}C (lit. 192 ^{o}C), which was used for next reactions without further purification. The disulfide could be easily reduced back to the thiol by lithium aluminium hydride using the method

described above. ^{1}H NMR ($CDCl_3$): δ 4.27 (4H, m), 4.13(5H, s). MS m/e (intensity): 434 (36.5, M^+), 337.9 (18), 271.9 (17.5), 217 (100), 151.9 (17), 56 (9.5).

Bromomethyltriphenylphosphonium Bromide.[24] In a 1 L flask fitted with condenser, a stirred solution of triphenylphosphine (104.9 g., 0.4 moles), methylene bromide (34.8 g., 0.2 moles), and toluene (500 mL) was heated at reflux for 24 h under nitrogen. The resulting suspension was filtered and the solid was dried at 80 ^{o}C (20 mm.) to yield tan crystals. The solid was dissolved in minimum methanol, reprecipitated with ethyl acetate, filtered, and washed with ether. The reprecipitation process was repeated one more time to give 33 g (38%) of white needles. The phosphonium salt was dried at 110 ^{o}C under vacuum for 48 h before being used; m.p. 238-240 ^{o}C, lit. m.p. 240-241 ^{o}C. ^{1}H NMR ($CDCl_3$): δ 7.97-7.92 (6H, m), 7.91-7.89 (3H, m), 7.70-7.67 (6H, m), 5.81 (2H, d, J = 5.7 Hz).

1-Bromo-2-ferrocenylethene (**FcCH=CHBr**). A slurry of KO*t*Bu (3.5 g, 31.25 mmol, 1.25 equiv.) in dry THF (100 mL) was added dropwise under argon to a slurry of bromomethyltriphenylphosphonium bromide (13.63 g, 31.25 mmol, 1.25 equiv.) in dry THF (100 mL) at -78 °C. After 1 h, a solution of ferrocenecarboxaldehyde (5.35 g, 25 mmol) in dry THF (20 mL) was added dropwise into the resulting light yellow suspension. The reaction mixture was allowed to warm to room temperature and stirred at room temperature until the reaction was complete by TLC (approx. 15 h). Water and diethyl ether (100 mL each) were added, and the layers were separated. The aqueous layer was extracted with more ether (2 x 100 mL); the combined ether extracts were washed with saturated aqueous sodium chloride (2 x 100 mL), dried over sodium sulfate, filtered, and evaporated under reduced pressure. The residue was dissolved into hexane (a large amount of triphenylphosphine oxide was poorly soluble and removed) and passed through a silica gel plug to yield a red oil or low melting point solid (5.6 g, 77%), which was an E/Z isomer mixture (ca. 1:1 ratio). (*Z*)-isomer: ^{1}H NMR ($CDCl_3$): δ 6.77 (1H, d, J = 7.8 Hz), 6.16 (1H, d, J = 7.8 Hz), 4.75 (2H, m), 4.29 (2H, m), 4.15 (5H, s); ^{13}C NMR ($CDCl_3$): δ 102.93, 101.43, 79.35, 69.7, 69.56, 69.36. (*E*)-isomer: ^{1}H NMR ($CDCl_3$): δ 6.78 (1H, d, J = 13.8 Hz), 6.24 (1H, d, J = 13.8 Hz), 4.29 (2H, m), 4.24 (2H, m), 4.16 (5H, s); ^{13}C NMR ($CDCl_3$): δ 135.19, 131.3, 82.06, 69.56, 68.36, 66.79.

Ferrocenyl(2-ferrocenylvinyl) Sulfide (**BFc2S**). A mixture of 1-ferrocenyl-2-bromoethene (0.291 g, 1 mmol), diferrocenyl disulfide (0.217 g, 0.5 mmol), copper (I) iodide (0.19 g, 1 mmol) and hexamethylphosphoric triamide (HMPA) (5 mL) was charged into a 25 mL flask equipped with a reflux condenser. The reaction mixture was heated for 2 h at 120-140 ^{o}C under argon, at approximately 80 ^{o}C the diferrocenyl disulfide was fully dissolved. The resulting dark suspension was cooled, treated with 50 mL water, and extracted with diethyl ether (3 x 50 mL). The organic phase was washed with brine, dried over Na_2SO_4 and evaporated to give a dark red gum. Chromatographic purification was achieved on silica gel using hexane to elute the unreacted FcCH=CHBr, hexane/CH_2Cl_2 (3:1) to elute an unknown by-product and the desired product as an orange solid (180 mg, 42.1%), which turned out to be a mixture of cis/trans isomers; m.p. 110 ^{o}C. (*E*)-isomer: ^{1}H NMR ($CDCl_3$): δ 6.24 (1H, d, J = 15.3 Hz), 6.04 (1H, d, J = 15.3 Hz), 4.37 (4H, m), 4.28 (4H, m), 4.23 (5H, s), 4.08 (5H, s); ^{13}C NMR ($CDCl_3$): δ 126.98, 125.77, 83.51, 81.8, 73.44, 69.38, 68.8, 66.46. (*Z*)-isomer: ^{1}H NMR ($CDCl_3$): δ 6.05 (2H, s), 4.55 (4H, m), 4.38 (4H, m), 4.25 (5H, s), 4.17 (5H, s); ^{13}C NMR ($CDCl_3$): δ 123.25, 122.61, 81.48, 78.45, 72.72, 69.87, 69.66, 68.95. IR (KBr pellet, cm^{-1}): 3091.3, 1639.1 (br), 1592.7, 1409, 1379, 1168.3, 1103.5, 1043.3, 1022, 1000, 821.3, 560.8. MS m/e (intensity): 428.1 (100, M^{+}), 275.1 (20), 214.1 (10), 186.1 (9), 121 (10), 57 (5), 43(4). Exact mass for $C_{22}H_{20}Fe_2S$: 427.99845, observed: 427.99668.

Ferrocene-1,1'-bis[2-(ferrocenylthio)vinyl] (TFc2S-A):

1,1'-Bis(2-bromovinyl)ferrocene [**Fc(CH=CHBr)$_2$**]. The same procedure for **FcCH=CHBr** was followed to synthesize the title compound (1.53 g, 77.2%) from bromomethyltriphenylphosphonium bromide ($[Ph_3PCH_2Br]^{+}[Br]^{-}$) (5.23 g, 12 mmol, 1.2 equiv.) and 1,1'-ferrocenedialdehyde (1.21 g, 5 mmol) in the presence of KO^{t}Bu (1.35 g, 12 mmol, 1.2 equiv.). The reaction mixture was stirred at room temperature for approx. 18 h. Purification was achieved by passing the crude material through a silica gel plug to yield the final product, which is an inseparable mixture of *trans,trans*, *trans,cis*, *cis,cis* isomers. The compound was very oxidatively unstable, and decomposed into black powder within two days which made long period storage fairly difficult. For this reason, the compound was always prepared freshly before use. ^{1}H NMR ($CDCl_3$): δ 6.76-6.50 (2H, m), 6.28-6.23 (2H, m), 4.74, 4.71 (ca. 2H, m), 4.29-4.25, 4.22 (6H, m). ^{13}C NMR

($CDCl_3$): δ 134.12, 130.47, 104.03, 103.42, 102.0, 83.12, 80.47, 71.18, 70.89, 70.77, 67.93. MS m/e (intensity): 395.9 (40, M^+), 236 (100), 179.1 (40), 145 (25), 89 (43), 38.8 (10).

1,1'-Bis[2-(ferrocenylthio)vinyl]ferrocene **(TFc2S-A).** The same procedure for **BFc2S** was used to synthesize the title compound (135 mg, 0.2 mmol, 40.2%) from ferrocene-1,1'-bis(2-bromovinyl) (198 mg, 0.5 mmol), diferrocenyl disulfide (217 mg, 0.5 mmol) and copper (I) iodide (190 mg, 1 mmol). The reaction mixture was refluxed in 5 mL HMPA at 120 ^oC for 2 h., and the crude product was purified by chromatography on silica gel using hexane/CH_2Cl_2 (3:1) to sequentially elute the unreacted 1,1'-bis(2-bromovinyl)ferrocene, an unknown ferrocenyl derivative byproduct, and the desired compound as a mixture of *cis/trans* isomers. **TFc2S-A** was achieved as an orange-red crystalline solid; m.p. 137-139 ^oC. (*E, E*)-isomer: ^1H NMR ($CDCl_3$): δ 6.25 (2H, d, J = 15.6 Hz), 6.04 (2H, d, J = 15.6 Hz), 4.38 (4H, t, J = 1.8 Hz), 4.27 (4H, t, J = 1.8 Hz), 4.23 (10H, s), 4.18 (4H, t, J = 1.8 Hz), 4.10 (4H, t, J = 1.8 Hz). ^{13}C NMR ($CDCl_3$): δ 127.64, 125.01, 84.36, 81.48, 73.41, 70.24, 69.77, 69.21, 67.46. (*Z, Z*)-isomer: ^1H NMR ($CDCl_3$): δ 6.05 (2H, d, J = 10.5 Hz), 5.91 (2H, d, J = 10.5 Hz), 4.46 (4H, t, J = 1.8 Hz), 4.41 (4H, t, J = 1.8 Hz), 4.30 (4H, t, J = 1.8 Hz), 4.26 (10H, s), 4.22 (4H, t, J = 1.8 Hz). ^{13}C NMR ($CDCl_3$): δ 125.1, 121.96, 82.77, 78.52, 72.73, 69.94, 69.83, 69.64, 69.56. (*E, Z*)-isomer: ^1H NMR ($CDCl_3$): δ 6.19 (1H, d, J = 15.6 Hz), 6.10 (1H, d, J = 10.5 Hz), 6.02 (1H, d, J = 10.5 Hz), 5.96 (1H, d, J = 15.6 Hz), 4.52 (4H, t, J = 1.8 Hz), 4.40 (4H, t, J = 1.8 Hz), 4.24 (4H, m), 4.25 (10H, s), 4.19 (4H, t, J = 1.8 Hz). ^{13}C NMR ($CDCl_3$): δ 127.08, 123.83, 123.64, 122.18, 84.40, 78.38, 73.51, 72.61, 70.30, 69.90, 69.77, 67.51. IR (KBr pellet, cm^{-1}): 3090, 2961, 1635.7 (br), 1590.6, 1409.3, 1260.2, 1104.3, 1021.3, 805.6, 722.5. MS m/e (intensity): 670 (100, M^+), 454 (3), 335 (13), 272 (17), 218 (12), 57.1 (6), 43(5). Exact mass for $C_{34}H_{30}Fe_3S_2$: 669.98371, observed: 669.98238.

Ferrocene-1,1'-bis[2-(ferrocenylvinyl)thio] (TFc2S-B).

1,2,3-Trithia-[3]-ferrocenophane (**FcS_3**). The title compound was prepared by modifying the literature procedures.[25] In a nitrogen-flushed 500 mL flask, ferrocene (8 g, 43 mmol) was dissolved in dry hexane (200 mL) and TMEDA (16 mL, 106 mmol, 23% excess) was added. The mixture was stirred while *n*-BuLi (39.6 mL of a 2.5 M solution in hexane, 99 mmol, 15% excess) was added dropwise. This produced a homogeneous

solution which was stirred overnight under argon at room temperature. An orange solid formed during this period. The hexane supernatant containing excess TMEDA, *n*-BuLi and unreacted ferrocene was removed through a cannula by a positive pressure of argon. Fresh dry oxygen-free hexane (80 mL) was added to the orange solid, the mixture was stirred and then allowed to settle, and the solvent was removed as above. This washing procedure was repeated once more.

The addition of dry oxygen-free 1,2-dimethoxyethane (300 mL) to washed 1,1'-dilithioferrocene·TMEDA mass gave a clear, deep orange red solution. Sublimed sulfur (6 g, 187 mmol) was then added to the rapidly stirred solution caused it to warm and darken. The resulting mixture was heated at reflux for 12 h, cooled and then filtered through a bed of "Celite". The filtrate was treated with diethyl ether (150 mL) and washed with 10% aqueous sodium hydroxide (3 x 100 mL). The combined aqueous fractions were washed with diethyl ether (3 x 100 mL). The combined ether fractions were dried over Na_2SO_4 and evaporated to give a dark semi-solid. The solid was passed through a short silica gel column, eluting with hexane, to remove impurities and remaining sulfur and yield an orange crystal, which is a mixture of the desired compound and recovered ferrocene. Fractional vacuum sublimation was used to separate ferrocene (1.0 mmHg, 70-75 ^{o}C) from **FcS_3** (0.3 mmHg, 160 ^{o}C) to afford an orange crystalline mass (5.54 g, 46%). 1,2,3-trithia-[3]-ferrocenophane is air stable and readily soluble in both polar and non-polar organic solvent. ^{1}H NMR ($CDCl_3$): δ 4.51 (2H, quintet, J = 1.2 Hz), 4.42 (2H, sextet, J = 1.2 Hz), 4.34 (2H, sextet, J = 1.2 Hz), 3.82 (2H, sextet, J = 1.2 Hz). MS m/e (intensity): 280 (100, M^{+}), 246 (5), 216 (13), 183.9 (45), 159.1 (6), 99.9 (12), 56 (10).

Ferrocene-1,1'-dithiol [**$Fc(SH)_2$**]. To a suspension of $LiAlH_4$ (1 g, 26 mmol, 2 equiv.) in dry diethyl ether (200 mL) was added, in small portions, 1,2,3-trithia-[3]-ferrocenophane (3.55 g, 12.7 mmol). The reaction mixture became warm and evolved hydrogen sulfide. After stirring under reflux for 2 h, the reaction mixture was poured onto 300 mL of ice-cold oxygen-free water. The addition of potassium hydroxide (5 g) gave an orange aqueous layer and a yellow ether layer. The aqueous layer was separated, extracted with diethyl ether (2 x 50 mL) and then acidified with concentrated HCl which caused the product to separate as a bright yellow suspension. The suspended material was

extracted into 300 mL of ether and the solvent was removed in vacuo, to give the product as bright yellow crystals (2.7 g, 85%). This material proved to be pure enough for most purposes. However, an analytical sample was prepared by sublimation (0.3 mmHg, 80 ^{o}C, water cooled probe) to give clear yellow crystals, m.p. 59-60 ^{o}C. The complex is moderately air sensitive in the solid; solutions, however, are more sensitive. ^{1}H NMR ($CDCl_3$): δ 4.29 (4H, t, J = 1.8 Hz), 4.19 (4H, t, J = 1.8 Hz), 2.87 (2H, s). MS m/e (intensity): 250 (100, M^{+}), 216.9 (21), 183.9 (22), 151.2 (18), 121 (9), 97 (16), 56 (9).

1,1'-Bis[2-(ferrocenylvinyl)thio]ferrocene (**TFc2S-B**). The same procedure for **BFc2S** was used to synthesize the title compound (120 mg, 0.179 mmol, 35.8%) from ferrocene-1,1'-dithiol (125 mg, 0.5 mmol), 1-ferrocenyl-2-bromoethene (291 mg, 1 mmol) and copper (I) iodide (190 mg, 1 mmol). The reaction mixture was refluxed in 5 mL HMPA at 120 ^{o}C for 2 h., and the crude product was purified by chromatography on silica gel using hexane/CH_2Cl_2 (3:1) to sequentially elute the unreacted FcCH=CHBr, an unknown ferrocenyl derivative byproduct, and the desired compound as a mixture of cis/trans isomers, which is an orange-red crystalline; m.p. 108 ^{o}C. (*E, E*)-isomer: ^{1}H NMR ($CDCl_3$): δ 6.29 (2H, d, J = 15.3 Hz), 6.13 (2H, d, J = 15.3 Hz), 4.42 (4H, t, J = 1.7 Hz), 4.32 (4H, t, J = 1.7 Hz), 4.26 (4H, t, J = 1.7 Hz), 4.22 (4H, t, J = 1.7 Hz), 4.09 (10H, s). ^{13}C NMR ($CDCl_3$): δ 126.97, 126.0, 83.33, 81.64, 74.19, 71.09, 69.54, 68.99, 66.56. (*Z, Z*)-isomer: ^{1}H NMR ($CDCl_3$): δ 6.10 (2H, d, J = 10.5 Hz), 6.05 (2H, d, J = 10.5 Hz), 4.57 (4H, t, J = 1.8 Hz), 4.46 (4H, t, J = 1.8 Hz), 4.36 (4H, t, J = 1.8 Hz), 4.26 (4H, t, J = 1.8 Hz), 4.17 (10H, s). ^{13}C NMR ($CDCl_3$): δ 123.31, 122.29, 83.25, 80.85, 73.75, 71.17, 71.10, 69.42, 68.92. IR (KBr pellet, cm^{-1}): 3093, 3010, 2922.6, 2862.9, 1645.8 (br), 1466.1, 1409.1, 1104.1, 1031.5, 819.7, 769.4. MS m/e (intensity): 670 (5, M^{+}), 434 (26), 338 (18), 272 (17), 218 (100), 152 (30), 97 (11), 55.9(13). Exact mass for $C_{34}H_{30}Fe_3S_2$: 669.98371, observed: 669.98635.

Results and Discussion

Synthesis

Preparations of Symmetric Linker-Bridged **TFc2** and **TFc4X** using Wittig and Horner-Wadsworth-Emmons (HWE) Reactions.

According to their structural characteristics, **TFc2** and –CH=CH-X-CH=CH- linked (except X = S and CO, which are not applicable) **TFc4X** could be prepared using Wittig related methodologies as illustrated in Figure 4.2. Following this strategy, there are two alternative synthetic pathways to achieve the constitution of the targeted compounds. The syntheses could be fulfilled either through route 1 (Figure 4.2) by olefinic condensation between one equivalent of bisylide of [1,1'-Fc($CH_2P^+Ph_3$)$_2$](I^-)$_2$ or 1,1'-Fc[$CH_2P(O)(OEt)$]$_2$ and two equivalents of appropriate monoaldehyde FcCH=CH-X-CHO (FcCHO for **TFc2**), or through route 2 (Figure 4.2) by coupling one equivalent of dialdehyde 1,1'-Fc(CH=CH-X-CHO)$_2$ [1,1'-Fc(CHO)$_2$ for **TFc2**] with two equivalent ylides of $FcCH_2P^+Ph_3I^-$. Apparently, these two synthetic routes use the same methodology but in the inverse manners. However, further considerations on accessibilities of the synthetic precursors suggested that route 1 is more practical since the preparations of a series of dialdehyde, 1,1'-Fc(CH=CH-X-CHO)$_2$, are synthetically more expensive and tedious, especially for X = 2,5-N-methylpyrrole, for which the preparation of the corresponding dialdehyde is a formidable work. Therefore, route 1 was selected as the initial preparative synthetic method.

Although [1,1'-Fc($CH_2P^+Ph_3$)$_2$](I^-)$_2$[21] and 1,1'-Fc[$CH_2P(O)(OEt)_2$]$_2$[20] are literature known compounds, a recent survey revealed that their synthetic applications have not yet been explored, which made the comparison between their reactivity for olefination reaction not on hand. Nevertheless, since (ferrocenylmethyl)triphenyl- phosphonium iodide or bromide, ($FcCH_2P^+Ph_3$)Y^- (Y = I or Br), were widely used as a synthetic genitor in forming the ferrocenylvinyl fragment via Wittig reaction, provided that the preparations of 1,1'-Fc($CH_2P^+Ph_3I^-$)$_2$ and 1,1'-Fc[$CH_2P(O)(OEt)_2$]$_2$ both involve three synthetic steps (Figure 4.3), we decided to first adopt 1,1'-Fc($CH_2P^+Ph_3I^-$)$_2$ as the potential candidate for the Wittig applications.

Following literature procedures[18, 21] (Figure 4.3), [1,1'-Fc($CH_2P^+Ph_3$)$_2$](I^-)$_2$ was synthesized by refluxing bis(ammonium methiodide), [1,1'-Fc($CH_2N^+Me_3$)$_2$](I^-)$_2$,[18] with

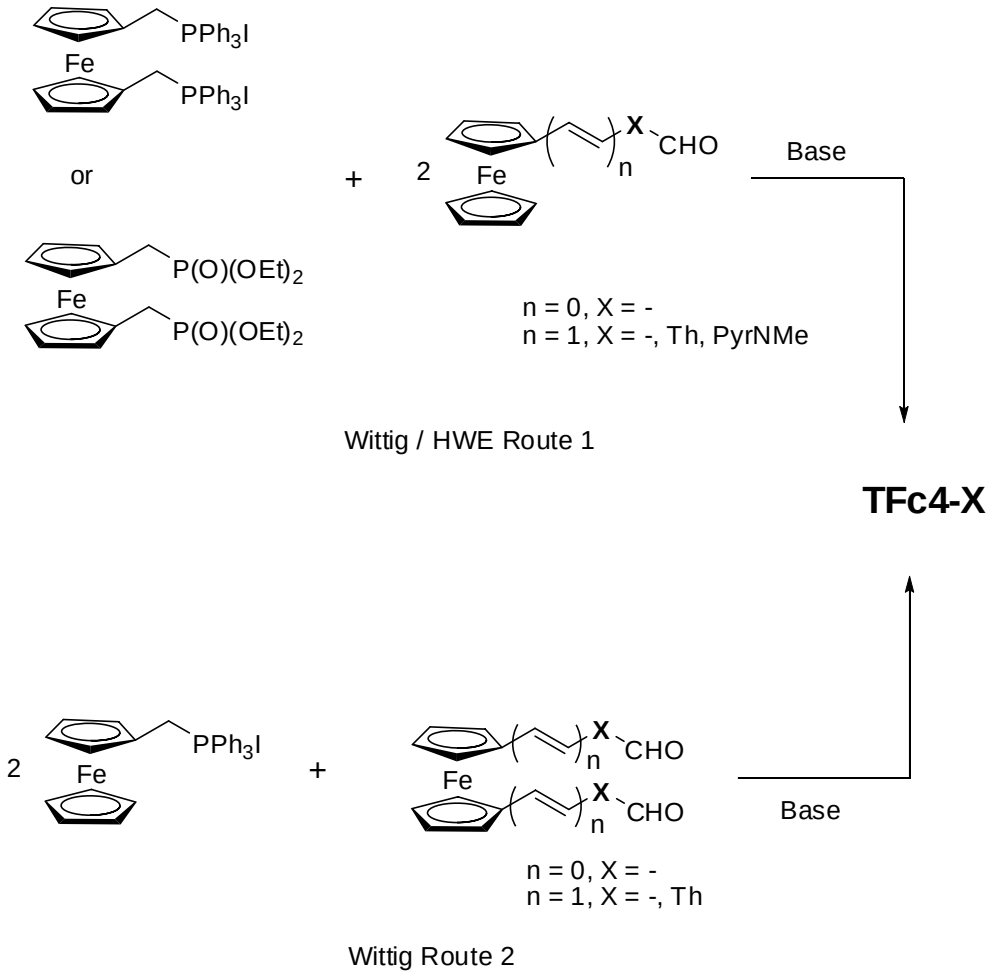

Figure 4.2 Projected synthetic routes for **TFc4X**s (X = -, Th, and PyrNMe).

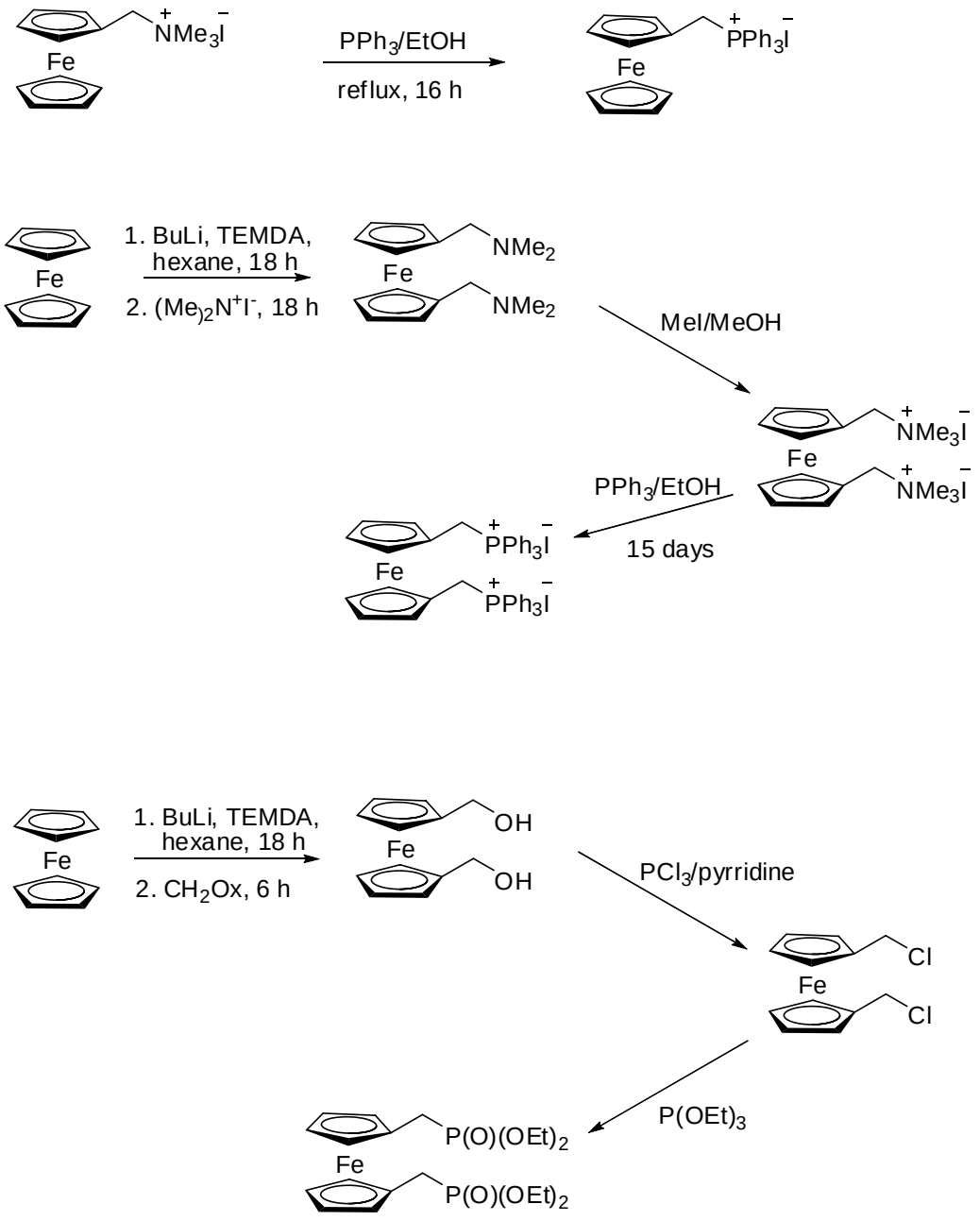

Figure 4.3 Synthesis of $FcCH_2P^+Ph_3I^-$, [1,1'-$Fc(CH_2P^+Ph_3)_2](I^-)_2$ and 1,1'-$Fc[CH_2P(O)(OEt)_2]_2$.

PPh_3 in absolute EtOH. Unlike that of its mono-phosphonium iodide analogue, $FcCH_2P^+Ph_3I^-$, which was readily formed[26] from $FcCH_2N^+Me_3I^-$ and PPh_3 by refluxing in the same media (also shown in Figure 4.3), generation of [1,1'-$Fc(CH_2P^+Ph_3)_2$]$(I^-)_2$ (vide supra) was very sluggish, which took 2-3 weeks (depending on the reaction scale) to afford a desirable yield (approx. 70%). The lengthening reaction time was not explained in the original report[21], but a careful examination on the X-ray diffraction record[27] illustrated the possible reason. As shown below, the two bulky triphenylphosphinylmethyl substituents on the two ferrocenyl Cp rings adopt a *syn* deposition with respect to each other. The obvious high degree of steric hindrance, therefore, must account for the slow formation of such architecture.

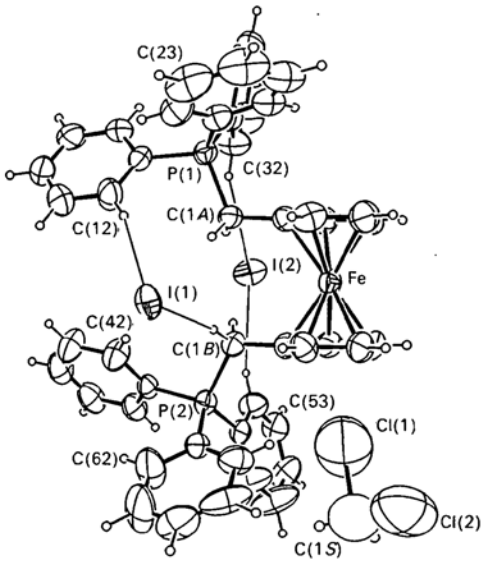

The transformation of [1,1'-$Fc(CH_2P^+Ph_3)_2$]$(I^-)_2$ into the corresponding bis-ylide with *t*BuOK was very ready, evidenced by the immediate formation a deep brown red solution upon introducing the base. After stirring (ca. 30 min), the bis-ylide was subjected to react with 2 equivalent of FcCHO for 3-4 hours to give **TFc2** in 53% yield, in contrast to the 78% yield achieved by reacting 2 equivalents of $(FcCH_2P^+Ph_3)I^-$ with 1 equivalents of $Fc(CHO)_2$ in the similar preparative manner.

Despite the successful demonstration of the first application of [1,1'-$Fc(CH_2P^+Ph_3)_2$]$(I^-)_2$ as a potential Wittig phosphonium reagent, further attempts to couple the same bis-ylide with other aldehydes such as FcCH=CHCHO and FcCH=CHThCHO

did not offer good results. The reactions were either hampered by extreme low conversion or by partially coupled product. This could again be attributed to the extremely congested surroundings of the methylene groups, at which site the Wittig intermediate oxaphosphetane was formed. To date, no further systematic efforts have been performed to optimize the reaction conditions to increase the yield or to overcome the synthetic failures. However, employing higher temperature, lengthening the reaction time or using solvent free synthesis[28] could be possible solutions to alleviate these situations. It will be an interesting investigation in the future to explore the potential of using [1,1'-Fc($CH_2P^+Ph_3$)$_2$](I^-)$_2$ as the synthetic alternatives in di-olefinating reactions. Moreover, it is worth mentioning that due to the intrinsic drawback of the conventional Wittig reactions, the product obtained for **TFc2** using the method stated above was a mixture of *cis/trans* isomers. Due to these reasons, we later switched to Horner-Wadsworth-Emmons (HWE) oriented reagent 1,1'-ferrocenyl-bis-(diethylmethylphosphonate), 1,1'-Fc[$CH_2P(O)(OEt)_2$]$_2$.

The synthesis of 1,1'-Fc[$CH_2P(O)(OEt)_2$]$_2$ was accomplished by modifying the literature procedures[20] (Figure 4.2). Reaction of 1,1'-dilithioferrocene with paraformaldehyde gave the diol 1,1'-Fc(CH_2OH)$_2$[29] which was chlorinated with PCl_3 to give the reactive dichloride 1,1'-Fc(CH_2Cl)$_2$ (Figure 4.3). This was reacted, without purification, with excess refluxing $P(OEt)_3$ to give 1,1'-Fc[$CH_2P(O)(OEt)_2$]$_2$, a brown oil.

HWE olefinations between 1,1'-Fc[$CH_2P(O)(OEt)_2$]$_2$ and 2 equivalents of an appropriate aldehye, FcCHO, (*E*)-FcCH=CHCHO and (*E*)-FcCH=CHPyr(NMe)CHO, in the presence of conventional HWE base, NaH, and catalytic amount of 15-crown-5, successfully furnished (*E,E*)-**TFc2**, (*E,E,E,E*)-**TFc4** and (*E,E,E,E*)-**TFc4PyrNM**e (Figure 4.4), respectively, after refluxing 18-24 hours in THF. The relatively long reaction time is crucial to guarantee the decent yields ranging from 45-65%. Later X-ray crystal structure (*vide infra*) revealed *syn* conformation with respect to the two ancillary ligands on the central ferrocenyl unit, which suggested that the di-phosphinylmethyl substituents on the Cp rings of the synthetic precursor, 1,1'-Fc[$CH_2P(O)(OEt)$]$_2$, may have *syn* disposition arrangement similar to that of [1,1'-Fc($CH_2P^+Ph_3$)$_2$](I^-)$_2$, which can lead to steric hindrance for reaction intermediates. Therefore, stronger base, extended reaction time and higher temperature are recommended to prompt the production and yield.

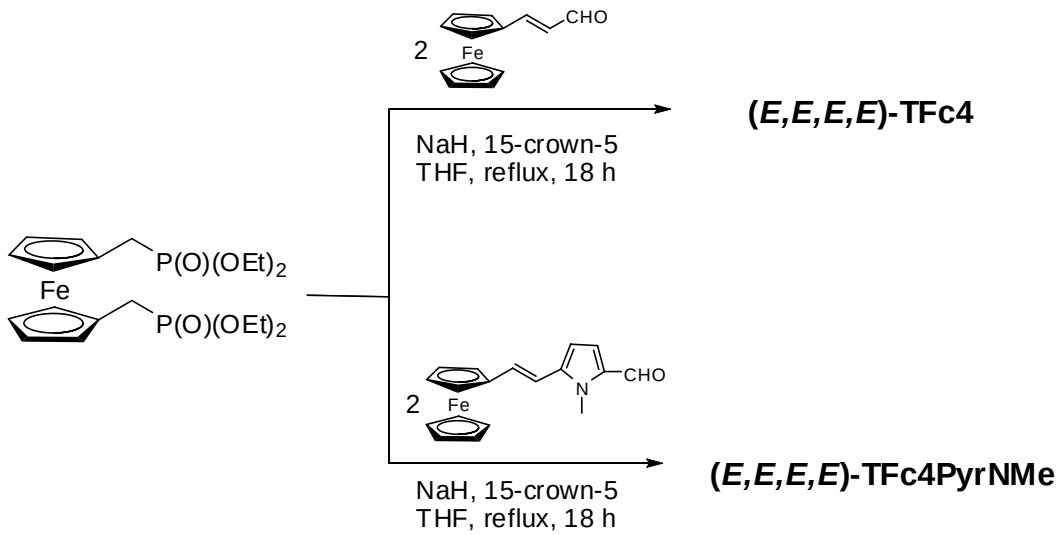

(*E*,*E*,*E*,*E*)-TFc4:

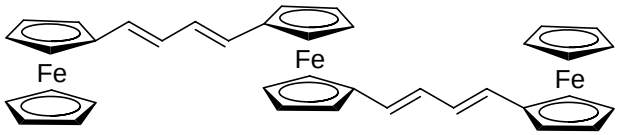

(*E*,*E*,*E*,*E*)-TFc4PyrNMe:

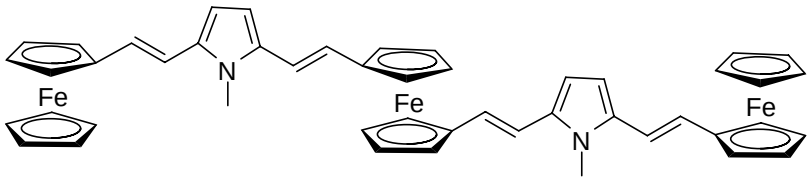

Figure 4.4 Synthesis of **TFc4** and **TFc4PyrNMe**.

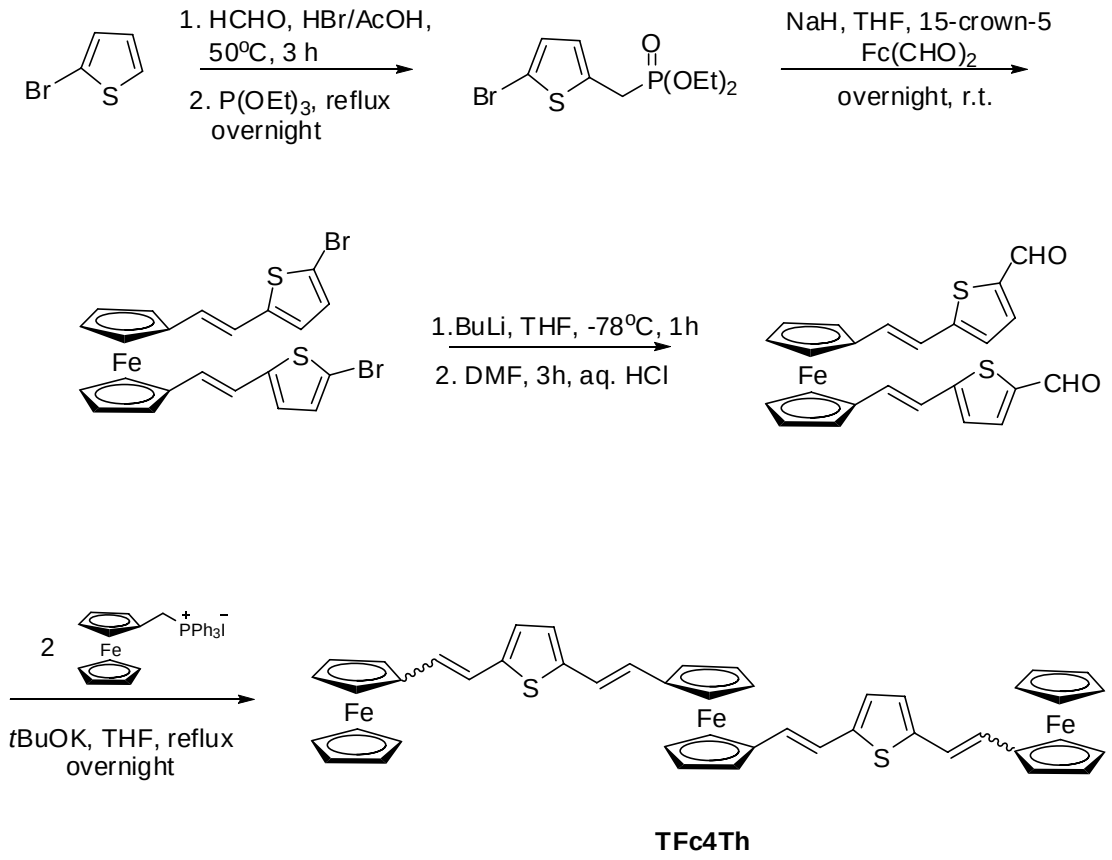

TFc4Th

Figure 4.5 Synthesis of **TFc4Th**.

Moreover, in each case, all newly formed olefinic bonds are characterized as *E*-form, which was supported by the ^{1}H NMR coupling constant (c.a. 16 Hz) and the strong IR band around 950 cm^{-1} originated from the vinyl C-H out-of-plane stretching mode. This was expected as the normal outcome of HWE reaction. Thus, we suggest to adopt the novel utility of 1,1'-Fc[$CH_2P(O)(OEt)_2$]$_2$ as a handy genitor for 1,1'-vinylene substituted ferrocene which otherwise won't be achievable. Finally, it is noteworthy that (*E,E,E,E*)-**TFc4PyrNMe** readily dissolves in CH_2Cl_2 and THF, (*E,E*)-**TFc2** and (*E,E,E,E*)-**TFc4**, however, only have very limited solubility in the same solvent, which was known for polyene-bridged diferrocenyl systems.[2]

To our surprise, the same HWE condensation between 1,1'-Fc[$CH_2P(O)(OEt)_2$]$_2$ and two equivalents of (*E*)-FcCH=CHThCHO did not go through successfully to offer the desired (*E,E,E,E*)-**TFc4Th**, which is in sharp contrast to its structural analogue, (*E,E,E,E*)-**TFc4PyrNMe**. Only some mono-coupled byproducts were recovered. After a few attempts by varying the reaction conditions, the situation still remained the same. At this moment, we can not provide a better explanation rather than the obvious steric effect and the possibly depreciated reactivity of the reaction intermediates stated earlier. For this reason, we later resorted synthetic route 2 (Figure 4.2) to eventually prepare the **TFc4Th.**

The synthetic pathway of **TFc4Th** was shown in Figure 4.5. The pivotal synthetic step is to prepare the 1,1'-bis(5-formylthiophen-2-ylvinyl)ferrocene, **1,1'-Fc(CH=CHThCHO)$_2$**, which was furnished via three major steps. Diethyl (5-bromo-thiophen-2-yl)methylphosphonate[22] was first prepared starting from 2-bromothiophene, which was treated with paraformaldehyde and HBr/AcOH in AcOH at 50 ^oC for 3 hours to afford the 2-bromo-5-bromomethylthiophene. This, as a crude product without further purification, was refluxed in $P(OEt)_3$ overnight to give the desired thiophene phosphonate. Conventional HWE reaction of two equivalents of (5-bromo-thiophen-2-yl)methylphosphonate with 1,1'-Fc$(CHO)_2$ in presence of NaH/15-crown-5 in THF at r.t. gave 1,1'-bis(5-bromothiophen-2-ylvinyl)ferrocene, **(*E,E*)-1,1'-Fc(CH=CHThBr)$_2$**, in excellent yield (95%), which was then converted to the corresponding dialdehyde **(*E,E*)-1,1'-Fc(CH=CHThCHO)$_2$** by lithiation with BuLi, followed by treatment with DMF and aqueous HCl to accomplish the transformation. **TFc4Th** was finally obtained through Wittig coupling between two equivalents of (ferrocenylmethyl)triphosphonium ylide and one equivalent of **(*E,E*)-1,1'-Fc(CH=CHThCHO)$_2$** in THF under reflux overnight. Purification was accomplished by several recrystallization of the crude product from MeOH and CH_2Cl_2, sequentially. The yield is 76% and the product demonstrated moderate solubility in common organic solvent as anticipated. ^1H NMR showed 85% (*E,E,E,E*)-product, which was isolated as pure species after careful recrystallization from CH_2Cl_2/hexane (1:1). It is worth stressing that heating in the final Wittig step is crucial to promote all-*E* product. Another comparison reaction conducted at r.t. afforded heavily mixed cis/trans isomers.

Preparation of **TFc4S**, **TFc4CO, TFc2CO-A** and **TFc2CO-B**

TFc4S was prepared by mixing dimethylthioether-a,a'-bis(triphenylphosphonium) bromide ($(CH_2PPh_3Br)_2S$), FcCHO and 1,1'-$Fc(CHO)_2$ in 2:2:1 stiochiometric ratio in MeOH and treated with NaOMe overnight to give a synthetic mixture as shown in Figure 4.6. Obviously this is not a clean chemistry, the major product is FcCH=CHSCH=CHFc, **BFc4S** (Chapter 2). However, roughly 13% of **TFc4S** was isolated after careful column chromatography. The proposed synthetic improvement for **TFc4S** was also included in Figure 4.6. Under this well-defined approach, **TFc4S** could be obtained by CuI/Pd promoted alkenyl thiol formation via the reaction of 1,1'-**$Fc(CH=CHBr)_2$** with two equivalents of alkenylthiol derivative, FcCH=CHSH, which can be accessed by modifying the literature procedures[30].

TFc4CO, **TFc2CO-A** and **TFc2CO-B** were easily obtained from base-catalyzed Clemmensen condensation as shown in Figure 4.7. It is important to underline that using THF as co-solvent to prepare **TFc2CO-A** is essential due to the low solubility of the intermediate FcC(O)CH=CHFcCHO in MeOH, which often isolated from the reaction mixture and undermined further reaction to the final product. **TFc2CO-B** was synthesized using the same procedures. The purple red product is not as robust as **TFc2CO-A**, therefore, purification usually was performed by fast processes such as flash chromatography.

Preparation of **TFc2S-A** and **TFc2S-B**

The most commonly used procedures to obtain alkenyl chalcogenides is from the reaction of alkenyl halide with chalcogenide anion under the assistance of transition metal catalyst.[31] We adopted a nucleophilic substitution reaction of alkenyl halides with diorganyl dichalcogenides as shown in Figure 4.9. Under this approach, several ferrocenethiol and ferrocenylalkenyl bromide derivatives were prepared beforehand as illustrated in Figure 4.8

Ferrocenethiol, FcSH, was achieved through multi-step reactions according to literature procedures[23, 32] (Figure 4.8). The foul-smelling oily FcSH is very instable and spontaneously dimerized into diferrocene disulfide, FcS-SFc, within two days in closed flask, evidenced by dissipation of the awful smell and solidification. Although the dimer form can be easily reduced back to FcSH with $LiAlH_4$ in THF, it is not necessary to do so

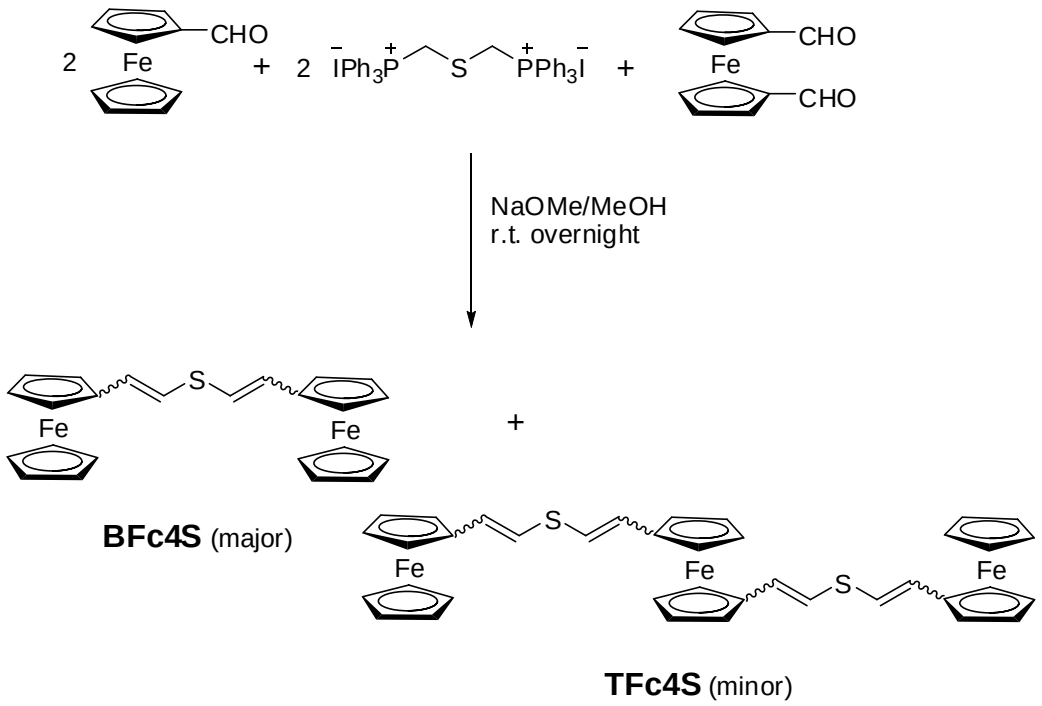

Improved synthesis (Projected) :

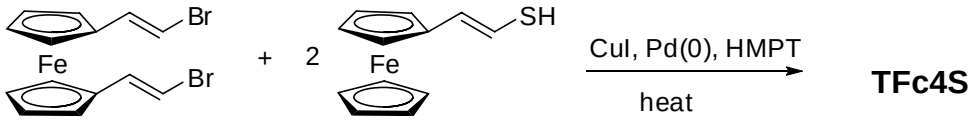

Figure 4.6 Synthesis of **TFc4S**.

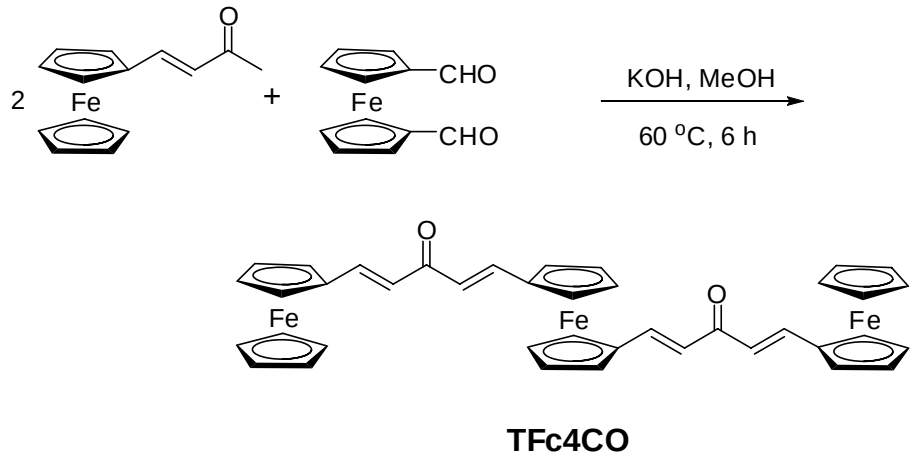

TFc4CO

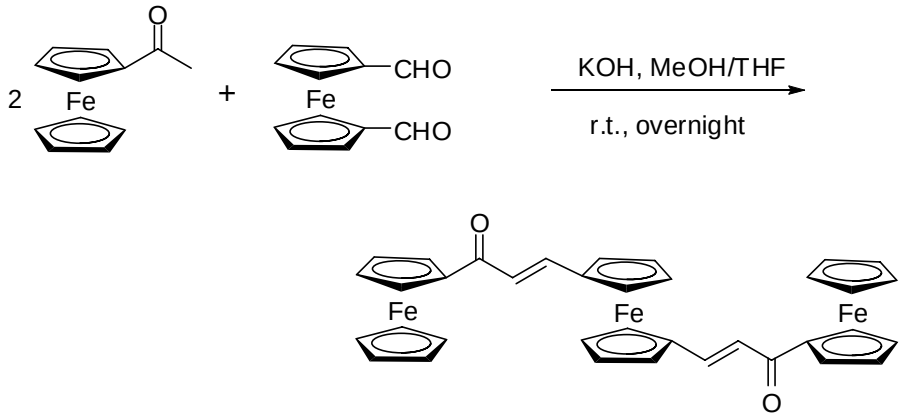

TFc2CO-A

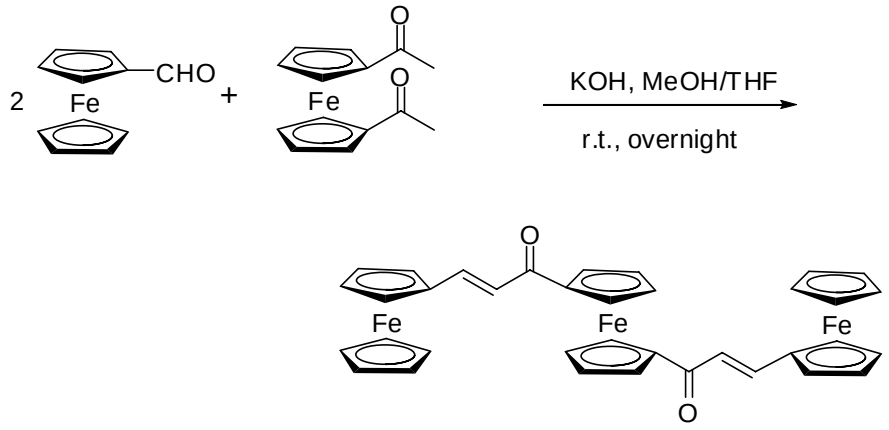

TFc2CO-B

Figure 4.7 Synthesis of **TFc4CO**, **TFc2CO-A** and **TFc2CO-B**.

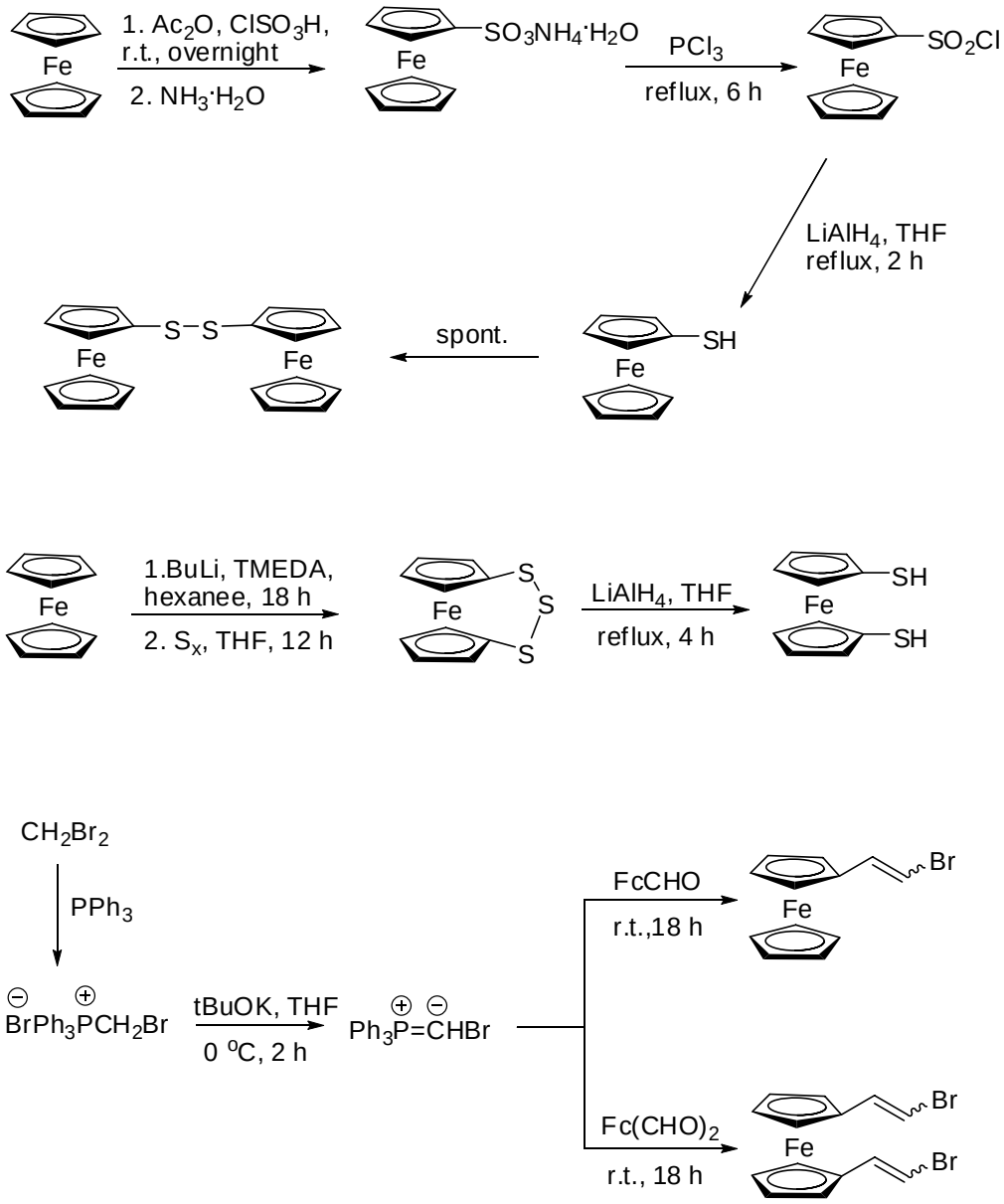

Figure 4.8 Synthesis of **FcS-SFc**, **1,1'-Fc(SH)$_2$**, **FcCH=CHBr** and **1,1'-Fc(CH=CHBr)$_2$**.

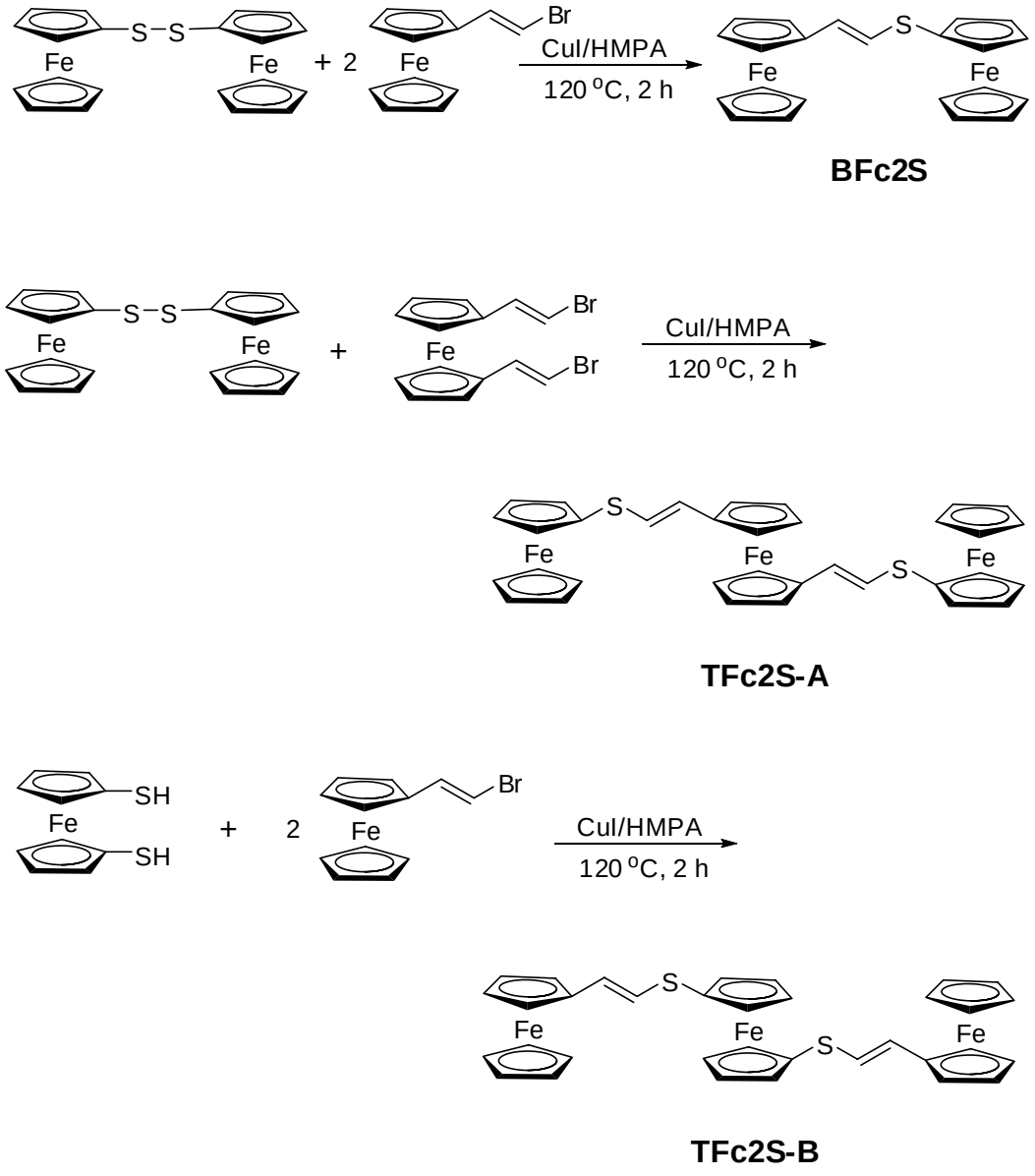

Figure 4.9 Synthesis of **BFc2S**, **TFc2S-A** and **TFc2S-B**..

since both the monomer and dimer serve the same synthetic purpose when current application is concerned.

The preparation of ferrocene-1,1'-dithiol[25], 1,1'-$Fc(SH)_2$, started with dilithiation of ferrocene with BuLi in the assistance of N,N,N'N'-tetramethylethylenediamine (TMEDA). The generated dilithioferrocene was allowed to react with elemental sulfur to give 1,2,3-trithia-[3]-ferrocenophane, $Fc(S)_3$, which was quantitatively converted to 1,1'-$Fc(SH)_2$ by –S-S-S- cleavage with $LiAlH_4$ under reflux in THF. Again, the dithiol tended to dimerize to the thermodynamically more stable form, which was used as is without further handling.

Treatment of bromomethyltriphenylphosphine bromide[24] with *t*BuOK in THF at ^oC conveniently afford the yellow colored bromomethylene ylide solution, which was allowed to react with FcCHO or 1,1'-$Fc(CHO)_2$ to form the olefinic products, 2-ferrocenylethenyl bromide, **FcCH=CHBr**, or ferrocene-1,1'-diyl-bis(ethenyl bromide), **1,1'-$Fc(CH=CHBr)_2$**, respectively. Obviously, the Wittig-guided syntheses were not stereoselective. Both E/Z (FcCH=CHBr) and combination of E/E, E/Z, and Z/Z [1,1'-$Fc(CH=CHBr)_2$] forms were obtained as the final products. Compared to the alternative Heck coupling approach[33], which is not stereoselective either, current procedures are certainly advantageous because of greater simplicity. Unlike **FcCH=CHBr**, the di-substituted analogue, **1,1'-$Fc(CH=CHBr)_2$**, is very unstable. The red compound decomposed to a black ferric-like powder within 24 hours in closed bottles. Therefore, it was always prepared freshly before use.

As stated earlier, synthesis of the alkenyl chalcogenide derivatives, **TFc2S-A** and **TFc2S-B**, was fulfilled through nucleophilic substitution upon heating dichalcogenide with alkenyl bromide in hexamethylphosphoric triamide (HMPA) in the presence of copper (I) iodide (Figure 4.9). Therefore, reaction between **FcS-SFc** with **1,1'-$Fc(CH=CHBr)_2$** afforded **TFc2S-A**, and coupling between **$Fc(SH)_2$** and two equivalents of **FcCH=CHBr** gave **TFc2S-B**, all in moderate yield (40-50%). For the sake of comparison, ferrocenyl(2-ferrocenylvinyl) sulfide, FcSCH=CHFc (**BFc2S**), was also prepared from **FcS-SFc** and **FcCH=CHBr** using the same reaction procedure.

X-ray Crystal Structures

Suitable crystals for X-ray diffraction analysis were grown from the concentrated solutions of CH_2Cl_2 through slow solvent evaporation. The availability of such single crystal was often limited by the solubility and structural regularity of each highly conjugated compound. Eventually, one synthetic precursor, **(*E,E*)-1,1'-Fc(CH=CHThCHO)$_2$**, one ferrocenyl dimer, **BFc2S**, along with four triferrocenes, **(*E,E*)-TFc2S-A**, **(*E,E*)-TFc2CO-A**, **(*E,E,E,E*)-TFc4Th** and **(*E,E,E,E*)-TFc4PyrNMe** offered good single crystals for X-ray crystallographic analysis. The X-ray molecular structures confirmed the identities of these compounds previously characterized by spectroscopic techniques. The ORTEP plots of these compounds are presented in Figure 4.10-4.15.

The crystal lattice of **(*E,E*)-1,1'-Fc(CH=CHThCHO)$_2$** consists of four molecules with two types of conformers, conformer A and conformer B, as shown in Figure 4.10. Both conformers show *syn* deposition in term of the two ancillary ligands. The vinylene bonds in each conformer all adopt the (*E*)-form. The differences between conformer A and B lie on the steric orientation of the two thiophene nuclei with respect to each other. The two stacked thiophene rings are displaced *anti* to each other in conformer A, but *syn* in conformer B. In conformer A, the two ancillary ligands are virtually coplanar, and the ligand through-space distances vary from 3.37 Å (C1A-C6A) to 3.79 Å (C13A-C20A), then back to 3.42 Å (C17A-C24A) at the formyl carbons. This nearly parallel arrangement gives rise to a more favorable π-π stacking interaction between the side chains. However, this disposition is under a cost of 9.12 ^{o} tilting between the two Cp rings. In contrast, the Cp rings in conformer B are perfectly parallel to each other. The *syn* thiophene rings are virtually overlapped to each other from the topside view. The two ancillary ligands smoothly increase their separation from 3.37 Å (C1B-C6B) to 3.78 Å (C17B-C24M), which is a consequence to release the small steric hindrance between the two ending formyl groups. In any event, the crystal structures of **1,1'-Fc(CH=CHThCHO)$_2$** represents a new sample where the intramolecular π-π interacting dominates the stereo-arrangement within a molecule.

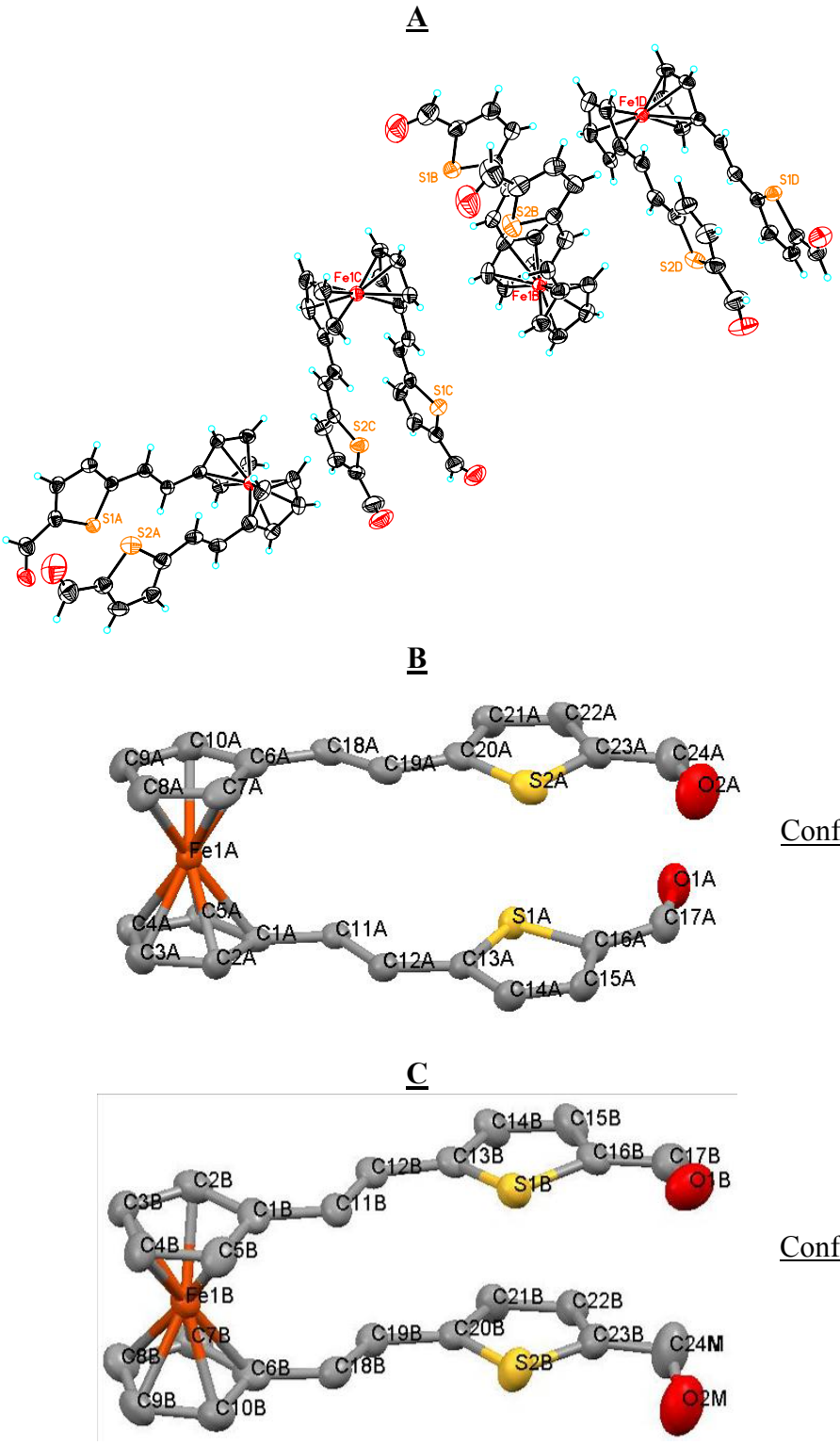

Conformer A

Conformer B

Figure 4.10 ORTEP diagram of **1,1'-Fc(CH=CHThCHO)$_2$**. The top crystal lattice (A) includes two types of geometric conformers, which are shown in the middle (B) and bottom (C) diagrams with hydrogen atoms escaped for clarity.

Slow evaporation of a CH_2Cl_2/hexane solution of **BFc2S** gave an orange red needle-like crystal. The single-crystal X-ray analysis confirmed the sample as an (*E*)-isomer (Figure 4.11). The structure has a fairly extended geometry with all the bond lengths and angles lying in the expected range. Both ferrocenyl units in **(E)-BFc2S** are normally eclipsed. The conjugation path between them is severely twisted, noted by a torsion angle of 97.40° between the two substituted Cp rings. The iron-iron distance is 8.79 Å.

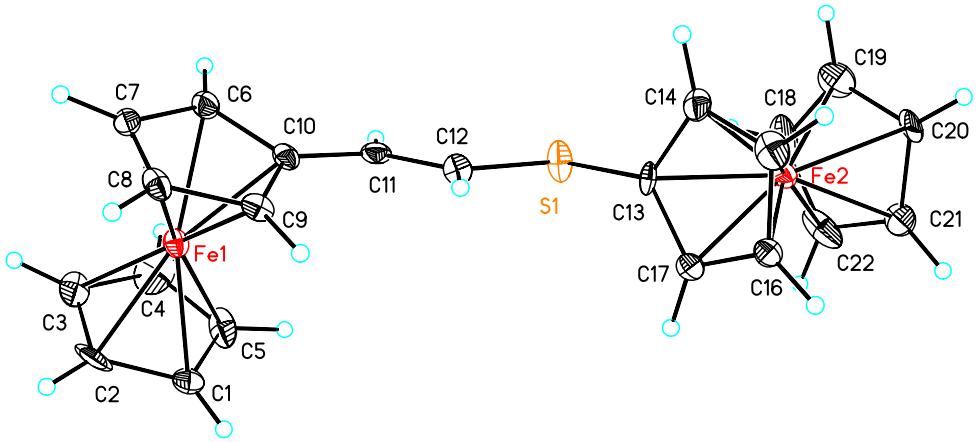

Figure 4.11 ORTEP plot of **BFc2S** with 50% anisotropic displacement ellipsoids.

The most striking structural feature of **(*E*,*E*)-TFc2S-A** is its *syn* disposition of the two side arms on the Cp rings of the central ferrocenyl unit as shown in Figure 4.12. Intuitively, this alignment will cause steric conflict between the bulky terminal ferrocenes. Meanwhile, there is no significant π-π stacking driving forces as previously described in **(*E*,*E*)-1,1'-Fc(CH=CHThCHO)$_2$**. Under the observed arrangement, the two ancillary ligands are *pseudo*-parallel to each other from the substituted Cp carbons to the sulfur atoms, at which point the two terminal ferrocenyl groups split into opposite direction to alleviate the steric hindrance between them. As better illustrated in the packing diagram (Figure 4.12), the two terminal ferrocenes adopt a face-to-edge

A

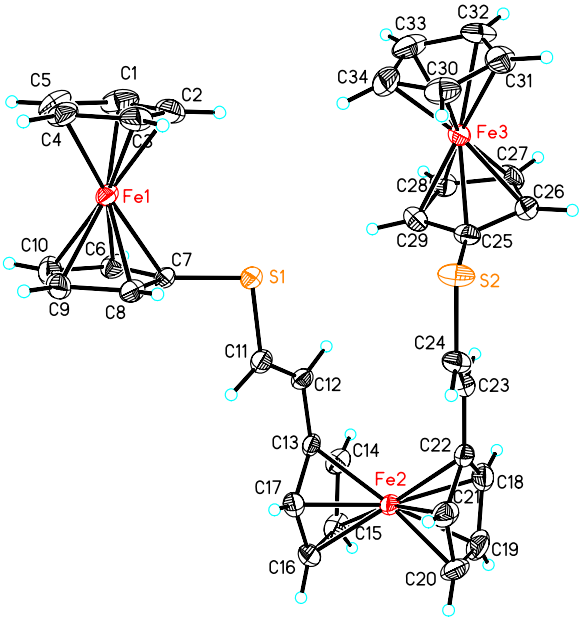

B

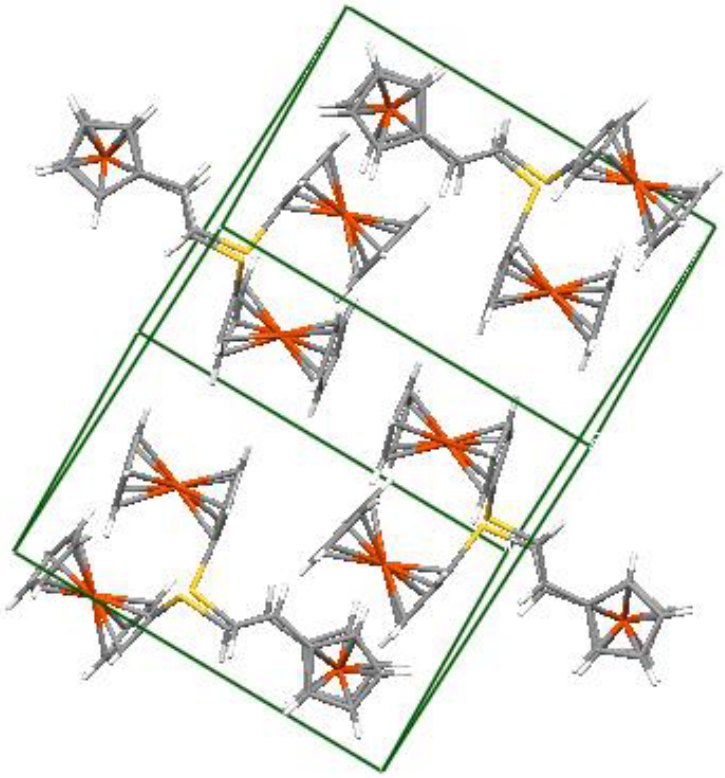

Figure 4.12 ORTEP plot (A) and unit cell packing form (B) of **(*E,E*)-TFc2S**.

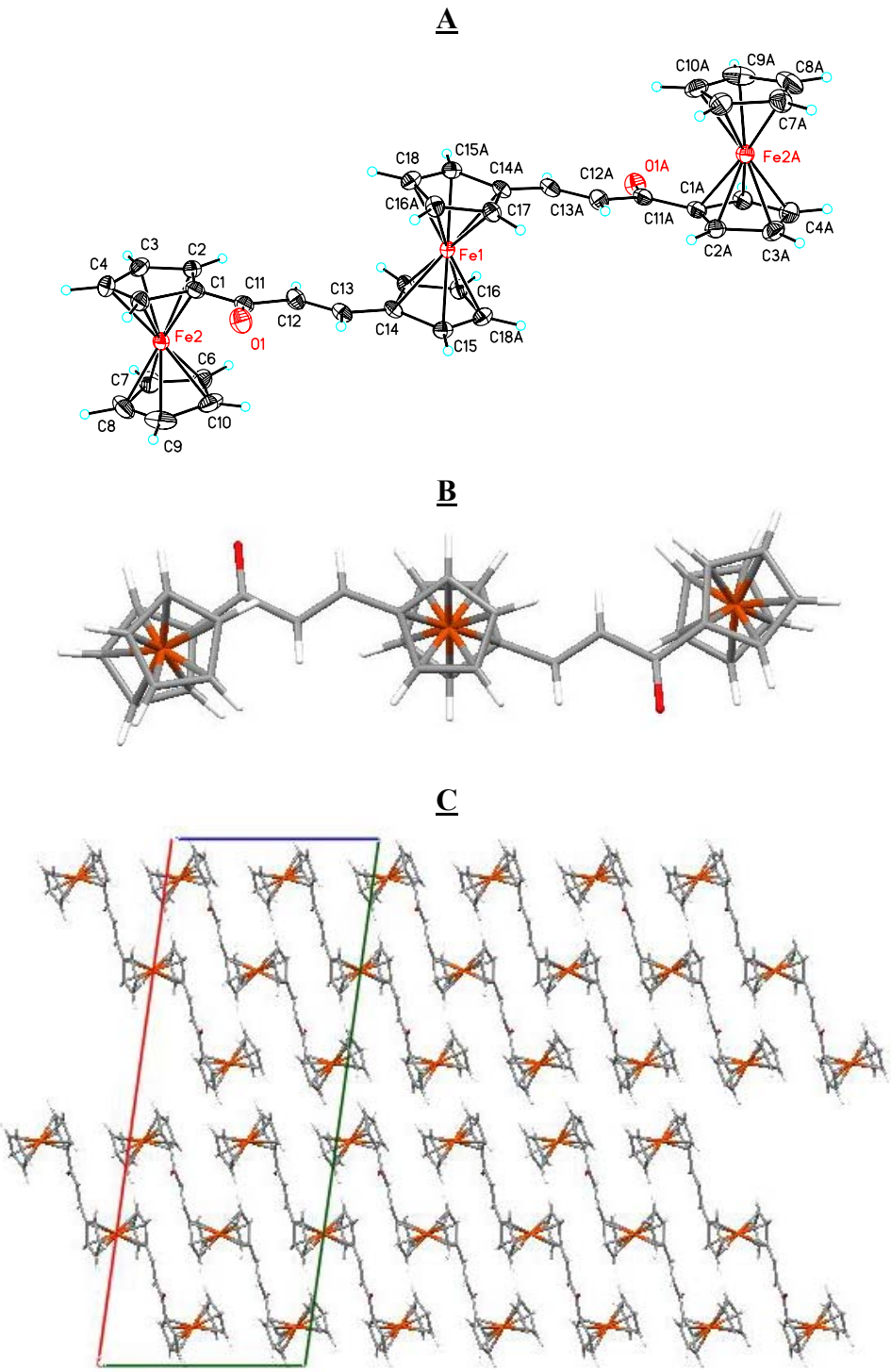

Figure 4.13 ORTEP plot (A), topside view (B) and packing diagram (C) of **(*E,E*)-TFc2CO-A**.

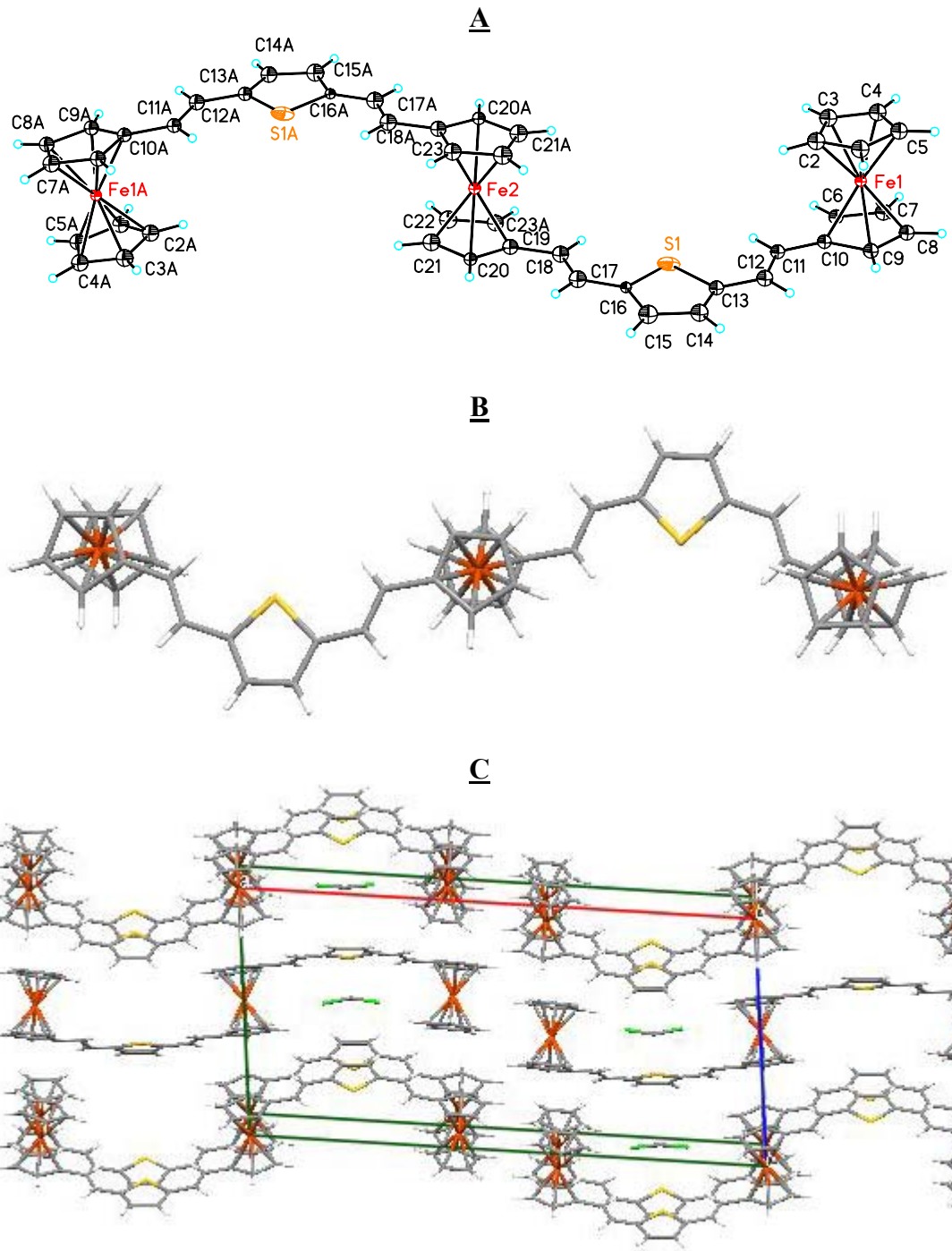

Figure 4.14 ORTEP plot (A), topside view (B) and packing diagram (C) of **(*E*,*E*,*E*,*E*)-TFc4Th**.

orientation with respect to the central unit, and 18.37° *endo*-incline to each other. The through space metal-to-metal distances of Fe(1)-Fe(2), Fe(2)-Fe(3), Fe(3)-Fe(1) are given as 8.81 Å, 7.76 Å, 7.19 Å, respectively, whereby the Fe(2) resides in the central ferrocene nucleus and the iron-iron distance between the two ending ferrocenyl groups is in the closest proximity due to the *syn* conformation of the two ancillary fragments. The possible reason for this stereochemistry can be ascribed to the packing effect or the predefined steric arrangement of the two side chains inherited from the synthetic precursor, **1,1'-Fc(CH=CHBr)$_2$**.

In contrast to **(*E,E*)-TFc2S-A**, **(*E,E*)-TFc2CO-A** (Figure 4.13) and **(*E,E,E,E*)-TFc4Th** (Figure 4.14) both crystallize into a very symmetric structure with many steric features similar to each other. They both possess an inversion center located at the iron atom of the central ferrocene nucleus. The three ferrocenyl groups displace progressively along the extended alignment. For both compounds, the two side substituents on the Cp rings of the central ferrocene nucleus are strictly *anti*, evidenced by a dihedral angle of 180° between them (Figure 4.13B and Figure 4.14B). More interestingly, while the Cp rings of the terminal ferrocenyl moieties take normal eclipse disposition, the two Cp rings of the central ferrocene nucleus utilize a nearly perfect staggered conformation, affording an average staggering angle of 36°. This kind of eclipse-to-stagger rotation is commonly observed in strain-contained ferrocenyl complexes to relieve the steric strains.[34] In **(*E,E*)-TFc2CO-A** and **(*E,E,E,E*)-TFc4Th**, however, there is no explicit driving force for such rotation to occur. The rotation seems exist to give rise to a perfectly symmetrical structure and a tight packing (Figure 4.13C and Figure 4.14C).

In **(*E,E*)-TFc2CO-A**, the two terminal ferrocenyl groups show *trans* conformation with respect to each other. The iron-iron-iron angle is perfectly 180°, giving a ladder shape displacement in the view of the steric arrangement of the three consecutive ferrocenes. The Fe(1)-Fe(2) and Fe(2)-Fe(2A) through-space distances are measured as 7.78 Å and 15.56 Å (precisely doubled value of Fe(1)-Fe(2)), respectively. Opposite to that of **(*E,E*)-TFc2CO-A**, the conformations among the ferrocenyl groups in **(*E,E,E,E*)-TFc4Th** are mutually *syn* to each other. The bridging organic ligands demonstrate high coplanarity with a maximum dihedral angle of 6.59°. All the bond lengths and angles in

(*E,E,E,E*)-TFc4Th lie in the expected range. The through-space metal-metal distances of Fe(2)-Fe(1), Fe(1)-Fe(1A) are measured as 11.0 Å and 22.0 Å, respectively.

The stereochemistry of **(*E,E,E,E*)-TFc4PyrNMe** (Figure 4.15) rather resembles to that of **(*E,E*)-TFc2S-A** in the aspect of the relative geometry between the two side arms attached on the central ferrocenyl rings, which adopts a *pseudo-syn* disposition. Different from **(*E,E*)-TFc2S-A**, however, the two side arms displace a 16.44^{o} torsion angle with respect to each other. This alleviates the even greater steric hindrance arising from the methyl substituents attached on the nitrogen atom of the pyrrole rings. Indeed, the two sterically proximate pyrrole rings point towards the opposite directions in regard to the orientation of their methyl-subsituents. This arrangement obviously avoids the otherwise steric conflict between the methyl groups. The dihedral angle between the substituted Cp ring [C(37)-C(41)]of the Fe3-incorporated terminal ferrocene and the connected Cp ring [C(6)-C(10)] of the central ferrocene nucleus [Fe(1)-incorporated] is approximately 0.59^{o}. Essentially, these two rings lie on the same plane. The pyrrolene ring bridging between these two Cp rings, however, tilts average 23.27^{o} from the plane passing through the two substituted Cp rings stated above. Therefore, the coplanarity along the conjugation pathway is moderately impaired due to the twisting of the central pyrrolene moiety. The second terminal ferrocene nucleus [Fe(2)-incorporated], in contrast, orientates close to perpendicularly to the middle ferrocene nucleus, which is mainly ascribed to the steric hindrance caused by the sterically proximate Fe(3) ferrocenyl group. In fact, the Fe(2) ferrocene nucleus arranges face-to-edge to the Fe(3) ferrocene nuleus, resulting in a Fe(2)-Fe(3) through-space distance of 6.18 Å, which is much shorter than the distances of Fe(1)-Fe(2) and Fe(1)-Fe(3) (12.69 Å and 11.98 Å, respectively). As shown in Figure 4.15, the conjugation pathway from the substituted Cp ring [C(19)-C(23)]of the Fe(2) ferrocene nucleus to the connected corresponding Cp ring [C(1)-C(5)] in the central ferrocene nucleus is severely distorted due to a series of twists along the Cp rings, the bridging vinylene and pyrrolene fragments, which in turn can account for some relevant effects on the electronic and electrochemical properties.

At this point, one may ask why the 1,1'-disubstituted ferrocenyl derivatives such as **(*E,E*)-TFc2S-A** and **(*E,E,E,E*)-TFc4PyrNMe** rather prefer a *syn* conformation regarding the two side chains even this arrangement obviously causes sterically

unfavorable geometry with no substantial intramolecular driving forces existing. The *anti* disposition represented by **(*E,E*)-TFc2CO-A** and **(*E,E,E,E*)-TFc4Th** should be more appealing to overcome the consequent steric problems. However, this *anti* conformation is rather rare from literature survey[35, 36]. Many approaches has been made in order to rationalize the *syn* conformational preference for the 1,1'-disubstituted ferrocene complexes by considering intra- and intermolecular interactions[37-39], but it is still an open controversy. The only conclusion we can draw from our examinations is that these conformational properties are either dominated by packing effects or inherited from the pre-defined conformational arrangement of the synthetic precursors.

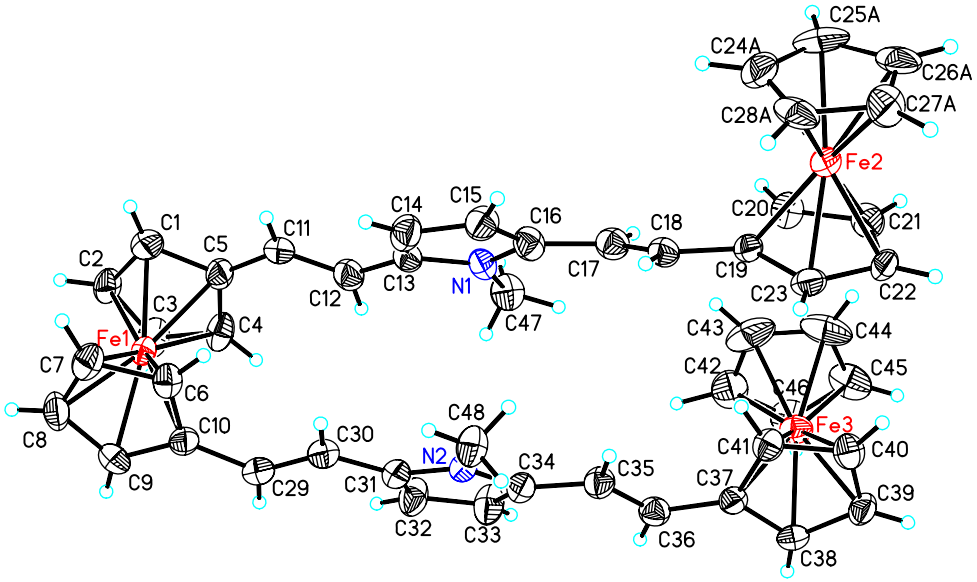

Figure 4.15 ORTEP plot of **(*E,E,E,E*)-TFc4PyrNMe** with 50% anisotropic displacement ellipsoids.

Electrochemistry

The cyclic voltammetric results of the triferrocenes are summarized in Table 4.1. Some electrochemical data of the relevant biferrocenes are also included in Table 4.1 to assist our understandings of the redox processes of their trimeric counterparts. All the electrochemical data are reported versus the Fc/Fc^+ as the internal reference. In this study, we still use *n*-$Bu_4N^+TFPB^-$ as the supporting electrolyte to avoid losing subtle information caused by ion-pairing effect with PF_6^-, BF_4^- or ClO_4^- as the counter anion.

TFc2:

In order to gain a basic insight of the electrochemical dependence of the triferrocenyl systems on their functionalized linking units, it is important to first examine the simplest trimeric compound herein, **TFc2**. Linked by a short vinyl bond between the adjacent ferrocene nuclei, **TFc2** revealed three oxidation waves (Figure 4.16), associating with the three redox centers along the molecular skeleton. The third oxidation wave is slightly off-scale and exhibits smaller peak intensity compared to the first two oxidation waves. This is commonly observed phenomenon for multiply-charged species due to its low stability at highly-oxidized state. The first oxidation wave (E_1) of **TFc2** is shifted to negative, -162 mV vs. Fc^+/Fc, indicating a electron-rich unit is first oxidized, which, apparently arises from the disubstituted central ferrocene nucleus. The interesting thing is that ΔE_1 (E_2- E_1) of **TFc2** (190 mV) is remarkably smaller than that of FcCH=CHFc (380 mV) (Figure 4.16). The peak separation is actually halved. The only possible explanation to this downgraded electronic interaction is the positive charge formed at the central ferrocene unit of the mono-cationic species relocalized to one of the juxtaposed ferrocenyl terminals immediately prior to the occurrence of the second anodic process to eliminate the otherwise close proximity between the two adjacent positive charges. By this charge relocalization, the electrostatic repulsion between the two positive charges is minimized to achieve a thermodynamically more stable state. In practice, this can only take place in a system with either a short iron-iron distance or a high electron delocalization (or both) such as in **TFc2**. Therefore, the redox processes and intermediate oxidative states of **TFc2** can be summarized in the following equations:

$$Fc\text{-}CH{=}CH\text{-}Fc\text{-}CH{=}CH\text{-}Fc \rightarrow Fc\text{-}CH{=}CH\text{-}Fc^+\text{-}CH{=}CH\text{-}Fc \rightarrow Fc^+\text{-}CH{=}CH\text{-}Fc\text{-}CH{=}CH\text{-}Fc^+ \rightarrow Fc^+\text{-}CH{=}CH\text{-}Fc^+\text{-}CH{=}CH\text{-}Fc^+ \quad (4.1)$$

Table 4.1 Electrochemical data[a] (from Cyclic Voltammetry) for the compounds.

Compounds	E^o_1 (mV)	E^o_2 (mV)	E^o_3 (mV)	E^o_4 (mV)	ΔE^o_1 [b] (mV)	ΔE^o_2 [c] (mV)
BFc2	-131	249			380	--
TFc2	-163	27	444[e]		190	417
FcSSFc	80	430			350	--
BFc2S	-50	310			360	--
TFc2S-A	-125	210	372		335	162
TFc2S-B	-20 [d]	355			375	--
BFc2CO	184	464			280	--
TFc2CO-A	205	340	615		135	275
TFc2CO-B	110	230	852		120	622
EE-TFc4	-155	30	255		185	225
TFc4	-170	-10	125		160	135
TFc4S	-80	90	425		170	335
TFc4CO	90	180	450[e]		90	270
TF4Th	-120	25	133		145	108
TFc4PyrNMe	-303	-78	200	580	225	278

[a] Obtained in CH_2Cl_2 solution containing 0.1 M Bu_4NTFPB. Scan rate 50 mV/s. [b] $\Delta E^o_1 = E^o_2 - E^o_1$; [c] $\Delta E^o_1 = E^o_3 - E^o_2$; [d] two-electron oxidation process; [e] semi-reversible oxidation process.

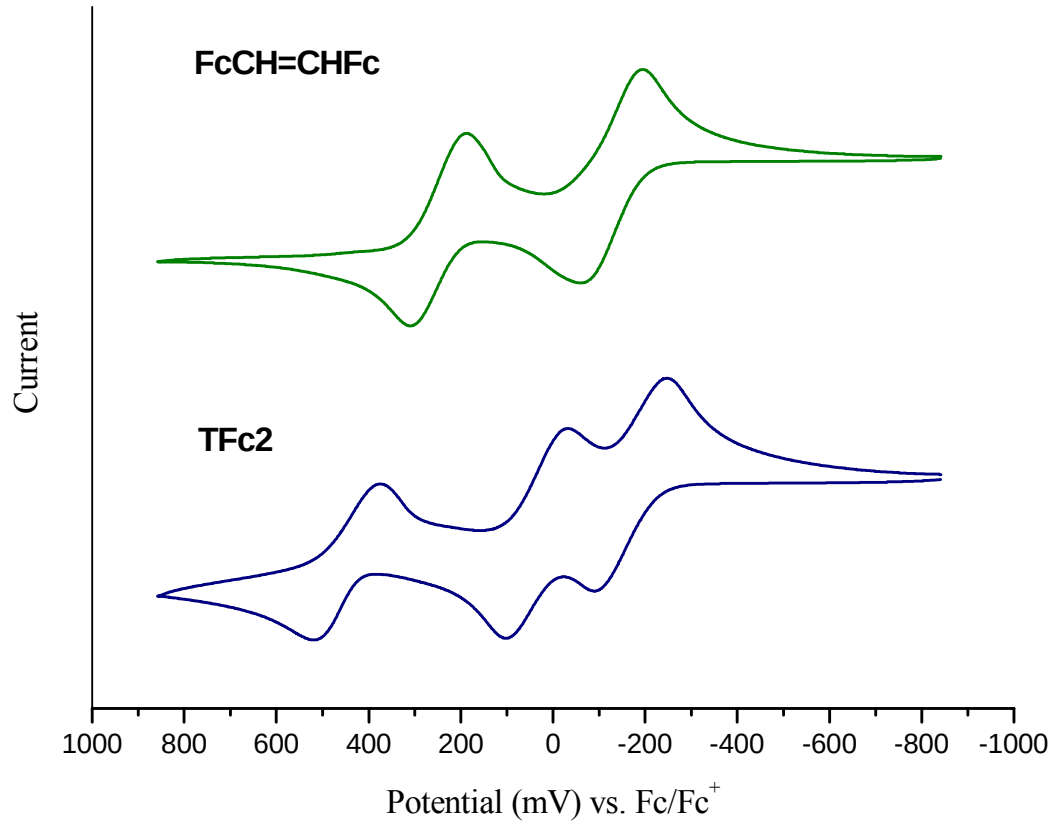

Figure 4.16 Cyclic voltammograms of FcCH=CHFc (**BFc2)** and **TFc2** in CH_2Cl_2/0.1 M Bu_4NTFPB. Scan rate 50 mV/s.

In fact, such dynamic redox processes have been observed in several ferrocenyloligomers, [40, 41] in which the ferrocene units are directly connected to each other or spaced by very short moieties such as $–Si(Me)_2-$. The dependence of the redox potentials on the number of ferrocene units has been interpreted based on the neighboring-site interaction model,[40, 41] originally presented by Aoki and Chen.[42]

Asymmetrical Triferrocenes:

Different from **TFc2**, which uses symmetrical vinyl spacer as the linker between the ferrocene nuclei, **TFc2X-A** and **TFc2X–B** adopt a functional atom/group, S or –C(O)-, along with a double bond as the bridging unit. By this mean, the newly inserted functional units play not only as a supporting manner for the electronic communications but also as a tuning factor determining the oxidation sequences. Structurally, for each

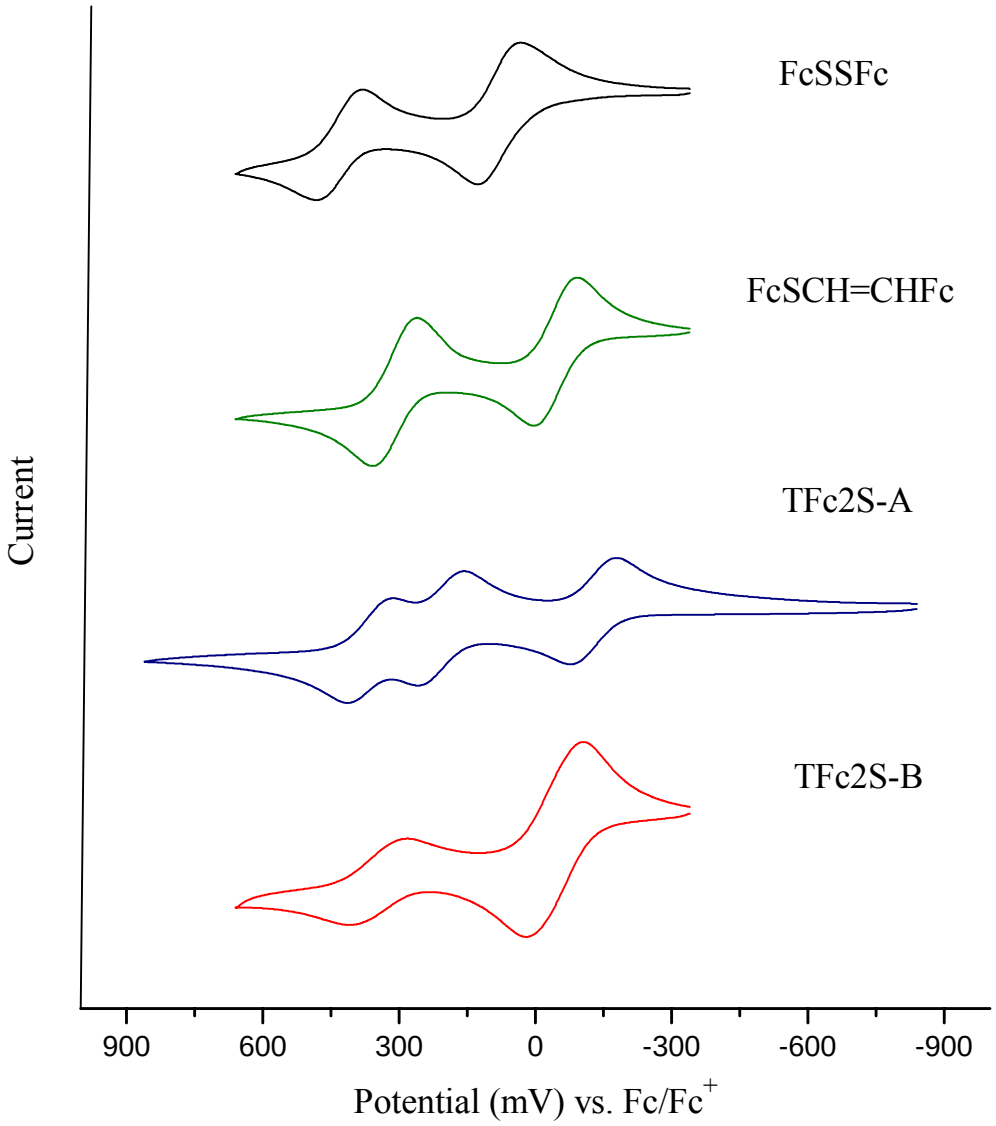

Figure 4.17 Cyclic voltammograms of **FcSSFc**, **BFc2S**, **TFc2S-A** and **TFc2S-B** in CH_2Cl_2/0.1 M Bu_4NTFPB. Scan rate 50 mV/s.

case of the **TFc2-X** (A and B) derivatives, the chemical environments of the two terminal ferrocenyl groups are identical and, at the meantime, significantly disparate from that of the central di-substituted ferrocenyl group. Ideally, another alternative ferrocene trimeric system, which is more 'symmetrical' (as shown below), is also desired for comparison studies, however, it is synthetically more difficult to achieve.

Fc-CH=CH-X-Fc-CH=CH-X-Fc

Before we start investigating the electrochemical behaviors of the sulfur-incorporated compounds **TFc2S-A** and **TFc2S-B**, it is dispensable to gain an insight of two relevant but simpler diferrocenylthio compounds, FcSSFc and FcSCH=CHFc (**BFc2S**). As shown in Figure 4.17, the cyclic voltammograms of both compounds reveal two redox waves with ΔEs of approximately the same magnitude around 350-360 mV. While the first oxidation of FcSSFc is 80 mV more positive than the unsubstituted ferrocene, the corresponding redox process of **BFc2S** takes place at -50 mV versus the Fc^+/Fc couple. This difference suggests that the sulfur-attached ferrocene has higher oxidation potential due to the electron-accepting sulfur atom. Inductively, in **BFc2S** the ferrocene unit directly connected to the vinyl moiety is the first redox center.

Several types of interactions between ferrocene nucleus and its directly substituted sulfur atom have been previously proposed[43, 44]. The sulfur atom can oppositely function both as an electron-donor through *pπ-pπ* interaction using its 3*p*-orbital (Scheme 4.1) and as an electron-acceptor via the electron-withdrawing *pπ-dπ* interaction between the molecular orbital of the Cp ring and the unoccupied *d*-orbital of the sulfur atom. Apparently, current CV data, especially the first oxidation of FcSSFc,

pπ-pπ pπ-dπ

Scheme 4.1 Orbital interactions between ferrocene nucleus and sulfur atom.

manifests that the latter interaction is more significant in varying the oxidation potential of sulfur-attached ferrocenes. Nevertheless, the large peak separation (350 mV) of the symmetrical FcSSFc, essentially results from the through-bond electronic coupling, is very similar to that of FcCH=CHFc (380 mV). Provided that the through-bond length of $C(Cp_1)$-S-S-$C(Cp_2)$ (5.57 A)[45] is slightly longer than that of $C(Cp_1)$-CH=CH-$C(Cp_2)$ (c.a. 4.32 A)[46], it is suggested that the sulfur-sulfur $p\pi$-$p\pi$ lone-pair overlapping resembles to the sp^2-sp^2 carbon-carbon overlapping in assisting through-bond electronic interaction, which is in good accordance with the result we described in Chapter 2. Finally, it's necessary to stress that the ΔE (360 mV) of **BFc2S** is an overall outcome of both the metal-metal through-bond electronic communication and the intrinsic chemical environmental difference between the two ferrocenyl end groups. After ruling out the chemical difference factor, 80-(-50) = 130 mV, roughly 360 – 130 = 230 mV is attributed to the intramolecular electronic interaction, which is in good resemblance to that of FcCH=CHCH=CHFc (220 mV) (Chapter 2).

The cyclic voltammograms of **TFc2S-A** and **TFc2S-B** are also shown in Figure 4.17. While **TFc2S-A** exhibits three one-electron oxidation waves, **TFc2S-B** shows a two-electron and a one-electron oxidation waves. Compared to that of **BFc2S**, the first oxidation of **TFc2S-A** is more negative (-125 mV), indicating the oxidation process was carried out at the central ferrocene nucleus which possesses more electron density due to the contribution from the two electron-donating side chain. In contrast, the first oxidation of **TFc2S-B** remains roughly the same as that of **BFc2S**. Together with the fact that this oxidation is a two-electron process, it is very clear the two vinylferrocenyl ending groups are oxidized simultaneously. The ΔE_1 (E_2 - E_1) value, 335 mV, of **TFc2S-A** is close but slightly less than the ΔE of **BFc2S** (360 mV), implying that the second oxidation arises from one of the ending group with the first positive charge localized at the central ferrocene unit. The slightly depressed ΔE_1 can be ascribed to a small charge draining effect from the central ferrocene unit to the third (unoxidized) ferrocenyl group through the linking bridge. It is a little surprising, however, that the ΔE (375 mV) of **TFc2S-B** is just a little larger than that of **BFc2S** since we shall anticipate even greater value due to the two charges pre-generated at the two terminal ferrocenes. The plausible reason is the two surfur atoms on the 1,1'-dithioferrocenyl moiety play as an electronic buffer due to

their high polarizability of their *pπ* lone-pair electrons. In summary, the oxidation processes of **TFc2S-A** and **TFc2S-B** can be described according to the following equations:

$$\text{Fc-SCH=CH-Fc-CH=CHS-Fc} \rightarrow \text{Fc-SCH=CH-Fc}^{+}\text{-CH=CHS-Fc} \rightarrow \text{Fc}^{+}\text{-SCH=CH-Fc}^{+}\text{-CH=CHS-Fc} \rightarrow \text{Fc}^{+}\text{-SCH=CH-Fc}^{+}\text{-CH=CHS-Fc}^{+} \quad (4.2)$$

and

$$\text{Fc-CH=CHS-Fc-SCH=CH-Fc} \rightarrow \text{Fc}^{+}\text{-CH=CHS-Fc-SCH=CH-Fc}^{+} \rightarrow \text{Fc}^{+}\text{-CH=CHS-Fc}^{+}\text{-SCH=CH-Fc}^{+} \quad (4.3)$$

In Figure 4.18, the CVs of **TFc2CO-A**, **TFc2CO-B**, and together with their model compound FcCH=CHC(O)Fc (**BFc2CO**) are shown. **BFc2CO** reveals two positive oxidation processes with oxidation potentials at 184 mV and 464 mV, originating from the vinylferrocenyl and carbonylferrocenyl groups, respectively. Unlike sulfur atom, carbonyl group is a pure electron-withdrawing element on the bridging backbone. The ΔE of **BFc2CO** (280 mV) mainly arises from the environmental difference between the two ferrocenes. Meanwhile, the existing weak coupling between the redox centers in carbonyl bridged system is associated with the through-bond inductive effect since the electron density of the conjugation pathway is highly lessened by the positively polarized carbon atom of the -C(O)- group, which prohibited the charge migration from occurring. Based on this knowledge, the three oxidation waves demonstrated by **TFc2CO-A** are assigned to the following processes:

$$\text{Fc-C(O)CH=CH-Fc-CH=CHC(O)-Fc} \rightarrow \text{Fc-C(O)CH=CH-Fc}^{+}\text{-CH=CHC(O)-Fc} \rightarrow \text{Fc}^{+}\text{-C(O)CH=CH-Fc}^{+}\text{-CH=CHC(O)-Fc} \rightarrow \text{Fc}^{+}\text{-C(O)CH=CH-Fc}^{+}\text{-CH=CHC(O)-Fc}^{+} \quad (4.4)$$

The first oxidation is ascribed to the central ferrocene nucleus for its comparatively higher electron density. The E_1 value is higher than that of **BFc2CO** due to the stronger inductive effect from two carbonyl groups on the side chains of the centeral ferrocenyl unit. Following similar logic, the oxidations of **TFc2CO-B** undergo with the following three redox processes:

$$\text{Fc-CH=CHC(O)-Fc-C(O)CH=CH-Fc} \rightarrow \text{Fc}^{+}\text{-CH=CHC(O)-Fc-C(O)CH=CH-Fc} \rightarrow \text{Fc}^{+}\text{-CH=CHC(O)-Fc-C(O)CH=CH-Fc}^{+} \rightarrow \text{Fc}^{+}\text{-CH=CHC(O)-Fc}^{+}\text{-C(O)CH=CH-Fc}^{+} \quad (4.5)$$

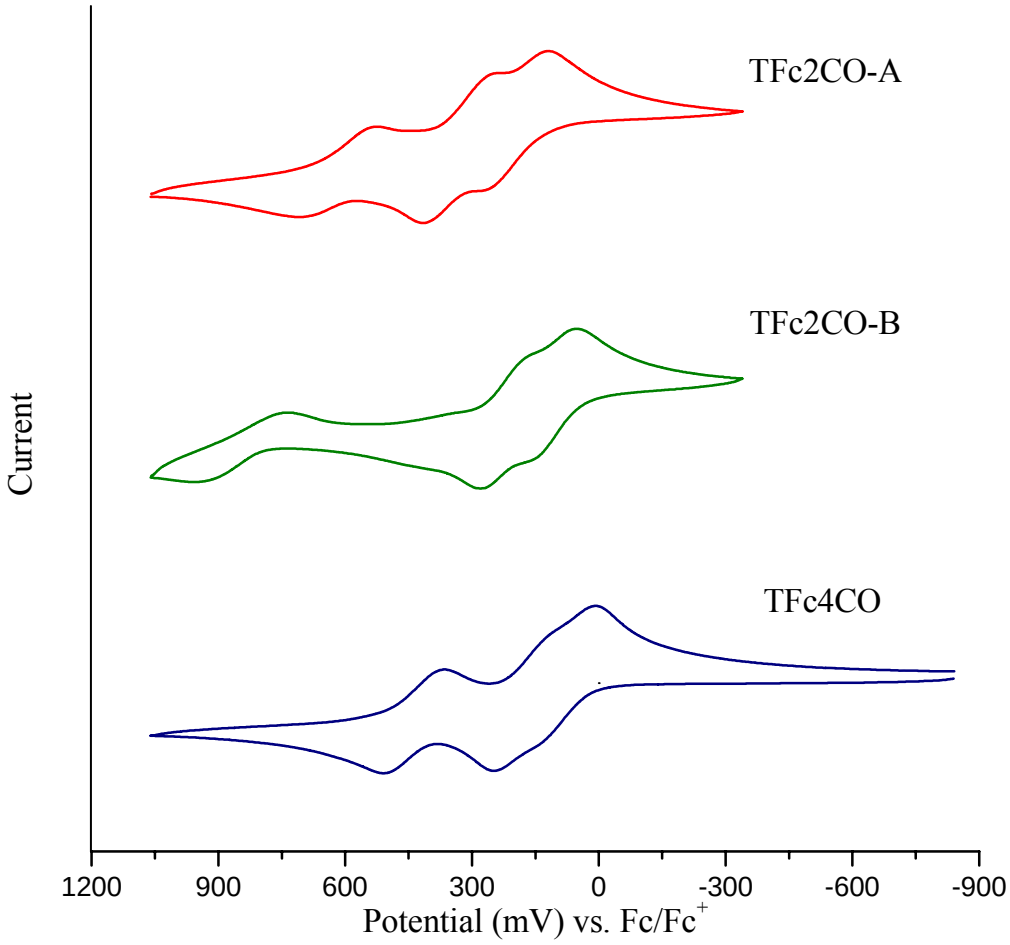

Figure 4.18 Cyclic voltammograms of **TFc2CO-A**, **TFc2CO-B** and **TFc4CO** in CH_2Cl_2/0.1 M Bu_4NTFPB. Scan rate 50 mV/s.

This time the central ferrocenyl moiety is oxidized last, which is obviously attributed to its extreme electron deficiency caused by the two carbonyl subsitutents on its Cp rings. The remarkable feature of the **TFc2CO-B**, however, is that the two identical ending ferrocenes are not oxidized simultaneously, indicating a long range electronic interaction, even the effect is fairly weak in term of ΔE_1, 120 mV. As electron or hole transfer is very unlikely for an electron-deficient conjugation system, this weak intramolecular interaction is assigned to the through-bond inductive effect.

So far, we have observed four oxidation patterns in five triferrocenyl systems, **TFc2** and **TFc2-X**s. The redox processes in these compounds are rather dynamic, which heavily rely on redox-redox distance, electron delocalization, tuning functional groups, inductive effect, etc. This in turn provides the opportunities to use these parameters to control the redox sequence among the metal centers along the conjugation path, which is essentially a generic model for electronic switches.

Symmetrical Compounds

The cyclic voltammogram of **(*E,E,E,E*)-TFc4** reveal three oxidation waves (Figure 4.19) with the first oxidation assigned to the central ferrocenyl unit due to the same reason described for **TFc2**. The ΔE_1 (185 mV) of **TFc4**, however, does not suggest a hole transfer process, i.e. charge relocalization, similar to that of **TFc2** because this value is not significantly deviated from the ΔE of the biferrocenyl analogue FcCH=CHCH=CHFc (220 mV). The decreased peak separation (ΔE_1) can be ascribed to the charge draining effect from the central ferrocene to the third unoxidized terminal ferrocene through the butadienyl side chain, which consequentially gives rise to a large ΔE_2 (225 mV). An interesting alternative of **(*E,E,E,E*)-TFc4** is its geometrically unspecified *cis/trans* isomeric mixture, *cis/trans*-**TFc4**, obtained from the corresponding Wittig reaction. While the first oxidation of *cis/trans*-**TFc4** appears at the approximately same position of that of **(*E,E,E,E*)-TFc4** (Figure 4.19), the second and the third oxidations are considerably more negative, giving ΔE_1 and ΔE_2 of 160 mV and 135 mV, respectively. This suggests that regio-regularity plays an important role in the polyene bridged systems comprising multiple redox centers. Apparently, all *E* arrangement provides more efficient channel for electronic communications.

The electrochemical behaviors of **TFc4-S** and **TFc4-Th** (Figure 4.19) are similar to that of **TFc4** in term of the negative shift of the first oxidation wave and the three one-electron redox pattern. Again, the central ferrocene unit is first to be oxidized, followed by sequential oxidations of the two ending ferrocenyl groups. Since –CH=CH-S-CH=CH- and –CH=CH-Th-CH=CH- are even weaker electron/hole transfer channel than the butadienyl bridge (Chapter 2), little charge-draining effect on the second oxidation was observed for **TFc4-S** and **TFc4-Th**. The ΔE_1s of both compounds are essentially same as their diferrocenyl analogues (**BFcVS** and **BFcVTh** in Chapter 2).

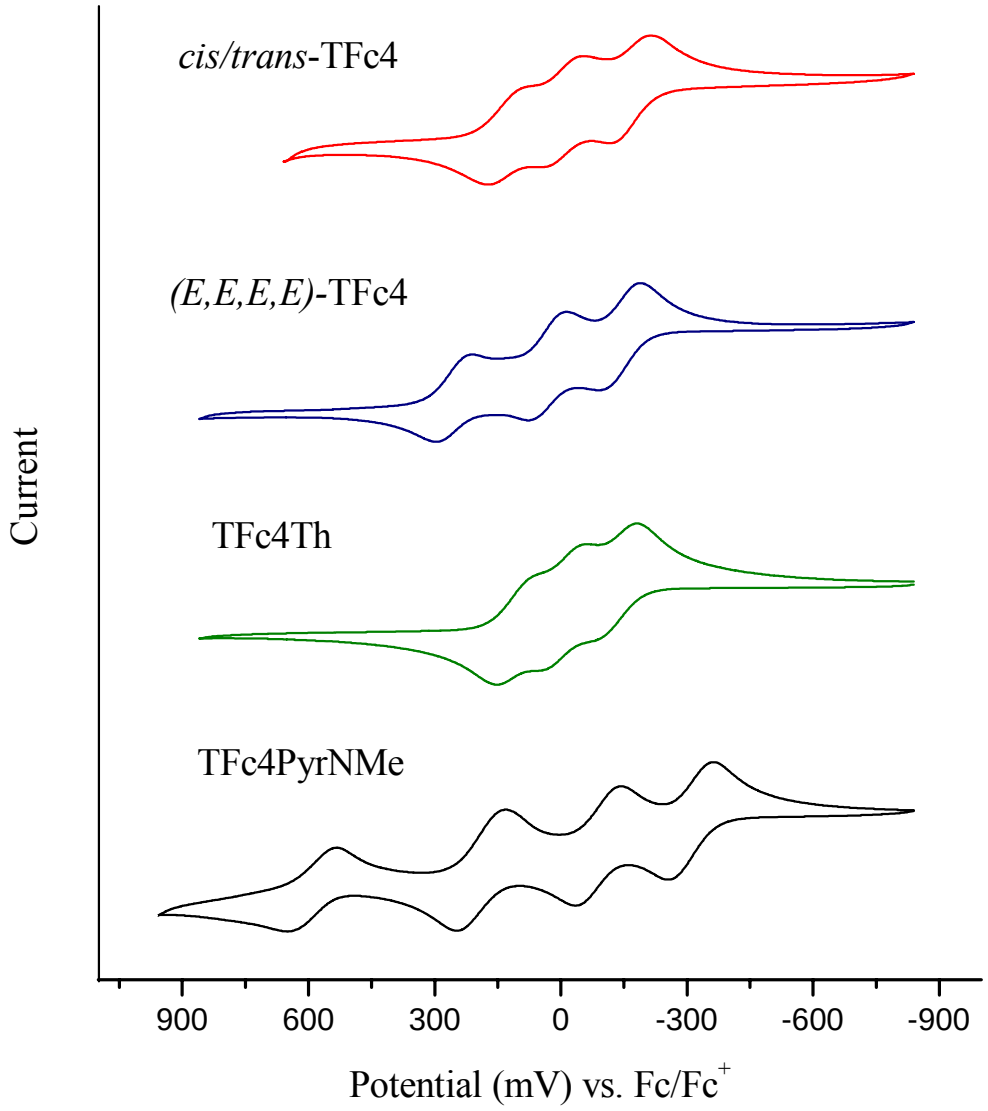

Figure 4.19 Cyclic voltammograms of cis/trans-**TFc4**, **(*E,E,E,E*)-TFc4**, **TFc4Th** and **TFc4PyrNMe** in CH_2Cl_2/0.1 M Bu_4NTFPB. Scan rate 50 mV/s.

Whereas the linking spacers in the triferrocenyl systems discussed so far merely function as electronic communication supporter and redox tuner, none of them electrochemically participate in the redox processes in the measurable extent. When pyrrolene moiety is incorporated as the X group in the **TFc4-X** series, the situation is totally changed as **TFc4PyrNMe** exhibited four oxidation waves as shown in Figure 4.19. Besides the three redox-active ferrocene nuclei, the additional redox process must be derived from one of the pyrrolene moieties since the oxidation potential of 2,5-divinyl substituted N-alkylpyrrole is very close to that of ferrocene, which has been extensively studied in the previous chapters. Indeed, careful examination of the electrochemical data of **TFc4PyrNMe** reveals some fascinating redox features actively partook and varied by the bridging pyrrolene units.

The further negated first oxidation wave (-303 mV) of **TFc4PyrNMe**, compared to that of the bis(2-ferrocenylvinyl)pyrrole analogue (**BFc4PyrNMe** shows E_1 = -250 mV in Chapter 3), arises from the central ferrocene nucleus due to the electron-donating effect from the two pyrrolene-contained side chains. The second oxidation (-78 mV), however, appears at a rather negative position, leading to a significantly lowered ΔE_1 (225 mV) compared to that of **BFc4PyrNMe** (380 mV). Again, since the second redox process presumably occurs at one of the terminal ferrocene nuclei, the considerably depreciated electronic coupling, indicated by ΔE_1, implies that the first positive charge relocalized from the central ferrocenyl unit to the adjacent pyrrolene moiety or to the even more distant un-oxidized terminal ferrocene immediately prior to the second oxidation process taking place, although the precise charge migration is difficult to tell by a single characterization technique, namely, by electrochemistry. Obviously, this charge arrangement is thermodynamically more stable for the dicatonic species of **TFc4PyrNMe** as previously observed in the dicationic species of **TFc2**. The consequentially generated tricationic and tetracationic species represent moderately increased ΔE_2 ($E_3 - E_2$ = 278 mV) and ΔE_3 ($E_4 - E_3$ = 280 mV), indicating the third and forth oxidations are even more profound processes, in which the newly formed positive charges are not able to escape beyond the system but mobilize dynamically to minimize the electrostatic repulsions, which gives rise to the overall redox processes as shown below,

Fc-V-Pyr-V-Fc-V-Pyr-V-Fc → Fc-V-Pyr-V-Fc^+-V-Pyr-V-Fc → [Fc-V-Pyr^+-V-Fc-V-Pyr-V-Fc^+ ←→ Fc^+-V-Pyr-V-Fc-V-Pyr-V-Fc^+] → Fc^+-V-Pyr-V-Fc^+-V-Pyr-V-Fc^+ → [Fc^+-V-Pyr^+-V-Fc-V-Pyr^+-V-Fc^+ ←→ Fc^+-V-Pyr^+-V-Fc^+-V-Pyr-V-Fc^+ ←→ Fc^+-V-Pyr-V-Fc^+-V-Pyr^+-V-Fc^+ ←→…..] (4.6)

where V and Pyr denote the vinylene and N-methylpyrrolene groups, respectively, for simplicity. It is worth stressing, however, these equations above are rather illustrative pictures which do not engage in many details for conceptual interpretation. As we can see, some of the charged species such as Fc-V-Pyr-V-Fc^+-V-Pyr-V-Fc certainly has more vibronic forms to gain higher stability. In addition, such dynamic oxidation process has been previously observed in oligoferrocenyl systems,[10, 40, 41] in which the ferrocenes are directly linked to each other or linked by a single-atom spacer (e.g. $SiMe_2$). The pyrrolene-incorporated triferrocenyl compound herein, however, shows even more subtle information, which needs more sophisticated investigation on the intermediate charged-states. This investigation is currently being undergone in our laboratory in a combinational manner involving techniques such as mixed-valence, ESR, Mossbauer spectroscopy along with theoretical calculations.

Intervalence Electronic Absorption

The mixed-valence (MV) species were generated using the same method described in previous chapters and the UV-Vis-NIR spectra were collected accordingly with successive addition of oxidants ($FcPF_6$ or magic blue). Our efforts in mixed-valence absorptions herein are mainly focused on the one-electron oxidized species, i.e. the monocationic triferrocene systems, which is more important to the interested properties. However, the discussion and developed model below are extensible to the dictionic counterparts and will be examined in the future studies.

Before we get into the spectroscopic details of each (or each group of) triferrocene mixed-valence species, it is important to first gain a basic understanding of the excited state electron transitions in triferrocenium systems and their difference from the corresponding biferrocene mixed-valence analogues. In mixed-valence biferrocenium system Fc^+-B-Fc, where B denotes a symmetrical bridging unit, the ground-state (Fc^+-B-Fc) and its photo-induced vibrationally excited state [Fc-B-Fc^+]* are two isoenergetic

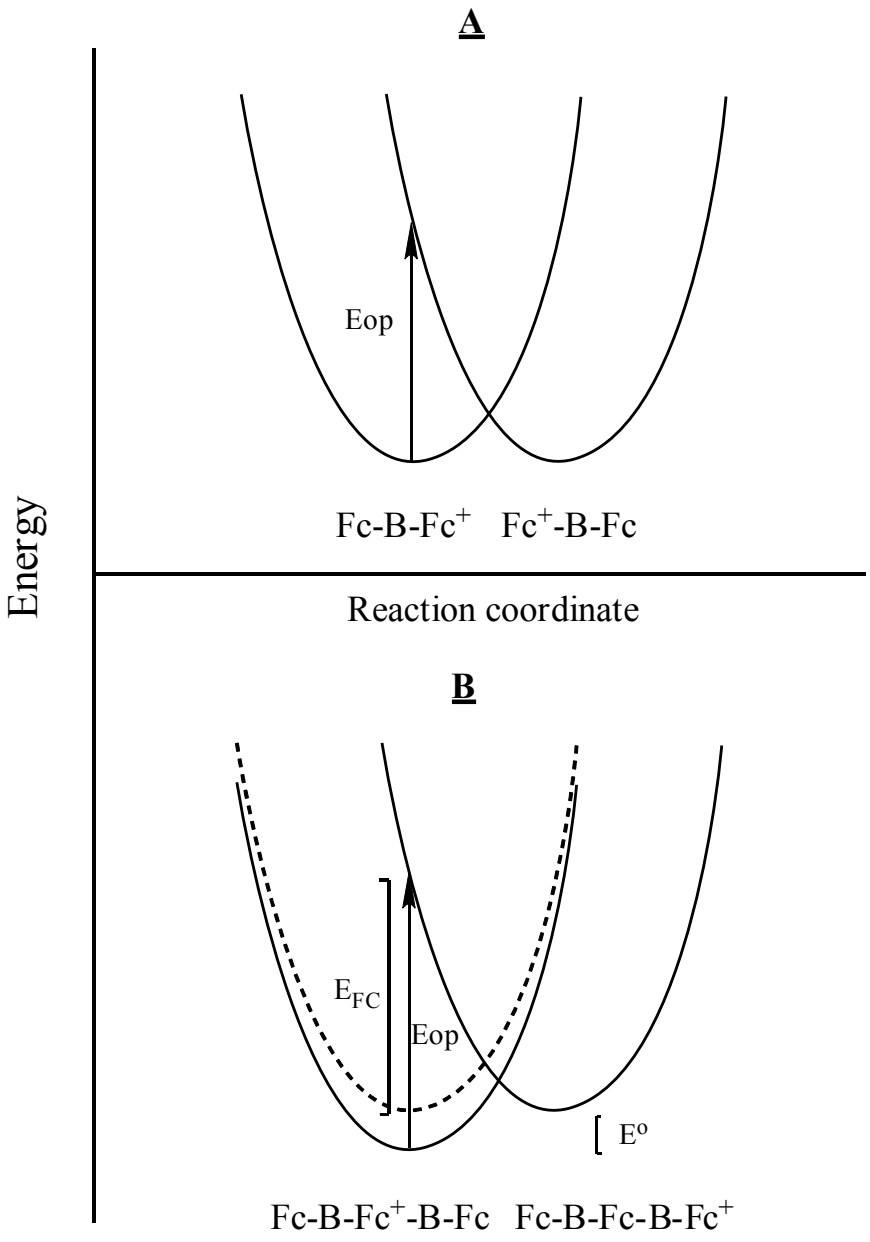

Figure 4.20 Schematic representation of potential coordinate diagrams for photo-induced electron transfer in biferrocenium and triferrocenium ions with symmetrical bridging linker B. A: the symmetrical case for the biferrocenium ion showing the transition Fc-B-Fc^+ + *hv* -> (Fc^+-B-Fc)*; B: the asymmetrical case for the triferrocenium ion showing the transition Fc-B-Fc^+-B-Fc + *hv* -> (Fc-B-Fc-B-Fc^+)*, E^o is the energy difference between the two isomeric oxidation states of the triferrocene cationic species.

isomers. Therefore, the two energy wells of these two states reside at the same energy level as illustrated in Figure 4.20A. For mixed-valence triferrocenes, however, the energy levels of these two wells are no longer the same (Figure 4.20B). This is a consequence of the asymmetrical structure of the triferrocenes, in which the two terminal ferrocenes are energetically identical (in all cases in this study) but different from the central ferrocene moiety. Thus, Fc-B-Fc^+-B-Fc and its photo-induced corresponding [Fc-B-Fc-B-Fc^+]* are energetically nonequivalent species with the latter possessing higher energy than the former due to relative instability. The free energy difference between the two states is represented as E^o in the potential energy-configurational coordination diagram shown in Scheme 4.2B. As described by Hush,[47] the energy for such an asymmetrical transition (E_{op}) will equal the sum of the Franck-Condon energy (E_{FC}) and the difference in energy (E^o) between the equilibrium vibrational states of Fc-B-Fc^+-B-Fc and the Fc-B-Fc-B-Fc^+, $E_{op} = E_{FC} + E^o$. For the intervalence charge transfer (IVCT)

$$\nu_{op} = \nu_{FC} + \nu^o \qquad (4.7)$$

where ν is the transition frequency in wave numbers.

The free energy difference (E^o) between the two oxidation state isomers can be estimated from the corresponding electrochemical data. Whereas the free energy of Fc-B-Fc^+-B-Fc is obtained directly from the first oxidation potential (E_1) of the neutral species, the energy of Fc-B-Fc-B-Fc^+ can be estimated from the corresponding oxidation potential of Fc-B-Fc^+ for a first approximation. This assumption is fairly reasonable for relatively less delocalized systems which are most of our cases. Meanwhile, a statistic factor should be counted in for Fc-B-Fc-B-Fc^+ species since there are two energetically equivalent ways of forming it, Fc-B-Fc-B-Fc^+ and Fc^+-B-Fc-B-Fc. This factor is small, (RT/nF)ln2 = 0.018 V, and nearly within the experimental error (±0.01 V). Thus, E^o and ν^o can be calculated as

$$E^o = E_{1(Fc\text{-}B\text{-}Fc\text{-}B\text{-}Fc)} - E_{1(Fc\text{-}B\text{-}Fc)} + 0.018 \qquad (4.8)$$

$$\nu^o = (10^7 \times E^o)/1240 \quad \text{(where } E^o \text{ is in eV)} \qquad (4.9)$$

Mixed-Valence Species With Symmetrical Linkers: **TFc2**$^+$, **TFc4**$^+$ and **TFc4Th**$^+$.

The one-electron oxidized MV spectra of **TFc2**$^+$, **TFc4**$^+$and **TFc4Th**$^+$ are shown in Figure 4.21, along with the spectra of their corresponding biferrcocenium analogues. The

summarized band parameters after spectral deconvolution and calculated Hush parameters (equations therein) are listed in Table 4.2.

Table 4.2 IVCT and LMCT band parameters, obtained from the spectral deconvolution, and calculated Hush parameters for the relevant cationic species.

	ν_{max} [cm^{-1}]	ε_{max} [$M^{-1}cm^{-1}$]	$\Delta\nu$ [cm^{-1}]	d_{da} [a] [Å]	V [b] [cm^{-1}]	α [c]
BFc2$^+$	5100	1620	3720	7.02 [d]	511 [j]	0.10
TFc2$^+$	5300	2440	3800	7.02 [d]	647 [j]	0.12
BFc4$^+$	5290	2320	3900	9.21 [d]	486 [j]	0.09
TFc4$^+$	5520	3600	3760	9.21 [d]	608 [j]	0.11
BFc4Th$^+$	6130	2770	4000	10.85	492 [j]	0.08
TFc4Th$^+$	6000	4020	4300	11 [e]	600 [j]	0.10
TFc4PyrNMe$^+$	6650	2950	2980	6.27	791 [k]	0.12
	4690	7300	2800	12.35 [e]	514 [j]	0.11
BFc2S$^+$	11790 [h]	245	1800		-	-
	9690 [i]	990	2995	5.73 [f]	607 [k]	0.06
	6710	190	2880	8.79	141 [j]	0.021
TFc2S$^+$	11850 [h]	609	2370		-	-
	9560 [i]	1320	3030	5.68 [g]	706 [k]	0.074
	7110	205	2700	8.28 [e]	155 [j]	0.022

[a] Spatial distance between electron donor and acceptor; [b] Hush coupling constant $V = 2.06 \times 10^{-2}(\varepsilon_{max}\cdot\Delta\nu_{1/2}\cdot\nu_{max})^{1/2}/d$; [c] delocalization efficient $\alpha = V/\nu_{max}$; [d] estimated from literature ref. 2; [e] average iron-iron distance of the two terminal Fe to the central Fe obtained from crystal structure; [f] distance between sulfur and vinyl-connected ferrocene Fe; [g] average sulfur-iron distance of the two side chain sulfur to the central Fe; [h] LMCT transition 1 as described in text; [i] LMCT transition 2, presumably from sulfur lone-pair electron to Fe^{III}; [j] IVCT transition; [k] LMCT transition.

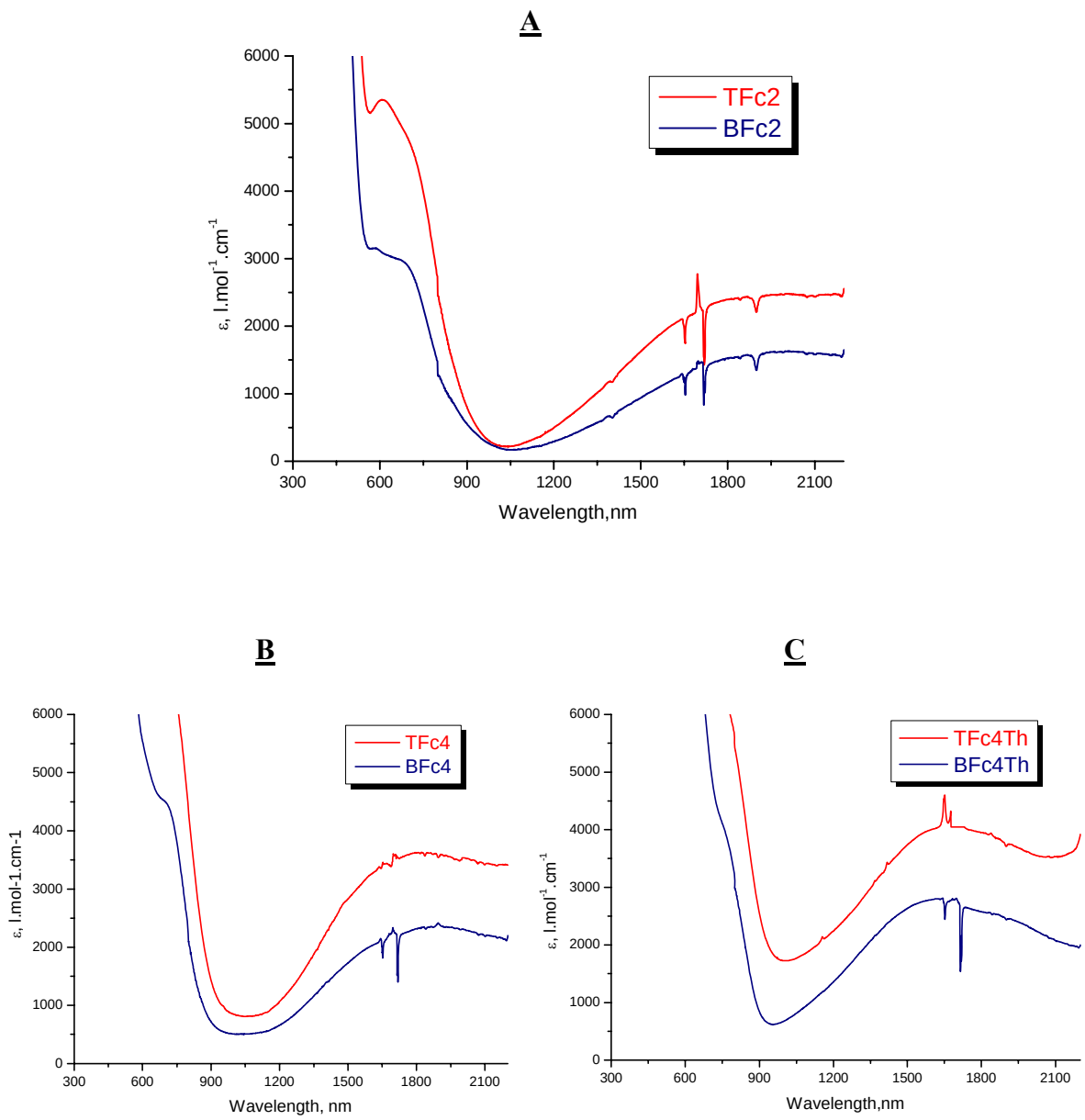

Figure 4.21 UV-Vis-NIR spectra of one-electron oxidized mixed-valence species. A: **TFc2**$^{+}$ and **BFc2**$^{+}$; B: **TFc4**$^{+}$ and **BFc4**$^{+}$; C: **TFc4Th**$^{+}$ and **BFc4Th**$^{+}$.

For each case, the λ_{max} of the low energy band, presumably the IVCT band, of the triferrocenium monocation appears at nearly the same position as that of its biferrocenium counterpart. This similarity in IVCT λ_{max} is not a surprise since the free energy difference E^o between the two equilibrium vibritional oxidation isomers is fairly small for these three triferrocenes. Taking **TFc2**$^+$ for instance, the calculated E^o from the data in table 4.1 is -0.014 V, which corresponds to a ΔG of 0.33 kcal/mol and ν^o of 113 cm^{-1}. This is a considerably small value to be detected and virtually negligible in a broad low energy IVCT band. Since $E^o \approx 0$, $Eop \approx E_{FC}$. If E_{FC} is nearly the same for **TFc2**$^+$ and **BFc2**$^+$, the IVCT ν values should also be nearly the same, which they are. For **TFc4**$^+$, however, the E^o is comparatively of significance, -0.06V, which means a blue-shift (483 cm^{-1}) to that of **BFc4**$^+$. As shown in table 4.2, we did observed a 230 cm^{-1} shifting to higher energy in **TFc4**$^+$. The variation between the experimental record and calculated result is still in the reasonable region since this value is still small to be accurately addressed under the experimental conditions. The other possible intrinsic reason for such difference could be ascribed to the slightly distorted potential energy surface of **TFc4**$^+$ from that of **BFc4**$^+$.

The molar extinction coefficients (ε_{max}) of the IVCT band for the triferrocenium monocations are considerably greater than for their corresponding biferrocenium monocationic analogues. The enhanced intensity for the mixed valence triferrocene ions can be attributed to the existence of equivalent transitions. In other words, there are two equivalent IVCT transitions from the full-filled dπ orbitals of the two terminal ferrocenes to the half-occupied central ferrocene dπ orbital, which gives rise to

$$Fc\text{-}B\text{-}Fc^+\text{-}B\text{-}Fc + h\nu \rightarrow (Fc\text{-}B\text{-}Fc\text{-}B\text{-}Fc^+)^* \text{ and}$$
$$Fc\text{-}B\text{-}Fc^+\text{-}B\text{-}Fc + h\nu \rightarrow (Fc^+\text{-}B\text{-}Fc\text{-}B\text{-}Fc)^* \qquad (4.10)$$

This additive effect in turn confirms our previous conclusion that the first oxidized moiety is located at the central ferrocene unit. In theory, such additive effect should lead to doubled ε_{max}, however, none of the triferrocenes demonstrated intensity increase to 100%. This implies that the electronic interactions among the iron centers are rather dynamic than static sum. Other exterior factors such as ion-pairing and solubility (triferrocenium ion is apparently less soluble than biferrocenium ion due to the extended conjugation) could also result in non-100% increased IVCT band. Due to the increased

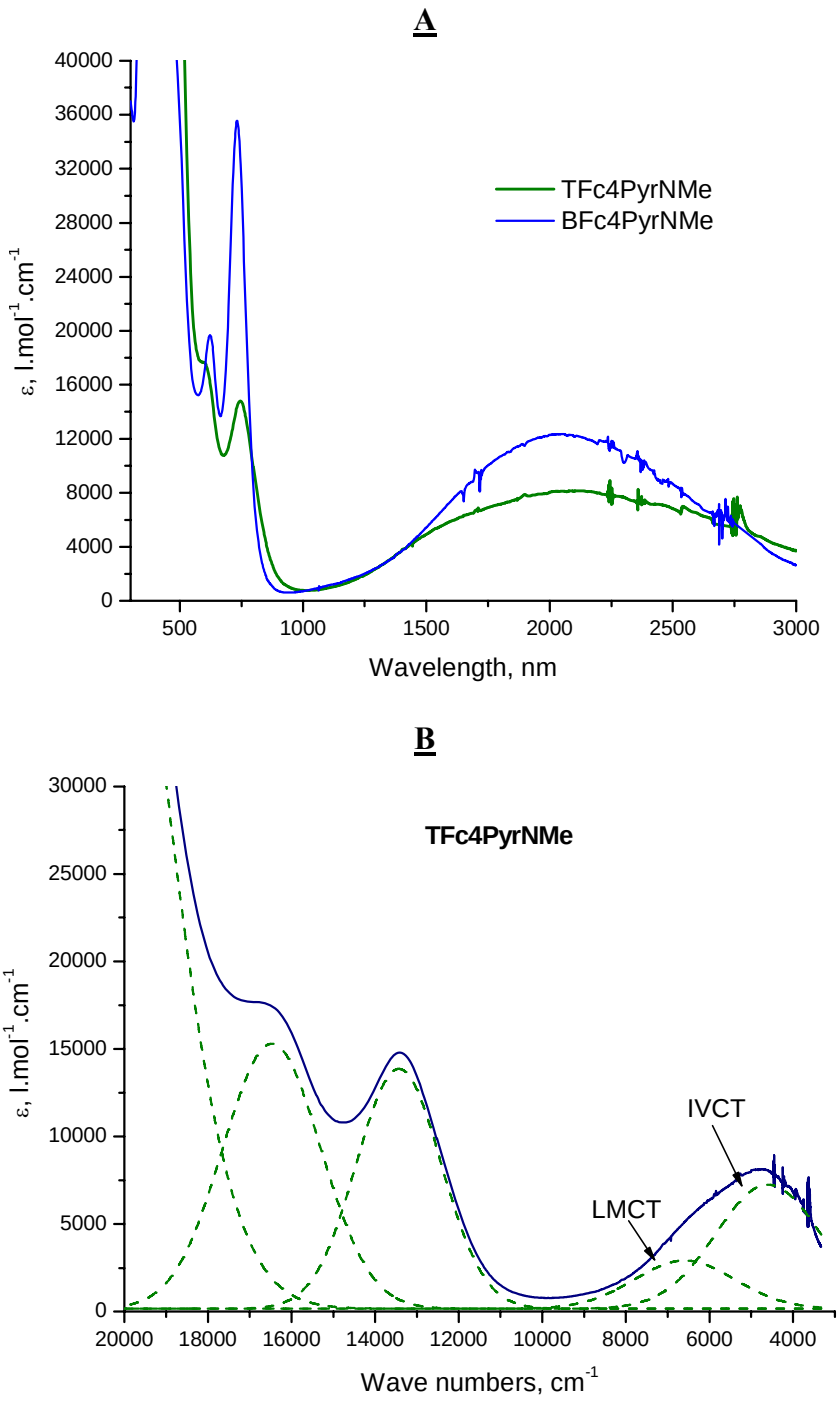

Figure 4.22 UV-Vis-NIR spectra of one-electron oxidized mixed-valence species, **TFc4PyrNMe**$^+$. A: **TFc4PyrNMe**$^+$ (green) and **BFc4PyrNMe**$^+$ (blue). The molar extinction efficient of **TFc4PyrNMe**$^+$ was calculated from the data obtained from 0.2 equivalent of $FcPF_6$ in presence to avoid possible formation dicationic species. B: deconvoluted bands (dashed lines) of **TFc4PyrNMe**$^+$, assuming gaussian-shaped absorptions.

ε_{max}, however, the calculated Hush electronic coupling constant and delocalization efficient of triferrocenes are all greater than the corresponding biferrocenes.

Mixed-valence Species With Vinylene-Pyrrolene-Vinylene as Linker: **TFc4PyrNMe$^+$**

Despite the fact that the bridging unit in **TFc4PyrNMe** is also symmetrical, the one electron-oxidized species **TFc4PyrNMe$^+$** exhibits substantially different spectroscopic behaviors from its triferrocenium peers discussed above. As shown in Figure 4.22A, compared to that of biferrocene analogue **BFc4PyrNMe$^+$**, the low energy envelope of **TFc4PyrNMe$^+$** features with decreased absorption intensity and broadened band width. Since it is confident that the first oxidation of **TFc4PyrNMe** derives from the central ferrocene unit due to the two strong electron-donating side chains as we discussed in the electrochemical section, the decreased intensity, or, in other words, the absence of the electron transfer additive effect in **TFc4PyrNMe$^+$** suggests that there is new mechanism involved which makes **TFc4PyrNMe$^+$** significantly disparate from the conventional triferrocene systems, i.e. the relatively localized systems.

It is important to realize that IVCT additive effect in triferrocene cations only occurs in the systems with the positive charge mostly localized on the central ferrocene which will give rise to an excitation Fc$^+$-B-Fc- pair as we observed for **TFc2$^+$**, **TFc4$^+$**, and **TFc4Th$^+$**. Given the fact that interaction between the IVCT transitions in these less delocalized systems is weak, the transition intensities therefore are additive. If delocalization is extensive, IVCT excitation will not be localized to a given Fc$^+$-B-Fc- pair, the IVCT transitions will interact, giving rise to delocalized excitation states. In **TFc4PyrNMe$^+$**, however, the situation is more complicated not only because of the enhanced electronic interaction between the ferrocenes but also the low band gap between the frontier HOMO ligand orbital and the Fe^{III} dπ orbital as we intensively discussed in Chapter 3. Such low band gap is further decreased in **TFc4PyrNMe$^+$** due to the decreased energy level of central iron orbital because the perturbation of two electron-rich side chains. It is very likely the positive charge initially generated at the central ferrocene group partially seeped into the pyrrolene-centered ancillary ligands. The significantly decreased intensity of the bridging-ligand-based π-π* transition band (centered at 742 nm in Figure 4.22A) might be accounted for such charge distribution.

Deconvolution of the **TFc4PyrNMe**$^+$ spectrum reveals two low energy Gaussians centered at 6652 cm^{-1} and 4690 cm^{-1}, respectively (Figure 4.22B). From our previous knowledge (Chapter 3), these two bands are assigned to pyrrolene-based LMCT and iron-iron interacted IVCT transitions, respectively, as marked in Figure 4.22B. The spectral data and calculated result according Hush equation are listed in Table 4.2. Compared to those of **BFc4PyrNMe**$^+$, the LMCT transition in **TFc4PyrNMe**$^+$ is explicitly presented and enhanced, and is apparently the consequence of additive effect of Fc-B^+- pair, where B is pyrrolene-centered bridging ligand; the decreased energy requirement (4690 cm^{-1}) for IVCT transition in **TFc4PyrNMe**$^+$ implies that the energy gap between Fe^{II} and Fe^{III} is further decreased due to promoted delocalization. The calculated Hush coupling constant, *V*, however, showed lowered electronic coupling in spite of the doubled IVCT interacting sources between the central Fe^{III} to the two terminal Fe^{II}. This contradiction might be ascribed to the competing of the LMCT process or the ineffectiveness of the Hush formalism in dealing with highly delocalized systems.[48-50] In fact, **TFc4PyrNMe**$^+$ represents a unique system in which multiply electronic interactions and vibrationally excited states can co-exist with charge more evenly distributed among the metal sites and organic components.

Mixed-valence species with asymmetrical linkers: **DFc2S**$^+$ and **TFc2S-A**$^+$

The one-electron oxidized mixed-valence spectra of **BFc2S**$^+$ and **TFc2S-A**$^+$ are shown in Figure 4.23, the corresponding spectral data are summarized in Table 4.2. As shown in Figure 4.23A, both mono-charged species show a major low energy band with roughly same λ_{max} around 1050 nm and negligible absorptions in the NIR region beyond 1500 nm. As we discussed in the electrochemical section, the positive charge of the monocations of these two species is localized at the vinyl-connected ferrocene group in **BFc2S**$^+$ and the doubly vinyl-linked central ferrocene in **TFc2S-A**$^+$. The positions of these bands suggest LMCT transitions presumably from the bridging Cp–SCH=CH-Cp ligand to the half-occupied Fe^{III} dπ orbital. The stronger LMCT band exhibited in **TFc2S-A**$^+$ is apparently attributed to the additive effect arising from two side chains on the central ferrocene unit. Although we have also attempted to reveal the similar spectra on **BFc2CO**, **TFc2CO-A** and **TFc2CO-B** using stronger oxidant, magic blue, none of them showed any noticeable NIR band. The lowest-energy absorption in these monocationc

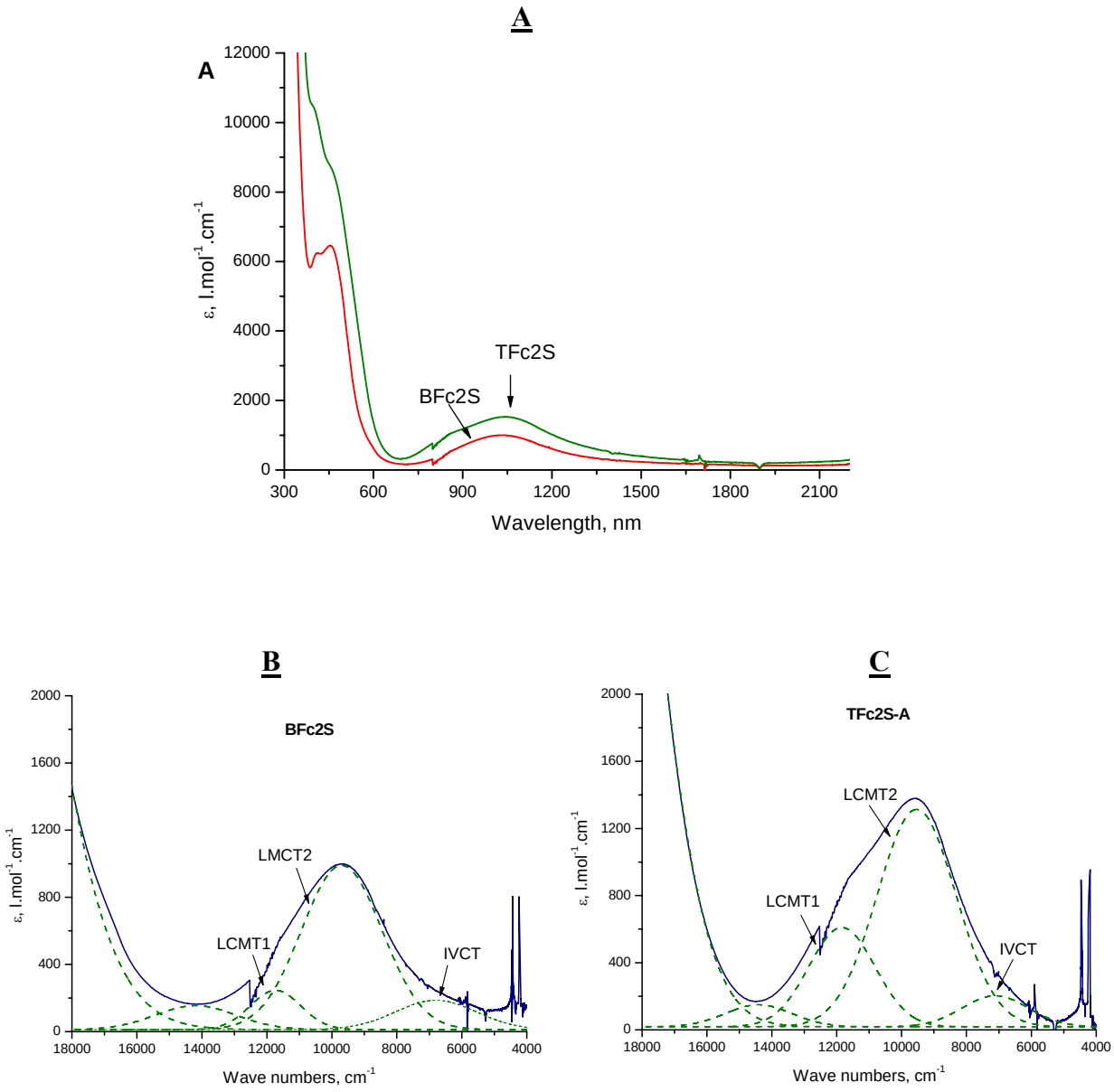

Figures 4.23. UV-Vis-NIR spectra of one-electron oxidized mixed-valence species, **BFc2S**$^{+}$ and **TFc2S-A**$^{+}$. A: spectra of **BFc2S**$^{+}$ (red line) and **TFc2S-A**$^{+}$ (green line); B and C: deconvoluted spectra in the NIR region of **BFc2S**$^{+}$ and **TFc2S-A**$^{+}$**,** respectively. The green dashed lines are the deconvoluted bands after curve fitting, assuming gaussian-shaped bands.

species is the Cp-to-Fe^{III} transition band appearing around 600 nm. Therefore, the highly electron-deficient –C(O)CH=CH- linker is essentially an insulator in supporting charge transport. The electronic interaction between the metal centers demonstrated in electrochemistry arises rather from inductive and electrostatic effects than superexchange or hopping mechanism.

Further band deconvolution on the spectra of **BFc2S**$^+$ in the NIR region (800 nm-2500 nm) revealed three discrete gaussians with absorption maxima at 11790 cm^{-1}(ε_{max} 246 $M^{-1}cm^{-1}$), 9690 cm^{-1} (ε_{max} 990 $M^{-1}cm^{-1}$) and 6710 cm^{-1} (ε_{max} 190 $M^{-1}cm^{-1}$), respectively, as shown in Figure 4.23B. Whereas the major 9690 cm^{-1} is still assigned to the LMCT transition, the higher energy shoulder band at 11790 cm^{-1} is a little bit of mystery. In fact, this shoulder band becomes more visible in **TFc2S-A**$^+$ as deconvolution shows three very similar gaussians (Figure 4.23B) with the c.a. 11790 cm^{-1} band even more intense and broader. The splitting of the LMCT bands could be ascribed to the electron transitions originated from different ligand orbitals, i.e. a Cp-vinyl-based and a Cp-sulfur-based ligand to metal charge transfers, with the former corresponding to the 11790 cm^{-1} band and the latter to the 9690 cm^{-1} band. This assignment is in accordance to the obviously promoted Cp-vinyl based LMCT band in **TFc2S-A**$^+$ which is a consequence of two vinyl-linked side chains on the central ferrocene. As to the very weak bands showing around 6710-7000 cm^{-1} in **BFc2S**$^+$ and **TFc2S-A**$^+$, we tentatively assign them as IVCT bands. The calculated Hush coupling constants are fairly small (around 150 cm^{-1}) (in Table 4.2) due to the low ε_{max}. This is expected and is in the similar magnitude as for other biferrocenyl systems containing heteroatom as the bridging spacers.[51]

Conclusion

We have prepared a series of novel triferrocene compounds linked by symmetric and asymmetric spacers with varied length of conjugation. X-ray structural analysis revealed very interesting patterns dominated either by intramolecular π-π stacking or packing effect. The electrochemical studies suggest that electron-hopping or charge relocalization is more likely when the conjugated linker is short, which allows thermodynamically more stable state to achieve in avoiding the Coulomb repulsion due to the close proximity between the neighboring positive sites. As the bridging spacer is elongated, the positive charge in the intermediate oxidation state is basically localized. Electronic interaction between the metal centers is presumably governed by the superexchange mechanism or through-bond inductive effect depending on the symmetrical property of the bridging spacer. In mixed-valence studies, such interaction exhibits additive effect in the symmetrically linked triferrocenes due to the existence of two isoenergetic oxidation state isomers (Fc-B-Fc-B-Fc^+)* and (Fc^+-B-Fc-B-Fc)* in the excited state. Such an additive effect can be considered as a characteristic of less or partial delocalization in the triferrocene system. When the electron delocalization effect is strong, as demonstrated by pyrrolene-mediated **TFc4PyrNMe**, both electrochemical and mixed-valence spectroscopic behaviors become unique. This is a consequence of redox-matching between the redox-active metal centers and the bridging organic ligand. Due to the low the energy gap between them, the bridging ligand acts more actively in supporting electron/hole transfer. Multiple electron hoppings among redox-active metal and organic sites become plausible in long range. This, again, guided our previous perspective in preparing highly delocalized conducting polymers. Finally, in asymmetrical triferrocene systems, we have discovered that, depending on the direction of the polar linking chain, the central ferrocene becomes a switching element, turning on or off the communication between the two ending ferrocenes, which provided a convenient prototype in designing molecular switches.

References

1. Tolbert, L. M.; Zhao, X.; Ding, Y.; Bottomley, L., *J. Am. Chem. Soc.* **1995,** 117, 12891-12892.

2. Ribou, A.-C.; Launay, J.-P. ; Sachtleben, M. L.; Li, H.; Spangler, C. W., *Inorg. Chem.* **1996,** 35, 3735-3740.

3. Skibar, W.; Kopacka, H.; Wurst, K.; Salzmann, C.; Ongania, K. H.; Fabrizi de Biani, F.; Zanello, P.; Bildstein, B., *Organometallics* **2004,** 23, 1024-1041.

4. Sato, M.; Kashiwagi, S.; Taniguchi, H.; Hiroi, M., *Jpn. J. Appl. Phys.* **1999,** 38, L1073-L1075.

5. Thomas, J. K. R.; Lin, J. T.; Wen, Y. S., *Organometallics* **2000,** 19, 1008-1012.

6. Nishihara, H.; Hirao, T.; Aramaki, K.; Aoki, K., *Synth. Metals* **1997,** 84.

7. Barlow, S.; O'Hare, D., *Chem. Rev.* **1997,** 97, 637 -669.

8. Pannell, K. H.; Dementiev, V. V.; Li, H.; Cervantes-Lee, F.; Nguyen, M. T.; Diaz, A. F., *Organometallics* **1994,** 13, 3644-3650.

9. Barlow, S.; Murphy, V. J.; Evans, J. S. O.; O'Hare, D., *Organometallics* **1995,** 14, 3461-3474.

10. Rulkens, R.; Lough, A. J.; Manners, I.; Lovelace, S. R.; Grant, C.; Geiger, W. E., *J. Am. Chem. Soc.* **1996,** 118, 12683-12695.

11. Hirao, T.; Kurashima, M.; Aramaki, K.; Nishihara, H., *J. Chem. Soc., Dalton Trans.* **1996**, 2929-2933.

12. Tárraga, A.; Molina, P.; Curiel, D.; Velasco, M. D., *Organometallics* **2001,** 20, 2145-2152.

13. Caballero, A.; Tárraga, A.; Velasco, M. D.; Espinosa, A.; Molina, P., *Organic Let.* **2005,** 7, 3171-3174.

14. Anderson, P. W., *Phys. Rev.* **1959,** 115, 2.

15. Marcus, R. A., *J. Chem. Phys.* **1965,** 43, 679-701.

16. Lambert, C.; Nöll, G.; Schelter, J., *Nat. Mater.* **2002,** 1, 69-73.

17. Petrov, E. G. M., V., *J. Phys. Chem. A* **2001,** 105, 10176.

18. Glidewell, C.; Royles, B. J. L.; Smith, D. M., *J. Organomet. Chem.* **1997,** 527, (1-2), 259-261.

19. Mueller-Westerhoff, U. T.; Yang, A.; Ingram, G., *J. Oragnomet. Chem.* **1993,** 463, 163-167.

20. Alley, S. R.; Henderson, W., *J. Organomet. Chem.* **2001,** 637-639 216–229.

21. Zakaria, C. M.; Morrison, C. A.; McAndrew, D.; Bell, W.; Gliden, C., *J. Organomet. Chem.* **1995,** 485, 201-207.

22. Mamane, V.; Ledoux-Rak, I.; Deveau, S.; Zyss, J.; Riant, O., *Synthesis* **2003**, (3), 455-467.

23. Herberhold, M.; Nuyken, O.; Poehlmann, T., *J. Organomet. Chem.* **1995,** 501, (1-2), 13-22.

24. Driscoll, J. S.; Grisley Jr., D. W.; Pustinger, J. V.; Harris, J. E.; Matthews, C. N., *J. Org. Chem.* **1964,** 29, 2427-2431.

25. Bishop, J. J.; Davison, A.; Katcher, M. L.; Lichtenberg, D. W.; Merrill, R. E.; Smart, J. C., *J. Organomet. Chem.* **1971,** 27, (2), 241-249.

26. Pauson, P. L.; Watts, W. E., *J. Chem. Soc.* **1963**, 2990-2996.

27. Glidewell, C.; Zakaria, C. M., *Acta Cryst.* **1994,** C50, 233-238.

28. Liu, W.; Xu, Q.; Ma, Y.; Liang, Y.; Dong, N.; Gan, D., *J. Organomet. Chem.* **2001** 625, 128-131.

29. Butler, I. R.; Cullen, W. R.; Ni, J.; Rettig, S. J., *Organometallics* **1985,** 4, 2196-2201.

30. Block, E.; Aslam, M., *J. Am. Chem. Soc.* **1985,** 107, (23), 6729-6731.

31. Ogawa, T.; Hayami, K.; Suzuki, H., *Chem. Let.* **1989**, (5), 769-72.

32. Knox, G. R.; Pauson, P. L., *J. Chem. Soc.* **1958**, 692-6.

33. Naskar, D.; Das, S. K.; Giribabu, L.; Maiya, B. G.; Roy, S., *Organometallics* **2000,** 19, (8), 1464-1469.

34. Togni, A.; Hayashi, T., *Ferrocenes: Homogeneous Catalysis-OrganicnSynthesis Materials-Science, VCH Publishers, New York, NY (USA)* **1995**.

35. Mata, J. A.; Peris, E., *J. Chem. Soc., Dalton Trans.* **2001**, (24), 3634-3640.

36. Mata, J. A.; Peris, E.; Llusar, R.; Uriel, S.; Cifuentes, M. P.; Humphrey, M. G.; Samoc, M.; Luther-Davies, B., *Eur. J. Inorg. Chem.* **2001**, (8), 2113-2122.

37. Braga, D.; Maini, L.; Paganelli, F.; Tagliavini, E.; Casolari, S.; Grepioni, F., *J. Organomet. Chem.* **2001,** 637-639, 609-615.

38. Braga, D.; Paganelli, F.; Tagliavini, E.; Casolari, S.; Cojazzi, G.; Grepioni, F., *Organometallics* **1999,** 18, (20), 4191-4196.

39. Braga, D.; Grepioni, F., *Chem. Commun. (Cambridge)* **1996**, (5), 571-578.

40. Aoki, K.; Chen, J.; Nishihara, H.; Hirao, T., *J. Electroanal. Chem.* **1996,** 416, 151-155.

41. Hirao, T.; Aramaki, K.; Nishihara, H., *Bull. Chem. Soc. Jpn.* **1998,** 71, 1817-1823.

42. Aoki, K.; Chen, J., *J. Electroanal. Chem.* **1995,** 380, 35-45.

43. Sato, M.; Tanaka, S.; Ebine, S.; Morinaga, K.; Akabori, S., *J. Organomet. Chem.* **1985,** 282, (2), 247-53.

44. Sato, M.; Tanaka, S.; Ebine, S.; Morinaga, K.; Akabori, S., *J. Organomet. Chem.* **1985,** 289, (1), 91-5.

45. Lu, J.; Li, M.; Bai, Y.; Hu, H.; Ma, H., *Synthesis and Reactivity in Inorganic and Metal-Organic Chemistry* **2003,** 33, (6), 999-1009.

46. Chen, Y. J.; Pan, D.-S.; Chiu, C.-F.; Su, J.-X.; Lin, S. J.; Kwan, K. S., *Inorg. Chem.* **2000,** 39, (5), 953-958.

47. Hush, N. S., *Prog. Inorg. Chem.* **1967,** 8, 391.

48. Westmoreland, T. D.; Wilcox, D. E.; Baldwin, M. J.; Mims, W. B.; Solomon, E. I., *J. Am. Chem. Soc.* **1989,** 111, 6106.

49. Salaymeh, F.; Berhane, S.; Yusof, R.; De la Rosa, R.; Fung, E. Y.; Matamoros, R.; Lau, K. W.; Zheng, Q.; Kober, E. M.; Curtis, J. C., *Inorg. Chem.* **1993,** 32, 3895.

50. Dong, Y.; Hupp, J. T., Hush-notfit2. *Inorg. Chem.* **1992,** 31, 3170.

51. Kurosawa, M.; Nankawa, T.; Matsuda, T.; Kubo, K.; Kurihara, M.; Nishihara, H., *Inorg. Chem.* **1999,** 38, 5113-5123.

CHAPTER 5

DOUBLY BRIDGED BINUCLEAR FERROCENOPHANES AND VINYLENE-ARYLENE-VINYLENE BRIDGED TRINUCLEAR FERROCENOPHANES: SYNTHESIS, STRUCTURE, ELECTROCHEMISTRY AND MIXED-VALENCE STUDIES.

Introduction

Binuclear transition-metal complexes bridged by conjugated spacers have been of great research interest for decades in the study of intramolecular electron transfer.[1-3] Electron or hole transport across mixed-valence metal centers is known to be conducted either by a through-space or by a through-bond mechanism.[1, 4-6] The through-space process is often observed in systems having electron donor and acceptors in close proximity so that spatial orbital overlap or through-space electron hopping between them is plausible. However, such space-based electron transfer is only effective to a very limited extent as it drops exponentially with enlarged donor-acceptor separation. Thus, long-range electronic communication is inevitably driven by a π-conjugated backbone. Such interaction is apparently a through-bond process and has been reported to be effective when the metal-metal distance is 13-carbons away, as demonstrated by Tolbert and Zhao in polymethine-linked biferrocenyl compounds.[7] To promote electronic interaction over long-ranges, multiple approaches have been employed, among which the most popular strategy is to modify the electronic configurations of both the bridging ligand and the metal centers so that the energy band gap between the HOMO of the bridging ligand and the metal dπ-orbitals is minimized. Using this approach, electron-delocalization can be maximized so as to allow electron transfer to take place over long distance. In contrast, since the through-bond electronic communication will be ultimately limited by the metal-metal separation, an alternative approach in seeking stronger intramolecular communication is to build multiple interacting channels between the metal

centers.[8-10] With two functionalizable Cp rings, ferrocene serves as a convenient redox-active species in constituting doubly-bridged system.

Doubly-linked biferrocenes (ferrocenophanes) bridged by longer than single atom chains are known in the literature.[11-13] Systems comprised of unsaturated bridges between two ferrocene nuclei are particularly interesting, and have attracted much research attention in recent years due to the potential for facile electronic communication.[14-16] Previously, we have investigated a large variety of singly-bridged biferrocenyl complexes of the type FcCH=CHXCH=CHFc, in which a functional atom/group X was varied across a common range of linking groups. The current study is designed to extend our interest in the through-bond electronic communication in binuclear systems. This time the terminal ferrocenes are linked by two identical bridging fragments still in the form of –CH=CHXCH=CH-. Again, the central X group is varied to give rise to a series of binuclear ferrocenophanes, in which two electron/hole conducting channels are established between the two ferrocene ends to facilitate the electronic interaction.

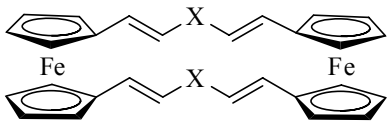

X = -, CH=CH, CH_2, S, C(O), CH=CHC(O), *o*-C_6H_4, 2,5-Th, 2,5-Fu, etc.

According to the structural characteristic of the ferrocenophanes herein, the bimetallic ferrocenophanes could, in most of the cases, be conveniently synthesized using Wittig-related condensation reactions, i.e. olefin forming reactions between equal equivalents of $Fc(CHO)_2$ and an appropriate bis-ylide. Apparently, this synthetic approach intrinsically introduced a possible competing polymerization process. Fine-tuning of the reaction parameters for each specific targeted compound, however, allowed us to promote the ring-closure process in forming the ferrocenophanes. Nevertheless, we also discovered that when the X group was an aromatic ring, the major ring-closure adduct is the trinuclear ferrocenophanyl macromolecules. This may be due to the additional spatial requirement needed in forming a ferrocene cycle because of the increased rigidity of the bridging fragment. Structural, electrochemical and mixed-

valence studies on this family of ferrocenophanes revealed some fascinating properties that would certainly enrich the chemistry in this area.

Experimental

General Methods

General methods such as NMR, IR, UV-Vis-NIR, cyclic voltammetry and X-ray crystallographic analysis described in Chapter 2 were followed. All chemicals were purchased from Aldrich or Acros and used without further purifications if not otherwise specified. The preparations of trimethylene bis(triphenylphosphonium) bromide (Chapter 2), 1,2-xylylenediphosphonate (Chapter 2), 1,4-xylylenediphosphonate (Chapter 2), bis(diethylphosphonylmethyl)pyrrole (Chapter 3), ferrocene-1,1'-diylbis(methyltriphenylphosphonium iodide) (Chapter 4), 1,1'-ferrocenedialdehyde (Chapter 4) and 1,1'-bis(2-formylvinyl)ferrocene (Chapter 4) have been depicted previously.

Synthesis

[4.4](1,1')Ferrocenophane-1,3,15,17-tetraene (1). To a suspension of ferrocene-1,1'-diylbis(methyltriphenylphosphonium iodide) [$Fc(CH_2PPh_3I)_2$] (990 mg, 1 mmol) in dry THF (40 mL) at 0 ^oC under argon, was added potassium *tert*-butoxide (269 mg, 2.4 mmol, 20% excess) in one portion. The solution was stirred for 30 min, whereupon it turned slowly from yellow to deep brown, at this point, 1,1'-bis(2-formylvinyl)ferrocene (300 mg, 1 mmol) was added as a solution in anhydrous THF (10 mL) via a cannula. The resultant mixture was slowly warmed to room temperature and stirred for ca. 12 h before 20 mL of water was introduced to quench the reaction. After removing the volatile solvent, the aqueous phase was extracted with diethyl ether (3 x 40 mL). The organic extract was then washed with saturated aqueous NaCl, dried over Na_2SO_4, and evaporated. Final purification was achieved by flash column chromatography on silica gel using CH_2Cl_2/hexane (1:2) as the eluent. The second major band was collected and concentrated to provide the product as an orange red powder (112 mg, 23.7%, based on the dialdehyde). ^1H NMR ($CDCl_3$): δ 6.04-5.97 (4H, m), 5.8-5.66 (ca. 2H, m), 5.51-5.43

(2H, m), 4.21 (8H, br), 4.13 (8H, br). MS m/e (intensity): 472.1 (100, M^+), 236.1 (31), 178 (9), 121.1 (8), 55.9 (4). Exact mass for $C_{28}H_{24}Fe_2$: 472.05768, observed: 472.05597.

[5.5](1,1')Ferrocenophane-1,4,16,19-tetraene (2). To a suspension of trimethylene bis(triphenylphosphonium) bromide (1.45 g, 2 mmol) in dry THF (ca. 50 mL) maintained at –78 ^oC was added *n*-buthyllithium (1.5 mL of a 1.6 M solution in hexane, 2.4 mmol). The resulting yellow colored solution was stirred for 30 min at –78 ^oC, and at room temperature for 2 h. The orange suspension was added to a solution of 1,1'-ferrocenedialdehyde (0.48 g, 2 mmol) in THF (ca. 10 mL) at –78 ^oC. The red mixture was stirred at –78 ^oC for 2 h, gradually warmed to room temperature and stirred for another three hours before being quenched by the addition of water (ca. 10 mL). The volatile solvent was evaporated under reduced pressure. The resulting aqueous solution was extracted with chloroform (3 x 50 mL). The organic extracts were combined, dried over $MgSO_4$, and evaporated. Purification was achieved by chromatography of the crude material on silica gel using chloroform as the eluent. The first band was collected and concentrated to afford a red oily gum (0.26 g, 52%). ^1H NMR ($CDCl_3$)*: δ 6.10 (4H, m, vinyl CH), 5.85 (ca. 2H, m, vinyl CH), 5.76 (2H, m, vinyl CH), 4.25 (8H, m, br), 4.16 (8H, m, br), 3.14 (1H, br, CH_2), 3.0 (2H, br, CH_2), 2.87 (1H, br, CH_2). MS m/e (intensity): 500 (100, M^+), 366 (7), 304 (5), 250 (34), 169 (13), 111.1 (10), 69.1 (16), 57.1 (21). (*: The NMR data indicated the presence of that a mixture of cis/trans isomers. The signals were broad due to the multiple overlap.)

[6.6](1,1')Ferrocenophane-1,3,5,17,19,21-hexaene (3). 1,1'-ferrocenedialdehyde (1.21 g, 5 mmol) and (*E*)-but-2-ene-1,4-diylbis(tributylphosphonium) dichloride (10 mL of a 0.5 M MeOH solution, 5 mmol) were placed in a 250 mL round bottom flask and dissolved in DMF (70 mL). A solution of sodium methoxide (12 mL of a 1.0 M solution in methanol, 12 mmol) was added dropwise with stirring, and the resulting mixture was stirred at 25 °C for 48 h and then at 90 °C for 2 h. After being concentrated to about 20 mL under vacuum, the reaction solution was poured into 200 mL of water, extracted with diethyl ether (3 x 150 mL), washed with saturated aqueous sodium chloride, and evaporated to dryness. The residue was purified by flash chromatography on silica gel, eluting with chloroform. The first band was collected and concentrated to yield a metallic copper colored compound (0.55

g, 42%). IR (KBr pellet, cm^{-1}): 3086, 3015.8, 2956.2, 2920.5, 1652.7, 1635.1, 1616.8, 1456.5, 1260.2, 1042.1, 986.2, 953, 931.9, 808.9, 495. MS m/e (intensity): 524.1 (100, M^+), 318 (5), 262 (33), 202.1 (6), 121 (4), 44 (5). Exact mass for $C_{32}H_{28}Fe_2$: 524.08898, observed: 524.08791.

[5.5](1,1')Ferrocenophane-3,18-dithia-1,4,16,19-tetraene (4). To a suspension of dimethylthioether-a,a'-bis(triphenylphosphonium) bromide (1.49 g, 2 mmol) and 1,1'-ferrocenedialdehyde (0.48 g, 2 mmol) in anhydrous MeOH (20 mL) at 0 ^oC, was added sodium methoxide (9.6 mL of a 0.5 M solution in MeOH, 4.8 mmol) under argon with stirring. The mixture was brought to room temperature, red solid started to separate from the solution upon 2 h stirring. After stirred overnight, the solution was concentrated to about 10 mL, cooled at 0^o C, and filtered to result in an orange powder which was washed twice with 5 mL petroleum ether. Further purification was achieved by recrystallization of the crude product from MeOH to yield the title compound as a red crystalline (0.35 g, 65%). ^1H NMR ($CDCl_3$): δ 6.2-6.42 (8H, m, major), 6.01 (m, minor), 4.47-4.54 (m, minor), 4.18-4.31 (8H, m, major). IR (KBr pellet, cm^{-1}): 3077.2, 3017.9, 2919.8, 1699.1, 1684.2 (br), 1590.8, 1455.3, 1379.3, 1242.5, 1041.5, 1027.3, 926.4, 808.4, 715.9, 490.7. MS m/e (intensity): 535.9 (100, M^+), 322 (10), 268 (42), 178.1 (12), 147 (9), 44 (21). Exact mass for $C_{28}H_{24}Fe_2S_2$: 536.00182, observed: 536.00042.

[5.5](1,1')Ferrocenophane-1,4,16,19-tetraene-3,18-dione (5).

1,1'-Bis(acetylvinyl)ferrocene [**Fc(CH=CHCOMe)$_2$**]. An aqueous solution of KOH (20 mL of a 2 M solution) was added at 0 ^oC to a solution of 1,1'-ferrocenedialdehyde (1.21 g, 5 mmol) in acetone (30 mL). The reaction mixture was stirred for 2 h at 0 ^oC and poured into cold water. The precipitate was filtered off and dried in air. No further purification was proceeded on the purple solid (1.26 g, 78%) since it is good enough for the following condensation reactions. Analytical sample was achieved by recrystallizing the crude product from CH_2Cl_2/hexane. ^1H NMR ($CDCl_3$): δ 7.14 (2H, d, J = 16 Hz), 6.21 (2H, d, J = 16 Hz), 4.79 (4H, br), 4.25 (4H, br), 2.25 (6H, s). ^{13}C NMR ($CDCl_3$): δ 197.90, 143.0, 125.97, 80.34, 72.82, 70.28, 27.65. IR (KBr pellet, cm^{-1}): 1633.1, 1616.3, 1595.2, 1351.4, 1261.8, 1048.8, 968.2, 821.4, 472.9.

[5.5](1,1')Ferrocenophane-1,4,16,19-tetraene-3,18-dione (**5**). Method A: A solution of 1,1'-ferrocenedialdehyde (0.726 g, 3 mmol), 1,1'-bis(2-acetylvinyl)ferrocene

(0.97 g, 3 mmol), and potassium hydroxide (2.1 g) in ethanol (50 mL) was heated at 60 ^{o}C for 10 h under an argon atmosphere. The completion of the reaction was monitored by TLC. After the crude product was filtered off, washed with water, ethanol, and ether, and then dried, the title compound was isolated as a purple solid (1.23 g, 78%). Analytical sample was obtained by recrystallizing the ferrocenophane from $CHCl_3$/hexane. ^{1}H NMR ($CDCl_3$): δ 7.42 (4H, d, J = 15 Hz), 6.20 (4H, d, J = 15 Hz), 4.53 (8H, br), 4.45 (8H, br). ^{13}C NMR ($CDCl_3$): δ 186.0, 141.3, 124.7, 80.9, 72.5, 72.3, 70.7. MS m/e (intensity): 528 (100, M^{+}), 450 (5), 384 (8), 264.1 (27), 190.1 (4), 121 (5), 43.9 (3). Exact mass for $C_{30}H_{24}Fe_2O_2$: 528.04751, observed: 528.04622.

Method B: A solution of 1,1'-ferrocenedialdehyde (0.97 g, 4 mmol), acetone (0.255 g, 4.4 mmol), and potassium hydroxide (1.5 g) in ethanol (30 mL) was heated at 60 ^{o}C for 10 h under an argon atmosphere. The completion of the reaction was monitored by TLC. After the crude product was filtered off, washed with water, ethanol, and ether, and then dried, identical compound was obtained as in method A (0.82 g, 78%).

[7.7](1,1')Ferrocenophane-1,4,6,18,20,23-hexaene-3,22-dione (6). A solution of 1,1'-bis(2-formylvinyl)ferrocene (0.59 g, 2 mmol), 1,1'-bis(2-acetylvinyl)ferrocene (0.64 g, 2 mmol), and potassium hydroxide (1.5 g) in ethanol (40 mL) was heated at 60 ^{o}C for 10 h under an argon atmosphere. The completion of the reaction was monitored by TLC. After the crude product was filtered off, washed with water, ethanol, and ether, and then dried, it was recrystallized from $CHCl_3$/hexane to afford the final product as a purple crystal (0.66 g, 57%). ^{1}H NMR ($CDCl_3$): δ 7.45 (2H, d, J = 15.6 Hz), 7.36 (2H, dd, J = 15 Hz, J = 11.7 Hz), 6.55 (2H, d, J = 15.3 Hz), 6.20 (2H, d, J = 15.6 Hz), 6.11 (2H, d, J = 15 Hz), 5.98 (2H, dd, J = 15.3 Hz, J = 11.7 Hz), 4.51 (4H, t, J = 1.8 Hz), 4.44 (4H, t, J = 1.8 Hz), 4.36 (4H, t, J = 1.8 Hz), 4.33 (4H, t, J = 1.8 Hz). ^{13}C NMR ($CDCl_3$): δ 187.4, 143.5, 141.4, 138.5, 127.2, 126.3, 125.1, 82.9, 80.8, 72.5, 72.3, 71.6, 71.4, 69.8. IR (KBr pellet, cm^{-1}): 3082.0, 1659.8, 1607.6, 1568.3, 1457.6, 1357.5, 1084.8, 1042.9, 992.9, 814.6, 539.2. MS m/e (intensity): 580 (100, M^{+}), 489 (3), 290 (21), 262 (7), 236 (6), 121 (4), 43.9 (11). Exact mass for $C_{34}H_{28}Fe_2O_2$: 580.07881, observed: 580.07977.

[2]orthocyclo[2]ferroceno[2]orthocyclo[2]ferrocenophane-1,9,21,29-tetraene (7). To NaH (240 mg, a 60% suspension in oil, 6 mmol) washed twice with dry hexane was added 15-crown-5 (88 mg, 0.4 mmol, 10%) in THF (20 mL) under argon. A mixture

of 1,1'-ferrocenedialdehyde (484 mg, 2 mmol) and tetraethyl 1,2-xylylenediphosphonate (Chapter 2) (831 mg, 2.2 mmol) in THF (30 mL) was added slowly and the suspension was heated at reflux under vigorous stirring overnight. After cooling to room temperature, the reaction was quenched by adding MeOH (5 mL), and the volatile solvent was evaporated under vacuum. The residue was extracted by CH_2Cl_2 (2 x 30 mL), the insoluble portion of the leftover was dissolved in 50 mL of water and extracted with CH_2Cl_2 (2 x 30 mL). The organic phase was combined and dried over $MgSO_4$, the solvent evaporated, and the red material was purified by column chromatography on silica gel (CH_2Cl_2/hexane 1:1). The first red band was collected and concentrated to yield the final product as an orange-red crystalline (110 mg, 17.6%); the following orange band was also collected which was identified presumably as oligmeric byproducts. NMR spectrum indicated that the final product contains two steric conformers, regarding the relative orientation of the two bridged phenylene rings to each other, i.e. syn and anti conformers, which was separated by preparative TLC chromatography (silica gel), eluting with CH_2Cl_2/hexane (1;3). *syn*-Conformer (intramolecular π-π stacking): ^{1}H NMR ($CDCl_3$): δ 6.96 (4H, dd, J = 3.6, 5.7 Hz), 6.83 (4H, dd, J = 3.3, 5.7 Hz), 6.68 (4H, d, J = 15.9 Hz), 6.09 (4H, d, J = 15.9 Hz), 4.49 (8H, t, J =1.7 Hz), 4.30 (8H, t, J =1.7 Hz). ^{13}C NMR ($CDCl_3$): δ 135.08, 126.52, 125.88, 125.29, 125.0, 85.78, 69.67, 67.57. IR (neat, cm^{-1}): 3044m, 2920m, 1777w, 1619m, 1591m, 1486m, 1243m, 1027m, 945s, 808s, 736s, 488s. *anti*-Conformer (non-stacking): ^{1}H NMR ($CDCl_3$): δ 7.27 (4H, dd, J = 3.6, 5.7 Hz), 7.04 (4H, dd, J = 3.3, 5.7 Hz), 6.89 (4H, d, J = 15.9 Hz), 6.52 (4H, d, J = 15.9 Hz), 4.38 (8H, t, J =1.7 Hz), 4.23 (8H, t, J =1.7 Hz). ^{13}C NMR ($CDCl_3$): δ 136.01, 128.86, 127.19, 126.60, 125.35, 85.06, 70.03, 68.40. MS m/e (intensity): 624.1 (100, M^+), 312 (45), 178.1 (7), 121 (4), 44 (5).

[2]paracyclo[2]ferroceno[2]paracyclo[2]ferrocenophane-1,9,21,29-tetraene (8) and [2]paracyclo[2]ferroceno[2]paracyclo[2]ferroceno[2]paracyclo[2]-ferrocenophane-1,9,21,29,31,39-hexaene (9). To NaH (240 mg, a 60% suspension in oil, 6 mmol) washed twice with dry hexane was added 15-crown-5 (88 mg, 0.4 mmol, 10%) in THF (20 mL) under argon. A mixture of 1,1'-ferrocenedialdehyde (484 mg, 2 mmol) and tetraethyl 1,4-xylylenediphosphonate (Chapter 2) (831 mg, 2.2 mmol) in THF (30 mL) was added slowly and the suspension was heated at reflux under vigorous

stirring overnight. After cooling to room temperature, the reaction was quenched by adding MeOH (5 mL), and the volatile solvent was evaporated under vacuum. The residue was extracted by CH_2Cl_2 (2 x 30 mL), the insoluble portion of the leftover was dissolved in 50 mL of water and extracted with CH_2Cl_2 (2 x 30 mL). The organic phase was combined and dried over $MgSO_4$, the solvent evaporated, and the red material was purified by flash chromatography on silica gel (CH_2Cl_2). The first red band was collected and concentrated to yield the final product as a red powder (156 mg, 25%). This product is the mainly the triferrocenophane **9** (ca. >90%). The trace amount of dimer **8** has more solubility than **9**, and therefore was removed by recrystallization from $CHCl_3$. Trimer **9**: ^{1}H NMR ($CDCl_3$): δ 7.46 (8H, s), 7.02 (4H, d, J = 16.2 Hz), 6.72 (4H, d, J = 16.2 Hz), 4.33 (8H, t, J = 1.6 Hz), 4.31 (8H, t, J = 1.6 Hz). ^{13}C NMR ($CDCl_3$): δ 136.74, 126.39 (aryl), 126.31, 126.02, 83.96, 69.83, 69.64. FABMS: *m/z* 936 [M^+] (trimer).

[2](2,5)thiopheno[2]ferroceno[2](2,5)thiopheno[2]ferrocenophane-1,8,20,27-tetraene (10) and [2](2,5)thiopheno[2]ferroceno[2](2,5)thiopheno[2]ferroceno[2]-(2,5)thiopheno[2]ferrocenophane -1,8,20,27,39,46-hexaene (11).

2,5-Bis(diethylphosphonylmethyl)thiophene. To a stirred solution of AIBN (0.48 g, 2.97 mmol) and N-bromosuccinimide (23 g, 129.6 mmol) in 100 mL of carbon tetrachloride was added 2,5-dimethylfuran (6.9 g, 61.5 mmol). The mixture was purged with argon for 1 h before it was heated at reflux for 4 h. The resulting brown suspension was allowed to cool to room temperature and vacuum-filtered to remove succinimide. The solvent was then removed under vacuum to afford a dark viscous oil, the crude product of 2,5-bis(bromomethyl)thiophene. This material was subjected to the next Arbuzov reaction without further purification due to its extreme sensitivity to air.

The dark oil was then carefully dissolved in triethylphosphite (15 mL) and heated at reflux for 5 h under argon. After removing the excess of triethylphosphite under reduced pressure at 140 ^{o}C, the residual oil was purified by column chromatography on silica gel using ethyl acetate as eluent to give the final product as a red liquid (16.5 g, 70%). ^{1}H NMR ($CDCl_3$): δ 6.80 (2H, d, J = 2.7 Hz), 4.10-4.0 (8H, sextet, J = 7.2 Hz), 3.25 (4H, d, J = 18.9 Hz, P-OCH_2), 1.26 (12H, t, J = 7.2 Hz). ^{13}C NMR ($CDCl_3$): δ 132.04, 127.46, 62.42, 29.13-27.22 (d, P-OCH_2), 16.50.

Preparation of thiophenoferrocenophanes **10** and **11**. To a stirred suspension of NaH (240 mg, a 60% suspension in oil, washed twice with dry hexane, 6 mmol) in THF (20 mL) was added a solution of 2,5-bis(diethylphosphonylmethyl)thiophene (770 mg, 2 mmol) in THF (25 mL) under argon. After 20 min, 1,1'-ferrocenedialdehyde (484 mg, 2 mmol) dissolved in THF (20 mL) was introduced via cannula. The reaction mixture was then stirred overnight at room temperature, quenched with water (30 mL), evaporated under vacuum to remove the volatile solvent, filtered and washed with another 30 mL of water. The red solid was then stirred vigorously in MeOH (30 mL) for a while before being filtered, followed by extraction with ca. 60 mL of chloroform (the insoluble portion is mainly the oligomeric byproduct). The organic phase was concentrated and purified by column chromatography on silica gel (chloroform) to afford a mixture of diferrocenophane **10** (minor, indicated by TLC) and triferrocenophane **11** (major) in form of red solid (180 mg, 28.3%). The ferrocenyl dimer and trimer demonstrated identical spectra under ^{1}H and ^{13}C NMR examinations, however, are separable by preparative TLC chromatography (silica gel), eluting with CH_2Cl_2/hexane (1:3). ^{1}H NMR ($CDCl_3$): δ 6.76 (6H, d, J = 15.6 Hz), 6.68 (6H, s, thiophene), 6.62 (6H, d, J = 15.6 Hz), 4.33 (24H, s). ^{1}H NMR (CD_2Cl_2): δ 6.76 (6H, d, J = 15.9 Hz), 6.69 (6H, s, thiophene), 6.62 (6H, d, J = 15.9 Hz), 4.36 (24H, s). ^{13}C NMR (CD_2Cl_2): 141.39, 126.17, 125.76, 120.48, 84.09, 70.03, 69.17. IR (neat, cm^{-1}): 3077.5w, 2918.3m, 2849.2m, 1761.6(br), 1611m, 1455.3m, 1374.7m, 1242.6m, 1040.5m, 1025.4m, 930.5s, 779.2s (br), 482.3s. FABMS: *m/z* 954 [M^{+}] (trimer).

[2](2,5)furano[2]ferroceno[2](2,5)furano[2]ferrocenophane-1,8,20,27-tetraene (12) and [2](2,5)furano[2]ferroceno[2](2,5)furano[2]ferroceno[2](2,5)-furano[2]ferrocenophane -1,8,20,27,39,46-hexaene (13)

2,5-Bis(diethylphosphonylmethyl)furan. The synthetic procedure for 2,5-bis(diethylphosphonylmethyl)thiophene was exactly followed to prepare the title compound. AIBN (0.48 g, 2.97 mmol), N-bromosuccinimide (23 g, 129.6 mmol) and 2,5-dimethylfuran (5.9 g, 61.5 mmol) were first reacted to give the crude 2,5-bis(bromomethyl)furan after simple workup. This material was extreme sensitivity to air, and therefore used immediately to the next Arbuzov reaction with triethylphosphite (15 mL). After column chromatography, the final product was obtained as a brown liquid (15

g, 66.4%). ^{1}H NMR ($CDCl_3$): δ 5.90 (2H, d, J = 2.7 Hz), 3.81-3.74 (8H, sextet, J = 7.2 Hz), 2.90 (4H, d, J = 19.2 Hz, P-OCH_2), 0.99 (12H, t, J = 7.2 Hz). ^{13}C NMR ($CDCl_3$): δ 144.99, 109.38, 62.19, 27.52-25.61 (d, P-OCH_2), 16.30.

Preparation of Furanoferrocenophanes **12** and **13**. General procedure as for DFc44-Th2 was used to prepare the title compounds. 2,5-Bis(diethylphosphonylmethyl)furan (740 mg, 2 mmol) and 1,1'-ferrocenedialdehyde (484 mg, 2 mmol) in THF was allowed to react overnight at room temperature in presence of NaH (6 mmol). The crude product was extracted with $CHCl_3$ to remove the insoluble oligomers and purified by column chromatography as described in DFc44-Th2. The recovered product, a red solid (175 mg, 29%), is mainly triferrocenophane adduct **13** with small amount of biferrocenophane derivative **12**, which was separated by preparative TLC chromatography. The dimer and trimer give the same ^{1}H and ^{13}C NMR spectra. ^{1}H NMR (CD_2Cl_2): δ 6.81 (4H, d, J = 15.9 Hz), 6.52 (4H, d, J = 15.9 Hz), 6.28 (4H, s), 4.40 (4H, t, J = 1.8 Hz), 4.36 (4H, t, J = 1.8 Hz). ^{13}C NMR (CD_2Cl_2): δ 153.1, 124.74, 115.17, 109.58, 84.33, 70.07, 68.96. IR (neat, cm^{-1}): 3080m, 2915m, 1764m, 1619m, 1555w, 1368m, 1273m, 1242m, 1015m, 940s, 808m, 764s, 652m, 485s. FABMS: *m/z* 906 [M^+] (trimer).

N,N'-dimethyl[2](2,5)pyrrolo[2]ferroceno[2](2,5)pyrrolo[2]ferrocenophane-1,8,20,27-tetraene (14) and N,N',N''-trimethyl[2](2,5)pyrrolo[2]ferroceno[2](2,5)-pyrrolo[2]ferroceno[2](2,5)pyrrolo[2]ferrocenophane-1,8,20,27,39,46-hexaene (15).

General procedure as for **10** and **11** was used to prepare the title compounds. 2,5-Bis(diethylphosphonylmethyl)pyrrole (760 mg, 2 mmol) and 1,1'-ferrocenedialdehyde (484 mg, 2 mmol) in THF was heated at reflux overnight in presence of $NaNHSi(Me)_3$ (6 mmol), instead of NaH. The crude material was washed with water, extracted with CH_2Cl_2 and purified by flash column chromatography on basic alumina, eluting with CH_2Cl_2 to yield a deep red solid (107 mg, 17%), which contains diferrocenophane **14** and triferrocenophane **15** in ratio of ca. 30:70, indicated by TLC. These ferrocenophanes are acid-sensitive and were not able to be separated by further chromatography manners due to decomposition on the absorbent. Recrystallization from CH_2Cl_2/hexane caused the diferrocenophane to first isolate from the solution as manifested by the X-ray crystallographic studies. Again, the ferrocene dimer and trimer showed identical spectra

in ^{1}H and ^{13}C NMR examinations. ^{13}C NMR (THF-d_8): δ 133.88, 125.13, 123.59, 122.53, 115.29, 114.01, 106.50(s), 84.99, 69.01, 68.53, 29.95, 29.64. IR (neat, cm^{-1}): 3090w, 2950w, 1741w, 1646m, 1618m, 1538m, 1442m, 1386m, 1269m, 1103m, 1040m, 940s, 814m, 752s, 480s. IR (neat, cm^{-1}): 3088w, 2921m, 1758w, 1620m, 1582m, 1538w, 1441m, 1385m, 1232m, 1021s, 931s, 806m, 747s, 483s. FABMS: *m/z* 945 [M^+] (trimer).

Results and Discussion

Synthesis and NMR Spectra

The ketone incorporated diferrocenophane derivatives **5** and **6** were all prepared through base-promoted Clemensen condensations as illustrated in Figure 5.2. The reactions proceeded smoothly upon mixing 1,1'-ferrocenyldialdehyde derivatives with equal equivalents of the appropriate1,1'-ferrocenyldiacetyl ketones in MeOH containing KOH. Heating was generally utilized to shorten the reaction time and increase the reaction yields (usually more than 70%). The bridging olefinic bonds were all found to be in *E* configuration in each final product as manifested by both proton NMR (coupling constant of c.a. 16 Hz) and IR (olefinic C-H out-of-plane stretching mode around 950 cm^{-1}) spectroscopy.

Although the single crystal X-ray structures of [n.n]ferrocenophane-diones (n = 5, 7) were not obtained due to the poor solubility of the complexes, it is noteworthy that the NMR chemical shifts of the vinylene protons were noticeably moved upfield in both compounds, compared to their singly-bridged diferrocenyl analogues. In [5.5]ferrocenophane **5**, for instance, the Fc-C<u>H</u>=CH-CO- and Fc-CH=C<u>H</u>-CO- protons exhibited magnetic resonance at 7.42 and 6.20 ppm, respectively. In contrast, the same protons of singly connected bis(2-ferrocenylvinyl)ketone showed chemical shifts at 7.62 and 6.58 ppm (Chapter 2), respectively. This suggests that [5.5]ferrocenophane **5** more likely adopts a *syn* steric arrangement with respect of the two linking bridges. In this conformation, the vinylene protons are exposed in the extra deshielding region stemming from the intramolecular π-π stacking between the two overlapped bridges, resulting in their upfield shifts. The *anti*-conformer, in contrast, does not provide such an effect and is expected to possess similar NMR properties as its singly-bridged analogue. Similar up-

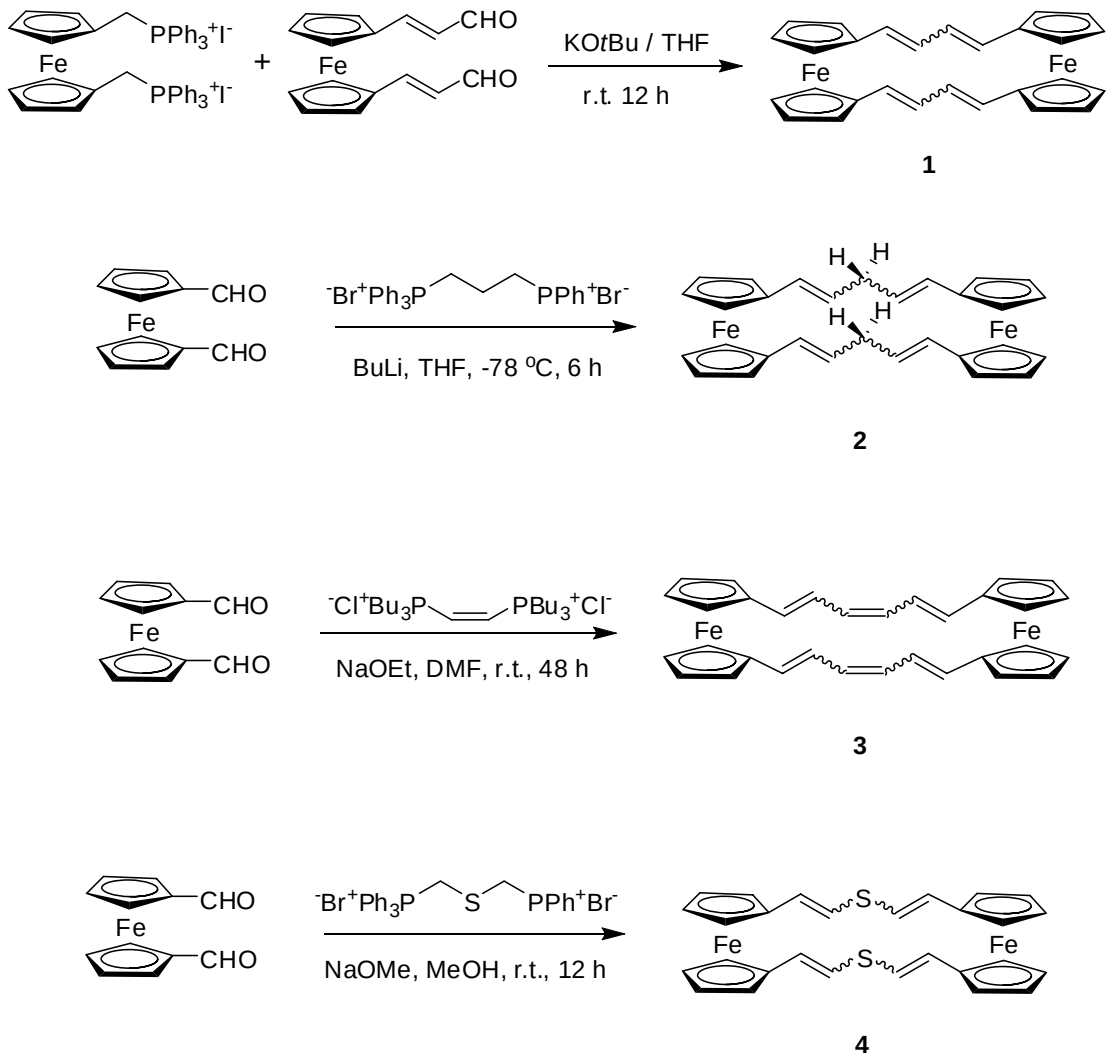

Figure 5.1 Synthesis of compounds **1-4** using Witting methodology.

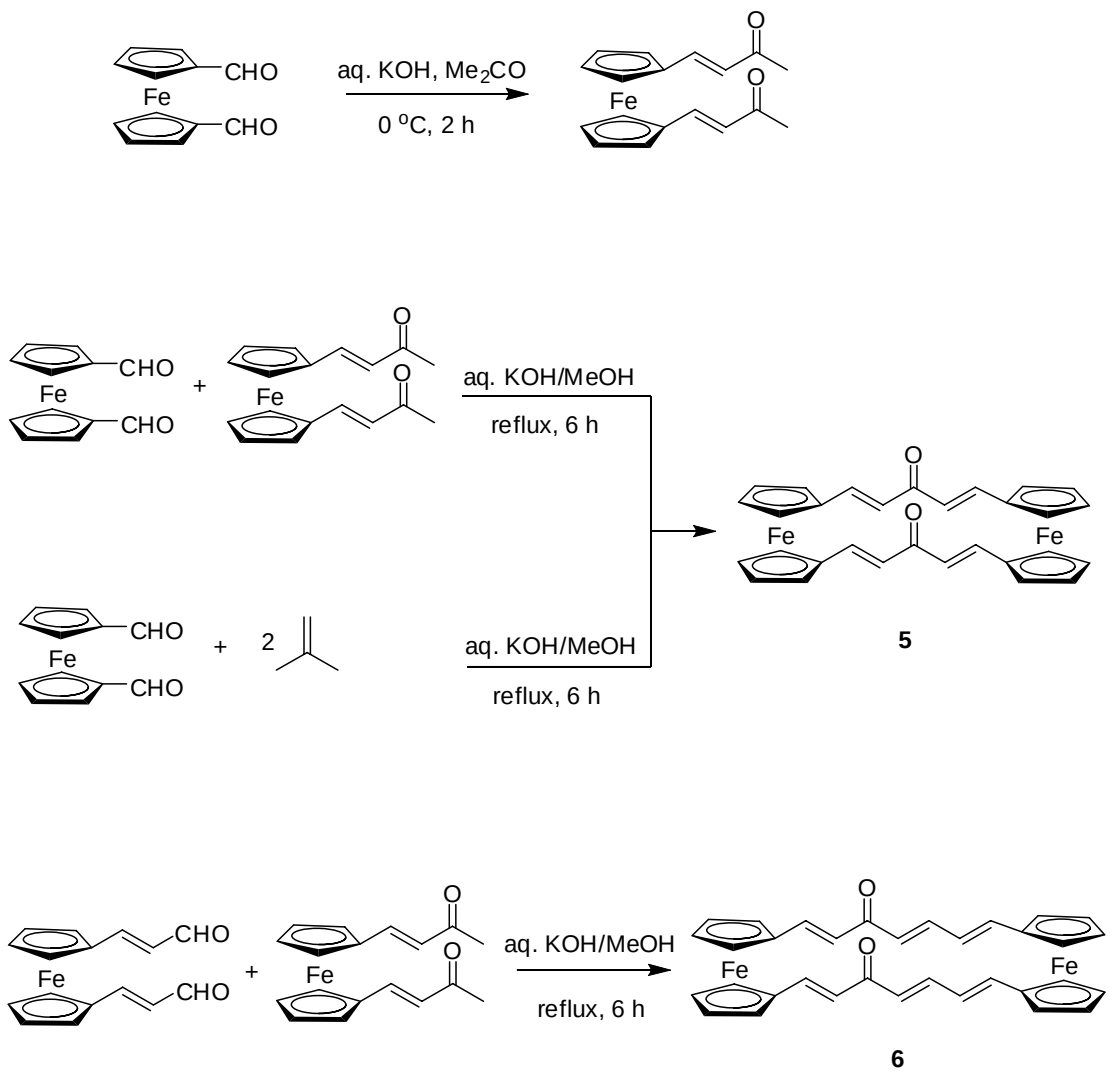

Figure 5.2 Synthesis of compounds **5** and **6**.

field shifts were also observed in the investigation of [7.7]ferrocenophane **6**, which likewise suggests a possibly exclusive *syn* conformation.

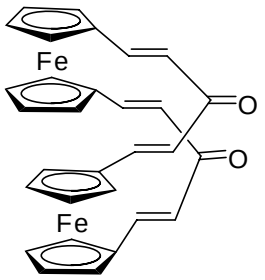

syn - **5**

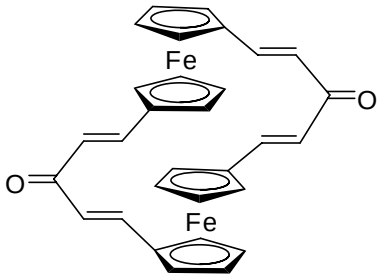

anti - **5**

The remaining ferrocenophanes were all prepared via a conventional Wittig or Wittig-Horner methodology (Figure 5.1 and 5.3-4), depending on the characteristic of the X functional group in the middle of the linking bridge for each specific compound. The general procedure for the synthesis of this series involved olefinic coupling between equal equivalent of 1,1'-ferrocenyldialdehyde and the corresponding bis-ylide. However, it is worth stressing that whereas Wittig-related reactions provided the most convenient method in preparing this series of structurally symmetrical compounds by ring closure mechanism, they also introduced a critical drawback, namely, the competing polymerization processes, which was detrimental to the desired product and yield. It has been observed that factors such as solvent, base, reaction temperature, reaction time, stereochemistry, and reactivity and bulkiness of the intermediate bis-ylide could all affect the outcome of the two competing processes. Among these reaction parameters, reaction temperature and stereochemistry play a major role since high reaction temperature commonly promoted polymerization and stereochemistry, in many cases, determined whether or not a sterically strained system could be formed. Therefore, our synthetic efforts in this work mainly focused on the enhancement of ring forming process by systematically optimizing the reaction conditions and choosing the suitable starting materials for each specific group of compounds.

Linearly bridged systems (X = S, CH_2, -, and CH=CH) were found more suitable for Wittig-oriented synthetic approach for the following reasons: 1. the easier accessibility of the starting bisphosphonium salts; 2. the ease of conducting the

olefination reaction at room or lower temperatures so as to depress the polymerization process; 3. the relative insensitivity of the stereochemistry due to the nature of the flexible bridging chains. In other words, the stereoselectivity of the vinyl bonds formed during the Wittig olefination (which is known for its non-E/Z specificity in most of cases) was not essential to the synthesis of the desired product. This was not the case when the bridging central X groups were aromatic rings. In such cases, the irregular vinylene linking unit caused serious ring closure problems as we shall see later. Additionally, the flexible linear chains were observed to facilitate the formation of the double-bridged adduct in a stepwise process that produced the [n.n]ferrocenophanes. However, this Wittig approach inevitably resulted in a mixture of stereo-isomers. Our attempts to make the all *E* derivatives using Horner-Wordworth- Emmons (HWE) reaction did not show any improvement and, instead, caused lower yields. Taking dithia-[5.5]ferrocenophane **4** for instance, although we had successfully adapted HWE reaction in preparing the singly-bridged analogue (*E,E*)-bis(ferrocenylvinyl)sulfide (**BFcVS** in Chapter 2), the (*E,E*)-**BFcVS** could only be achieved with heating. When we applied the same procedure to the HWE reaction between 1,1'-$Fc(CHO)_2$ and the corresponding diphosphonate $[(EtO)_2P(O)CH_2]_2S$, the stereoselectivity was diminished in the recovered product (major *trans* with minor *cis* double bonds evidenced by NMR spectroscopy). This is probably due to the structural confinement of cyclic bimetallic ferrocenophane which is not favorable to the relevant free rotation in forming the thermodynamically more stable *E* orientation. Furthermore, due to the heating required for the HWE reaction, the yield of the final ferrrocenophane **4** was lower than that obtained in the corresponding Wittig reaction conducted at room temperature (Figure 5. 3). The low yield might be attributed to the heat-induced polymerization. Similar comparison studies on [6.6]ferrocenophane **3** gave the same observation.

The final synthetic pathways for ferrocenophanes, **1**, **2**, **3** and **4**, linked by linear hydrocarbon or heteroatom-mediated hydrocarbon spacers, are shown in Figure 5.1. These synthetic routes are the optimized procedures from a series of systematic examinations, which were dedicated to achieve the highest conversion by varying the suitable solvent, base, and reaction temperature in a combinational manner. As stated earlier, only geometrically isomeric mixtures (*cis/trans*) were obtained for each

compound. The yields vary from 65% (compound **4**) to 24% (compound **1**). The low yield of [4.4]ferrocenophane **1** is mainly ascribed to the sterically hindered nature of the synthetic intermediate ferrocene-1.1'-bis[(methylphosphonium)ylide] (Chapter 4) and the sterically more strained structure of the product due to its short bridging linkers. The employment of an alternative bis-ylide, the bis-ylide of 1,1'-$Fc(CH_2P(O)(OEt)_2)_2$ (Chapter 4), with the corresponding HWE reaction procedure did not offer ring closure adduct, possibly because of the required long reaction time and refluxing condition, which led to polymeric product only.

Our initial attempts to prepare vinylene-arylene-vinylene doubly-bridged bimetallic ferrocenophane were focused on the phenylene-centered derivatives (X = *p*-Ph and *o*-Ph) using the Wittig methodology, i.e., to react equal equivalent of 1,1'-$Fc(CHO)_2$ with the corresponding bis-ylide of *p*-$(CH_2PPh_3Br)_2C_6H_4$ or *o*-$(CH_2PPh_3Br)_2C_6H_4$. Unfortunately, only some trace amounts of sterically unselective *p*-phenylene derivatives were obtained, while the *o*-phenylene counterpart did not offer any doubly-bridged product. A careful examination on the structural features of this kind of aryleneferricenophanes suggested that owing to the rigidity of the aromatic rings, the associated doubly-bridged species were more difficult to achieve since the first bridged fragment could not freely rotate to a sterically favorable position to allow the second bridging step, namely, the ring closure process, to occur. Intrinsically, this kind of doubly-bridged diferrocenophanes contains more steric strain than the linearly doubly-bridged systems. In addition, study of the crystal structures of singly-bridged diferrocenyl analogues (Chapter 2 and 3) indicated that the steric regularity of the vinylenes (i.e. all *E* configuration) were essential to the coplanarity of the bridging conjugation pathway, which in turn should enhance the structural feature of the doubly-bridged system so that the ring-closure step could be conducted in a more favorable and decent way. Based on this knowledge, we later resorted to the HWE approach to prepare the arylene-mediated binuclear ferrocenophanes.

Orthocycloferrocenophane **7** was eventually achieved by refluxing a mixture of equal equivalent of 1,1'-$Fc(CHO)_2$ and diphosphonate in THF in the presence of NaH (Figure 5.3). During the workup procedures, some poorly soluble orange-red components were isolated, which were presumably the corresponding oligomeric and polymeric

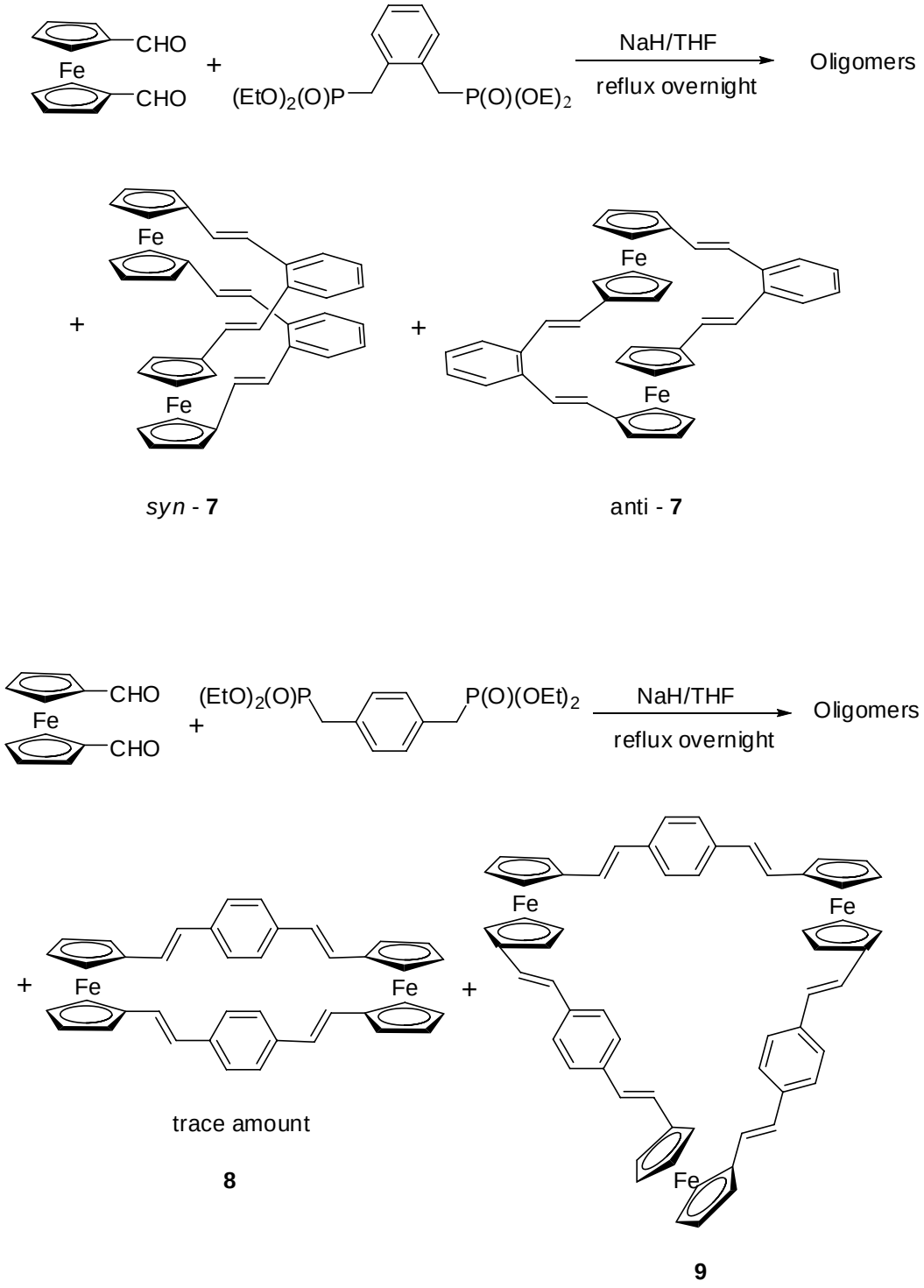

Figure 5.3 Synthesis of compounds **7-9**. Compound **7** was obtained with two conformational isomers in roughly 1:1 ratio. In preparing paracycloferrocenophanes, ferrocene trimer **9** was recovered as the major product with trace amount of ferrocene dimer **8** in presence.

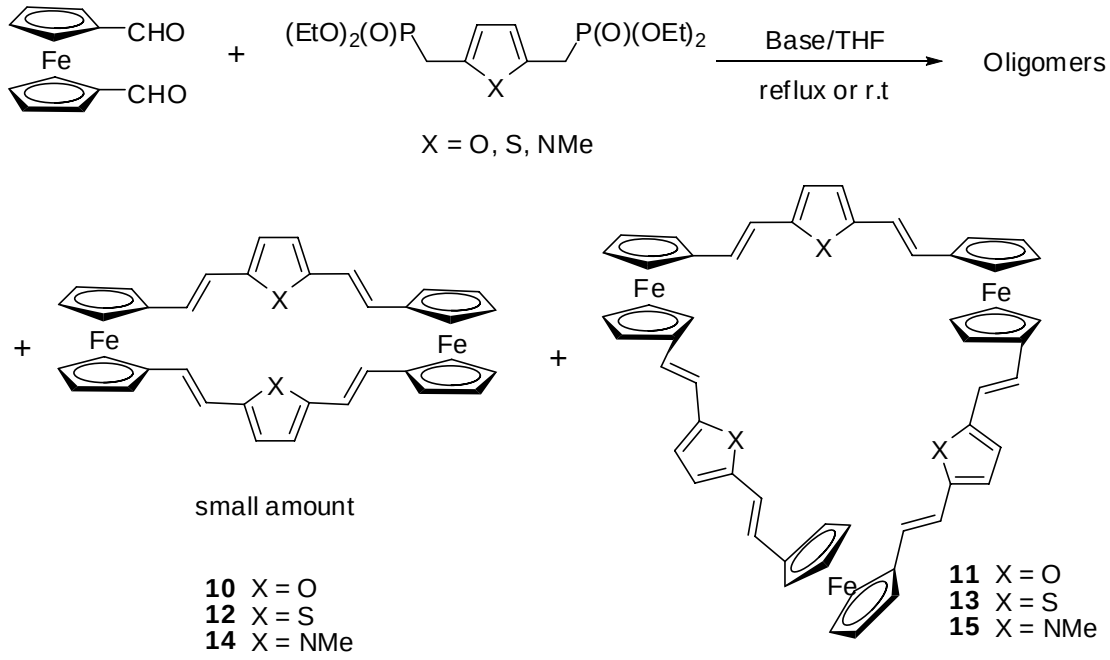

Figure 5.4 Synthesis of compounds **10-15**. In each case, the ferrocene trimer was obtained as the major heteorocycloferrocenophanyl product.

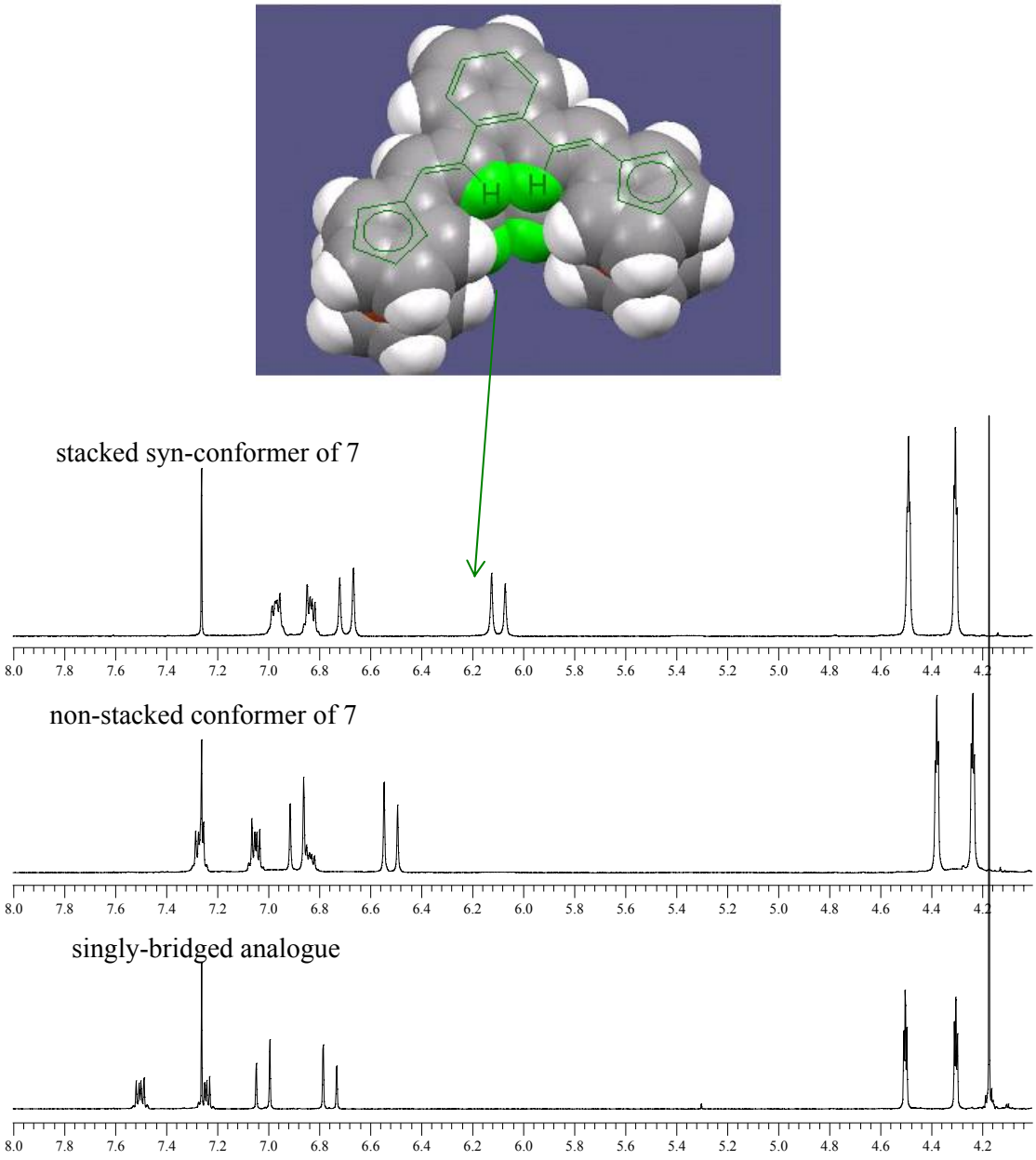

Figure 5.5 ^{1}H NMR spectra of the stacked *syn*-conformer (top) and non-stacked conformer (middle) of compound **7** and their singly-bridged analogue (bottom) in $CDCl_3$. The top diagram is the space-filling model obtained from the single crystal structure of **7**, which illustrates the π-π stacking effect on the high-field shifts of the proton signals due to the shielding effect caused by the ligand aromatic π-cloud.

byproducts. The crude product was subjected to flash column chromatography (silica gel) using CH_2Cl_2-hexane (1:1) as the eluant to afford an orange-red crystalline solid in 18% yield. Proton NMR spectroscopy revealed two distinguishable components present in the final product in an approximate 1:1 ratio. Both components demonstrated only the *trans* olefinic signals (coupling constant 15.9 Hz) and one pair of ferrocenyl signals in the area of 4.22-4.99 ppm. Further separation by preparative TLC chromatography eluting with CH_2Cl_2-hexane (1:3) afforded two distinct species. Mass spectroscopic examinations on these two species revealed the same molecular ion peak at m/z 624 (no higher molecular peaks were detected by FAB and MALDI for each case), which affirmed our expectation of two geometric conformers of the targeted ferrocenophane. Single crystal structural analysis of one of the isomers confirmed the *syn* face-to-face parallel disposition of the two ligands, which suggested strong intramolecular π-π stacking interaction (vide infra). Therefore, the second conformer of **7** was assigned as an either *anti* or off-parallel adduct (Figure 5.3).

Transannular π-π interactions including face-to-face interactions between parallel arenes and face-to-edge interactions or homoconjugation in rigid T-shaped geometries have been observed in cyclophanes, spiropolyenes, and dihydropyrenes and are usually accompanied by high-field shifts in the ^{1}H NMR spectrum.[17, 18]

The refined proton NMR spectra of the two conformers of **7** are shown in Figure 5.5, together with the NMR spectrum of their singly-bridged analogue 1,2-bis(ferrocenylvinyl)benzene (**BFcV*o*Ph** in Chapter 2). In contrast to the ^{1}H NMR spectrum of **BFcV*o*Ph**, the signals of the bridging fragments (both the *o*-phenylene and vinylenes) of both ferrocenophane conformers all experience an upfield shift. In particular, the up-field shifts in the face-to-face ferrocenophane conformer are more significant because of anisotropic shielding in the stacked framework. The markedly upfield shifted doublet at 6.05 ppm is assigned to the vinylene protons (in total number of four) immediately adjacent to the phenylene groups. The up-field shift, approximately of 1 ppm in comparison with the corresponding chemical shift of the singly-bridged species, indicates that these protons are sterically enclosed inside the π-cloud of the stacked Cp-vinylene-(*o*-phenylene)-vinylene-Cp fragments, the consequent diamagnetic ring current gives rise to high level of shielding effect. The illustration of this phenomenon can be

better viewed from the top diagram in Figure 5.5, where the space-filling geometry of the α-Hs on the interior boundary of the π-cloud is responsible for the magnetic shielding. The concurrent solid- (crystal structure, vide infra) and solution-state (NMR spectrum in $CDCl_3$) observations of the intramolecular π-π stacking forms suggest that solvation between the co-facial arene rings is impossible.

Paracycloferrocenophane, furanoferrocenophane, thiophenoferrocenophane and pyrroloferrocenophane were prepared through the same HWE manner as that of orthocycloferrocenophane analogue. In each case, poorly soluble oligomeric and polymeric materials were observed as the major byproduct, which significantly limited the desired ring closure process and resulted in low yields. Lowering the reaction temperature to ambient conditions was found to promote cycloferrocenophane adducts in the case of furan and thiophene derivatives. However, no olefination reactions were proceeded under the same condition when p-phenylene and 2,5-pyrrolene were used. The difference arose from the high reactivity of the 2,5-substituted furan and thiophene diphosphonates in the bis-ylide formation process, whereupon color change was immediately observed when they were exposed to NaH at room temperature. In contrast, ylides of p-phenylene and pyrrolene diphosphonates required heating to be generated using the same base. Although no extensive effort was pursued to maximize the ring closure product at the time of this writing, we proposed to use a combination of stronger base (e.g. BuLi), lower temperature (e.g. -78 ^{o}C), and longer reaction time to minimize the competing polymerization process and ideally enhance the formation of cycloferrocenophanes.

After comprehensive characterization, and to our surprise, the cycloferrocenophanes obtained above turned out to be mostly the trimetallic cycloferrocenophanes (as shown in Figure 5.3-4) and small amounts of the initially intended bimetallic cycloferrocenophanes **8**, **10**, **12** and **14**. The most appealing evidence came from electrochemical studies, whereby all the assumed bimetallic ferrocenophanes exhibited three distinct peaks which indicated the existence of the third metal center. MALDI mass spectroscopic examination and single crystal X-ray analysis (e.g. thiophenoferrocenophane **13**) both supported this conclusion for all four species. ^{1}H NMR spectroscopy, however, was of limited use in distinguishing bimetallic from

trimetallic ferrocenophanes due to their highly symmetrical structures. There is no need to stress that elemental analysis gave identical results in both cases. It is logically clear then that the steric restriction of the rigid vinylene-arylene-vinylene bridging units and the confined Cp rings of ferrocene nuclei require more space to allow the ring closure to occur. Doubly bridged paracyclo-, furano-, thiopheno-, and pyrroloferrocenophanes were sterically unfavorable adducts comparing to their trimetallic ferrocenophanyl counterparts. The obvious difference in achieving doubly bridged bimetallic orthocycloferrocenophane **7** as major product apparently stemmed from the protrusion of the *ortho*-phenylene ring out of the linking framework between the two ferrocene units.

Separation of the bimetallic from trimetallic ferrocenophanes proved very difficult. Recrytallization from chloroform was generally utilized to partially remove the bimetallic species since trimetallic component intuitively possesses lower solubility. Preparative TLC chromatography was then affected to produce the pure trimetallic ferrocenophanes as the major product. Paracycloferrocenophanes **9**, however, exhibited very low solubility, resembling that of its singly-bridged diferrocenyl analogue (Chapter 2), and making the purification process even more difficult. Pyrroloferrocenophanes **14** and **15**, on the other hand, were very acid-sensitive and unstable upon extensive exposure to silica gel or alumina without pre-handling with basic solution of Et_3N, which unfortunately resulted in poorer separation.

Despite the relatively large size of the trimetallic cycloferrocenophanes, their NMR spectra are rather simple and clear, owing to the highly symmetrical structures. As exemplified by thiophenoferrocenophane **13**, only four distinct proton signals in an integral ratio of 1:1:1:4 were revealed in its ^{1}H NMR spectrum (Figure 5.6), corresponding to the vinylene (6.76 ppm), thiophenylene (6.68 ppm), vinylene (6.62 ppm), and ferrocenylene (4.33 ppm) protons in the macromolecule. The coupling constant (15.6 Hz) of the vinylene units indicated the *E* geometry as expected; the two types of protons in the ferrocenyl nucleus merge to a single peak in this particular molecule. In the ^{13}C NMR spectrum (Figure 5.6), the four downfield peaks (120-145 ppm) were assigned to two types of thiophenylene and two types of vinylene carbons. The signals at 84.09 (Cp-C connected to the vinyl bond), 70.03 and 69.17 ppm clearly

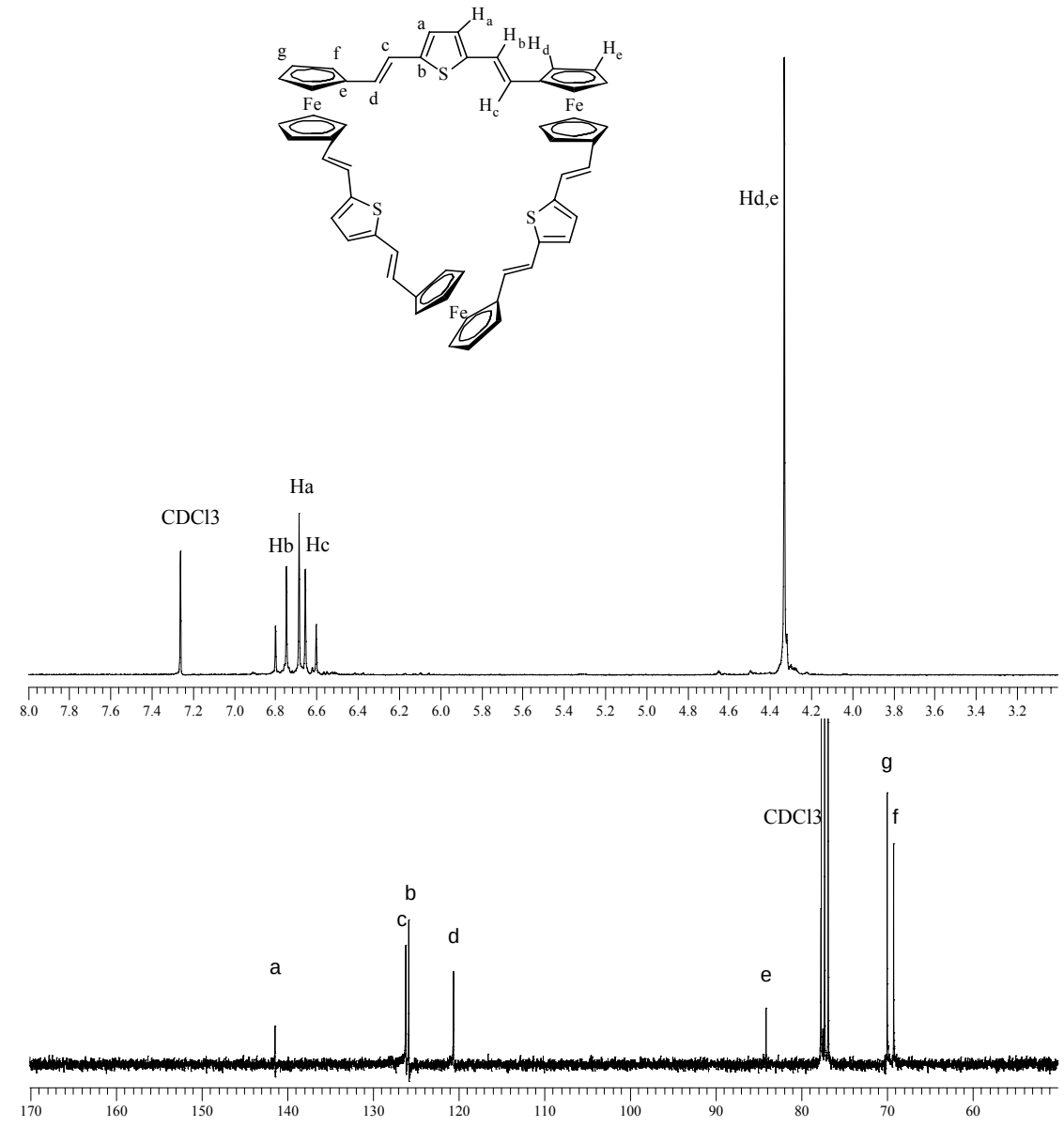

Figure 5.6 ^{1}H (top) and ^{13}C (bottom) NMR spectra of thiophenoferrocenophane **13** in $CDCl_3$.

derived from three types of ferrocenyl carbons. Indeed the NMR spectra of the recovered small amount of bimetallic thiophenoferrocenophane **12** were found to be identical to its trimetallic analogue **13**, which again was consistent with the symmetrical structure and, on the other hand, suggests that the stereochemistry of **12** does not adopt an effective π-π stacking disposition between the two linking pathways as seen of **7** where up-field chemical shifts were detected.

X-ray Structural Analysis

Suitable crystals for X-ray structural analysis were obtained by slow solvent evaporation of the corresponding CH_2Cl_2 solution. The availability of such crystals relied primarily on the solubility of the ferrocenophanes as most of them show limited solubility due to high level of conjugation. For this reason, only three compounds, namely **7**, **13** and **14** eventually afforded crystals suitable for X-ray diffraction studies. The ORTEP plots as well as packing diagrams are shown in Figure 5.7-5.10. To our knowledge, the literature known crystal structures of diferrocenophanes are mainly associated with [1.1]ferrocenophane compounds[19, 20] or very large and less strained systems.[21] Structural characterization of multi-metallic ferrocenophane is even rare. In fact, the crystallographic studies herein not only provide a number of interesting features of a series of novel ferrocenophane systems, but also present fascinating samples to assess the impact of steric strain, stereochemistry, molecular motion, intra- and intermolecular π-π stacking on metrical parameters, intramolecular self-assembly and crystal packing preference.

In principle, doubly-bridged ferrocenophanes are believed to be a subject to considerable steric strains due to the strict structural confinement. This is especially the case when the bridging units are [(*E*)-vinylene]-arylene-(*E*)-vinylene]s, which add up more strain due to the rigiditiy of the well-defined double bonds and aromatic functional fragments. Essentially, in a very limited spatial environment, six aromatic rings (including four cyclopentadineyl nuclei) linked by four vinylene bonds are contained within two ferrocenyl pivot skeleton. The steric limitations are more acute in N-methyl substituted pyrroloferrocenophane derivatives such as **14**, in which the methyl groups introduce extra steric hindrance arising from their close proximity. It has been well

established for ferrocenyl complexes that the intrinsic steric strains can be relieved in two ways,[22] and both are associated with the relative dispositions of the two Cp rings within a ferrocene unit: one by rotating from an eclipsed to a staggered disposition, and two by tilting from the normal parallel disposition. For aryloferrocenophanes **7** and **14**, little tilting is observed as the two cyclopentadienyl rings are only slightly tilted (dihedral angles 3.2-4.5^{o}).

In Figure 5.7, *syn*-**7** demonstrates well-defined structural features. The two cyclopentadienyl (Cp) rings of each ferrocene nucleus possess nearly perfectly eclipsed disposition. The two vinylene-(*ortho*-phenylene)-vinylene bridging fragments lie on the same side with regard to the crossing line between the two metal centers and the relative positions of the Cp/*o*-Ph/Cp rings of each ligand can be visualized as the three vertices of a triangle. The two sandwich-slicing ligands are virtually coplanar along the conjugation pathways and, again, are nearly perfectly parallel to each other. Little variation of the ligand separation is revealed. The ligand distance gradually and smoothly increases from 3.44 Å (C5-C10) to 3.65 Å (C15-C25). From the vertical topside view, the upper ligand almost fully superimposes the bottom ligand at each carbon and hydrogen point. Apparently, this idealized stereochemistry of compound **7** maximizes intramolecular π-π stacking and minimizes steric strains. Interestingly, the crystal structure of the corresponding singly-bridged counterpart, (*E,E*)-1,2-bis(ferrocenylvinyl)benzene (Chapter 2), does not even show a coplanar conjugation pathway as one of its terminal ferrocenes severely twisted from the conjugation backbone. The well regulated stereo-arrangement of orthocycloferrocenophane **7** exemplifies an intramolecluar self-assembly driven by steric constraint and intramolecular π-stacking interaction. Consequentially, the related electronic and electrochemical properties should be perturbed accordingly.

Besides the remarkable feature discussed above, the crystal packing form of **7** is also unique. Figure 5.8A presents two-dimensional packing network of the crystal lattice of **7** as viewed down the c-axis. For clarity, the hydrogen atoms were omitted. As can be seen, the unit cell consists of 18 molecules, and every six molecules organize very nicely to form a subunit giving rise to a very round circle. Within each circle, the twelve ferrocenyl moieties of the six molecules are evenly distributed on the boundary, with the

bridging ligands, namely, the ortho-phenylene rings of each molecule, displaced inside a sphere with orientation uniformly pointing at the center that. This gives rise to another

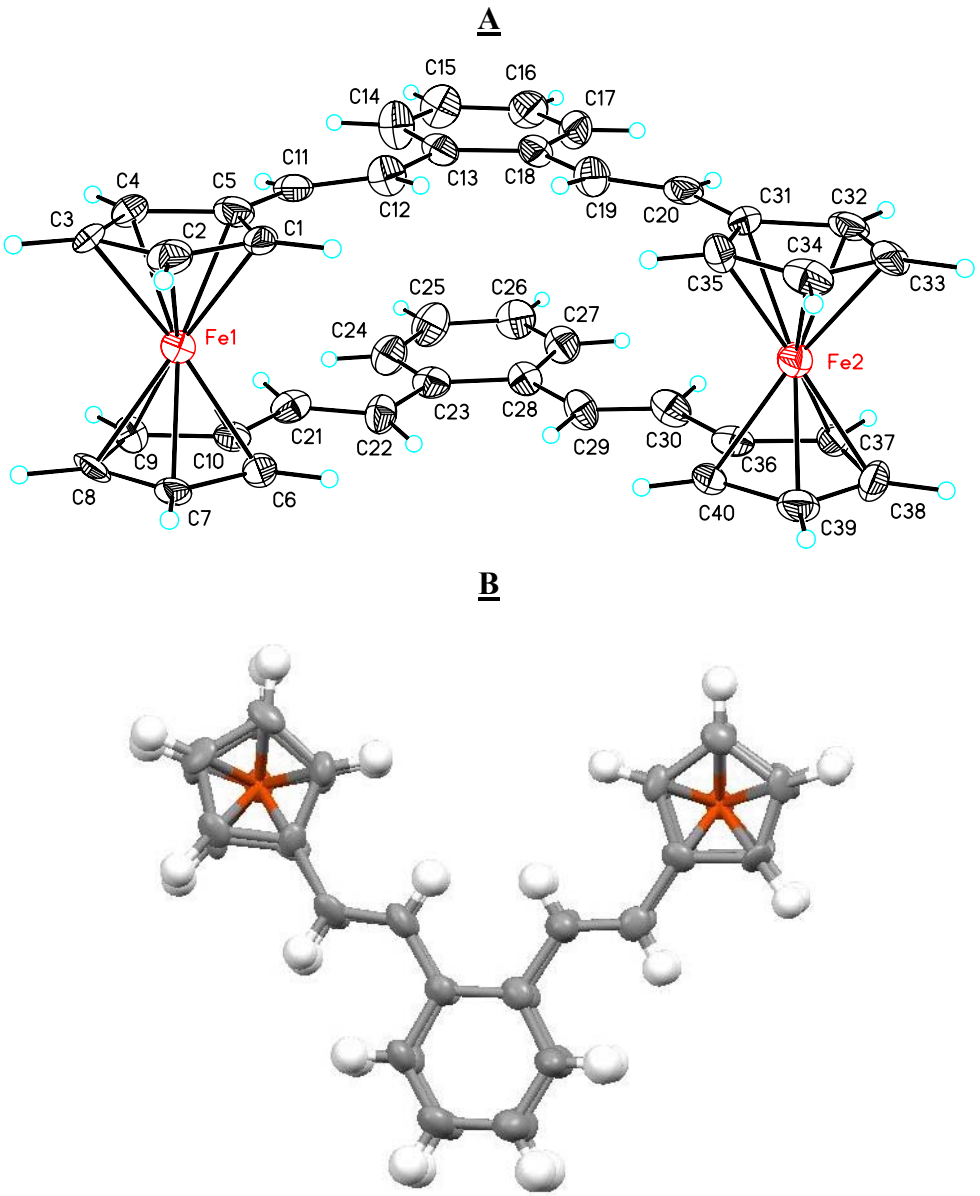

Figure 5.7 Crystal structure of orthocycloferrocenophane **7**. A: ORTEP plot of **7** with 50% anisotropic displacement ellipsoids; B: topside view showing the eclipcised ferrocenes and the *syn*-orientation of the two bridging ligands, which gives rise to effective intramolecular π-π stacking interaction.

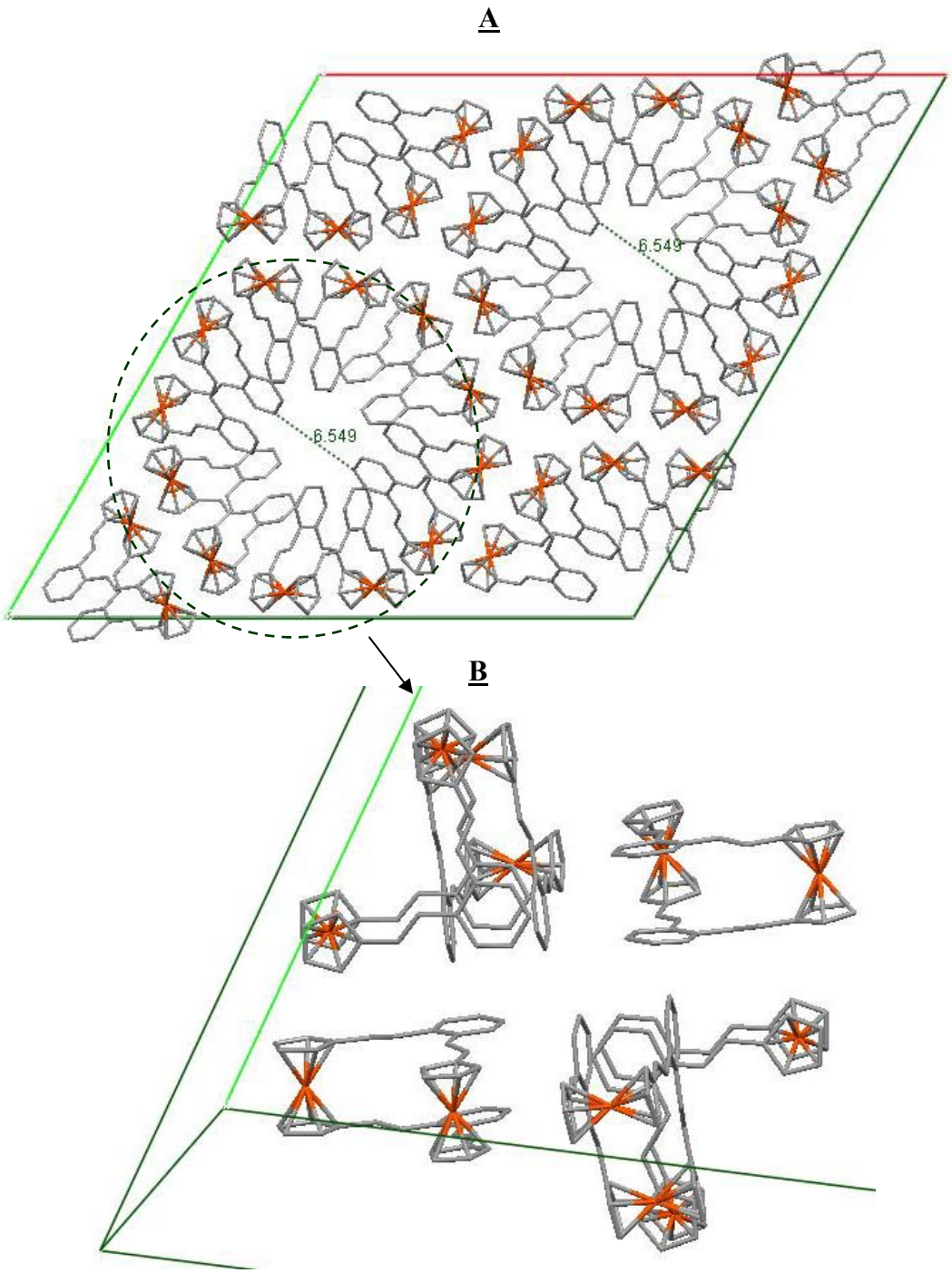

Figure 5.8 Unit cell packing form of orthocycloferrocenophane **7**. A: unit cell packing form of **7** viewing from c-axis. Each unit cell contains 18 orthocycloferrocenophane molecules, with every 6 grouped molecules forming a round circle viewed from c-axis; B: diagram viewed from another angle showing the 3-d arrangement of the grouped molecules (highlighted in A). Virtually the molecules are mutually perpendicular to the neighboring molecules.

interior circle shaped by the twelve *ortho*-phenylene rings, eventually leaving a three-dimensional central vacancy with diameter of 4.57 Å, taking the hydrogen atoms into account. In this 2-D networking picture, each unit cell contains essentially three circles described above, with the corner molecules constructing circles with other molecules in the neighboring unit cells. The contact between two circles can be depicted as edge-to-edge or back-to-back in the view of the orientation of the juxtaposing ferrocene nuclei. Three-dimensionally, each molecule within a subunit is mutually perpendicular to its adjacent two molecules as shown in Figure 5.8B. Accordingly, the ferrocene nuclei of each molecule take a face-to-edge orientation with respect to their neighboring ferrocene nuclei. Whereas the packing form of compound **7** is certainly unique, the driving force for this striking organization is still unclear. One can imagine that intermolecular π-π interactions could play an important role since the aromatic phenylene rings of each subgroup molecules all cluster in the steric center described above. However, the mutual perpendicular orientation between the neighboring molecules rules out such interaction, at least, π-π stacking interations. Another possibility is a solvent mediated effect, since the steric vacancy represented by the center of the three dimensional 'sphere' could accommodate a solvent molecule could be accommodated there and hold the surrounding aromatics. Unfortunately, no evidence was found for this hypothesis. The only 'conclusion' we can draw from the observations is that the coplanar and parallel ligand feature of each distinct molecule allows the most efficient packing. Clustering molecules into subunits and organizing the protruded aromatic fragments together provide an efficient mechanism for tight packing.

As mentioned earlier, the N-methylpyrrolene-incorporated ferrocenophane possesses additional steric strains due to the introduction of the methyl groups on the pyrrole nuclei. It is reasonable to expect that multiple tilting and distortions necessitating the sacrifice of the coplanarity of the ligand conjugation backbone may be required to accommodate such a high degree of strain. In contrast, the actual X-ray structural analysis, shown in Figure 5.9, reveals no serious twisting and distortions. In particular, the ligand coplanarity even persists better than that of the singly-bridged analogue, 2,5-bis(ferrocenylvinyl)-N-methylpyrrole (in Chapter 3). The pyrrole nuclei only show little distortion from coplanarity (maximum dihedral angle 4.16^{o}). The ligand separation is

A

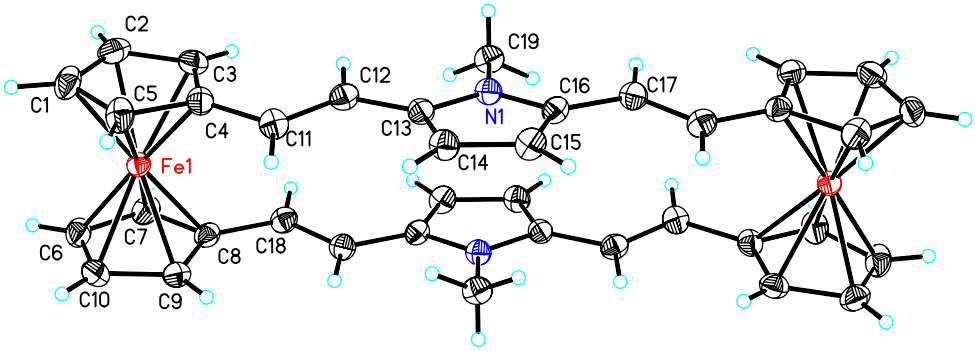

B

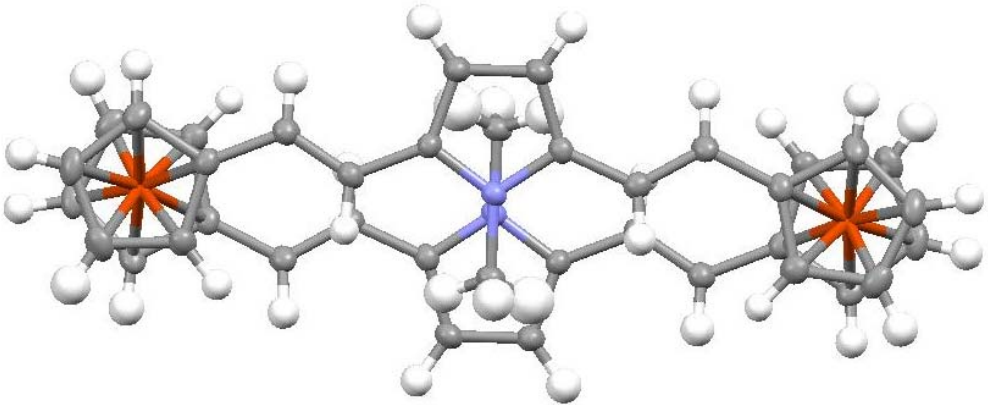

Figure 5.9 Crystal structure of pyrroloferrocenophane **14**. A: ORTEP plot of **14** with 50% anisotropic displacement ellipsoids; B: topside view showing the staggered ferrocenes and the *anti*-orientation of the two bridging pyrrolene moieties with respect to each other.

nearly persistent along the conjugation pathways. No significant titling with respect to the two Cp rings of the ferrocene nuclei was observed. In fact, these well-shaped structural features are the consequences of two major molecular motions and steric arrangements, which are, presumably, the key factors for relaxing the intramolecular strains: (1) the two Cp rings of each ferrocene nucleus rotate from an eclipsed to a staggered disposition with an average staggering angle of 26.25^{o}. As a consequence, the paired Cp substituted C-C bonds such as C4-C11 and C8-C18 bonds are no longer superimposed on each other. Instead, they rotate away and give a dihedral angle of 48.27^{o}; (2) the methyl substituents on the top and bottom pyrrole moieties in Figure 5.9 lie on opposite sides of the line crossing between the two metal centers. This effectively avoids the steric conflict between the methyl groups otherwise. Under these arrangements, the two bridging conjugated chains are prevented from overlapping with each other (Figure 5.9B) so that intramolecular π-π stacking is essentially broken. Obviously, the stereochemistry of **14** is steric-strain dominated.

Compared to bimetallic ferrocenophanes, the trimetallic ferrocenophane **13** (Figure 5.10) in principle contains less steric strain owing to the enlarged cyclic skeleton. However, due to the three-dimensional molecular constraints, several structural compromising features are observed. First, the paired Cp rings in the three ferrocene nuclei demonstrate different degrees of tilting. Whereas the Fc2 (Fe2-incorporated ferrocenyl unit) and Fc3 show little tilting (5.38^{o} and 4.8^{o}, respectively) with respect to the paired Cp rings, the tilting level of Fc1 is quite noticeable (9.12^{o}) and indicative of more steric strain at this joining point. Second, all the ferrocenyl units exhibit pseudo-*syn* conformation in terms of their two ancillary ligands, but none of the paired disubstituents is parallel. The dihedral angles between C10-C11 and C1-C51 bonds (Fc1), C18-C19 and C28-C29 bonds (Fc2), and C36-C37 and C46-C47 bonds (Fc3) are 68.4^{o}, 28.68^{o}, and 60.5^{o}, respectively. Relevantly, the degrees of rotation from eclipsed to staggered disposition for the three ferrocene nuclei are different. Fc1 is almost eclipsed, Fc3 is slightly staggered (average staggered angle 8.23^{o}), and Fc2 is heavily rotated (average staggered angle 21.26^{o}). Lastly, the three bridging linkers show varied conjugation efficiencies. While the coplanarity of the conjugation pathway between Fc2 and Fc3 is persisted, the first conjugation halfway from Fc2 to Fc1 also presents high degree of

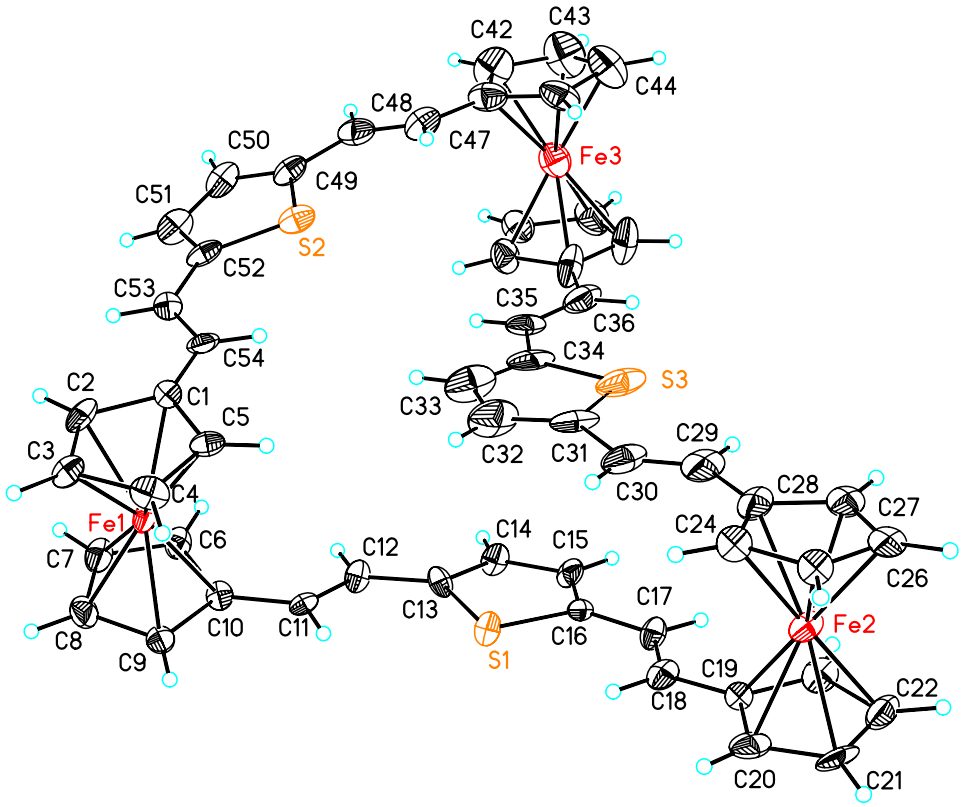

Figure 5.10 ORTEP plot of compound **13** with 50% anisotropic displacement ellipsoids.

coplanarity from the corresponding Fc2 Cp ring to the central thiophene nucleus (S1-incorporated thiophene was denoted as Th1, same for Th2 and Th3). In fact, the two ancillary ligands on Fc2 are nearly parallel and exhibit some extent of π-π overlapping between the Th1 and Th3 rings as shown in Figure 5.10. It is necessary to underline, however, that the π-π interaction in this case is very limited as the top (C29-C30) and bottom (C18-C17) vinylene bonds are oriented along different directions (staggered). The second halfway fragment (from Th2 to the corresponding Fc1 Cp ring), however, shows some distortion, which is evidenced by a torsion angle of 11.09^{o} between the Th2 and Cp (C6-C10) rings. Similarly, the conjugation pathway between Fc1 and Fc3 is also distorted from coplanarity. In deed, the distortion between the Fc1 Cp (C1-C5) and Th2 rings (dihedral angle 18.34^{o}) is the highest in the conjugation system of this molecule.

From the stereochemistry of **13**, the following bond forming sequences and corresponding molecular motions could be easily deducted. The bridging linker between Fc2 and Fc3 ought to be the first fragment to be established since it possesses the highest coplanarity in absence of notable steric hindrance. Following this is the connection between Fc2 and Fc1, upon which the two ancillary ligands substituted to the Fc2 Cp rings should ideally exhibit more parallel and π-π interaction features as the model compound 1,1'-Fc(CH=CHThCHO)$_2$ does (Chapter 4). At this point, no Cp ring tilting should be observed for any of the three ferrocenyl groups; the Cp ring dispositions of Fc3 and Fc1 should be the normal eclipsed style; and the same conformation for Fc2, however, may contain some staggering feature since the current molecular constitution consists of certain steric hindrance arising from the proximity between the two ending ferrocenyl groups (Fc3 and Fc1). A possible mechanism to relieve the steric congestion is either to orientate the Fc1 to a sterically more favorable direction or to have the Cp rings of Fc2 slightly staggered to keep the side ligand terminals apart from each other. The last step of forming the final architecture of **13** is accomplished by the ring closure process between Fc1 and Fc3, with which the molecular construction is finalized together with an introduction of serious steric strains. The steric strains are accommodated by a series of molecular motions: (1) the tilting from parallel position of the Cp pairs, especially the Fc1 unit; (2) the distortions from coplanarity highlighted by the degraded conjugation between the Fc1 Cp rings and their substituted side ligands; and (3) the rotation from an

eclipsed to a staggered conformation of the Fc2 and Fc3 groups, especially the Fc2 nucleus. Obviously, the concentrated steric distortions around the Fc1 group suggest that this is the location where the ring closure step is carried out.

Electrochemistry

The cyclic voltammetric data of the cycloferrocenophanes are summarized in Table 5.1. The oxidation potentials are reported versus Fc/Fc^+ couple. All the electrochemical studies are conducted in CH_2Cl_2, unless stated otherwise, using $Bu_4N^+TFPB^-$ as the supporting electrolyte.

In general, all the bimetallic ferrocenophanes present two well-resolved reversible oxidation waves. Except for [5.5]ferrocenophane-dione **5** and [7.7]ferrocenophane-dione **6**., the rest of the bimetallic ferrocenophanes exhibit the first oxidation (E_1) at a more negative potential than both the Fc/Fc+ couple and their singly-bridged diferrocenyl analogues. This is attributed to the increased electron density and extended conjugation on the ferrocene vicinity. The degree of such negative shift is associated with the electron richness of the X group/atom in this class of doubly-bridged diferrocenyl compounds.

Due to the electron-withdrawing nature of the carbonyl group, the first oxidations of [5.5]ferrocenophane-dione **5** and [7.7]ferrocenophane-dione **6**, however, appear at rather positive potential versus Fc/Fc^+ couple and are even more positive than those of their singly-bridged diferrocenyl counterparts. This positive shift is certainly a result of the accumulated electron-withdrawing effect from the electron-deficient double linkages.

It is a common assumption that the difference between E_2 and E_1 (ΔE) of a symmetrically linked bimetallic complex is considered as an important parameter in judging the capacity of the linking spacer to conduct intramolecular electronic communication between the two metal centers. As shown in Table 5.1, the ΔE values of doubly-bridged diferrocenophanes **1-7** vary from 140 to 400 mV with [4.4]ferrocenophane **1** showing the largest peak separation due to its shortest conjugation length. On the other extreme, [5.5]ferrocenophane **2** has the smallest ΔE-- clearly because of the broken conjugation at the central methylene group. The increasing order of the ΔEs of this series of compounds is in good agreement with the peak-separation trend of the singly-bridged diferrocenyl analogues described in chapter 2. Furthermore, the ΔE value

Table 5.1 Electrochemical data[a] (from Cyclic Voltammetry) for the compounds

Comp.	E^o_1 (mV)	E^o_2 (mV)	E^o_3 (mV)	ΔE^o_1[b] (mV)	ΔE^o_s[c] (mV)	Increased[d] ΔE^o (%)
1	-180	225		405	220	84%
2	-40	100		140	115	21%
3	-165	150		315	180	75%
4	-135	150		285	165	76%
5	245	465		220	125	76%
6	140	375		235	N/A	-
7	-54	160		214	130	65%
10	-240	60		300	160	87.5%
9	-47	53	121	100	90	-
11	-155	19	170	174	160	-
13	-125	27	142	152	140	-
15	-388	-88	887[e]	300	365	-

[a] Obtained in CH_2Cl_2 solution containing 0.1 M Bu_4NTFPB; scan rate 50 mV/s, oxidation potential reported vs. Fc/Fc^+ couple; [b] $E^o_2 - E^o_1$; [c] ΔE of the singly-bridged analogue; [d] % = $(\Delta E^o_1 - \Delta E^o_s)/\Delta E^o_s$ x 100%, only applicable to the doubly-bridged system; [e] semi-reversible oxidation process.

of each doubly-bridged ferrocenophane is unexceptionally increased compared to that of its singly-bridged counterparts. Except for compound **2**, the increased percentages range from 64% to 88% depending on the X-linking unit. The enhanced peak-separation, i.e. stronger intramolecular interaction, apparently arises from the doubled bridging channels between the redox termini, which is consistent with the observations previously reported for the duel-linked systems.[14] Given the fact that the iron-iron distance (> 8.5Å) has been well-separated in a strictly confined framework for the ferrocenophanes herein, through-space charge transfer could be virtually ruled out since such motion drops exceptionally with the increasing metal-metal distance. Therefore, the observed electronic interactions must originate from a through-bond mechanism.

Careful examination on the electrochemical behaviors of the ferrocenophanes prepared via Wittig reactions (i.e. compounds **1-4**) reveals a slightly broadened second oxidation wave (Figure 5.11-12). Such broadening often represents a major peak accompanied with a shoulder at a more negative position. A possible explanation to this observation is related to the co-presence of the unseparable isomeric species. In other words, due to the synthetic method (Wittig reaction) used in preparing these compounds, several *cis/trans* isomers are present in the substrate. The difference in stereochemistry of the two linking fragments may affect the efficiency of the electronic coupling between the two ferrocene ends. While the steric effect on electrochemistry may not be significant for the singly-bridged diferrocenyl species due to the flexible rotation of the linear chain during the consecutive oxidation processes, it is no longer negligible for the doubly-bridged systems, for which the restricted structural confinement inhibits such free rotation. Therefore, for compounds such as **1**, isomers with more regular conjugation pathways (**1c** in the structures shown below) will presumably have more effective electron-communicating means, which consequently results in the second oxidation to appear at more positive potential, and vice versa. The broadened second oxidation wave reflects the overall mixing of the corresponding redox processes. In contrast, such broadening feature is not observed in compounds with unambiguously-defined all-*E* vinylene bonds such as **7** and **10**.

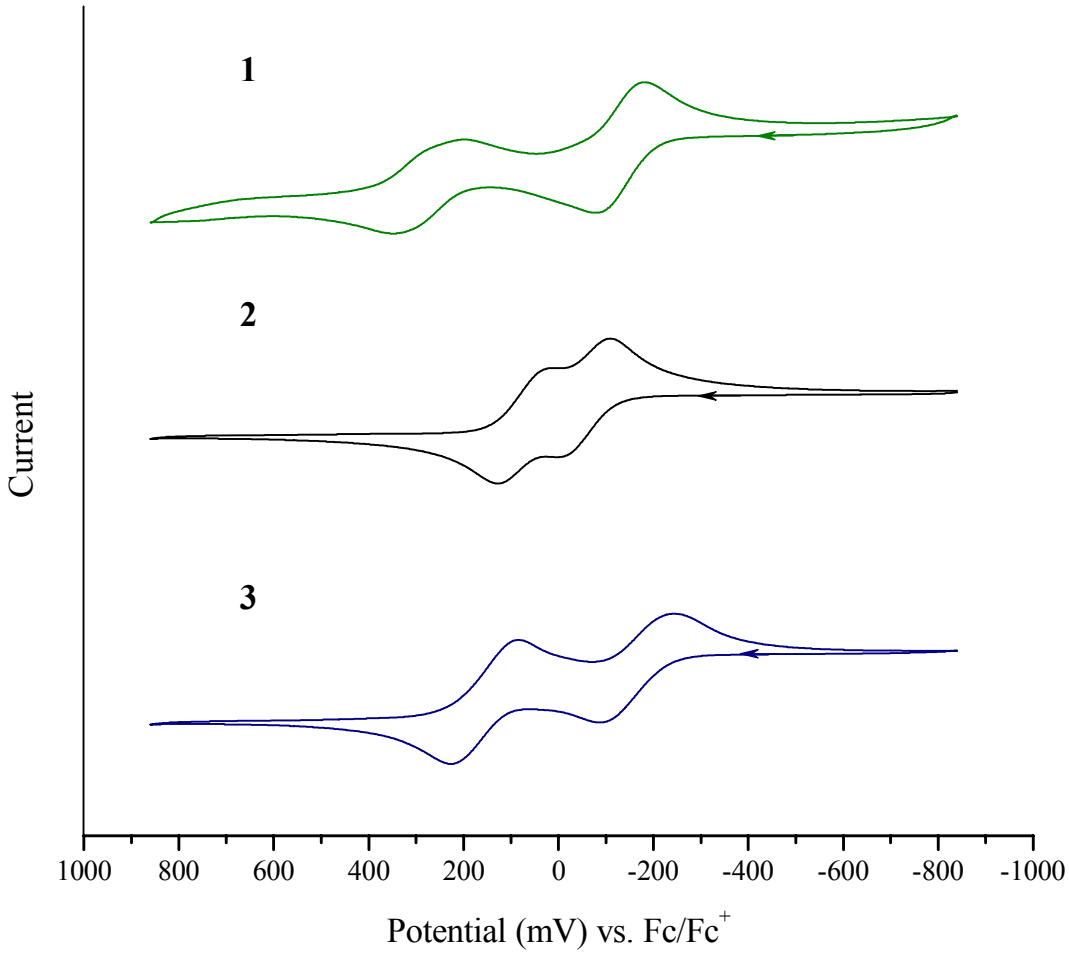

Figure 5.11 Cyclic voltammograms of [4.4]ferrocenophane **1**, [5.5]ferrocenophane **2** and [6.6]ferrocenophane **3** in CH_2Cl_2/0.1M Bu_4NTFPB. Scan rate 50 mV/s. The oxidation potentials are reported versus Fc/Fc^+ couple as the internal reference

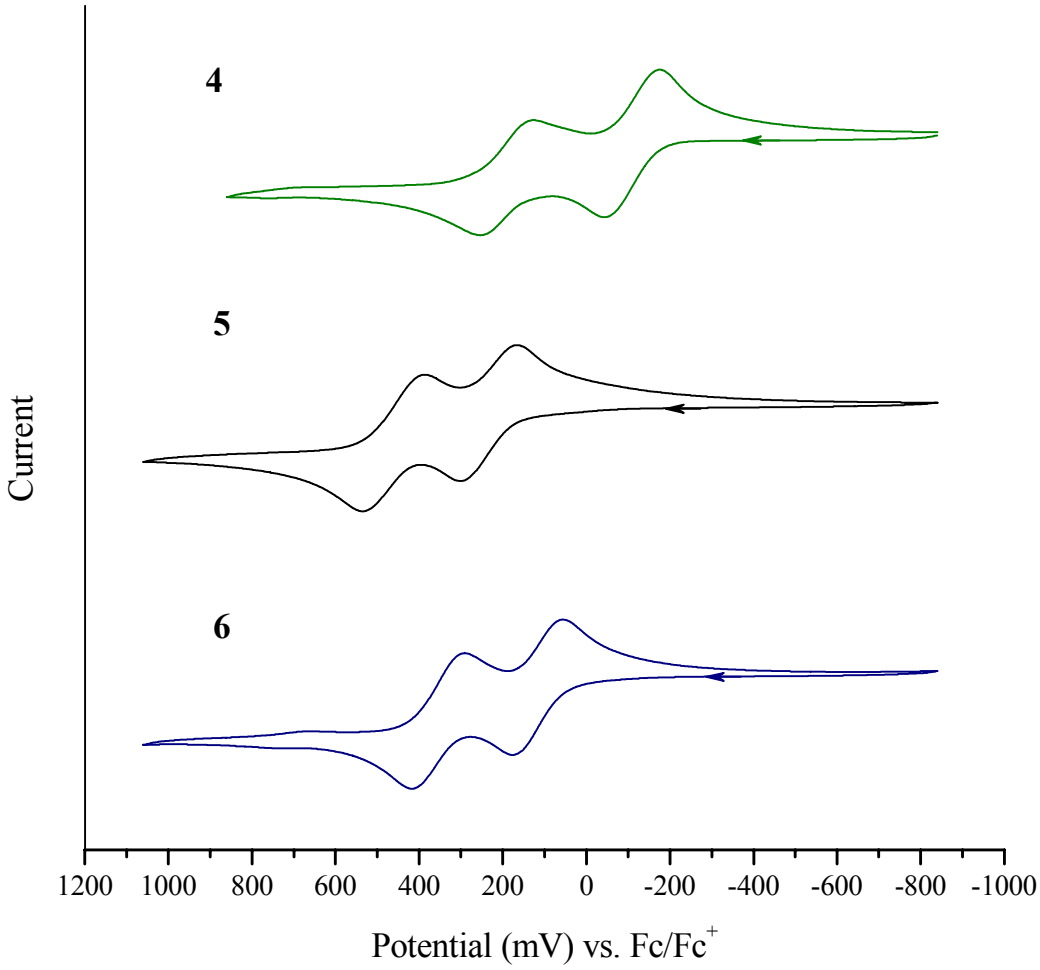

Figure 5.12 Cyclic voltammograms of dithia[5.5]ferrocenophane **4**, [5.5]ferrocenophane-dione **5** and [7.7]ferrocenophane-dione **6** in CH_2Cl_2/0.1 M Bu_4NTFPB. Scan rate 50 mV/s. The oxidation potentials are reported versus Fc/Fc^+ couple as the internal reference

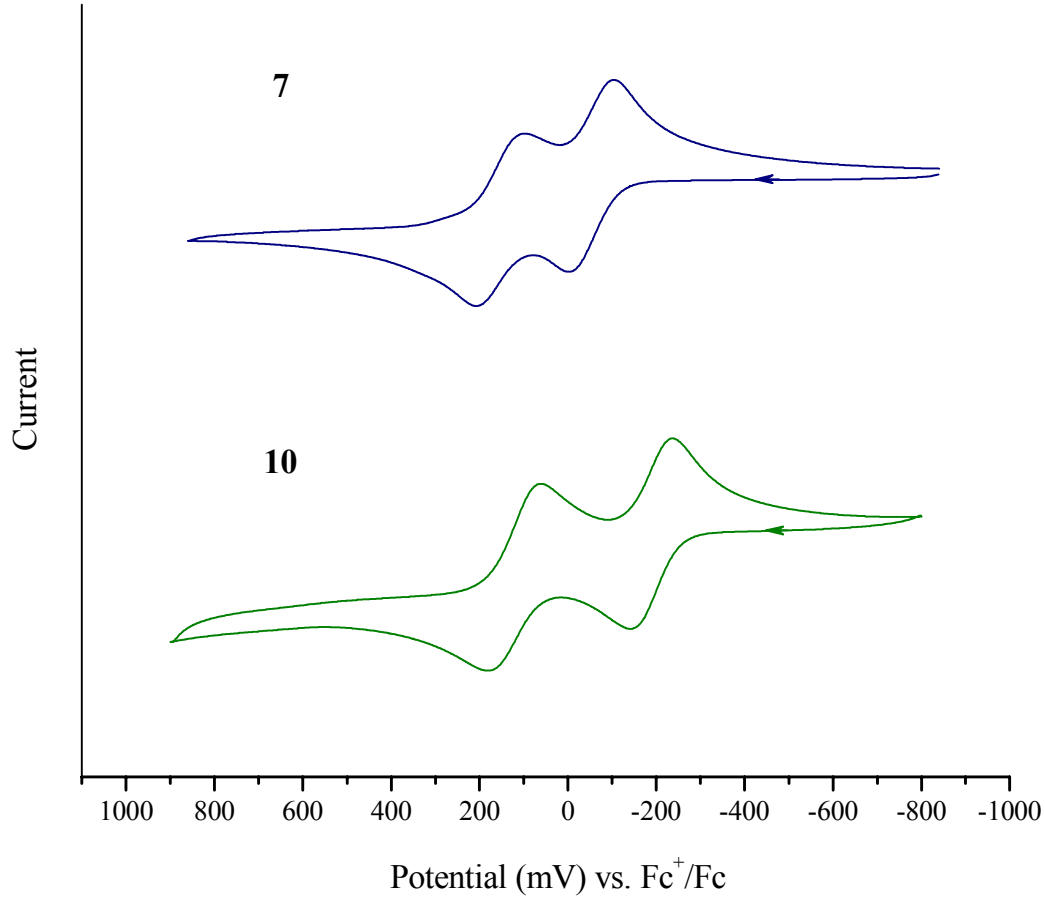

Figure 5.13 Cyclic voltammograms of orthocyclo-diferrocenophane **7** and furano-diferrocenophane **10** in CH_2Cl_2/0.1 M Bu_4NTFPB. Scan rate 50 mV/s. The oxidation potentials are reported versus Fc/Fc^+ couple as the internal reference

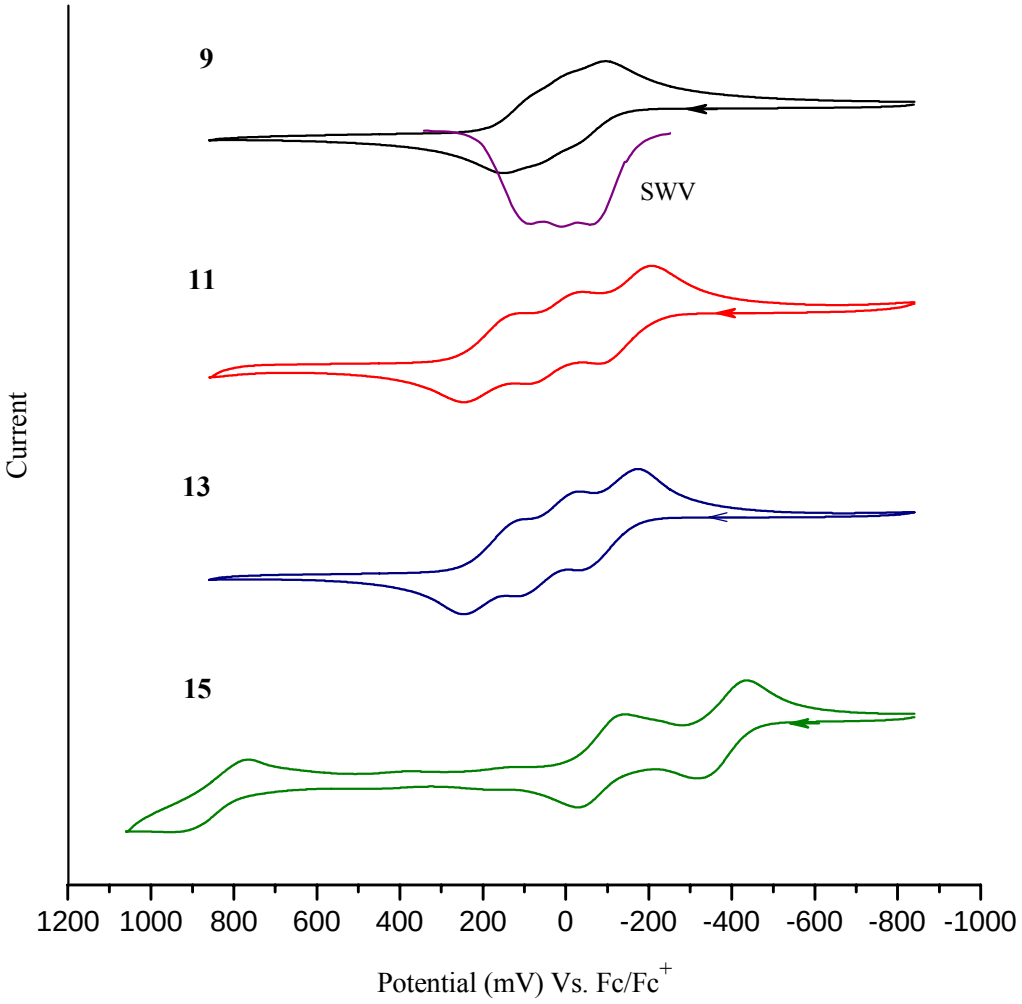

Figure 5.14 Cyclic voltammograms of paracyclo-triferrocenophane **9**, furano-triferrocenophane **11**, thiopheno-triferrocenophane **13** and pyrrylo-triferrocenophane **15** in CH_2Cl_2/0.1M Bu_4NTFPB. Scan rate 50 mV/s. The oxidation potentials are reported versus Fc/Fc^+ couple as the internal reference. Square wave voltammogram of triferrocenophane 9 (inset spectrum in purple color) indicated three closely-spaced oxidation processes corresponding to the three ferrocene groups.

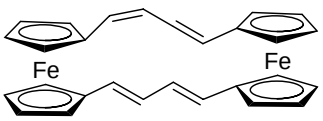

1a

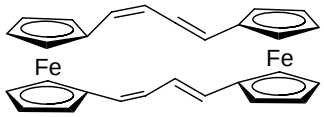

1b

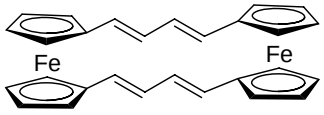

1c

It is also noteworthy that [7.7]ferrocenophane-dione **6** is the only asymmetric diferrocenophane examined in this study. The chemical environments of the two ferrocene units are apparently different. The lowered $E_1$of **6**, compared to that of [55]ferrocenophane-dione **5**, originates from the oxidation of the ferrocene moiety four carbons away from the carbonyl group. While the ΔE of [5.5]ferrocenophanedione **5** (220 mV) merely represents the degree of the through-bond intramolecular communication between the two metal centers, that of [7.7]ferrocenophane-dione **6** (235 mV) should not be considered as a correct measure of such interaction. In fact, the ΔE value of **6** is the sum of the through-bond electronic interaction and the intrinsic electronic difference between the two ferrocene termini.

For orthocycloferrocenophane **7**, the most speculative aspect is whether the steric conformers, *syn* and *anti*, will behave differently in electrochemistry. As the *syn*-conformer possesses a face-to-face overlapping between the two vinylene-phenylene-vinylene conjugated segments, the manifested π-π stacking between them may perturb the charge transfer process upon oxidation. Nevertheless, comparison studies on the two conformers showed an identical oxidation pattern with virtually the same oxidation potentials and peak separation. This observation implies the followings: (1) the electronic communication between the redox centers is primarily a through-bond process; (2) super-exchange is the more suggested mechanism than electron hopping as the latter could be potentially mediated by the π-π stacking effect in the electron transfer process; and (3) under the applied conditions of the electrochemical measurements, the difference between the steric conformers is not significant enough to be detected.

For trimetallic ferrocenophanes **9**, **11** and **13**, each macromolecule demonstrates three reversible peaks in 1:1:1 ratio, corresponding to the three ferrocene moieties. The peak-separations (ΔE_1 and ΔE_2) of thiophene- and furan-linked species **11** and **13** are larger than that of *p*-phenylene linked analogue **9** due to the less aromatic conjugation chains. All peak splittings are within the normal level indicating a rather localized electronic interaction among the metal centers.

Pyrroloferrocenophane **15**, however, exhibits markedly different oxidation pattern compared to other trimetallic compounds. Cyclic voltammetric analysis of **15** reveals three oxidation waves at -0.388 V, -0.088 V and 0.887 V. It is not a surprise that the first oxidation appears at an even more negative potential due to the electron-donating pyrrolene ligands disubstituted on the ferrocene nuclei. The ΔE_1 (300 mV), however, is noticeably smaller than that of N-methylbis(2-ferreocenylvinyl)pyrrole (365 mV, Chapter 3). Given the fact that N-alkyl substituted 2,5-divinyl- pyrrolene nucleus possesses a formal oxidation potential close to that of ferrocene (Chapter 3), the redox-matching between the metal and organic components in **15** essentially gives rise to a highly delocalized system. The decreased ΔE_1 suggests that the second positive charge is generated at a location further distant from the first ferrocenium moiety, i.e. at the pyrrolene unit as shown below. This electronic arrangement establishes an electrostatically more stable state for the dicationic species by having the two positive charges mostly apart. For the same reason, removing one more electron from $\mathbf{15}^{2+}$ results in the positive charges evenly distributed on the three ferrrocene units in $\mathbf{15}^{3+}$. The charge delocalizing feature of $\mathbf{15}^{3+}$ clearly accounts for the enlarged ΔE_2 (800 mV). The third oxidation is effectively influenced by the neighboring charges within the cyclic structure, which makes it more difficult to take place. The small burst peak appearing at 0.125 V is presumably derived from the presence of small amount of bimetallic **14** (or other impurities), which is very difficult to remove by chromatography.

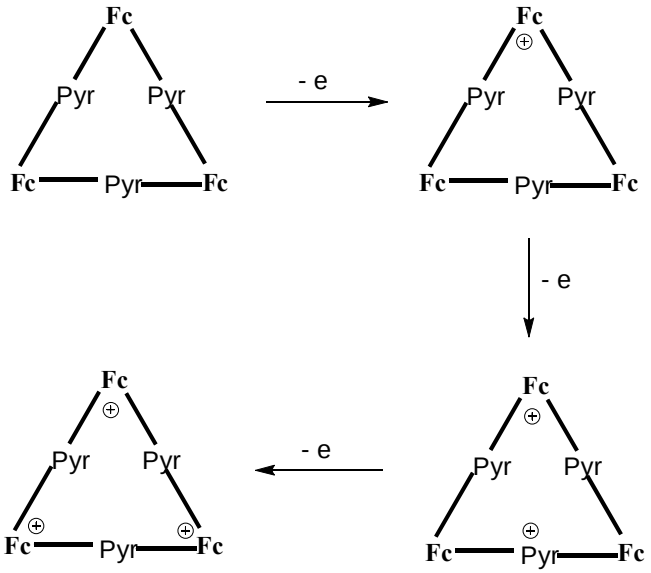

Mixed-Valence Intervalence Absorption

Our efforts on the examination of intervalence charge transfer (IVCT) absorption in this study are still focused on the one-electron oxidized species. The mixed-valence species was generated using the same method described in the previous chapters. The interested neutral compound was dissolved in CH_2Cl_2 as a 2-4 x 10^{-4} M solution and mixed with $FcPF_6$ or $Ar'_3N^+SbCl_6^-$ (magic blue, Ar' = *p*-BrC_6H_4) (when higher oxidative strength is needed such as for dione 5 and 6) in the same solvent. The resulting solution was then immediately subjected to UV-Vis-NIR measurement. A series of such measurement was taken with 0.2-1.0 equivalent of oxidant present for each of the neutral compound so that a medium value of the calculated molar extinction coefficient was adopted as the reasonably reported value. The concentration of the monocationic species at equilibrium was determined from the physically reasonable solution to the quadratic equation (Eq. 5.1), in which $[M^+]$ is the concentration of monocation at equilibrium, C_M is the concentration of M in reaction mixture (i.e. neutral, monocation and dication), C_{OX} is the concentration of $Fc^+PF_6^-$ in reaction mixture and K_c is the comproportionation constant.

$$(0.25 - (1/K_c))[M^+]^2 - (0.5C_M)[M^+] + (0.25C_{OX})(2C_M - C_{OX}) = 0 \qquad (5.1)$$

However, it is necessary to point out that the solubility of the mono-charged species of bimetallic and trimetallic ferrocenophanes is poorer than the singly-bridged

diferrocenyl analogues in some of the cases, depending on both the extent of conjugation and the nature of the bridging unit. Although lowering the concentration or using smaller equivalent of oxidant (e.g. 0.2-0.5 equivalent) generally gives better result in avoiding miscalculation of the actual [M^+], overestimation of the [M^+] is still possible for some of the systems due to undetectable isolation of the mixed-valence species from solution. This in turn leads to an underestimation of the molar extinction coefficient (ε_{max}) as we shall see in the following discussion. To resolve this problem, replacing the counterion PF_6^- with the bulky Ar'_4B^- (Ar' = 3,5-$(CF_3)_2C_6H_3$) is recommended to promote the solubility of the monocations in the future work.

In general, the mixed-valence species of [5.5]ferrocenophane **2**, [5.5]ferrocenophane-dione **5** and [7.7]ferrocenophane-dione **6** showed little or negligible IVCT band due to the broken conjugation (for **2**) and highly-deficient electron density (for **5** and **7**) on the bridging units. The mixed-valence spectrum of paracycloferrocenophane $\mathbf{9}^+$ is highly skewed due to the poor solubility of both of the neutral and mono-cationic species, which made the spectral analysis impossible. The rest of the monocations all exhibit one or multiple low energy bands in NIR region after spectral deconvolution. The bands are attributed to ligand-to-metal charge transfer (LMCT), IVCT and interconfigurational (IC) transition depending on the specificity of the bridging unit. The mixed-valence absorption spectra of doubly-bridged bimetallic ferrocenophanium $\mathbf{1}^+$, $\mathbf{2}^+$, $\mathbf{4}^+$, $\mathbf{7}^+$ and trimetallic ferrocenophanium $\mathbf{11}^+$, $\mathbf{13}^+$ and $\mathbf{15}^+$ are shown in Figure 5.17-5.20, together with the corresponding singly-bridged analogues for comparisons. The deconvoluted spectral parameters, calculated Hush parameters and delocalization efficient (equations therein) are summarized in Table 5.2. The detailed explanation will be described in the following discussions.

Doubly-Bridged Bimetallic Ferrocenophanes

The absorption spectra of polyene doubly-bridged diferrocenium $\mathbf{1}^+$ and $\mathbf{2}^+$ are shown in Figure 5.17. For each case, the IVCT band exhibits a c.a. 100 nm red-shift in comparison with that of the singly-bridged analogues. In fact, such bathochromic shift of IVCT band was observed for all the di- and triferrocenophane monocations containing electron-donating bridging linker. This indicates that the energy difference between the half-occupied Fe^{III} and full-filled Fe^{II} dπ orbitals is decreased due to the perturbation of

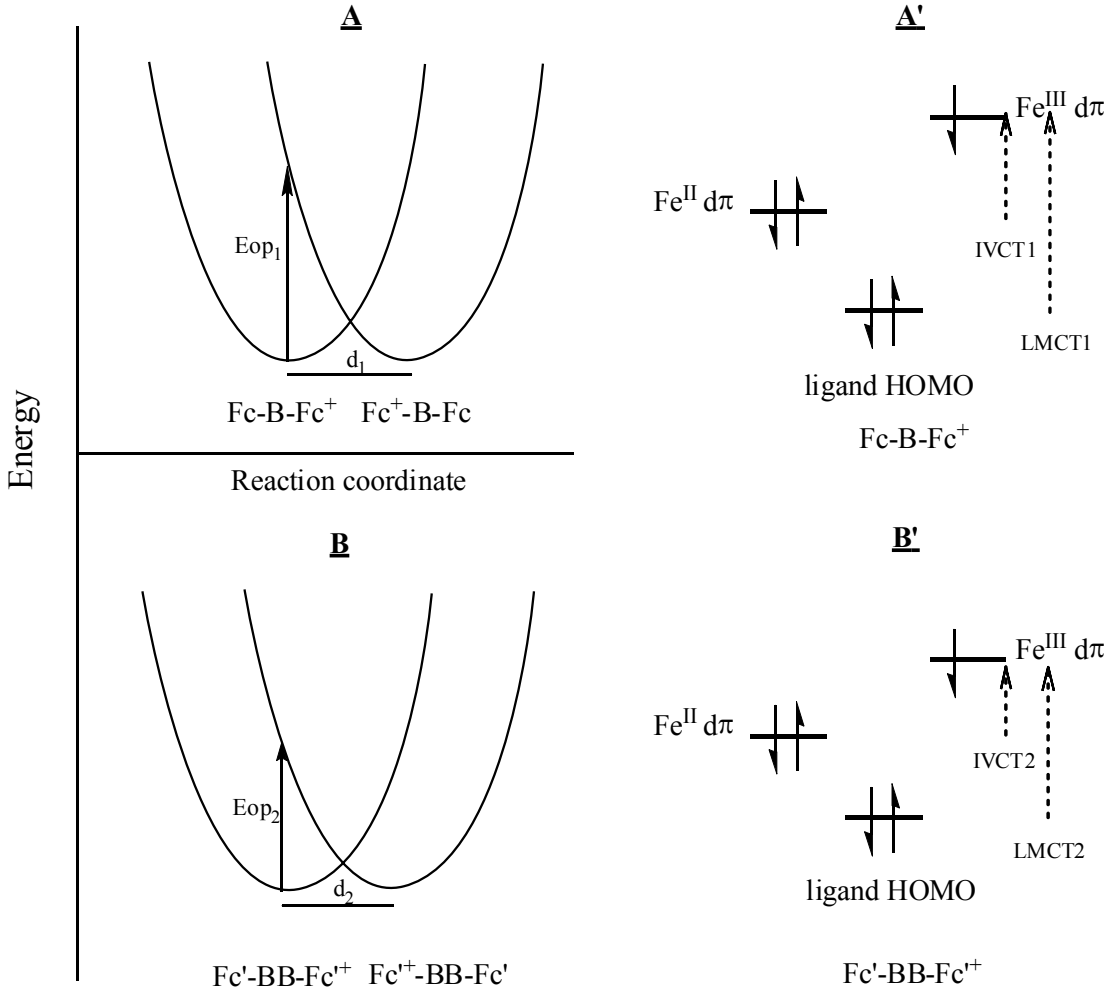

Figure 5.15 Schematic representation of potential coordinate and orbital configurational diagrams for photo-induced electron transfer in singly-bridged biferrocenium and doubly-bridged biferrocenium ions with symmetrical bridging linker B. A and A': singly-bridged diferrocenyl system; B and B': dinuclear ferrocenophanyl system, where –BB- denotes the double linkers. Note: d: metal-metal distance; IVCT: intervalence charge transfer; LMCT: ligand-to-metal charge transfer.

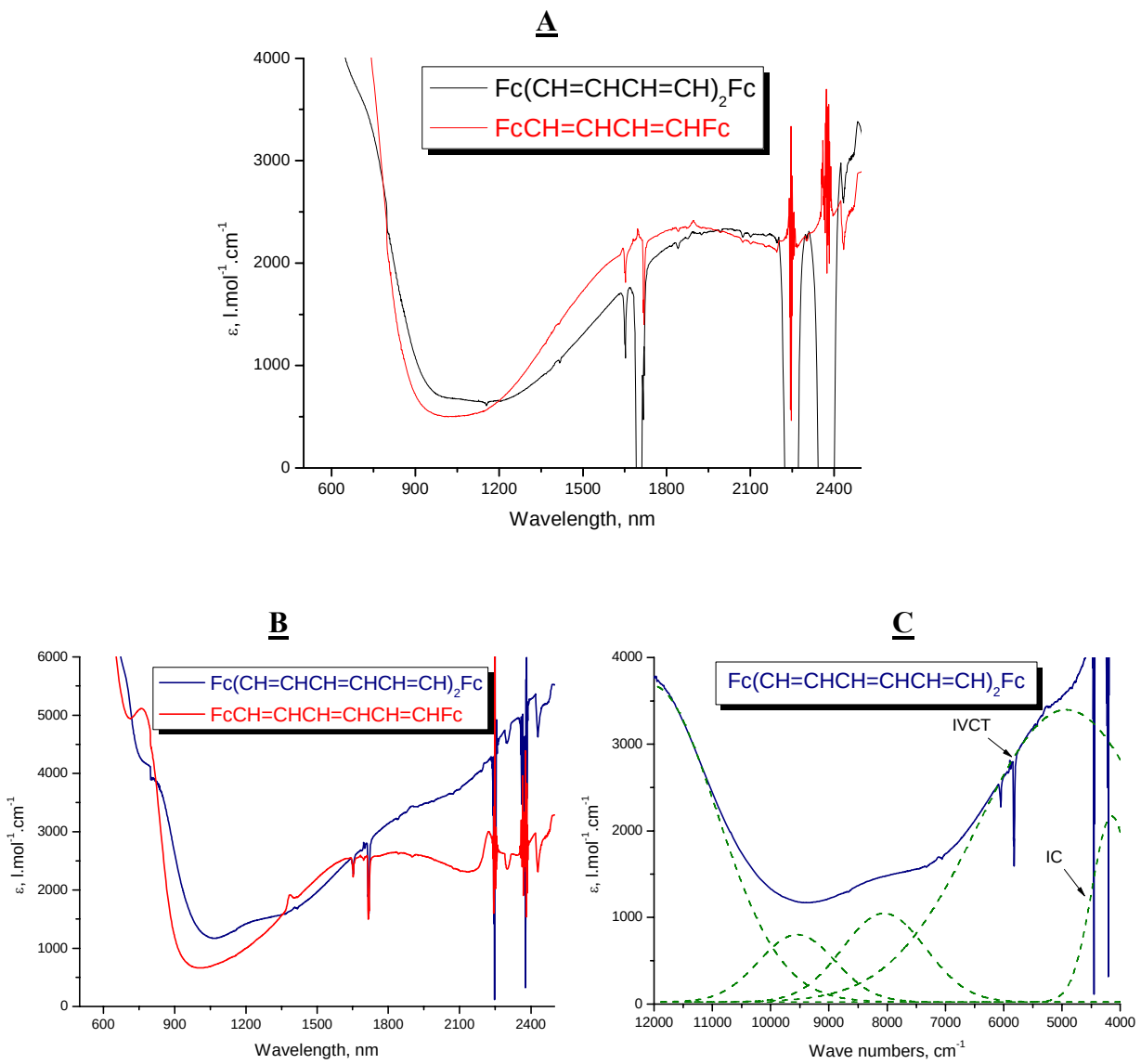

Figure 5.16 UV-Vis-NIR spectra of mixed-valence species $\mathbf{1}^+$ and $\mathbf{2}^+$. A: spectra of $\mathbf{1}^+$ (black line) and singly-bridged $Fc^+CH{=}CHCH{=}CHFc$ (red line); B: spectra of $\mathbf{2}^+$ (blue line) and singly-bridged $Fc^+CH{=}CHCH{=}CHCH{=}CHFc$ (red line); C: deconvoluted curve-fitting bands (green dashed lines) of $\mathbf{2}^+$ in NIR region.

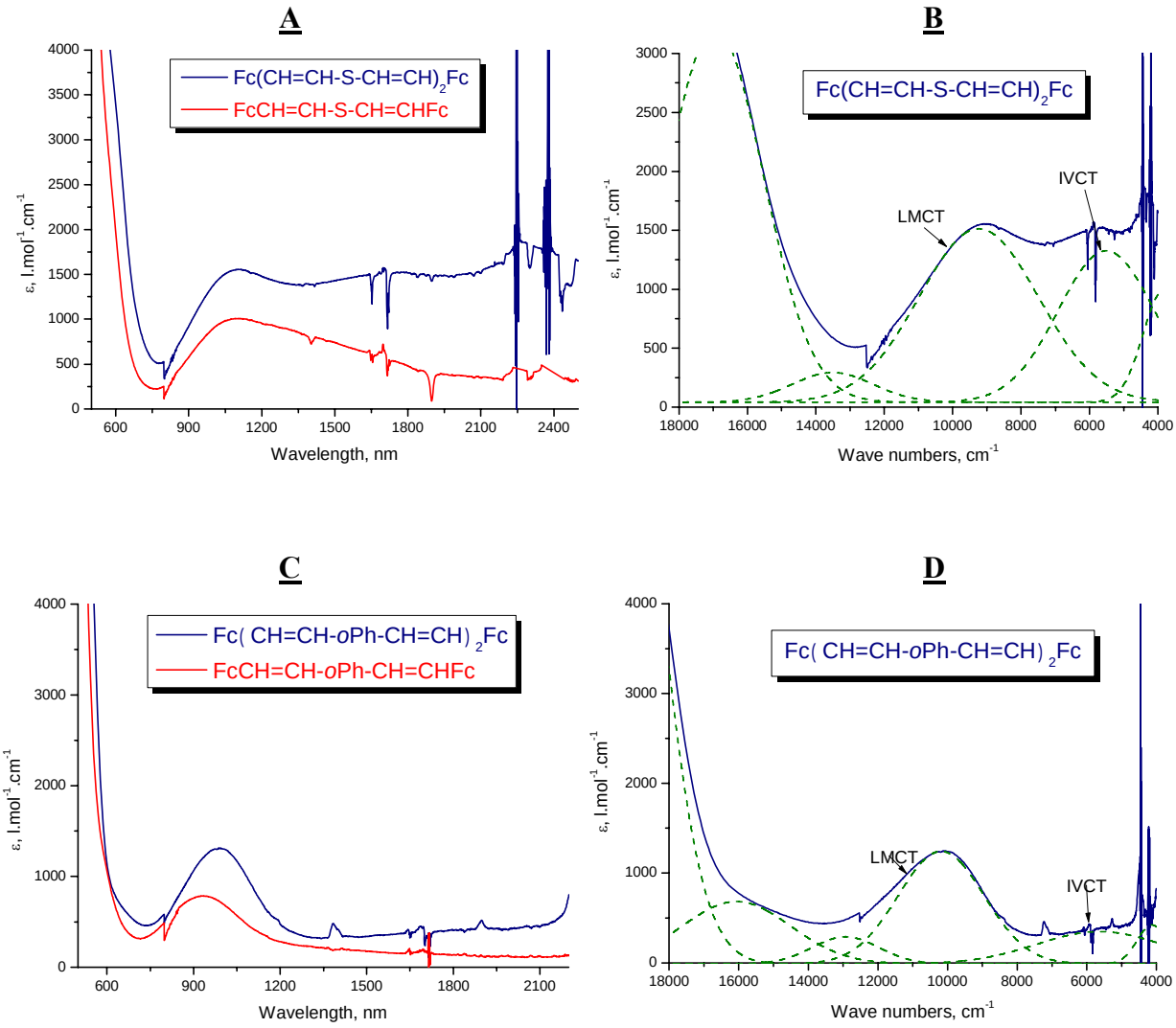

Figure 5.17 UV-Vis-NIR spectra of mixed-valence species $\mathbf{4}^{+}$ and $\mathbf{7}^{+}$. A: spectra of $\mathbf{4}^{+}$ (blue line) and singly-bridged analogue $Fc^{+}CH{=}CHSCH{=}CHFc$ (red line); B: deconvoluted curve-fitting bands (green dashed lines) of $\mathbf{4}^{+}$ in Vis-NIR region; C: spectra of $\mathbf{7}^{+}$ (blue line) and singly-bridged analogue $Fc^{+}CH{=}CH$-oPh-$CH{=}CHFc$ (red line); D: deconvoluted curve-fitting bands (green dashed lines) of $\mathbf{7}^{+}$ in Vis-NIR region.

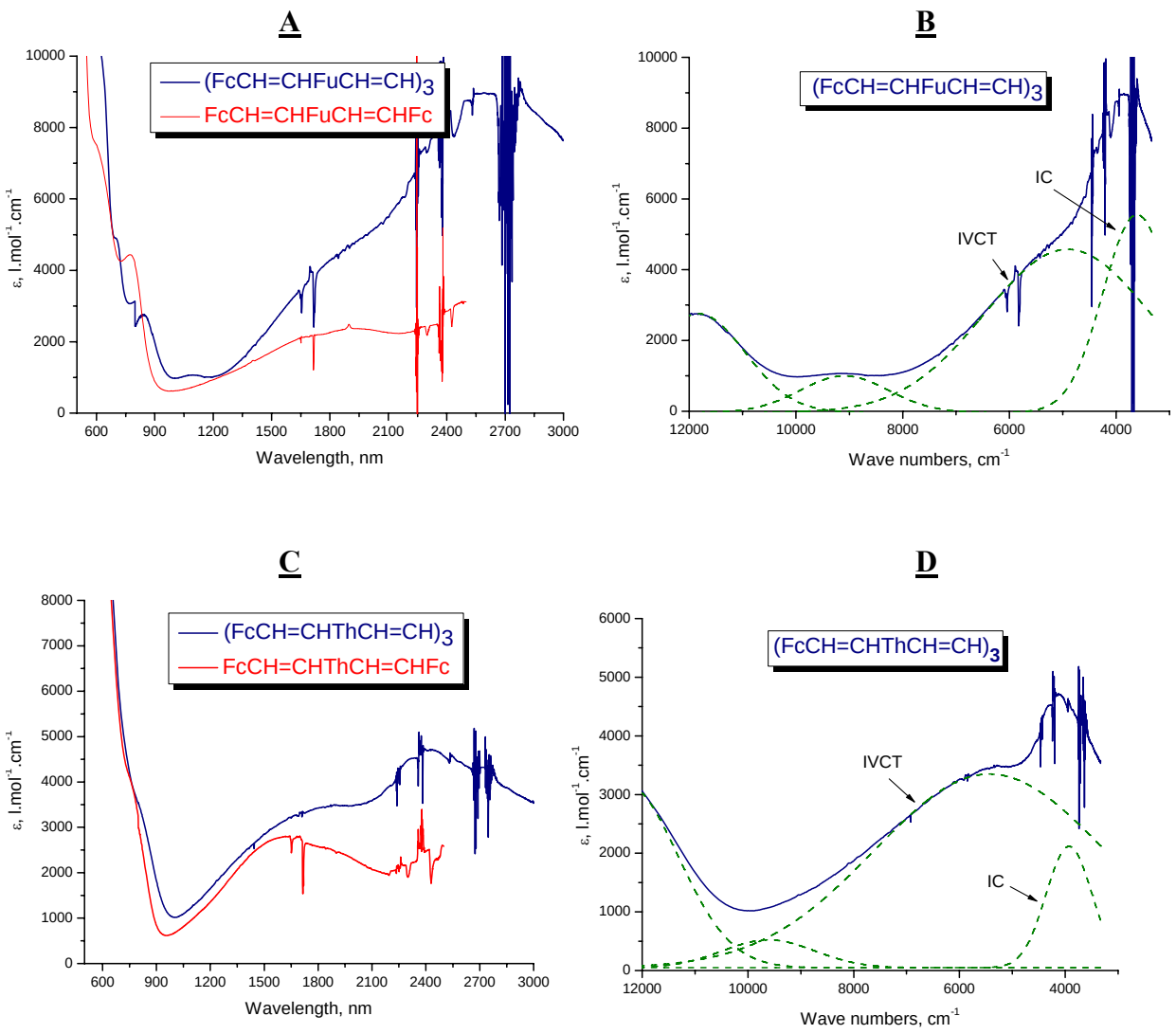

Figure 5.18 UV-Vis-NIR spectra of mixed-valence species **11**$^+$ and **13**$^+$. A: spectra of **11**$^+$ (blue line) and singly-bridged analogue $Fc^+CH{=}CH\text{-}C_4H_2O\text{-}CH{=}CHFc$ (red line); B: deconvoluted curve-fitting bands (green dashed lines) of **11**$^+$ in NIR region; C: spectra of **13**$^+$ (blue line) and singly-bridged analogue $Fc^+CH{=}CH\text{-}C_4H_2S\text{ -}CH{=}CHFc$ (red line); D: deconvoluted curve-fitting bands (green dashed lines) of **13**$^+$ in NIR region.

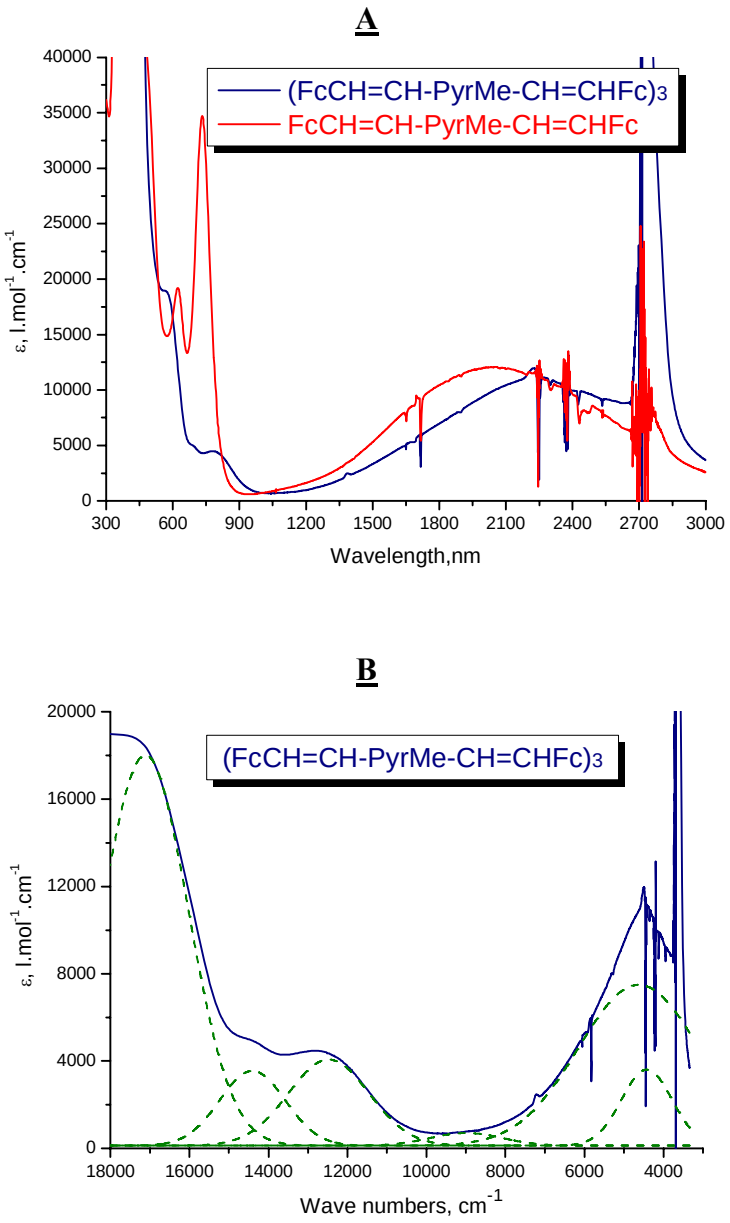

Figure 5.19 UV-Vis-NIR spectra of mixed-valence species **15**$^{+}$. A: spectra of **15**$^{+}$ (blue line) and singly-bridged analogue $Fc^{+}CH{=}CH\text{-}C_4H_2N(Me)\text{-}CH{=}CHFc$ (red line); B: deconvoluted curve-fitting bands (green dashed lines) of **15**$^{+}$ in Vis-NIR region;

Table 5.2 IVCT and LMCT band parameters, obtained from the spectral deconvolution, and calculated Hush parameters for the selected cationic species.

	ν_{max} [cm^{-1}]	ε_{max} [$M^{-1}cm^{-1}$]	$\Delta\nu$ [cm^{-1}]	d_{mm} [a] [Å]	V [b] [cm^{-1}]	α [c]
BFc4^{+} [d]	5290	2320	3900	9.21	487 [j]	0.092
1^{+}	5020	2300 [i]	3400	8.59 [e]	473 [i,j]	0.094
BFc6^{+} [d]	5660	2590	4040	11.54	432 [j]	0.076
2^{+}	5050	3400	3600	11.05 [e]	461 [j]	0.091
BFcVS^{+} [d]	9257 [h]	965	4176	5.47 [g]	724 [k]	0.078
	6020	440	3640	9.78	206 [j]	0.034
4^{+}	9240 [h]	1515	4010	5.82 [e,g]	835 [k]	0.090
	5512	1320	3320	9.68 [e]	329 [j]	0.060
BFcVoPh^{+} [d]	10770 [h]	780	3600	-	-	-
	6060	162	4486	10.14	134 [j]	0.022
7^{+}	10180 [h]	1240	2910	-	-	-
	5630	340	4260	8.38	221 [j]	0.039
BFcVFu^{+} [d]	5250	2320	4600	10.37	468 [j]	0.089
11^{+}	4950	4550	3670	11.45 [e,f]	515 [j]	0.104
BFcVTh^{+} [d]	6130	2770	4000	10.85	492 [j]	0.080
13^{+}	5410	3350 [i]	5240	11.45 [f]	552 [i,j]	0.102
15^{+}	4600 [l]	7450	3740			
	4420 [m]	3630	1490			

[a] Spatial iron-iron distance obtained from crystal structure if not otherwise stated; [b] Hush coupling constant $V = 2.06 \times 10^{-2}(\varepsilon_{max} \cdot \Delta\nu_{1/2} \cdot \nu_{max})^{1/2}/d$; [c] delocalization efficient $\alpha = V/\nu_{max}$; [d] singly-bridged analogue obtained from Chapter 2; [e] obtained from theoretical calculation; [f] average iron-iron distance between the three metal centers; [g] average sulfur-iron distance; [h] LMCT transition as described in text; [i] possibly underestimated due to partial insolubility of the monocationic species; [j] IVCT transition; [k] LMCT transition; [l] undetermined, might be the overlapped LMCT and IVCT bands; [m] undetermined, might be the IC band.

the two ancillary ligands substituted on the Cp rings of the ferrocene units. The potential energy-configurational coordinate diagram and orbital electronic configuration of singly-bridged diferrocenium and the corresponding doubly-bridged diferrocenium monocations are illustrated in Figure 5.15, in which Fc^{+}-B-Fc and Fc'^{+}-BB-Fc' denote the singly-bridged and doubly-bridged mixed-valence diferroceniums, respectively, and B represents the linking spacer between the ferrocene units. As diagrammatically shown in Figure 5.15 A and B, the decrease of photo-induced electron transition energy (Eop_2) in Fc'^{+}-BB-Fc' could be conceptually interpreted that the potential energy surface of the doubly-bridged system is distorted to wider from the case for Fc^{+}-B-Fc, assuming that the metal-to-metal distances, d_1 and d_2 (in Figure 5.15 A and B), in both cases are roughly the same. Accordingly, upon association with two electron-sufficient substituents, the Fe^{II} and Fe^{III} dπ orbitals in doubly-bridged Fc'^{+}-BB-Fc' are reorganized to give rise to lower energy gap between the two metal sites (Figure 5.15 B'). In both viewpoints, the resulting IVCT transition of Fc'^{+}-BB-Fc' will lead to red-shifted absorption compared to that of Fc^{+}-B-Fc.

On the other hand, the IVCT molar absorption intensity is expected to be stronger in the doubly-bridged systems than in the singly-bridged analogue due to the additive effect arising from the duel channels of electronic interaction. This is clearly elucidated by [6.6]ferrocenophanium $\mathbf{2}^{+}$ (Figure 5.16B). The [4.4]ferrocenophanium $\mathbf{1}^{+}$, however, only demonstrates similar IVCT ε_{max} as $Fc^{+}CH{=}CHCH{=}CHFc$ (Figure 5.16A), which is ascribed to the possibly undervalued molar absorption of $\mathbf{1}^{+}$ due to the isolation of the poorly soluble $\mathbf{1}^{+}PF_6^{-}$ from the tested solution. Therefore, the calculated Hush coupling constant and delocalization efficient (in Table 5.2) are also underestimated due to the same reason. Last, the sharp and intense band appearing around 2400 nm in both $\mathbf{1}^{+}$ and $\mathbf{2}^{+}$ is assigned to the interconfigurational (IC) electron transition from the full-filled dπ orbital to the half-occupied dπ orbital of the Fe^{III} center. This IC band generally appears as a sharp and narrow band with half band width around 1000 cm^{-1}. The intensity and broadness of this band are commonly increased by the electron-donating effect from the substituents on the ferrocenium Cp ring, which is especially the case when the ferrocenium group is disubstituted.

In Figure 5.17A, dithia[5.5]ferrocenophanium $\mathbf{4}^+$ exhibits an apparently different band shape in the NIR region from that of the singly-bridged analogue $Fc^+CH=CHSCH=CHFc$ (**BFcVS**$^+$ in Chapter 2). Spectral deconvolution of the $\mathbf{4}^+$ absorption spectrum gave rise to three well-shaped gaussians in the low energy area fitting very well to the original spectrum (Figure 5.17B), with the lowest energy band (centered at c.a. 4000 cm^{-1}) assigned to the IC transition. The first NIR band centered at 9240 cm^{-1} (1082 nm) appears at nearly the same position as that of the singly-bridged **BFcVS**$^+$ and is assigned to the sulfur-based ligand-to-metal charge transfer (LMCT). The promoted intensity of this band is clearly because of the additive effect arising from two bridging –CH=CHSCH=CH- units. The second band centered at 5520 cm^{-1} (1810 nm) is assigned to the IVCT transition between the interacting metal centers. Whereas the IVCT transition in **BFcVS**$^+$ is fairly weak and only appears as a buried band in the tailing section of the LMCT band, the corresponding IVCT band in $\mathbf{4}^+$ is explicitly visible and possesses absorption strength comparable to the LMCT band. The IVCT band of $\mathbf{4}^+$ is red-shifted from that of **BFcVS**$^+$ for the same reason as previously described for the doubly-bridged system, the intensity is almost tripled from that of the singly-bridged analogue. Such electronic interaction enhancement can not be understood only as the consequence of the additive effect due to the double bridging-chains, but also, probably more essentially, as the better orbital mixing between the bridging ligand and metal centers. Apparently, intramolecular communication through the heteroatom mediated conjugation backbone is greatly increased due to comprehensive orbital reorganization and overlapping once the second bridging unit is introduced, even such interaction is still weak (V_{ab} = 329 cm^{-1}).

For orthocycloferrocenophanium $\mathbf{7}^+$, the major low energy absorption is still the LMCT band appearing around 1100 nm (Figure 5.17C). This band is red-shifted in comparison with that of the singly-bridged analogue. Such bathochromic shift could be attributed to the decreased band gap between the ligand HOMO orbital and the Fe^{III} dπ orbital as illustrated in Figure 5.15 B', which mainly arises from the stabilized Fe^{III} dπ orbital due to the two substituents. The IVCT band of $\mathbf{7}^+$ is not of significance, evidenced by ε_{max} = 340 and V_{ab} = 220 cm^{-1}, and is consistent with our previous conclusion (Chapter 2) that ortho-phenylene is an unfavorable spacer in supporting electronic interaction.

Trimetallic Ferrocenophanes

The triferrocenophanes in many aspects resemble to the doubly-bridged biferrocenophanes. The symmetrical structure gives rise to three energetically and electronically identical metal centers. The potential energy surface wells, optical intervalence transition energy (Eop), frontier orbital electronic configurations and energy gap between the Fe^{II} and Fe^{III} dπ orbitals shown in Figure 5.15B & B' for doubly-bridged diferrocenophanium ion can be essentially applied to the one-electron oxidized mixed-valence triferrocenophanium species with little modification.

Meanwhile, the intervalence optical transition for trimetallic ferrocenophanium monocation should give rise to two interleaved points. On the one hand, unlike the 'asymmetrical' non-cyclic triferrocenium studied in previous chapter (Chapter 4), the ground state and vibrationally excited state of the monocationic triferrocenophanium species are energetically equivalent oxidation state isomers due to the cyclic and symmetrical structure of the macromolecule. On the other hand, like the non-cyclic triferrocenium analogue, two equivalent IVCT transitions may occur in the photo-induced electron transfer process, which will lead to the IVCT intensity enhancement due to the additive effect.

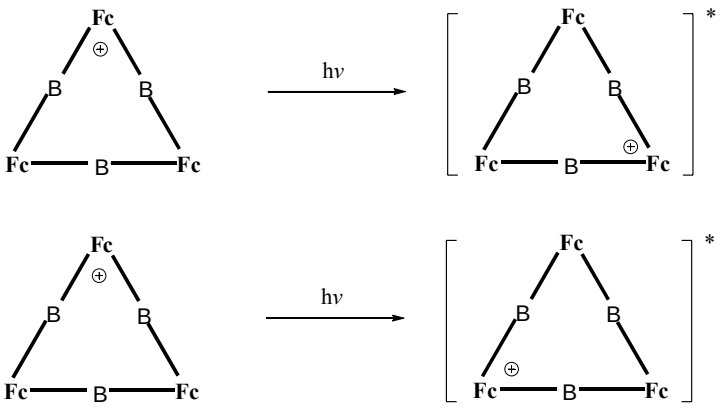

The one-electron oxidized mixed-valence spectra of furanoferrocenophanium $\mathbf{11}^{+}$ and thiophenoferrocenophanium $\mathbf{13}^{+}$ and the corresponding deconvoluted spectra are shown in Figure 5.18. Both the cyclic triferrocenophanium ions exhibit red-shifted IVCT bands in comparison with their singly-bridged diferrocenium anologues, due to the same

reason proposed for the doubly-bridged diferrocenophanium ion (shown schematically in Figure 5.15 B & B'). The highly increased intensity of the IVCT band in $\mathbf{11}^+$ is ascribed to both the additive effect of the duel transitions and the internal electronic configuration change of the relevant interacting orbitals. The IVCT band of $\mathbf{13}^+$, however, demonstrates limited intensity enhancement compared to that of $\mathbf{11}^+$. The possible reason for this observation is ascribed to the poorer solubility of the thiophenoferrocenophanium species, which results in an underestimated molar extinction coefficient. Finally, both trinuclear ferrocenophaniums revealed a strong IC band in the into-IR area, which is commonly observed for the ferrocenium moiety disubstituted by electron-rich groups.

So far, the binuclear and trinuclear ferrocenophanes discussed above are partially delocalized systems, in which the bridging fragment is basically an electronic interaction mediator but not a redox-participant, and the IVCT bands from different iron donors do not interfere each other to give a new type of absorption. When it comes to the pyrrolene-mediated trimetallic ferrocenophanium $\mathbf{15}^+$, the situation is quite different. As shown in Figure 5.19A, the low-energy envelope of $\mathbf{15}^+$ is bathochromically shifted more than 200 nm in comparison with that of the singly-bridged diferrocenium analogue. The band shape is indeed highly skewed. Although spectral deconvolution gives two fully overlapped gaussians, centered at 4600 and 4420 cm^{-1}, respectively, fitting pretty well to the original low-energy envelope (Figure 5.19B), the reliability of such fitting is not unquestionable to lead to unambiguous scientific interpretations. However, the band-width and position of the 4420 cm^{-1} band suggests a likely IC transition. Qualitatively, the low energy absorption of $\mathbf{15}^+$ could derive from both the LMCT and IVCT transitions. The energy band between the HOMO of bridging ligand and Fe^{III} dπ orbital in $\mathbf{15}^+$ is certainly lowered to minimum since the energy of iron dπ orbital is further decreased in $\mathbf{15}^+$ due to the additional electron-rich substituent. As we have extensively discussed in the previous chapters, the energy level of 2,5-divinyl-substituted pyrrolene ligand is very close to that of the corresponding connected ferrocene. Further lowering the energy level of the Fe^{III} orbital in $\mathbf{15}^+$ is very likely to give rise to a highly delocalized system due to the greatly mixed ligand and metal orbitals. In addition, the conventional IVCT and LMCT transitions in the cyclic macromolecule may heavily interact with each other to result in new type of transition in the category of delocalized system.

Finally, although the electronic coupling in binuclear and trinuclear ferrocenophanes is implicitly increased, the V and α values (Table 5.2) suggests that this family of ferrocenophanes belongs to Robin-Day class II systems in which the degree of delocalization is still limited.

Conclusion

Our initial intention in preparing a series of novel doubly-bridged diferrocenes via Wittig-related or base-promoted condensation reactions turned out to be successful when the linking units were linear hydrocarbon chains. The relatively higher flexibility of the conjugated backbone in these systems accounted for the achievement of the ring-closure process in completing the second bridge, which afforded the final product. When it came to the cases with the more rigid arylene nucleus incorporated as the central unit of the bridging fragment, the trimetallic ferrocenophanes were instead observed as the major ring-closure adducts. Apparently, this is due to the increased rigidity of the linking frameworks which requires extra space to allow the statistic ring-forming process. In all cases, polymerization accompanied as the major competing process, which resulted in low yielding for the desired ferrocenophanes. Therefore, it is strongly recommended to use the combination of strong base and low temperature to improve the yields.

Electrochemical studies of the doubly-bridged diferrocenes reveal greatly enhanced electronic interaction, as evidenced by the enlarged peak-separations (ΔEs). The enhancement in ΔE ranges from 50-90% greater for the doubly-bridged systems than their singly-bridged analogues. Such increased electronic coupling clearly derives from the through-bond communication due to the structurally confined diferrocenophane framework. Preliminary results of the mixed-valence absorption are in good agreement with this conclusion as manifested by the greater V and α values for each bimetallic ferrocenophane containing the electron-sufficient bridging ligands. In the meantime, it also suggests that the increased electronic coupling between the metal centers arises not only from the additive effect due to the existence of the duel channels in supporting electronic communication, but also from the perturbation of the energy gap between the frontier ligand HOMO and the iron dπ orbital upon introduction of a second electron-rich

substituent on the ferrocene Cp ring. Similarly, such additive electronic interaction and orbital perturbation effect are extended to the trimetallic cycloferrocenophanes when the bridging ligand possesses less delocalized features. When the delocalization is strong as we have observed in the pyrrolene-incorporated trinuclear ferrocenophane, the redox-matching between the metal and ligand centers gives rise to rather dynamic redox processes, in which both superexchange and electron-hopping can co-exist in supporting electron transfers within the cyclic systems.

References

1. Barlow, S.; O'Hare, D. *Chem. Rev.* **1997,** 97, 637 -669.
2. Fraysse, S.; Londiet, C.; Launay, J.-P. *Tetrahedron Lett.* **1998,** 39, 7873-7876.
3. Schimanke, H.; Gleiter, R. *Organometallics* **1998,** 17, 275-277.
4. Lambert, C.; Nöll, G.; Schelter, J., *Nat. Mater.* **2002,** 1, 69-73.
5. Elliott, C. M.; Derr, D. L.; Ferrere, S.; Newton, M. D.; Liu, Y. P. *J. Am. Chem. Soc.* **1996,** 118, 5221-5228.
6. Sun, D. L.; Rosokha, S. V.; Lindeman, S. V.; Kochi, J. K. *J. Am. Chem. Soc.* **2003,** 125, 15950-15963.
7. Tolbert, L. M.; Zhao, X. *J. Am. Chem. Soc.* **1997,** 119, 2291.
8. Levanda, C.; Bechgaard, K.; Cowan, D. O. *J. Org. Chem.* **1976,** 41, 2700-2704.
9. Dinolfo, P. H.; Hupp, J. T. *J. Am. Chem. Soc.* **2004,** 126, 16814-16819.
10. Dinolfo, P. H.; Williams, M. E.; Stern, C. L.; Hupp, J. T. *J. Am. Chem. Soc.* **2004,** 126, 12990-13001.
11. Kasahara, A.; Izumi, T. *Chemistry Letters* **1978**, (1), 21-4.
12. Kramer, J. A.; Hendrickson, D. N. *Inorganic Chemistry* **1980,** 19, (11), 3330-7.
13. Izumi, T.; Shimizu, I.; Kasahara, A. *Kenkyu Hokoku - Asahi Garasu Kogyo Gijutsu Shoreikai* **1980,** 36, 331-48.
14. Fabian, K. H. H.; Lindner, H.-J.; Nimmerfroh, N.; Hafner, K. *Angew. Chem. Int. Ed.* **2001,** 40, (18), 3402-3405.
15. Heo, R. W.; Lee, T. R. *J. Organomet. Chem.* **1999,** 578, (1-2), 31-42.
16. Caballero, A.; Lloveras, V.; Tárraga, A.; Espinosa, A.; Velasco, M. D.; Vidal-Gancedo, J.; Rovira, C.; Wurst, K.; Molina, P.; Veciana, J. *Angew. Chem. Int. Ed.* **2005,** 44, 1977-1981.
17. Jiang, J.; Lai, Y.-H. *J. Am. Chem. Soc.* **2003,** 125, 14296-14297.
18. Ting, Y.; Lai, Y.-H. *J. Am. Chem. Soc.* **2004,** 126, 909-914.
19. Zechel, D. L.; Foucher, D. A.; Pudelski, J. K.; Yap, G. P. A.; Rheingold, A. L.; Manners, I. *J. Chem. Soc., Dalton Trans.: Inorg. Chem.* **1995**, (11), 1893-9.
20. Mizuta, T.; Imamura, Y.; Miyoshi, K.; Yorimitsu, H.; Oshima, K. *Organometallics* **2005,** 24, 990-996.

21. Li, G.; Song, Y.; Hou, H.; Linke Li, L.; Fan, Y.; Zhu, Y.; Meng, X.; Mi, L. *Inorg. Chem.* **2003,** 42, 913-920.

22. Togni, A.; Hayashi, T., Fc-release strain. *Ferrocenes: Homogeneous Catalysis-Organic Synthesis Materials-Science, VCH Publishers, New York, NY (USA)* **1995**.

CHAPTER 6

BIS(STYRYLPYRROLE)S LINKED BY –CH=CH-X-CH=CH- SPACERS: A CHARGE MOBILITY STUDY ON CONJUGATED ORGANIC OLIGOMERS

Introduction

Since the charge mobility in linked dimetallic complex relies heavily on the mixing of the frontier HOMO orbital of the bridging ligand and the metal dπ orbitals, the effectiveness of electronic coupling of the organic wire linked transition metal complexes are often governed by the redox-matching between the redox-active metal center and bridging organic component. For this reason, in our previous studies, most of the biferrocenyl compounds in the form of FcCH=CH-X-CH=CHFc are characterized as weakly-coupled systems and therefore classified into Robin-Day's class II or class I. To overcome such limitation caused by the metal-ligand orbital mixing problem, one of the most important strategies is to replace the metal probe with a redox-active organic component. Thus, organic mixed-valence (MV) compounds have recently attracted increasing attention. Many different redox centers have been investigated, including quinones and imides,[1] dioxaborines,[2] nitro groups,[3, 4] and perchlorotriphenylmethyl centers[5] in anionic organic MV systems, and hydrazines,[6] 1,4-dialkoxybenzenes,[7, 8] and various triarylamines[9, 10] in cationic systems. These purely organic compounds tend to exhibit stronger intersite coupling than their transition-metal-based analogues due to this obvious advantage. For some of the strongly coupled systems, their pronounced electronic features have provoked great interest in study of class II/III transitions. Moreover, another general interest in these organic materials stems from the fact that they provide insight into the behavior of optical and organic electronic materials. Some of the organic materials are therefore used as electron/hole transport components in optoelectronic devices such as photoconductors, photorefractive materials, or organic light-emitting devices.[11, 12]

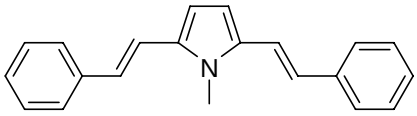

E^o = 0.08 V
vs. Fc/Fc^+

(E,E)-N-methyl-2,5-distyrylpyrrole

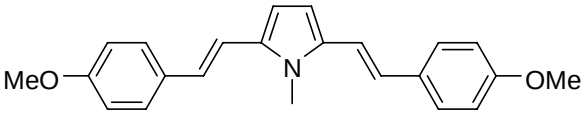

E^o = -0.07 V
vs. Fc/Fc^+

(E,E)-N-methyl-2,5-bis(4-methoxystyryl)pyrrole

Figure 6.1 Distyrylpyrrole compounds.

Previously, we have demonstrated that the oxidation potentials of two distyrylpyrrole derivatives (Figure 6.1) are very close to that of the unsubstituted ferrocene (Chapter 3). The redox processes are apparently pyrrole-based, due to the electron rich heteroaromatic ring. Based on this fact, we have examined a series of diferrocenyl and triferrocenyl complexes linked by a variety of pyrrolene-based spacers. All of them showed greatly enhanced electronic interactions due to the redox-matching between the redox-active metal centers and the bridging organic component. However, the electronic transition studies, especially the intervalence charge transfer (IVCT) absorptions, were often complicated by other coexisting optical processes such as ligand-to-metal charge transfer (LMCT) and Fe^{III} interconfigurational (IC) transition, which sometimes made the interpretation of the electronic behaviors very difficult. This, together with the intrinsic limitation of transition metal complexes stated earlier prompted us to seek a purely organic system to investigate the charge transfer abilities of certain bridging wires. Inspired by our previous research, 2,5-substituted *N*-methylpyrroles automatically emerged to surface as an ideal electron donor and acceptor moiety due to their synthetic convenience, low oxidation potential and reversibly oxidizable properties.

In this study, we report a series of –CH=CH-X-CH=CH- linked bis(styrylpyrrole) compounds. The chemical structures of the model compounds are shown in Figure 6.2. In this manner, we still keep our conventional –CH=CH-X-CH=CH- linkage, which allows

variation of the electronic property of the bridging component by varying the X functional group on the one hand, on the other hand, the terminal ferreocenes of the FcCH=CH-X-CH=CHFc compounds (Chapter 2) are replaced with two redox-active organic components, i.e. the styrylpyrroles, which have essentially the same oxidation potentials. According to the nature of the central X units, the electronic mediators can be divided into four categories: 1) heteroatom (S), 2) linear unsaturated double bond, 3) phenylic groups, which vary with *para*-, *ortho*-, and *meta*-phenyl rings, and 4) heteroarylic rings such as furan, thiophene and pyrrole. As can be seen, structurally, these symmetrical organic compounds can also be considered as vinylene spaced heterologue arylic oligomers. In addition, the end styryl groups are also configured with three different substituents, i.e. -OMe, -H, and -CN at the *para* position of the phenyl ring (**B** in Figure 6.2). The purpose of introducing a *para*-substituent on phenyl ring is two-fold: first, to stabilize the *para* phenyl proton which is suspected to be vulnerable for electrophilic attack, as recorded in literature;[13] second, to act as a tuning factor in alternating the photochemical, electrochemical and electronic transition properties of the oligomers.

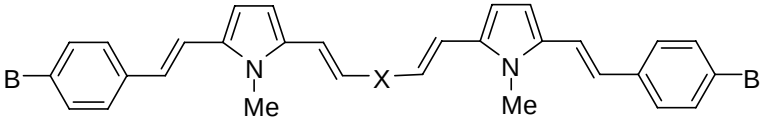

X	**B**= CN	H	OMe
S	**1a**	**1b**	**1c**
CH=CH	**2a**	**2b**	**2c**
p-$C_6H_2(OC_{12}H_{25})_2$	**3a**	**3b**	**3c**
C_4H_2S	**4a**	**4b**	**4c**
C_4H_2O	**5a**	**5b**	**5c**
C_4H_2NMe	**-**	**6b**	**-**
o-C_6H_4	**7a**	**7b**	**7c**
m-C_6H_4	**8a**	**-**	**--**

Figure 6.2 Chemical structures of a series of bis(styrylpyrrole)-based compounds.

Experimental

General Methods

General methods described in Chapter 2 were followed. All chemicals were purchased from Aldrich or Acros and used without further purification unless specified otherwise. All diphosphonates used for HWE condensation reactions were prepared according to the procedures depicted in previous chapters. Electrochemical studies were performed using 0.1 M Bu_4NTFPB as supporting medium in a CH_2Cl_2 solution. Oxidative UV-Vis-NIR absorptions were measured in CH_2Cl_2 solution, in the range of 0.5-2 x 10^{-4} M, using $Fc^+PF_6^-$ or magic blue as the oxidation agent.

Fluorescence studies were performed on a SPEX 386SX Fluor meter. Fluorescence quantum yields of the compounds were all determined in CH_2Cl_2, using Rhodamine 6G or Couramin 6 in aerated ethanol (EtOH) as the standard reference. Absolute quantum yields were subsequently calculated from the following equation:

$$\varphi = (F/F_{ref}) \times (A_{ref}/A) \times [n_D(CH_2Cl_2)/n_D(EtOH)]^2 \times \varphi_{ref} \qquad (6.1)$$

where φ_{ref} is the fluorescence quantum yield of the standard reference in EtOH, $n_D(CH_2Cl_2) = 1.4242$ and $n_D(EtOH) = 1.3594$ are the refractivity indices of EtOH and CH_2Cl_2, respectively, F and F_{ref} are the areas under the fluorescence spectra of the substrate (in CH_2Cl_2) and standard reference (in EtOH), and A_{ref} and A are the corresponding absorbance of the two molecules recorded at the excitation wavelength.

Column chromatography was performed on silica gel (40 mesh, 60Å, Fisher). Deactivated silica gel chromatography was achieved by washing the packed column with corresponding eluant containing 3% of triethylamine and then with pure eluent to remove the triethylamine.

Synthesis

General Procedure for *trans*-aryl-2-(*N*-methylpyrrol-2-yl)ethane.

To a stirred suspension of NaH (2.4 g, a 60% suspension in oil, 60 mmol, washed twice with dry hexane) in dry THF (100 mL) was added a solution of the appropriate diethyl benzylphosphonate (50 mmol) in THF (50 mL) dropwise under argon at r.t. The resulting suspension was stirred for 20 minutes before 1-methyl-2-pyrrolecarboxyaldehyde (5.45 g, 50 mmol) in THF (30 ml) was added slowly and the reaction mixture was heated to reflux for 4 h. The mixture was cooled and quenched with

water (20 ml). Volatile solvent was then removed under reduced pressure, the residues dissolved in CH_2Cl_2 (100 mL), washed with H_2O (3 x 100 mL) and dried over Na_2SO_4.The solvent was evaporated, the crude product was purified by flash column chromatography on silica gel eluting with CH_2Cl_2/hexane (1:1) to yield the targeted compound.

***trans*-2-(*p*-Cyanostyryl)-*N*-methylpyrrole (trans-(4-cyanophenyl)-2-(*N*-methylpyrrol-2-yl)ethene) (9a).** The general procedure above was used to prepare the title compound from diethyl 4-cyanobenzylphosphonate.Yellow solid, m.p. = 135 ^oC. 92% yield. ^1H NMR ($CDCl_3$): δ 7.57 (2H, d, J = 8.1 Hz, Ar), 7.48 (2H, d, J = 8.1 Hz, Ar), 7.05 (1H, d, J = 15.9 Hz, vinyl), 6.80 (1H, d, J = 15.9 Hz, vinyl), 6.69 (1H, dd, J = 2.7, 1.8 Hz, Pyr), 6.58 (1H, dd, J = 3.6, 1.8 Hz, Pyr), 6.18 (1H, dd, J = 3.6, 2.7 Hz, Pyr), 3.71 (3H, s, NCH_3). ^{13}C NMR ($CDCl_3$): δ 142.755, 132.67, 131.36, 126.37, 125.18, 123.50, 120.64, 119.53, 109.71, 109.08, 108.63, 34.46.

***trans*-2-Styryl-*N*-methylpyrrole (trans-phenyl-2-(*N*-methylpyrrol-2-yl)ethane) (9b).** The general procedure above was used to prepare the title compound from diethyl benzylphosphonate. Pale yellow solid, m.p. = 71 ^oC. 94% yield. ^1H NMR ($CDCl_3$): δ 7.47 (2H, d, J = 7.2 Hz, Ar), 7.36 (2H, t, J = 7.5 Hz, Ar), 7.25 (1H, t, J = 7.5 Hz, Ar), 6.98 (1H, d, J = 16.2 Hz, vinyl), 6.87 (1H, d, J = 16.2 Hz, vinyl), 6.66 (1H, dd, J = 2.7, 1.8 Hz, Pyr), 6.53 (1H, dd, J = 3.6, 1.8 Hz, Pyr), 6.19 (1H, dd, J = 3.6, 2.7 Hz, Pyr), 3.71 (3H, s, NCH_3). ^{13}C NMR ($CDCl_3$): δ 138.14, 132.24, 128.90, 127.23, 126.24, 126.21, 123.86, 117.35, 108.53, 106.96, 34.40.

***trans*-2-(*p*-Methoxystyryl) -*N*-methylpyrrole (trans-(4-methoxyphenyl)-2-(*N*-methylpyrrol-2-yl)ethane) (9c).** The general procedure above was used to prepare the title compound from diethyl 4-methoxybenzylphosphonate. Pale yellow solid, m.p. = 90-91 ^oC. 93.8% yield. ^1H NMR ($CDCl_3$): δ 7.38 (2H, d, J = 8.7 Hz, Ar), 6.87 (2H, d, J = 8.7 Hz, Ar), 6.83 (2H, s, vinyl), 6.62 (1H, dd, J = 2.7, 1.8 Hz, Pyr), 6.45 (1H, dd, J = 3.6, 1.8 Hz, Pyr), 6.15 (1H, dd, J = 3.6, 2.7 Hz, Pyr), 3.83 (3H, s, OCH_3), 3.71 (3H, s, NCH_3). ^{13}C NMR ($CDCl_3$): δ 159.09, 132.52, 130.94, 127.35, 126.03, 123.41, 115.42, 114.34, 108.35, 106.25, 108.63, 55.57, 34.35.

General Procedure for *trans*-2-styryl-*N*-methylpyrrole-5-carboxaldehyde.

The formylation of the 2-substituted-*N*-methylpyrrole derivatives were achieved by Vilsmeier reaction.[14] The Vilsmeier reagent was prepared by mixing dimethyl formamide (DMF) and phosphorus oxychloride at 0 ^{o}C. This was cannulated dropwise to an ice-cooled solution of the appropriate *N*-methylpyrrole in DMF (30 mL). After the addition, the reaction mixture was allowed to warm to r.t. and stirred for 4h. The resulting yellow/green solution was then quenched with water and subsequently treated with excess of 10% aqueous NaOH solution. The yellow suspension was extracted with CH_2Cl_2, and washed with more diluted NaOH, water and brine solution sequentially. The combined organic extracts were dried over $MgSO_4$ and evaporated to dryness to afford the crude product, which was purified by column chromatography on silica gel using CH_2Cl_2/hexane (1:1) as eluant.

***trans*-2-(*p*-Cyanostyryl)-*N*-methylpyrrole-5-carboxaldehyde (10a).** The general procedure above was used to synthesize the title compound from **9a**. Yellow solid, m.p. = 190 ^{o}C. 74% yield. ^{1}H NMR ($CDCl_3$): δ 9.54 (1H, s, CHO), 7.64 (2H, d, J = 8.1 Hz, Ar), 7.56 (2H, d, J = 8.1 Hz, Ar), 7.10 (2H, s, vinyl), 6.93 (1H, d, J = 4.5 Hz, Pyr), 6.62 (1H, d, J = 4.5 Hz, Pyr), 4.06 (3H, s, NCH_3). ^{13}C NMR ($CDCl_3$): δ 179.66, 141.15, 140.47, 133.33, 132.84, 130.72, 127.18, 124.94, 119.04, 118.73, 111.48, 109.10, 32.67.

***trans*-2-Styryl-*N*-methylpyrrole-5-carboxaldehyde (10b).** The general procedure above was used to synthesize the title compound from **9b**.Yellow solid, m.p. = 85 ^{o}C. 88% yield. ^{1}H NMR ($CDCl_3$): δ 9.48 (1H, s, CHO), 7.48 (2H, d, J = 7.2 Hz, Ar), 7.37 (2H, t, J = 7.5 Hz, Ar), 7.30 (1H, t, J = 7.5 Hz, Ar), 7.09 (1H, d, J = 16.2 Hz, vinyl), 6.94 (1H, d, J = 16.2 Hz, vinyl), 6.89 (1H, d, J = 4.5 Hz, Pyr), 6.55 (1H, d, J = 4.5 Hz, Pyr), 4.01 (3H, s, NCH_3). ^{13}C NMR ($CDCl_3$): δ 179.23, 141.80, 136.73, 133.31, 132.76, 129.10, 128.71, 126.89, 125.17, 115.22, 108.21, 32.67.

***trans*-2-(*p*-Methoxystyryl)-*N*-methylpyrrole-5-carboxaldehyde (10c).** The general procedure above was used to synthesize the title compound from **9c**. Yellow solid, m.p. = 100-101 ^{o}C . 60% yield. ^{1}H NMR ($CDCl_3$): δ 9.47 (1H, s, CHO), 7.43 (2H, d, J = 8.7 Hz, Ar), 7.05 (1H, d, J = 16.2 Hz, vinyl), 6.91 (2H, d, J = 8.7 Hz, Ar), 6.89 (1H, d, J = 5.2 Hz, Pyr), 6.81 (1H, d, J = 16.2 Hz, vinyl), 6.52 (1H, d, J = 5.2 Hz, Pyr), 4.03

(3H, s, OCH_3), 3.83 (3H, s, NCH_3). ^{13}C NMR ($CDCl_3$): δ 179.04, 160.20, 142.35, 133.09, 132.53, 129.53, 128.23, 125.32, 114.53, 113.03, 107.75, 55.59, 32.61.

General Procedure for Distyrylpyrrole Oligomers. The oligomers were synthesized via the traditional Horner-Emmons-Wittig reaction. To a stirred suspension of NaH (104 mg, a 60% suspension in oil, 2.6 mmol, washed with dry hexane) in dry THF (10 mL) was added a solution of the appropriate tetraethyl aryldiphosphonate (1.1 mmol) in THF (10 mL) dropwise under argon at r.t. The resulting suspension was stirred for 10 minutes before the corresponding aldehyde (2 mmol) in THF (20 mL) was added slowly and the reaction mixture was heated to reflux for 2-6 h. After cooling the colored mixture was quenched with water (2 mL). The volatile solvent was then removed under reduced pressure, the residues dissolved in CH_2Cl_2 (50 mL), washed with H_2O (3 x 30 mL), dried over $MgSO_4$ and evaporated to afford the crude product. Purification was generally achieved by recrystallization from MeOH if not other specified.

Bis[2-[5-(p-cyanostyryl)-N-methylpyrrol-2-yl]vinyl]sulfide (1a). Prepared from bis(diethylphosphonylmethyl)sulfide and **10a** as the general method above; reaction time 4h. The title compound was obtained as an orange red solid, m.p. 225-226 ^oC, 58% yield. ^1H NMR ($CDCl_3$): δ 7.57 (4H, d, J = 8.4 Hz, Ar-CN), 7.48 (4H, d, J = 8.4 Hz, Ar-CN), 7.04 (2H, d, J = 15.9 Hz, vinyl), 6.82 (2H, d, J = 15.9 Hz, vinyl), 6.64 (2H, d, J = 15.0 Hz, vinyl), 6.60 (2H, d, J = 15.0 Hz, vinyl), 6.59 (2H, d, J = 3.9 Hz, Pyr), 6.41 (2H, d, J = 3.9 Hz, Pyr), 3.64 (6H, s, NCH_3). ^{13}C NMR ($CDCl_3$): δ 142.51, 134.02, 132.70, 126.35, 124.13, 120.65, 120.20, 119.86, 119.46, 109.81, 109.26, 108.30, 30.94. IR (neat, cm^{-1}): 3012w, 2925w, 2213m, 1619m, 1591s, 1551m, 1441m, 1298m, 1170m, 1117w, 934m, 917m, 854m, 751m, 638, 543m. FABMS: *m/z* 498 [M^+].

Bis[2-(5-styryl-*N*-methylpyrrol-2-yl)vinyl]sulfide (1b). Prepared from bis(diethylphosphonylmethyl)sulfide and **10b** as the general method above; reaction time 4h. The title compound was obtained as a yellow solid, m.p. 165-166 ^oC, 56% yield. ^1H NMR ($CDCl_3$): δ 7.44 (4H, d, J = 7.5 Hz, Ar), 7.34 (4H, t, J = 7.5 Hz, Ar), 7.22 (2H, t, J = 7.2 Hz, Ar), 6.95 (2H, d, J = 16.2 Hz, vinyl), 6.86 (2H, d, J = 16.2 Hz, vinyl), 6.59 (2H, d, J = 15.0 Hz, vinyl), 6.54 (2H, d, J = 15.0 Hz, vinyl), 6.51 (2H, d, J = 4.2 Hz, Pyr), 6.40 (2H, d, J = 4.2 Hz, Pyr), 3.63 (6H, s, NCH_3). ^{13}C NMR ($CDCl_3$): δ 137.94, 133.67, 132.90, 128.93, 127.35, 126.97, 126.21, 120.36, 119.44, 117.02, 107.84, 107.65, 30.94.

IR (neat, cm^{-1}): 3022w, 1619m, 1593m, 1441m, 1381m, 1294m, 1235w, 1041w, 945s, 916s, 839m, 766s, 684s. 495m. FABMS: *m/z* 448 [M^+].

Bis[2-[5-(p-methoxystyryl)-*N*-methylpyrrol-2-yl]vinyl]sulfide (1c). Prepared from bis(diethylphosphonylmethyl)sulfide and **10c** as the general method above; reaction time 4h. The title compound was obtained as a yellow solid, m.p. 172 ^oC, 73% yield. ^1H NMR ($CDCl_3$): δ 7.37 (4H, d, J = 8.7 Hz, Ar-OMe), 6.87 (4H, d, J = 8.7 Hz, Ar-OMe), 6.84 (2H, d, J = 15.9 Hz, vinyl), 6.78 (2H, d, J = 15.9 Hz, vinyl), 6.58 (2H, d, J = 15.0 Hz, vinyl), 6.51 (2H, d, J = 15.0 Hz, vinyl), 6.45 (2H, d, J = 3.9 Hz, Pyr), 6.38 (2H, d, J = 3.9 Hz, Pyr), 3.84 (6H, s, OCH_3), 3.61 (6H, s, NCH_3). ^{13}C NMR ($CDCl_3$): δ 159.2, 134.01, 132.53, 130.78, 127.41, 126.80, 120.47, 119.04, 115.10, 114.39, 107.71, 107.01, 55.57, 30.91. IR (neat, cm^{-1}): 3023w, 2919w, 2835w, 1620m, 1601m, 1571m, 1443m, 1300m, 1245m, 1171m, 1107s, 948m, 916m, 810m, 765m, 615m. FABMS: *m/z* 508 [M^+].

1,6-Bis[5-(p-cyanostyryl)-*N*-methylpyrrol-2-yl]hexa-1,3,5-triene (2a). Prepared from tetraethyl (2*E*)-butene-1,4-diphosphonate and **10a** as the general method above; reaction time 4h. The title compound was obtained as a purple red solid, decomposed > 200 ^oC, 55% yield. ^1H NMR ($CDCl_3$): δ 7.57 (4H, d, J = 8.4 Hz, Ar-CN), 7.49 (4H, d, J = 8.4 Hz, Ar-CN), 7.10 (2H, d, J = 15.9 Hz, vinyl), 6.8 (2H, d, J = 15.9 Hz, vinyl), 6.65 (3H, m, vinyl), 6.55-6.45 (5H, m, pyrrole and vinyl), 6.31-6.17 (2H, m, vinyl), 3.66, 3.63 (6H, s, NMe). IR (neat, cm^{-1}): 2920m, 2851m, 2219m, 1615w, 1591s, 1442m, 1375m, 1232m, 1170m, 1107m, 1018s, 937s, 808m, 743m, 636m. FABMS: *m/z* 492 [M^+].

1,6-Bis(5-styryl-*N*-methylpyrrol-2-yl)hexa-1,3,5-triene (2b). Prepared from tetraethyl (2*E*)-butene-1,4-diphosphonate and **10b** as the general method above; reaction time 6h. The title compound was obtained as a deep red solid, m.p. 263-265 ^oC, 52% yield. ^1H NMR ($CDCl_3$): δ 7.44 (4H, d, J = 7.5 Hz, Ar), 7.33 (4H, t, J = 7.5 Hz, Ar), 7.12 (2H, t, J = 7.2 Hz, Ar), 7.03-6.86 (6H, m, vinyl), 6.78-6.65 (1H, m, vinyl), 6.59-6.45 (5H, m, Pyr and vinyl), 6.3-6.17 (2H, m, vinyl-center), 3.69-3.61 (6H, multiple singlets, NCH_3). IR (neat, cm^{-1}): 3019m, 1611m, 1586m, 1530m, 1443m, 1405m, 1316m, 1243m, 1112m, 1036m, 986s, 942s, 849m, 754s, 682s, 640m. FABMS: *m/z* 442 [M^+].

1,6-Bis[5-(*p*-methoxystyryl)-*N*-methylpyrrol-2-yl]hexa-1,3,5-triene, MeO-6-OMe. Prepared from tetraethyl (2*E*)-butene-1,4-diphosphonate and **10c** as the general method above; reaction time 6h. The title compound was obtained as a purple red solid, decomposed > 190 ^{o}C, 48% yield. IR (neat, cm^{-1}): 3013w, 2943w, 2834w, 1600s, 1571m, 1506s, 1440m, 1402m, 1300m, 1244m, 1132m, 1027m, 981m, 943m, 846m, 759m, 635m. FABMS: *m/z* 502 [M^{+}].

1,4-Bis[2-[5-(*p*-cyanostyryl)-*N*-methylpyrrol-2-yl]vinyl]-2,5-dodecyloxybenzene (3a). Prepared from 2,5-bis(diethylphosphonylmethylene)-1,4-didodecoxybenzene and **10a** as the general method above; the resulting red reaction mixture was heated at reflux for 2h. The crude product was suspended in MeOH (20 mL), sonicated for 15 min and filtered to yield a deep red solid, m.p.130 ^{o}C, 91% yield.. ^{1}H NMR ($CDCl_3$): δ 7.57 (4H, d, J = 8.4 Hz, Ar-CN), 7.48 (4H, d, J = 8.4 Hz, Ar-CN), 7.19 (2H, d, J = 16.2 Hz, vinyl), 7.10 (2H, d, J = 16.2 Hz, vinyl), 7.09 (2H, d, J = 15.9 Hz, vinyl), 6.98 (2H, s, Ar-center), 6.83 (2H, d, J = 15.9 Hz, vinyl), 6.66 (2H, d, J = 3.9 Hz, Pyr), 6.59 (2H, d, J = 3.9 Hz, Pyr), 4.04 (4H, t, J = 6.6 Hz, CH_2O-dodecyl), 3.73 (6H, s, NCH_3), 1.89-1.27 (40H, m), 0.87 (6H, t, J = 6.9 Hz). ^{13}C NMR ($CDCl_3$): δ 151.33, 142.71, 136.24, 132.97, 132.68, 126.75, 126.27, 123.53, 120.32, 119.54, 117.31, 111.15, 109.57, 108.43, 69.68, 32.16, 30.89, 29.94, 29.61, 26.57, 22.93, 14.37. IR (neat, cm^{-1}): 2916m, 2847m, 2216m, 1615m, 1589s, 1551m, 1504m, 1413w, 1345m, 1228m, 1171m, 1043w, 953m, 937m, 855m, 757m, 721m, 636m. FABMS: *m/z* 910 [M^{+}].

1,4-Bis[2-(5-styryl-*N*-methylpyrrol-2-yl)vinyl]-2,5-dodecyloxybenzene (3b). Prepared from 2,5-bis(diethylphosphinylmethylene)-1,4-didodecoxybenzene and **10b** as the general method above; the resulting pink red reaction mixture was heated at reflux for 2h. The crude product was suspended in MeOH (20 mL), sonicated for 15 min and filtered to yield a pink red powder, m.p. 125-126 ^{o}C, 84% yield. ^{1}H NMR ($CDCl_3$): δ 7.46 (4H, d, J = 7.2 Hz, Ar), 7.34 (4H, t, J = 7.5 Hz, Ar), 7.22 (2H, t, J = 7.5 Hz, Ar), 7.17 (2H, d, J = 16.2 Hz, vinyl), 7.09 (2H, d, J = 16.2 Hz, vinyl), 7.0 (2H, d, J = 15.9 Hz, vinyl), 6.99 (2H, s, Ar-center), 6.88 (2H, d, J = 15.9 Hz, vinyl), 6.58 (4H, s, Pyr), 4.04 (4H, t, J = 6.3 Hz, CH_2O-dodecyl), 3.72 (6H, s, NCH_3), 1.89-1.27 (40H, m), 0.88 (6H, t, J = 6.9 Hz). ^{13}C NMR ($CDCl_3$): δ 151.26, 138.11, 134.99, 133.87, 128.91, 127.20, 126.80, 126.46, 126.16, 122.22, 117.55, 117.18, 111.10, 108.06, 69.73, 32.17, 30.91, 29.95,

29.62, 26.58, 22.94, 14.38. IR (neat, cm^{-1}): 2917m, 2848m, 1618m, 1594m, 1503m, 1466m, 1345m, 1228s, 1197m, 1122w, 1036m, 941s, 865m, 759s. FABMS: *m/z* 860 [M^+].

1,4-Bis[2-[5-(p-methoxystyryl)-*N*-methylpyrrol-2-yl]vinyl]-2,5-dodecyloxybenzene (3c). Prepared from 2,5-bis(diethylphosphinylmethylene)-1,4-didodecoxybenzene and **10c** as the general method above; the resulting pink red reaction mixture was heated at reflux for 2h. The crude product was suspended in MeOH (20 mL), sonicated for 15 min and filtered to yield a bright red powder, m.p. 124-125 ^oC, 83% yield. ^1H NMR ($CDCl_3$): δ 7.40 (4H, d, J = 9 Hz, Ar-OMe), 7.15 (2H, d, J = 16.2 Hz, vinyl), 7.08 (2H, d, J = 16.2 Hz, vinyl), 6.99 (2H, s, Ar-center), 6.87 (4H, d, J = 9 Hz, Ar-OMe), 6.87 (2H, d, J = 15.9 Hz, vinyl), 6.81 (2H, d, J = 15.9 Hz, vinyl), 6.55 (2H, d, J = 3.9 Hz, Pyr), 6.51 (2H, d, J = 3.9 Hz, Pyr), 4.05 (4H, t, J = 6.3 Hz, CH_2O-dodecyl), 3.83 (6H, s, OCH_3), 3.70 (6H, s, NCH_3), 1.86-1.27 (40H, m), 0.88 (6H, t, J = 6.9 Hz). ^{13}C NMR ($CDCl_3$): δ 159.13, 151.24, 134.62, 134.23, 130.97, 127.37, 126.79, 126.30, 121.83, 117.60, 115.30, 114.40, 111.04, 107.84, 107.45, 69.73, 55.56, 32.20(NCH_3), 30.88, 29.98, 29.64, 26.60, 22.96, 14.40. IR (neat, cm^{-1}): 2918m, 2848m, 1606m,1572m, 1506s, 1464m, 1299m, 1246s, 1171m, 1033m, 946s, 865w, 799m, 761m, 642w. FABMS: *m/z* 920 [M^+].

2,5-Bis[2-[5-(p-cyanostyryl)-*N*-methylpyrrol-2-yl]vinyl]thiophene (4a). Prepared from 2,5-bis(diethylphosphonylmethyl)thiophene and **10a** as the general method above; reaction time 2h. The title compound was obtained as a black solid, m.p. 234-235 ^oC, 85.7% yield. ^1H NMR ($CDCl_3$): δ 7.58 (4H, d, J = 8.4 Hz, Ar-CN), 7.49 (4H, d, J = 8.4 Hz, Ar-CN), 7.07 (2H, d, J = 16.2 Hz, vinyl), 6.98 (2H, d, J = 16.2 Hz, vinyl), 6.88 (2H, s, thiophene), 6.77 (2H, d, J = 15.9 Hz, vinyl), 6.72 (2H, d, J = 15.9 Hz, vinyl), 6.65 (2H, d, J = 3.9 Hz, Pyr), 6.57 (2H, d, J = 3.9 Hz, Pyr), 3.72 (6H, s, NCH_3). ^1H NMR (tetrahydrofuran-d_8): δ 7.62 (8H, s, Ar-CN), 7.32 (2H, d, J = 15.9 Hz, vinyl), 7.04 (2H, d, J = 15.6 Hz, vinyl), 6.92 (2H, d, J = 15.9 Hz, vinyl), 6.90 (2H, s, thiophene), 6.82 (2H, d, J = 15.6 Hz, vinyl), 6.65 (2H, d, J = 4.2 Hz, Pyr), 6.57 (2H, d, J = 4.2 Hz, Pyr), 3.75 (6H, s, NCH_3). ^{13}C NMR (tetrahydrofuran-d_8): δ 142.93, 142.04, 134.72, 133.56, 132.22, 126.68, 126.23, 123.26, 120.42, 119.98, 118.68, 116.12, 109.71, 109.44, 108.39, 29.71.

IR (neat, cm^{-1}): 3040w, 2216m, 1614m, 1588s, 1550m, 1440m, 1387m, 1265m, 1170m, 1041m, 920m, 854m, 810m, 763m, 545m. FABMS: *m/z* 548 [M^+].

2,5-Bis[2-(5-styryl-*N*-methylpyrrol-2-yl)vinyl]thiophene (4b). Prepared from 2,5-bis(diethylphosphonylmethyl)thiophene and **10b** as the general method above; reaction time 2h. The title compound was obtained as a red solid, m.p. 230-231 ^oC, 72% yield. ^1H NMR ($CDCl_3$): δ 7.45 (4H, d, J = 7.5 Hz, Ar), 7.34 (4H, t, J = 7.5 Hz, Ar), 7.22 (2H, t, J = 7.5 Hz, Ar), 6.98 (2H, d, J = 16.2 Hz, vinyl), 6.94 (2H, d, J = 16.2 Hz, vinyl), 6.85 (2H, s, thiophene), 6.80 (2H, d, J = 15.9 Hz, vinyl), 6.72 (2H, d, J = 15.9 Hz, vinyl), 6.6-6.5 (4H, m, Pyr), 3.71 (6H, s, NCH_3). ^1H NMR (tetrahydrofuran-d_8): δ 7.47 (4H, d, J = 7.2 Hz, Ar), 7.28 (4H, t, J = 7.5 Hz, Ar), 7.16 (2H, t, J = 7.5 Hz, Ar), 7.10 (2H, d, J = 16.2 Hz, vinyl), 6.99 (2H, d, J = 15.9 Hz, vinyl), 6.88 (2H, d, J = 16.2 Hz, vinyl), 6.86 (2H, s, thiophene), 6.81 (2H, d, J = 15.9 Hz, vinyl), 6.54 (2H, d, J = 4.2 Hz, Pyr), 6.51 (2H, d, J = 4.2 Hz, Pyr), 3.73 (6H, s, NCH_3). ^{13}C NMR (tetrahydrofuran-d_8): δ 141.94, 138.42, 134.17, 13.53, 128.51(p), 126.68, 126.23, 125.92 (p), 119.04, 117.10, 116.31, 107.93 (multi), 29.71. IR (neat, cm^{-1}): 3032w, 1614m, 1592m, 1531m, 1443m, 1386m, 1266m, 1235m, 1043m, 932s, 765s, 741s, 683s, 535m. FABMS: *m/z* 498 [M^+].

2,5-Bis[2-[5-(p-methoxystyryl)-*N*-methylpyrrol-2-yl]vinyl]thiophene (4c). Prepared from 2,5-bis(diethylphosphonylmethyl)thiophene and **10c** as the general method above; reaction time 2h. The title compound was obtained as a red solid, m.p. 226-228 ^oC, 53% yield. ^1H NMR (tetrahydrofuran-d_8): δ 7.41 (4H, d, J = 8.7 Hz, Ar), 6.98 (2H, d, J = 16.2 Hz, vinyl), 6.91 (2H, d, J = 15.9 Hz, vinyl), 6.87 (2H, s, thiophene), 6.84 (4H, d, J = 8.7 Hz, Ar), 6.80 (2H, d, J = 16.2 Hz, vinyl), 6.74 (2H, d, J = 15.9 Hz, vinyl), 6.52-6.45 (4H, m, Pyr), 3.77 (6H, s, OCH_3), 3.71 (6H, s, NCH_3). ^{13}C NMR (tetrahydrofuran-d_8): δ 158.85, 145.77, 134.58, 133.06, 132.80, 131.03, 127.07, 126.04, 120.59, 118.57, 116.79, 114.94, 113.99, 108.10, 107.24, 54.63, 29.69. IR (neat, cm^{-1}): 3018w, 2834w, 1618m, 1598m, 1517m, 1506s, 1439m, 1386m, 1301m, 1246s, 1172m, 1109w, 1026m, 920s, 845m, 755s, 643m. FABMS: *m/z* 558 [M^+].

2,5-Bis[2-[5-(*p*-cyanostyryl)-*N*-methylpyrrol-2-yl]vinyl]furan (5a). Prepared from 2,5-bis(diethylphosphonylmethyl)furan and **10a** as the general method above; reaction time 2h. The title compound was obtained as a black solid, m.p. 235 ^oC, 80.4% yield. ^1H NMR ($CDCl_3$): δ 7.58 (4H, d, J = 8.4 Hz, Ar-CN), 7.49 (4H, d, J = 8.4 Hz, Ar-

CN), 7.08 (2H, d, J = 16.2 Hz, vinyl), 6.94 (2H, d, J = 16.2 Hz, vinyl), 6.72 (2H, d, J = 15.9 Hz, vinyl), 6.66 (2H, d, J = 15.9 Hz, vinyl), 6.64 (2H, d, J = 3.9 Hz, Pyr), 6.56 (2H, d, J = 3.9 Hz, Pyr), 6.34 (2H, s, furan), 3.75 (6H, s, NCH_3). ^{1}H NMR (tetrahydrofuran-d_8): δ 7.62 (8H, s, Ar-CN), 7.32 (2H, d, J = 15.9 Hz, vinyl), 7.03 (2H, d, J = 15.9 Hz, vinyl), 6.91 (2H, d, J = 15.9 Hz, vinyl), 6.72 (2H, d, J = 15.9 Hz, vinyl), 6.66 (2H, d, J = 3.9 Hz, Pyr), 6.56 (2H, d, J = 3.9 Hz, Pyr), 6.39 (2H, s, furan), 3.78 (6H, s, NCH_3). ^{13}C NMR (tetrahydrofuran-d_8): δ 153.63, 142.95, 135.03, 133.63, 132.32, 126.22, 123.15, 120.43, 118.70, 114.83, 114.06, 110.76, 109.68, 109.46, 108.31, 29.76. IR (neat, cm^{-1}): 3037w, 2929w, 2215m, 1616m, 1549s, 1525m, 1431m, 1349m, 1265m, 1169m, 1112w, 929m, 849m, 762m, 554m. FABMS: *m/z* 532 [M^+].

2,5-Bis[2-(5-styryl-*N*-methylpyrrol-2-yl)vinyl]furan (5b). Prepared from 2,5-bis(diethylphosphonylmethyl)furan and **10b** as the general method above; reaction time 2h. The title compound was obtained as a red solid, m.p. 233-235 ^{o}C, 72% yield. ^{1}H NMR ($CDCl_3$): δ 7.45 (4H, d, J = 7.2 Hz, Ar), 7.34 (4H, t, J = 7.5 Hz, Ar), 7.22 (2H, t, J = 7.5 Hz, Ar), 6.99 (2H, d, J = 16.2 Hz, vinyl), 6.92 (2H, d, J = 16.2 Hz, vinyl), 6.69 (2H, d, J = 15.9 Hz, vinyl), 6.63 (2H, d, J = 15.9 Hz, vinyl), 6.58-6.5 (4H, m, Pyr), 6.32 (2H, s, furan), 3.74 (6H, s, NCH_3). ^{13}C NMR ($CDCl_3$): δ 153.37, 138.02, 133.99, 132.24, 128.92, 127.29, 126.87, 126.19, 117.05, 115.00, 110.82, 108.19, 30.94. ^{1}H NMR (tetrahydrofuran-d_8): δ 7.47 (4H, d, J = 7.5 Hz, Ar), 7.28 (4H, t, J = 7.5 Hz, Ar), 7.16 (2H, t, J = 7.5 Hz, Ar), 7.12 (2H, d, J = 15.9 Hz, vinyl), 7.02 (2H, d, J = 15.9 Hz, vinyl), 6.88 (2H, d, J = 15.9 Hz, vinyl), 6.67 (2H, d, J = 15.9 Hz, vinyl), 6.54 (2H, d, J = 3.9 Hz, Pyr), 6.51 (2H, d, J = 3.9 Hz, Pyr), 6.34 (2H, s, furan), 3.76 (6H, s, NCH_3). ^{13}C NMR (tetrahydrofuran-d_8): δ 153.59, 138.44, 134.23, 133.85, 128.51, 126.67, 125.92, 125.76, 117.13, 115.03, 113.16, 110.17, 107.93, 107.84, 29.75. IR (neat, cm^{-1}): 3020w, 1615m, 1592m, 1558w, 1493m, 1385m, 1233m, 1120w, 1013m, 945s, 761s, 689s, 543m. FABMS: *m/z* 482 [M^+].

2,5-Bis[2-[5-(*p*-methoxystyryl)-*N*-methylpyrrol-2-yl]vinyl]furan (5c). Prepared from 2,5-bis(diethylphosphonylmethyl)furan and **10c** as the general method above; reaction time 2h. The title compound was obtained as a red solid, decomposed > 190 ^{o}C, 65% yield. ^{1}H NMR (tetrahydrofuran-d_8): δ 7.40 (4H, d, J = 8.7 Hz, Ar), 7.00 (2H, d, J = 16.2 Hz, vinyl), 6.97 (2H, d, J = 15.9 Hz, vinyl), 6.84 (4H, d, J = 8.7 Hz, Ar), 6.82 (2H, d,

J = 16.2 Hz, vinyl), 6.64 (2H, d, J = 15.9 Hz, vinyl), 6.48 (2H, d, J = 3.9 Hz, Pyr), 6.46 (2H, d, J = 3.9 Hz, Pyr), 6.32 (2H, s, furan), 3.77 (6H, s, OCH_3), 3.73 (6H, s, NCH_3). ^{13}C NMR (tetrahydrofuran-d_8): δ 159.30, 153.58, 134.61, 133.38, 131.05, 127.06, 125.79, 115.04, 113.99, 112.75, 109.94, 107.74, 107.24, 54.64, 29.87. IR (neat, cm^{-1}): 3030w, 2917w, 2827w, 1600m, 1571m, 1506s, 1448m, 1386m, 1242s, 1170m, 1024m, 928m, 845w, 757m, 642w. FABMS: *m/z* 542 [M^+].

1,2-Bis[2-[5-(*p*-cyanostyryl)-*N*-methylpyrrol-2-yl]vinyl]benzene (7a).

Prepared from 1,2-bis(diethylphosphonylmethyl)benzene and **10a** as the general method above; reaction time 4h. The title compound was obtained as an orange red solid, m.p. 174 °C, 54.4% yield. ^1H NMR ($CDCl_3$): δ 7.58 (4H, d, J = 8.4 Hz, Ar-CN), 7.54 (2H, dd, J = 2.7, 6.0 Hz, Ar-center), 7.49 (4H, d, J = 8.4 Hz, Ar-CN), 7.27 (2H, dd, J = 2.7, 6.0 Hz, Ar-center), 7.25 (2H, d, J = 15.6 Hz, vinyl), 7.09 (2H, d, J = 15.9 Hz, vinyl), 6.86 (2H, d, J = 15.6 Hz, vinyl), 6.84 (2H, d, J = 15.9 Hz, vinyl), 6.65 (2H, d, J = 3.9 Hz, Pyr), 6.59 (2H, J = 3.9 Hz, Pyr), 3.72 (6H, s, NCH_3). ^{13}C NMR ($CDCl_3$): δ 142.58, 135.10, 135.42, 133.15, 132.71, 127.79, 126.57, 126.35, 125.64, 124.03, 120.25, 119.49, 119.26, 109.77, 109.48, 108.47, 30.94. IR (neat, cm^{-1}): 3033w, 2917w, 2216m, 1615m, 1590s, 1551m, 1451m, 1353m, 1266m, 1171m, 1034w, 935s, 851m, 744s, 639m, 540m. FABMS: *m/z* 542 [M^+].

1,2-Bis[2-(5-styryl-*N*-methylpyrrol-2-yl)vinyl]benzene (7b). Prepared from 1,2-bis(diethylphosphonylmethyl)benzene and **10b** as the general method above; reaction time 4h. The title compound was obtained as a yellow solid, m.p. 183-184 °C, 52% yield. ^1H NMR ($CDCl_3$): δ 7.54 (2H, dd, J = 2.7, 6.0 Hz, Ar-center), 7.46 (4H, d, J = 7.5 Hz, Ar), 7.28-7.23 (6H, m, Ar-center and vinyl), 7.22 (2H, t, J = 7.5 Hz, Ar), 6.99 (2H, d, J = 15.9 Hz, vinyl), 6.89 (2H, d, J = 16.2 Hz, vinyl), 6.87 (2H, d, J = 15.9 Hz, vinyl), 6.58 (4H, s, Pyr), 3.71 (6H, s, NCH_3). ^{13}C NMR ($CDCl_3$): δ 138.01, 136.27, 134.24, 134.06, 128.92, 127.46, 127.30, 126.87, 126.49, 126.21, 124.64, 119.54, 117.08, 108.02, 107.91, 30.93. IR (neat, cm^{-1}): 3030w, 1613m, 1591m, 1460m, 1388m, 1237m, 1175m, 1047w, 944s, 746s, 694s, 618m. FABMS: *m/z* 492 [M^+].

1,2-Bis[2-[5-(*p*-methoxystyryl)-*N*-methylpyrrol-2-yl]vinyl]benzene (7c). Prepared from 1,2-bis(diethylphosphonylmethyl)benzene and **10c** as the general method above; reaction time 4h. The title compound was obtained as a yellow solid, m.p. 183-

184 ^{o}C, 52% yield. to afford a yellow solid, m.p. 200-201 ^{o}C, 48% yield. ^{1}H NMR ($CDCl_3$): δ 7.53 (2H, dd, J = 2.7, 6.0 Hz, Ar-center), 7.39 (4H, d, J = 8.7 Hz, Ar-OMe), 7.23 (2H, dd, J = 2.7, 6.0 Hz, Ar-center), 7.22 (2H, d, J = 15.9 Hz, vinyl), 6.91 (4H, d, J = 8.7 Hz, Ar-OMe), 6.87 (4H, s, vinyl), 6.86 (2H, d, J = 15.9 Hz, vinyl), 6.57 (2H, d, J = 3.9 Hz, Pyr), 6.51 (2H, J = 3.9 Hz, Pyr), 3.83 (6H, s, OCH_3), 3.69 (6H, s, NCH_3). ^{13}C NMR ($CDCl_3$): δ 159.18, 136.31, 134.41, 133.88, 130.86, 127.41, 126.70, 126.44, 124.27, 119.59, 115.19, 114.40, 107.93, 107.29, 55.58, 30.91. IR (neat, cm^{-1}): 3010w, 2937w, 2834w, 1599m, 1570m, 1507s, 1442m, 1299w, 1244s, 1172m, 1026m, 934m, 850m, 746m, 599m, 518m. FABMS: *m/z* 552 [M^+].

1,3-Bis[2-[5-(p-cyanostyryl)-*N*-methylpyrrol-2-yl]vinyl]benzene (8a). Prepared from 1,3-bis(diethylphosphonylmethyl)benzene and **10a** as the general method above; reaction time 4h. The title compound was obtained as an orange solid, m.p. 269-270 ^{o}C, 55% yield. ^{1}H NMR ($CDCl_3$): δ 7.58 (4H, d, J = 8.4 Hz, Ar-CN), 7.49 (4H, d, J = 8.4 Hz, Ar-CN), 7.37-7.33 (4H, m, Ar-center), 7.09 (2H, d, J = 16.2 Hz, vinyl), 7.01 (2H, d, J = 16.2 Hz, vinyl), 6.92 (2H, d, J = 15.9 Hz, vinyl), 6.84 (2H, d, J = 15.9 Hz, vinyl), 6.65 (2H, d, J = 3.9 Hz, Pyr), 6.59 (2H, J = 3.9 Hz, Pyr), 3.75 (6H, s, NCH_3). ^{13}C NMR ($CDCl_3$): δ 142.61, 138.20, 135.13, 133.13, 132.70, 127.62, 126.34, 124.98, 124.59, 123.95, 120.27, 119.50, 117.06, 109.74, 109.53, 108.50, 30.96. IR (neat, cm^{-1}): 3008w, 2216m, 1617m, 1589s, 1530m, 1488m, 1386m, 1297m, 1266m, 1171m, 1118m, 1033m, 940s, 857m, 769s, 684m. FABMS: *m/z* 542 [M^+].

Results and Discussion

Synthetic Procedures

The general synthetic route is shown in Figure 6.3. The 2-styryl-*N*-methylpyrroles **9a-c** were first prepared via a conventional Horner-Wadsworth-Emmons (HWE) condensation reaction of *N*-methylpyrrole-2-carboxaldehyde with the corresponding *p*-substituted phenylmethylphosphonates, which were either commercially accessible or conveniently synthesized from *p*-substituted benzylic bromides and triethylphosphine via a simple Arbuzov reaction as illustrated in Figure 6.3. This procedure benefited not only from high yields (> 90%) but also from exclusive *E* products, as evidenced by the vinylic

coupling constant (ca. 16 Hz) in ^{1}H NMR spectroscopy. The 2-styryl-*N*-methylpyrroles were then converted to the corresponding *N*-methylpyrrolecarboxaldehydes **10a-c** by a Vilsmeier reaction.[14] The formylations were completed in DMF at room temperature in the presence of $POCl_3$. However, unlike formylation of other arylic or heteroarylic analogues, the pyrrole derivatives were more acid-sensitive and therefore resulted in moderate yields (50-70%).

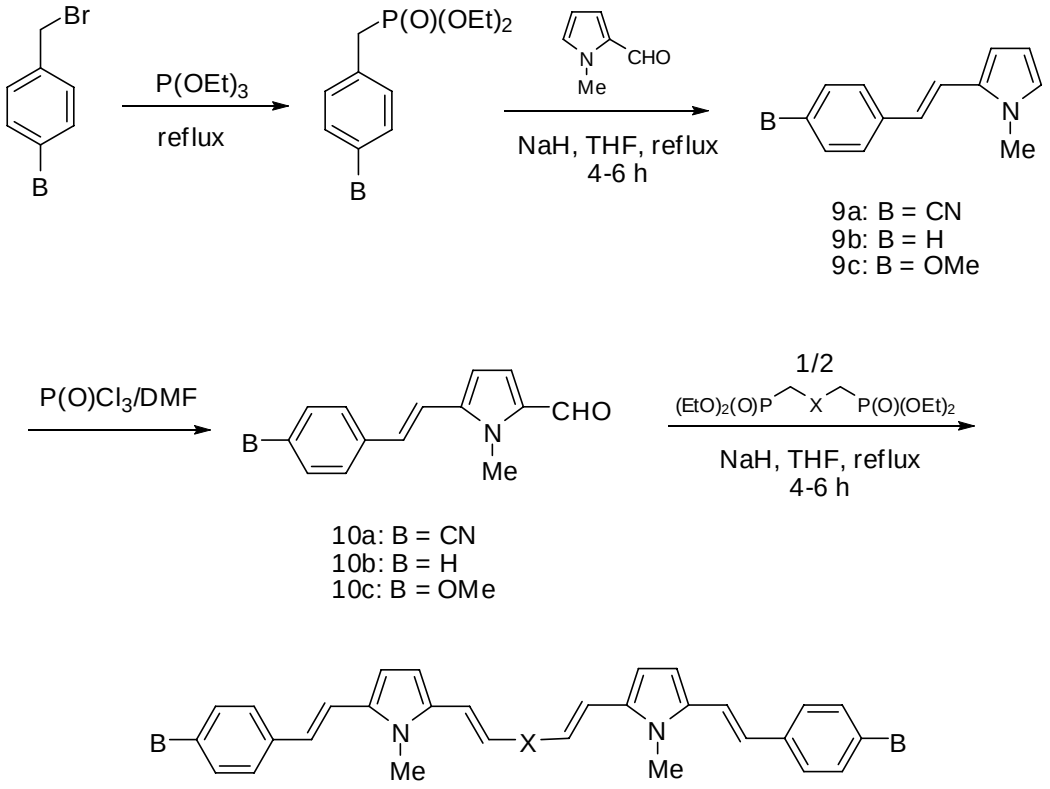

Figure 6.3 Synthetic route for the bis(styrylpyrrole)-based compounds.

Another HWE olefinic coupling between the diphosphonates containing an appropriate central X unit and two equivalents of the corresponding pyrrolecarboxaldehyde **10a-c** afforded the targeted oligomers. For most of the compounds, purification was accomplished by multiple recrystallization from MeOH or EtOH since the highly conjugated oligomers are insoluble or poorly soluble in protic polar solvents. When column chromatography was necessary, deactivated silica gel or basic alumina was always used as the absorbent because the pyrrole-based oligomers

were found to be acid sensitive. A trace amount of acid can trigger an oxidation on the pyrrole moieties, which often led to severe product loss during the purification procedures if the compounds were not carefully protected from contact with acidic reagent. The final yields therefore relied, in most of the cases, not on the reaction conversion (which is high for most of the compounds) but on the compound robustness during the purification process.

Both ^{1}H NMR and IR spectroscopy attested that the two vinyl bonds built in the final HWE step both adopted an *E* geometry when the central X group is an aromatic or heteroaromatic ring, giving rise to all *E* products. For sulfur centered derivatives **1a-c**, this stereoselectivity was also dominating. The only exceptions are **2a-c**, where the X group is a –C=C- double bond, which indicated a *cis/trans* mixture. The possible reason is attributed to the low thermal barrier required for the interexchange between the two intermediate oxaphosphatane forms due to the flexibility of the double bond..

Although we have also obtained the crude oligomers containing *p*-phenylene as the central unit with high conversions, all the three substances (B = -CN, -H and -OMe), unfortunately, are not soluble in any organic solvent, which made successive purification and characterization impossible. Therefore, it necessitates the introduction of the lateral alkoxy chains on the 2,5-positions of the *p*-phenylene ring to improve the solubility, which gave rise to compounds **3a-c**.

Physical Properties

All the pyrrole-based oligomers are powder solids with a color ranging from bright yellow to black. In general, a -CN substituted compound is darker than its –H and –OMe substituted analogues, and the colors of the –H and –OMe end-capped derivatives are basically the same. For instance, sulfur centered **1b** and **1c** are yellow, **1a** is orange red; thiophene centered **4b** and **4c** are red, **4a** is black. Moreover, the heteroaromatic ring centered (X = furan, thiophene, pyrrole) oligomers are deeper colored than the phenylenes and their heteroatom centered counterparts.

Although most of the organic oligomers herein are soluble in polar solvents such as THF, DMF and insoluble or poorly soluble in protic solvents such as MeOH, their solubility in other common organic solvents, CH_2Cl_2, $CHCl_3$ and acetone, varies. All

sulfur (**1a-c**), didodecyloxy substituted *para*-phenylene (**3a-c**) and *ortho*-phenylene (**7a-c**) centered compounds are very soluble in methylene chloride. The rest of the oligomers, however, only dissolve to limited extent in the same solvent. This is in line with the literature record for heteroaromatic oligomers. Related to that, we also tried to obtain the single crystals of these oligomers to allow an X-ray crystallographic study, however, most of the compounds were isolated from solution as amorphologic powders after slow solvent evaporation. The only promising compounds for this purpose were the long chain alkoxy substituted species **3a-c**, especially cyano-substituted **3a**, which afforded fiber-like needles upon recrystallizing from CH_2Cl_2/hexane (1:1) for long period of time. Unfortunately, the crystals were still too thin to be suitable for the X-ray analysis.

NMR Spectroscopy

For arylenevinylene oligomers, the steric regulation of the unsaturated double bonds had important consequences to their optical and electronic properties.[15, 16] One of our major concerns for current distyrylpyrrole-based oligomers was to construct chemically symmetrical structures. The key steps were to form the geometrically selective double bonds, preferentially in *E*-configuration, between the aromatic rings. This was successfully fulfilled though well-defined HWE olefinations as evidenced by the NMR spectroscopy.

The exemplifying ^{1}H NMR spectra of *p*-phenyl centered compound **3c** and furan derivative **5a** are shown in Figure 6.4 and Figure 6.5, respectively. For **5a** in THF-d_8, there are eight distinct peaks in the aromatic and vinylic region (ca. 7.5-6.3 ppm) with an integral ratio of 4:1:1:1:1:1:1:1, sequentially from low field to high field (see inset of Figure 6.5). The slightly broadened singlet at 7.4 ppm is assigned to the protons of the end-capping phenyl groups. The two types of phenylic protons (H_h and H_i in Figure 6.5) obviously merge at the same resonance position in THF-d_8. However, they appear as two discrete doublets in $CDCl_3$ (see details in the experimental section). The four well separated doublets appearing in the region of 7.12-6.66 ppm are derived from two pairs of vinylic protons belonging to two kinds of double bonds, in which one double bond bridges the phenylic and pyrrolic rings, and the other double bond links the pyrrolic ring and the central furan group. The coupling constants, 16.2 and 15.9 Hz,

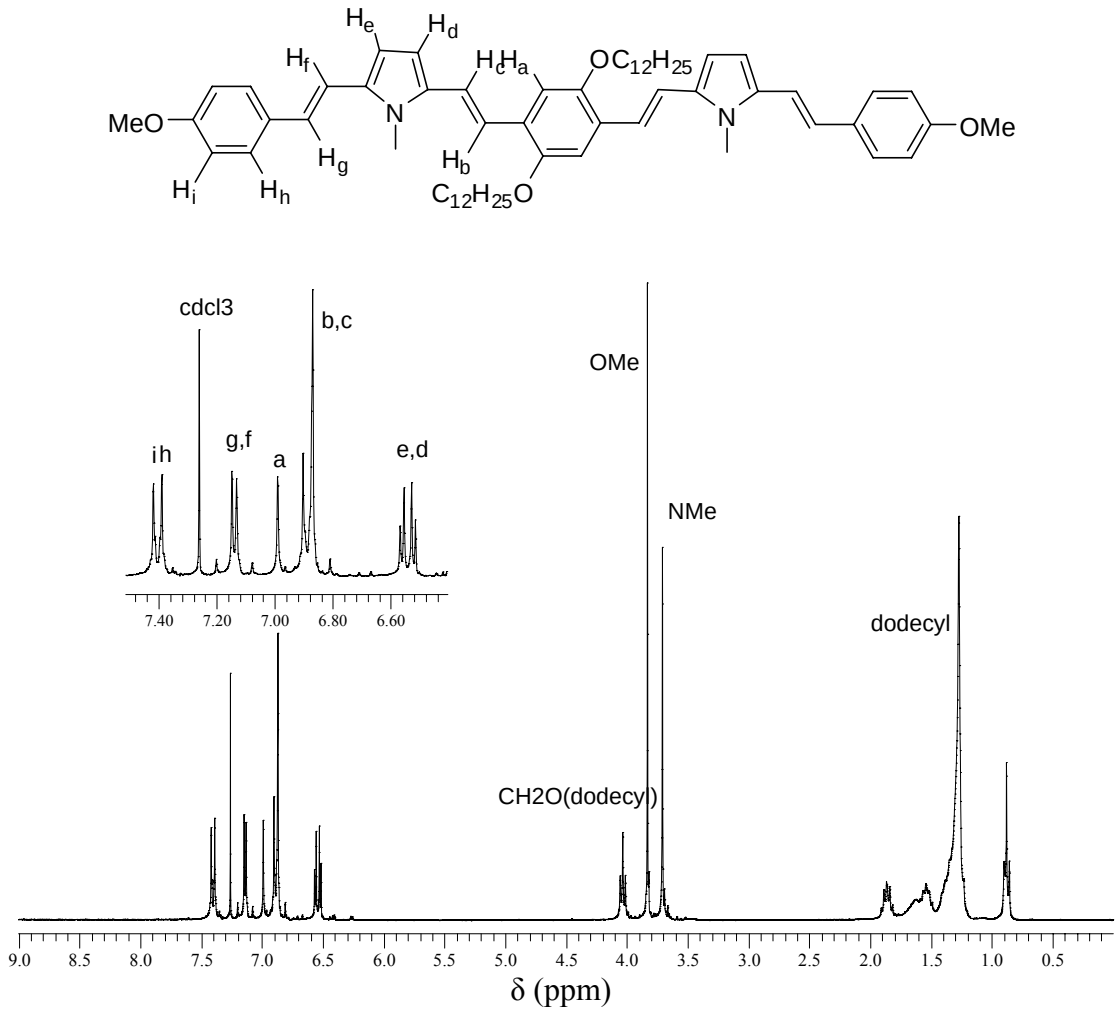

Figure 6.4 ^{1}H NMR spectrum of **3c** in $CDCl_3$.

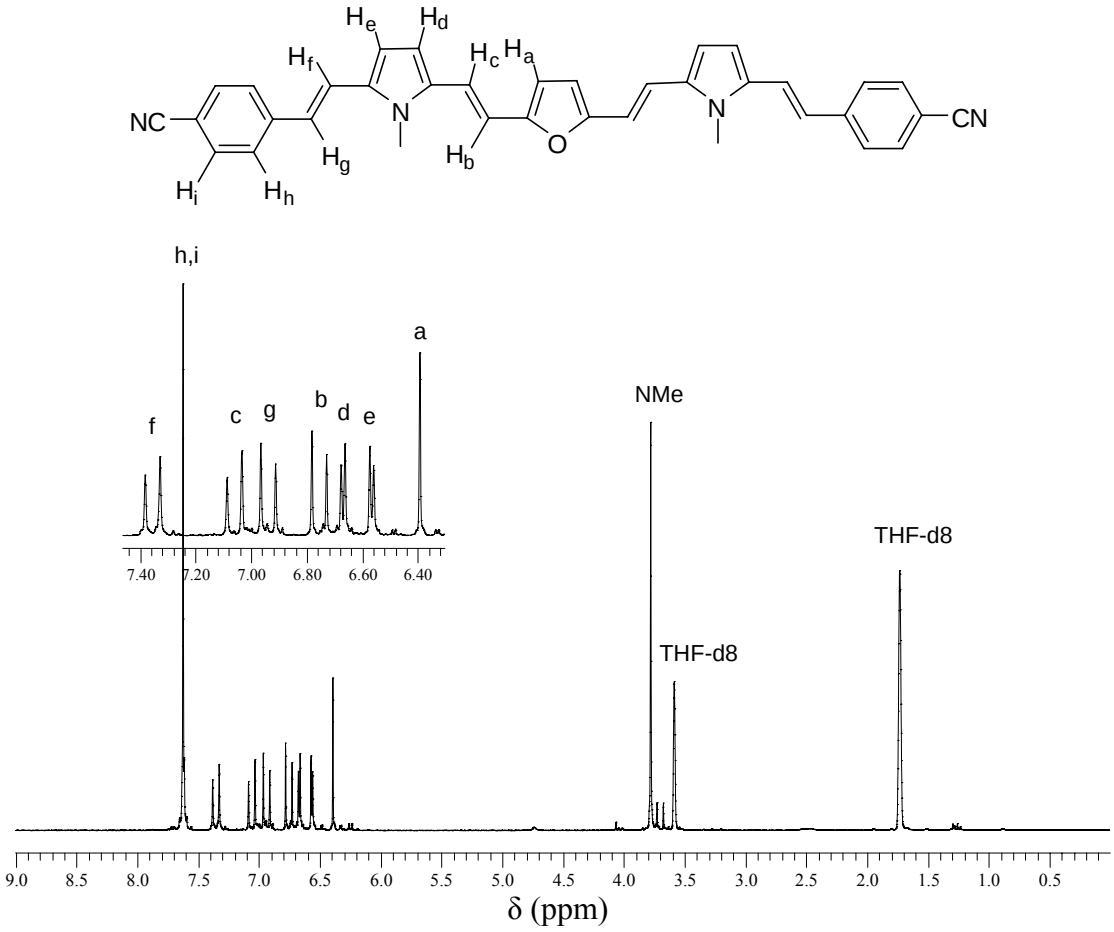

Figure 6.5 ^{1}H NMR spectrum of **5a** in THF-d_8.

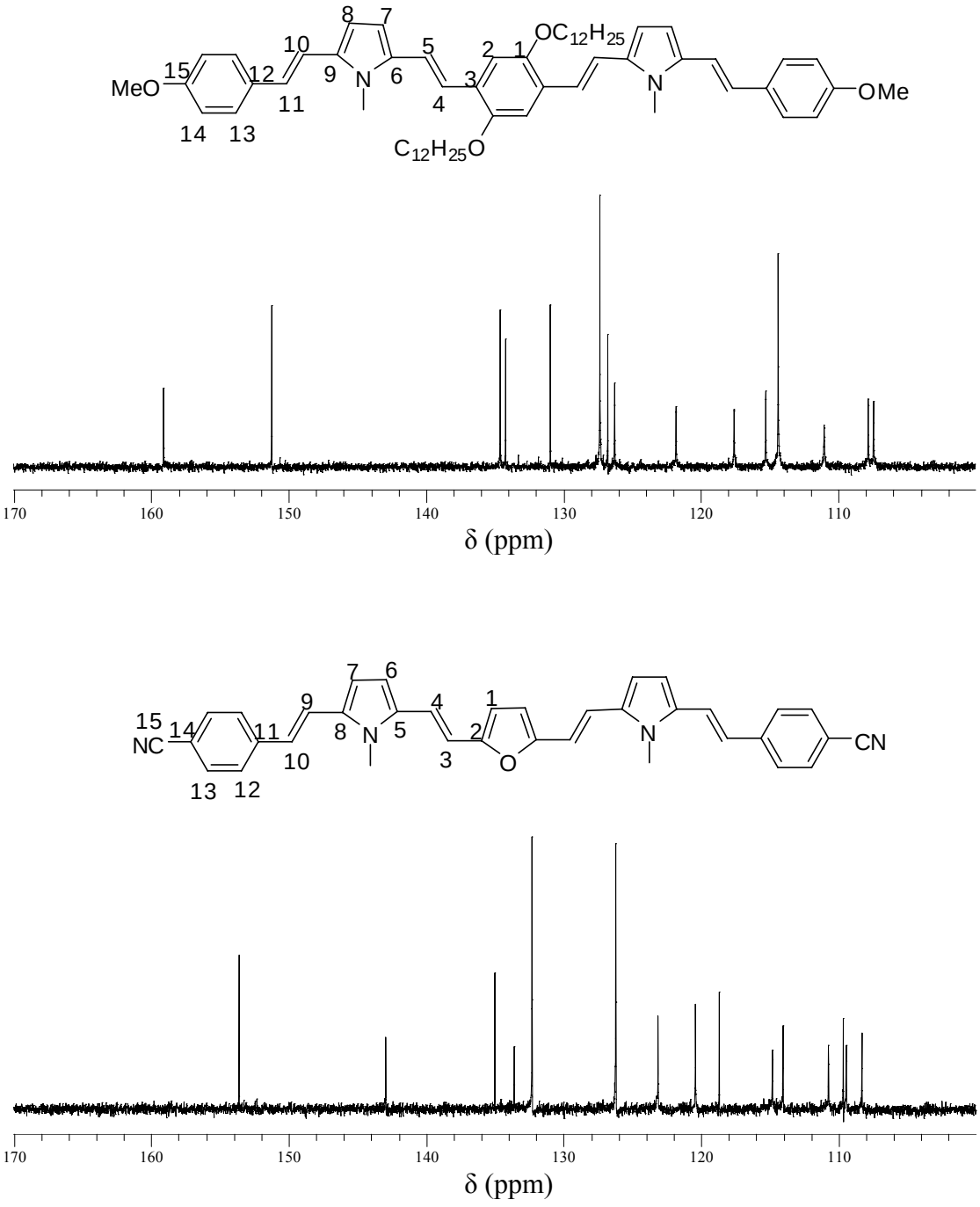

Figure 6.6 ^{13}C NMR spectra of **3c** (top) and **5a** (bottom) in the aromatic and vinylic region.

manifest that all vinyl bonds adopt a *trans* (*E*) configuration, which is also confirmed by the out-of-plane stretching mode at ca. 940 cm^{-1} in IR spectroscopy. Due to the unsymmetrical substitution at the 2,5- positions of the pyrrolene ring, two distinct pyrrolic protons appear at 6.5 and 6.4 ppm, respectively. Finally, the two furan protons exhibit a singlet peak at 6.35 ppm due to the chemical equivalency of the identical substituents at each side of this heteroaromatic ring.

^{13}C NMR spectra of **3c** and **5a** in the low field (100-170 ppm) are shown in Figure 6.6. For **5a**, there are fifteen peaks appearing in the aromatic and unsaturated bond region (ca. 155-105 ppm). The peak at 118.70 ppm is assigned to the cyano carbon. The rest of the signals originate from fourteen different unsaturated carbons along the conjugation backbone. Both ^{1}H and ^{13}C NMR spectra suggest that this oligomer possesses precisely-defined structure, which is highly symmetrical and regulated.

Last, as mentioned in the synthetic discussion, due to the poorly defined *cis, trans* geometry of the double bonds around the central vinyl unit, the ^{1}H NMR spectra of the linear polyene bridged oligomers, **2a**, **2b** and **2c**, show complicated signals in the vinylic region. The percentage of the *E,E*-isomer is estimated as approximately 70%. In contrast, the isomeric scenario is not observed for the sulfur centered series, even they both embrace a flexible X unit, i.e. double bond versus sulfur atom, in comparison with the relatively rigid aromatic X group for other oligomers. The possible reason for the enhanced stereoselectivity of divinyl sulfide **1a-c** has been discussed in previous chapters (see Chapter 2) and is ascribed to the stabilizing effect from the sulfur atom to the intermediate carbonanion and the consequent oxaphosphanate form in favor of formation of a *trans* double bond.

UV-Vis Absorption and Fluorescence

The optical parameters, including absorption maxima (λ_{max}), emission maxima (λ_{em}) and fluorescence quantum yields (φ), of the oligomers are listed in Table 6.1. The selected absorption and emission spectra are shown in Figure 6.7-6.9.

UV-Vis absorptions. The UV-Vis absorption maxima ($\lambda_{max)}$ of the mixed-aromatic oligomers fall in the region of 400-520 nm (Table 6.1) in CH_2Cl_2. The onset of

Table 6.1 UV-Vis absorption and fluorescence parameters for the oligomers.[a]

X	B = CN		H		MeO	
	Abs. (nm)	Em.(nm) (Q.Y.)[b]	Abs. (nm)	Em.(nm) (Q.Y.)[b]	Abs. (nm)	Em.(nm) (Q.Y.)[b]
S	436	562 (0.29)	407	496 (0.031)	407	492 (0.02)
CH=CH	497	636 (<0.01)	478	583/626 (<0.01)	478	584/620 (<0.01)
p-$C_6H_2(OC_{12}H_{25})_2$	494	591 (0.63)	473	553 (0.51)	475	567 (0.55)
C_4H_2S	513	604/640 (0.04)	498	576/602 (0.05)	499	588/617 (0.07)
C_4H_2O	422/507	640 (0.05)	388/484	567/603 (0.032)	390/489	567/602 (0.03)
C_4H_2NMe	-	-	465	573/596 (0.31)	-	-
o-C_6H_4	420/446	562 (0.64)	385/420	540 (0.50)	386/419	544 (0.50)
m-C_6H_4	439	522 (0.14)	-	-	-	-

[a] Obtained from the CH_2Cl_2 solutions, [b] fluorescence quantum yield.

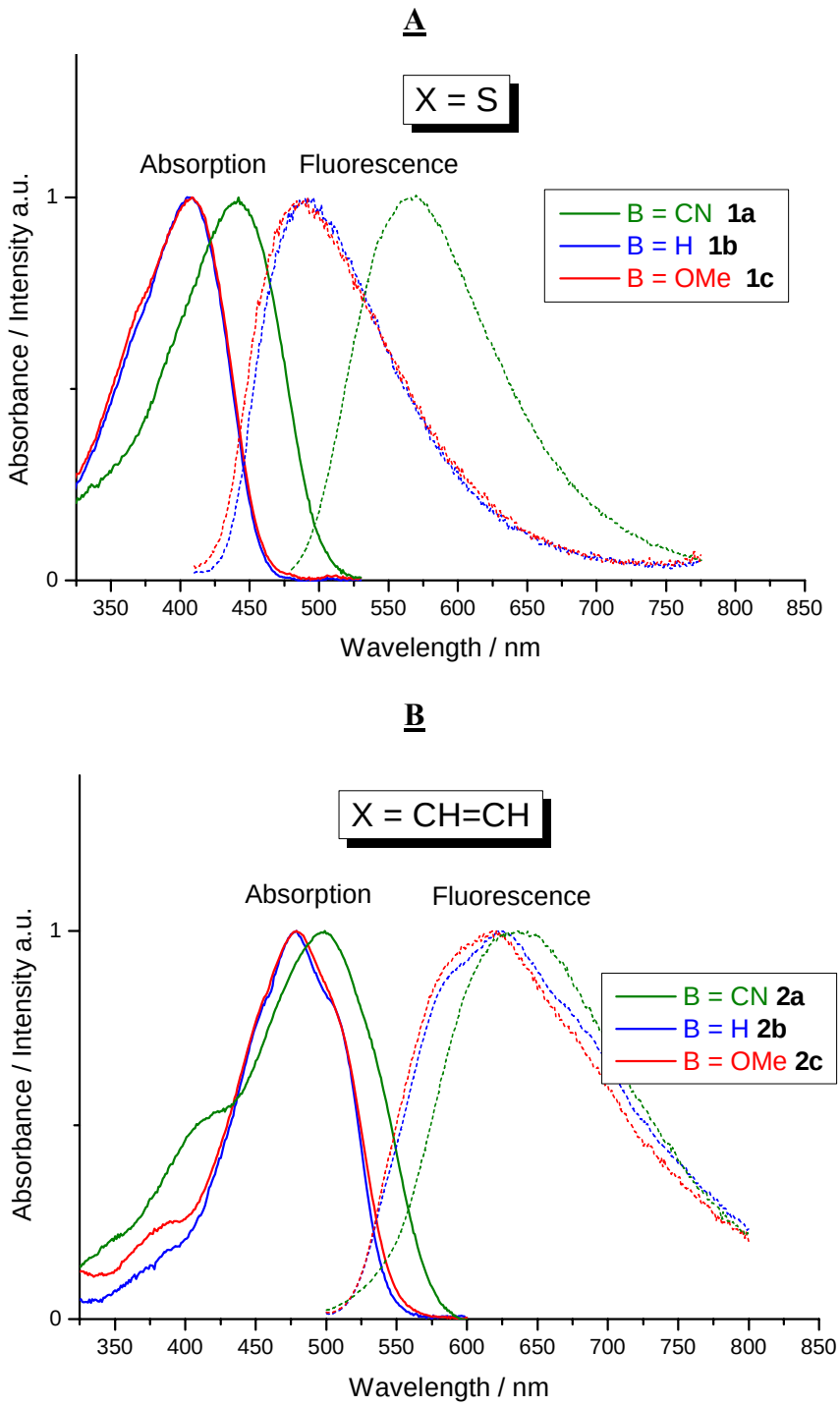

Figure 6.7 Normalized absorption (solid lines) and fluorescence (dashed lines) spectra of compounds **1a-c** (A) and **2a-c** (B).

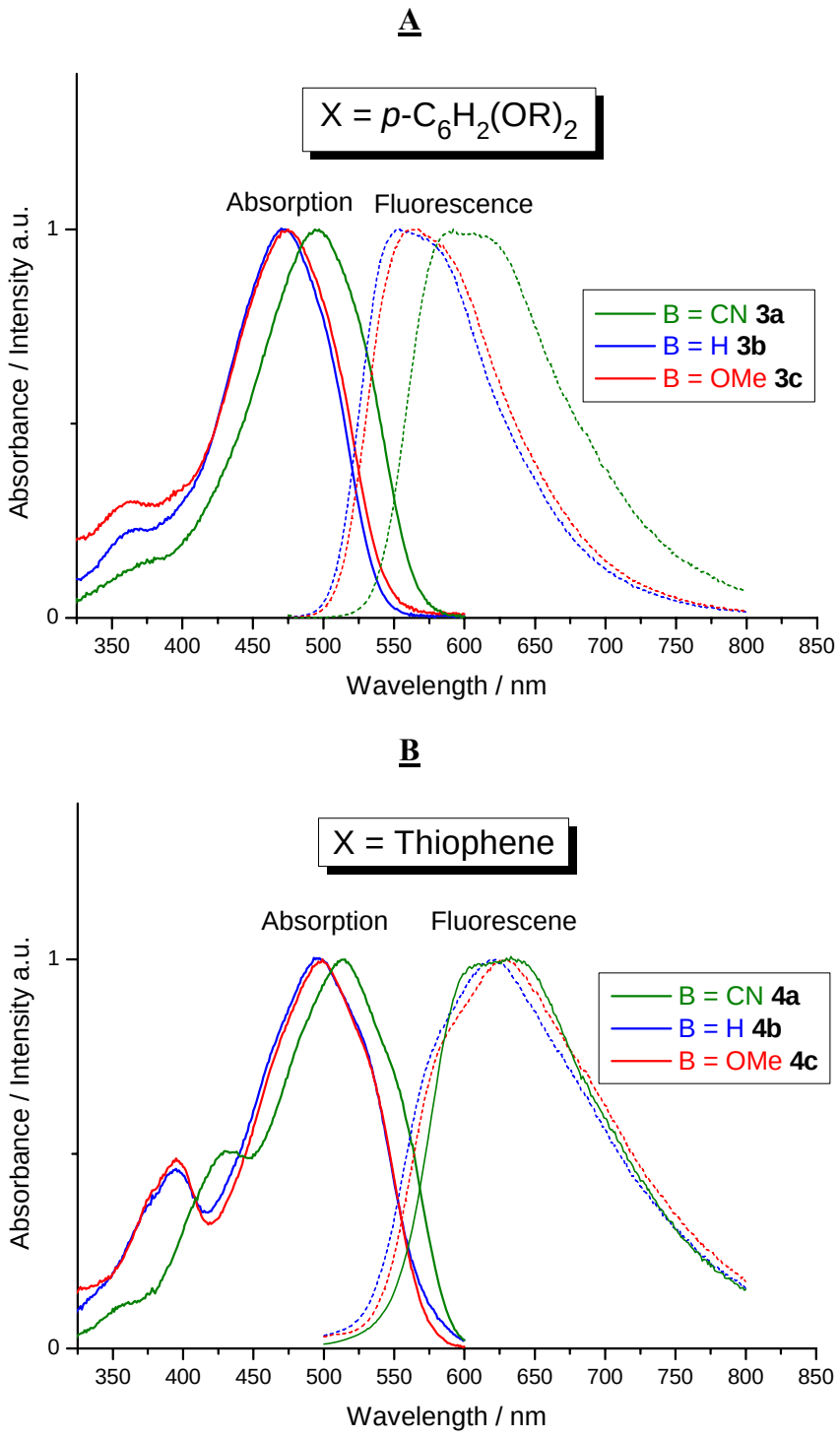

Figure 6.8 Normalized absorption (solid lines) and fluorescence (dashed lines) spectra of compounds **3a-c** (A) and **4a-c** (B).

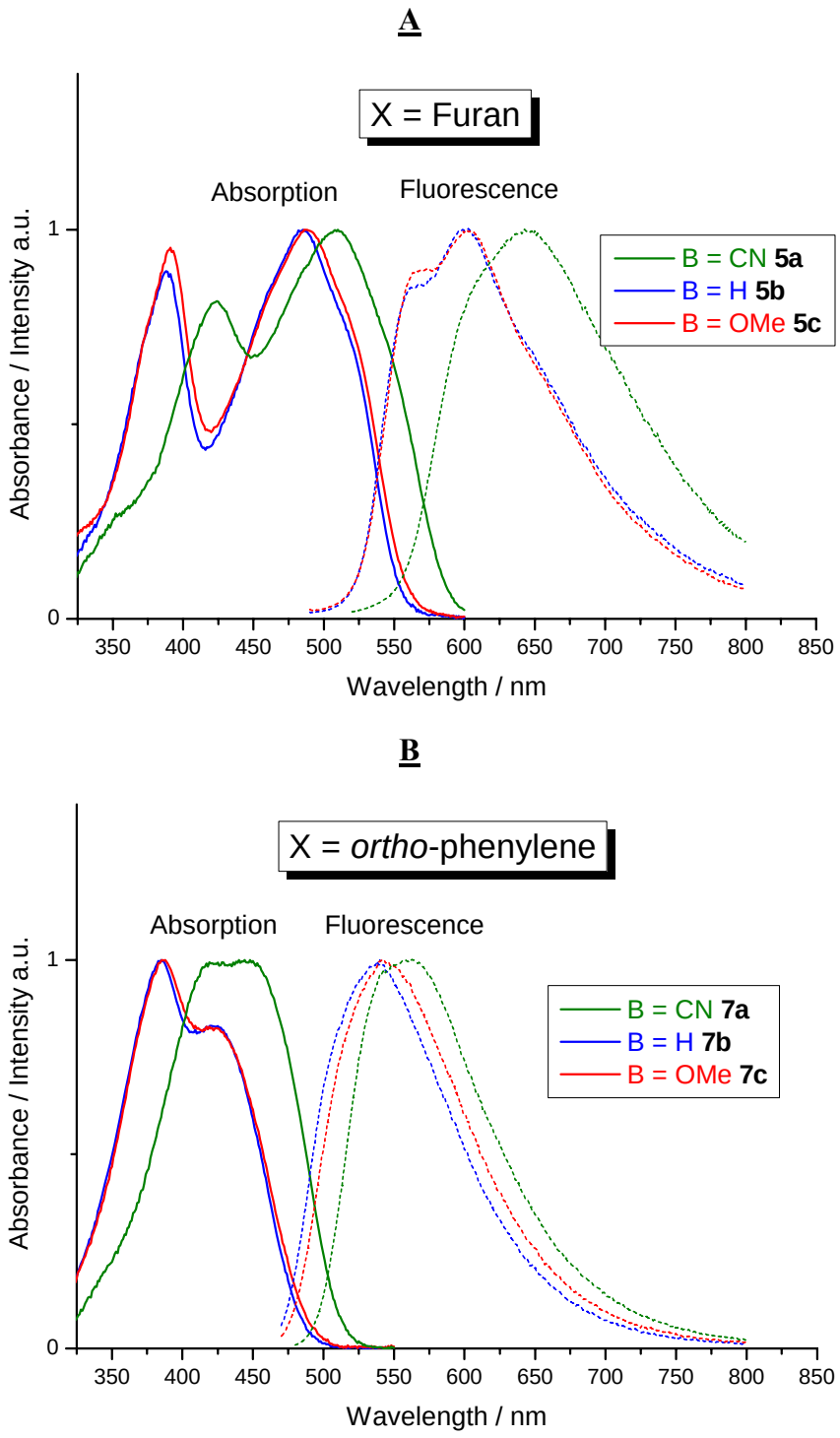

Figure 6.9 Normalized absorption (solid lines) and fluorescence (dashed lines) spectra of compounds **5a-c** (A) and **7a-c** (B).

the π-π* transition (Eg) varies as a function of the X group, B substituent, magnitude of conjugation and steric effect for these oligomers.

For each subgroup with a fixed central X unit, the cyano-substituted compound always absorbs at a wavelength ca. 20-30 nm longer than its methoxy-substituted or un-substituted analogues, while the absorption maxima of the latter compounds are almost the same. It has been known that both electron withdrawing and electron donating groups in the *para*-position of the end phenyl group in an oligomeric molecule shift the absorption bathochromically.[17] The absence of obvious red-shift for methoxy-substituted compounds for current cases may arise from two opposite effects: on the one hand, the electron-donating –OMe group can elevate the HOMO energy of the oligomer by interacting with the frontier orbital of the conjugated component with its occupied π orbitals; on the other hand, the steric distortion introduced by such group may reduce the conjugation effectiveness of the oligomeric backbone and thus raise the LUMO energy level, giving rise to overall slightly changed energy gap. In contrast, the linear attribute of the cyano substituent brings little influence on the conjugation geometry. The bathochromic shift caused by the –CN groups is mainly because the LUMO energy is lowered more than the HOMO energy by coupling with the anti-bonding π* orbitals of the cyano groups, which results in a narrowed band gap.

For different central X units, the λ_{max} shifts to longer wavelength with an increasing number of aromatic rings, consistent with the expected behavior for conjugated systems. Therefore, the sulfur bridged compounds, **1a-c**, exhibit the highest energy absorption due to the presence of a heteroatom in the midway of the conjugation path. However, their absorption maxima (407-430 nm) are still red-shifted in comparison with that of the model compound, 2,5-distyrylpyrrole (396 nm), meaning that the lone pair p-orbital in the sulfur atom still overlaps with the neighboring double bonds in maintaining the conjugation to some extent. When the sulfur atom is replaced by an unsaturated double bond, the absorption energies are shifted ca. 60-70 nm to lower energy and are in the same magnitude as those of aromatic rings.

Finally, steric factors play a remarkable role in influencing the absorption behaviors. For instance, if we compare the absorption maxima of the phenyl end-capped compounds 4b, 5b and 6b, the pyrrole-centered derivative **6b** (465 nm) reveals a higher

S_0-S_1 transition energy difference than its thiophene- (**4b**, 498 nm) and furan-centered (**5b**, 485 nm) analogues. One of the reasons for such a blue-shift is that the methyl substituent on the central pyrrole nucleus somewhat distorts the conjugation coplanarity to release the steric conflict with the adjacent methyl groups on the neighboring pyrrole rings. For the same steric reason, the *ortho*-phenylene (**7a-c**) and *meta*-phenylene (**8a**) derivatives all present rather high energy absorption maxima in comparison with the *para*-phenylene derivatives (**3a-c**). Apparently, the 1,2- or 1,3- substitutions of two bulky side chains on the central phenylene group is sterically very unfavorable in maintaining the planarity of the whole molecule. Compromising the steric strains will result in downgraded conjugation and therefore enlarged HOMO-LUMO band gap and shift the absorption to higher energy. Related to the steric effect, the vinyl bonds between the arylene rings in current oligo(arylenevinylene) series are crucial in lowering the energy band gap. In comparison with oligoarylene or oligoheteroarylene, the vinyl spacers in oligo(heteroarylenevinylene) effectively reduce the steric hindrance between the adjacent aromatic rings. It is especially the case when the repeating unit is *N*-alkylpyrrole since the alkyl attachment can severely twist the coplanarity of the oligomeric/polymeric backbone and lower the level of π-conjugation, thus leading to degraded optical and electronic properties.

Fluorescence properties. The normalized absorption and emission spectra of some of the compounds are shown in Figure 6.7-6.9. Again, the emission behaviors of the mixed-aromatic oligomers alter greatly with the central X group and the B end-capping substituent. In general, the Stokes shifts vary from 90 to 130 nm depending on the specific structures, which is in the normal range for these kinds of oligomers. The emission spectra of methoxy substituted compound and its phenyl end-capped analogue (B = H) are always close to identical as their close similarity in the absorption spectra, thus, resulting in a nearly same Stokes shift. The emission of the corresponding cyano substituted derivative, however, is much more red-shifted and the Stokes shift is also greater. The extreme case can be exemplified by the sulfur centered compounds **1a-c** (Figure 6.7A), in which **1b** and **1c** exhibit a Stokes shift of ca. 90 nm, while the corresponding value for **1a** is 126 nm. The larger Stokes shift indicates that the emitting state is different from the state reached by absorption, i.e. the fluorophore is excited to the

singlet states (S_1, S_2, etc.) with an energy level much higher than the lowest vibrational level of first excited electronic state (S_1), where the light emission occurs after thermal conversions have taken place.

The fluorescence quantum yields (φ) depend greatly on the X and B groups as well as indicated in Table 6.1. For each subgroup with a fixed X central unit, a methoxy substituent plays a small role in altering the quantum yield, while a cyano group unexceptionally enhances the quantum yield, which is in line with the literature record.[16] It is especially the case for the sulfur centered oligomer **1a**, which has a fluorescence quantum efficiency of 0.29, about 10 times greater than those of **1b** and **1c**. Among the different X groups, -C=C- centered derivatives are the least fluorescently efficient. All three species, **2a-c,** showed very low φ values less than 0.01. This behavior has been observed for polyene linked diphenyl and dithienyl compounds, and is attributed to the presence of the lowest excited singlet states of different symmetry, whose relative stabilization depends on the extent of the conjugation and then affects the nature of the lowest excited state.[18-20] The low quantum yields for the hexatrienyl linked compounds are thus indicative of a forbidden transition between the symmetry mismatched excited and ground states. This may also explain the low φ values for flexible chain linked compounds **1b** and **1c**. The greatly enhanced φ value for the cyano-substituted oligomer **1a** can be attributed to the alteration of the excited state symmetry by the electron-withdrawing group so that a symmetrically allowed transition will occur. For compounds in which the central X is an aromatic ring, the quantum yield decreases in the order of *para*-phenyl, *ortho*-phenyl > pyrrole > *meta*-phenyl > thiophene, furan. Indeed, the fluorescence efficiencies of the *para*-phenylene (**3a-c**) and *ortho*-phenylene (**7a-c**) derivatives are most pronounced. Each of them reveals a φ value no less than 0.5. Aside from that, it is also interesting to note that the heteroaryl rings differ greatly in fluorescent properties as the tripyrrole oligomer **6b** shows rather impressive quantum efficiency (0.31), in sharp comparison to the low φ values exhibited by thiophene (0.05) and furan (0.032) centered analogues. Conceptually, such variation has to do with the excited state symmetry, radiationless decay, intersystem crossing to triplet state, etc. A full interpretation of current results inevitably requires more experimental support and theoretical calculation treatment, which are underway. Other photophysical and

photochemical properties of the mixed-aromatic oligomers such as fluorescence life time (τ), radiative decay, triplet properties and photoreactivity are also planned for further investigations.

Electrochemistry

The cyclic voltammetric results for the oligomers are collected in Table 6.2. All electrochemical measurements were conducted using Bu_4NTFPB as the supporting electrolyte in CH_2Cl_2, and the oxidation potentials are reported versus the ferrocene/ferrocenium couple, which was used as the internal reference for each measurement. The sampled cyclic voltammgrams are also shown in Figure 6.10-6.12. As indicated in Table 6.2, the electrochemical behaviors of the organic oligomers vary with the central X unit and the terminal B group. While compounds **2a-c** (X = CH=CH), **3a-c** (X = *para*-$C_6H_2(OC_{12}H_{25})_2$), **4a-c** (X = thiophene), **5a-c** (X = furan) and **6b** (X = pyrrole, B = H) exhibited two reversible oxidation waves which are presumably pyrrole-based, **7a-c** (X = *ortho*-C_6H_4) and **8a** (X = *meta*-C_6H_4), however, only presented irreversible oxidations due to compound decompositions.

For each three compounds with a fixed central X group, the B *para*-substituent on the end-capping phenyl group plays a noticeable role in alternating both the first oxidation and peak separation. On the one hand, the first oxidation potential (E_1) increases in the order of -OMe < -H < -CN, which is a consequence of the substituent effect on perturbing the HOMO energy level. An electron donating group (-OMe) elevates the HOMO, resulting in a lowered first oxidation, while an electron withdrawing group (-CN) operates inversely so that the compound is more difficult to oxidize. On the other hand, the peak separation (ΔE) increases in the order of -CN > -H > -OMe. This is because in the dicationic state, the electron-withdrawing cyano groups on the terminal phenyl group push the positive charges into the bridging fragment so that the two positive charges are closer to each other, leading to a thermodynamically unfavorable state, which consequentially requires higher energy. The net result accounts for an enlarged peak separation between the first and second oxidation. In contrast, the electron-donating methoxy groups stabilize the positive charges so that they can lie further apart from each other with largest separation. Such electronic arrangement makes the dicationic species

relatively easier to achieve and gives rise to a lower second oxidation potential (E_2) and smaller ΔE. Such a phenomenon is in evidence in Figure 6.10-6.11.

Table 6.2 Electrochemical data[a] (from Cyclic Voltammetry) for the oligomers.

Comp	X	B = CN		H		MeO	
		E_1[b] (mV)	ΔE[c] (mV)	E_1[b] (mV)	ΔE[c] (mV)	E_1[b] (mV)	ΔE[c] (mV)
1a-c	S	93 (semi)	306 (semi)	-68 (ir)	n/a	-100 (ir)	n/a
2a-c	CH=CH	-84	165	-244	138	-267	96
3a-c	*p*-$C_6H_2(OC_{12}H_{25})_2$	-24	177	-150	158	-184	158
4a-c	C_4H_2S	-36	190	-157	151	-210	149
5a-c	C_4H_2O	-80	192	-180	152	-230	118
6b	C_4H_2NMe	-	-	-380	340	--	--
7a-c	*o*-C_6H_4	180 (ir)	n/a	50 (ir)	n/a	-20 (ir)	n/a
8a	*m*-C_6H_4	220 (ir)	n/a	--	--	--	--

[a] Obtained in CH_2Cl_2 solution containing 0.1 M NBu_4TFPB as the supporting electrolyte. Scan rate 50 mV/s. semi = semi-reversible redox process, ir = irreversible oxidation. [b] first oxidation potential vs. Fc/Fc^+ couple; [c] the oxidation potential difference between $E_{1/2}{}^2$ and $E_{1/2}{}^1$.

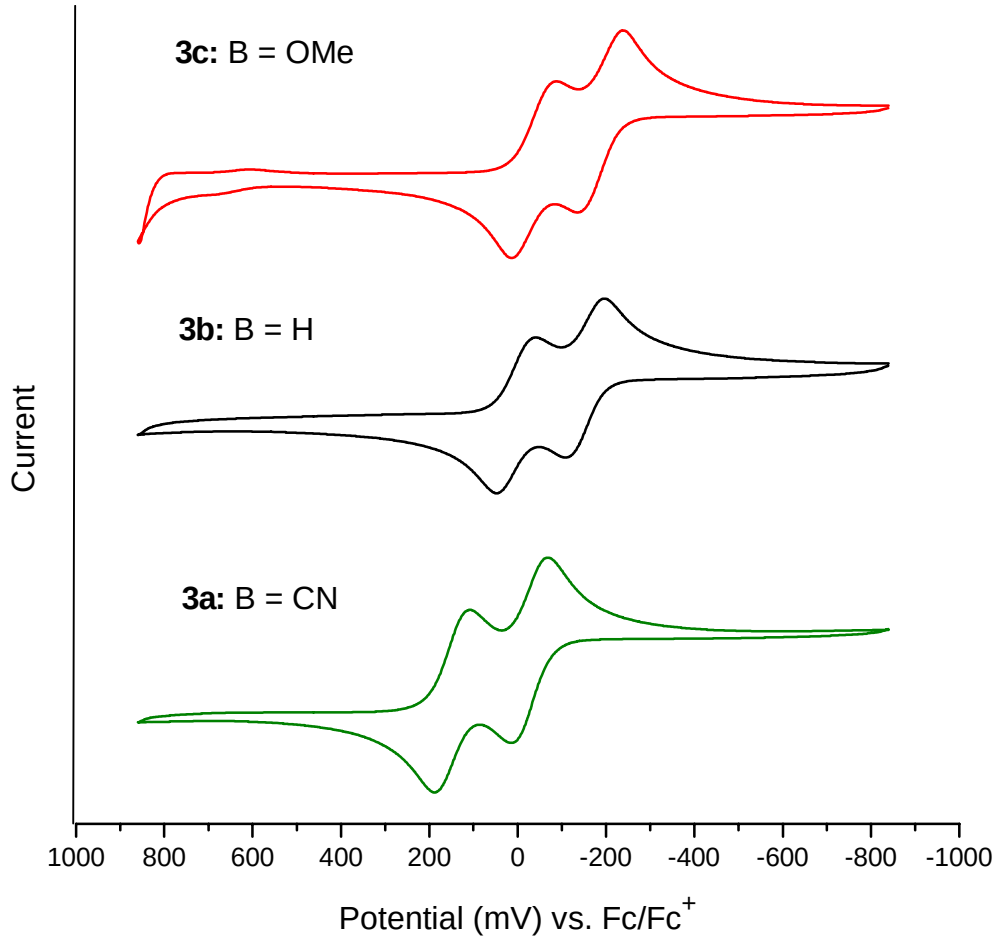

Figure 6.10 Cyclic voltammograms of **3a**, **3b** and **3c** in a CH_2Cl_2 solution containing 0.1M Bu_4NTFPB. Scan rate: 50 mV/s.

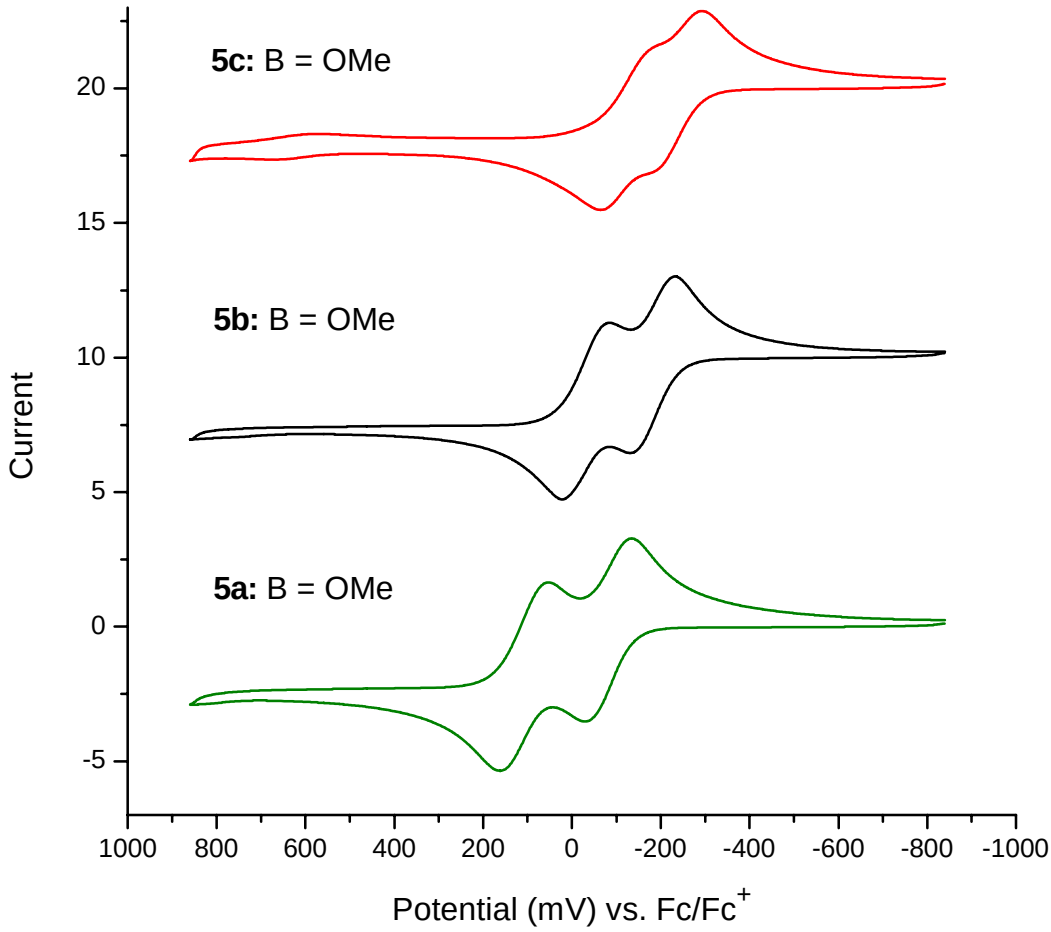

Figure 6.11 Cyclic voltammograms of **5a**, **5b** and **5c** in a CH_2Cl_2 solution containing 0.1M Bu_4NTFPB. Scan rate: 50 mV/s.

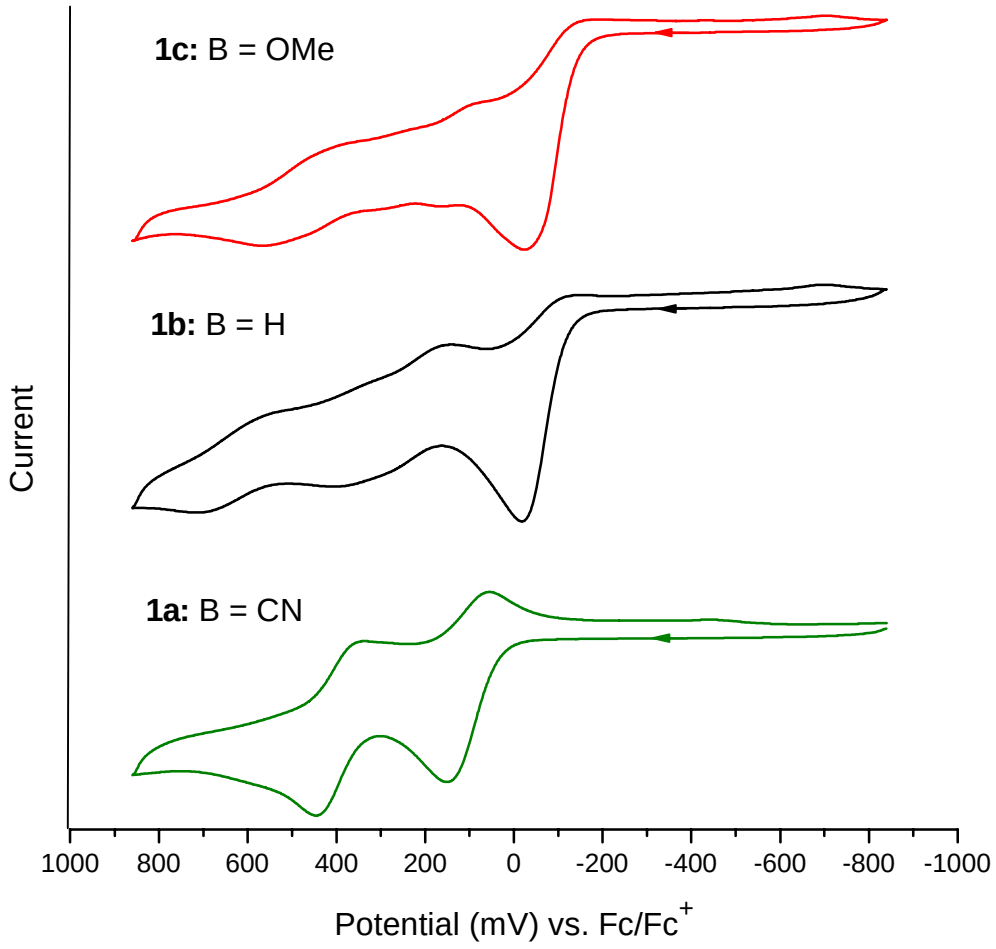

Figure 6.12 Cyclic voltammograms of **1a**, **1b** and **1c** in a CH_2Cl_2 solution containing 0.1M Bu_4NTFPB. Scan rate: 50 mV/s.

For tripyrrole derivative **6b**, the oxidation profile is expected to be different from the rest of the compounds since the electron-richest moiety is located at the central pyrrolene unit due to the accumulated electron-donating effect from the electron-rich side chains. Therefore, the first oxidation of **6b** is mostly negatively shifted (-380 mV vs. Fc/Fc^{+}). The rather moderate ΔE (340 mV) suggests that in the dicationic state the two positive charges are not immediately adjacent to each other. In other words, the initial positive charge has migrated to one of the side pyrrolene groups before the second anodic reaction so that the resulting positive charges are mostly separated to eliminate the strong electrostatic repulsion otherwise. This observation has been observed in many occasions in our previous research (Chapter 2-5) for highly delocalized systems.

In order to gain a further insight of the electrochemical behaviors of the organic oligomers, it is interesting to compare them with their bimetallic FcCH=CHXCH=CHFc analogues. For most of the organic compounds, the corresponding peak separations, ΔEs, are slightly enlarged, especially for those with –CN substituents. The most enhanced species are the dialkoxy-*p*-phenylene derivatives (**3a-c)**, which demonstrated peak separations in the same magnitude of their furan (**4a-c)** or thiophene (**5a-c**) counterparts. The corresponding bis(2-ferrocenylvinyl) analogues, instead, showed differentiable coupling strengths in the order of furan > thiophene > dialkoxy-*p*-phenylene (Chapter 2). However, such ΔE enhancements are considerably more moderate, ranging from 0% to 60% depending on both the X and B groups (60% is the extreme case for **3a**, the average increase is below 20%). This is somewhat unexpected if we consider the redox alteration in the framework of mixed-valence (MV) electronic interaction since the metal-ligand orbital mixing problem has been intrinsically circumvented in current cases. More surprisingly, the1,6-hexatrienyl bridged compounds **2a-c** (X = C=C) showed the smallest peak separations in these series even their nominal pyrrole-to-pyrrole distances are shorter and the hexatrienyl spacer was observed as a more efficient linker in supporting electron transfer than other –CH=CH-X-CH=CH- bridging components (Chapter 2, 4 and 5). Furthermore, the peak separations of **2a**, **2b** and **2c** (165 mV, 138 mV and 96 mV, respectively) are all smaller than their biferrocenyl analogue **$Fc(CH=CH)_3Fc$** (180 mV, in Chapter 2). These facts are suggestive that the oxidation processes of the organic

compounds underwent different mechanism from those of the diferrocenyl complexes. Most likely, for the organic oligomers, the positive charge in the first oxidized state is delocalized along the molecular axis, the progressive oxidations were governed rather by the HOMO and SOMO energy levels of the successive oxidation states than by the electronic coupling between two discrete redox sites with different oxidation states. This hypothesis was later confirmed by the electronic absorption studies on the intermediate oxidized species (*vide infra*).

Finally, the electrochemical behaviors of sulfur bridged compounds **1a-c** vary greatly with the peripheral attachment on the terminal phenyl groups as shown in Figure 6.12.Whereas the methoxy end-capped compound **1c** exhibited highly skewed CV sweeping due to compound decomposition, the cyano substituted analogue **1a** showed two semi-reversible oxidation waves. Apparently, the electrophilic substituents (-CN) stabilize both the monocationic and dicationic species of the electron-rich oligomer. Apart from that, the ΔE of **1a** (306 mV) is notably superior to any other compound in this study (Table 6.2). For this case, we believe that intramolecular electronic coupling is at work since the π-conjugation is considered partially broken at the central sulfur atom. The positive charge generated in the intermediate monocationc species was likewise more localized at one of the pyrrole moieties and effectively perturbed the successive oxidation through the linking spacer. The greatly increased peak separation, in contrast to that of FcCH=CH-S-CH=CHFc (170 mV, Chapter 2), is mainly attributed to the enhanced charge delocalization in the organic system.

Electronic Spectra of the Monocations

Oligomers subjected to electronic spectroscopic studies are **2a-c**, **3a-c**, **4a-c**, **5a-c** and **6b**, the rest of the oligomers are not suitable due to the decomposition of the charged species as depicted in the earlier discussions. The radical cations of the oligomers were generated using ferrocenium hexafluorophosphate ($FcPF_6$) as the oxidizing agent. This was based on the fact that $FcPF_6$ has a mild oxidation strength which allowed a better control in achieving the intermediate oxidation state of the oligomers, i.e. the monocationic species. In addition, the side product, ferrocene, did not interfere with the vis-NIR absorptions, since it only has negligible absorption around 460 nm ($\varepsilon_{max} < 300$

$L \bullet M^{-1} \bullet cm^{-1}$).[21] We also tried tris(4-bromophenyl)aminium hexafluoroantimonate (TBA or magic blue); however, the oxidation strength was rather strong and often led to over-oxidation and loss of subtle information otherwise available. Solutions containing monocations were obtained by the addition of $FcPF_6$ solution to a large excess (>10 equiv.) of the neutral substrate solutions in a concentration around 0.5-1 x 10^{-4} mol/L. These solutions were then investigated using Vis-NIR spectroscopy. However, most of the cyano-substituted monocations were poorly soluble or insoluble in CH_2Cl_2. The charged species either immediately precipitated from solution upon *in situ* oxidation or aggregated into a black solid in very short period of time. Therefore, only the absorption spectra of $\mathbf{3a}^+$ and $\mathbf{5a}^+$ were obtained with underestimated intensity (ε_{max}) due to the visible precipitation (the long chain alkyl chain $\mathbf{3a}^+$ indeed improved the solubility). In principle, the solubility of the monocations can be enhanced by using bulky free coordinating anions such as $TFPB^-$. This will involve preparing the corresponding $FcTFPB^-$, which is left for future work. With the qualitative spectrum of $\mathbf{3a}^+$ and $\mathbf{5a}^+$ at this stage, we can still have a basic understanding of the substituent effects on the monocations since the electronic absorptions of cyano derivatives are very close to those of the unsubstituted species.

The UV-Vis-NIR absorption spectra of the radical cations are shown in Figure 6.13-6.14. All monocations exhibited a pair of very intense absorptions in the NIR and visible region, respectively. For some of the cases, e.g. $\mathbf{3a\text{-}c}^+$, the two strong absorptions (M1 and M2 in Figure 3.13A) are each accompanied with a shoulder transition on the higher energy side (M1' and M2', respectively). The line-shape and intensity of the NIR bands suggest that these absorptions are no longer associated with an intervalence charge transfer. If we assume an IVCT transition for the lowest energy bands, the predicted half bandwidths from Hush theory[22] ($\nu_{1/2}$[Hush] = 2310 x ν_{max}, in cm^{-1}) will be three to four times broader than the observed band width, as shown in Table 6.3. In addition, all these lowest energy bands are characterized as asymmetrical in terms of $\nu_{1/2}$[high]/$\nu_{1/2}$[low], where $\nu_{1/2}$[high] and $\nu_{1/2}$[low] are twice the half-widths on the high- and low-energy side of the band, respectively. In contrast, an IVCT band is defined as a symmetrical broad band. Therefore, these features are in good line with the Robin-Day's class III

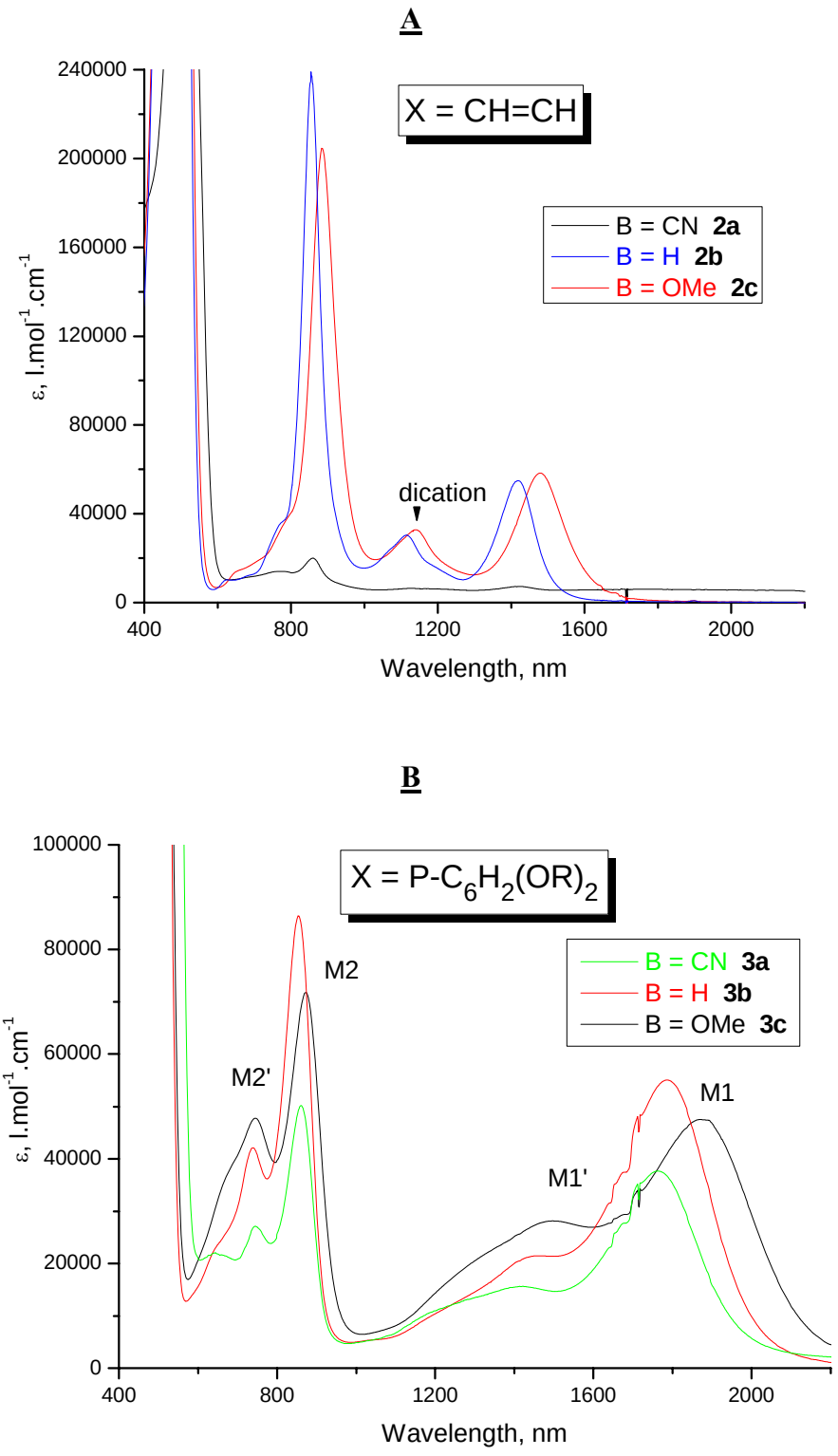

Figure 6.13 Vis-NIR absorption spectra of the cationic species of **2a-c** (A) and **3a-c** (B).

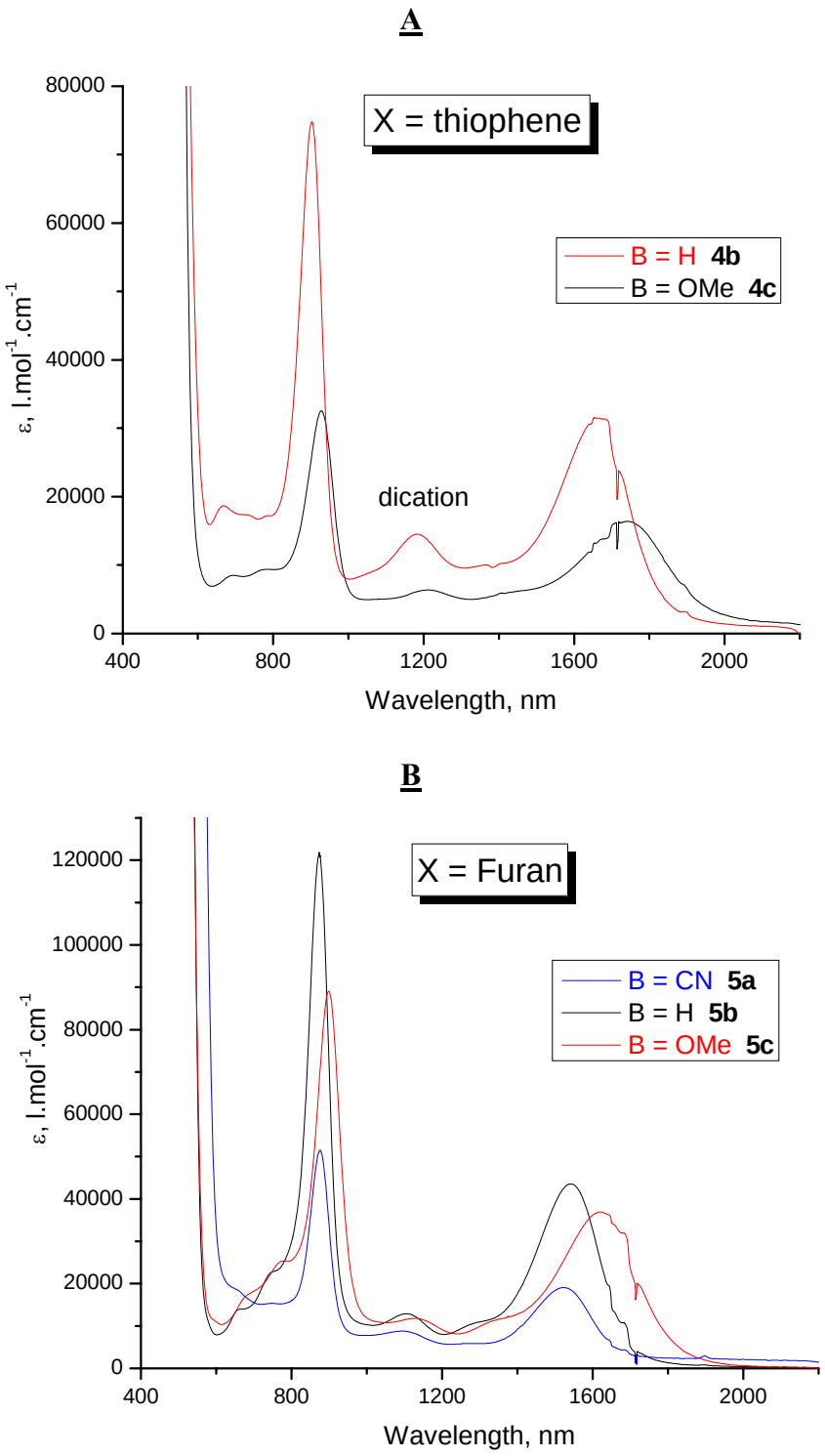

Figure 6.14 Vis-NIR absorption spectra of the cationic species of **4a**, **4b** (A) and **5a-c** (B).

Table 6.3 Band shape data of the lowest energy band of the cationic species in CH_2Cl_2.

	ν_{max} (cm^{-1})[a]	$\nu_{1/2}$[high] (cm^{-1})[b]	$\nu_{1/2}$[obs] (cm^{-1})[c]	$\nu_{1/2}$[low] (cm^{-1})[d]	$\nu_{1/2}$[Hush] (cm^{-1})[e]	$\nu_{1/2}$[high]/ $\nu_{1/2}$[low]
2b$^+$	7060	680	702	724	4040	0.94
2c$^+$	6770	778	741	704	3950	1.11
3a$^+$	5670	1142	938	734	3620	1.56
3b$^+$	5600	1220	988	756	3595	1.61
3c$^+$	5330	1544	1171	798	3500	1.93
4b$^+$	5990	1190	911	632	3720	1.88
4c$^+$	5750	1306	1064	822	3640	1.59
5a$^+$	6570	1048	890	732	3900	1.43
5b$^+$	6480	1078	887	696	3870	1.55
5c$^+$	6170	1202	985	768	3775	1.57

[a] Absorption maximum of the lowest energy band in cm^{-1}. [b] Twice the bandwidth at half-height of the high-energy side. [c] Observed bandwidth at half-height. [d] Twice the bandwidth at half-height of the low-energy side. Predicted bandwidth of half-height, $\nu_{1/2}[Hush] = (2310 \times \nu_{max})^{1/2}$.

transitions.[23-25] In other words, the radical cations of the pyrrole-based oligomers are fully delocalized systems, and the optical transition no longer involves charge transfer between the redox sites with different oxidation state and is therefore not accompanied by a net dipole moment change. Instead, the optical spectra shown in Figure 6.13 and 6.14 are in the same absorption patterns observed for the radical cations of oligothiophene,[26-28] oligopyrrole,[29] and oligoheterocycles, [30-32] which serve as the model compounds for the polaron theory[33, 34] of conducting polymers. The results of the corresponding spectroscopy are generally interpreted in the framework of molecular orbital (MO) theory, which is suitably applicable to our current cases.

Based on the MO theory, the MO diagrams of the oligomers in the neutral and radical cation states are shown in Figure 6.15, the optical transition energies are listed in Table 6.4. In Figure 6.x., the second highest occupied and lowest unoccupied molecular orbitals are dubbed (HOMO - 1) and (LUMO + 1), and the midgap singly occupied molecular orbital is (SOMO). The lowest energy transition of neutral oliogmers (N), located at 2.45-2.67 eV (Table 6.4), is assigned to the fundamental π-π* transition between the HOMO and LUMO levels. Upon removal of one electron from the HOMO of a closed-shell neutral oligomer, significant geometrical deformation of the molecule occurs which leads to a major rearrangement of the MO energy levels for the produced radical cation. This will give rise to two strong subgap electronic absorption transitions, M1 and M2, in the NIR and visible regions, respectively. The lowest energy band M1 essentially corresponds to a transition between the HOMO and SOMO, while M2 derives from a transition between singly occupied SOMO and LUMO.

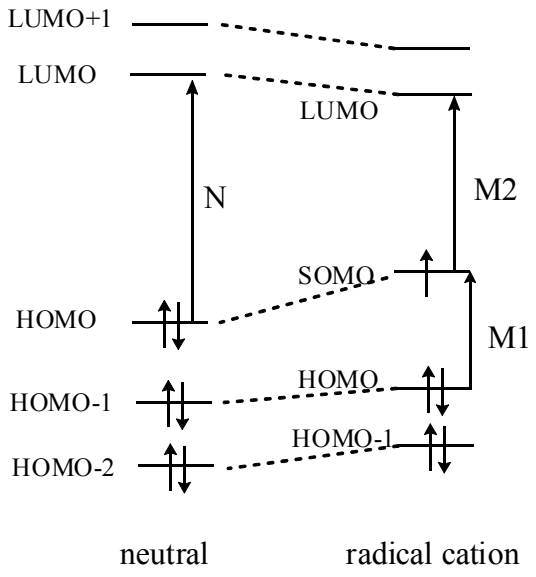

Figure 6.15 Molecular orbital diagram of the oligomers in neutral and cationic states.

Table 6.4 Optical transition energies of the oligomers.

Oligomer	N (eV)	Radical cation			
		M1 (eV)	M1' (eV)	M2 (eV)	M2' (eV)
2b	2.59	0.88	--	1.45	--
2c	2.59	0.84	--	1.4	--
3a	2.51	0.7	0.87	1.44	1.66
3b	2.62	0.69	0.86	1.45	1.68
3c	2.61	0.66	0.83	1.42	1.67
4b	2.49	0.74	--	1.37	--
4c	2.48	0.71	--	1.34	--
5a	2.45	0.81	--	1.42	--
5b	2.56	0.8	0.96[a]	1.42	1.66[a]
5c	2.54	0.76	0.92[a]	1.38	1.62[a]
6b	2.67	0.94	--	1.59	--
		Ridical cation π-dimer			
		D1 (eV)		D2 (eV)	
$(\mathbf{6b})_2^{2+}$		1.06		1.71	

[a] Very weak absorption.

For some of the cases, M1 and M2 are accompanied with a side shoulder band M1' and M2', respectively, appearing at higher energy around 0.17-0.26 eV to the paired absorption band. The shoulder absorptions are especially pronounced for $\mathbf{3a}^+$-$\mathbf{3c}^+$ (Figure 6.13B). This phenomenon is not uncommon for oxidized thiophene,[26, 27, 35] pyrrole,[29] *p*-phenylene,[36] 2,5-thienylenevinylene,[37] *p*-phenylenevinylene,[38] and other heterocycle oligomers.[32] The electronic origin of these bands is difficult to determine because it may involve transitions between the HOMO, SOMO and LUMO levels. Several postulated assignments have been proposed, and each theory has been the source of great

controversy.[28, 39, 40] To date, it is generally accepted that these sideband absorptions may be due to vibronic transitions,[40] which is consistent with a C=C stretching mode that would strongly couple to the electronic structure.[41] The weak bands appearing around 1100-1200 nm for each oxidized species are due to the dicationic absorptions caused by the disproportionation equilibrium from the radical cation to the dication and neutral forms.

As indicated in Table 6.4, the energies required for M1 and M2 transitions in current series are altered by the B-substituent and the central X group. In general, an electron-rich group moves the absorptions to lower energy, and *vice versa*. Thus, for a given X series, the methoxy end-capped compounds always display the M1 and M2 bands red-shifted about 0.03-0.04 eV to those of the cyano substituted and the phenyl end-capped derivatives. On the other hand, for different X central groups with the same B substituent, the transition energy of M1 decreases in the order of pyrrole > -C=C > furan > thiophene > 2,5-dialkoxy-*p*-phenylene, the M2 energy varies in the same trend but relatively less sensitive. The notably high energy required for the tripyrrole derivative $\mathbf{6b}^+$ is probably because the different charge distribution profile since the positive charge is more centered at the middle pyrrole unit. For other X bridged cationic species, however, the two side pyrrole units are believed to accommodate the positive charge to greater extent. This can have important consequences in alternating the electronic configuration so that $\mathbf{6b}^+$ apparently has the biggest HOMO and SOMO energy difference. In comparison with the aromatic ring centered analogues, $\mathbf{2a}^+$-$\mathbf{2c}^+$ (X = CH=CH) show higher energy M1 transitions due to the lower degree of π-conjugation.

It is also noteworthy that the HOMO-SOMO energy gap of the radical cations of the distyrylpyrrole-based oligomers herein are considerably lower than the literature values for other oligoheterocycles in the similar degree of conjugation. For instance, the M1 transition energy of $\mathbf{6c}^+$ (0.66 eV) is essentially the same value as that of the singly oxidized nonithiophene ($9T^+$) (0.67 eV);[42] the corresponding energy for $\mathbf{2c}^+$ is identical to that of sexithiophene radical cation ($6T^+$) (0.84 eV);[26, 42] and oligopyrrole $[PhPyr_3Ph]^+$ and $[PhPyr_4Ph]^+$ showed M1 transition at 1.32 and 1.13 eV,[29] respectively, which are much higher than any cationic species in this study. The lowered energy for M1 transition in current cases can be attributed to the following causes: 1). pyrrole, especially *N*-alkyl

substituted pyrrole, generally alters the absorption bathochromically due to its higher electron density; 2). the vinylene spacers play an important role in decreasing the steric distortion otherwise caused by the immediate proximity of the aromatic rings (especially for *N*-alkylpyrroles), which leads to greater coplanarity of the conjugation backbone and therefore decreased energy gap; 3). utilization of a less electron-rich X mediator between the two pyrrolene moieties causes the positive charge unevenly distributed among the aromatic rings, which has essential consequence in altering the electronic configuration and HOMO-SOMO energy gap (as exemplified by $\mathbf{6b}^+$ vs. other cationic oligomers). We believe this is very suggestive in seeking low energy gap oligomers or polymers and appealing for more investigations in future work.

Finally, the successive oxidation of tripyrrole derivative **6b** showed remarkably different spectrum development in comparison with those of other oligomers. To illustrate such difference, the oxidation evolution spectra of **3b** and **6b** are shown in Figure 6.16. For $\mathbf{3b}^+$, the radical cationic absorption bands, M1, M1', M2 and M2', continuously grew in the course of progressive oxidation (Figure 6.16A). The absorptions were saturated when one equivalent of $FcPF_6$ was introduced and the band shape and intensity persisted with up to two equivalents of oxidant in presence (note that $FcPF_6$ is not strong enough to convert $\mathbf{3b}^+$ into the dicationic species). In contrast, the absorption spectra of **6b** were highly dependent on the doping level (Figure 6.16B). Initially, two bands (M1 and M2), arising from the corresponding radical cation $\mathbf{6b}^+$, were found at low and high energy, respectively. Each of these two bands has an associated second transition (D1 and D2) at higher energy (shifted by about 0.22 eV), which is attributed to the formation of a spinless π-dimer of the cation radical. As the doping level is increased, the dimer transition bands D1 and D2 quickly dominate the absorption spectrum, accompanied with progressive disappearance of the M1 and M2 bands at the same time. Further introduction of oxidant causes an ill-resolved spectrum mainly because of the isolation of the consequently formed dication from solution. Indeed, dimerization of radical cation is a common phenomenon for singly-oxidized heterocycle oligomers such as oligothiophenes[43, 44] and oligopyrroles.[29] By analogy of the generally recognized dimerization theory,[29, 43] Figure 6.17 depicts the energy-level diagram for $\mathbf{6b}^+$ and the corresponding $\mathbf{(6b)_2}^{2+}$. The energy levels for the dimer species are constructed by formal

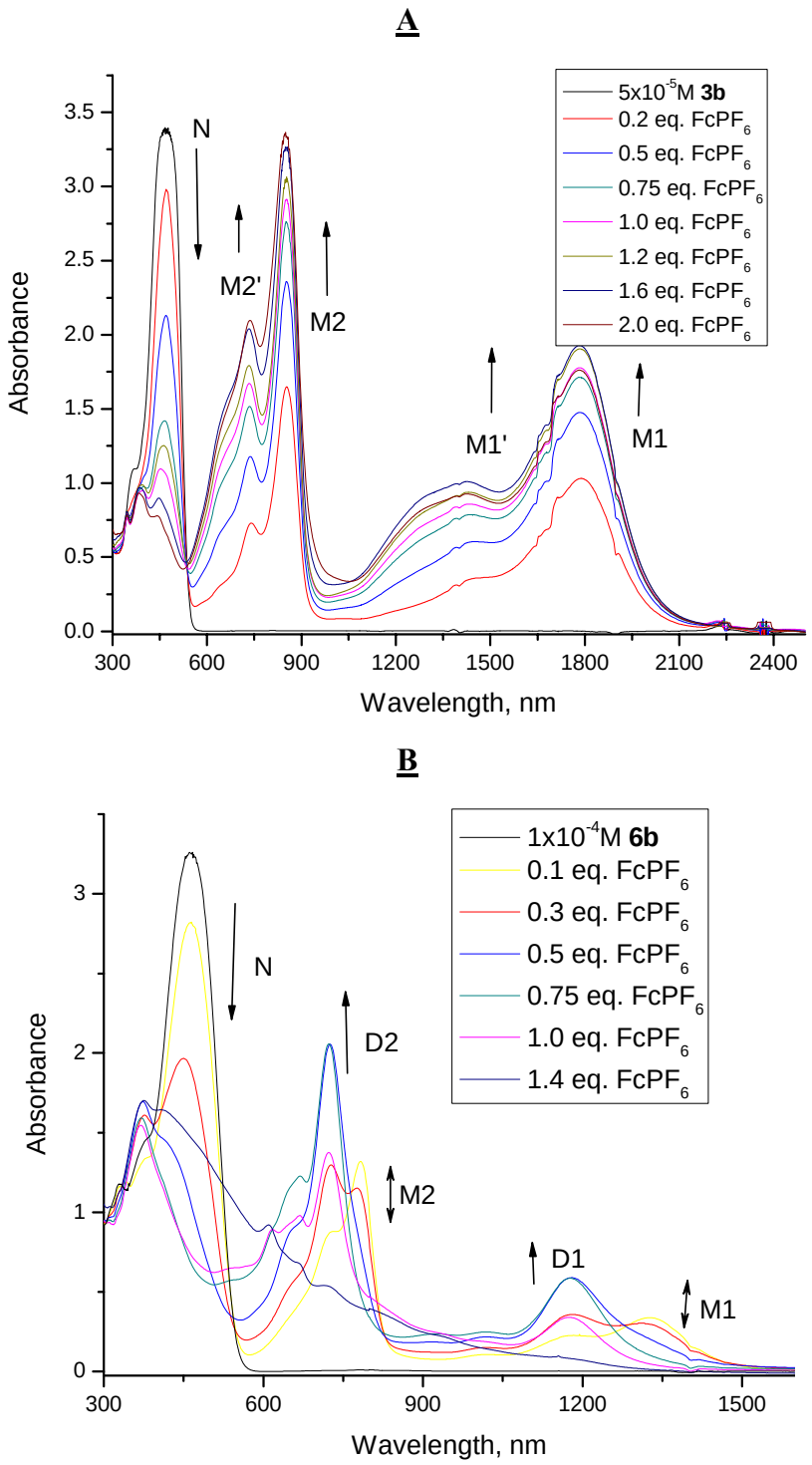

Figure 6.16 UV-Vis-NIR spectrum evolution of oligomer **3b** (A) and **6b** (B) upon progressive oxidation.

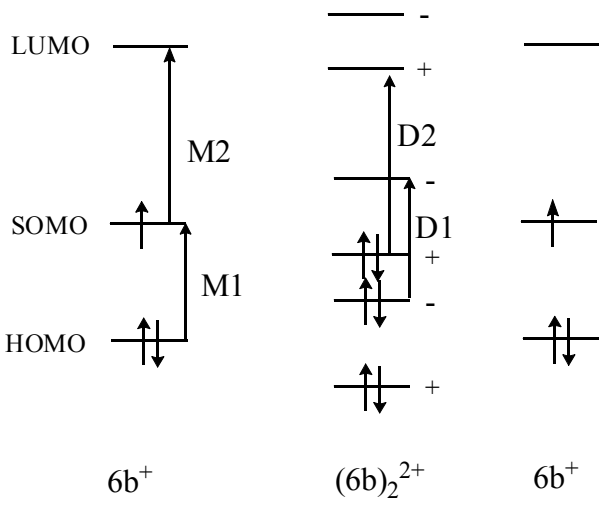

Figure 6.17 Schematic energy diagram for radical cation **6b**$^+$ and the corresponding π-dimer **(6b)$_2$**$^{2+}$.

linear combination of the monomer MOs. The π-interaction between two cation radicals to give a π-dimer will cause a splitting of frontier orbitals into bonding (+) and anti-bonding (-) levels. In the dimer, the D1 (anti-bonding to anti-bonding) and D2 (bonding to bonding) transitions are dipole-allowed and polarized along the long axis of the oligomer. For **(6b)$_2$**$^{2+}$, the D1 and D2 transitions are shifted to higher energy by 0.22 eV regarding the M1 and M2 transitions (Table 6.4), comparable with the corresponding shifts found for the oligopyrrole,[29] oligothiophene[43-46] and other π-radical ion dimers.[29, 47] Such a blue shift is a well-known observation and has been attributed to the interaction between transition dipole moments on the adjacent cation radicals (Davydov shift),[47] although other phenomena may contribute such as different splittings of frontier orbitals upon dimerization.

Although no clear-cut reason that dimerization occurrs only to **6b**$^+$ but not to other oligomer radical cations (e.g. **3b**$^+$) is in evidence, we believe it must be associated with the charge distribution pattern along the conjugation backbone and the dipole moment of the whole molecule. Other factors such as steric effect may also account for the absence of dimer formation for some specific oligomer radical cations such as **3a**$^+$, **3b**$^+$ and **3c**$^+$. In these cases, the flexible long alkyl chains may hinder the association of the cations. Generally, the two side pyrrole moieties would carry more positive charge

than the central X unit when the X unit is not a pyrrole group. Thus, the charge is not concentrated on one redox site, which is not the case for **6c**$^{+}$. This will change the dipole moment of the radical cations and their interchain interactions. Moreover, this may also explain why dimerization is a common phenomenon for homo-oligomers such as oligopyrrole and oligothiophene but not for alternating pyrrole-thiophene oligomers.[31] Further investigations are planned to confirm such postulation by variable temperature NIR/ESR studies and theoretical calculation treatments.

Conclusion

Our initial attempt to develop distyrylpyrrole-based mixed-valence organic compounds resulted in highly delocalized systems. In most of the cases, when the π-conjugation is persisted, a class III system was built, which is especially convincing in the Vis-NIR absorption studies of the singly-oxidized species. The narrow, intense and asymmetrical low energy absorptions suggested that the positive charge in the monocation was fully delocalized along the whole molecule. Therefore, interpretation of the electronic data was conducted in the framework of the polaron and molecular orbital theories. Accordingly, the successive oxidations in electrochemistry should not be considered as the result of electronic coupling between two redox sites with different oxidation states; instead, the discrete oxidations are directly linked to the HOMO and SOMO energy levels of the neutral and cationic species. The only exceptions for such treatment are the sulfur bridged derivatives, in which the π-conjugation is considered partially broken at the midway heteroatom. The unusual large peak separation demonstrated by cyano-substituted compound **1a** was thus attributed to the mixed-valence interactions due to the enhanced charge delocalization in the organic system. This speculation could be easily tested by intervalence absorption examinations if the solubility and stability of the monocationic species could be improved by the employment of free-coordinating counterion such as TFPB^{-}.

Aside from this, we also discovered that the one-electron doped (polaron) mixed-arylene oligomers have unique electronic properties in comparison with other conventional homologous oligomers. Due to the different electron affinity of each arylic

group along the conjugated backbone, the delocalized positive charge is believed to be unevenly distributed among the aromatic centers. The profound consequence to the resulting electronic structures may account for the low HOMO-SOMO energy gap and the absence of the formation of π-dimer for the radical cationic species. Furthermore, on the basis of the charge mobility decreases when π-dimers are generated, it is suggested that π-dimers do not contribute to interchain electron-transfer and that a hopping transport of charges is unlikely to be mediated by such species.[48] Our current results are very implicative in designing highly conductive oligomeric or polymeric materials. An extended full investigation of the organic oligomers on their electronic profile (by theoretical calculations), dication (bipolaron) characterization, electric conductivity, photophysical and photochemical properties, and their potential as optical and organic electronic materials is therefore imperative and currently undergoing.

References

1. Jozefiak, T. H.; Miller, L. L., *J. Am. Chem. Soc.* **1987,** 109, 6560-6561.

2. Risko, C.; Barlow, S.; Coropceanu, V.; Halik, M.; Brédas, J.-L.; Marder, S. R., *Chem. Commun.* **2003**, 194-195.

3. Stephen, F.; Nelsen, S. F.; Konradsson, A. E.; Weaver, M. N.; Telo, J. P., *J. Am. Chem. Soc.* **2003,** 125, 12493-12501.

4. Nelsen, S. F.; Weaver, M. N.; Zink, J. I., *J. Am. Chem. Soc.* **2005,** 127, 10611-10622.

5. Bonvoisin, J.; Launay, J.-P.; Rovira, C.; Veciana, J., *Angew. Chem., Int. Ed. Engl.* **1994,** 44, 2106-2109.

6. Nelsen, S. F.; Ismagilov, R. F.; Powell, D. R., *J. Am. Chem. Soc.* **1996,** 118, 6313-6314.

7. Lindeman, S. V.; Rosokha, S. V.; Sun, D.; Kochi, J. K., *J. Am. Chem. Soc.* **2002,** 124, 843-855.

8. Rosokha, S. V.; Sun, D.-L.; Kochi, J. K., *J. Phys. Chem. A 2002, 106, 2283* **2002,** 106, 2283-2292.

9. Lambert, C.; Nöll, G., *J. Am. Chem. Soc.* **1999,** 121, 8434-8442.

10. Barlow, S.; Risko, C.; Chung, S.-J.; Tucker, N. M.; Coropceanu, V.; Jones, S. C.; Levi, Z.; Bredas, J.-L.; Marder, S. R., *J. Am. Chem. Soc.* **2005,** 127, 16900-16911.

11. Selby, T. D.; Blackstock, S. C., *J. Am. Chem. Soc. 1998, 120, 12155* **1998,** 120, 12155-12156.

12. Borsenberger, P. M.; Weiss, D. S., *Organic Photoreceptors for Xerography; Marcel Dekker: New York,* **1998**.

13. Strauss, S. H., *Chem. Rev.* **1993**, 927-942.

14. de Meheas, M., *Bull. SOC. Chim. Fr.* **1962**, 1989.

15. Martinez-Ruiz, P.; Behnisch, B.; Schweikart, K.-H.; Hanack, M.; Lüer, L.; Oelkrug, D., *Chem. Eur. J.* **2000,** 6, 1294-1301.

16. Greenham, N. C.; Moratti, S. C.; Bradley, D. D. C.; Friend, R. H.; Holmes, A. B., *Nature* **1993,** 365, 628-630.

17. Nakatsuji, S.; Matsuda, K.; Uesugi, Y.; Nakashima, K.; Akiyama, S.; Katzer, G.; Fabian, W., *J. Chem. Soc. Perkin Trans.* **1991,** 2, 861-867.

18. Allen, M. T.; Whitten, D. G., *Chem. Rev.* **1989,** 89, 1690-1702.

19. Bartocci, G.; Spalletti, A.; Becker, R. S.; Elisei, F.; Floridi, S.; Mazzucato, U., *J. Am. Chem. Soc.* **1999,** 121, 1065-1075.

20. Orlandi, G.; Zerbetto, F.; Zgierski, M. Z., *Chem. ReV.* **1991,** 91, 867-891.

21. Sohn, Y. S.; Hendrickson, D. N.; Gray, H. B., *J. Am. Chem. Soc.* **1971,** 93, 3603-3612.

22. Hush, N. S., *Prog. Inorg. Chem.* **1967,** 8, 391.

23. Brunschwig, B. S.; Creutz, C.; Sutin, N., *Chem. Soc. ReV.* **2002,** 31, 168-184.

24. Demadis, K. D.; Hartshorn, C. M.; Meyer, T. J., *Chem. ReV.* **2001,** 101, 2655-2686.

25. Nelsen, S. F., *Chem.--Eur. J.* **2000,** 6, 581-588.

26. Fichou, D.; Horowitz, G.; Xu, B.; Garnier, F., *Synth. Met.* **1990,** 39, 243-259.

27. Fichou, D.; Horowitz, G.; Garnier, F., *Synth. Met.* **1990,** 39, 125-131.

28. Fichou, D.; Xu, B.; Horowitz, G.; Garnier, F., *Synth. Met.* **1991,** 41, 463-469.

29. van Haare, J. A. E. H.; Groenendaal, L.; Havinga, E. E.; Janssen, R. A. J.; Meijer, E. W., *Angew. Chem., Int. Ed. Engl.* **1996,** 35, 638-640.

30. Parakka, J. P.; Chacko, A. P.; Nikles, D. E.; Wang, P.; Hasegawa, S.; Maruyama, Y.; Metzger, R. M.; Cava, M. P., *Macromolecules* **1996,** 29, 1928-1933.

31. Parakka, J. P.; Jeevarajan, J. A.; Jeevarajan, A. S.; Kispert, L. D.; Cava, M. P., *Adv. Mater.* **1996,** 8, 54-59.

32. van Haare, J. A. E. H.; Groenendaal, L.; Havinga, E. E.; Meijer, E. W.; Janssen, R. A. J., *Synth. Met.* **1997,** 85, 1091-1092.

33. Heeger, A. J.; Kivelson, S.; Schriefer, J. R.; Su, W. P., *Rev. Mod. Phys.* **1988,** 60, 781.

34. Lu, Y., *Solitons und Poluron.s in Conducting Polymers, World Scientific, Singapore* **1988**, ( ).

35. Chang, A.-C.; Miller, L. L., *Synth. Met.* **1987,** 22, 71-78.

36. Khanna, R. K.; Jiang, Y. M.; Creed, D., *J. Am. Chem. SOC.* **1991,** 113, 5451-5453.

37. Spangler, C. W.; Liu, P.-K., *Synth. Met.* **1991,** 44, 259-269.

38. Spangler, C. W.; J., H. T., *Synth. Met.* **1991,** 44, 85-93.

39. Deussen, M.; Bässler, H., *Chem. Phys.* **1992,** 164, 274-257.

40. Guay, J.; Kasai, P.; Dim, A.; Wu, R.; Tour, J. M.; Dao, L. H., *Chem. Mater.* **1992,** 4, 1097-1105.

41. Rughooputh, S. D. D. V.; Hotta, S.; Heeger, A. J.; Wudl, F. J., *Polym. Sci., Polym. Phys. Ed.* **1987,** 25, 1071-1078.

42. van Haare, J. A. E. H.; Havinga, E. E.; van Dongen, J. L. J.; Janssen, R. A. J.; Cornil, J.; Brédas, J. L., *Chem.- Eur. J.* **1998,** 4, 1509-1522.

43. Bäuerle, P.; Segelbacher, U.; Maier, A.; Mehring, M., *J. Am. Chem. Soc.* **1993,** 115, 10217-10223.

44. Bäuerle, P.; Segelbacher, U.; Gaudl, K. U.; D. Huttenlocher, D.; Mehring, M., *Angew. Chem. Int. Ed. Engl.* **1993,** 32, 76-78.

45. Hill, M. G.; Mann, K. R.; Miller, L. L.; Penneau, J. F., *J. Am. Chem. Soc.* **1992,** 114, 2728-2730.

46. Hapiot, P.; Audebert, P.; Monnier, K.; Pernaut, J. M.; Garcia, P., *Chem. Mater.* **1994,** 6, 1549-1555.

47. Torrance, J. B.; Scott, B. A.; Welber, B.; Kaufman, F. B.; Seiden, P. E., *Phys. Rev. B* **1979,** 19, 730-741.

48. Lacroix, J. C.; Chane-Ching, K. I.; Maquere, F.; Maurel, F., *J. Am. Chem. Soc.* **2006,** 128, 7264-7276.

APPENDIX

ADDITIONAL SYNTHETIC PROCEDURES AND RESULTS

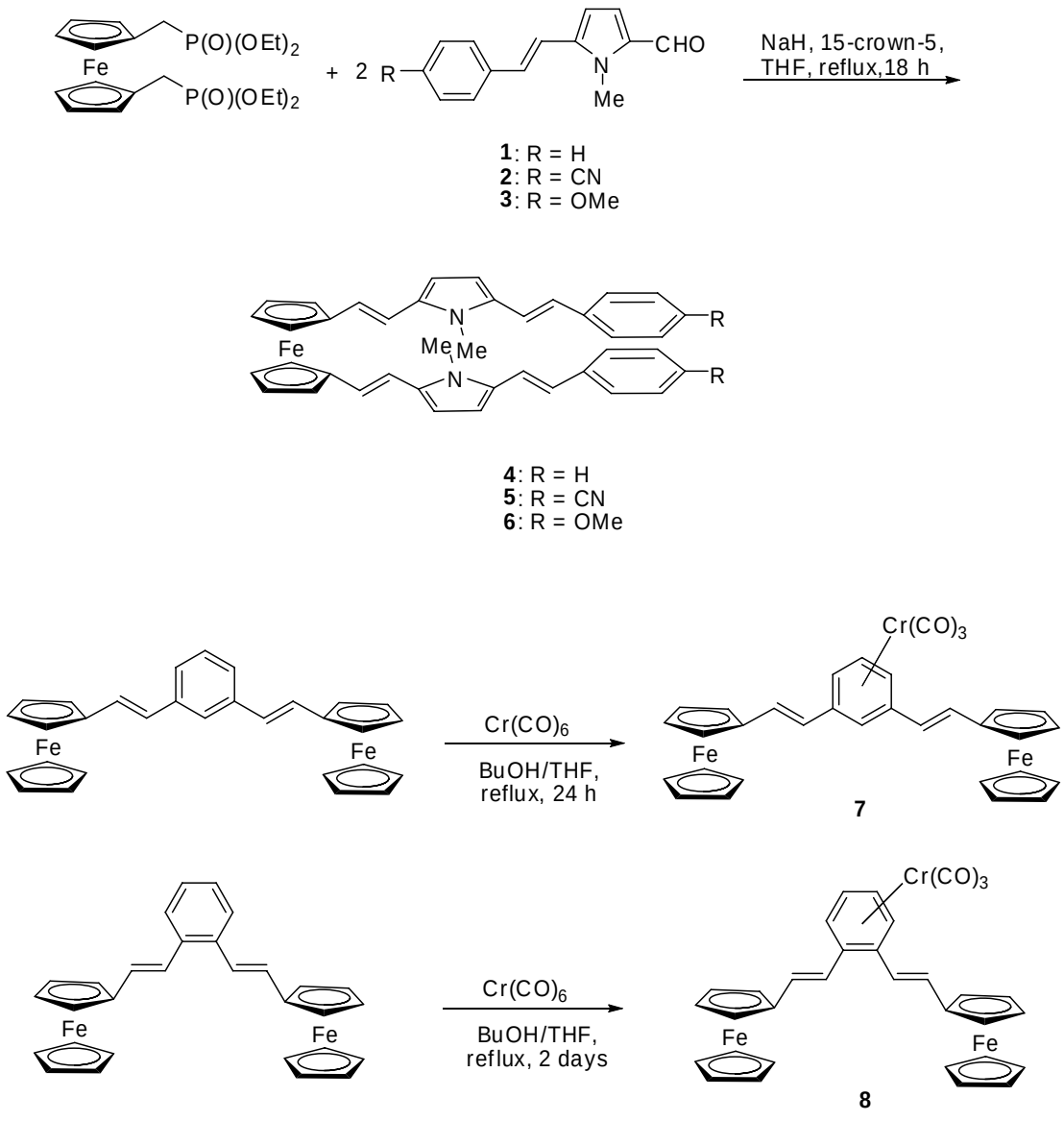

Figure A.1. Synthesis of compounds **4-8**.

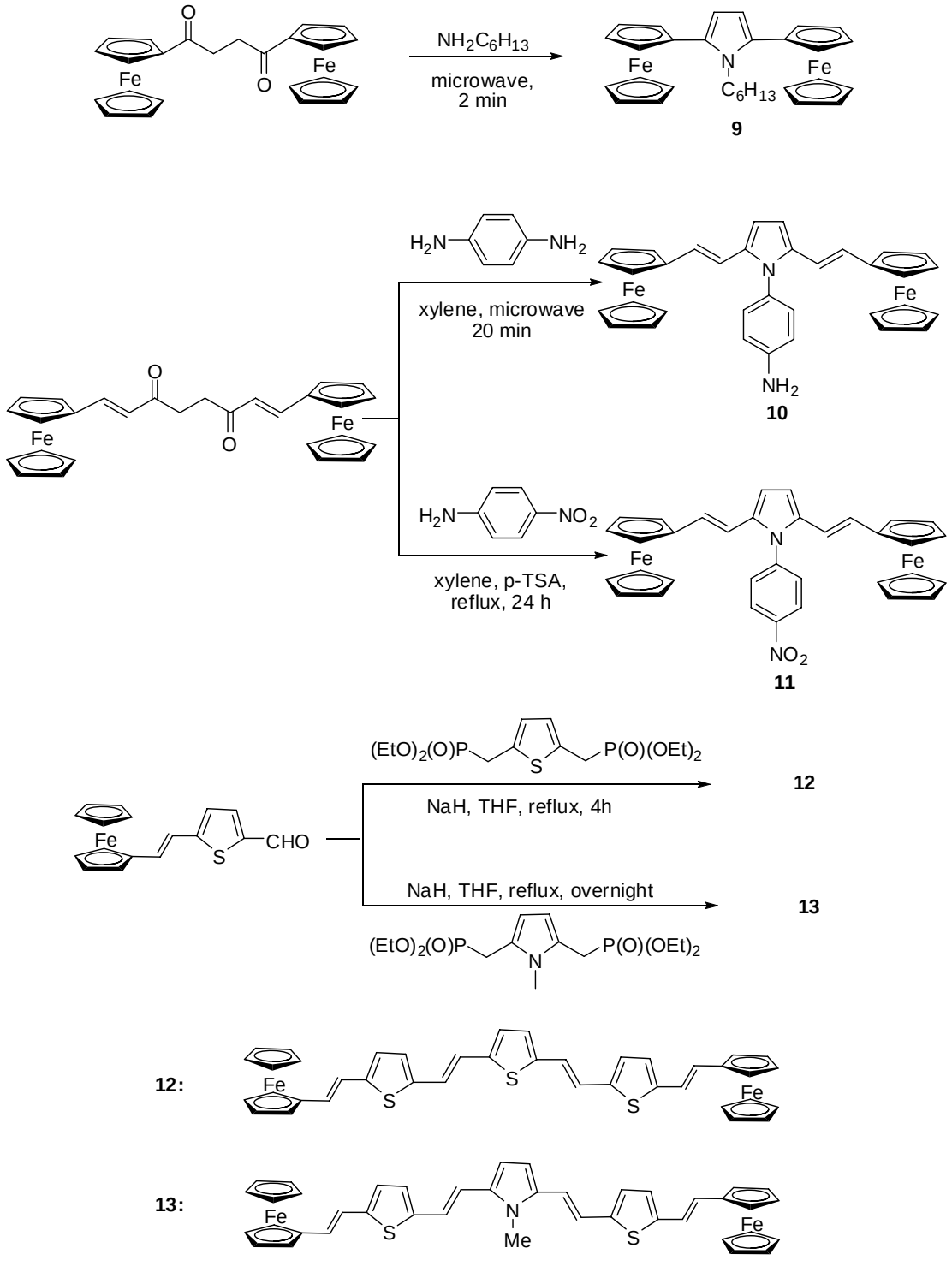

Figure A.2. Synthesis of compounds **9-12**.

Synthesis

(*E,E,E,E*)-1,1'-Bis[2-(5-styryl-*N*-methylpyrrol-2-yl)vinyl]ferrocene (4). To a stirred suspension of NaH (104 mg, a 60% suspension in oil, 2.6 mmol, washed with dry hexane) in dry THF (15 mL) was added a solution of 1,1'-ferrocenyl-bis(diethylmethylphosphonate) (535 mg, 1.1 mmol) and 4 drops of 15-crown-5 in THF (20 mL) dropwise under argon at r.t. The resulting suspension was stirred for 10 minutes before *trans*-2-styryl-*N*-methylpyrrole-5-carboxaldehyde (Chapter 6) (474 mg, 2 mmol) in THF (20 mL) was added slowly. The reaction mixture was heated to reflux for 18 h, cooled, and quenched with water (5 mL). The volatile solvent was then removed under reduced pressure, the residues dissolved in CH_2Cl_2 (60 mL), washed with H_2O (3 x 30 mL), dried over $MgSO_4$ and evaporated to afford the crude product. Purification was achieved through flash column chromatography on alumina gel using CH_2Cl_2 as eluent to afford a red crystalline solid (0.43 g, 72%). ^{1}H NMR (CD_2Cl_2): δ 7.44 (4H, d, J = 7.0 Hz), 7.33 (4H, t, J = 7.2 Hz), 7.21 (2H, t, J = 7.2 Hz), 6.94 (2H, d, J = 15.9 Hz), 6.82 (2H, d, J = 15.9 Hz), 6.55 (2H, d, J = 15.9 Hz), 6.49 (2H, d, J = 3.9 Hz, Pyr), 6.42 (2H, d, J = 15.9 Hz), 6.36 (2H, d, J = 3.9 Hz, Pyr), 4.42 (4H, t, J = 1.8 Hz), 4.28 (4H, t, J = 1.8 Hz), 3.35 (6H, s). ^{13}C NMR (CD_2Cl_2): δ 138.13, 134.35, 132.87, 128.79, 126.89, 125.96, 125.45, 123.29, 117.22, 115.34, 107.67, 106.55, 85.44, 69.92, 67.74, 30.06, 29.92. IR (neat, cm^{-1}): 3026w, 2920m, 1625w, 1586s, 1529m, 1440s, 1358m, 1267s, 1095s, 942s, 758s, 686s, 494m. MS m/e (intensity): 600.2 (100, M^+), 328.1 (20), 272.2 (7), 256.1 (7), 181.1 (4), 115.1 (4).

(*E,E,E,E*)-1,1'-Bis[2-[5-(*p*-cyanostyryl)-*N*-methylpyrrol-2-yl]vinyl]ferrocene (5). The general synthetic procedure for compound **4** was followed. 1,1'-Ferrocenyl-bis(diethylmethylphosphonate) (535 mg, 1.1 mmol) was allowed to react with *trans*-2-(*p*-cyanostyryl)-*N*-methylpyrrole-5-carboxaldehyde (Chapter 6) (524 mg, 2 mmol) under reflux in THF for 18 h with the assistance of NaH (104 mg, a 60% suspension in oil, 2.6 mmol, washed with dry hexane) and 15-crown-5 (4 drops). The title compound was achieved as a purple red crystalline solid (340 mg, 52%). ^{1}H NMR (CD_2Cl_2): δ 7.41 (4H, d, J = 8.7 Hz), 7.31 (4H, d, J = 8.7 Hz), 6.99 (2H, d, J = 16.2 Hz, vinyl), 6.75 (2H, d, J = 16.2 Hz, vinyl), 6.58 (2H, d, J = 3.9 Hz, pyr), 6.55 (2H, d, J = 15.9 Hz, vinyl), 6.39 (2H, d, J = 3.9 Hz, pyr), 6.36 (2H, d, J = 15.9 Hz, vinyl), 4.43 (4H, d, J = 1.8 Hz), 4.29 (4H, d,

J = 1.8 Hz), 3.25 (6H, s). ^{13}C NMR (CD_2Cl_2): δ 142.63, 135.53, 132.42, 131.77, 125.83, 124.02, 122.10, 120.36, 119.34, 115.13, 109.29, 109.12, 107.02, 85.15, 70.03, 67.83, 29.96. IR (neat, cm^{-1}): 2914w, 2844.2w, 2213.7m, 1620.1m, 1589.3s(br), 1550.5m, 1442.1m, 1405.0m, 1300.1m, 1212.8w, 1168.8, 1030.9m, 950.1m, 931m, 807.6m, 756m, 538.5m. MS m/e (intensity): 650.2 (100, M^+), 353.1 (25), 296.1 (38), 169 (5), 43.8 (28).

(*E,E,E,E*)-1,1'-Bis[2-[5-(*p*-methoxystyryl)-*N*-methylpyrrol-2-yl]vinyl]ferrocene (6). The general synthetic procedure for compound **4** was followed. 1,1'-Ferrocenyl-bis(diethylmethylphosphonate) (535 mg, 1.1 mmol) was allowed to react with *trans*-2-(*p*-methoxystyryl)-*N*-methylpyrrole-5-carboxaldehyde (Chapter 6) (534 mg, 2 mmol) in THF under reflux for 18 h in the presence of NaH (104 mg, a 60% suspension in oil, 2.6 mmol, washed with dry hexane) and 15-crown-5 (4 drops). The title compound was achieved as a red crystalline solid (430 mg, 65%), m.p. 203-205 ^{o}C. ^{1}H NMR (CD_2Cl_2): δ 7.28 (4H, d, H = 8.7 Hz, Ar), 6.84 (2H, d, J = 15.9 Hz), 6.78 (2H, d, J = 15.9 Hz), 6.75 (4H, d, H = 8.7 Hz, Ar), 6.57 (2H, d, J = 15.9 Hz), 6.45 (2H, d, J = 15.9 Hz), 6.44 (2H, d, J = 3.9 Hz, Pyr), 6.38 (2H, d, J = 15.9 Hz), 4.40 (4H, t, J = 1.8 Hz), 4.27 (4H, t, J = 1.8 Hz), 3.80 (6H, s), 3.26 (6H, s). ^{13}C NMR (CD_2Cl_2): δ 158.94, 133.85, 133.11, 130.87, 127.13, 125.23, 122.62, 115.45, 115.30, 114.97, 106.98, 106.34, 85.47, 69.79, 67.73, 55.37, 29.87. IR (neat, cm^{-1}): 2927.3w (br), 2827.6w, 2040.6w, 1619.2m, 1600.9m, 1507.7s, 1447.5m, 1301.1m, 1244.1s, 1172.6m, 1146.5m, 1027.3s, 934.4s, 788s, 759.1s, 642.2m, 482.6m. MS m/e (intensity): 660.2 (94, M^+), 447 (28), 358.1 (18), 301.1 (100), 213.1 (12), 121.1 (12), 43.9 (38).

(*E,E*)-1,3-Bis(2-ferrocenylvinyl)-η^6-Cr(CO)$_3$benzene (7). (*E,E*)-1,3-Bis(2-ferrocenylvinyl)benzene (Chapter 2) (0.25 g, 0.50 mmol) and $Cr(CO)_6$ (0.33 g, 1.5 mmol) were dissolved in 40 mL of Bu_2O/THF (10:1), and the solution was refluxed for 24 h. After being cooled to room temperature, the solution was passed through a pad of Celite. The filtrate was concentrated and chromatographed on silica gel with CH_2Cl_2/hexane (1:1) as eluent. After evaporation of the solvent, the product was obtained as an orange red solid in 70% yield (0.222 g) based on the 1,3-bis(2-ferrocenylvinyl)benzene. ^{1}H NMR ($CDCl_3$): δ 6.87 (4H, d, J = 15.9 Hz), 6.27 (4H, d, J = 15.9 Hz), 5.59 (1H, s), 5.54 (1H, t, J = 6.0 Hz), 5.39 (2H, t, J = 6.0 Hz), 4.45 (4H, t, J = 1.8 Hz), 4.34 (4H, t, J = 1.8 Hz), 4.18 (10H, s). ^{13}C NMR ($CDCl_3$): δ 233.82, 130.74,

121.81, 107.94, 93.85, 88.07, 87.57, 81.58, 70.0, 69.92, 69.74, 67.52, 67.41. IR (neat, cm^{-1}): 1942.8s, 1860.6s (br), 1631.6m, 1529.9m, 1407.7m, 1040.5m, 949.0m, 831.3m, 808.1m, 685.1s, 623.7s, 484.1s.

(*E,E*)-1,2-Bis(2-ferrocenylvinyl)-η^6-Cr(CO)$_3$benzene (8). The general synthetic procedure for compound **7** was used to prepare the title compound (206 mg, 65%) from (*E,E*)-1,2-bis(2-ferrocenylvinyl)benzene (Chapter 2) (0.25 g, 0.50 mmol) and $Cr(CO)_6$ (0.33 g, 1.5 mmol), reaction time 2 days. The final product was obtained as an orange solid. ^{1}H NMR ($CDCl_3$): δ 6.81 (4H, d, J = 15.9 Hz), 6.57 (4H, d, J = 15.9 Hz), 5.66 (2H, m), 5.39 (2H, m), 4.52 (2H, t, J = 1.8 Hz), 4.41 (2H, t, J = 1.8 Hz), 4.33 (4H, m), 4.18 (10H, s). ^{13}C NMR ($CDCl_3$): δ 233.73, 132.20, 119.77, 105.84, 91.65, 90.51, 81.93, 70.0, 69.88, 69.73, 68.32, 66.69. IR (neat, cm^{-1}): 1952.9s, 1893.5s, 1851.2s, 1625.3m, 1413.6m, 1105.6m, 963.2m, 816.4s, 663.3s, 626.0s. MS m/e (intensity): 634 (5, M^+), 550 (20), 498 (100), 312.1 (23), 249 (20), 186 (10), 121 (10).

***N*-Hexyl-2,5-diferrocenylpyrrole (9)**. 1,4-Diferrocenyl-butane-1,4-dione (114 mg, 0.25 mmol) and hexylamine (3 mL) were taken in a conical test tube and thoroughly mixed with stirring. The resulting mixture was irradiated in microwave at 200 Watt for 2 min and cooled to room temperature. After the excess hexylamine was removed under vacuum, the mixture was diluted in 20 mL CH_2Cl_2, washed with water (2 x 20 mL) and dried over Na_2SO_4. Upon removing the volatile solvent, the residue was purified by flash column chromatography (silica gel) using CH_2Cl_2/hexane (1:1) as eluent to yield the title compound as a pale yellow solid (106 mg, 82%). ^{1}H NMR (CD_2Cl_2): δ 6.31 (2H, s), 4.39 (4H, t, J = 1.8 Hz), 4.27 (4H, t, J = 1.8 Hz), 4.19 (10H, s), 4.08 (2H, t, J = 5.0 Hz), 1.47 (2H, br), 1.21 (6H, br), 0.87 (3H, t, J = 6.3 Hz). ^{13}C NMR (CD_2Cl_2): δ 130.45, 108.86, 80.35, 69.53, 68.69, 68.08, 44.62, 31.62, 31.49, 26.48, 22.73, 13.96. MS m/e (intensity): 519.1 (100, M^+), 434 (8), 368 (6), 259.5 (12), 191 (3), 121 (3).

(*E,E*)-Bis(2-ferrocenylvinyl)-*N*-(*p*-aminophenyl)pyrrole (10). 1,8-Diferrocenyl-octa-1,7-diene-3,6-dione (102 mg, 0.2 mmol), 1,4-diaminobenzene (108 mg, 1 mmol) and xylene (4 mL) were taken in a conical test tube and thoroughly mixed with stirring. The resulting mixture was irradiated in microwave at 200 Watt for 20 min and cooled to room temperature. After removal of xylene under vacuum, the mixture was diluted in 20 mL CH_2Cl_2, washed with water (2 x 20 mL) and dried over Na_2SO_4. Upon removing the

volatile solvent, the residue was purified by flash column chromatography (silica gel) using CH_2Cl_2/hexane (1:1) as eluent to yield the title compound as a red crystalline solid (94 mg, 81%). ^{1}H NMR ($CDCl_3$): δ 7.08 (2H, d, J = 7.6 Hz), 6.79 (2H, d, J = 7.6 Hz), 6.52 (2H, s), 6.48 (2H, d, J = 16.2 Hz), 6.18 (2H, d, J = 16.2 Hz), 4.26 (4H, t, J = 1.8 Hz), 4.16 (4H, t, J = 1.8 Hz), 4.07 (10H, s), 3.87 (2H, br). ^{13}C NMR ($CDCl_3$): δ 146.48, 134.68, 129.97, 128.64, 123.61, 116.39, 115.37, 106.29, 84.67, 69.36, 68.81, 66.58. IR (neat, cm^{-1}): 3468.1m, 3361.7m, 3087.3m, 1771.5w, 1613.3m, 1513.1s, 1412.0m, 1232.1m, 1102.9m, 1024.1m, 998.7m, 928.9s, 801.3s, 729.2m. MS m/e (intensity): 578.2 (100, M^+), 576.2 (12), 513.1 (5), 391.1 (11), 289.1 (14), 120.1 (7).

(*E,E*)-Bis(2-ferrocenylvinyl)-*N*-(*p*-nitrophenyl)pyrrole (11). 1,8-Diferrocenyl-octa-1,7-diene-3,6-dione (202 mg, 0.4 mmol), 1-amino-4-nitrobenzene (163 mg, 1.2 mmol) and catalytic amount of *p*-TSA (5 mg) were dissolved in xylene (20 mL), heated at reflux under argon for 24 h and cooled to room temperature. After removal of the solvent under reduced pressure, the residue was dissolved in CH_2Cl_2 (40 mL), washed with water (3 x 20 mL), dried over $MgSO_4$ and evaporated. The crude product was purified by flash column chromatography (silica gel), eluting with CH_2Cl_2/hexane (1:1), to afford the final product as a dark yellow solid (24 mg, 10%) after solvent evaporation. The major byproduct was (*E,E*)-bis(2-ferrocenylvinyl)furan. ^{1}H NMR ($CDCl_3$): δ 8.41 (2H, d, J = 8.8 Hz), 7.50 (2H, d, J = 8.8 Hz), 6.61 (2H, d, J = 16.2 Hz), 6.59 (2H, s), 6.11 (2H, d, J = 16.2 Hz), 4.26 (4H, t, J = 1.8 Hz), 4.21 (4H, t, J = 1.8 Hz), 4.09 (10H, s). ^{13}C NMR ($CDCl_3$): δ 147.98, 134.19, 129.87, 125.85, 125.13, 124.76, 114.72, 107.81, 83.79, 69.38, 69.23, 66.68. IR (neat, cm^{-1}): 3071.3m, 1766.9w, 1591.9m, 1517.3s, 1495.2m, 1409.0m, 1335.1s, 1104.5m, 1026.1m, 943.7m, 801.4s, 481.2s. MS m/e (intensity): 608.1 (100, M^+), 562.1 (4), 440 (6), 375 (8), 304 (10), 242.1 (4), 120.1 (8).

(*E,E,E,E*)-2,5-Bis{2-[5-(2-ferrocenylvinyl)-thiophen-2-yl]vinyl}thiophene (12). To a stirred suspension of NaH (120 mg, a 60% suspension in oil, washed twice with dry hexane, 3 mmol) in THF (20 mL) was added a solution of 2,5-bis(diethylphosphonylmethyl)thiophene (Chapter 5) (384 mg, 1 mmol) in THF (25 mL) under argon. After 20 min, (*E*)-2-(2-ferrocenylvinyl)thiophene-5-carboxaldehyde (Chapter 2) (644 mg, 2 mmol) dissolved in THF (20 mL) was introduced via cannula. The reaction mixture was heated at reflux for 4 h, cooled to room temperature, quenched

with water (30 mL), evaporated under vacuum to remove the volatile solvent and extracted with CH_2Cl_2 (3 x 30 mL). The organic layers was combined, washed with water (2 x 50 mL), dried over $MgSO_4$ and evaporated under reduced pressure. The residue was stirred vigorously in MeOH (20 mL) for 10 min and filtered, this washing procedure was repeated once more. The crude product was then recrystallized from CH_2Cl_2 to yield the title compound as a purple solid powder (520 mg, 72%). ^{1}H NMR (CD_2Cl_2): δ 6.92 (4H, s, vinyl), 6.88 (2H, s, Th), 6.87 (2H, d, J = 3.6 Hz, Th), 6.78 (2H, d, J = 3.6 Hz, Th), 6.73 (2H, d, J = 15.6 Hz, vinyl), 6.63 (2H, d, J = 15.6 Hz, vinyl), 4.45 (4H, t, J = 1.8 Hz), 4.31 (4H, t, J = 1.8 Hz), 4.15 (10H, s). FABMS: *m/z* 720 [M^+].

(*E,E,E,E*)-2,5-Bis{2-[5-(2-ferrocenylvinyl)-thiophen-2-yl]vinyl}-*N*-methylpyrrole (13). The general synthetic procedure for compound **12** was followed. 2,5-Bis(diethylphosphonylmethyl)-*N*-methylpyrrole (Chapter 3) (381 mg, 1 mmol) was reacted with (*E*)-2-(2-ferrocenylvinyl)thiophene-5-carboxaldehyde (Chapter 2) (644 mg, 2 mmol) under reflux in THF overnight in the presence of NaH (120 mg, a 60% suspension in oil, 3 mmol, washed with dry hexane). The final product was achieved as a red solid (380 mg, 54%). ^{1}H NMR ($CDCl_3$): δ 6.93 (2H, d, J = 15.6 Hz, vinyl), 6.80 (2H, s, Th), 6.78 (2H, d, J = 15.9 Hz, vinyl), 6.75 (2H, s, Th), 6.73 (2H, d, J = 15.6 Hz, vinyl), 6.61 (2H, d, J = 15.9 Hz, vinyl), 6.53 (2H, s, Pyr), 4.42 (4H, t, J = 1.8 Hz), 4.29 (4H, t, J = 1.8 Hz), 4.15 (10H, s), 3.68 (3H, s, NCH_3). ^{13}C NMR ($CDCl_3$): δ 141.92, 141.55, 133.88, 127.24, 126.57, 125.76, 120.03, 119.70, 116.12, 108.35, 83.22, 69.53, 69.48, 67.01, 30.76. IR (neat, cm^{-1}): 3088m, 3023m, 2923m, 1754m, 1691m, 1596m, 1388m, 1237m, 1103m, 1025m, 926s, 785s, 643m, 479s. MS m/e (intensity): 716.9 (100, M^+), 614.9 (18), 504 (30), 359 (10), 227 (12), 121 (90), 40.9 (39).

A

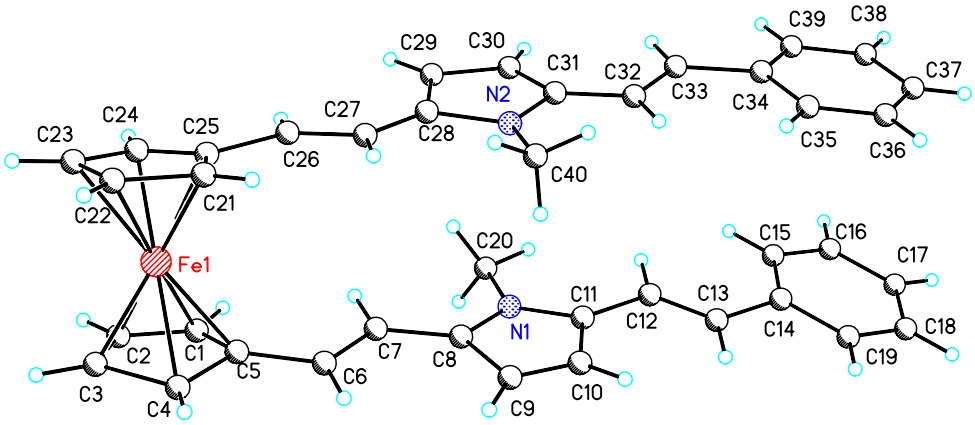

B

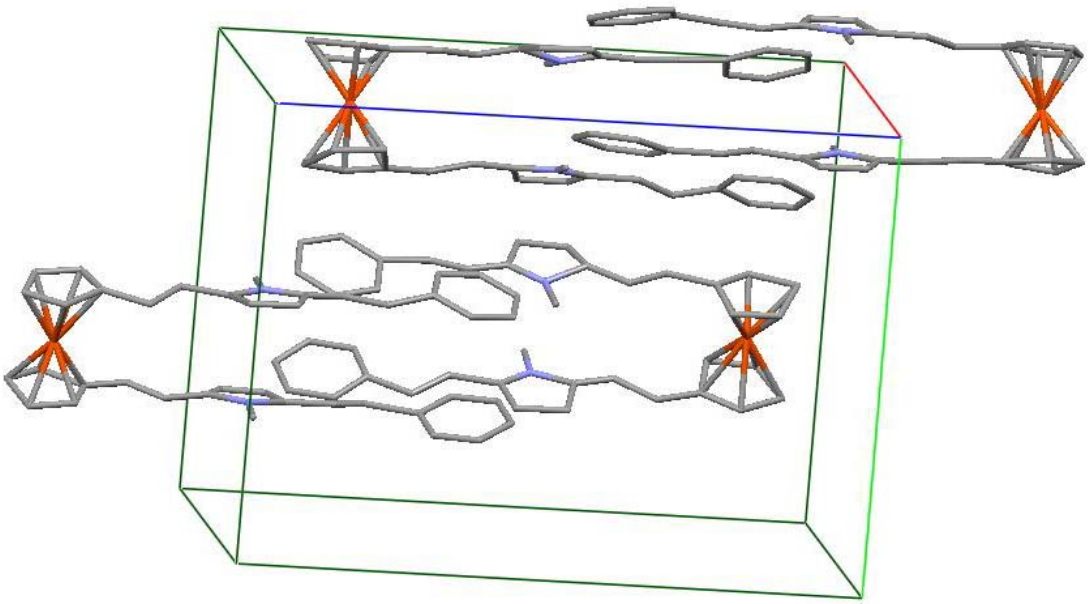

Figure A.3. ORTEP plot (A) and unit cell packing diagram (B) of compound **4**.

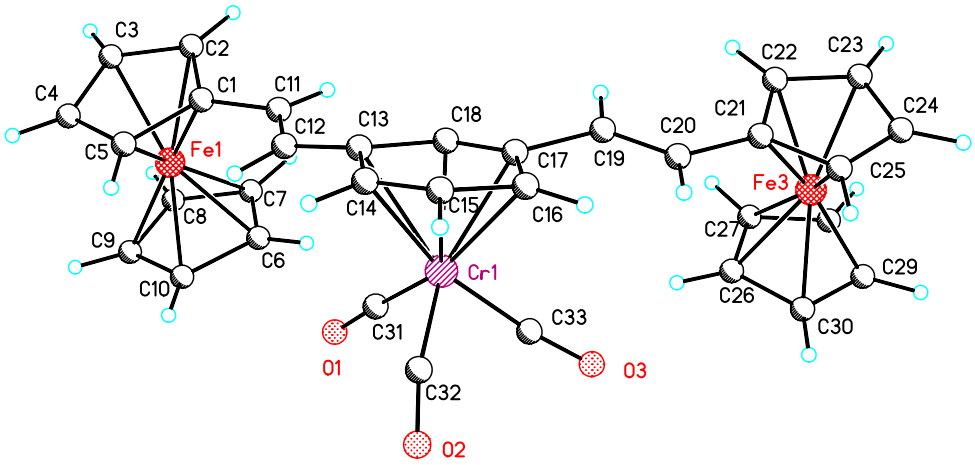

Figure A.4. ORTEP plot of compound **7**.

Table A1. Electrochemical data[a] (from Cyclic Voltammetry) of the compounds.

Compounds	E_1 (mV)	E_2 (mV)	E_3 (mV)	E_4 (mV)	ΔE_1 [b] (mV)	ΔE_2 [c] (mV)
4	-270	122	1057		392	935
5	-163	323			486	
6	-278	12	724	912	290	712
7	38	113	840[e]		75	727
8	34	169[e]			135	
9	-200	280			480	
10	-250	113	785		363	672
11	-147	106	956[f]		253	850
12	-20[d]	511	972[f]		531	461
13	-167	12	174	852[f]	179	162

[a] Obtained in CH_2Cl_2 containing 0.1 M Bu_4NTFPB. E (mV versus Fc/Fc^+) are the arithmetic average of the anodic and cathodic peak potentials. Scan rate: 50 mv/s. [b] $\Delta E_1 = E_2 - E_1$. [c] $\Delta E_2 = E_3 - E_2$. [d] Two-electron oxidation. [e] Irreversible. [f] Semi-reversible.

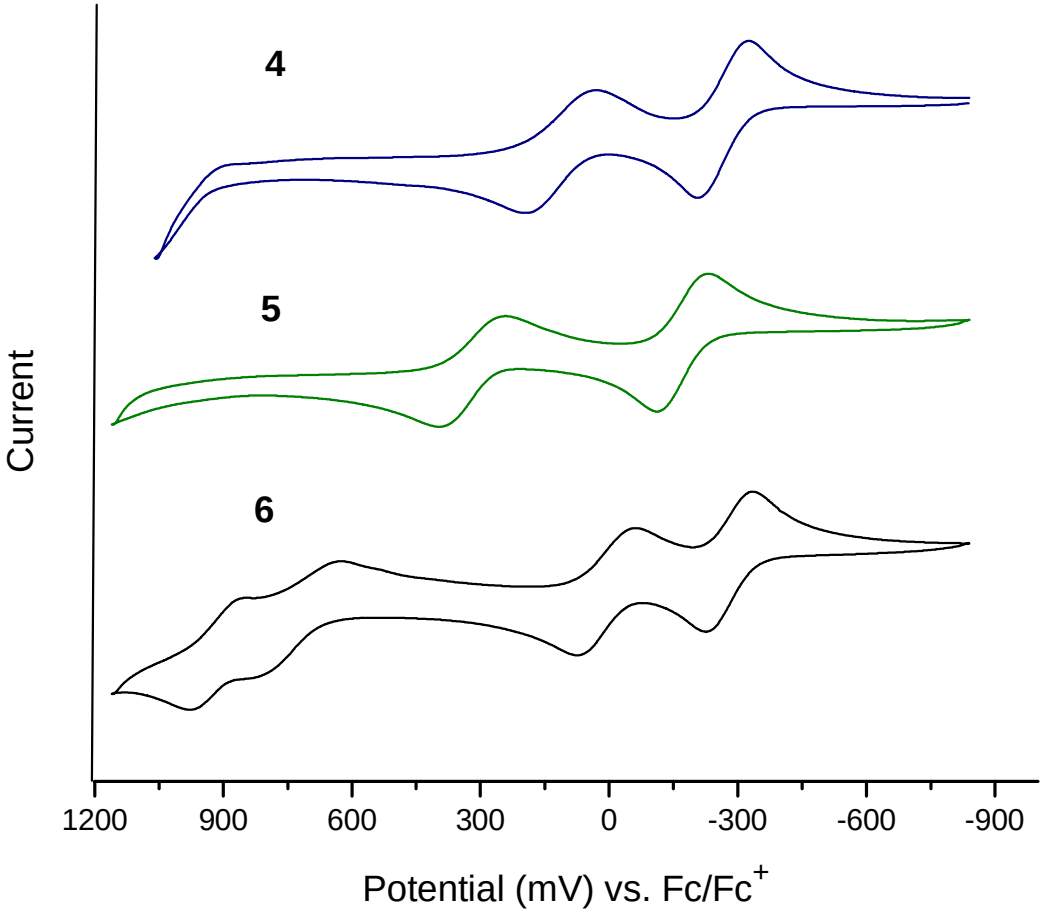

Figure A.5. Cyclic voltammograms of **4, 5** and **6** in a CH_2Cl_2 solution containing 0.1 M Bu_4NTFPB. Scan rate: 50 mV/s.

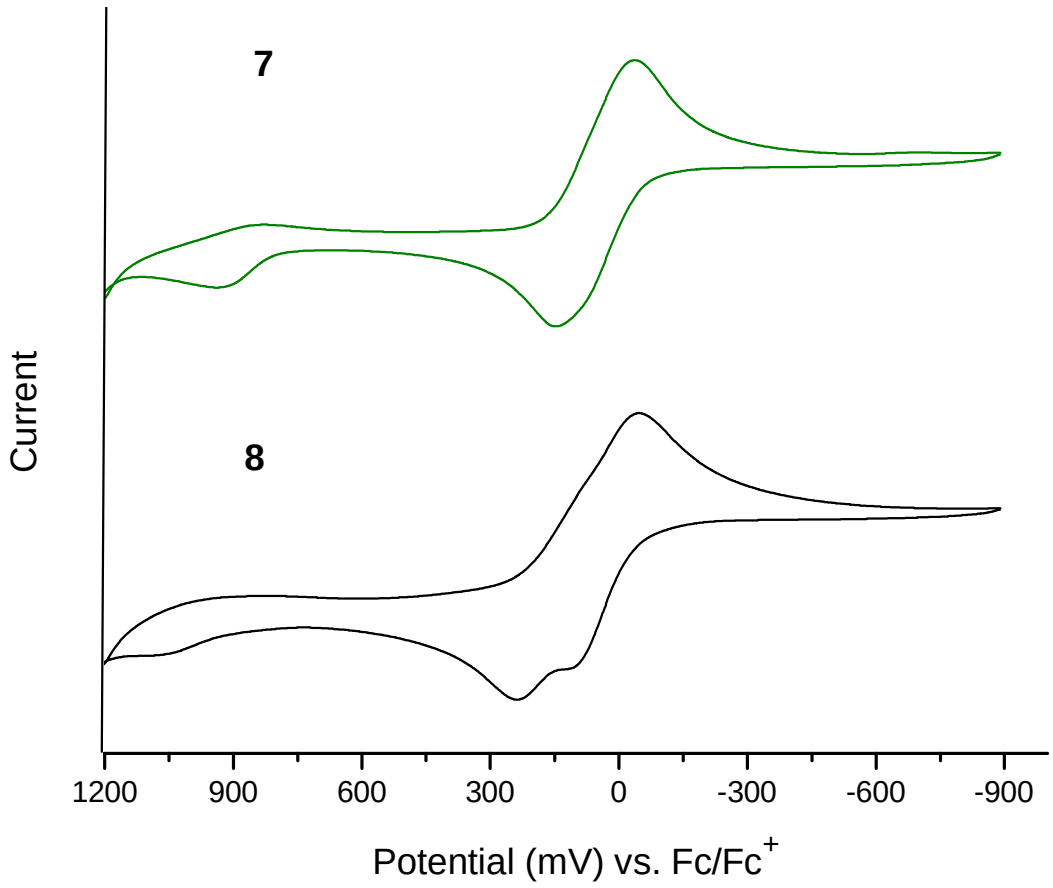

Figure A.6. Cyclic voltammograms of **7** and **8** in a CH_2Cl_2 solution containing 0.1 M Bu_4NTFPB. Scan rate: 50 mV/s.

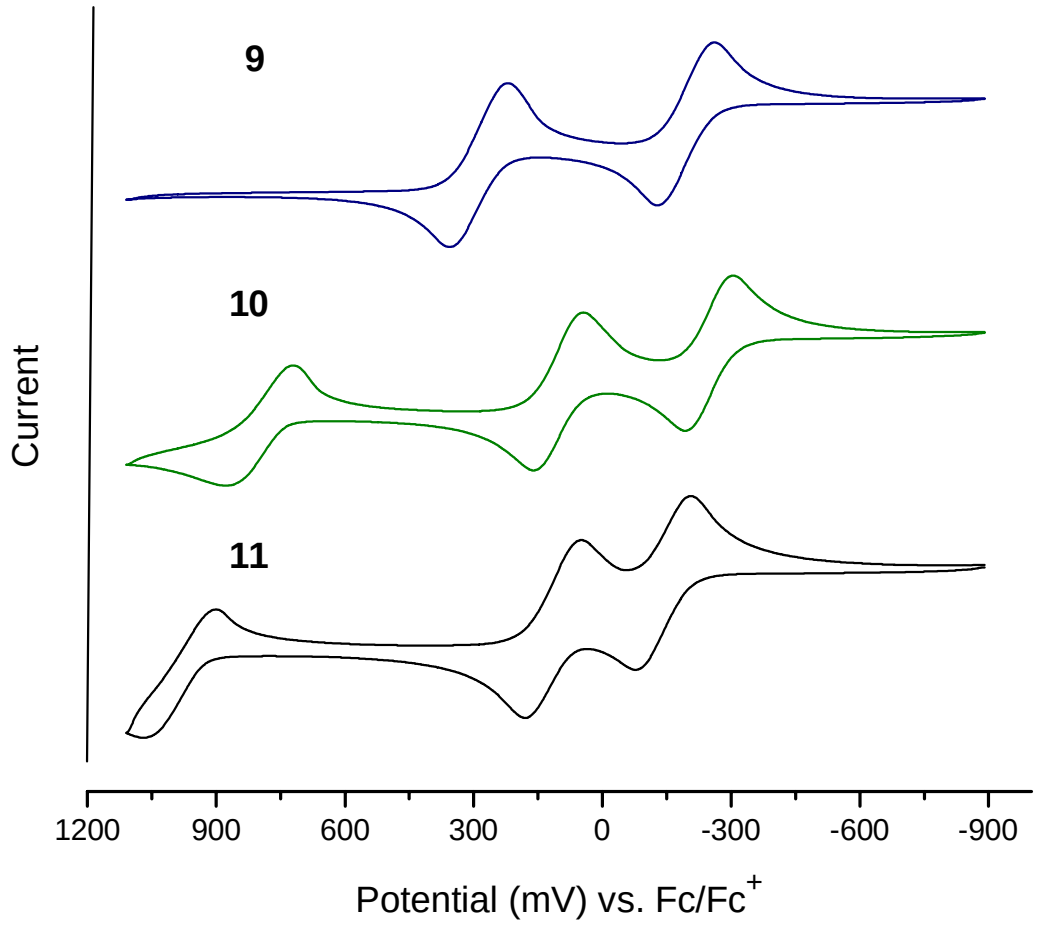

Figure A.7. Cyclic voltammograms of **9, 10** and **11** in a CH_2Cl_2 solution containing 0.1 M Bu_4NTFPB. Scan rate: 50 mV/s.

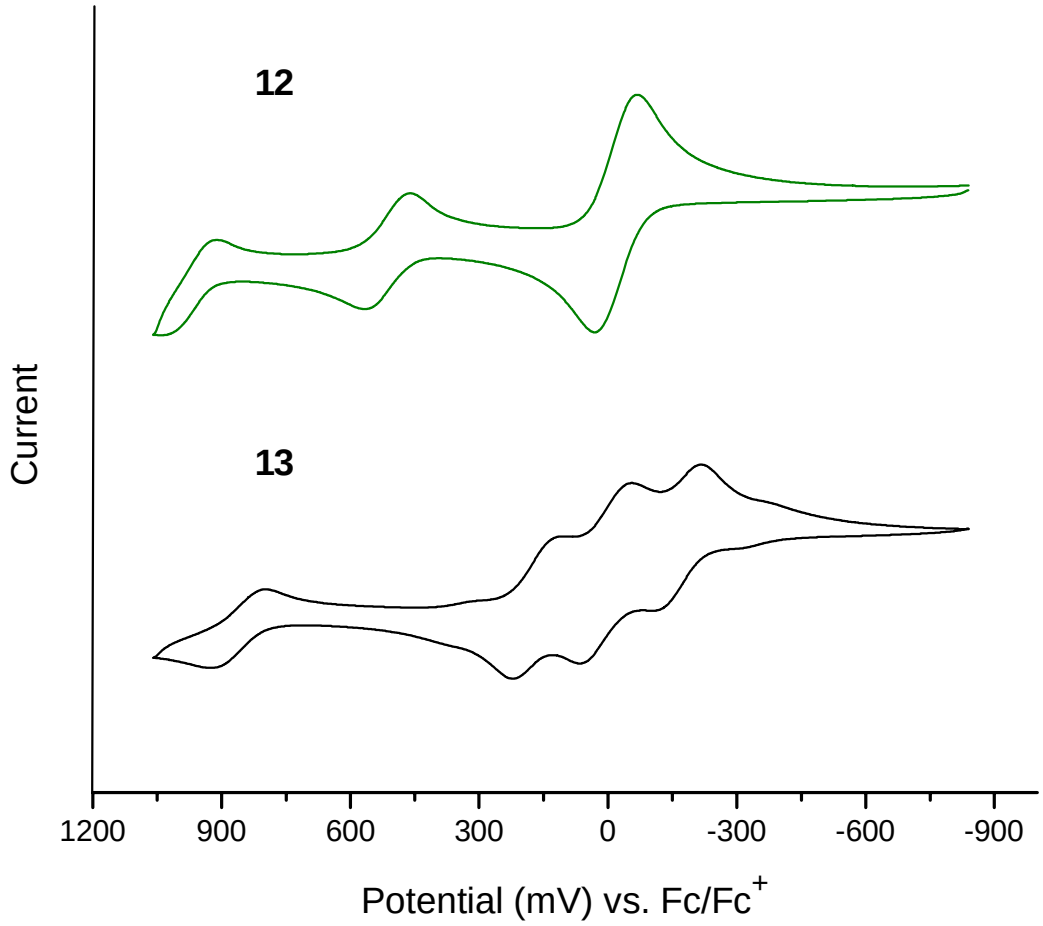

Figure A.8. Cyclic voltammograms of **12** and **13** in a CH_2Cl_2 solution containing 0.1 M Bu_4NTFPB. Scan rate: 50 mV/s.

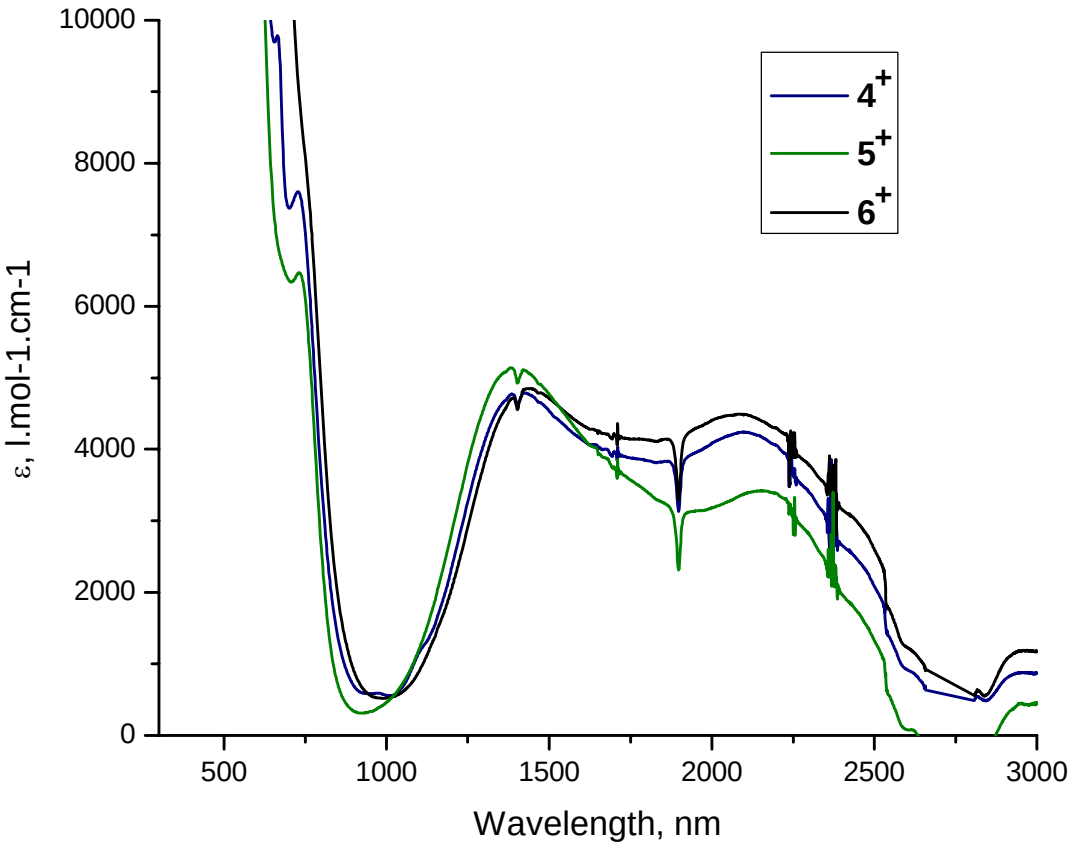

Figure A.9. UV-Vis-NIR spectra of the monocationic species $\mathbf{4}^+$, $\mathbf{5}^+$ and $\mathbf{6}^+$ in CH_2Cl_2.